Funding: ARO, DoE, NDSEG

Acknowledgments:

Dr. François Génin (LLNL)
Dr. Arieh Karger (Radiation Monitoring Devices)
Dr. Alf Bjørseth (Scanwafer)
Dr. Tom Mates (UCSB)
Dr. John Chervinsky (Harvard University)
Prof. Cynthia Friend (Harvard University)
Prof. Mike Aziz (Harvard University)

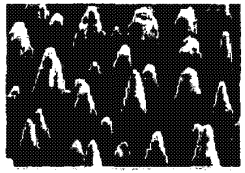
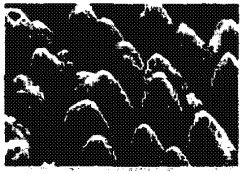
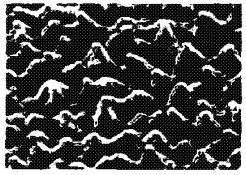
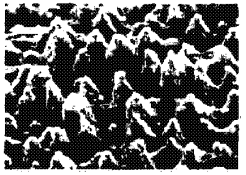
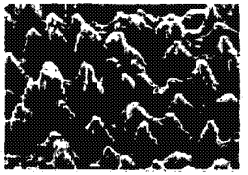
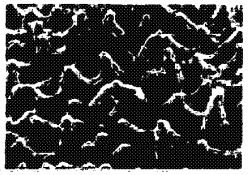
For a copy of this talk and additional information, see:

http://mazur-www.harvard.edu

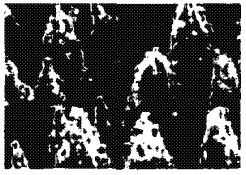
SIONYX1403000029.0010

SAMSUNG EX. 1002 - 2744/4148

Materials

	SF_6	Cl_2	N_2	air	vacuum
Si					
Ti		reacts			

Only in SF_6:



Ge



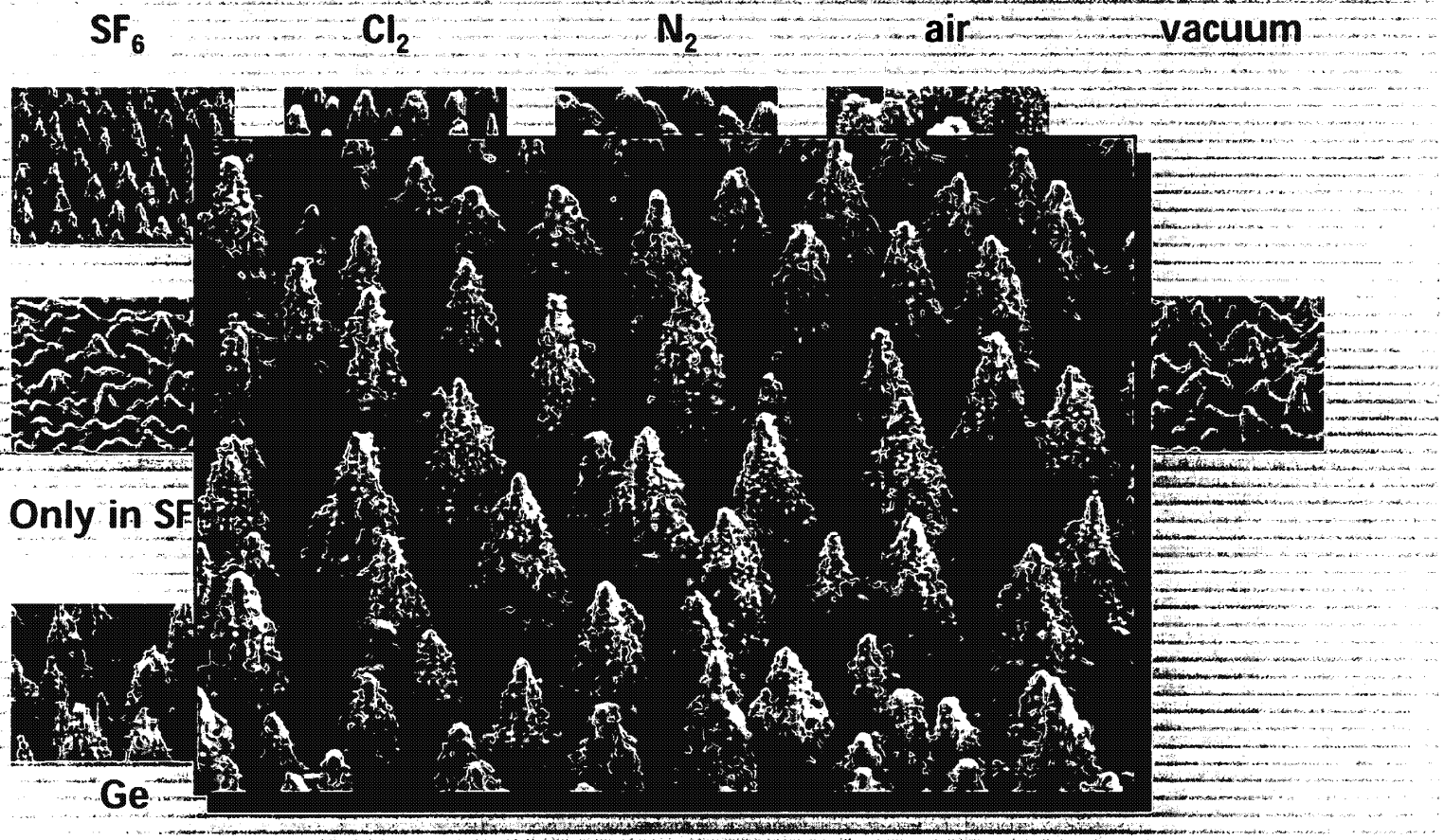
InP

No spikes in SF_6: Ag, Al, Cu, Pd, Pt, Rh, Ta and GaAs

SIONYX1403000029.0011

SAMSUNG EX. 1002 - 2745/4148

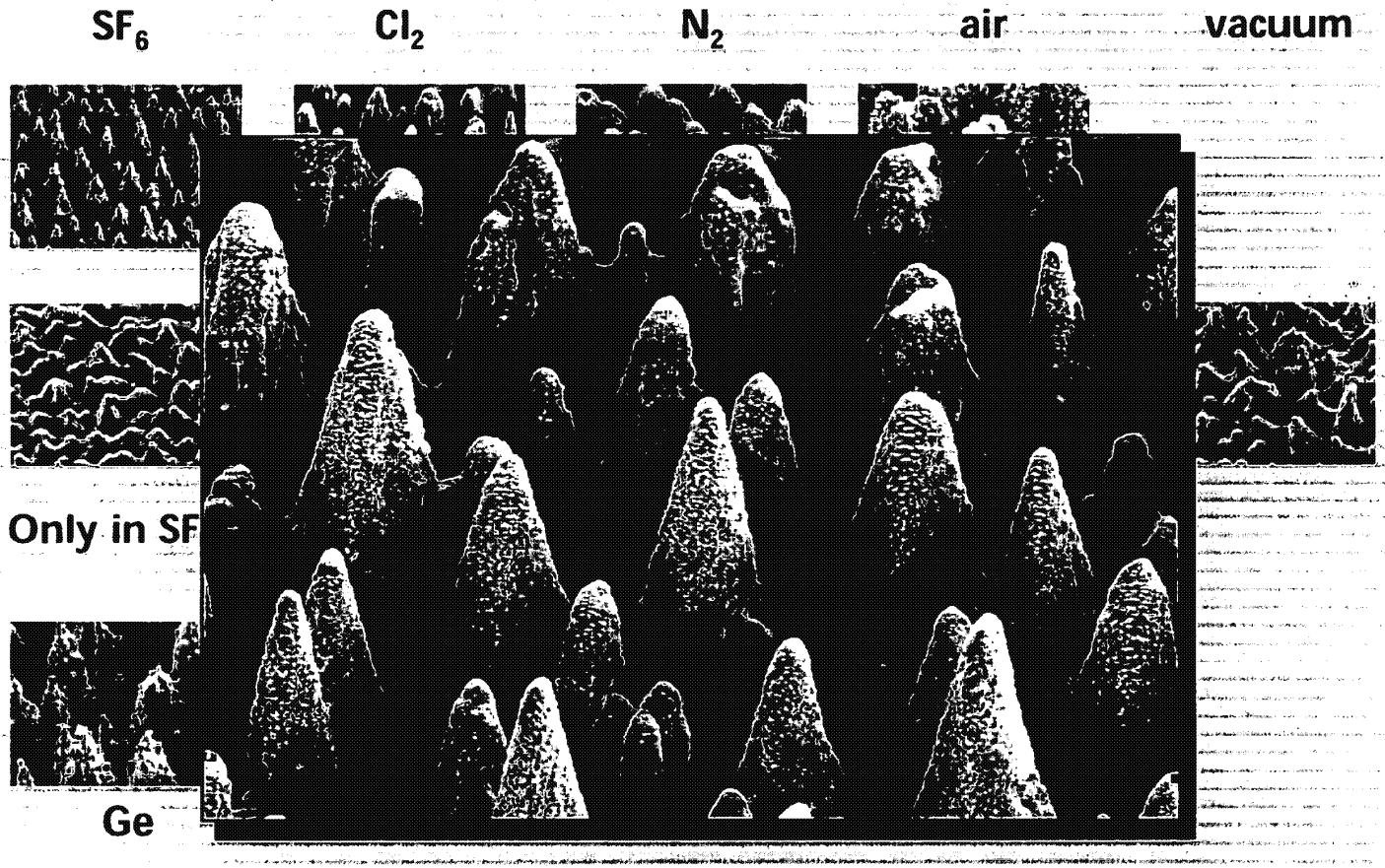
Materials



No spikes in SF_6: Ag, Al, Cu, Pd, Pt, Rh, Ta and GaAs

SAMSUNG EX. 1002 - 2746/4148
SIONYX1403000029.0012

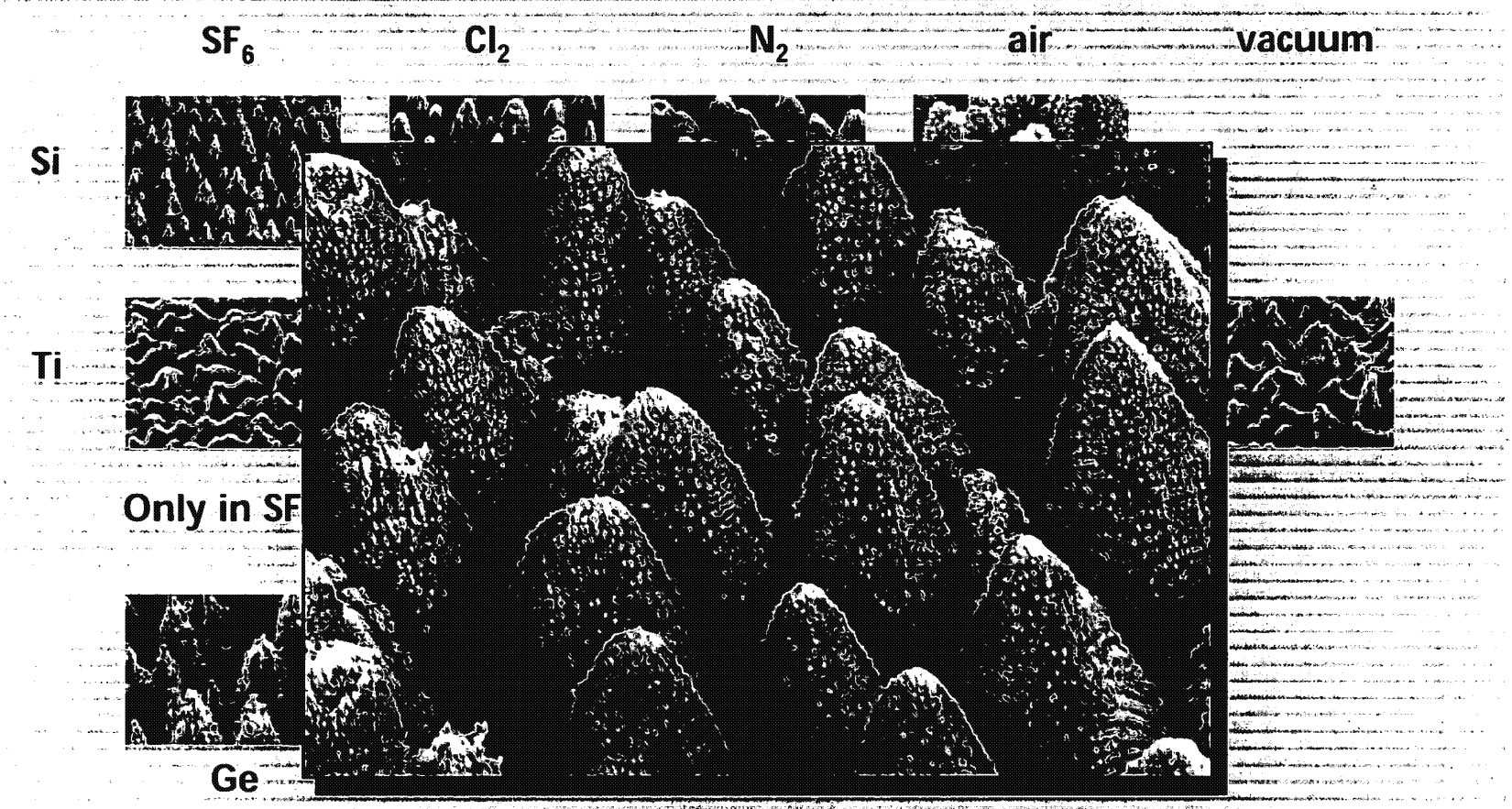
Materials



No spikes in SF_6: Ag, Al, Cu, Pd, Pt, Rh, Ta and GaAs

SAMSUNG EX. 1002 - 2747/4148
SIONYX1403000029.0013

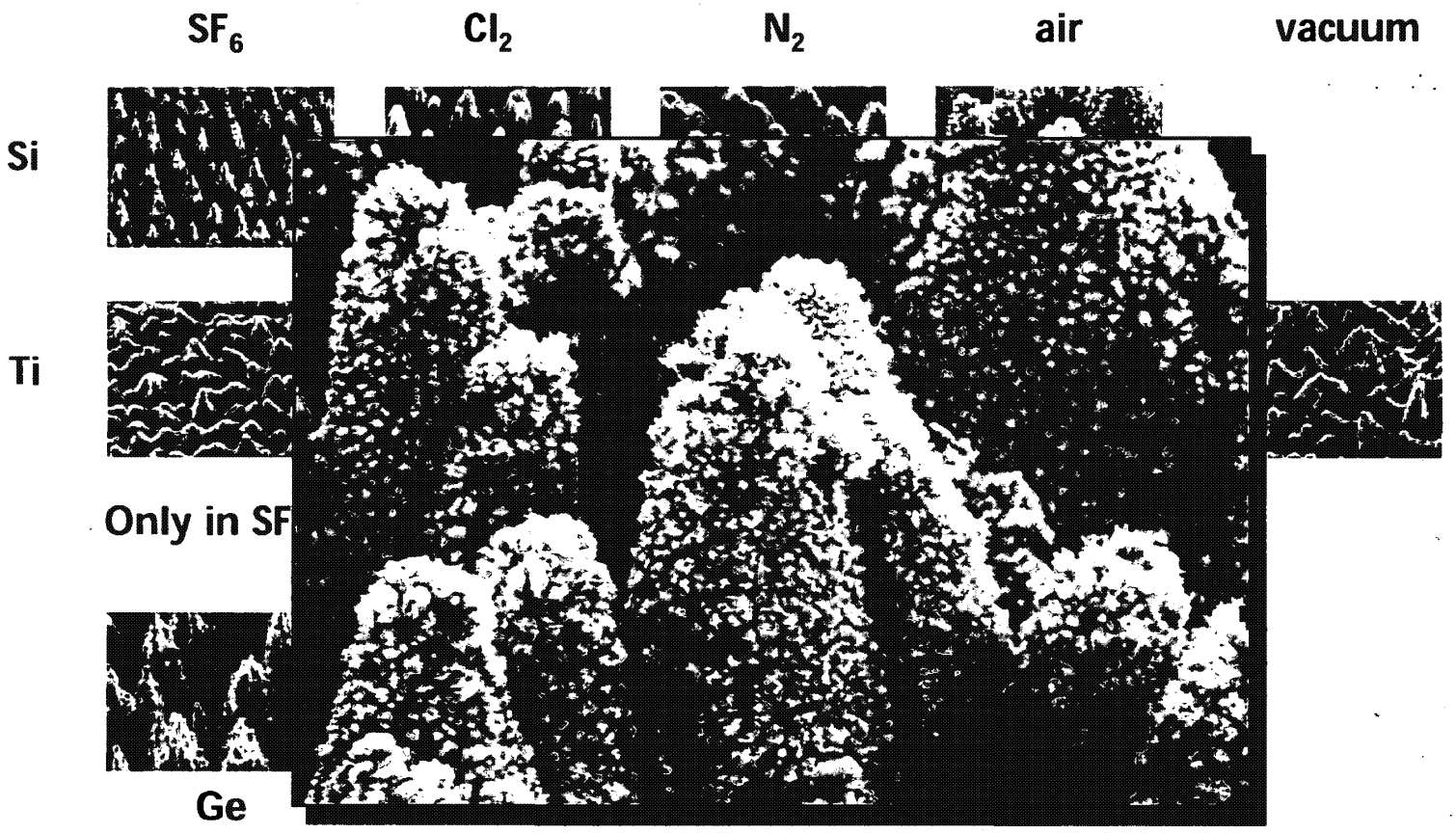
Materials



No spikes in SF_6: Ag, Al, Cu, Pd, Pt, Rh, Ta and GaAs

SAMSUNG EX. 1002 - 2748/4148
SIONYX1403000029.0014

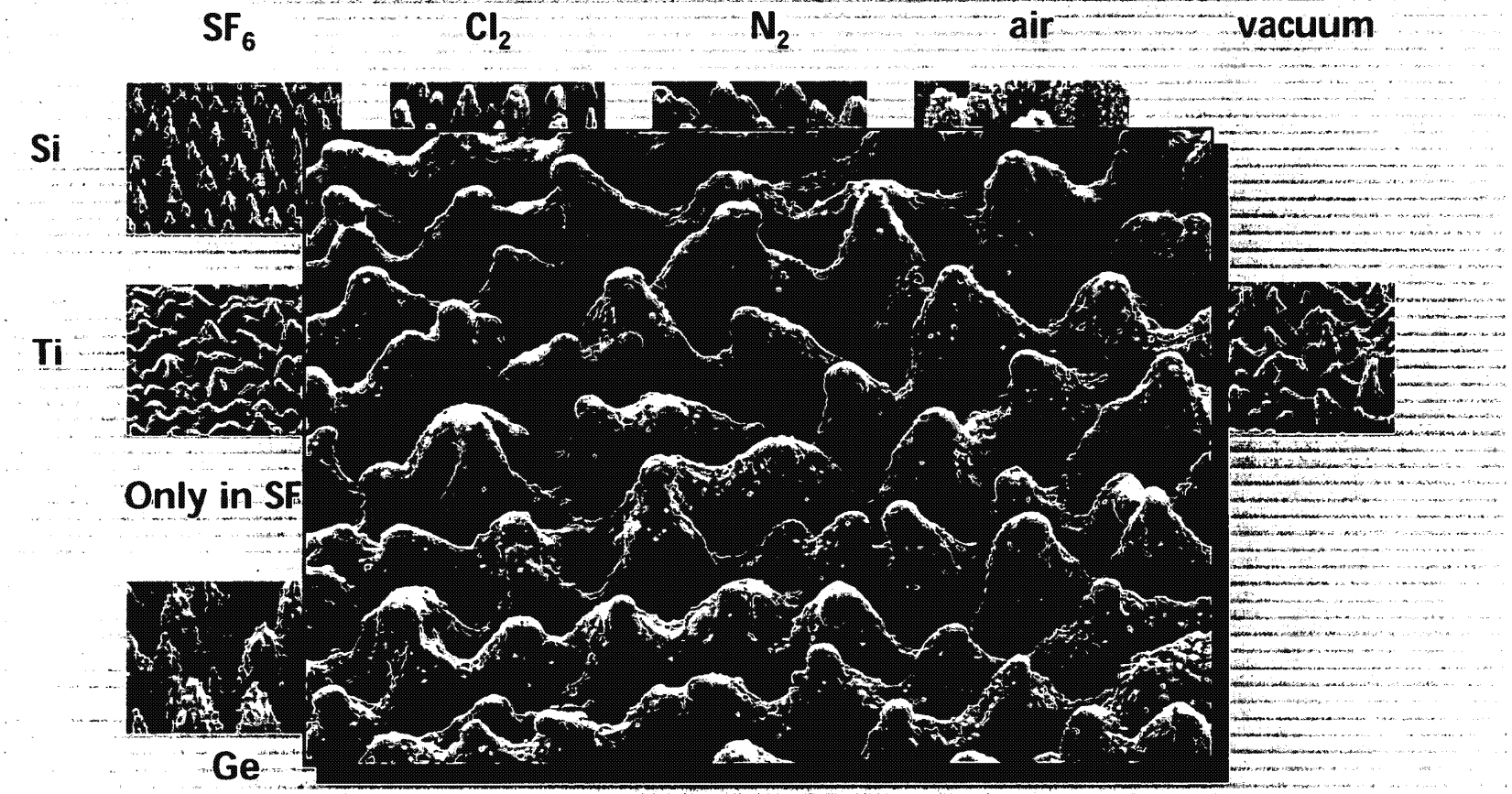
Materials



No spikes in SF_6: Ag, Al, Cu, Pd, Pt, Rh, Ta and GaAs

SAMSUNG EX. 1002 - 2749/4148
SIONYX1403000029.0015

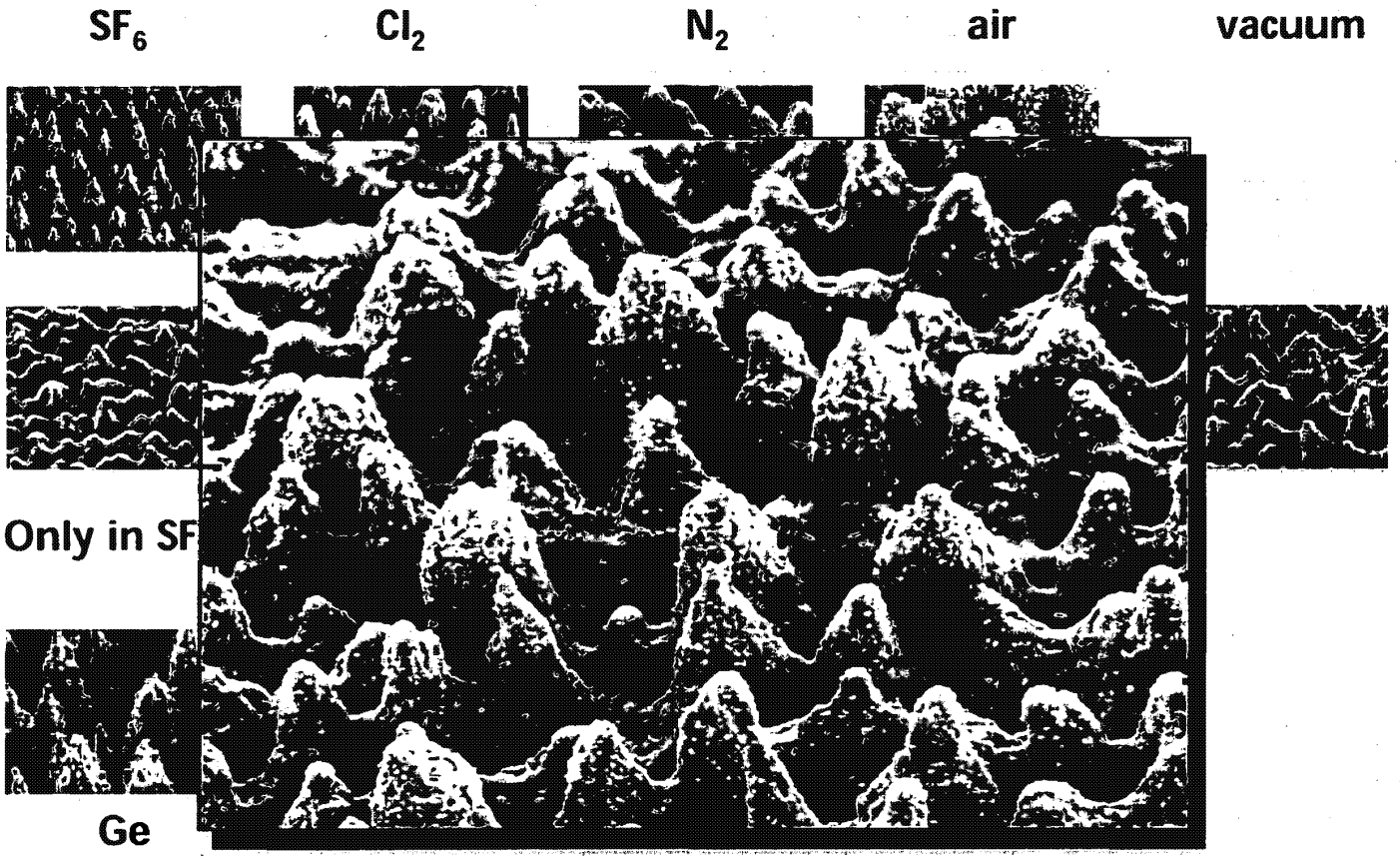
Materials



No spikes in SF_6: Ag, Al, Cu, Pd, Pt, Rh, Ta and GaAs

SAMSUNG EX. 1002 - 2750/4148
SIONYX1403000029.0016

Materials

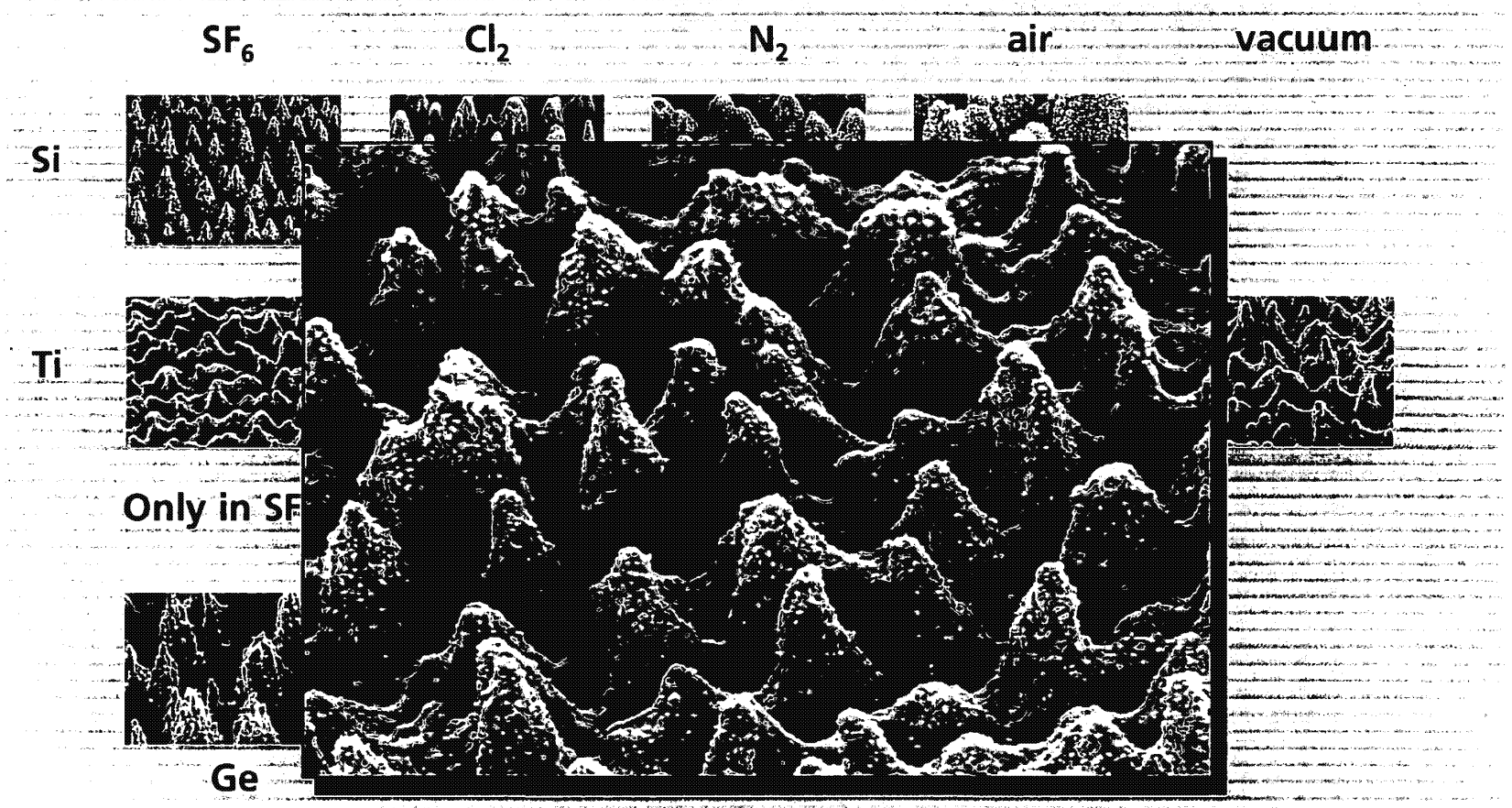


No spikes in SF_6: Ag, Al, Cu, Pd, Pt, Rh, Ta and GaAs

SIONYX1403000029.0017

SAMSUNG EX. 1002 - 2751/4148

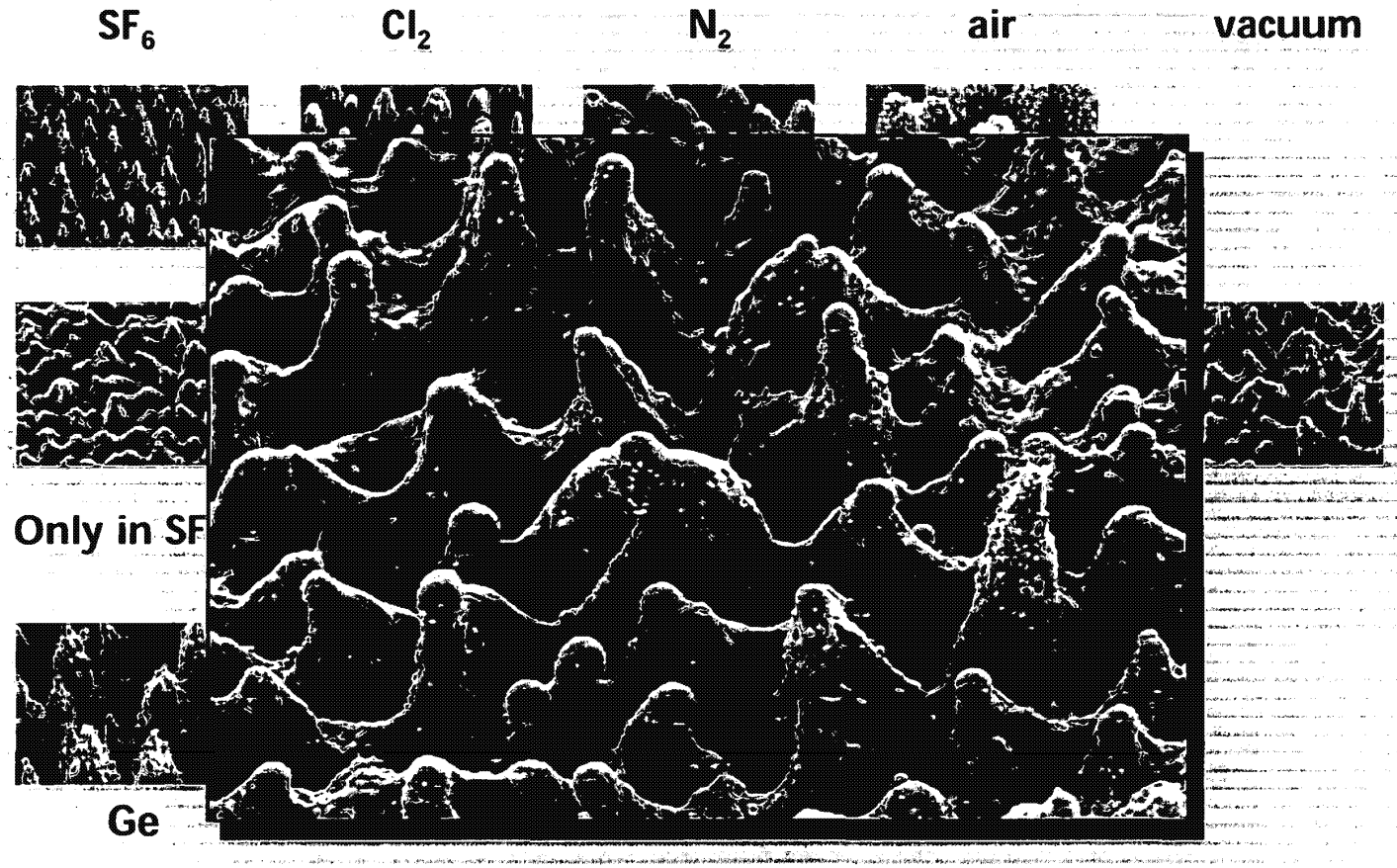
Materials



No spikes in SF_6: Ag, Al, Cu, Pd, Pt, Rh, Ta and GaAs

SAMSUNG EX. 1002 - 2752/4148
SIONYX14030000029.0018

Materials



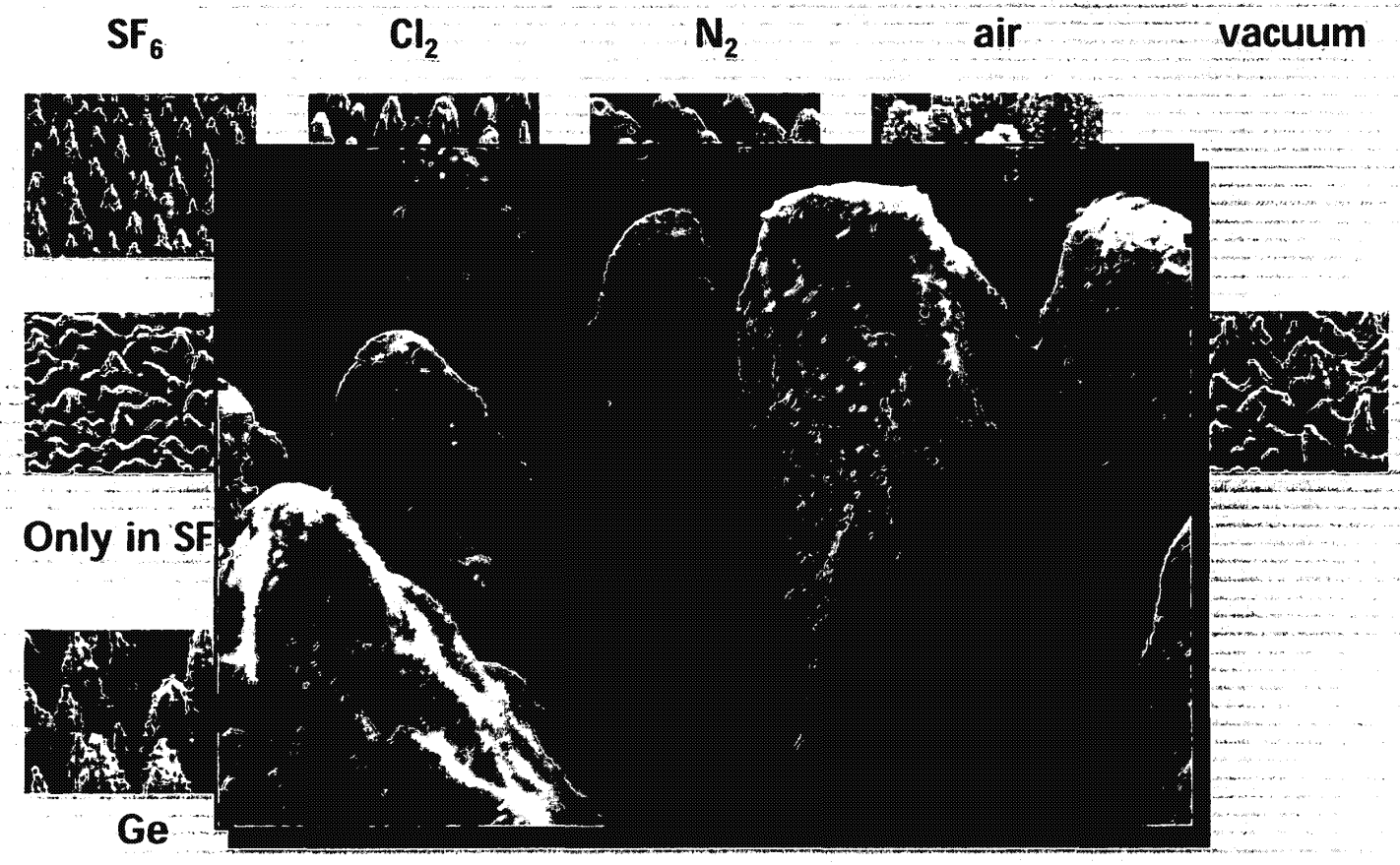
No spikes in SF_6: Ag, Al, Cu, Pd, Pt, Rh, Ta and GaAs

SAMSUNG EX. 1002 - 2753/4148

SIONYX1403000029.0019

SAMSUNG EX. 1002 - 2754/4148

Materials



No spikes in SF_6: Ag, Al, Cu, Pd, Pt, Rh, Ta and GaAs

SIONYX1403000029.0021
SAMSUNG EX. 1002 - 2755/4148

C5

Femtosecond Laser-Assisted Microstructuring of Silicon for Novel Detector, Sensing and Display Technologies

James E. Carey and Eric Mazur
Harvard University, Department of Engineering and Applied Physics, 29 Oxford Street, Cambridge, MA 02138, Tel: +1 617-495-8729, Fax: +1 617-255-4622, email: mazur@physics.harvard.edu

Arrays of sharp, conical microstructures are obtained by stucturing the surface of a silicon wafer using femtosecond laser-assisted chemical etching. The one step, maskless structuring process drastically changes the optical, material and electronic properties of the original silicon wafer. These properties make microstructured silicon viable for use in a wide range of commercial devices including solar cells, infrared photodetectors, chemical and biological sensors, and field emission devices.

Previously, we reported the formation of sharp, micrometer-sized conical structures in quasi-ordered arrays after irradiating a silicon surface with hundreds of femtosecond-laser pulses in the presence of sulfur containing gases [1,2]. Figure 1 shows a scanning electron micrograph of the microstructured silicon surface at an angle of 45°. The laser irradiation also creates a nanometer scale, highly disordered sulfur-doped surface layer. The combinration of sulfur-doped surface layer and conical microstructures results in near-unity absorption of light from 250 nm to 2500 nm [2,3].

We recently found that the laser-affected surface layer forms a photodiode junction with the undisturbed substrate wafer beneath. Figure 2 shows the *I-V* characteristics of this junction in a dark environment. The high absorption of light from 250 nm to 2500 nm and the photodiode junction allow us to fabricate silicon-based photodetectors for both the visible and the near infrared [4]. The spectral responsivity (wavelength dependence of photocurrent per unit incident power) for such a device is shown in Figure 3. At a small bias of –0.1 V, the responsivity in the visible is nearly ten times greater than that of commercially available silicon PIN photodiodes. At wavelengths with energies below the band gap of ordinary silicon (1200-1650 nm) the reponsivities are five orders of magnitude higher than responsivities measured in Si avalanche photodiodes before amplification. We are also working toward creating efficient photovoltaic devices that take advantage of the extended wavelength absorption region. Nearly a third of sunlight is at energies below the band gap of silicon and is therefore not converted into usable energy by conventional silicon solar cells. We hope to use the simple microstructuring process to make silicon-based solar cells that convert more of the sun's spectrum into electric energy.

In addition to its striking optical properties, microstructured silicon displays remarkable field emission characteristics. The rapidly growing field of field emission devices requires unique emitting materials that are robust, easily fabricated, and that have favorable emission characteristics. Figure 3 shows an *I-V* measurement for a 2 x 2 mm^2 area of microstructured silicon. The low turn-on fields and high current yields make the textured silicon ideal for use in field emission displays, ion thruster propulsion, and microwave amplification.

SAMSUNG EX. 1002 - 2756/4148

In this talk we will present the unique optical and electronic properties of microstructured silicon, discuss the formation process of the conical microstructures, and review the chemical and structural make-up of the surface that are responsible for the novel optoelectronic properties. We will also discuss future directions for this technique including structuring of new materials, incorporation of new ambient gases, and better control over the position and density of the microstructures themselves (Figure 4).

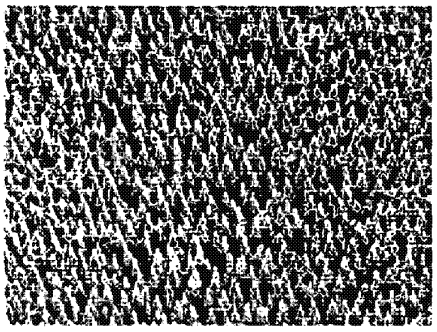


Figure 1: A scanning electron micrograph of silicon microstructures taken at a 45° angle and 3000x magnification.

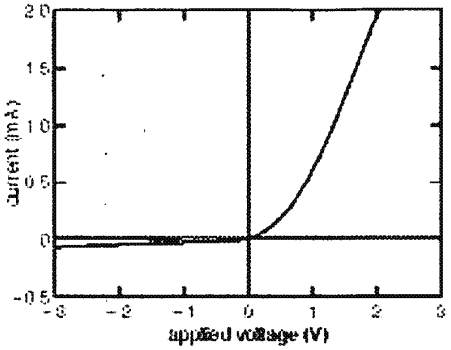


Figure 2: Current-voltage characteristics of microstructured silicon photodiode without illumination.

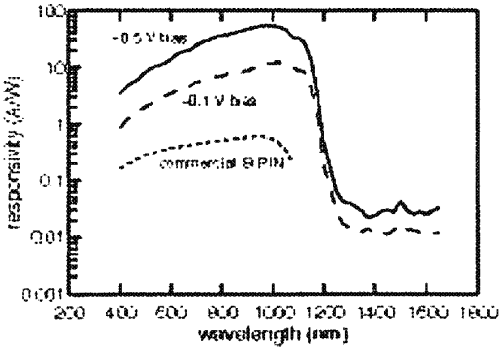


Figure 3: Spectral responsivity (wavelength dependence of photocurrent per unit incident power) of microstructured silicon device at two bias values. The responsivity of a commercial silicon PIN photodiode is shown for comparison.

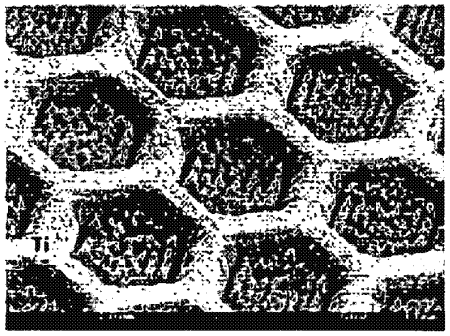
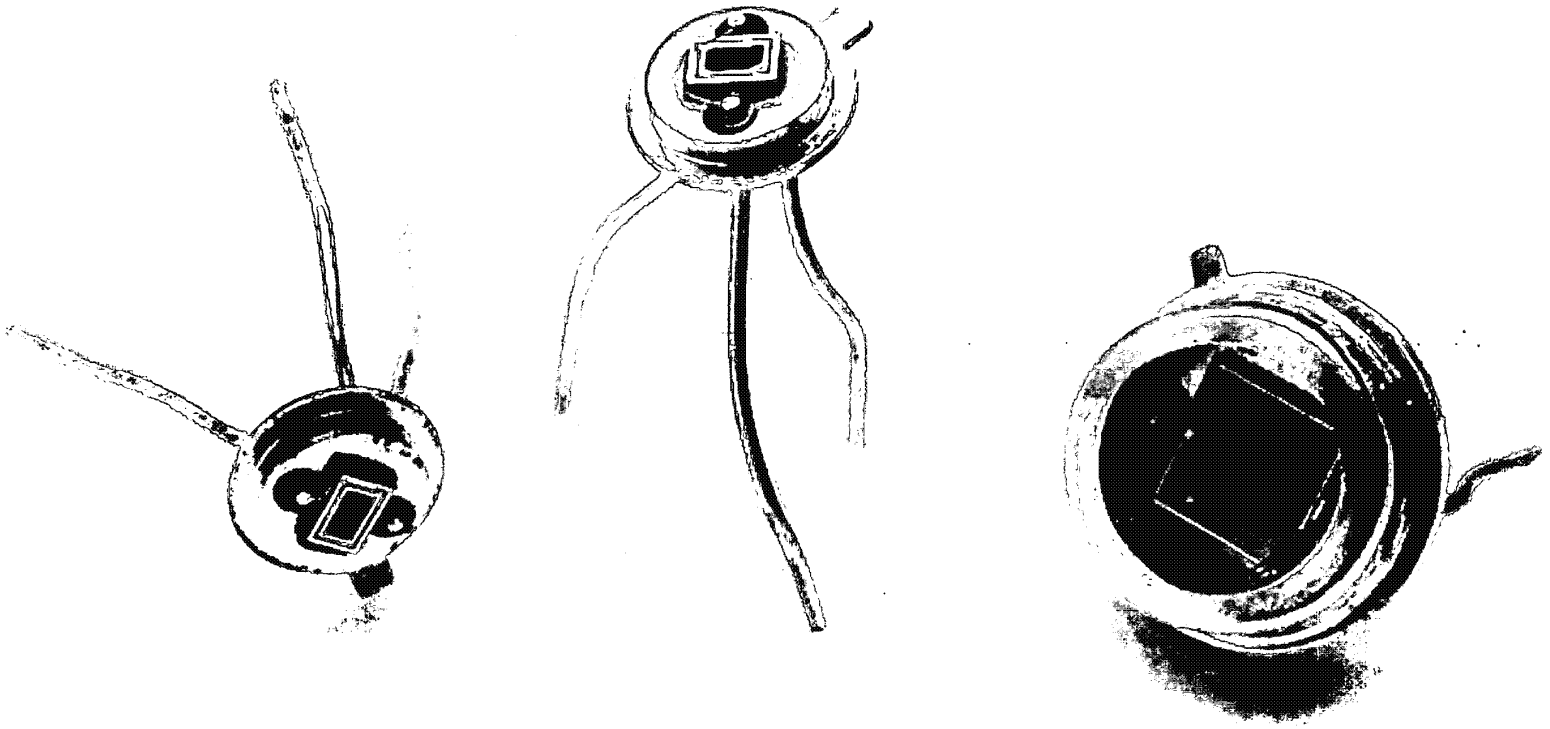


Figure 4: A scanning electron micrograph of structures made on Titanium using a spatial mask to control their organization.

[1] T. H. Her, R. J. Finlay, C. Wu, S. Deliwala, and E. Mazur, *Appl. Phys. Lett.* **73**, 1673-1675 (1998).
[2] C. Wu, C. H. Crouch, L. Zhao, J. E. Carey, R. Younkin, J. A. Lenvinson, R. M. Farrell, P. Gothoskar, A. Karger, and E. Mazur *Appl. Phys. Lett.* **78**, 1850-1852 (2001).
[3] R. Younkin, J. E. Carey, E. Mazur, J. A. Levinson, and C. M. Friend, *J. Appl. Phys.* **93**, 2626 (2003).
[4] J. E. Carey, C. H. Crouch, M. A. Sheehy, M. Shen, C. M. Friend and E. Mazur, *submitted to Applied Physics Letters.*

SAMSUNG EX. 1002 - 2757/4148

Femtosecond laser-assisted microstructuring of silicon for novel detector, sensing and display technologies



2003 LEOS Annual Meeting
Tucson, AZ, 29 October 2003

SIONYX1403000029.0024

SAMSUNG EX. 1002 - 2758/4148

SAMSUNG EX. 1002 - 2759/4148

and also....

Tsing-Hua Her
Shrenik Deliwala
Richard Finlay
Michael Sheehy
Brian Tull
Jeffrey Warrander
Claudia Wu
Rebecca Younkin

Dr. John Chervinsky
Dr. Joshua Levinson

Dr. François Génin (LLNL)
Dr. Richard Farrell
Dr. Arieh Karger (RMD)
Dr. Richard Meyers (RMD)

Prof. Michael Aziz
Prof. Cynthia Friend
Prof. Li Zhao (Fudan)

SAMSUNG EX. 1002 - 2760/4148

Introduction

irradiate with 100-fs 10 kJ/m^2 pulses

SAMSUNG EX. 1002 - 2761/4148

Introduction

SAMSUNG EX. 1002 - 2762/4148

Introduction

"black silicon"

SAMSUNG EX. 1002 - 2763/4148

SIONYX1403000029.0030

SAMSUNG EX. 1002 - 2765/4148

SAMSUNG EX. 1002 - 2766/4148

SAMSUNG EX. 1002 - 2767/4148

Introduction

SAMSUNG EX. 1002 - 2768/4148

Introduction

- maskless etching process
- self-organized, tall microstructures
- highly light absorbing

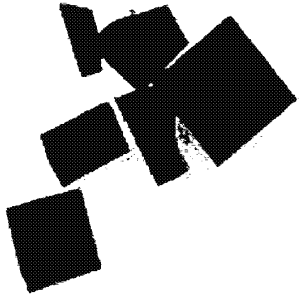


SIONYX1403000029.0035

SAMSUNG EX. 1002 - 2769/4148

Outline

- properties
- structural and chemical analysis
- detectors
- outlook

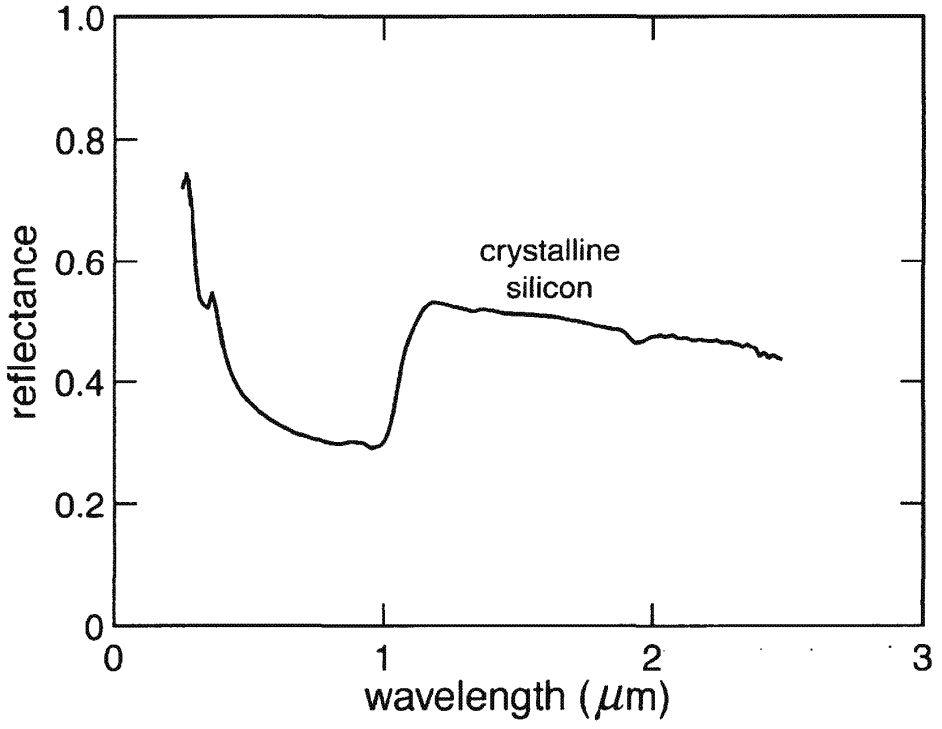


SIONYX14030000029.0036

SAMSUNG EX. 1002 - 2770/4148

Properties

reflectance (integrating sphere)

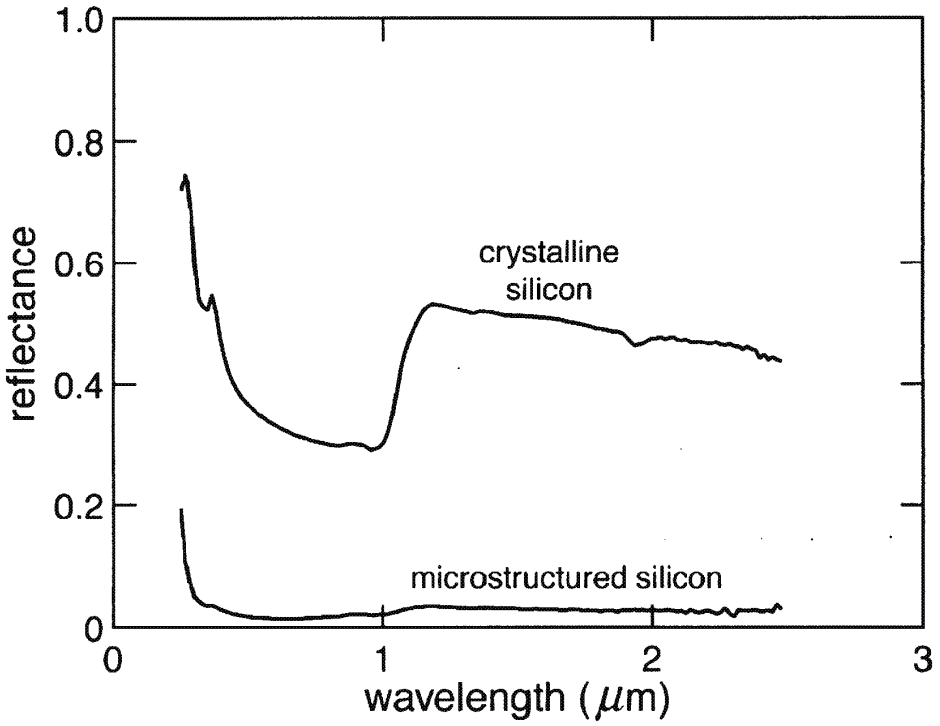


SIONYX1403000029.0037

SAMSUNG EX. 1002 - 2771/4148

Properties

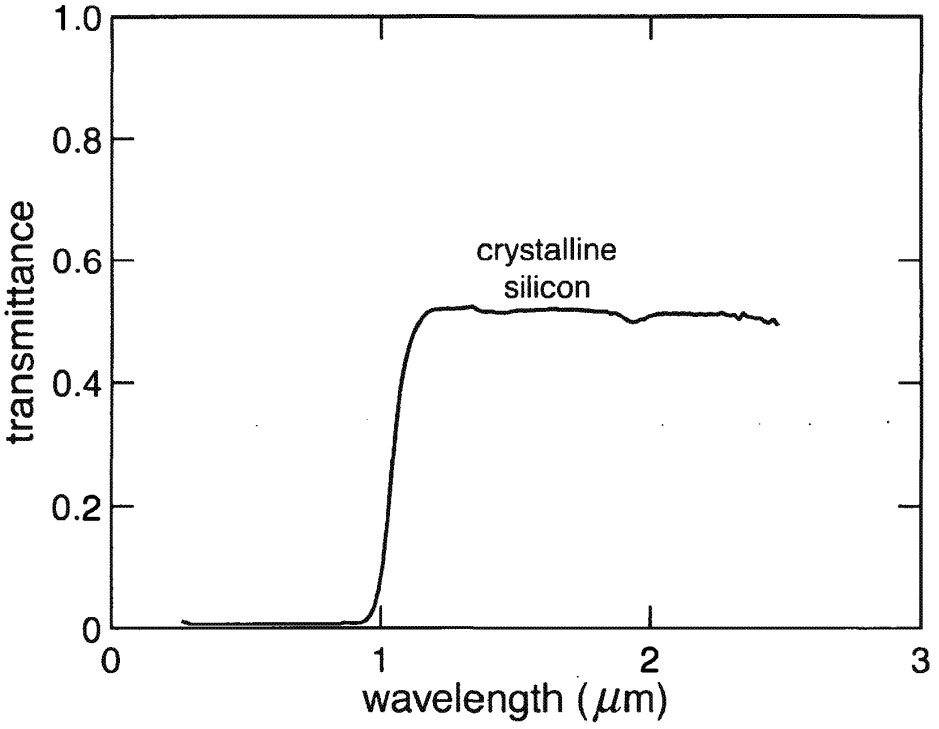
reflectance (integrating sphere)



SAMSUNG EX. 1002 - 2772/4148
SIONYX14030000029.0038

Properties

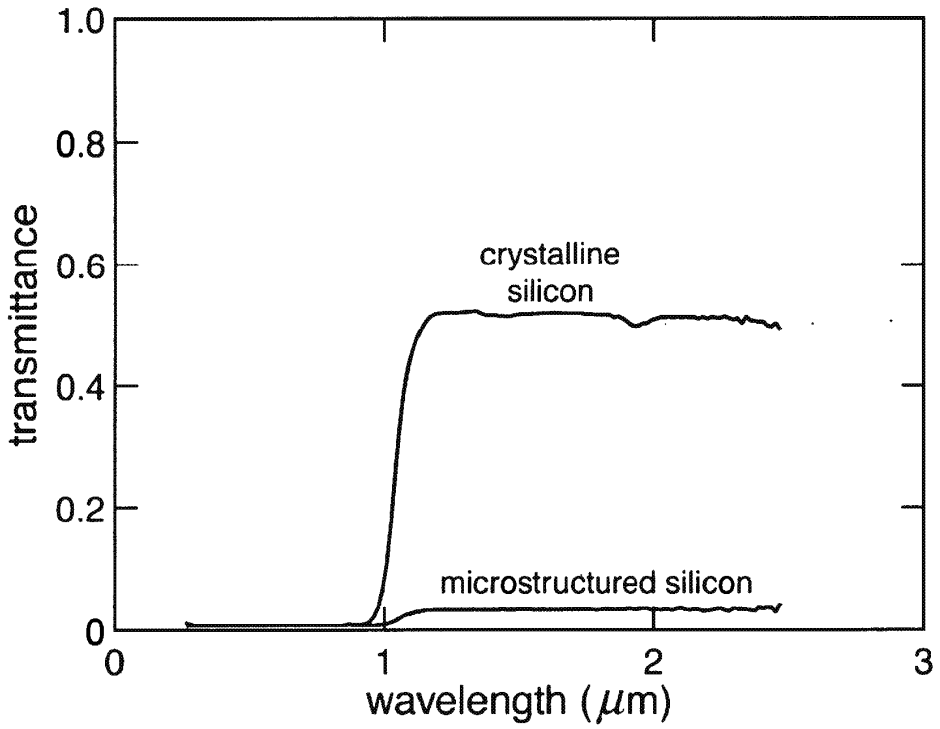
transmittance (integrating sphere)



SAMSUNG EX. 1002 - 2773/4148
SIONYX14030000029.0039

Properties

transmittance (integrating sphere)

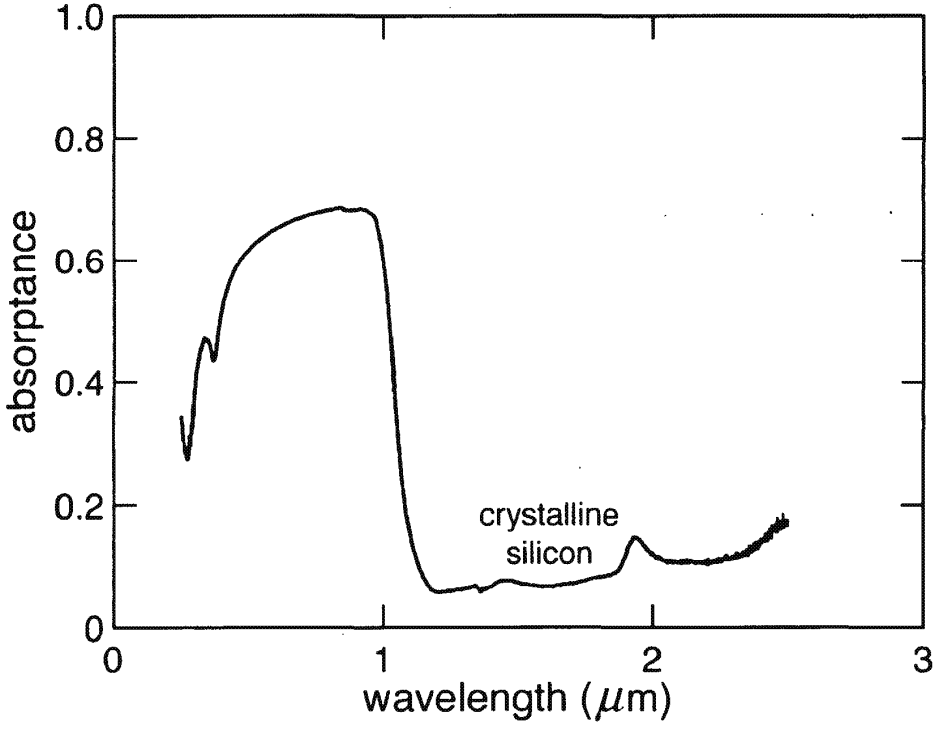


SIONYX1403000029.0040

SAMSUNG EX. 1002 - 2774/4148

Properties

absorptance (1 – *R* – *T*)

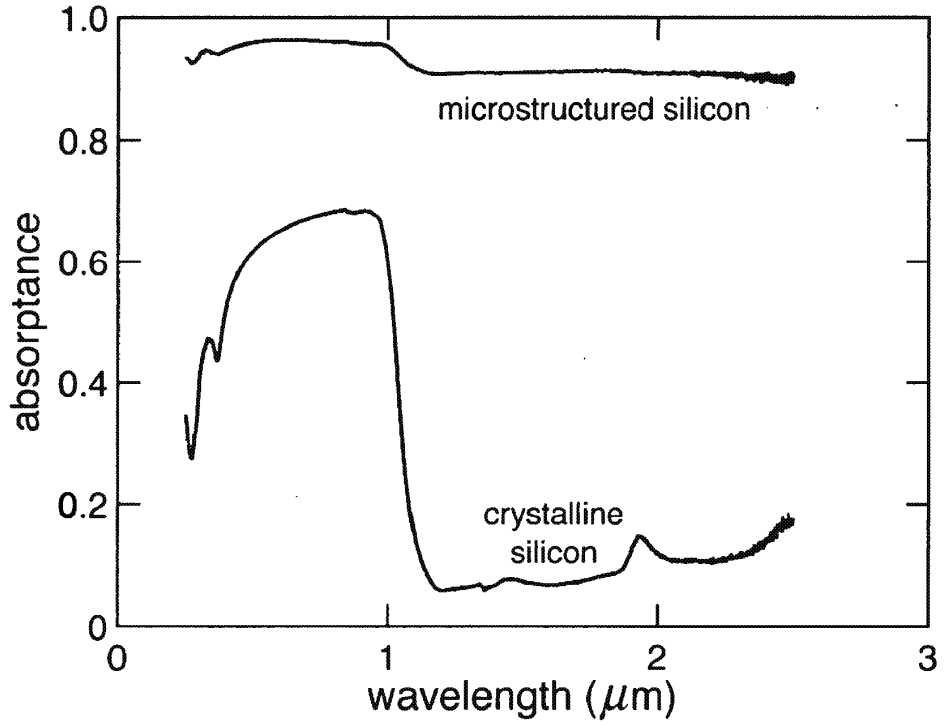


SIONYX1403000029.0041

SAMSUNG EX. 1002 - 2775/4148

Properties

absorptance (1 – *R* – *T*)



SIONYX1403000029.0042

SAMSUNG EX. 1002 - 2776/4148

Properties

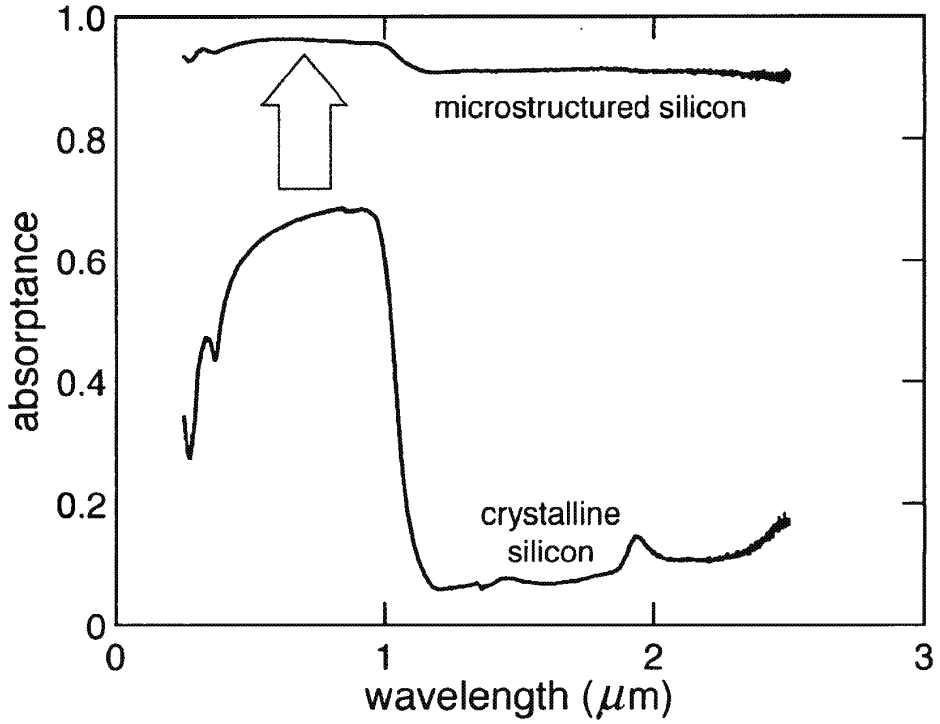
What causes the near-unity absorptance?

SAMSUNG EX. 1002 - 2777/4148

SIONYX1403000029.0044

Properties

multiple reflections enhance absorption

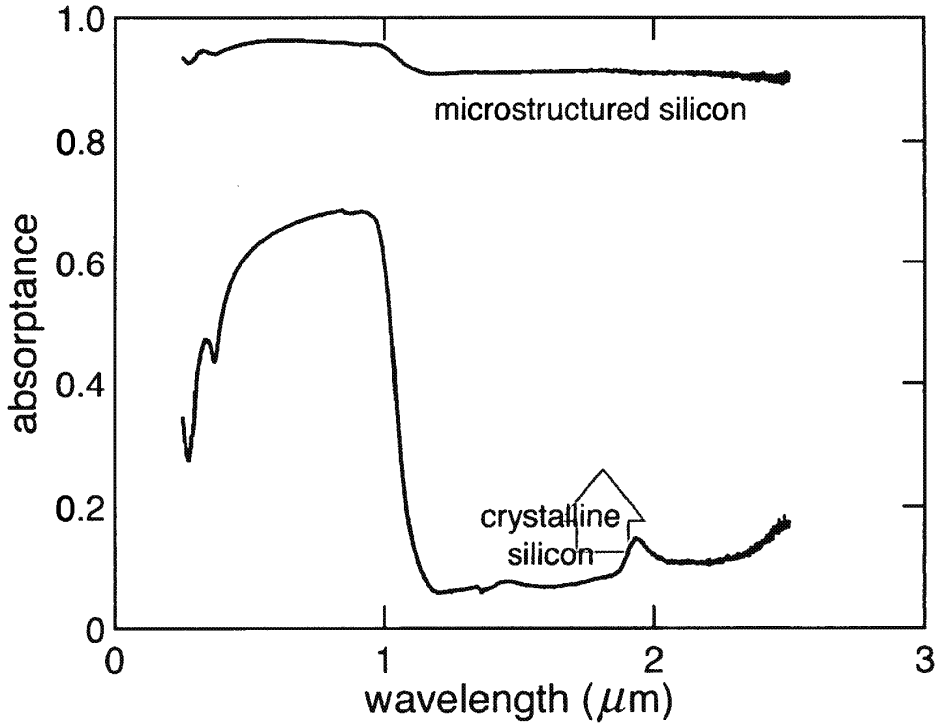


SIONYX1403000029.0045

SAMSUNG EX. 1002 - 2779/4148

Properties

multiple reflections enhance absorption

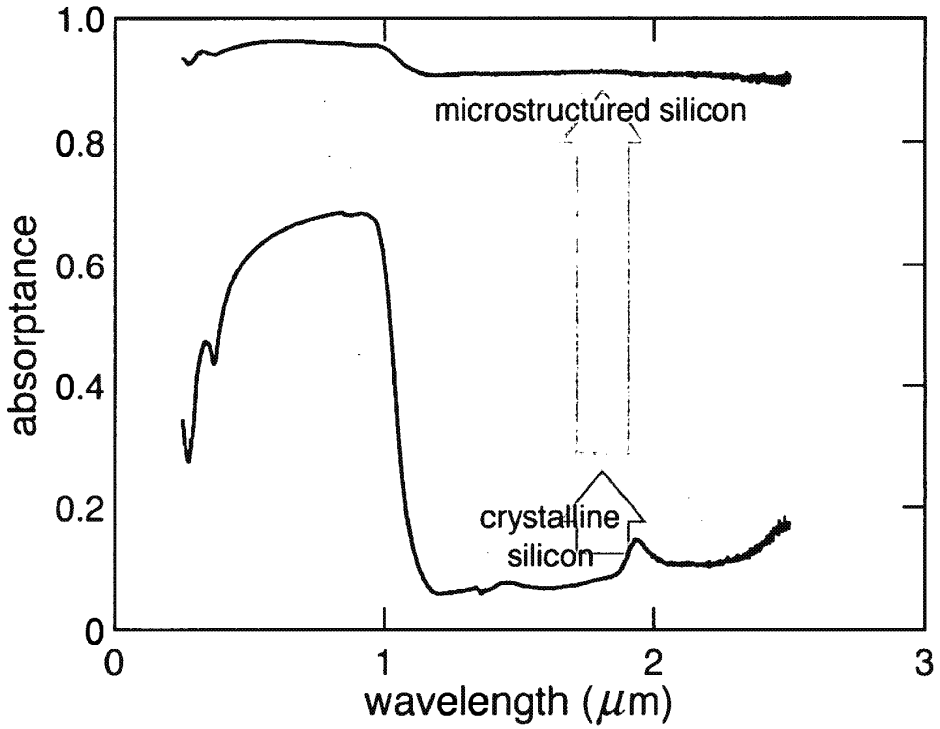


SIONYX1403000029.0046

SAMSUNG EX. 1002 - 2780/4148

Properties

electronic band structure changes



SIONYX1403000029.0047

SAMSUNG EX. 1002 - 2781/4148

Properties

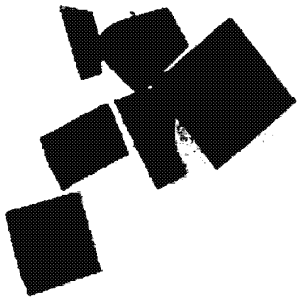
- enhanced absorption in visible
- enhanced photoelectron generation in visible
- near unity absorption in IR
- visible photoluminescence
- strong field emission

SIONYX1403000029.0048

SAMSUNG EX. 1002 - 2782/4148

Outline

- properties
- structural and chemical analysis
- detectors
- outlook



SIONYX1403000029.0049

SAMSUNG EX. 1002 - 2783/4148

Structural and chemical analysis

Band structure changes: defects and/or impurities

SIONYX1403000029.0050

SAMSUNG EX. 1002 - 2784/4148

Structural and chemical analysis

SAMSUNG EX. 1002 - 2785/4148

Structural and chemical analysis

SAMSUNG EX. 1002 - 2786/4148

Structural and chemical analysis

cross-sectional
Transmission Electron
Microscopy



SIONYX1403000029.0053

SAMSUNG EX. 1002 - 2787/4148

Structural and chemical analysis

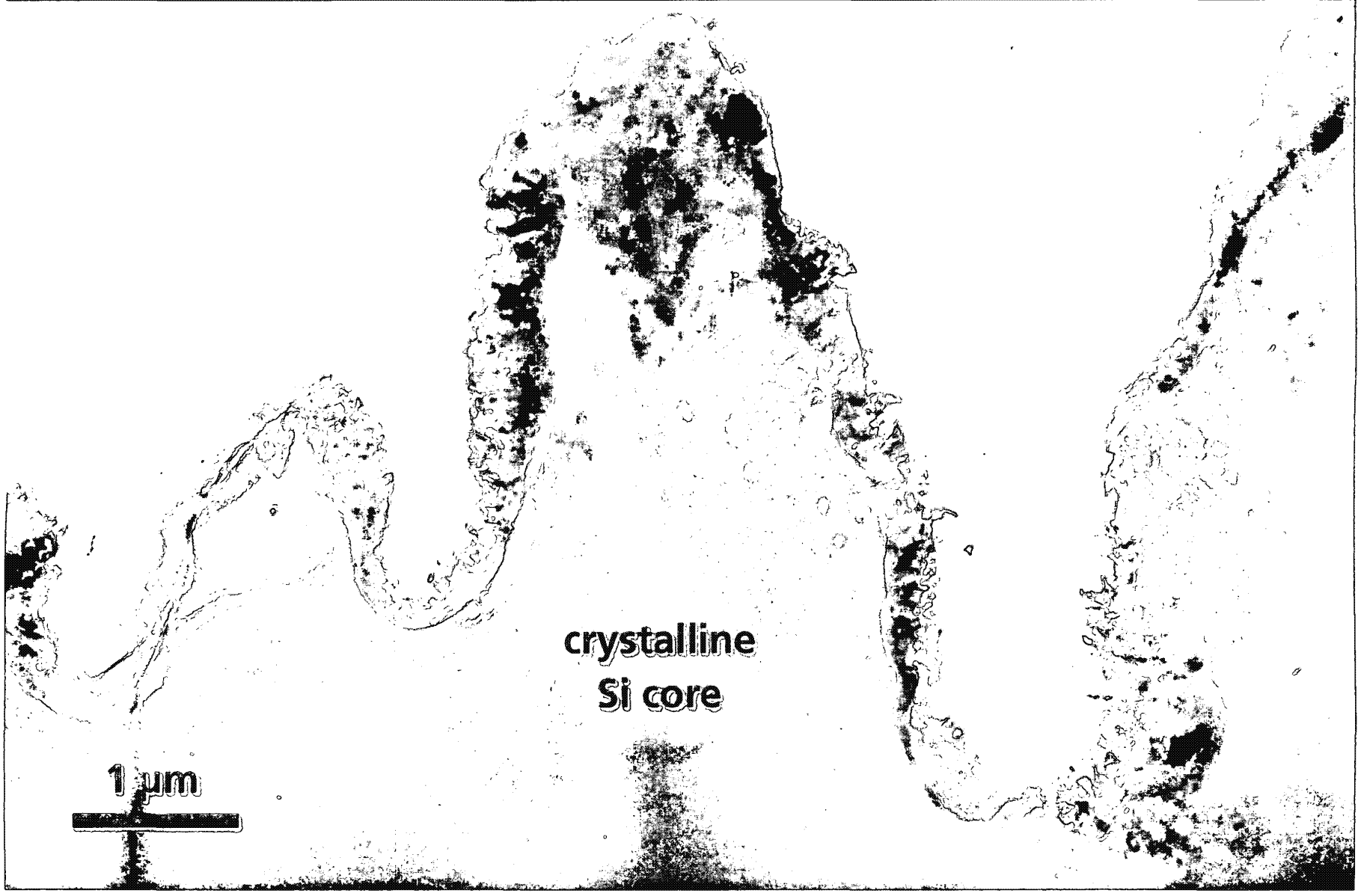
M. Wall, F. Génin (LLNL)

SIONYX1403000029.0054

SAMSUNG EX. 1002 - 2788/4148

SIONYX1403000029.0055

Structural and chemical analysis



SIONYX140300029.0056

SAMSUNG EX. 1002 - 2790/4148

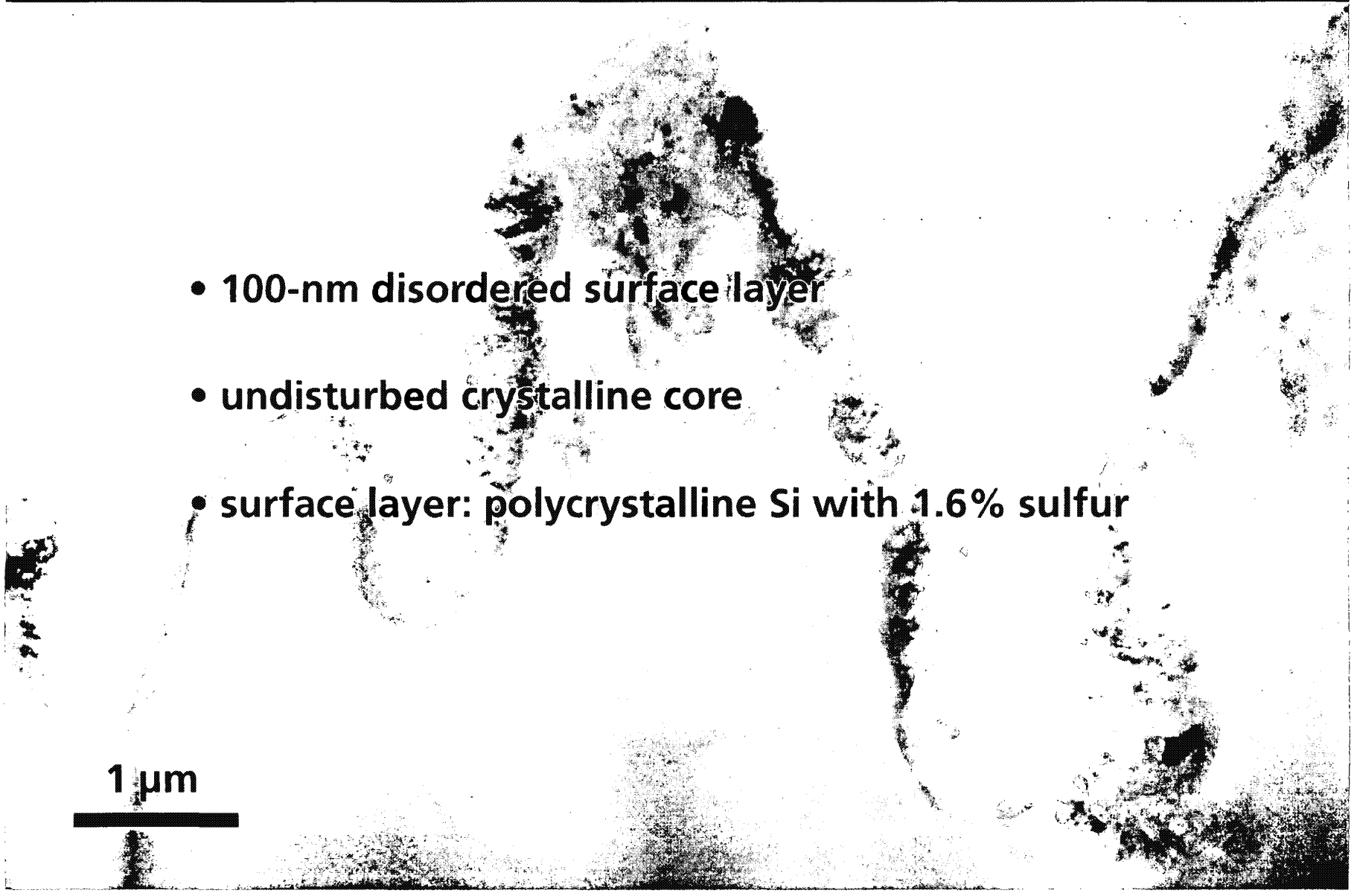
SIONYX1403000029.0057

SAMSUNG EX. 1002 - 2791/4148

Structural and chemical analysis

SIONYX1403000029.0058

Structural and chemical analysis



SIONYX1403000029.0059

SAMSUNG EX. 1002 - 2793/4148

Structural and chemical analysis

Microstructure with different gases:

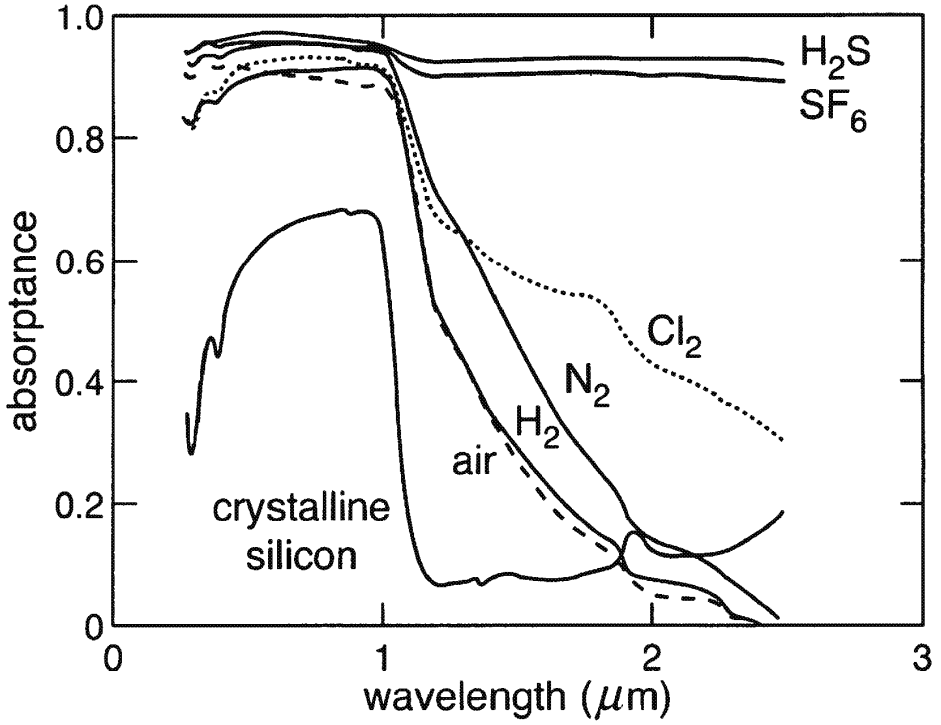
- **gas species incorporated into surface layer**
- **sulfur required for below band gap absorption**

SIONYX1403000029.0060

SAMSUNG EX. 1002 - 2794/4148

Structural and chemical analysis

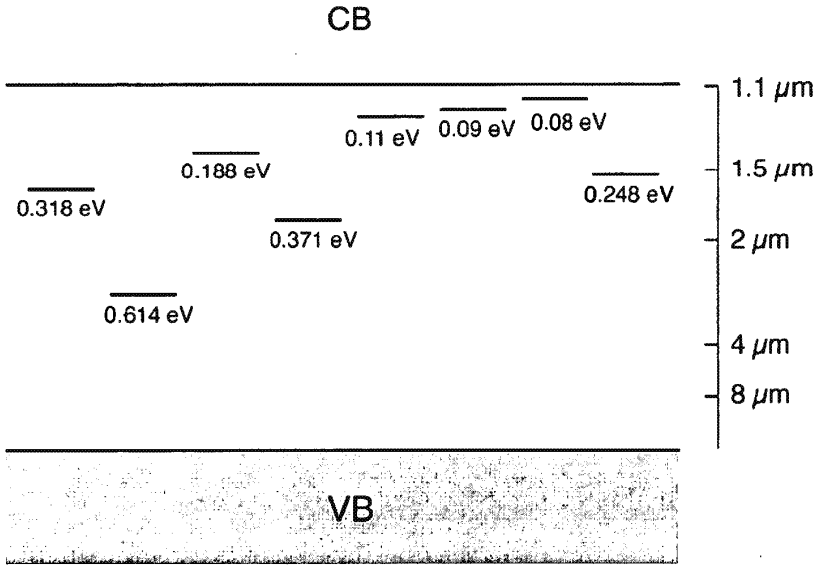
microstructure with different gases



SAMSUNG EX. 1002 - 2795/4148
SIONYX14030000029.0061

Structural and chemical analysis

1 part in 10^6 sulfur introduces states in gap

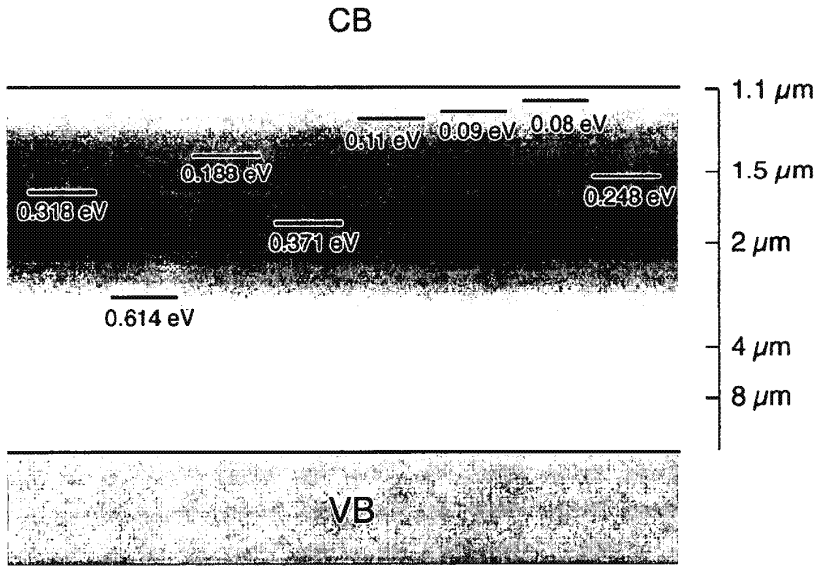


Janzén *et al.*, Phys. Rev. B 29, 1907 (1984)

SAMSUNG EX. 1002 - 2796/4148
SIONYX1403000029.0062

Structural and chemical analysis

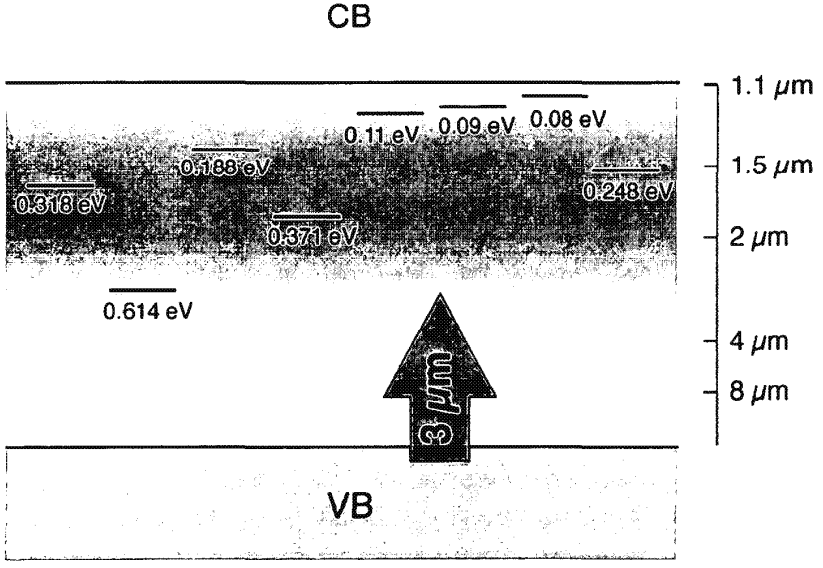
at high concentration states broaden into band



SAMSUNG EX. 1002 - 2797/4148
SIONYX1403000029.0063

Structural and chemical analysis

absorption extends into infrared

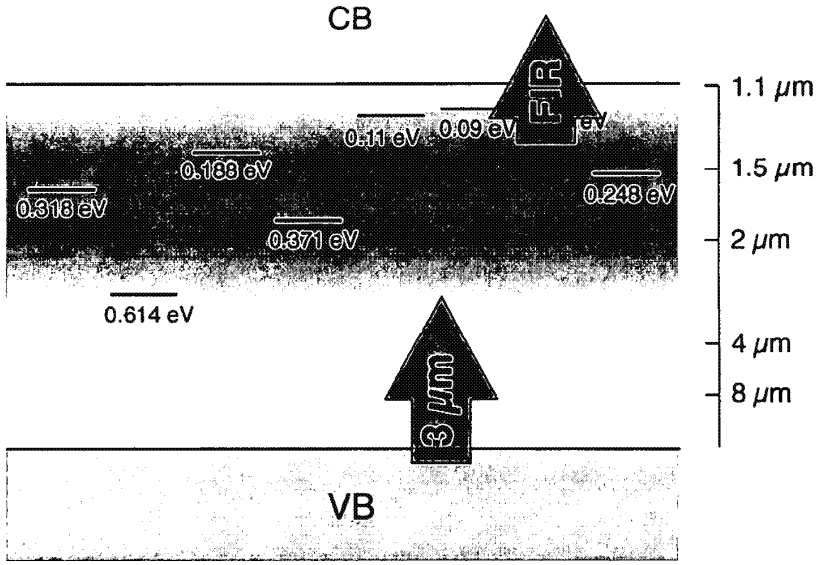


SIONYX1403000029.0064

SAMSUNG EX. 1002 - 2798/4148

Structural and chemical analysis

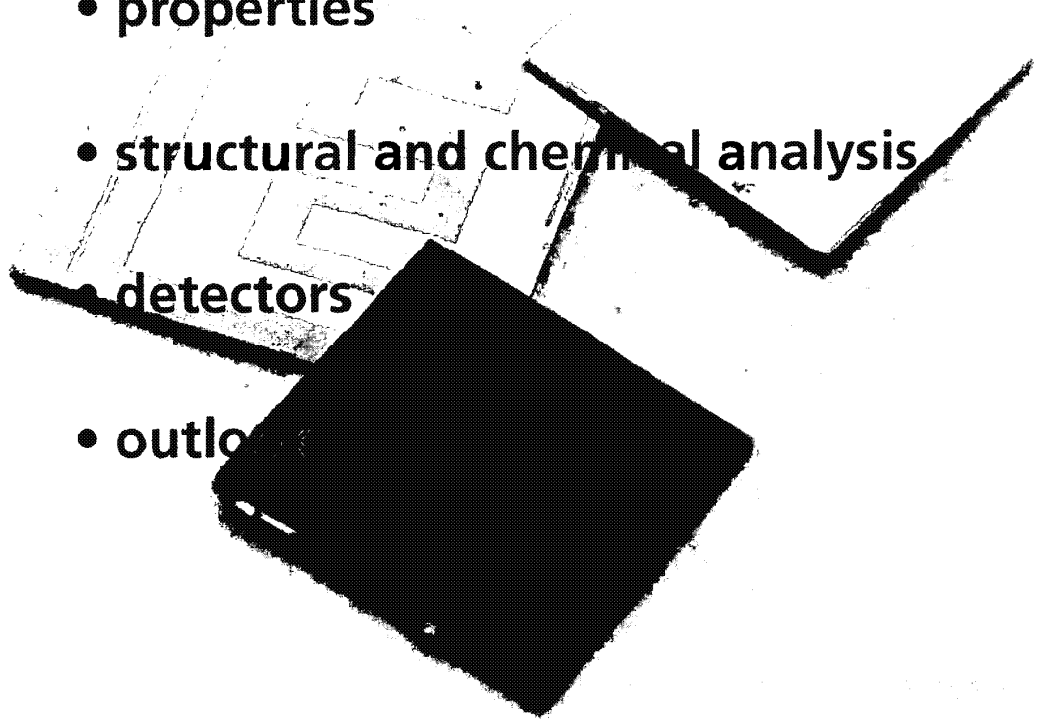
sulfur has 6 valence electrons: donor states?



SAMSUNG EX. 1002 - 2799/4148
SIONYX14030000029.0065

Outline

- properties
- structural and chemical analysis
- detectors
- outlook

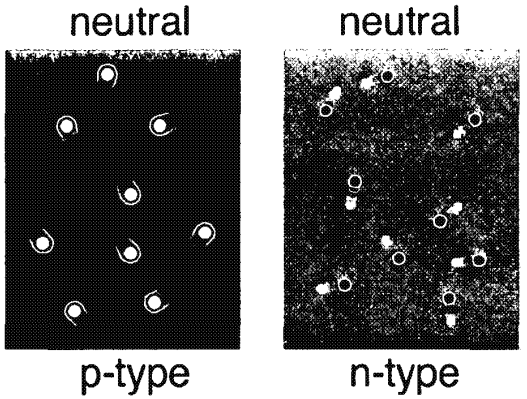


SIONYX14030000029.0066

SAMSUNG EX. 1002 - 2800/4148

Detectors

join acceptor and donor type Si

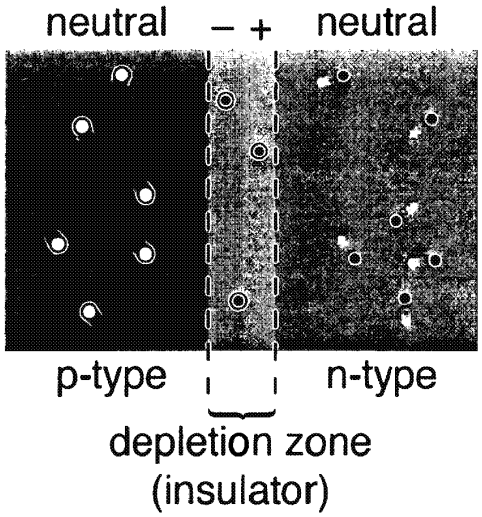


SIONYX14030000029.0067

SAMSUNG EX. 1002 - 2801/4148

Detectors

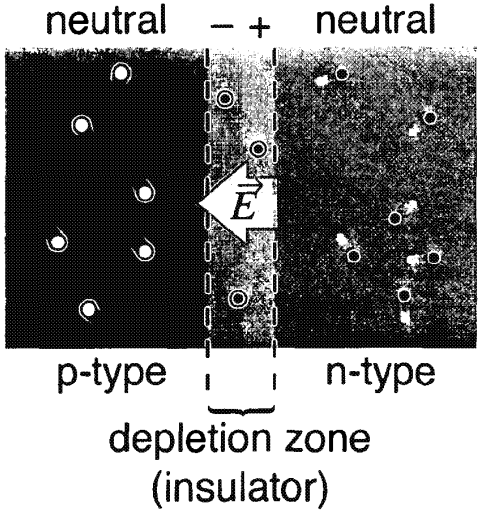
join acceptor and donor type Si



SAMSUNG EX. 1002 - 2802/4148
SIONYX14030000029.0068

Detectors

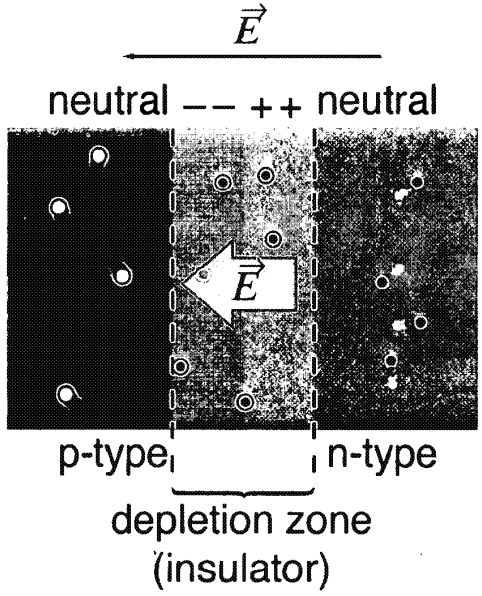
depletion zone with strong E-field



SAMSUNG EX. 1002 - 2803/4148
SIONYX1403000029.0069

Detectors

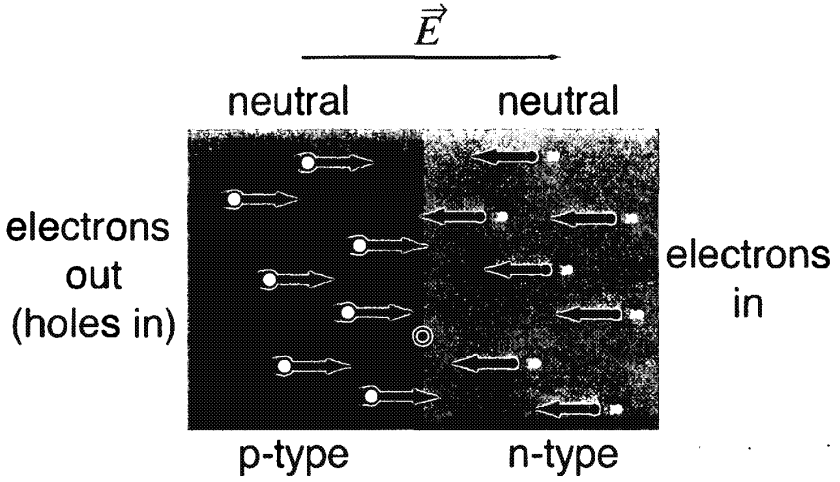
reverse bias: depletion zone grows



SAMSUNG EX. 1002 - 2804/4148
SIONYX1403000029.0070

Detectors

forward bias: current flows

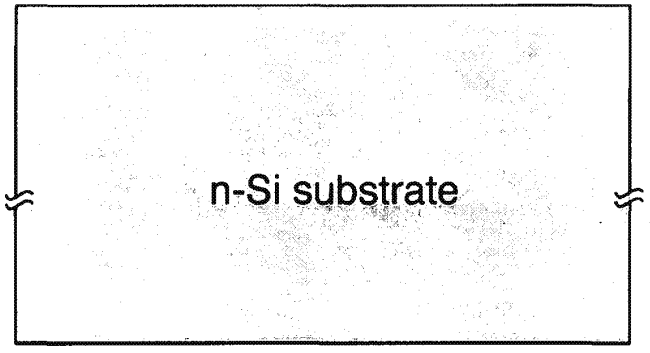


SIONYX14030000029.0071

SAMSUNG EX. 1002 - 2805/4148

Detectors

black silicon/n-type silicon junction

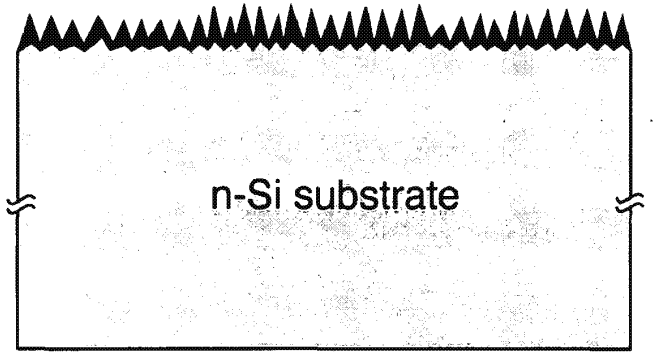


SIONYX1403000029.0072

SAMSUNG EX. 1002 - 2806/4148

Detectors

black silicon/n-type silicon junction

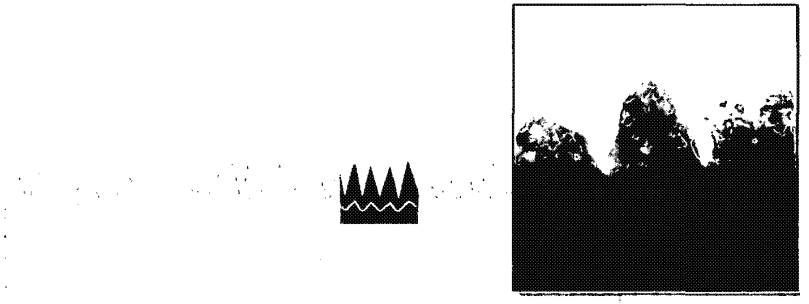


SIONYX1403000029.0073

SAMSUNG EX. 1002 - 2807/4148

Detectors

black silicon/n-type silicon junction

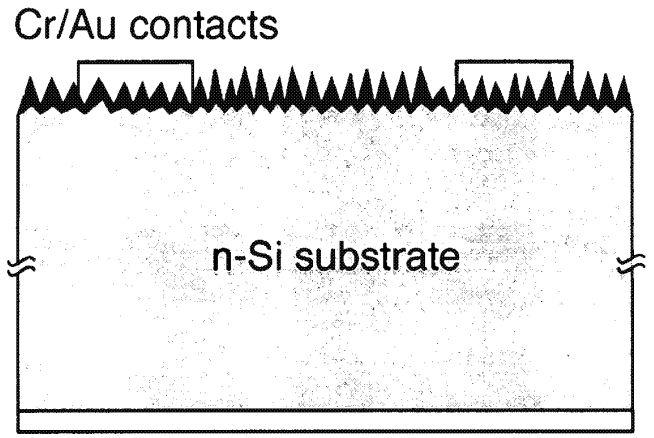


SIONYX1403000029.0074

SAMSUNG EX. 1002 - 2808/4148

Detectors

black silicon/n-type silicon junction

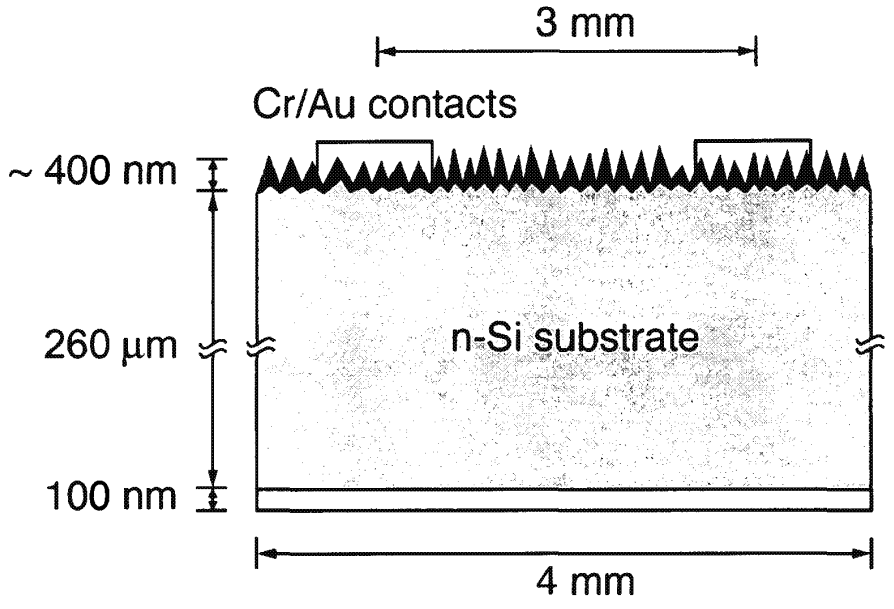


SIONYX1403000029.0075

SAMSUNG EX. 1002 - 2809/4148

Detectors

black silicon/n-type silicon junction

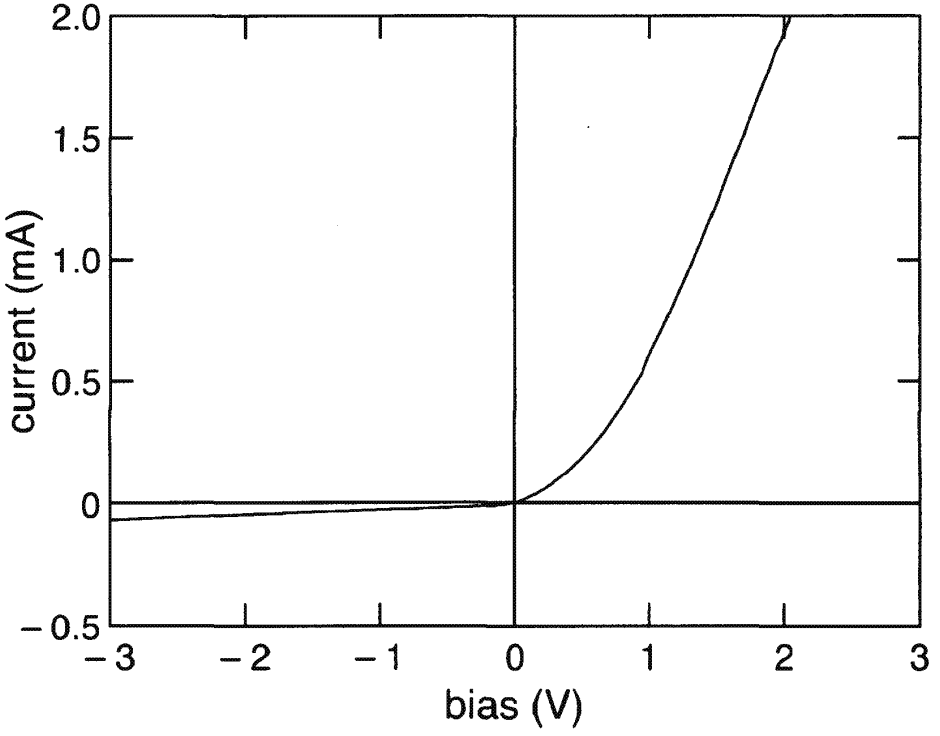


SIONYX1403000029.0076

SAMSUNG EX. 1002 - 2810/4148

Detectors

IV characteristics

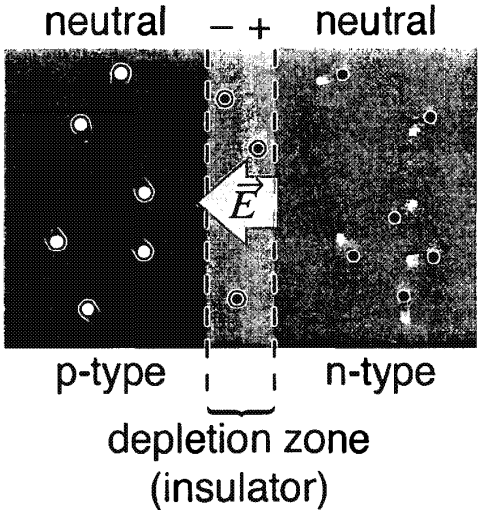


SIONYX1403000029.0077

SAMSUNG EX. 1002 - 2811/4148

Detectors

photodiode operation

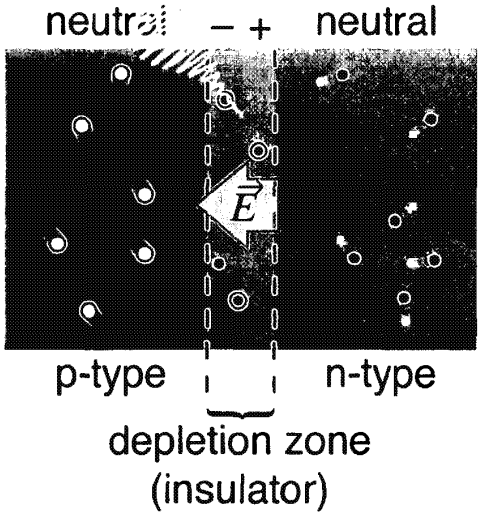


SIONYX14030000029.0078

SAMSUNG EX. 1002 - 2812/4148

Detectors

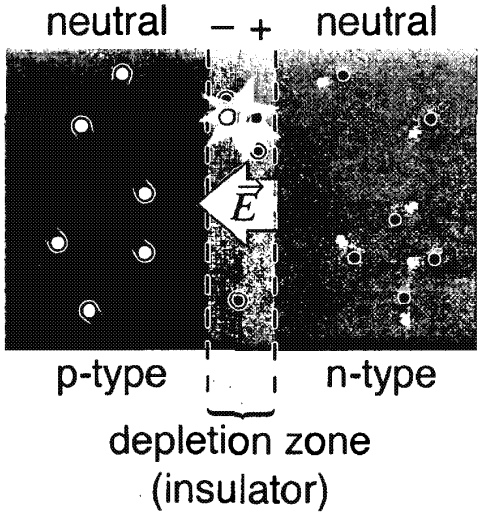
photodiode operation



SIONYX1403000029.0079
SAMSUNG EX. 1002 - 2813/4148

Detectors

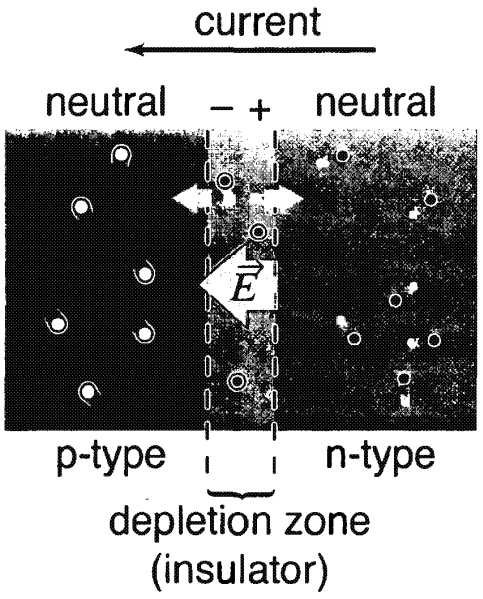
incident photon creates electron-hole pair



SIONYX14030000029.0080
SAMSUNG EX. 1002 - 2814/4148

Detectors

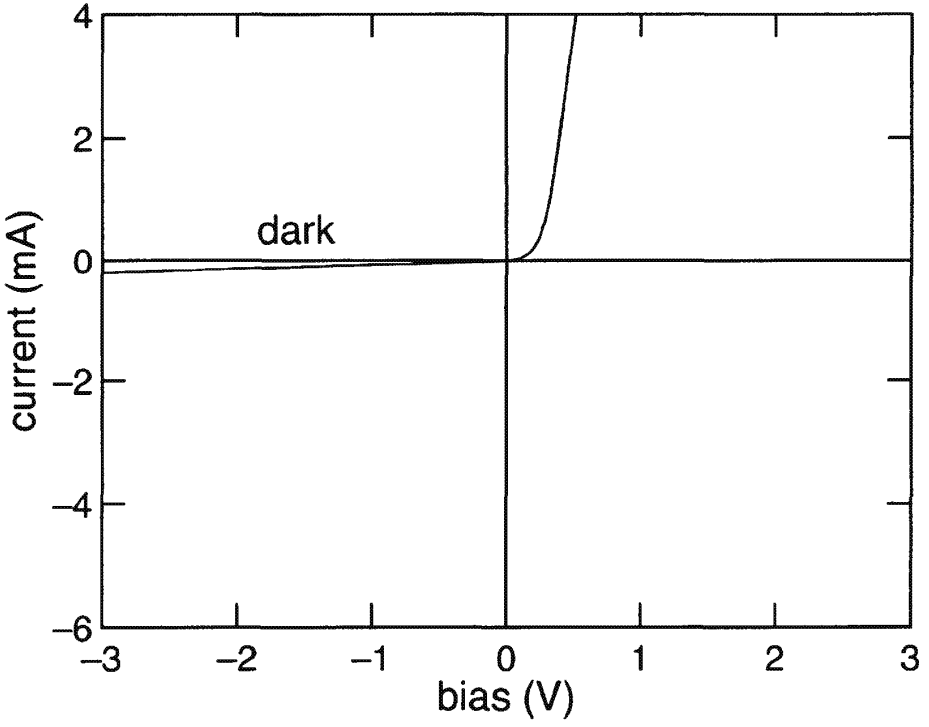
E-field separates eh-pair causing current



SIONYX14030000029.0081
SAMSUNG EX. 1002 - 2815/4148

Detectors

IV characteristics

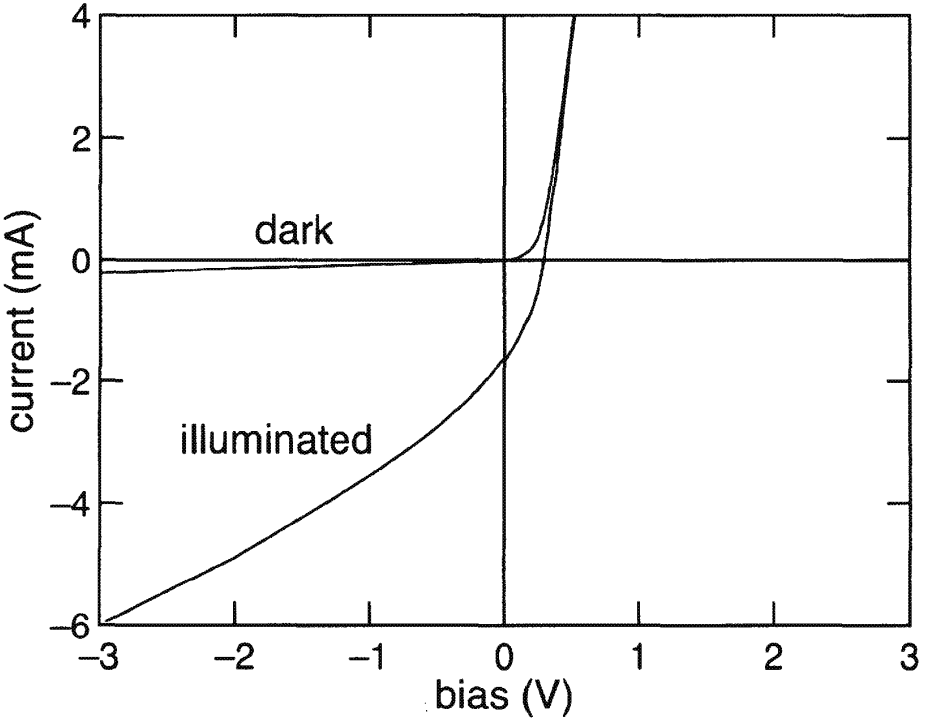


SIONYX14030000029.0082

SAMSUNG EX. 1002 - 2816/4148

Detectors

IV characteristics

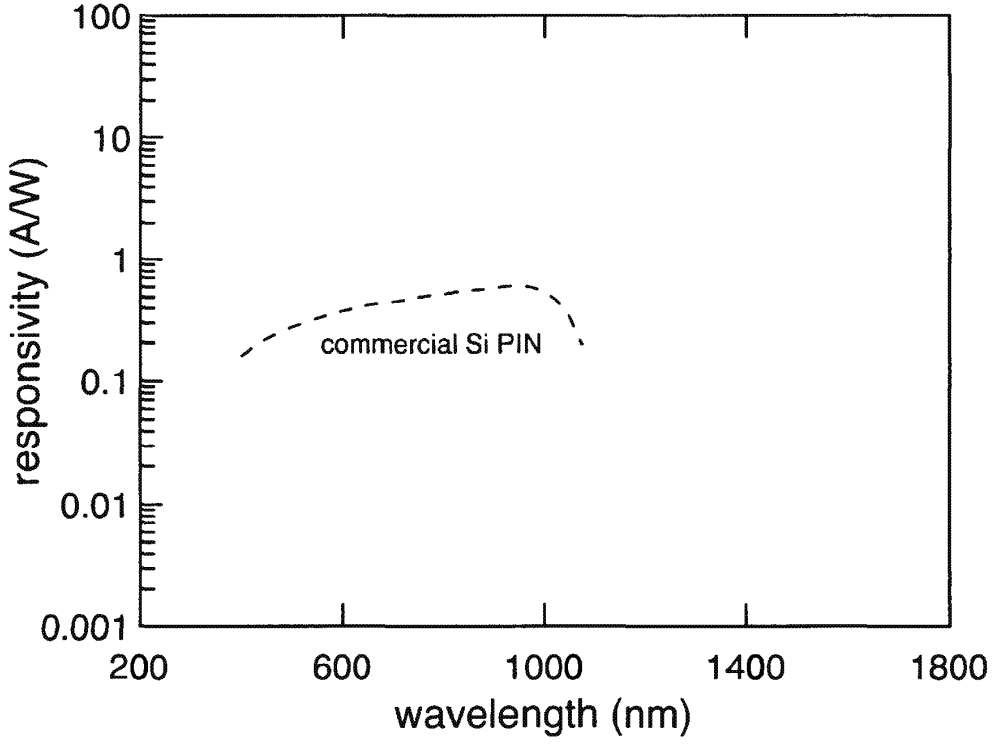


SIONYX14030000029.0083

SAMSUNG EX. 1002 - 2817/4148

Detectors

responsivity

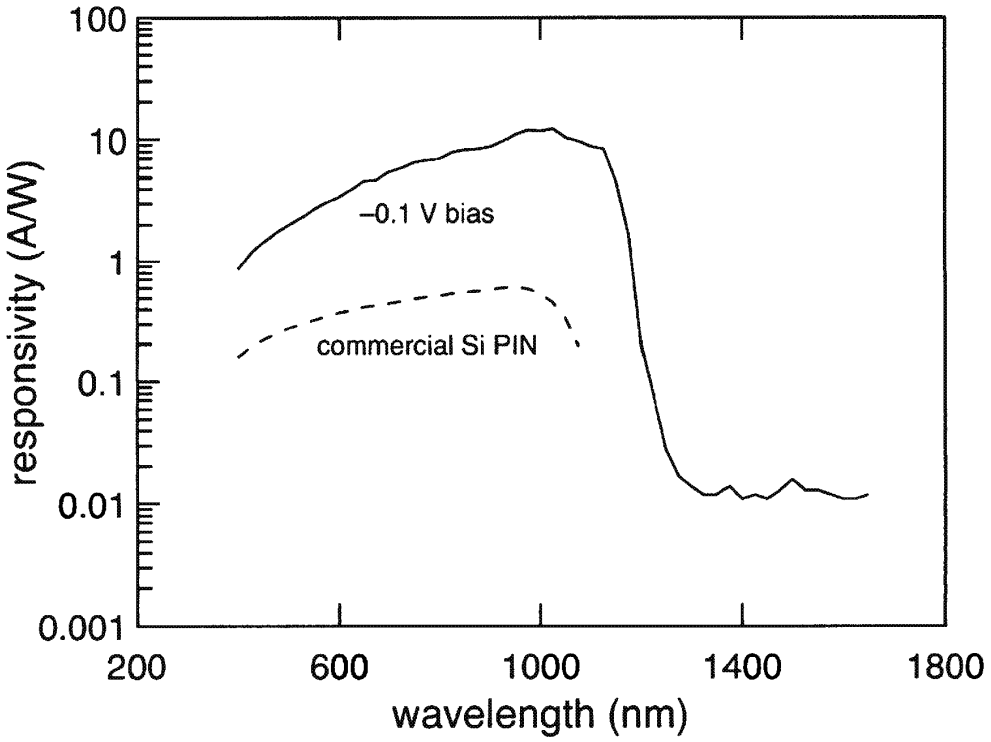


SIONYX1403000029.0084

SAMSUNG EX. 1002 - 2818/4148

Detectors

responsivity

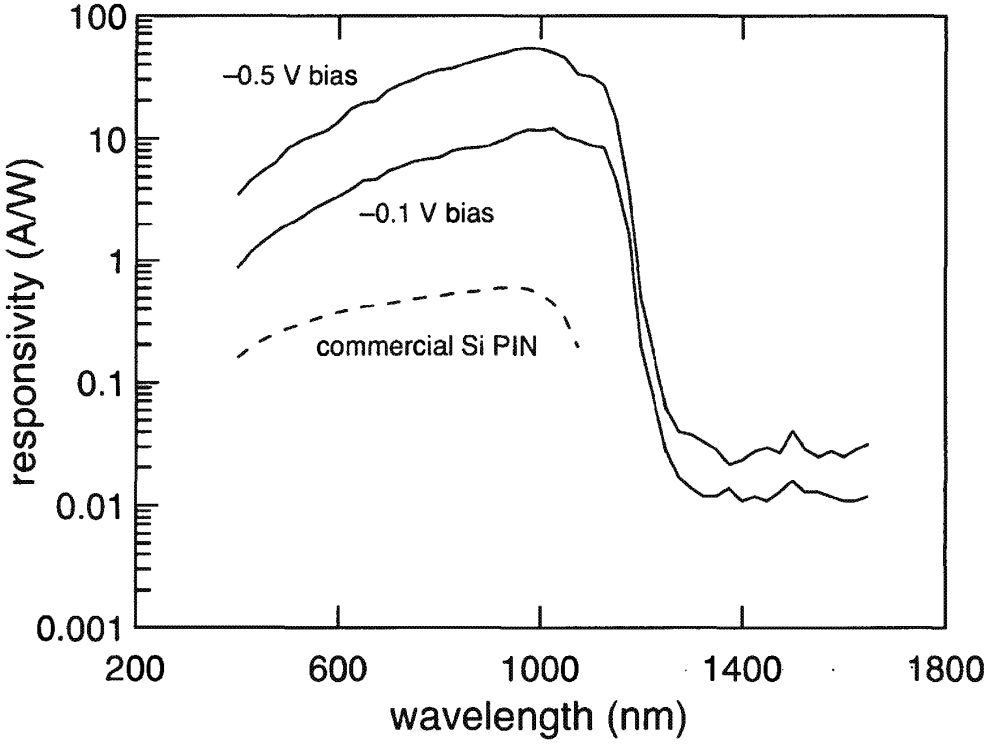


SIONYX14030000029.0085

SAMSUNG EX. 1002 - 2819/4148

Detectors

responsivity

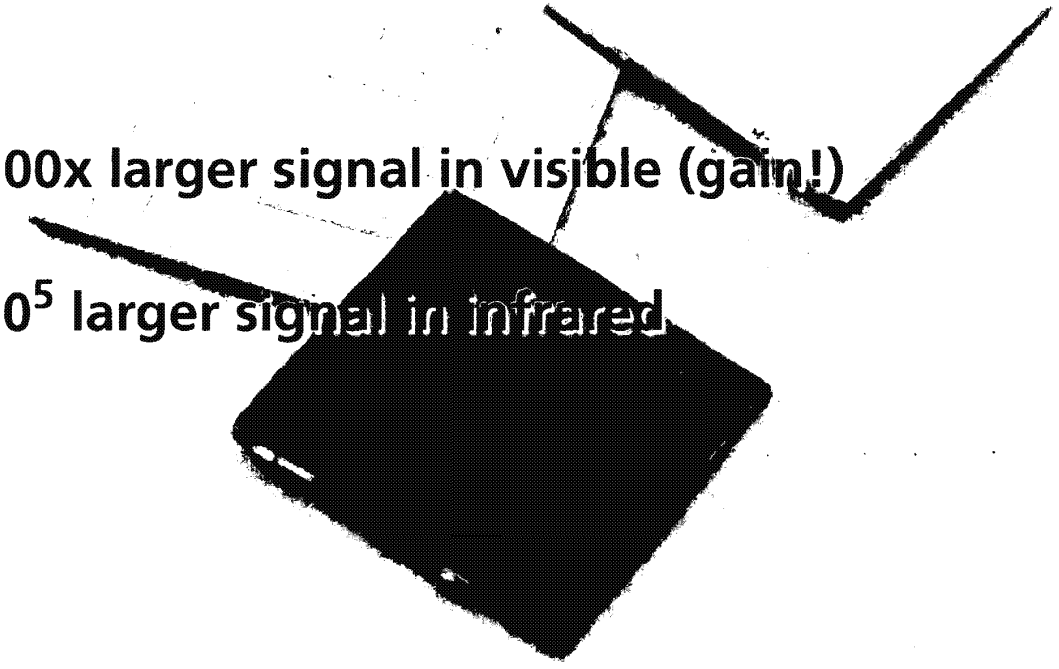


SIONYX1403000029.0086

SAMSUNG EX. 1002 - 2820/4148

Detectors

Black silicon photodiode (at 0.5 V bias):



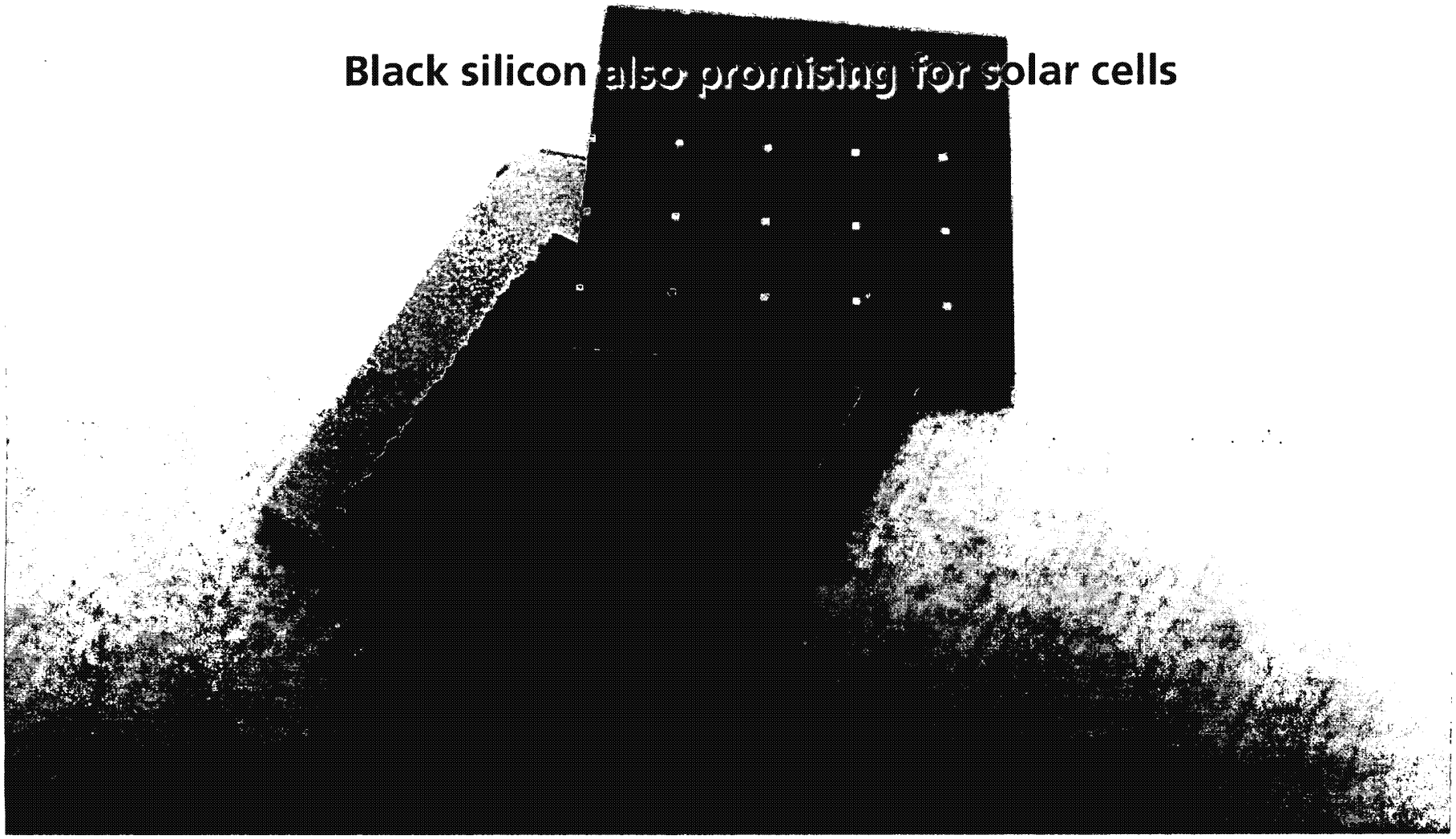
- **100x larger signal in visible (gain!)**
- **10^5 larger signal in infrared**

SIONYX1403000029.0087

SAMSUNG EX. 1002 - 2821/4148

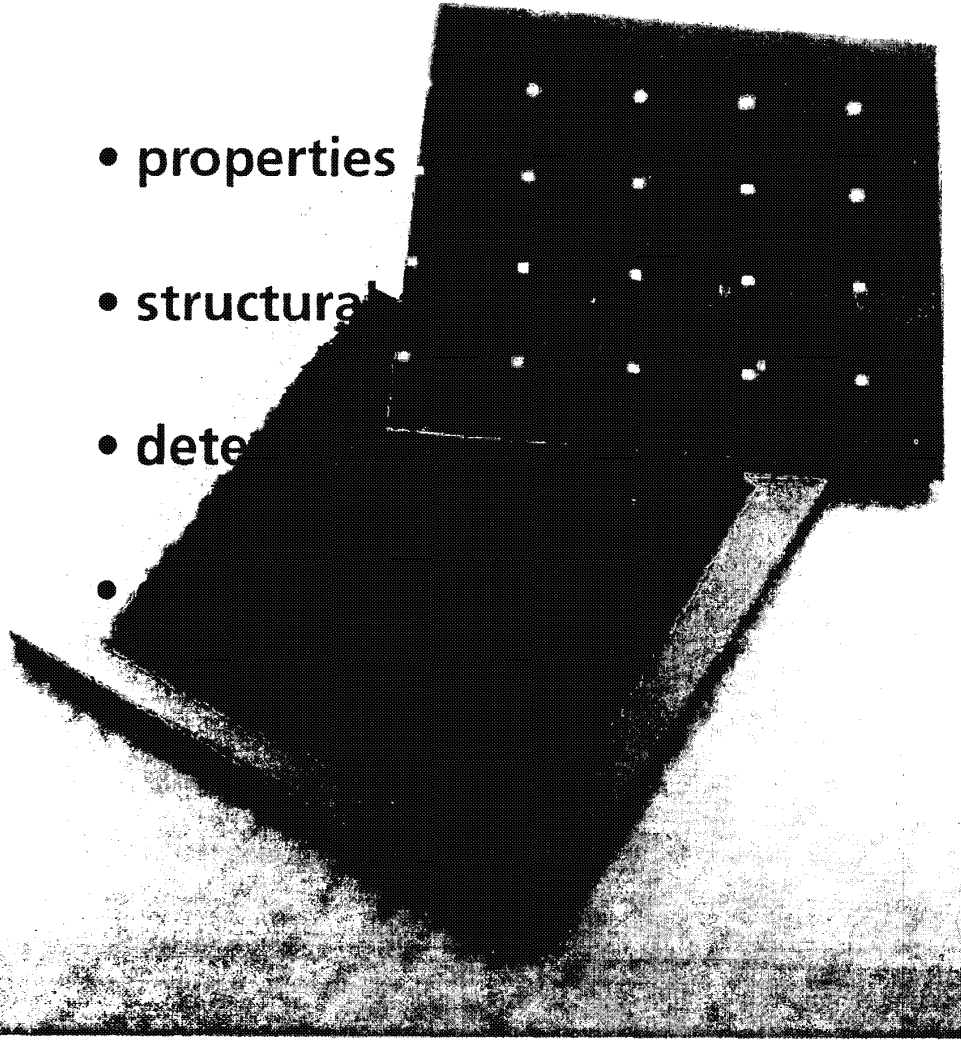
Detectors

Black silicon also promising for solar cells



SAMSUNG EX. 1002 - 2822/4148

Outline



- properties
- structura
- dete
-

SAMSUNG EX. 1002 - 2823/4148

SIONYX14030000029.0089

Outlook

A forest of silicon spikes could revolutionise solar cells and give you painless injections. **Bruce Schechter** peers into the mysterious world of black silicon

TALL, DARK AND STRANGER

WE ALL love stories of serendipity. They seem to hark back to a time when a fogged photographic plate or a filthy Petri dish could change the world. Even today, when financial constraints keep the role of chance to a minimum, science is still sometimes a spontaneous act, a freelance exploration of the unknown. It often starts in front of a blackboard when one scientist says, "I wonder what would happen if . . .", and the other one replies, "Let's give it a try."

The result of one such conversation two years ago in Eric Mazur's laboratory at ...rd University is a new form of sil- ... soot. What started life as ...ow has patents ... be-

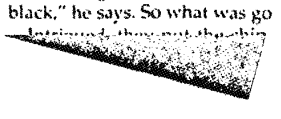
semiconductors with a powerful laser. In the early 1990s, Mazur's was the first academic lab in the world to get its hands on a femtosecond laser. This device produces pulses of light that are hundreds of billions of times brighter than the Sun. Its immense power is delivered extremely quickly: each pulse lasts a mere fraction of a trillionth of a second.

These flashes of laser light have provided researchers with a new way to probe the characteristics of many materials (*New Scientist*, 19 February 2000, p 34). Mazur's group was using the powerful femtosecond pulses to study the surface chemistry of metals. But Her, who is now at the Lawrence Livermore Laboratory in Calif- ...ia, had been wondering for years what ...ld do to semiconductors like ... tried it, so there

around the laboratory," he claims.

Well, it was almost the only reason. A short laser pulse will break down SF_6 into sulphur and fluorine radicals, which will attack a silicon substrate. "Hydrogen fluoride is used to etch silicon. So we thought maybe the SF_6 would decompose and then the fluorine would somehow react with the silicon," Mazur explains.

With no clearer idea than this, th researchers began firing 100-femtosecor pulses of laser light through the wind of their chamber, through the SF_6 gas onto the shiny silicon wafer. After f about 100 pulses they cracked the se the chamber and removed the wafer saw a tiny black spot at the focal p the laser beam. A burn, perhaps. that Mazur knew that silicon does "You can get silicon oxide, bu' black," he says. So what was go



New Scientist 13, 34 (2001)

SIONYX14030002600900

SAMSUNG EX. 1002 - 2824/4148

• **detector technology**

A forest of silicon spikes could revolutionise solar cells and give you painless injections. **Bruce S** peers into the my world of black sili



TALL, D AND STRANGER

WE ALL love stories of serendipity. They seem to hark back to a time when a fogged photographic plate or a tilting Petri dish could change the world. Even today, when financial constraints keep the role of chance to a minimum, science is still sometimes a spontaneous act, a freelance exploration of the unknown. It often starts in front of a blackboard when one scientist says, "I wonder what would happen if . . .", and the other one replies, "Let's give it a try."

The result of one such conversation two years ago in Eric Mazur's laboratory at [illegible] University is a new form of sil[illegible] spot. What started life as [illegible] way has patents [illegible] be[illegible]

semiconductors with a powerful laser. In the early 1990s, Mazur's was the first academic lab in the world to get its hands on a femtosecond laser. This device produces pulses of light that are hundreds of billions of times brighter than the Sun. Its immense power is delivered extremely quickly: each pulse lasts a mere fraction of a trillionth of a second.

These flashes of laser light have provided researchers with a new way to probe the characteristics of many materials (*New Scientist*, 19 February 2000, p 34). Mazur's group was using the powerful femtosecond pulses to study the surface chemistry of metals. But Her, who is now at the Lawrence Livermore Laboratory in California, had been wondering for years what would do to semiconductors like [illegible] tried it, so there [illegible] around the laboratory," he claims.

Well, it was almost the only reason. A short laser pulse will break down SF$_6$ into sulphur and fluorine radicals which will attack a silicon substrate. Hydrogen fluoride is used to etch silicon. So we thought maybe the SF$_6$ would decompose and then the fluorine would somehow react with the silicon," Mazur explains.

With no clearer idea than this, researchers began firing 500 femtosecond pulses of laser light through the window of their chamber, through the SF$_6$ gas, onto the shiny silicon wafer. After about 100 pulses they cracked the seal, flushed the chamber and retrieved the wafer. They saw a tiny black spot at the focal point of the laser beam. A quick peep-through that Mazur knew that silicon does not [illegible] can get silicon oxide [illegible] Black [illegible] esn't. So what was go[illegible]

New Scientist 13, 34 (2001)

SIONYX1403000029.0091

SAMSUNG EX. 1002 - 2825/4148

- **detector technology**
- **solar cells**

A forest of silicon spikes could revolutionise solar cells and give you painless injections. **Bruce S** peers into the my world of black sili



TALL, D AND STRANGER

WE ALL love stories of serendipity. They seem to hark back to a time when a fogged photographic plate or a filthy Petri dish could change the world. Even today, when financial constraints keep the role of chance to a minimum, science is still sometimes a spontaneous act, a freelance exploration of the unknown. It often starts at the foot of a blackboard when one scientist says, 'I wonder what would happen if ...', and the other one replies, 'Let's give it a try.'

The result of one such conversation two years ago in Eric Mazur's laboratory at [illegible] University is a new form of sil[illegible] stuff. What started life as [illegible] two US patents [illegible] be[illegible]

semiconductors with a powerful laser. In the early 1990s, Mazur's was the first academic lab in the world to get its hands on a femtosecond laser. This device produces pulses of light that are hundreds of billions of times brighter than the Sun. Its immense power is delivered extremely quickly, each pulse lasts a mere fraction of a trillionth of a second.

Those flashes of laser light have provided researchers with a new way to probe the characteristics of many materials (*New Scientist*, 19 February 2000, p 40). Mazur's group was using the powerful femtosecond pulses to study the surface chemistry of metals. But Her, who is now at the Lawrence Livermore Laboratory in California, had been conducting tests on a slice of [illegible] to see what happened to semiconductors like [illegible] if [illegible] so there [illegible] around the laboratory," he claims.

Well, it was almost the only reason. A spare laser pulse with Brook Jewett, SF into sulphur and fluorine radicals, which will attack a silicon substrate. Hydrogen fluoride is used to etch silicon. So [illegible] thought maybe the SF, would decompose and then the fluorine would somehow react with the silicon. Mazur explains:

With no clearer idea than this, the researchers began firing femtosecond pulses of laser light through the window of their chamber, through the SF, gas and into the shiny silicon wafer. After about 100 pulses they cracked the seal, lifted the lid and removed the wafer. They saw a tiny black spot at the focal point of the laser beam. A quick microscope test [illegible] Mazur knew that silicon [illegible] [illegible] [illegible] [illegible] [illegible]

New Scientist 13, 34 (2001)

SIONYX1403000029.0092

SAMSUNG EX. 1002 - 2826/4148

- **detector technology**
- **solar cells**
- **display technology**

A forest of silicon spikes could revolutionise solar cells and give you painless injections. **Bruce S.** peers into the my[illegible] world of black sili[illegible]



TALL, D[illegible] AND STRANGER

WE ALL love stories of serendipity. They seem to hark back to a time when a fogged photographic plate or a filthy Petri dish could change the world. Even today, when financial constraints keep the role of chance to a minimum, science is still sometimes a spontaneous act, a reckless exploration of the unknown. It often starts in front of a blackboard, when one scientist says, "I wonder what would happen if ..." and the other one replies, "Let's give it a try."

The result of one such conversation two years ago in Eric Mazur's laboratory at Harvard University is a new form of silicon. What started his[illegible] was[illegible] way has patents [illegible] ... ive semiconductors with a powerful laser. In the early 1990s, Mazur's was the first academic lab in the world to get its hands on a femtosecond laser. This device produces pulses of light that are hundreds of billions of times brighter than the Sun. Its immense power is delivered extremely quickly: each pulse lasts a mere fraction of a trillionth of a second.

These flashes of laser light have provoked researchers with a new way to probe the characteristics of many materials (*Science*, vol 288, p 1758). Mazur's group was using the powerful femtosecond pulses to study the surface chemistry of metals. But Her, who is now at the Lawrence Livermore Laboratory in California, had been wondering for years what he did to semiconductors [illegible] ... the [illegible] trees around the laboratory. "He claims [illegible]

Well, it was almost the only reason. A short laser pulse with enough power to irradiate sulphur dioxide or some radicals which will attack a silicon substrate. Hydrogen fluoride is used to etch silicon. So it thought maybe the gas would decompose and then the fluorine would somehow react with the silicon. Mazur explains:

With no clearer idea than this, the researchers began firing femtosecond pulses of laser light through the window of their chamber, through the SF$_6$ gas onto the shiny silicon wafer. After about 30 pulses they could see that the surface had changed colour and textured like velvet. Even to the naked eye, tiny flecks spot the face of the laser beam. A guess perhaps that Mazur knew that silicon [illegible] "And we got silicon oxide [illegible] black. [illegible] SF$_6$ Mazur's group [illegible]

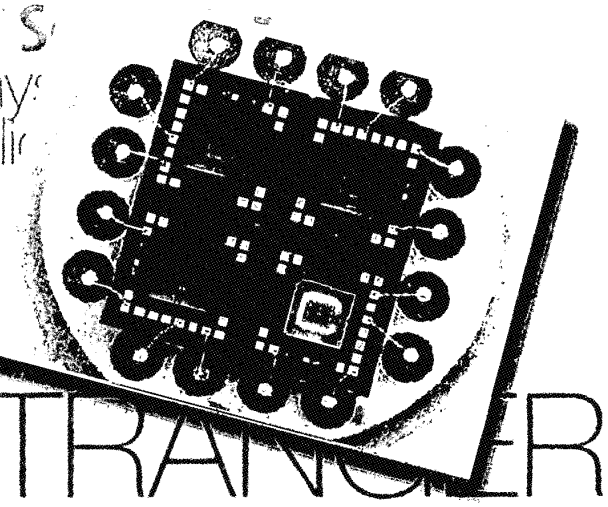
New Scientist 13, 34 (2001)

SIONYX1403000026.0093

SAMSUNG EX. 1002 - 2827/4148

- detector technology
- solar cells
- display technology
- biosensing

A forest of silicon spikes could revolutionise solar cells and give you painless injections. Bruce S[illegible] peers into the mys[illegible]orld of black sili[illegible]



TALL, D[illegible] AND STRANG[illegible]ER

WE ALL love stories of serendipity. They seem to hark back to a time when a fogged photographic plate or a dribby Petri dish could change the world. Even today, when financial constraints keep the role of chance to a minimum, science is still sometimes a spontaneous act, a reclame exploration of the unknown. It often starts in front of a blackboard when one scientist says, "I wonder what would happen if ..." and the other one replies, "Let's give it a try."

The result of one such conversation two years ago in Eric Mazur's laboratory at Harvard University is a new form of silicon. What started life as a [illegible] has patents [illegible] bec[illegible] semiconductors with a powerful laser. In the early 1990s, Mazur's was the first academic lab in the world to get its hands on a femtosecond laser. This device produces pulses of light that are *hundreds of billions* of times brighter than the Sun. Its immense power is delivered extremely quickly: each pulse lasts a mere fraction of a trillionth of a second.

These flashes of laser light have provided researchers with a new way to probe the characteristics of many materials (*New Scientist*, 19 February 2000, p 34). Mazur's group was using the powerful femtosecond pulses to study the surface chemistry of metals. But Her, who is now at the Lawrence Livermore Laboratory in California, had been wondering for years what would happen to semiconductors like [illegible] around the laboratory," he claims.

Well, it was almost the only reason. A short laser pulse will break down Si, into sulphur and fluorine radicals which will attack a silicon substrate. Hydrogen fluoride is used to etch silicon. So we thought maybe the SF, would decompose and then the fluorine would somehow react with the silicon," Mazur explains.

With no clearer idea than this, the researchers began firing femtosecond pulses of laser light through the wind[illegible] of their chamber, through the SF, gas onto the shiny silicon wafer. After about 500 pulses they cracked the [illegible] their camera and retrieved the wafer. [illegible] saw a tiny black spot at the focal [illegible] the laser beam. A hunch, perhaps, that Mazur knew that silicon does [illegible] You can get silicon's side [illegible] back," he says. So [illegible]

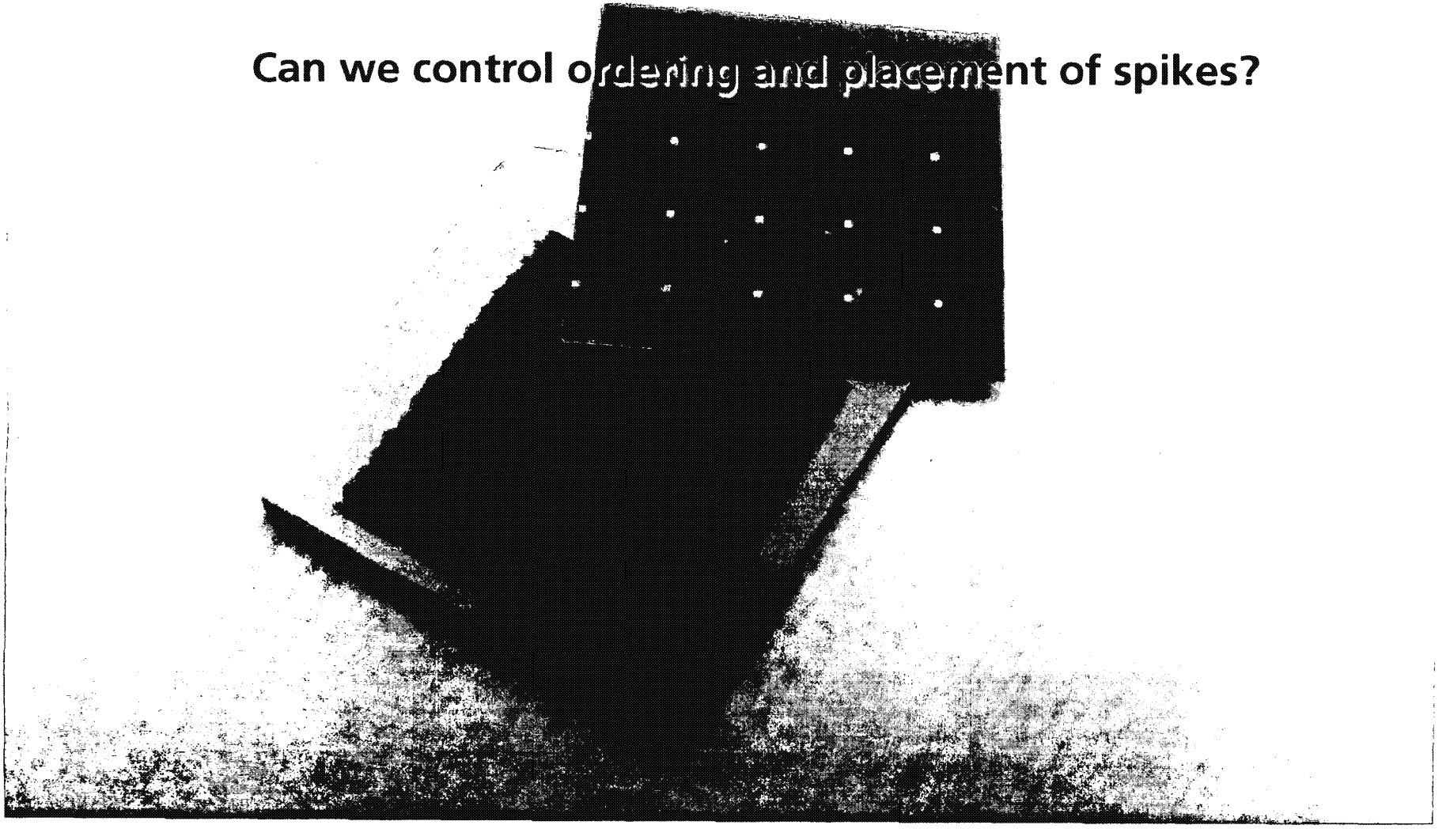
New Scientist 13, 34 (2001)

SIONYX1403000029.0064

SAMSUNG EX. 1002 - 2828/4148

Detectors

Can we control ordering and placement of spikes?



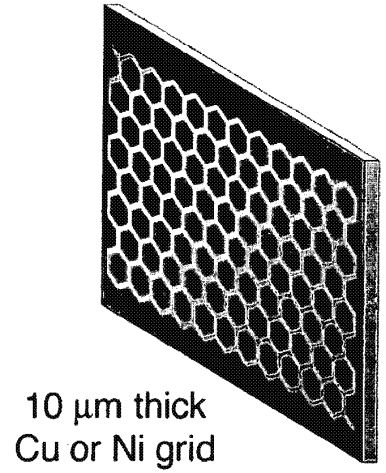
SAMSUNG EX. 1002 - 2829/4148

Outlook

SAMSUNG EX. 1002 - 2830/4148

Outlook

place grid in front of sample

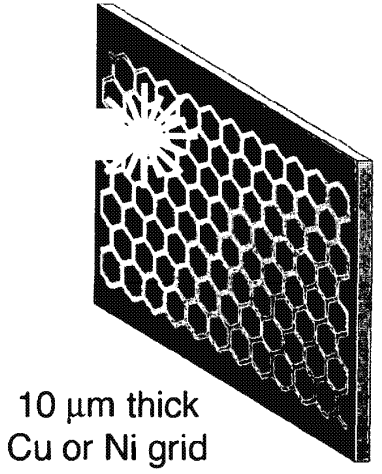


SIONYX1403000029.0097

SAMSUNG EX. 1002 - 2831/4148

Outlook

scan laser beam



10 μm thick
Cu or Ni grid

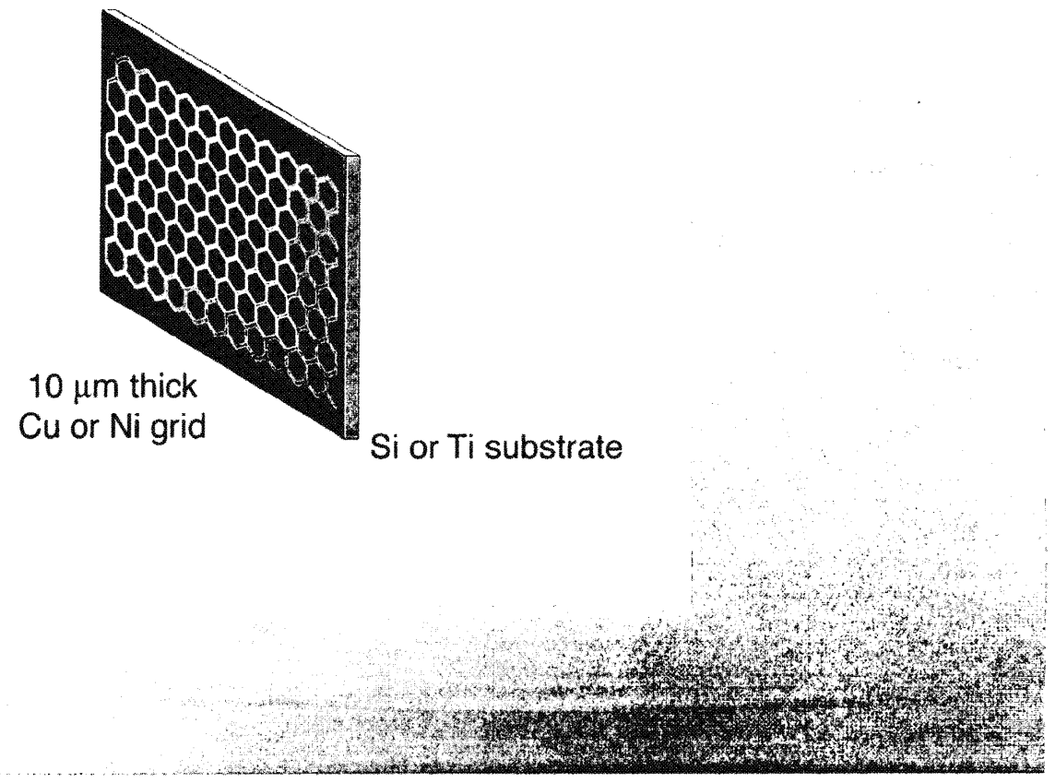
Si or Ti substrate

SIONYX1403000029.0098

SAMSUNG EX. 1002 - 2832/4148

Outlook

scan laser beam

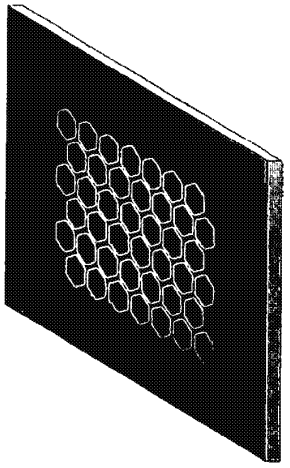


SIONYX1403000029.0099

SAMSUNG EX. 1002 - 2833/4148

Outlook

remove grid



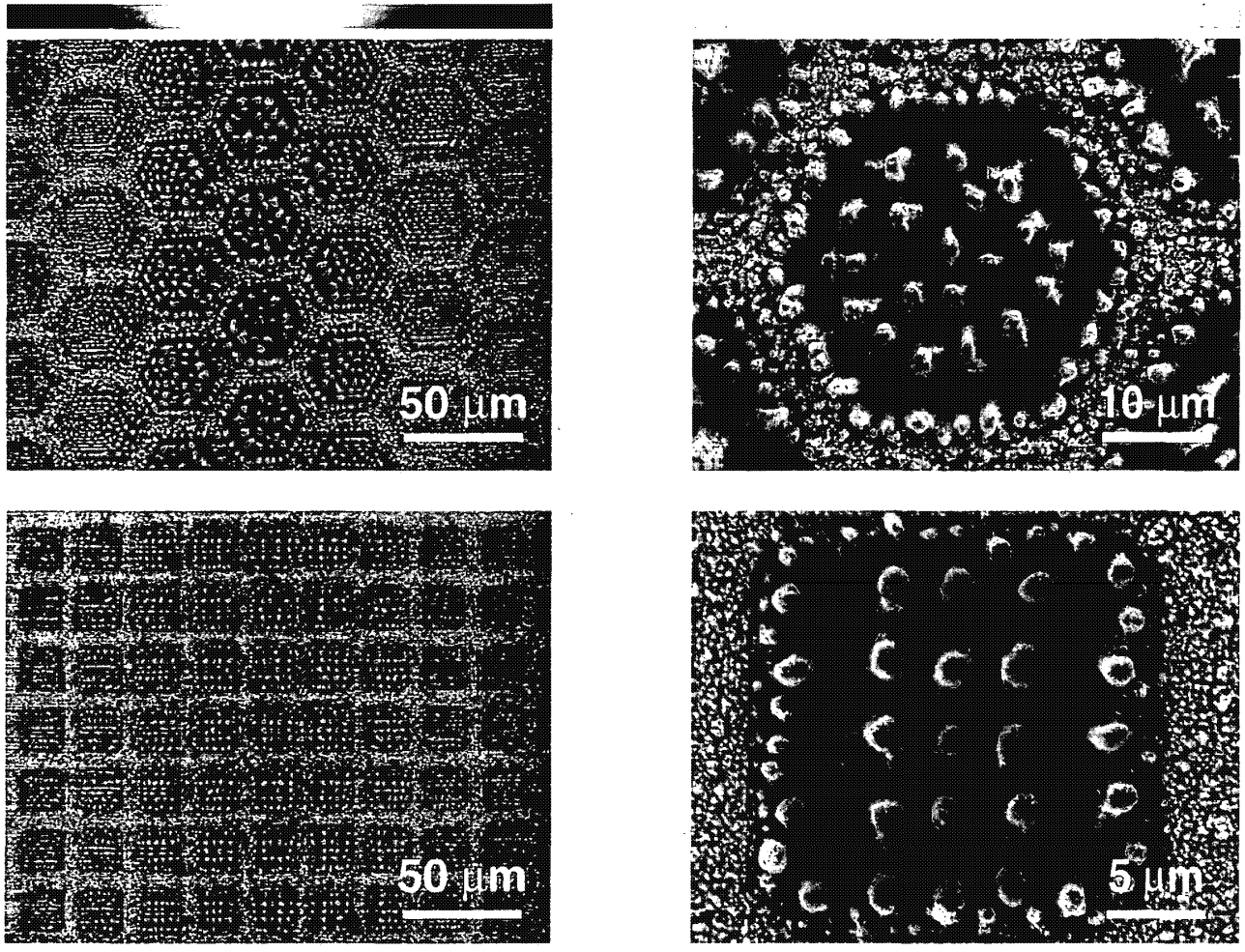
Si or Ti substrate

SIONYX1403000029.0100

SAMSUNG EX. 1002 - 2834/4148

SIONYX1403000029.0101

Outlook



Appl. Phys. Lett., **82**, 1715 (2003)

SIONYX1403000029.0102

SAMSUNG EX. 1002 - 2836/4148

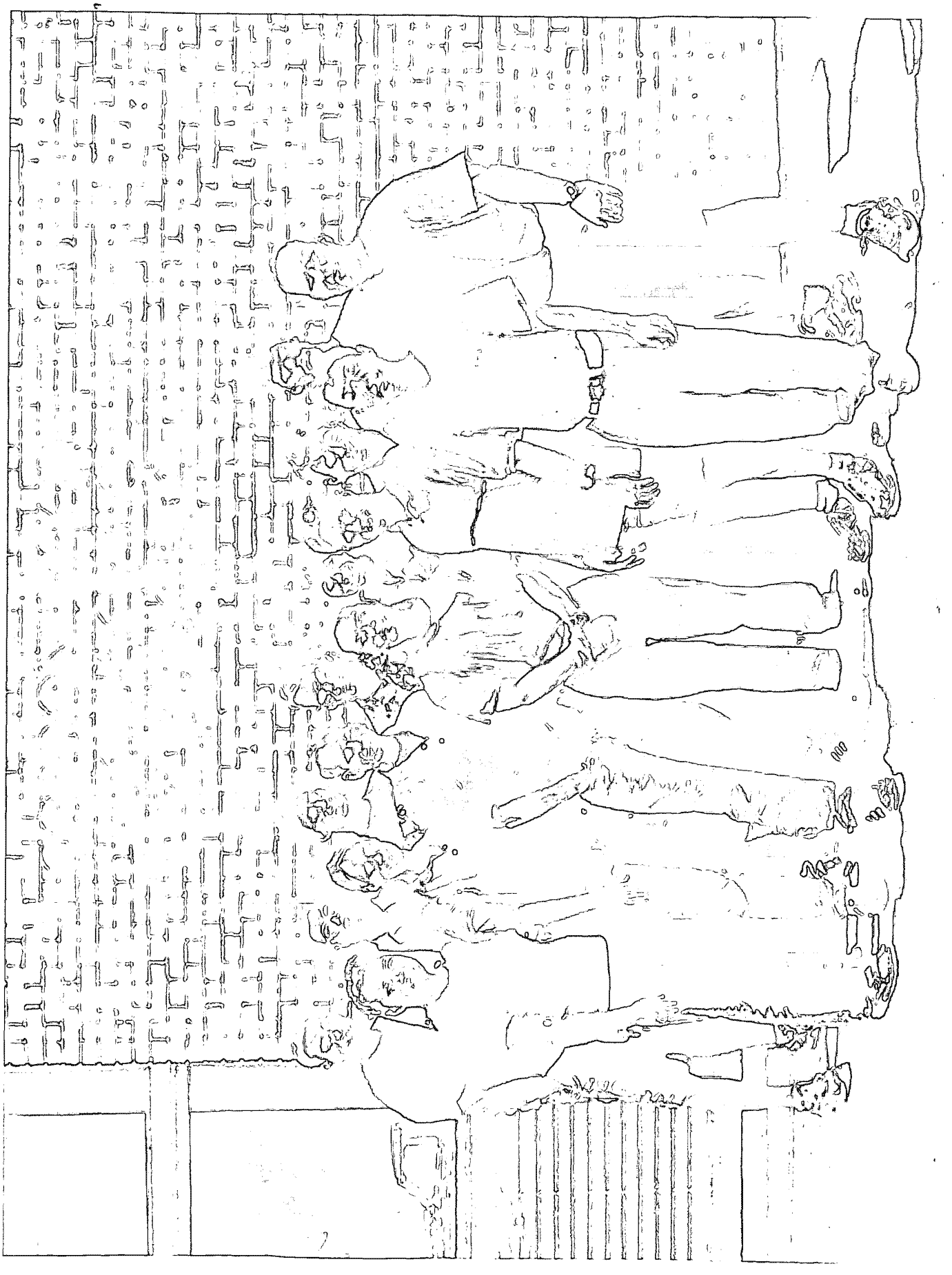
Summary

Summary

- near unity absorption from near-UV to near-IR
- maskless process, easily integrated with microelectronics
- grid improves positioning and spacing
- many promising applications

SIONYX1403000029.0104

SAMSUNG EX. 1002 - 2838/4148



SIONYX1403000029.0105

SAMSUNG EX. 1002 - 2840/4148

e4

High sensitivity silicon-based VIS/NIR photodetectors

J. E. Carey and E. Mazur

Harvard University, Division of Engineering & Applied Sciences and Department of Physics, 9 Oxford St, Cambridge, MA 02138, USA
jcarey@fas.harvard.edu

Abstract:

We fabricate silicon-based photodiodes using a simple femtosecond-laser microstructuring technique. The detectors are ten times more sensitive than commercial silicon PIN photodiodes at visible wavelengths and can be used at wavelengths up to 1650 nm.

© 2003 Optical Society of America

OCIS codes: (040.6040) Silicon; (040.3060) Infrared

Silicon is the most commonly used semiconductor in microelectronics and optoelectronic devices but a band gap of 1.07 eV limits the photoresponse to wavelengths shorter than 1100 nm. Consequently, silicon photodetectors are insensitive to the two primary telecommunications wavelengths, 1300 nm and 1550 nm. Therefore, extending the sensitivity of silicon-based photodetectors to longer infrared wavelengths is an active area of research [1, 2, 3].

We previously reported that silicon surfaces microstructured in the presence of sulfur containing gases with high-intensity femtosecond laser pulses have near-unity absorption from the near-ultraviolet (250 nm) to the near-infrared (2500 nm)[4, 5]. Here we report that under reverse bias, these microstructured surfaces can be used to fabricate photodiodes that are sensitive to infrared wavelengths up to 1650 nm and that have greatly enhanced photoresponse to visible wavelengths.

We irradiate n-doped, Si (111) wafers (ρ = 800–1200 $\Omega \cdot$ cm) with a 1-kHz train of 100-fs laser pulses at normal incidence in an 0.67-bar atmosphere of SF_6. Each pulse has an average fluence of 4 kJ/m^2 and a 1/e spot size of 150 x 150 mm^2. In order to structure an area larger than this spot size, the silicon wafer is translated relative to the laser beam at a speed such that any given spot on the surface is exposed to an average of 500 pulses. The resulting surface is covered with conical microstructures that are 2–3 μm tall and spaced by 2–3 μm; the uppermost few hundred nanometers of the microstructures are modified, with crystalline silicon beneath [6].

Electrical
contacts are then fabricated by thermal evaporation of a 4-nm layer of chrome followed by a 100-nm layer of gold on both the structured and unstructured sides. Metal is deposited on the entire unstructured side; on the microstructured side, metal is deposited in two circular areas 1 mm in diameter and 3 mm apart center-to-center. The resulting devices have a 2 × 4 mm^2 active area. Figure 1 shows a schematic diagram of a vertical cross-section through the device and a bright-field transmission electron micrograph of a cross-section of the interface between the laser-affected surface layer.

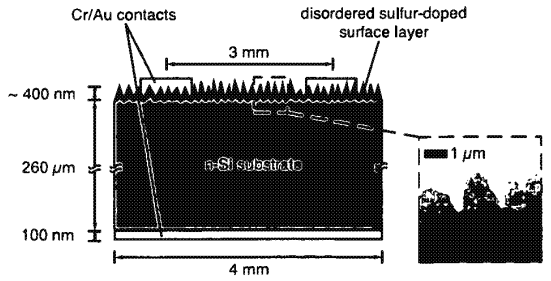


Fig. 1. Schematic diagram of a vertical cross-section through the microstructured silicon photodiode. The dashed box shows a bright-field transmission electron micrograph of the interface between the disordered layer and the crystalline silicon substrate.

SIONYX1403000029.0107

SAMSUNG EX. 1002 - 2841/4148

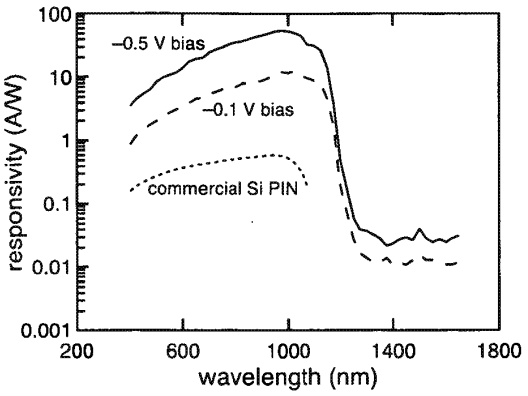


Fig. 2. Spectral responsitivity (wavelength dependence of photocurrent per unit incident power) of microstructured silicon photodiode at a bias of –0.1 V and –0.5 V. The spectral responsivity of the silicon photodiode used for calibration is also shown.

Figure 2 shows the spectral responsivity of the microstructured silicon at a bias of –0.1 V and –0.5 V as well as the responsivity of the standard silicon PIN photodiode used for calibration. At a bias of –0.1 V, the responsivity of the device is greater than 1 A/W for wavelengths from 400 nm to 1175 nm, with a peak responsivity of 12.1 A/W at 975 nm. These responsivities are nearly ten times greater than those of commercially available silicon PIN photodiodes. At longer wavelengths (1200–1650 nm), the responsivity is weaker, but still remarkably high for silicon based devices. For a bias of –0.5 V bias, the responsivity is 38 mA/W at 1300 nm and 25 mA/W at 1550 nm – four orders of magnitude higher than responsivities measured in silicon avalanche photodiodes before amplification [7].

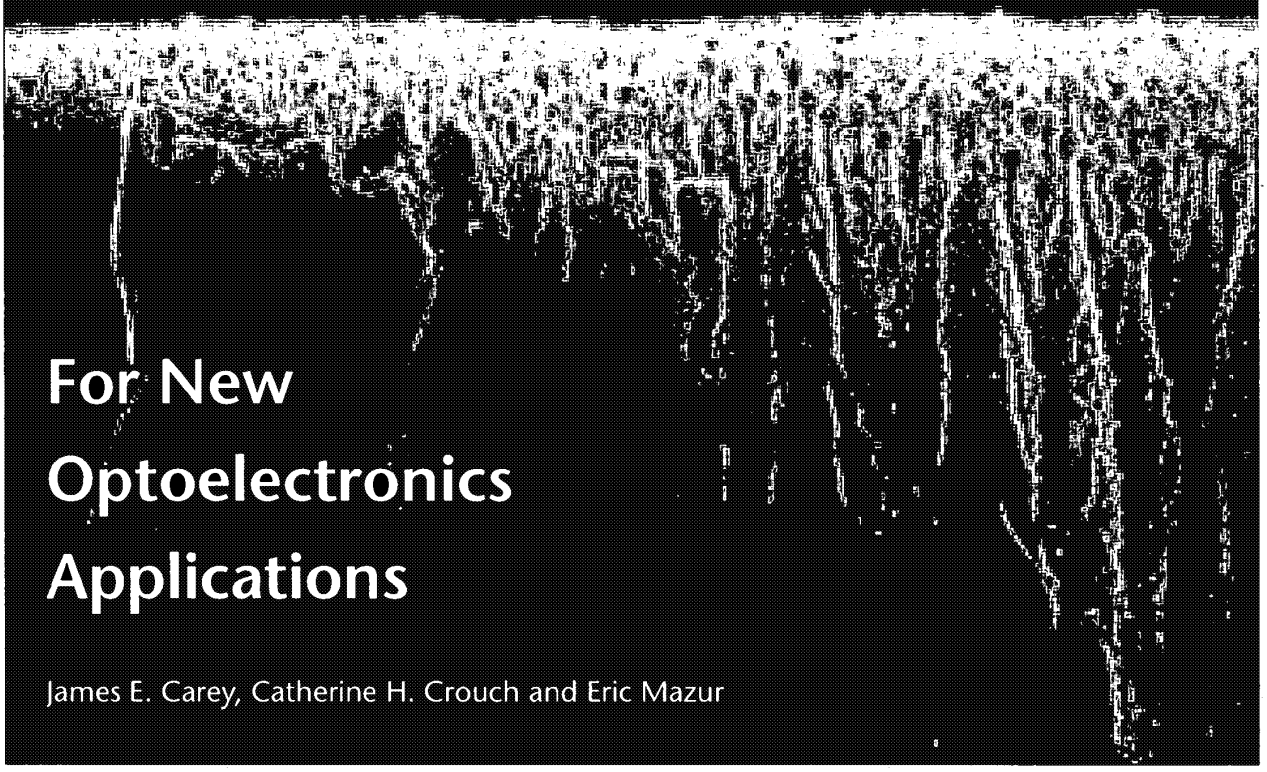
References

1. A. Loudon, P. Hiskett, G. Buller, R. Carline, D. Herbert, W. Y. Leong, and J. Rarity, *Opt. Lett.*, **27**, 219 (2002).
2. Z. Lo, R. Jiang, Y. Zheng, L. Zang, Z. Chen, S. Zhu, X. Cheng, and X. Liu, *Appl. Phys. Lett.*, **77**, 1548 (2000).
3. M. Elkurdi, R. Boucaud, S. Sauvage, O. Kermarrec, Y. Campidelli, D. Bensahel, G. Saint-Girons, and I. Sagnes, *Appl. Phys. Lett.*, **80**, 509 (2002).
4. C. Wu, C. H. Crouch, L. Zhao, J. E. Carey, R. Younkin, J. A. Levinson, E. Mazur, R. M. Farrell, P. Gothoskar, and A. Karger, *Appl. Phys. Lett.*, **78**, 1850 (2001).
5. R. Younkin, J. E. Carey, E. Mazur, J. A. Levinson, and C. M. Friend, *J. Appl. Phys.*, **93**, 2626 (2003).
6. C. H. Crouch, J. E. Carey, M. Shen, E. Mazur, and F. Y. Genin, *submitted to Appl. Phys. A.*
7. M. Ghioni, A. Lacaita, G. Ripamonti, and S. Cova, *IEEE J. Quantum Electronics*, **28**, 2678 (1992).

SAMSUNG EX. 1002 - 2842/4148

C6

Femtosecond-Laser-Assisted Microstructuring



For New Optoelectronics Applications

James E. Carey, Catherine H. Crouch and Eric Mazur

Silicon, thoroughly characterized and inexpensive, is the most widely used substrate for semiconductor microelectronics. From computer chips to photodetectors, silicon has found its way into countless commercial applications. Ordinary silicon has certain limitations as far as optoelectronics is concerned, however. For example, because it is transparent to the near-infrared radiation wavelengths used for telecommunications (1.3 μm and 1.55 μm), it cannot be used to detect these wavelengths. Because of its indirect bandgap, it is also a poor light emitter. We developed a technique for microstructuring silicon surfaces with femtosecond laser pulses that overcomes some of these shortcomings. The resulting microstructured surfaces have novel optoelectronic properties that provide new functionality for silicon.[1,2]

After we irradiate the surface of a silicon wafer with a 1-kHz train of 100-fs, 800-nm laser pulses of fluence 8kJ/m^2 in an environment of sulfur hexafluoride (SF_6), the originally shiny surface of the wafer becomes velvet black. Scanning electron microscopy reveals that the laser-treated surface is covered with a quasi-ordered array of conical microstructures. Figure 1 (page 34) shows a macroscopic view of a microstructured silicon wafer and a scanning electron micrograph of the surface. Areas ranging from tens of micrometers to tens of millimeters in diameter can be microstructured without the use of lithographic masks. The process also yields reproducible average spacing, height and aspect ratio of the conical microstructures.

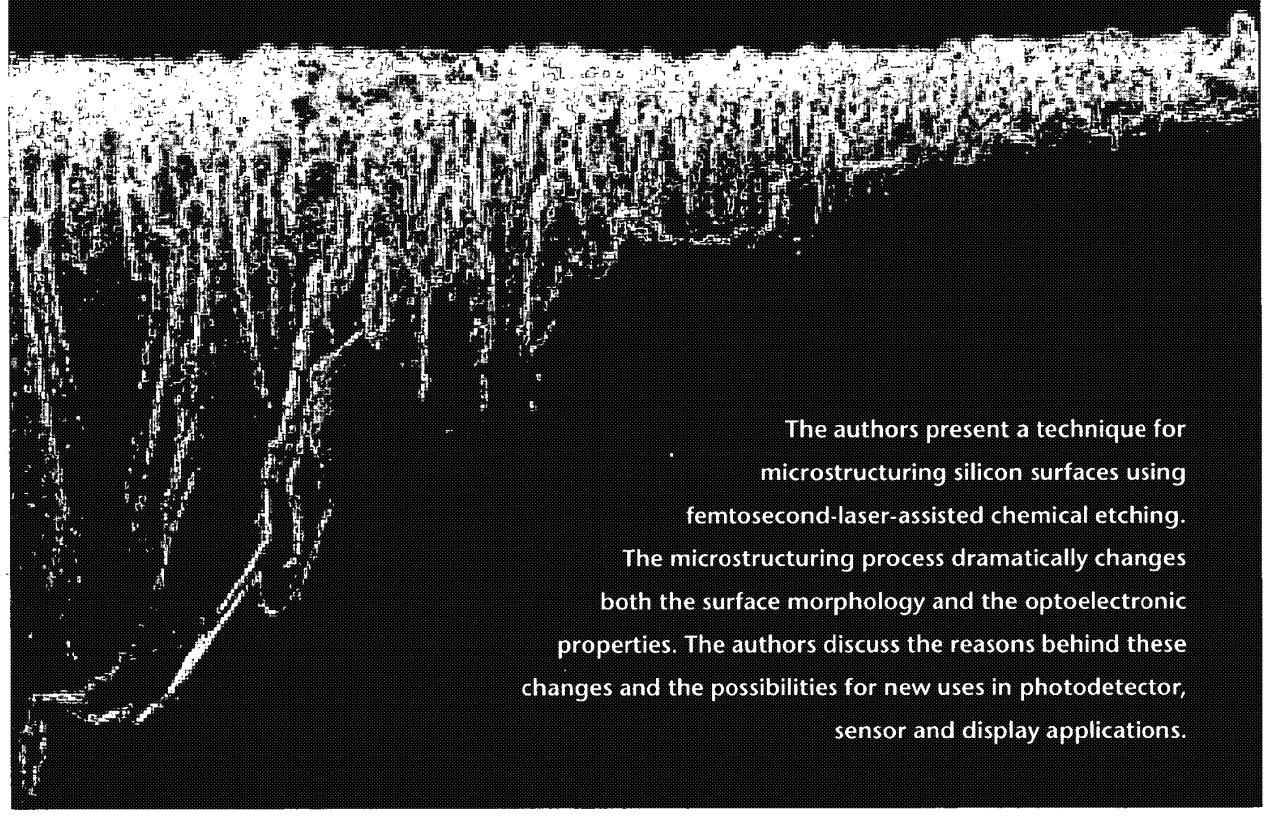
A series of scanning electron micrographs showing the development of the surface structure is shown in Fig. 2. When the first laser pulse strikes the silicon surface, the energy deposited in the material near the surface creates a plasma, melting the surface and producing a plume of ablated material. The plasma dissociates the normally inert SF_6 molecules, and fluorine radicals react with the molten silicon surface. The volatile species created in these reactions can either travel away from the surface with the expanding plasma or diffuse into the molten surface. After a few microseconds, the surface

1047-6938/03/02/0032/5-$15.00 © Optical Society of America

SIONYX1403000029.0109

SAMSUNG EX. 1002 - 2843/4148

of Silicon Surfaces



The authors present a technique for microstructuring silicon surfaces using femtosecond-laser-assisted chemical etching. The microstructuring process dramatically changes both the surface morphology and the optoelectronic properties. The authors discuss the reasons behind these changes and the possibilities for new uses in photodetector, sensor and display applications.

resolidifies and some of the ejected material is redeposited. When the next laser pulse strikes this roughened surface, the incident laser light reflects off the sides of the protrusions and more energy is absorbed in the valleys between protrusions than on the tips of the protrusions. Subsequent pulses therefore preferentially remove material between protrusions, resulting in the formation of conical microstructures.

Optical properties of microstructured silicon

The striking blackness of the microstructured surfaces indicates that the optical properties of the silicon substrate have been altered. To quantify the optical properties, we measured the transmittance and reflectance of a microstructured sample using a spectrophotometer equipped with a spherical detector that collects all transmitted or scattered light. The spherically integrated reflectance, R, and transmittance, T, were then used to obtain the absorptance, A, of the material using the formula: $A=1-R-T$. Figure 3 shows the absorptance of silicon measured before and after microstructuring in an SF_6 atmosphere as a function of wavelength from 250 nm to 2500 nm. The absorptance for visible wavelengths increases from about 65% to nearly 95%, giving rise to the black appearance of the surface after microstructuring.

The increased absorption of visible light can be explained by the multiple reflections that occur when incident light strikes the sharp conical microstructures. Based on the geometry of the microstructures, we find that incident light on average experiences four reflections. Using the optical properties of unstructured silicon, we find that the overall absorptance of the sample in the visible region of the spectrum increases to over 90% after four reflections.

Multiple reflections, however, cannot account for the surprisingly high absorption of light with wavelengths from 1.1 to 2.5 μm. Because the minimum in the bandgap energy of silicon is 1.07 eV, corresponding to a wavelength of about 1.1 μm, the absorptance of infrared light by intrinsic, unstructured silicon is very small. Simply increasing the number of reflections cannot cause the observed

SIONYX1403000029.0110

SAMSUNG EX. 1002 - 2844/4148

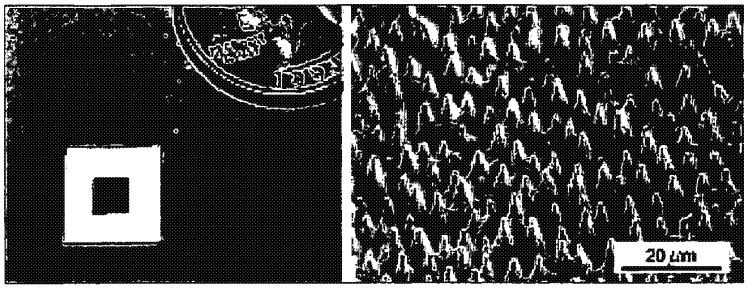


Figure 1. *Left:* Picture of a microstructured silicon wafer. The microstructured area appears black to the eye in contrast to the silvery appearance of the unstructured area. *Right:* A scanning electron micrograph of the microstructured surface.

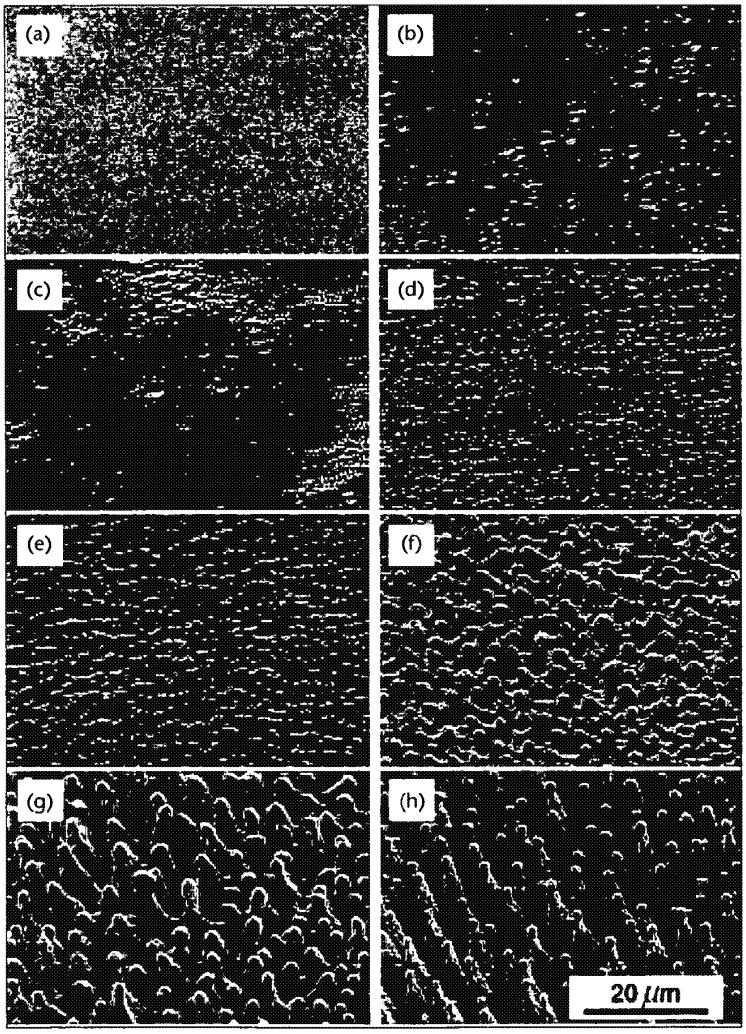


Figure 2. Series of scanning electron micrographs showing the development of the surface morphology with increasing number of laser pulses. The number of laser pulses shown are: (a) 0, (b) 1, (c) 2, (d) 5, (e) 8, (f) 20, (g) 50 and (h) 600 pulses. The spot size of the incident beam has a diameter of 150 μm, larger than the area shown in the micrographs.

near-unity infrared absorptance. Furthermore, thermal annealing of the microstructured surface causes a significant drop in infrared absorptance without changing the surface morphology. We therefore conclude that the band structure of the material is very different from that of ordinary silicon.

The high infrared absorptance of microstructured silicon opens up the possibility of developing broadband silicon photodetectors sensitive to infrared regions of the spectrum. To function as a photodetector, however, the absorption must create photocarriers that can be collected and turned into an electronic signal. In collaboration with Radiation Monitoring Devices of Watertown, Massachusetts, we performed a proof-of-principle experiment to demonstrate that microstructured silicon can be used for infrared photodetection. By microstructuring the detection area of a commercial avalanche photodiode, we produced a significant increase in the photocurrent generated by 1.3 μm radiation. The unstructured avalanche photodiode showed no response to 1.3 μm radiation at bias voltages below 900 volts. After microstructuring, the photodiode responded to illumination at 1.3 μm with bias voltages as low as 400 V and the photocurrent generated for bias voltages above 900 V increased three-fold. We also demonstrated a thirty percent increase in the quantum efficiency of avalanche photodiodes at 1.064 μm. Inexpensive silicon-based photodetectors at these wavelengths would be extremely useful for both research and communications.

Field emission properties of microstructured silicon

When a potential difference is applied across sharp tips, such as those of microstructured silicon, the electric field lines are concentrated near the tips, greatly enhancing the strength of the electric field in the vicinity of the tip. This geometric enhancement can make the electric field so strong that it reduces the potential barrier for electrons to escape from the material. If the barrier is lowered far enough, quantum mechanical tunneling allows electrons to be emitted from the surface, a process known as field emission. Cathodes based on field emis-

SIONYX1403000029.0111

SAMSUNG EX. 1002 - 2845/4148

sion are much more efficient than those based on thermionic emission from resistive heating, such as those found in conventional cathode ray tubes.

We have found that silicon microstructured in SF_6 has remarkable field emission characteristics. Figure 4 shows the current versus voltage characteristics for a 2 × 2 mm² sample of microstructured silicon. The so-called turn-on field—that is, the magnitude of the applied electric field necessary to achieve an emission current density of 10 nA/mm²—is only 1.2 V/μm, equal to the lowest turn-on field achieved with carbon nanotube field emitters. Moreover, microstructured silicon achieves a stable current density that is slightly higher than that of carbon nanotubes (12 versus 10 mA/mm², respectively[3]) at an applied field of 100 V/μm and the silicon microstructures are more robust as field emitters than those based on carbon nanotubes. Emission remains constant for several days even at high current and the field emission properties do not degrade after months of exposure to the atmosphere.

Because of the potential for efficient and inexpensive operation, the development of silicon-based field emitters has recently received much attention. Possible applications of field emission arrays include flat panel displays and microwave amplification. Conventional techniques for fabricating micrometer-sized silicon-tip arrays require a multistep process, including photolithography, etching and oxidation. Femtosecond laser microstructuring, on the other hand, provides a simple one-step method for fabricating powerful and efficient silicon-based field-emission arrays.

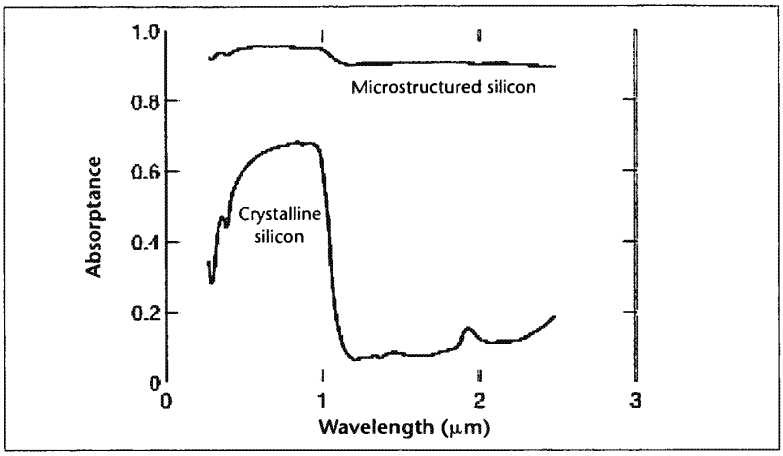


Figure 3. Absorptance of crystalline silicon and microstructured silicon as a function of wavelength from 250 nm to 2500 nm.

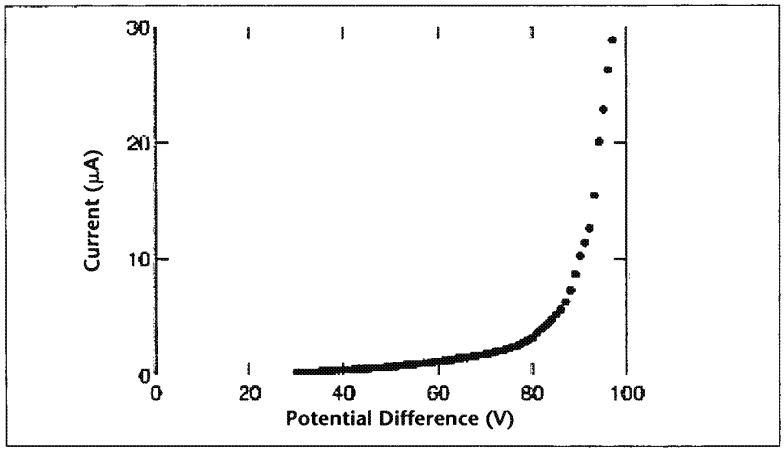


Figure 4. Current versus voltage characteristics for microstructured silicon with an anode-cathode spacing of 20 μm.

What causes the altered optoelectronic properties?

As stated earlier, the high infrared absorptance indicates that the band structure of the structured silicon is different from that of ordinary silicon. We investigated the chemical and structural composition of the structured surface to determine what might be responsible for the altered band structure. Using secondary ion mass spectrometry, we characterized the chemical species present at the surface of the microstructures formed in SF_6. Briefly, an energetic beam of ions is used to sputter secondary ions off the surface; the chemical composition of the sputtered material is then analyzed by means of mass spectrometry. The measurements show that sulfur makes up about 1 part in 10^3 of the surface. Other groups have reported incorporation of elements into silicon after irradiation with longer-pulse and continuous wave lasers, but the concentrations previously reported are orders of magnitude smaller than the concentrations we obtain with femtosecond irradiation.[4,5]

Studies of crystalline silicon doped with sulfur by diffusion implantation show that sulfur concentrations of 1 part in 10^9 produce localized donor states within the bandgap.[6] We believe that at the very high concentrations of sulfur achieved after femtosecond laser microstructuring in SF_6, these states broaden to form an impurity band within the bandgap. This allows infrared light to promote electrons from this impurity band into the conduction band.

In addition, the large concentration of electrons at higher energy states contributes to the field emission current, which explains the high emission currents we observe.

SIONYX1403000029.0112

SAMSUNG EX. 1002 - 2846/4148

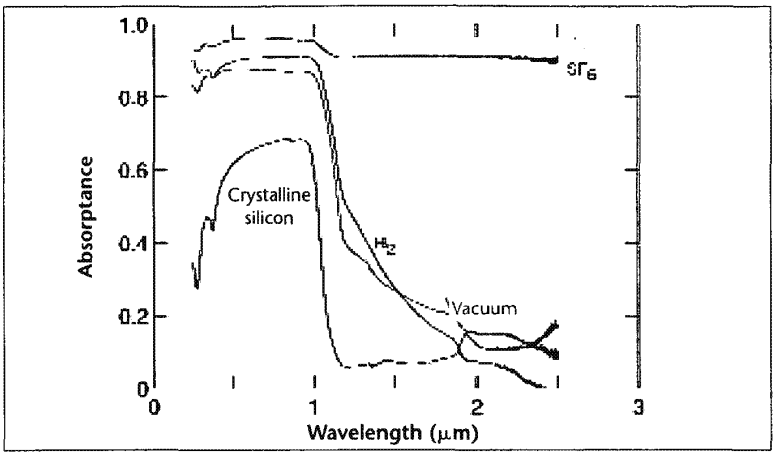


Figure 5. Absorptance of silicon microstructured in various sulfur-containing and non-sulfur-containing environments as a function of wavelength from 250 nm to 2500 nm.

By microstructuring silicon in other gases, we obtained additional evidence for the role of sulfur. Figure 5 shows the absorptance for silicon microstructured in these different gases. A silicon wafer irradiated in an ambient atmosphere of Cl_2 is covered in microstructures that are similar in morphology to those made in SF_6, but does not display high infrared absorption or high field emission current. Furthermore, silicon microstructured in H_2S exhibits near-unity infrared absorption, whereas silicon microstructured in H_2 does not. Finally, annealing a SF_6 sample decreases both the sulfur concentration and the near-infrared absorptance by approximately a factor of two. These observations strongly suggest that sulfur impurities are responsible for the high infrared absorptance and field emission current of the microstructures formed in SF_6.

Future directions

By altering the morphology and optoelectronic properties of silicon, we have created a novel material for near-infrared light detection and field emission devices. By varying the sample material, laser conditions, and the ambient gas, we can also produce other surfaces with unique optoelectronic properties. For example, after irradiating a silicon wafer in air, we obtain the rounded microstructures with a large amount of nanostructure shown in the top of Fig. 6. Chemical analysis of the air-structured sample shows that the irradiation forms a layer of silicon-rich silica, or SiO_x ($x<2$), at the surface. This substoichiometric silicon dioxide surface is photoluminescent, highly robust, and does not degrade over time when exposed to air.[7]

Because microstructuring increases the surface area of the material by more than an order of magnitude, it offers a promising strategy for making silicon-based chemical or biological sensors. We are therefore developing approaches for terminating the microstructured surface with molecules that have attachment sites for specific chemical species. Changes in an optoelectronic property of the surface, such as photoluminescence, can then be used to monitor attachment of this chemical species.

Finally, by covering the substrate with a copper grid containing micrometer-scale holes, we have made patterned regions of microstructures as shown in the bottom of Fig. 6.[8] These pixel-sized regular arrangements of microstructures are ideal for field emission displays. In addition to restricting the area of the surface exposed, the masks impose sharp boundary conditions on the irradiated material and produce more regularly arranged microstructures within each pixel.

The novel optoelectronic properties and ease of integration into microelectronics make microstructured silicon an attractive substrate for use in detectors, sensors and display technologies. We continue to find new applications and properties of interest from substrates microstructured using femtosecond laser pulses.

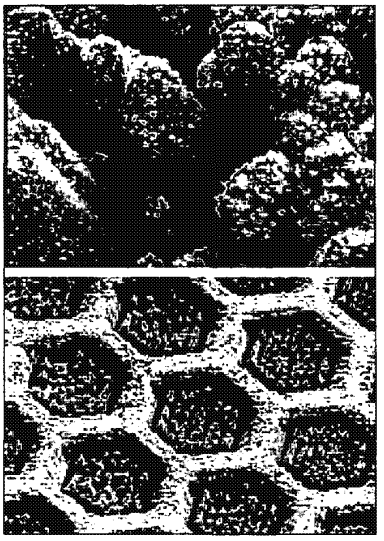


Figure 6. *Top:* Scanning electron micrograph of a silicon surface microstructured in air. *Bottom:* Scanning electron micrograph of a titanium surface microstructured with a hexagonal copper grid covering the substrate.

Acknowledgments

The authors thank Rebecca Younkin, Michael Sheehy, Mengyan Shen, Cynthia Friend, Tom Mates, Rick Meyers, Richard Farrell and Arieh Karger for their participation in the experiments described in this article. This work was funded by the Army Research Office, the National Science Foundation and the Department of Energy. James Carey acknowledges the NDSEG for fellowship support throughout these experiments.

References

Please see OPN Feature Article References, page 49.

James E. Carey (jcarey@fas.harvard.edu) is a research assistant in the Division of Engineering and Applied Sciences, Harvard University, Cambridge, Massachusetts. Catherine H. Crouch is a post-doctoral fellow in the Division of Engineering and Applied Sciences at Harvard University. Eric Mazur is a professor in the Department of Physics and Division of Engineering and Applied Sciences at Harvard University.

SIONYX1403000029.0113

SAMSUNG EX. 1002 - 2847/4148

Feature Article References

Note: References in OPN feature articles are published exactly as submitted by the authors.

Optoelectronic Microsystems Integration for System-on-a-Package and System-on-a-Chip Applications 26

Nan Marie Jokerst, Martin A. Brooke, Sang-Yeon Cho, Dae-Ik Kim, Mikkel Thomas and Suzanne Fike

1. S. K. Tewksbury and L. A. Hornak, "Optical clock distribution in electronic systems," Journ. VLSI Sig. Pro., vol. 16, 1997, pp. 225-246.
2. Rassaian, M.; Beranek, M.W., "Quantitative characterization of 96.5Sn3.5Ag and 80Au20Sn optical fiber solder bond joints on silicon micro-optical bench substrates," IEEE Trans. on Adv. Pack., vol. 22, 1999, pp. 86-93.
3. S. J. Walker and J. Jahns, "Optical clock distribution using integrated free-space optics," Opt. Comm., vol. 90, 1992, pp. 359-371.
4. P. J. Delfyett, D. H. Hartman, and S. Z. Ahmad, "Optical clock distribution using a mode-locked semiconductor laser-diode system," Journ. of Light. Tech., vol. 9, 1991, pp. 1646-1649.
5. B. Bihari, J. Gan, L, Wu, Y. Liu, S. Tang, and R. T. Chen, "Optical clock distribution in supercomputers using polyimide-based waveguides," Proc., Opto. Intercon. Vl., San Jose, CA, Jan. 1999, pp. 123-133.
6. David A. B. Miller, "Rationale and Challenges for Optical Interconnects to Electronic Chips," Proc. of the IEEE, vol. 88, 2000, pp. 728-749.
7. Y. Liu, E. Strezelecka, J. Nohava, M. Hibbs-Brenner, E. Towe, "Smart-Pixel Array Technology for Free-Space Optical Interconnects," Proceedings of the IEEE, vol. 88, No. 6, p. 764-768June, 2000.
8. Jokerst, N.M.; Brooke, M.A.; Laskar, J.; Wills, D.S.; Brown, A.S.; Vrazel, M.; Jung, S.; Joo, Y.; Chang, J.J., "Microsystem optoelectronic integration for mixed multisignal systems," IEEE Journal on Special Topics in Quantum Electronics Millenium Issue, Vol. 6, No. 6, pp. 1231-1239, November/December, 2000.
9. Chang, J.J.; Jung, S.; Vrazel, M.; Jung, K.; Lee, M.; Brooke, M.A.; Jokerst, N., "Hybrid optically interconnected microprocessor: an InP I-MSM integrated onto a mixed-signal CMOS analog/microprocessor IC," Proceedings of the International Society for Optical Engineering, Vol. 4089, pp.708-714, 2000.
10. S. Cho, N. Jokerst, "Polymer waveguide optical interconnections for electrical interconnection substrates," Proceedings of the IEEE Conference on Lasers and Electro-Optics, pp. 161-162, Long Beach, CA, May, 2002.
11. S. Fike, B. Buchanan, N. M. Jokerst, M. Brooke, T. Morris, S. DeWeerth, "8 X 8 Array of Thin Film Photodetectors Vertically Electrically Interconnected to Silicon Circuitry," IEEE Photonics Technology Letters, Vol. 7, No. 10, pp. 1168-1170, October, 1995.
12. S. Wilkinson, J. Tabler, N. Jokerst, M. Brooke, R. Leavitt, "An 8*8 array of resonant cavity enhanced light emitting diodes integrated onto silicon grayscale (32 level) driver circuitry," Proceedings of the IEEE LEOS 9th Annual Meeting, Boston, MA, Vol. 2, p.277-8, Nov. 18-19, 1996.

Femtosecond-Laser-Assisted Microstructuring of Silicon Surfaces for New Optoelectronics Applications 32

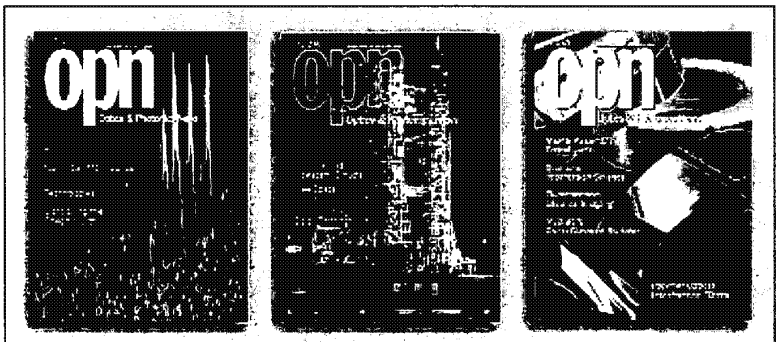
James E. Carey, Catherine H. Crouch and Eric Mazur

1. T.-H. Her, R. J. Finlay, C. Wu, and E. Mazur, Appl. Phys. A **70**, 383 (2000).
2. C. Wu, C. H. Crouch, L. Zhao, J. E. Carey, R. Younkin, J. A. Levinson, E. Mazur, R.M. Farrell, P. Gothoskar, and A. Karger, Appl. Phys. Lett. **78**, 1850 (2001).
3. J.-M. Bonard, H. Kand, T. Stockli, and L.-O. Nilsson Solid State Electronics, vol. **45**, p. 893, (2001).
4. A. Pokhmurska, O. Bonchik, S. Kiyak, G. Savitski, A. Gloskovsky, Appl. Surf. Sci. **154-155**, 712-715 (2000).
5. Y. Hatanaka, M. Niraula, A. Nakamura, T. Aoki, Appl. Surf. Sci. **175-176**, 462-467 (2001).
6. E. Janzen, R. Stedman, G. Grossman, and H.G. Grimmeiss, Phys. Rev. B **29**, 1907-1918 (1984).
7. C. Wu, C.H. Crouch, L. Zhao, and E. Mazur, Appl. Phys. Lett. **81**, 1999-2001 (2002).
8. M. Shen, C. H. Crouch, J. E. Carey. R. Younkin, M. Sheehy. C. M. Friend, E. Mazur, submitted to Appl. Phys. Lett.

Structural Colors in Nature and Butterfly-Wing Modeling 38

Gérard Tayeb, Boris Gralak and Stefan Enoch

1. A. R. Parker, R. C. McPhedran, D. R. McKenzie, L. C. Botten and N. A. Nicorovici, "Photonic engineering: Aphrodite's iridescence," Nature 409, 36-37 (2001).
2. H. Ghiradella, "Light and color on the wing: structural colors in butterflies and moths," Applied Optics **30**, 3492-3500 (1991).
3. B. Gralak, G. Tayeb and S. Enoch. "Morpho butterflies wings color modeled with lamellar grating theory," Optics Express Vol. 9, No. 11, 567-578 (2001).
4. P. Vukusic, J.R. Sambles, C.R. Lawrence and R.J. Wootton, "Quantified interference and diffraction in single *Morpho* butterfly scales," Proceedings: Biological Sciences, The Royal Society of London **266**, 1403 -1411 (1999).
5. Colourware, Colour FAQ, http://www.colourware.co.uk/cpfaq.htm
6. CVRL Color & Vision database, http://www.cvrl.org/
7. Charles A. Poynton, Color technology, http://www.poynton.com/ColorFAQ.html
8. Color Science, http://www.physics.sfasu.edu/astro/color.htm



OPN online

Search feature articles from January 2002

Information for advertisers

Author guidelines

www.osa-opn.org

SIONYX1403000029.0114

SAMSUNG EX. 1002 - 2848/4148

Femtosecond-laser Microstructuring of Silicon for Novel Optoelectronic Devices

A thesis presented

by

James Edward Carey III

to

The Division of Engineering and Applied Sciences

in partial fulfillment of the requirements

for the degree of

Doctor of Philosophy

in the subject of

Applied Physics

Harvard University

Cambridge, Massachusetts

July 2004

SIONYX1403000029.0115

SAMSUNG EX. 1002 - 2849/4148

©2004 by James Edward Carey III

All rights reserved.

SIONYX1403000029.0116

SAMSUNG EX. 1002 - 2850/4148

Femtosecond-laser Microstructuring of Silicon for Novel Optoelectronic Devices

Eric Mazur James E. Carey III

ABSTRACT

This dissertation comprehensively reviews the properties of femtosecond-laser microstructured silicon and reports on its first application in optoelectronic devices. Irradiation of a silicon surface with intense, short laser pulses in an atmosphere of sulfur hexafluoride leads to a dramatic change in the surface morphology and optical properties. Following irradiation, the silicon surface is covered with a quasi-ordered array of micrometer-sized, conical structures. In addition, the microstructured surface has near-unity absorptance from the near-ultraviolet (250 nm) to the near-infrared (2500 nm). This spectral range includes below-band gap wavelengths that normally pass through silicon unabsorbed.

We thoroughly investigate the effect of experimental parameters on the morphology and chemical composition of microstructured silicon and propose a formation mechanism for the conical microstructures. We also investigate the effect of experimental parameters on the optical and electronic properties of microstructured silicon and speculate on the cause of below-band gap absorption. We find that sulfur incorporation into the silicon surface plays an important role in both the formation of sharp, conical microstructures and the near-unity absorptance at below-band gap wavelengths.

Because of the novel optical properties, femtosecond-laser microstructured silicon has potential application in numerous optoelectronic devices. We use femtosecond-laser microstructured silicon to create silicon-based photodiodes that are one hundred times more sensitive than commercial silicon photodiodes in the visible, and five orders of magnitude more sensitive in the near-infrared. We also create femtosecond-laser microstructured silicon solar cells and field emission arrays.

SIONYX1403000029.0117

SAMSUNG EX. 1002 - 2851/4148

Table of Contents

Abstract *iii*

Table of Contents *iv*

List of Figures *vii*

List of Tables *x*

Acknowledgements *xi*

Citations to Published Work *xiv*

1 Introduction **1**

2 Femtosecond-laser microstructured silicon **4**
2.1 Background 5
2.2 Apparatus and procedure 8

3 Morphology and chemical composition **13**
3.1 Effect of shot number 14
3.1.1 Surface morphology 14
3.1.2 Surface layer structure and composition 21
3.2 Spot samples *vs.* translated samples 24
3.3 Effect of fluence 27
3.3.1 Surface morphology 27
3.3.2 Surface layer structure and composition 30
3.4 Effect of pulse duration 31
3.4.1 Surface morphology 32
3.4.2 Surface layer structure and composition 34
3.5 Effect of laser wavelength 36
3.5.1 Surface morphology 36
3.5.2 Surface layer structure and composition 38
3.6 Effect of polarization and propagation direction 38
3.6.1 Surface morphology 39

SIONYX1403000029.0118

SAMSUNG EX. 1002 - 2852/4148

3.6.2 Surface layer structure and composition . . . 40
3.7 Effect of ambient gas . . . 40
3.7.1 Surface morphology . . . 40
3.7.2 Surface layer structure and composition . . . 47
3.8 Effect of ambient gas pressure . . . 49
3.8.1 Surface morphology . . . 50
3.8.2 Surface layer structure and composition . . . 50
3.9 Effect of annealing . . . 51
3.9.1 Surface morphology . . . 51
3.9.2 Surface layer structure and composition . . . 52
3.10 Effect of silicon substrate properties . . . 53
3.11 Summary of chemical composition (RBS data) and trends . . . 53
3.12 Discussion . . . 55

4 Optical and electronic properties 61
4.1 Optical measurements . . . 62
4.1.1 Optical properties of femtosecond-laser microstructured silicon . . . 63
4.1.2 Effect of shot number . . . 64
4.1.3 Effect of fluence . . . 65
4.1.4 Effect of pulse duration . . . 65
4.1.5 Effect of laser wavelength, polarization, and propagation direction . 67
4.1.6 Effect of ambient gas . . . 67
4.1.7 Effect of gas pressure . . . 69
4.1.8 Effect of annealing . . . 69
4.1.9 Effect of silicon substrate properties . . . 71
4.2 Electronic measurements . . . 71
4.2.1 Hall effect and resistivity measurements: procedure and apparatus . 71
4.2.2 Results . . . 76
4.3 Discussion . . . 81

5 Femtosecond-laser microstructured silicon photodiodes 86
5.1 Introduction to photodiodes: the *p*-*n* junction . . . 87
5.2 Femtosecond-laser microstructured silicon photodiodes . . . 94
5.2.1 Experimental . . . 96
5.2.2 Results . . . 98
5.3 Optimization and discussion . . . 110

6 Solar cells, field emission, and future directions 117
6.1 Solar cells and renewable energy . . . 118
6.2 Femtosecond-laser microstructured silicon solar cells . . . 119
6.2.1 Introduction to solar cells . . . 119
6.2.2 Recent progress . . . 122
6.3 Field emission from femtosecond-laser microstructured silicon surfaces . . . 126
6.3.1 Introduction to field emission . . . 126
6.3.2 Field emission results . . . 131

SIONYX1403000029.0119

SAMSUNG EX. 1002 - 2853/4148

6.4 Future directions 134

7 Summary and outlook **135**

References **138**

SIONYX1403000029.0120

SAMSUNG EX. 1002 - 2854/4148

List of Figures

2.1 Morphology of femtoscond-laser microstructured silicon. 5
2.2 Optical properties of femtosecond-laser microstructured silicon. 7
2.3 Microstructuring apparatus. 9

3.1 Evolution of surface morphology with increasing shot number. 15
3.2 Fourier analysis of a silicon surface after 2 laser pulses in SF_6. 16
3.3 Fourier analysis of a silicon surface after 5 laser pulses in SF_6. 17
3.4 Fourier analysis of a silicon surface after 10 laser pulses in SF_6. 18
3.5 A sideview of a cleaved microstructured silicon sample. 19
3.6 Fourier analysis of a silicon surface after 500 laser pulses in SF_6. 21
3.7 Transmission electron micrographs of samples made with 10 and 500 laser pulses. 22
3.8 Comparison of morphology for stationary and translated samples. 25
3.9 Morphology of stationary sample made with changing pulse energy. 26
3.10 Morphology of samples made at different fluences. 27
3.11 Morphology variation in a single irradiated spot. 29
3.12 Self-ordered silicon nano-islands formed with low fluence irradiation. 30
3.13 Transmission electron micrographs of samples made with fluence 8 kJ/m^2 and 4 kJ/m^2. 31
3.14 Morphology of samples made with two pulse durations: 100 femtoseconds and 30 nanoseconds. 32
3.15 Microstructure separation for several pulse durations. 34
3.16 Transmission electron micrographs of samples made with femtosecond and nanosecond laser pulses. 35
3.17 Evolution of surface morphology with increasing shot number for samples made with 400 nm laser pulses. 37
3.18 Morphology of samples made with different laser polarizations. 39
3.19 Morphology of samples made with different gas species. 41
3.20 Fourier analysis of a silicon surface after 2 laser pulses in vacuum. 43
3.21 Fourier analysis of a silicon surface after 50 laser pulses in vacuum. 44
3.22 Fourier analysis of a silicon surface after 200 laser pulses in vacuum. 45
3.23 Fourier analysis of a silicon surface after 500 laser pulses in vacuum. 46

SIONYX1403000029.0121

SAMSUNG EX. 1002 - 2855/4148

3.24 Morphology of samples made with different gas species at high magnification. 47
3.25 Fractional concentration of chemical species for different ambient gases. . . 49
3.26 Morphology of samples made in different pressures of SF_6. 50
3.27 Morphology of samples after annealing. 51
3.28 Transmission electron micrographs of samples before and after annealing. . 52

4.1 Optical properties of femtosecond-laser microstructured silicon. 63
4.2 Optical properties of microstructured silicon at different shot numbers. . . . 64
4.3 Optical properties of microstructured silicon at different fluences. 65
4.4 Optical properties of microstructured silicon at different pulse durations. . . 66
4.5 Optical properties of microstructured silicon for different ambient gas species. 67
4.6 Optical properties of microstructured silicon for different pressures of SF_6. . 69
4.7 Optical properties of microstructured silicon after annealing. 70
4.8 A silicon sample prepared for resistivity and Hall voltage measurements. . . 73

5.1 Creation of a *p*-*n* junction. 88
5.2 A *p*-*n* junction in thermal equilibrium. 90
5.3 The effect of an externally applied voltage (electric field) on a *p*-*n* junction. 91
5.4 Current-voltage characteristics of a *p*-*n* diode. 94
5.5 Schematic diagrams of a femtosecond-laser microstructured silicon photodiode. 97
5.6 Current-voltage characteristics of microstructured silicon photodiodes after annealing. 99
5.7 Responsivity of microstructured silicon photodiodes after annealing. 100
5.8 Current-voltage characteristics of microstructured silicon photodiodes made with different fluences. 101
5.9 Responsivity of microstructured silicon photodiodes made with different fluences. 102
5.10 Current-voltage characteristics of microstructured silicon photodiodes made with different substrate dopings. 103
5.11 Responsivity of microstructured silicon photodiodes made with different substrate dopings. 104
5.12 Responsivity measurements with no applied bias (quantum efficiency). . . . 105
5.13 Responsivity with increasing back bias. 107
5.14 Current-voltage characteristics and responsivity measurements with decreasing temperature. 108
5.15 Photodiode characteristics for a heavily sulfur doped amorphous silicon layer and a laser annealed surface layer. 109
5.16 Photodiode characteristics for an optimized femtosecond-laser microstructured silicon photodiode. 111

6.1 Spectral irradiance distribution of the solar spectrum. 120
6.2 The difference between photoconductive and photovoltaic mode. 121
6.3 Maximum power rectangle and fill factor of a solar cell. 123
6.4 Current-voltage characteristics for femtosecond-laser microstructured silicon solar cells under one sun illumination. 124

SIONYX1403000029.0122

SAMSUNG EX. 1002 - 2856/4148

6.5 Energy level arrangement versus position for field emission from a metal surface. 128
6.6 Energy level arrangement versus position for field emission from a semiconductor surface. 130
6.7 Field emission measurement apparatus. 131
6.8 Field emission measurements from a silicon surface microstructured in SF_6. 132
6.9 Field emission measurements from silicon surfaces microstructured in N_2, Cl_2, and air. 133

SIONYX1403000029.0123

SAMSUNG EX. 1002 - 2857/4148

List of Tables

3.1 Summary of sulfur concentration data. 54
3.2 Summary of the trends in morphology and composition with experimental parameters. 55

4.1 Electronic properties of microstructured silicon made at different fluences. . 77
4.2 Electronic properties of microstructured silicon after annealing. 78
4.3 Electronic properties of microstructured silicon for p-doped substrates. . . . 79
4.4 Electronic properties of microstructured p-doped substrates after annealing. 80

SIONYX1403000029.0124

SAMSUNG EX. 1002 - 2858/4148

Acknowledgements

Without the support of family, friends, and coworkers, I never would have reached this point. Today, I am putting the finishing touches on my dissertation and thereby completing my doctorate. As my last task in this process, I want to thank everyone who has helped me along the way.

I would first like to thank my advisor Eric Mazur and the Mazur group itself. When I first arrived at Harvard, I found it to be quite a challenge. I honestly did not think I would be able to finish. However, the supportive environment that Eric and the rest of the Mazur group provided helped me overcome my initial fears. Since joining the group, Eric has granted me enormous freedom in my pursuits. He taught me how to be a good researcher, the importance of motivating your audience, when teaching or speaking in front of an audience, and how to clearly convey ideas. I greatly enjoyed having Eric as a mentor and friend over these past five years.

There are many members of the Mazur group that I wish to thank. I begin with the elder members who made me feel so welcome five years ago. Adam, Albert, Nan, Claudia, Paul, Chris Schaffer, Chris Roeser, and Jon were all wonderful colleagues and quick with any advice or help I needed when I joined the group. In particular, I thank Chris R. for showing me the right way to do pretty much everything; and Jon for simultaneously keeping me focused on finishing and wasting precious research time with random conversation.

SIONYX1403000029.0125

SAMSUNG EX. 1002 - 2859/4148

I also would like to thank the younger students that have come along and are the future of the group. Rafael, Iva, and Maria made my time here more enjoyable with every day. It feels as though we have banded together to fight through the struggles of graduate school. I thank Rafa for being thoughtful and generous no matter what the situation; Iva for keeping my spirits high and keeping me in shape; and Maria for being such a good friend and a good sport when I occasionally joked around at her expense. I would also like to thank Alex and Veronica for showing me how a postdoc is done, and for being such wonderful people and welcome additions to the group. There have also been some recent additions to the graduate student supply in Sam, Loren, Geoff, and Prakriti. I hope to get to know all of you better, and that your time here will be as rewarding as mine has been.

Then there are all the people I have had the pleasure of working directly alongside: Catherine, Michael, Rebecca, Brian, Mengyan, Claudia, Li, and Josh. I owe all of you a debt of gratitude for your friendships and your hard work that contributed so much to my own progress. I would especially like to thank Catherine and Michael, who were there with me through most of this experience and made each working day a pleasure. I also want to wish Brian luck with carrying on our work; I know it is in good hands.

Lastly, I would like to thank my family and friends for being so loving and supportive. My friends may not even know what I actually do in graduate school, but they always helped me through hard times and helped me relax when needed. I thank Guy for being the best roommate and friend a Harvard graduate student could as for. Most of all, I thank my parents and my sisters, Charlene, Beth, and Tina. They made me who I am today and any successes I have can be attributed to them. They raised me right and I can be proud of what I have accomplished because I know that they are proud of me. I would also like to thank the rest of my family including all my brother-in-laws, Rich, Steve, and Mike, for being good friends and the brothers I never had. Many thanks to my loving and

SIONYX1403000029.0126

SAMSUNG EX. 1002 - 2860/4148

wonderful girlfriend Beth; you have been so patient, understanding, and caring during this last push toward my degree. Your support made everything seem easier and possible.

It is a nearly impossible task to adequately thank everyone for helping me through these last five years. I consider myself extremely lucky to have the friends and loved ones that I have, and to have found myself surrounded by good friends and cohorts at work. Thank you everyone, my future is bright because of you.

James Carey
Cambridge, Massachusetts
August, 2004

Acknowledgements of Financial Support

This thesis is based on work supported by the Department of Energy under contract DE-FC36-016011051 and by the Army Research Office under contract DAAD19-99-1-0009. My time in graduate school was partially funded by a fellowship provided by the Department of Defense.

SIONYX1403000029.0127

SAMSUNG EX. 1002 - 2861/4148

Citations to Published Work

Parts of this dissertation cover research reported in the following articles:

[1] J. E. Carey, C. H. Crouch, M. A. Sheehy, M. Shen, C. Friend, and E. Mazur, "High sensitivity silicon-based VIS/NIR photodetectors," *to be submitted to Optics Lett.*, 2004.

[2] C. H. Crouch, J. E. Carey, M. Shen, E. Mazur, and F. Y. Genin, "Infrared absorption by sulfur-doped silicon formed by femtosecond laser irradiation," *accepted for publication in Appl. Phys. A*, 2004.

[3] C. H. Crouch, J. E. Carey, J. M. Warrender, M. J. Aziz, E. Mazur, and F. Y. Genin, "Comparison of structure and properties of femtosecond and nanosecond laser-structured silicon," *Appl. Phys. Lett.*, vol. 84, p. 1850, 2004.

[4] J. E. Carey, C. H. Crouch, and E. Mazur, "Femtosecond-laser-assisted microstructuring of silicon surfaces," *Optics and Photonics News*, p. 32, February 2003.

[5] R. J. Younkin, J. E. Carey, E. Mazur, J. Levinson, and C. Friend, "Infrared absorption by conical silicon microstructures made in a variety of background gases using femtosecond-laser pulses," *J. Appl. Phys.*, vol. 93, p. 2626, 2003.

[6] M. Y. Shen, C. H. Crouch, J. E. Carey, R. Younkin, M. Sheehy, C. M. Friend, and E. Mazur, "Formation of regular arrays of silicon microspikes by femtosecond laser irradiation through a mask," *Appl. Phys. Lett.*, vol. 82, p. 1715, 2003.

[7] C. Wu, C. H. Crouch, L. Zhao, J. E. Carey, R. J. Younkin, J. Levinson, E. Mazur, R. M. Farrel, P. Gothoskar, and A. Karger, "Near-unity below-band gap absorption by microstructured silicon," *Appl. Phys. Lett.*, vol. 78, p. 1850, 2001.

SIONYX1403000029.0128

SAMSUNG EX. 1002 - 2862/4148

To My Parents –

for always teaching and keeping me grounded.

SIONYX1403000029.0129

SAMSUNG EX. 1002 - 2863/4148

I am a great believer in luck and I find the harder I work, the more I have of it.

THOMAS JEFFERSON

SIONYX1403000029.0130

SAMSUNG EX. 1002 - 2864/4148

Chapter 1

Introduction

Silicon is the most prevalent semiconductor used in microelectronics and photonics. Second only to oxygen in earthly abundance, silicon is produced in higher volume for lower cost than any other semiconductor. Its readily grown oxide made silicon the material of choice for the semiconductor device industry. A band gap of 1.07 eV leads to efficient detection of visible light and conversion of sunlight into electricity. Easily integrated with other microelectronics, silicon is used in many forms (including crystalline, amorphous, and porous) in numerous opto-electronic devices.

However, silicon has several shortcomings: as an indirect band-gap material, it is a poor light emitter; silicon cannot be used to detect many important communications wavelengths; and silicon solar cells fail to convert nearly a third of the suns' spectrum into electricity. A large research effort is directed at manipulating the properties of silicon to overcome these shortcomings. Despite the existence of other semiconductor materials that can better detect longer wavelengths, it is the low cost and easy integration with existing silicon fabrication techniques that drives research to find new forms and uses of silicon.

This dissertation describes a method for using the intense conditions created at

SIONYX1403000029.0131

SAMSUNG EX. 1002 - 2865/4148

the focus of a femtosecond laser pulse to create a new form of silicon with unique optical and electronic properties. Through an interdisciplinary effort that involves ultrafast optical techniques and material science, we investigate the reasons for the unique properties and apply our conclusions toward creating novel optoelectronic devices. Although our methods can be used to create a wide variety of interesting materials, we concentrate on femtosecond-laser microstructured silicon surfaces for use in photodetectors, photovoltaics, and field emission devices.

Organization of the dissertation

Chapter 2 is a brief review of the history and context of femtosecond-laser microstructuring of silicon. We also introduce the microstructuring apparatus and procedure.

Chapter 3 examines the effect of experimental parameters on surface morphology and chemical composition. The intense conditions at the focus of the laser cause ablation and melting of the silicon surface; the molten surface evolves and interacts with chemical species present in the ambient gas before resolidifying with an altered morphology. The inclusion of sulfur into the surface during laser irradiation is crucial in conical microstructure formation.

Chapter 4 examines the effect of experimental parameters on the optical and electronic properties of the laser-disordered surface layer. Silicon microstructured in a sulfur hexaflouride environment has near-unity absorptance for both the visible and near-infrared spectrum. The increased absorption is a result of surface texturing and inclusion of high levels of sulfur in a nonequilibrium arrangement. Annealing to high temperatures eliminates absorption in the near-infrared and greatly increases the number of donor carriers contributed by implanted sulfur atoms.

Chapter 5 presents the use of femtosecond-laser microstructured silicon to make

SIONYX1403000029.0132

SAMSUNG EX. 1002 - 2866/4148

highly sensitive photodiodes for the visible and near-infrared. We successfully create silicon-based photodetectors that utilize the extended absorption range of surfaces microstructured in sulfur hexaflouride. Large gain at small applied biases is responsible for the high sensitivity of the photodiodes. The gain mechanism is related to disorder in the surface layer and is eliminated with annealing to high temperatures.

Chapter 6 presents the use of femtosecond-laser microstructured silicon to make novel solar cells and field emission arrays. Lessons learned while creating photodiodes help identify and remedy past problems in these areas. We demonstrate femtosecond-laser microstructured silicon solar cells for the first time and these solar cells show great potential for use in thin film solar cells. We also present results for field emission from microstructured surfaces with low turn-on fields and high emission currents.

Chapter 7 summarizes the work contained within the dissertation and comments on the future of the research. Past successes and current progress indicate that femtosecond-laser microstructuring has numerous potential future applications.

SIONYX1403000029.0133

SAMSUNG EX. 1002 - 2867/4148

Chapter 2

Femtosecond-laser microstructured silicon

Six years ago, we reported the first observation of conical microstructures formed on the surface of silicon following irradiation with femtosecond laser pulses in an atmosphere of sulfur hexaflouride. A serendipitous and quite unexpected result, femtosecond-laser microstructured silicon was born from experiments on ultrashort laser pulse induced chemical reactions at semiconductor surfaces. In the ensuing six years, we investigated both the formation and physical properties of microstructured silicon; our experimental goals and motivations have grown from solely morphological curiosity to applications in novel semiconductor devices.

This chapter presents a brief introduction to the history of our work and its context in the area of laser microstructuring of semiconductor surfaces. We begin with a description of our initial experiments and how our motivations and goals have changed with time. We also describe comparable work being done on laser microstructuring of semiconductor surfaces. At the end of the chapter, we present the experimental apparatus and procedure

SIONYX1403000029.0134

SAMSUNG EX. 1002 - 2868/4148

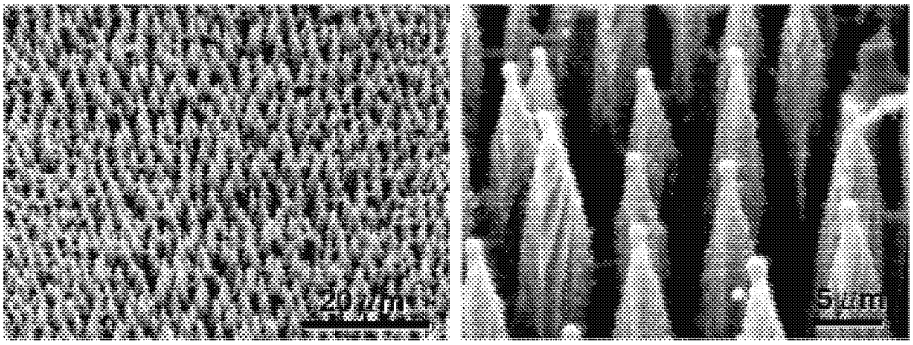


Figure 2.1: Scanning electron micrographs of typical surface morphologies for femtosecond-laser microstructured silicon at two magnifications. Both micrographs are taken at a 45° angle.

used in making femtosecond-laser microstructured silicon.

2.1 Background

We first reported on the formation of conical microstructures on silicon in 1998 [1, 2]. Irradiation of a silicon surface with several hundred femtosecond-laser pulses of fluence 10 kJ/m^2 in an atmosphere of sulfur hexaflouride (SF_6) results in a quasi-ordered array of micrometer-sized, conical structures (see Figure 2.1). The morphology of the microstructures exhibits spontaneous ordering and sharpness unmatched by other laser structuring methods at the time.

Since the early 1970's, researchers have reported on the appearance of spontaneous periodic surface ripples following laser irradiation [3, 4, 5]. The ripples, later named Laser Induced Periodic Surface Structures (LIPPS), are small undulations on the surface with spatial periods closely related to the central wavelength of the laser. These structures share the spontaneous ordering seen in femtosecond-laser microstructured silicon, but not the dramatic surface topography. A decade later, the formation of conical microstructures with

SIONYX1403000029.0135

SAMSUNG EX. 1002 - 2869/4148

laser irradiation was first reported [6]. The laser "sputter-cones" were initially an unwanted byproduct of laser sputtering of targets in pulsed laser deposition experiments. Although conical, sputter-cones are irregular, disordered across the surface, and more blunt than our microstructures. In the mid to late 1990's, a few research groups began examining more exotic structure formation on silicon following laser irradiation [7, 8, 9, 10]. The structures formed in these experiments also lacked the sharpness and ordering of structures formed with femtosecond-laser irradiation in an atmosphere of SF_6.

Because the morphology of our microstructures is unique, initial experiments focused on formation mechanisms and the influence of experimental conditions on morphology. These early experiments provided clear evidence that the ambient gas plays a critical role in the formation of sharp conical microstructures [1]. Surfaces irradiated in nitrogen, helium, or vacuum have much blunter structures than surfaces structured in sulfur hexaflouride or chlorine. Experiments were performed to determine the effect of laser parameters such as fluence, pulse duration, and polarization on surface morphology [11, 2]. These experiments were carried out in hopes of determining how the sharp, ordered structures are formed. Howevere, determining the formation mechanism proved to be a formidable problem, which we continue to study today (see Chapter 3). After we reported on the formation of conical microstructures, a few other research groups took notice of the unique surface morphologies following laser irradiation in sulfur hexaflouride and began their own work on the subject [12, 13, 14, 15].

While the focus of these other groups has remained solely on unique surface morphologies [16, 17], our work changed significantly in 2000 because of another unique property of femtosecond-laser microstructured silicon. In addition to forming ordered, conical microstructures, laser irradiation transforms the originally grey, mirror-like surface of polished silicon into a dark, velvety black. The structured surface's deep black appearance led us

SIONYX1403000029.0136

SAMSUNG EX. 1002 - 2870/4148

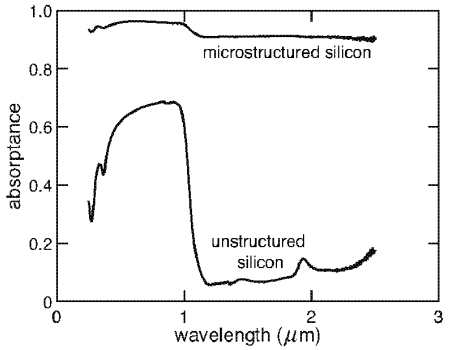


Figure 2.2: Absorptance of femtosecond-laser microstructured silicon as a function of wavelength. The absorptance of unstructured silicon is shown for reference. The large drop in absorptance of unstructured silicon at 1.1 μm corresponds to the band gap energy of crystalline silicon.

to refer to it as "black silicon[1]." The altered appearance of the surface indicated that the optical properties of the surface are modified during laser irradiation. In order to quantify the change, we measured the absorptance of a microstructured surface for wavelengths from the near-unltraviolet to the near-infrared [18, 19]. Figure 2.2 shows the absorptance of femtosecond-laser microstructured silicon as compared to unstructured silicon. Microstructured silicon has much higher absorptance across the entire spectrum, including near-unity absorptance at below-band gap wavelengths. The increased absorption in the visible is consistent with the black appearance, but high absorptance at wavelengths longer than 1.1 μm was quite surprising. Because crystalline silicon has a band gap energy of 1.07 eV, absorptance in crystalline silicon drops precipitously for wavelenghts longer than 1.1 μm (shown in the absorptance measurement of unstructured silicon). Though an interesting result from a scientific point of view, the below-band gap absorbtance also holds great promise for application in silicon based optoelectronics. At this point, the scope of our work expanded to include both investigating the formation mechanism and the source of

[1]In this dissertation, we refer to the irradiated surfaces as either femtosecond-laser microstructured silicon or, simply, microstructured silicon.

SIONYX1403000030.0001

SAMSUNG EX. 1002 - 2871/4148

near-unity absorptance at below-band gap wavelengths [20] (see Chapter 4).

This dissertation contains a comprehensive review of our recent work on femtosecond-laser microstructured silicon. We present explanations of both the formation mechanism and the source of below-band gap absorption. In addition, the later chapters represent the latest significant change in our work over the last six years; using what we know about the structured surface, we transitioned from investigation to application and present novel optoelectronic devices made with femtosecond-laser microstructured silicon.

As electronic devices continue to get smaller, researchers are searching for novel ways of achieving small self-assembled active devices over large areas. Although still a very young field, the interaction of intense femtosecond laser pulses with semiconductor surfaces holds great promise. The extreme conditions at the focus of an intense femtosecond pulse give rise to new physics and material interactions. Also, under the proper conditions, short laser pulses can be used to create nanometer-scale self-ordered structures [17, 21]. The combination of self-ordering and unique material properties make femtosecond-laser structuring of semiconductors a valuable tool for future progress of microelectronic devices.

The preceding history, along with the following description of our experimental apparatus and procedures, lays the foundation for discussion of results presented in the remainder of this dissertation.

2.2 Apparatus and procedure

The procedure and apparatus for creating microstructured silicon has evolved since the original experiments [1]. Single crystal silicon wafers are cut to the desired size for each experiment, typically 10 mm x 10 mm squares. Each square is then cleaned with a fifteen minute ultrasonic bath in trichloroethylene, followed by a fifteen minute ultrasonic bath

SIONYX1403000030.0002

SAMSUNG EX. 1002 - 2872/4148

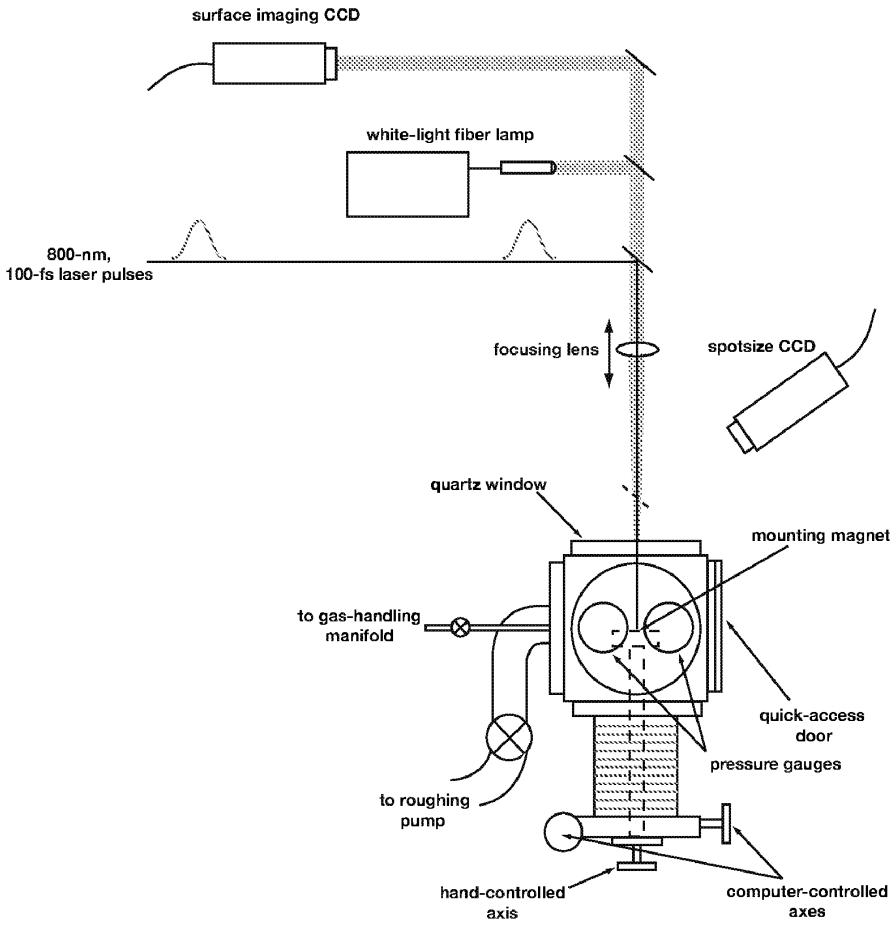


Figure 2.3: A schematic diagram of the apparatus used for microstructuring silicon with femtosecond laser pulses. Samples are loaded through the quick-access door and attached to the mounting magnet.

in acetone, and lastly a fifteen minute ultrasonic bath in methanol. After cleaning, the cut squares are left to soak in a methanol bath. At the time of microstructuring, squares are removed from the methanol bath and dried with a nitrogen gas flow. They are then attached (with carbon tape) to a magnetizable sample holder for mounting on a magnet inside the sample processing chamber.

The main piece of the sample processing chamber is a 4.5 inch stainless steel cube

SIONYX1403000030.0003

SAMSUNG EX. 1002 - 2873/4148

with Conflat connections on each of the six sides. Attached to the back side of the cube is a three axis, precision motion controller from Thermionics^{TM} vacuum products. This controller contains two orthogonal micrometer precision axes driven by computer controlled SilverMax^{TM} motors. The third axis is hand controlled with 1 mil precision. The controller translates a one-inch diameter stainless steel rod which supports a 2" diameter mounting magnet in the center of the cube; samples attached to a magnetizable sample holder are attached to the mounting magnet. Attached to the bottom of the cube is a corrosive compatible, Edwards^{TM} two-stage roughing pump that can evacuate the chamber to a base pressure of approximately 10^{-3} torr. In order to monitor the chamber pressure, we use two pressure gauges. For measuring higher pressures ($1 - 760$ torr) we use an MKS^{TM} Baratron capacitance manometer; for lower pressure ($10^{-3} - 1$ torr) we use a platinum coated Convectron gauge. Attached to one side of the chamber is a leak valve and stainless steel gas-handling manifold. The leak valve and manifold allow us to attach and admit up to five different background gases. An optical grade, 4.5 inch quartz window is attached to the front of the chamber to allow laser access. Lastly, a quick-access viewport door is attached to the remaining side. This door allows for rapid sample loading and removal as well as a means to observe the sample surface safely during microstructuring.

The laser used in the majority of our experiments is a regeneratively amplified, femtosecond Ti:sapphire system with a central wavelength of 800 nm. Femtosecond laser pulses are generated with a Kapteyn-Murnane^{TM} kit pumped by a 5-W Coherent^{TM} Verdi diode laser. The femotsecond pulses are regeneratively amplified in a second Ti:sapphire crystal that is pumped by a Quantronix^{TM} YLF nanosecond laser. Following amplification, the laser pulses are approximately 100 fs, have a center wavelength of 800 nm, and are at a repitition rate of 1 kHz. Further details of this laser system are described elsewhere [22, 23, 2].

SIONYX1403000030.0004

SAMSUNG EX. 1002 - 2874/4148

The laser is focused through the quartz window and onto the sample surface using a 250-mm focal length, anti-reflection coated, plano-convex lens. The lens is mounted on a single axis linear translation stage and positioned such that the focal point is behind the sample. By moving the lens, and therefore the position of the focus, we can vary the laser spot size at the sample surface from a diameter of 30 μm to 250 μm. In order to measure the spot size, we place a CCD (Charge-Coupled Device) camera at the exact same optical distance (from the lens) as the sample surface. A flipper mounted mirror redirects the laser beam onto the camera and we determine the spot size on the sample surface from the measured spot size on the camera. We image white-light reflected off of the sample surface with a second CCD camera in order to monitor progress during microstructuring.

Samples attached to a magnetizable sample holder are loaded through the access door and attached to the mounting magnet. Samples are then positioned in the center of the magnet to allow for maximum translation. The chamber is evacuated to a base pressure of 10^{-3} torr and then filled to the desired pressure with an ambient gas (typically 0.67 bar of sulfur hexafluoride). The sample is then irradiated with a 1-kHz train of 100-femtosecond, 800-nm laser pulses. The fluence of each pulse is set by picking a spot size (typically 150 μm) and using a waveplate/polarizing cube combination to vary the pulse energy. We can irradiate either a single spot or use the motion controller to translate the sample relative to the laser beam. If translated, the sample is moved in a simple raster scan pattern. We can pattern square areas up to 20 mm x 20 mm. By using a shutter and varying the horizontal translation speed, the average number of pulses hitting a given spot on the sample can be controlled. Following irradiation, the chamber is evacuated and purged with nitrogen gas. The chamber is then brought up to atmosphere, samples are removed via the access-door, and the optical access window is cleaned to remove material that may have stuck to it during microstructuring. The resulting morphology and optical properties depend heavily on the

SIONYX1403000030.0005

SAMSUNG EX. 1002 - 2875/4148

parameters of the experiment, including shot number, fluence, pulse duration, ambient gas species, ambient gas pressure, and laser wavelength.

SIONYX1403000030.0006

SAMSUNG EX. 1002 - 2876/4148

Chapter 3

Morphology and chemical composition

The experimental procedure for femtosecond-laser microstructuring silicon involves several variable parameters. Among these parameters are the number of incident laser pulses, the laser fluence, wavelength, pulse duration, ambient gas species and pressure, substrate doping and crystalline orientation, and annealing temperature. We examine the extent to which these parameters affect the final morphology and chemical composition of the microstructured surface. This analysis sheds light on formation mechanisms responsible for the unique microstructures.

The quasi-ordered array of microstructures shown in Chapter 2 (Figure 2.1) are made with the following experimental conditions: irradiation of an n-doped silicon wafer (n-Si(111), 260 μm thick, resistivity $\rho = 8 - 12$ Ω·m) with an average of 500 laser pulses (100 fs, central wavelength 800 nm, fluence 8 kJ/m^2) in 0.67 bar of SF_6. For historical reasons we choose these as our standard conditions. We vary the aforementioned parameters and employ microscopy and chemical measurements to monitor changes in the surface

SIONYX1403000030.0007

SAMSUNG EX. 1002 - 2877/4148

morphology and composition.

3.1 Effect of shot number

In this section we investigate how the surface morphology and chemical composition evolves with increasing number of pulses; all other parameters are kept at standard conditions.

3.1.1 Surface morphology

Figure 3.1 shows the surface evolution with increasing numbers of pulses, from 1 to 600. Each scanning electron micrograph (SEM) shows a different irradiated spot; the micrographs are not taken of the same spot in between pulses. Over the course of several hundred laser pulses, the quasi-ordered array of microstructures forms without the use a mask. We discuss the formation of conical microstructures in two parts: the early formation stage (for pulses one to ten) and late stage formation (for pulses 10 and up).

Early stage

Following the first laser pulse, small defects appear that are randomly scattered across the irradiated area. These defects resemble a burst bubble of molten silicon with a circular ripple pattern surrounding some of the larger defects. They are likely the result of instabilities in temperature of the molten surface at a defect or impurity.

With the second pulse, a distinct, regular ripple pattern appears on the surface. The ripples occur at a wavelength close to the central wavelength of the laser light and their long axis is perpendicular to the laser polarization. The ripple formation is a well-understood phenomenon termed Laser Induced Periodic Surface Structures (LIPSS) [5, 3, 4]. In this fluence regime, the ripples are the result of capillary waves excited in molten silicon

SIONYX1403000030.0008

SAMSUNG EX. 1002 - 2878/4148

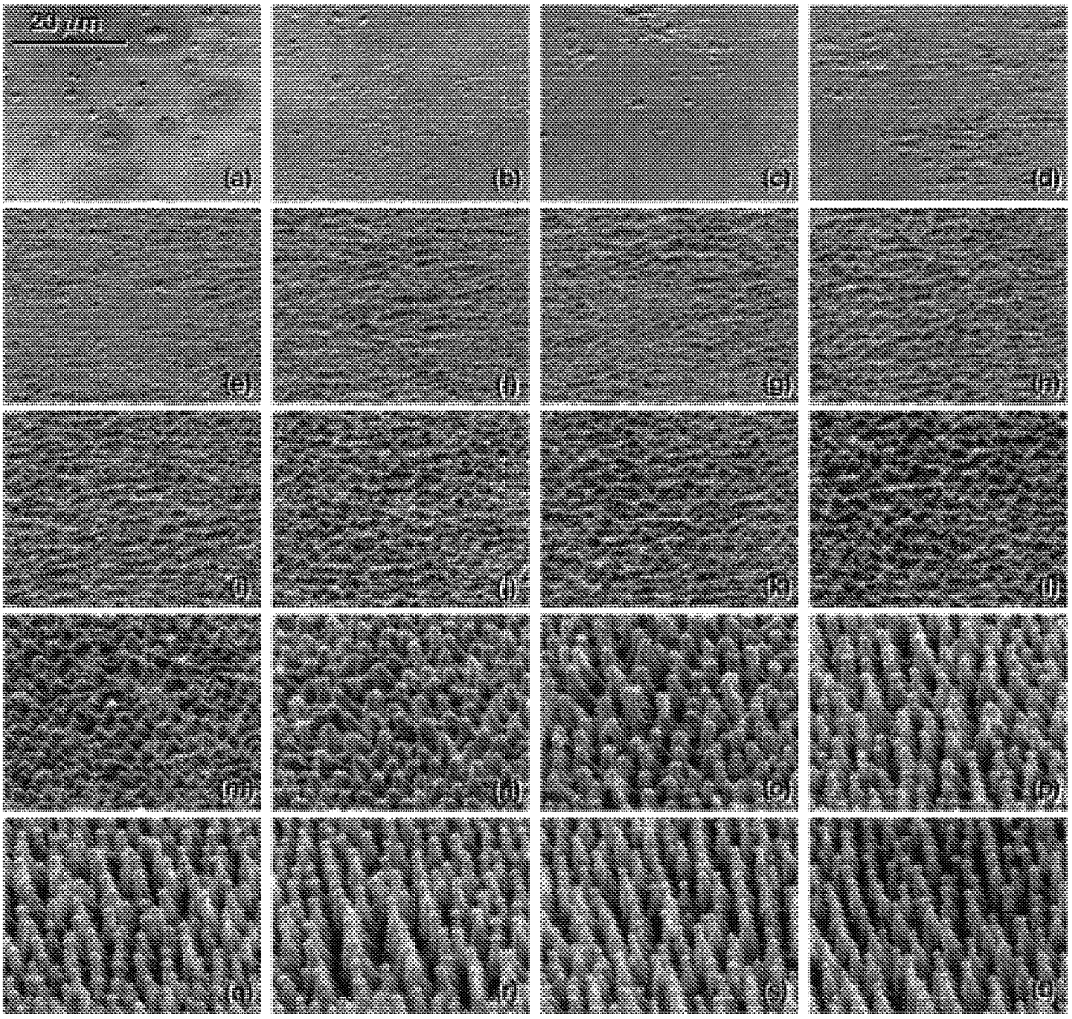


Figure 3.1: Scanning electron micrographs of a silicon surface after (a) 1, (b) 2, (c) 3, (d) 4, (e) 5, (f) 6, (g) 7, (h)8, (i)9, (j)10, (k)12,(l)15, (m) 20, (n) 30, (o) 50, (p) 70, (q) 100, (r) 200, (s) 400, and (t) 600 laser pulses. Each SEM is taken at a 45° angle to the surface with the same magnification.

SIONYX1403000030.0009

SAMSUNG EX. 1002 - 2879/4148

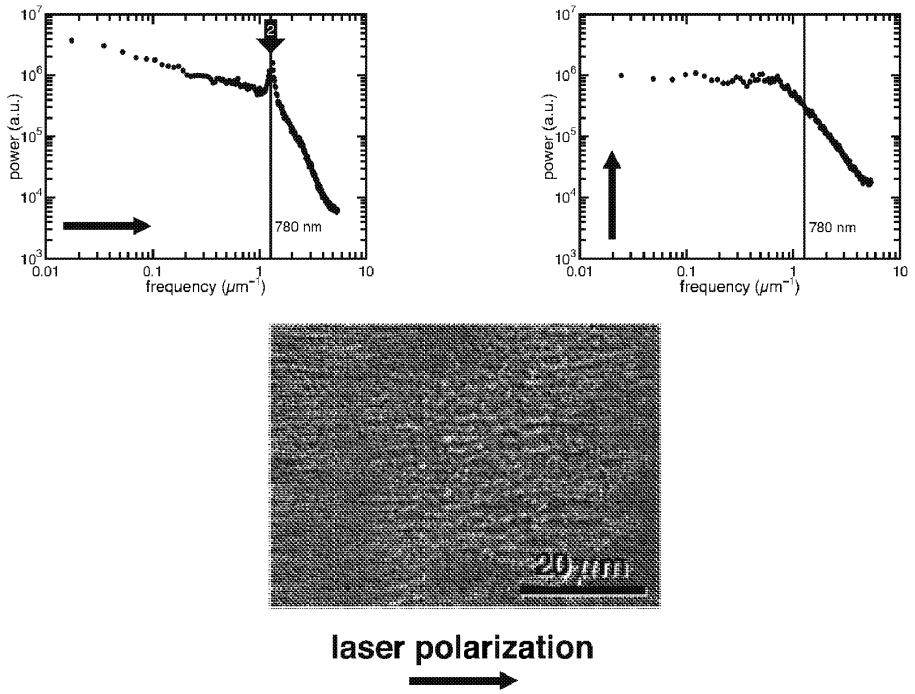


Figure 3.2: Fourier analysis of line-outs taken in the vertical and horizontal direction of a silicon surface after 2 laser pulses. The scanning electron micrograph is taken normal to the surface.

through interference between the incident and scattered laser light [24, 25]. We analyze the periodicity of patterns, like the ripples, with Fourier transforms of scanning electron micrographs for both the vertical and horizontal directions. Figure 3.2 shows the Fourier analysis of a surface after 2 laser pulses. The horizontal direction shows a strong peak at a frequency corresponding to the ripple period. There is no visible pattern in the vertical direction and, likewise, there is no peak in the Fourier power spectrum.

During pulses 3, 4 and 5 the morphology transitions from laser induced periodic surface structures to a stage in the formation process that is not well understood. In this second stage, the ripples begin to coarsen and "bead-up" along their long axis. The peak that appears in the horizontal Fourier power spectrum (after two pulses) diminishes; there is

SIONYX1403000030.0010

SAMSUNG EX. 1002 - 2880/4148

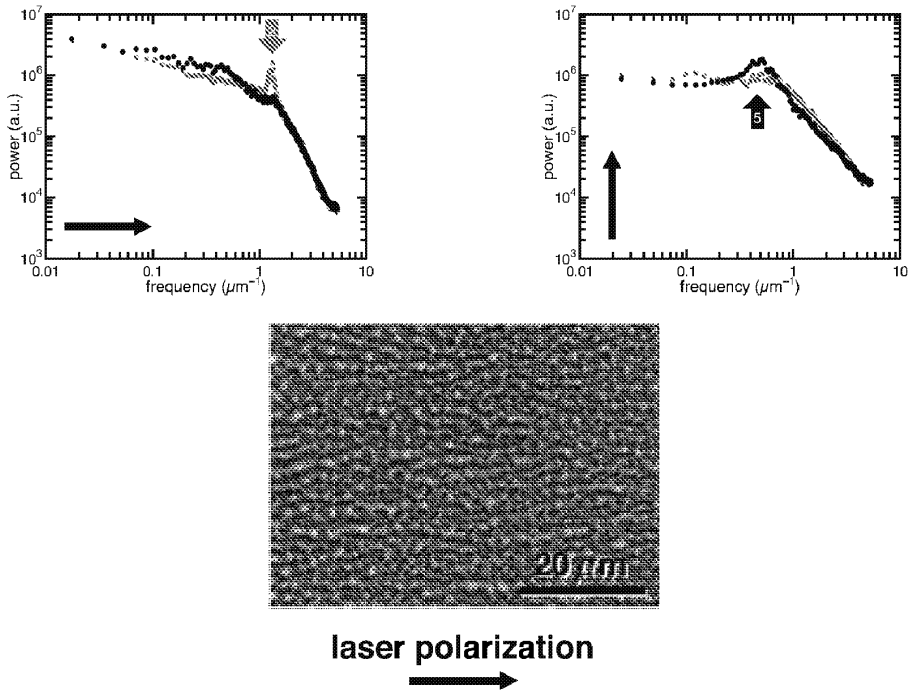


Figure 3.3: Fourier analysis of line-outs taken in the vertical and horizontal direction of a silicon surface after 5 laser pulses. The scanning electron micrograph is taken normal to the surface.

no longer a distinguishable surface pattern in the horizontal direction. However, the beads that form from the ripples are spaced by about 2 μm, parallel to the laser polarization; their spacing leads to a peak in the vertical direction of the Fourier power spectrum. Figure 3.3 shows the Fourier analysis after five incident pulses.

For pulses 5 to 10, the peak in the vertical direction grows and shifts toward slightly smaller frequencies (larger spacing). After the tenth pulse, the peak of this feature is at a frequency corresponding to a bead spacing of about 3.5 μm. In addition, a peak in the Fourier signal is beginning to appear in the horizontal direction. Figure 3.4 shows the Fourier analysis of the surface after ten incident pulses. At this point the characteristic wavelengths/spacings for the final microstructures are set. This marks the end of the early

SIONYX1403000030.0011

SAMSUNG EX. 1002 - 2881/4148

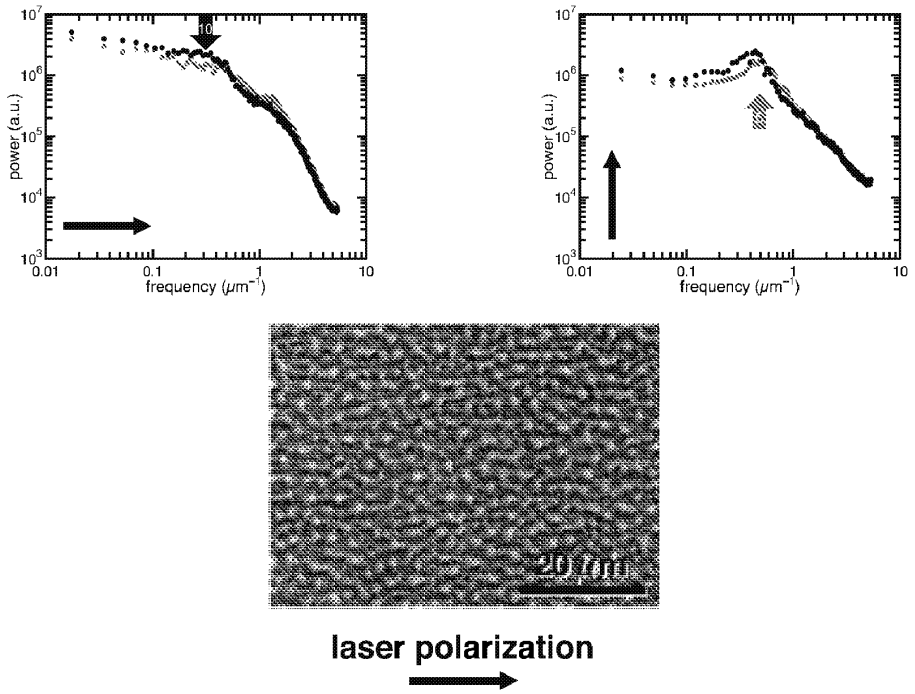


Figure 3.4: Fourier analysis of line-outs taken in the vertical and horizontal direction of a silicon surface after 10 laser pulses. The scanning electron micrograph is taken normal to the surface.

stage of formation.

To summarize, during the early stage of formation we see three important patterns emerge at different pulse numbers. A ripple pattern at the wavelength of the laser forms after the second pulse, with the ripples' long axis perpendicular to the laser polarization. After the fifth pulse, the ripple pattern coarsens significantly and beads begin to form along the ripples at a spacing larger than the wavelength of the laser. By the tenth pulse, the beads become more pronounced and a characteristic spacing for both the vertical and horizontal directions emerges. What causes the transition from the one-dimensional ripple pattern to the two-dimensional pattern of beads is not clear. We speculate that the spacing and size of the beads depends strongly on capillary waves and surface tension, which are in

SIONYX1403000030.0012

SAMSUNG EX. 1002 - 2882/4148

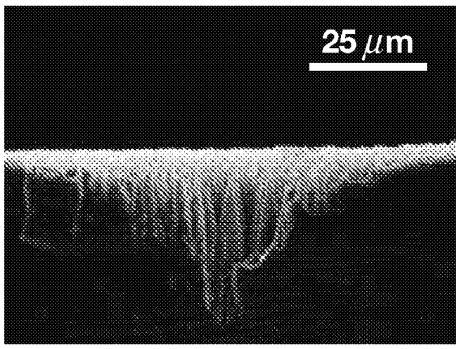


Figure 3.5: A sideview of a microctured silicon sample, cleaved through an irradiated spot. The tips of the microstructures are all at or below the original wafer surface.

turn influenced by impurities in the surface layer, melt depth, and temperature. We will see later in this chapter that these characteristic spacings and morphology depend heavily on other parameters such as ambient gas and fluence.

Late stage

At the end of the early formation stage, a two-dimensional pattern of beads emerges (Figure 3.4). This pattern remains in essentially the same arrangement throughout the entire late stage formation. From pulse ten to several hundred pulses, the final conical microstructures are etched out of the surface, with the beads ending up as the peaks of the cones. Incident laser pulses preferentially remove material to the sides of the beads, leaving the conical structures behind. Figure 3.5 shows that the tips of all microstructures are at or below the surface of the original silicon wafer and that the conical structures are etched out rather than grown.

During late stage formation, the beads serve two purposes. First, they act as protective caps from the incident laser energy. The reason for the beads resilience is not well known. However, in similar conical structures formed during ion sputtering, concentrations

SIONYX1403000030.0013

SAMSUNG EX. 1002 - 2883/4148

of impurity atoms seed cone growth and protect regions of the substrate; implanted impurity atoms lower the sputter yield, thus seeding cone placement and growth [26]. Another example of conical structures are naturally formed snow structures called *penitentes* that form on glaciers or snow fields at high altitudes. For these structures, which resemble meter-scale versions of silicon conical microstructures, higher dirt concentration at the tips reduces melting at the peaks relative to the "cleaner" snow to the sides of the peaks [27]. Likewise, impurity atom implantation during laser irradiation might reduce ablation rates from the beads and is a likely reason for their resilience.

The second effect of the beads is to concentrate laser light into the valleys between the beads. Briefly, incoming photons that strike the side of the beads have a higher incident angle than those that hit the top of the bead. Because reflectivity is high at large incident angles, a majority of the light striking the side of the beads reflects off and is absorbed in the pits where it strikes at an angle closer to normal [18]. An increase in absorbed light raises the energy concentration within the pits and results in more material ablation and preferential etching inside the pits. This effect becomes more pronounced as the beads sharpen into microstructures and the angles of the sides become steeper.

In the late stage of formation, there is little change in the spacing of the surface pattern. The spacings in the horizontal and vertical direction move to slightly longer wavelengths as the microstructures are etched from the surface. A final Fourier analysis of the surface after 500 incident pulses is shown in Figure 3.6. The average spacing of the microstructures is about 3-4 μm in the direction both perpendicular and parallel to the laser polarization.

SIONYX1403000030.0014

SAMSUNG EX. 1002 - 2884/4148

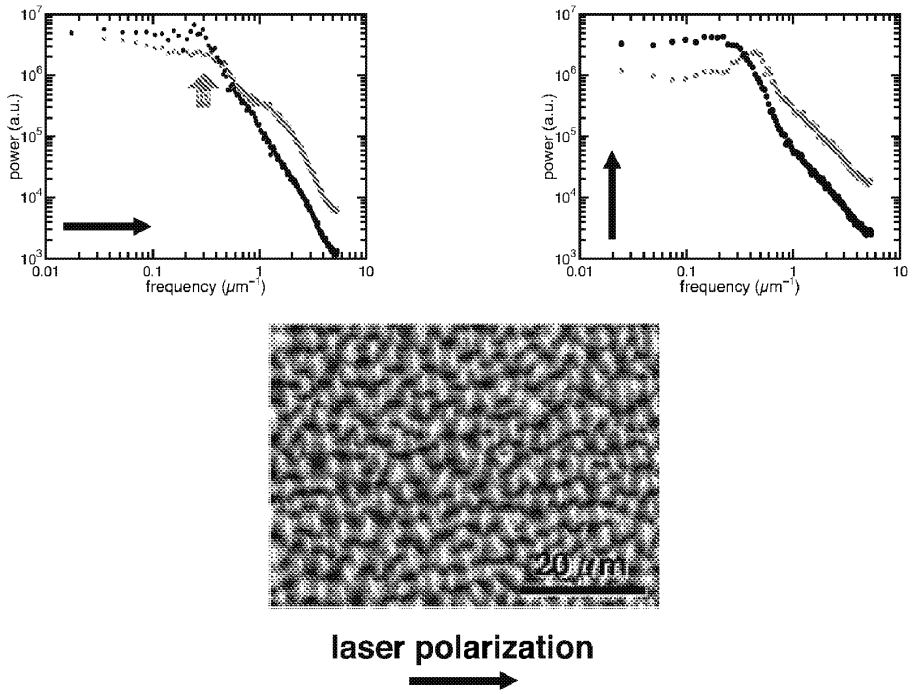


Figure 3.6: Fourier analysis of line-outs taken in the vertical and horizontal direction of a silicon surface after 500 laser pulses. The scanning electron micrograph is taken normal to the surface.

3.1.2 Surface layer structure and composition

After discussing the morphology of the surface on a micrometer scale, we now take a closer look and examine chemical composition and nanometer scale structure of the surface.

Surface layer structure

In addition to scanning electron micrographs of the surface, we performed bright-field transmission electron microscopy (TEM) on cross-sections prepared from samples after 10 and 500 laser pulses. These micrographs are shown in Figure 3.7[1]. Visual examination

[1]TEM sample preparation, micrographs, and x-ray analysis were provided by M. Wall and Dr. F. Génin from Lawrence Livermore National Laboratory

SIONYX1403000030.0015

SAMSUNG EX. 1002 - 2885/4148

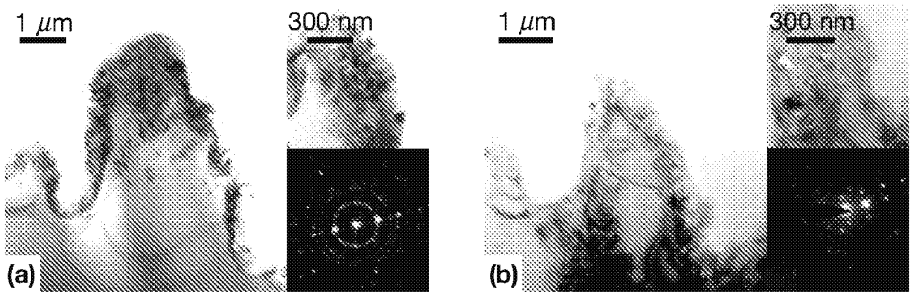


Figure 3.7: Transmission electron micrographs of the surface after (a) 500 and (b) 10 pulses. The disordered surface layer of both samples is similar in thickness and structure. Insets: (upper) high-magnification view of the disordered region at the tip of the microstructure and (lower) selected area electron diffraction pattern obtained from the disordered region.

indicates that (for both samples) there is a disordered layer that is several hundred nanometers thick and made up of nanocrystallites (~10–50 nm in diameter) and nanopores. The disordered surface layer after 10 pulses is similar to that for 500 pulses, despite much smaller conical microstructures. Although we do not have transmission electron micrographs for other pulse numbers, the fact that the surface layer formed with just 10 pulses is similar in both thickness and structure to that formed with 500 pulses suggests that the surface layer may reform with each laser pulse once the pattern of microstructures is established.

Selected area diffraction (SAD) indicates that for both samples, the surface layer (insets to Figure 3.7) has significant crystalline order. It is also possible that amorphous-like material is present between nanocrystalline grains. Research has shown that the structure of the intergranular phase in nanocrystalline silicon is similar to that of bulk amorphous silicon [28] and amorphous material has long been observed following short pulsed laser irradiation [29, 30]. Selected area diffraction indicates that the substrate below the disordered layer is undisturbed crystalline silicon.

SIONYX1403000030.0016

SAMSUNG EX. 1002 - 2886/4148

Chemical composition

To determine the effect of shot number on chemical composition we employed Rutherford backscattering spectrometry (RBS) [31] and energy dispersive X-ray (EDX) [32] emission spectroscopy. As a rough gauge, EDX measurements indicate that there is a large amount of sulfur ($\sim$ 1 at. %) in the disordered surface layer and no measurable amount of impurity species in the crystalline silicon beneath. We used RBS to make more precise measurements of the chemical composition in the surface layer. We measured the backscattering spectrum from 2.0-MeV alpha particles collected with an annular solid state detector. To determine the chemical composition of the microstructured material, we compared the measured RBS spectra to simulated spectra [33] from planar material. The spectra measure only the average sulfur concentration in the uppermost 100 nm of the surface; the RBS signal from deeper sulfur is masked by the silicon signal. However, because EDX indicates that there are no chemical changes below the structurally modified layer, we simulate only the top layer to determine sulfur concentrations. RBS spectra indicate that the modified surface layer consists of oxidized silicon with fluorine and sulfur impurities; etching the samples in 5% HF for 4 minutes removes the fluorine and the oxide without changing the sulfur concentration. To simplify simulation of the spectra, we took RBS spectra for samples etched in HF[2]. These measurements show that the concentration of sulfur increases with increasing shot number up to about 50 pulses. The amount of sulfur increases from roughly 0.2 at. % for the sample made with two pulses to roughly 0.7 at. % for the sample made with 50 pulses. Additional pulses have little effect; the sample made with 500 pulses also has 0.7 at. % sulfur. These results are summarized as a part of Table 3.1 near the end of the chapter.

[2]The conditions and considerations for RBS measurements is true for all RBS data presented in this disseration

SIONYX1403000030.0017

SAMSUNG EX. 1002 - 2887/4148

3.2 Spot samples *vs.* translated samples

Before moving on to other parameters that affect morphology, we discuss a subtlety of the experimental process. As mentioned in the experimental procedure section (Section 2.2), we make samples in two ways: we either leave a sample stationary and irradiate a single spot, or translate the substrate relative to the laser beam in order to structure larger areas. With the rest of the experimental parameters left the same, there are two visible differences between translated and stationary samples. The first is that the microstructures in the stationary samples have a micrometer-sized sphere at the tip while the translated samples are sharper and lack the sphere at the tip. The second is that translated samples have a larger amount of nanoscale particles spread across the surface. An extreme example of these two differences is shown in Figure 3.8. The left frame shows microstructures from a stationary sample and the right shows those made while translating the sample relative to the laser beam. The left frame has fewer nanoscale particulates on the surface and much larger, rounder tips (some of the scanning electron micrographs in this chapter are from stationary samples and some are from translated samples).

The nanoscale particles on translated samples are redeposited material from the ejected plume. For each irradiated spot there is a ring of material around the spot. On a stationary sample all of this debris lies away from the area where microstructures form. However, on a translated sample, the debris from other irradiated regions lands back in previously irradiated regions. The density of nanoscale material varies a great deal along the surface of a translated sample and there is no recognizable pattern to the variation in concentration. In addition, many of these particles can be washed off in a brief ultrasonic methanol bath.

The reason for the presence or lack of spheres at the tip is a little harder to

SIONYX1403000030.0018

SAMSUNG EX. 1002 - 2888/4148

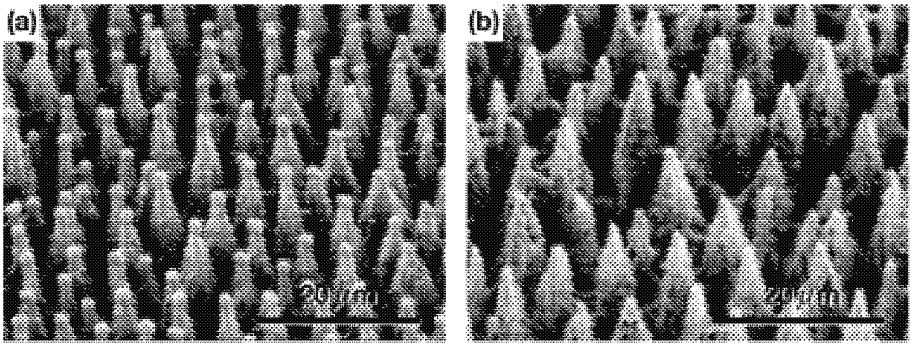


Figure 3.8: Scanning electron micrographs of (a) a stationary sample and (b) a translated sample. The stationary sample has spherical ball tips while the the translated sample has sharper tips and more nanoscale debris along the surface.

determine than the presence of nanometer-scale particles. The spherical tips have been observed previously on nanosecond laser formed microstructures and are explained as a resolidied molten droplet of silicon [7, 8, 10]. In addition to the spherical tips, other groups observe microstructure growth above the original substrate surface. These research groups contend that no significant build-up can occur from material "climbing" the sides of the microstructure and that the material at the tip must be redeposited ablated material from the silicon rich plume above the molten surface [10]. The spherical tips of our silicon microstructures are most likely resolidified droplets of redeposited silicon.

However, redeposition does not explain why the spherical balls are only present for stationary samples. We speculate that the varying fluence at each point on the surface during translation melts the spherical ball tips. Under our standard conditions, a single spot on the surface is irradiated with approximately 500 laser pulses. However, the intensity of these pulses is not constant as the Gaussian profile of the beam passes over a spot. That is, a given spot on the surface is first struck by the leading edge of the gaussian beam, which is at a lower fluence than the center of the beam. The higher fluences of the beam center

SIONYX1403000030.0019

SAMSUNG EX. 1002 - 2889/4148

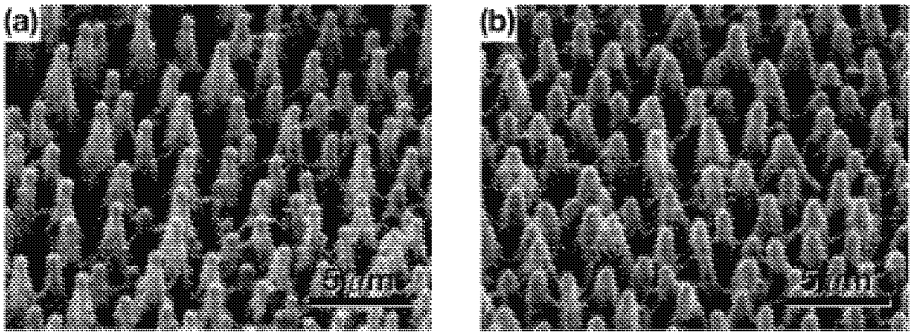


Figure 3.9: Scanning electron micrographs of (a) a single spot irradiated with 500 laser pulses under standard conditions and (b) a single spot irradiated under the same conditions as (a), but with the energy of each pulse varied to simulate the gaussian profile of the laser as it passes over the surface during translation. The spherical balls at the tips disappear with varying the energy of each pulse.

then pass over the spot, but, as the trailing edge passes over, the spot is again exposed to lower fluence irradiation. If a spot is exposed to fluences below the ablation threshold but above the melting threshold, the spherical tips melt, flow, and wet the sides of the conical microstructures. In addition, no material is available for redeposition at the tips because no ablation occurs.

To test this hypothesis, we simulated the changing fluences for a translated sample by leaving the sample stationary but varying the fluence of each incident pulse. To do this we used a low pulse repetition rate and a variable neutral density filter to adjust the power of each pulse and simulate an increasing and then decreasing fluence. We matched the highest fluence of the filtered pulses to match the fluence of pulses at our standard conditions. The results are shown in Figure 3.9. The spherical tips do indeed disappear. In fact, if the experiment is carried out by simply decreasing the fluence with each pulse, we see the same results.

SIONYX1403000030.0020

SAMSUNG EX. 1002 - 2890/4148

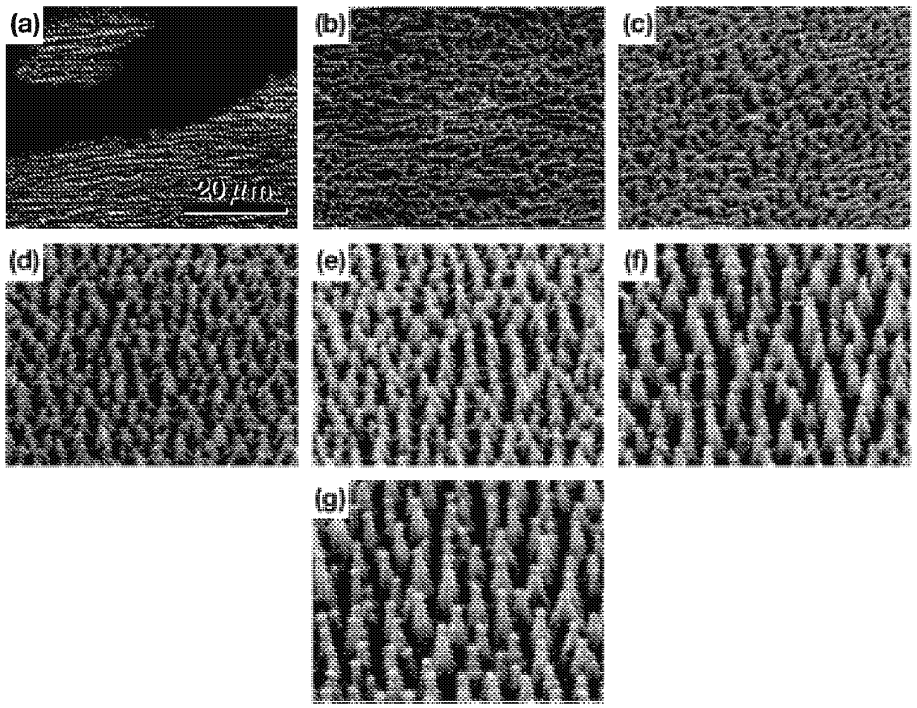


Figure 3.10: Scanning electron micrographs of a silicon surface after irradiation with laser pulses of fluence (a) 2 kJ/m^2, (b) 3 kJ/m^2, (c) 4 kJ/m^2, (d) 5 kJ/m^2, (e) 6 kJ/m^2, (f) 7 kJ/m^2, and (g) 8 kJ/m^2. Each SEM is taken at a 45° angle to the surface with the same magnification.

3.3 Effect of fluence

The final morphology also greatly depends on the fluence of the incident laser pulses. In this section we examine morphology at different fluences while keeping all other experimental parameters at our standard conditions.

3.3.1 Surface morphology

Figure 3.10 shows the variation in surface morphology for average fluence from 2 kJ/m^2 to 8 kJ/m^2. The change in morphology with increasing fluence strongly resembles the stages of development seen with increasing shot number (Figure 3.1). With increasing

SIONYX1403000030.0021

SAMSUNG EX. 1002 - 2891/4148

fluence (at constant shot number) the morphology goes from laser induced periodic surface structures, to a coarsened surface, to the sharp microstructures of our standard conditions.

At an average fluence of 2 kJ/m^2 the surface is altered in sporadic patches and the damage that occurs resembles laser induced periodic surface structures. At this fluence the laser is only melting the surface and no ultrafast melting or ablation occurs [34]. Some of the surface remains undisturbed because this average fluence is just above the threshold fluence for melting (1.5 kJ/m^2). Continued irradiation at this fluence does not result in development of sharp, conical microstructures. At a fluence of 3 kJ/m^2, the surface is covered by a coarsened ripple pattern with spacings longer than the wavelength of the laser light. This fluence is above the ultrafast melting threshold and very close to the ablation threshold for silicon (3.1 kJ/m^2) [34]. Continued irradiation at this fluence does not result in development of sharp, conical microstructures. At a fluence of 4 kJ/m^2, the morphology resembles the surface after 15 laser pulses in the shot number series (Figure 3.1). With continued irradiation at this fluence, conical microstructures *do* develop. As we continue to increase the fluence from 5 to 8 kJ/m^2, the changes in morphology resemble the progression from tens of laser pulses to 500 pulses. For fluences above 8 kJ/m^2 (up to 12 kJ/m^2), the surface morphology looks very similar to the 8 kJ/m^2 samples with a small increase in microstructure height and a thinning of the cone body. At very high fluences (>12 kJ/m^2), many times the ablation threshold fluence, material removal becomes extreme and instead of conical structures, we make a gaussian shaped hole in the surface. These high fluences are often used for fast machining and cutting of silicon because a large amount of material is removed with each pulse [35].

An important trend to notice in Figure 3.10 is that, with increasing fluence, there is an increase in both the microstructure height and distance between microstructures. These

SIONYX1403000030.0022

SAMSUNG EX. 1002 - 2892/4148

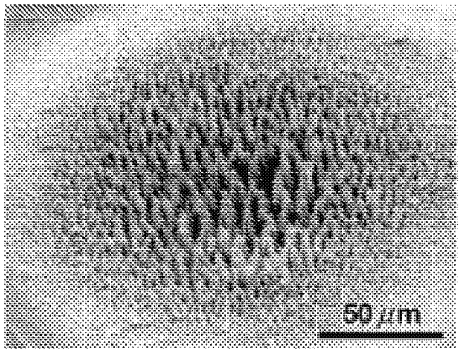


Figure 3.11: A scanning electron micrograph of (a) a single spot irradiated at a fluence of 10 kJ/m^2. From the guassian fluence profile, the different morphologies that occur can be seen in a single spot.

two dimensions are, in fact, correlated according to

$$h \propto d^{2.4\pm0.1} \tag{3.1}$$

with microstructure height h, and separation distance d [11]. Perhaps the clearest illustration of how fluence affects the morphology of the surface is to look at an entire irradiated spot at 10 kJ/m^2 (Figure 3.11). One can see all the different morphologies from ripples at the edge to tall conical structures in the center, showing the gaussian fluence profile of the laser beam.

As an aside, if we take a look at the surface at the low end of the tested fluences (2 kJ/m^2), there are some interesting surface morphologies to note. As we see in Figure 3.10 (a), the surface is altered in sporadic patches; some of the surface appears unchanged. Upon closer examination of areas that appear unchanged, we find regions of ordered silicon islands that are about 10-nm in diameter (Figure 3.12). Similar ordering of nanostructures has been observed by other researchers [16] and are likely the result of scattering from dust particles on the surface. We have not rigorously analyzed this behavior, but we may investigate these morphologies further because self-ordering of nanometer-scale structures

SIONYX1403000030.0023

SAMSUNG EX. 1002 - 2893/4148

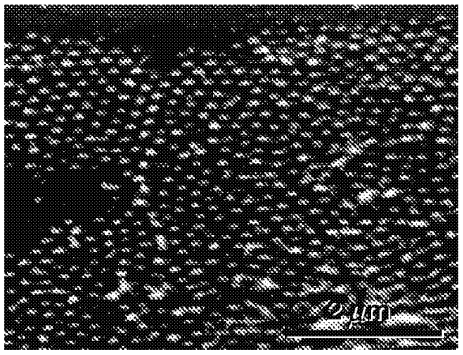


Figure 3.12: Nanometer scale self-ordered silicon islands formed at low fluence (2 kJ/m^2).

is an active area of research.

3.3.2 Surface layer structure and composition

In addition to the micrometer-scale morphology, we take a closer look at the nanoscale structure and chemical composition of the surface for different fluences.

Surface layer structure

Figure 3.13 shows transmission electron micrographs of samples made with fluence 4 kJ/m^2 and 8 kJ/m^2. As was the case for shot number, the surface layer for both fluence samples are similar despite differences in microstructure size. Both have a several hundred nanometer thick, disordered surface layer, made up of nano-crystallites (~10–50 nm in diameter) and nanopores. Selected area diffraction indicates that for both fluences, the surface layer (insets to Figure 3.13) has significant crystalline order with a strong possibility that amorphous-like material is present between the nanocrystalline grains (see Section 3.1.2).

SIONYX1403000030.0024

SAMSUNG EX. 1002 - 2894/4148

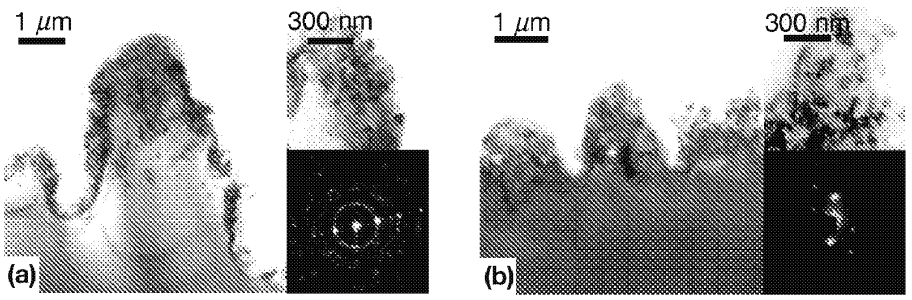


Figure 3.13: Transmission electron micrographs of samples made with (a) 8 kJ/m^2 and (b) 4 kJ/m^2. The disordered surface layer of both samples is similar in thickness and structure. Insets: (upper) high-magnification view of the disordered region at the tip of the microstructure and (lower) selected area electron diffraction pattern obtained from the disordered region.

Chemical composition

To determine the effect of fluence on chemical composition we employ the tools listed in section 3.1.2. Rutherford backscattering spectrometry (RBS) indicates that the concentration of sulfur increases with increasing fluence. The amount of sulfur increases from roughly 0.3 at. % for a sample made with 2.5 kJ/m^2 to roughly 0.7 at. % for the sample made with 8 kJ/m^2 pulses. Higher fluences do not increase the concentration significantly; samples made with 10 kJ/m^2 pulses also have 0.7 at. % sulfur. These results are summarized as a part of Table 3.1 near the end of the chapter.

3.4 Effect of pulse duration

Varying the duration of the pulse from femtoseconds to nanoseconds changes the overall size and shape of the microstructures. In this section we examine morphology of microstructures for nanosecond and femtosecond pulses. We also comment on the effect of a less drastic change in pulse duration through poor compression of a spectrally dispersed femtosecond pulse.

SIONYX1403000030.0025

SAMSUNG EX. 1002 - 2895/4148

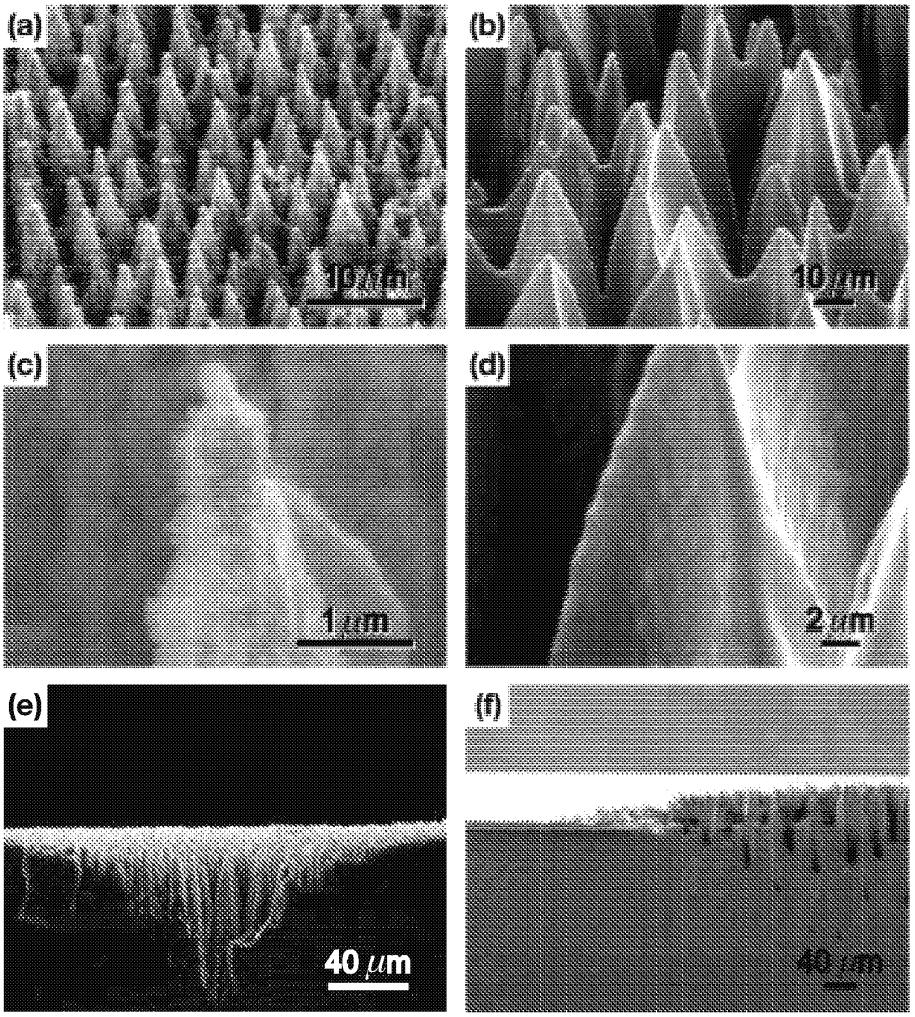


Figure 3.14: Scanning electron micrographs comparing surface morphology for two different pulse durations. ((a), (c), (e)) show microstructures made with 100-fs pulses and ((b), (d), (f)) show microstructures made with 30-ns laser pulses.

3.4.1 Surface morphology

The conditions used for creating nanosecond-laser-formed structures were matched with the initial work and conditions of Perdraza *et al.* [10]. A KrF+ excimer laser delivered a train of 248-nm, 30-ns laser pulses with a flat-top spatial profile and a fluence of 30 kJ/m^2

SIONYX1403000030.0026

SAMSUNG EX. 1002 - 2896/4148

onto a sample in a vacuum chamber filled with 1 bar of SF_6. Pedraza *et al.* found that about 1500 laser pulses produce fully-formed conical structures, so we used an average of 1500 pulses per spot.

Figure 3.14 shows the results for the nanosecond-laser-formed microstructures as compared to femtosecond-laser-formed microstructures. In both cases, the microstructures are roughly conical, but the structures formed with the femtosecond laser ((a), (c), (e)) are one-fifth the size of those formed with the nanosecond laser ((b), (d), (f)). The femtosecond-formed structures are roughly 8 μm tall and separated by 4 μm; the nanosecond-formed structures are roughly 40 μm tall and separated by 20 μm. Again, the tips of the femtosecond-formed structures are at the level of the original surface of the wafer (e), while the nanosecond-formed structures protrude above the original surface (f). Finally, the femtosecond-formed structures are covered with nanoparticles 10–50 nm in diameter deposited on the structures during fabrication (Figure 3.14 (c)), while the surface of the nanosecond-formed structures is much smoother, with 500 nm-size protrusions that appear to grow out of the surface (Figure 3.14 (d))[3].

We have also examined the effect of increasing the duration of our femtosecond laser pulses from 100 femtoseconds to 10 picoseconds by changing the compression of a spectrally dispersed femtosecond pulse [11]. In this work, the separation between microstructures is plotted as a function of pulse duration (Figure 3.15), but separation distance is related to the height by Formula 3.1. For increasing pulse duration, the microstructure separation decreases from 100 femtoseconds to 5 picoseconds but then begins to increase again. The transition at 5 ps duration might be the point at which microstructures switch from being below the surface to growing above like the nanosecond-formed-microstructures

[3]Changing the pulse duration has a drastic effect on the morphology. However, other parameters were changed in the above experiment (pressure, wavelength, fluence). From examining the effects of varying these parameters in this chapter we are confident that it is the pulse duration that causes the morphological differences shows in Figure 3.14.

SIONYX1403000030.0027

SAMSUNG EX. 1002 - 2897/4148

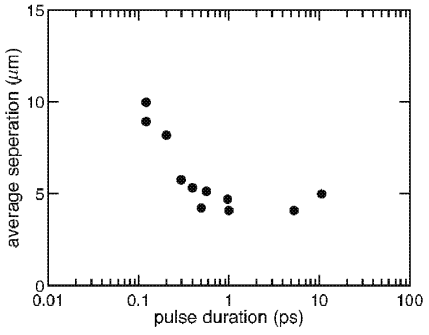


Figure 3.15: Average microstructure separation as a function of pulse duration. Separation distance is correlated to average microstructure height. Adapted from [11].

shown in Figure 3.14.

3.4.2 Surface layer structure and composition

The large difference in micrometer-scale morphology indicates a large difference in the formation process for nanosecond pulses and femtosecond pulses. We examine the nanoscale structure and chemical composition to see if there are also large differences in these characteristics.

Surface layer structure

Figure 3.16 shows transmission electron micrographs for a femtosecond-laser-formed sample and a nanosecond-laser-formed sample. Again, with the femtosecond-formed structures, there is a highly disordered layer of silicon a few hundred nanometers thick, made up of nanocrystallites and nanopores. Selected area diffraction (SAD) indicates that the core is crystalline and the surface layer is polycrystalline or microcrystalline (upper inset to (a)). The nanosecond-formed structures likewise have a crystalline core, but the disordered layer is thinner (150 nm or less) and covers only parts of the structures; the tips of

SIONYX1403000030.0028

SAMSUNG EX. 1002 - 2898/4148

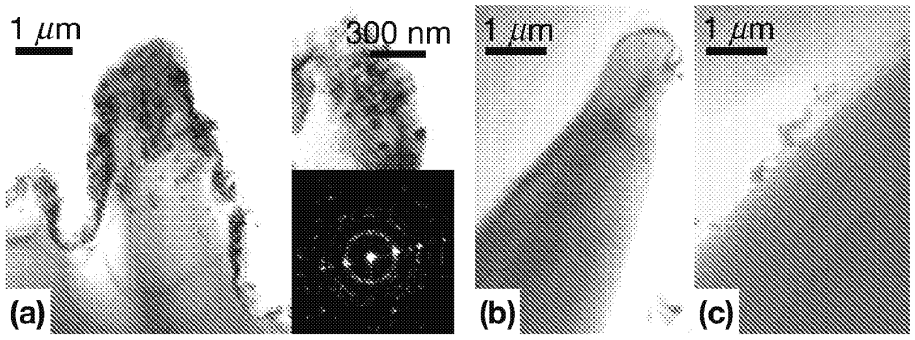


Figure 3.16: Comparison of transmission electron micrographs of (a) cross-section of femtosecond-laser-formed microstructure (insets: (upper) higher magnification view of disordered material, (lower) selected area electron diffraction pattern obtained from the tip of the sample); (b) cross-section of tip of nanosecond-laser-formed microstructure; and (c) cross-section of side of nanosecond-laser-formed microstructure. The disordered layer on the nanosecond-formed microstructures is too thin to take a selected area diffraction pattern.

the structures are single crystal and free of extended defects. Although the bases of the nanosecond-formed structures (visible in Figure 3.14 (f)) cannot be observed in the transmission electron micrographs, they are visible to ion channeling, which averages over the projected surface. We observed good channeling for nanosecond-formedstructures, which indicates that, even at the bases, the surface of the nanosecond-formed structures is more ordered than the surface of the femtosecond-formed structures. There is not a thick enough disordered surface layer to perform SAD on the nanosecond-formed microstructures.

Chemical composition

To determine the concentration of sulfur, we perform Rutherford backscattering spectrometry (RBS) and ion channeling on the femtosecond and nanosecond-structured samples; we compare the measured RBS spectra to simulated [33] spectra from planar material. The RBS spectra of the femtosecond-structured samples indicate that the sulfur concentration in the uppermost 100 nm is about 0.7 at. % before annealing and about 0.5

SIONYX1403000030.0029

SAMSUNG EX. 1002 - 2899/4148

at. % after annealing (see Section 3.7.2). The sulfur signal obtained with ion channeling is slightly lower than that obtained with randomly aligned RBS, suggesting that some of the sulfur impurities are substitutional. The femtosecond-structured samples, in contrast, channel poorly ($\chi_{min}^{(Si)} \sim 50\%$) and the reduction in sulfur signal with channeling is comparable in magnitude to the possible sources of error. Hence we can only determine that between 20% and 70% of the sulfur in the unannealed femtosecond-structured sample is substitutional, and we cannot determine how much sulfur is substitutional in the annealed femtosecond-structured sample. In the nanosecond-structured samples, the sulfur concentration in the observable near-surface region is about 0.5 at. % before annealing, and about 0.4 at. % after annealing. The nanosecond-structured samples show much stronger silicon channeling ($\chi_{min}^{(Si)} = 5.6\%$ before and 6.6% after annealing), and nearly half of the sulfur is substitutional (43% $\pm$ 7% before and 48% $\pm$ 8% after annealing). The sulfur concentration is therefore very similar in the two types of structures, but much more of the affected material in the nanosecond-structured samples is single crystal than in the femtosecond-structured samples, and a great deal of the sulfur is definitely substitutional in the nanosecond-structured samples. These results are summarized as a part of Table 3.1 near the end of the chapter.

3.5 Effect of laser wavelength

The laser wavelength also affects the final morphology of the microstructures. In this section we use second harmonic generation [36] to examine how laser radiation with a central wavelength of 400 nm (*vs.* 800 nm) affects morphologly.

3.5.1 Surface morphology

We used second harmonic generation to convert our 800-nm laser pulses into pulses with a central wavelength of 400 nm. Conversion efficiencies below 30% result in a lower

SIONYX1403000030.0030

SAMSUNG EX. 1002 - 2900/4148

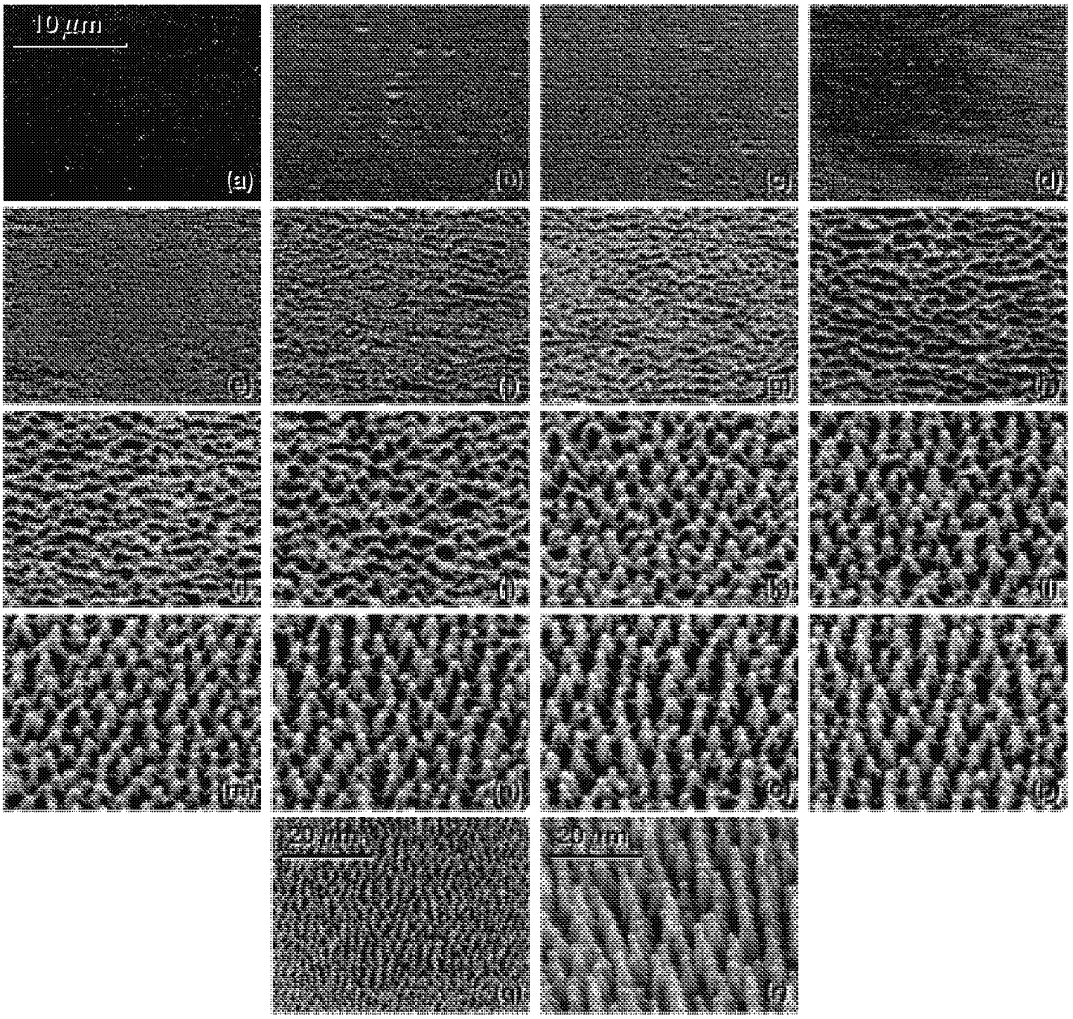


Figure 3.17: Scanning electron micrographs of a silicon surface after (a) 1, (b) 2, (c) 3, (d) 4, (e) 5, (f) 7, (g) 10, (h) 15, (i) 20, (j) 30, (k) 50, (l) 75, (m) 100, (n) 200, (o) 300, (p) 500 laser pulses with a center wavelength of 400 nm. Each SEM is taken at a 45° angle to the surface with the same magnification. Frames (q) and (r) show the final morphology for 400 nm and 800 nm radiation, respectively. The structures are smaller and more dense for 400 nm radiation.

SIONYX1403000030.0031

SAMSUNG EX. 1002 - 2901/4148

pulse energy so, in order to maintain a fluence of 8 kJ/m^2, we use a smaller spot with a diameter of 85 μm. Figure 3.17 shows the evolution of the silicon surface irradiated with 400-nm pulses. The development follows the same progression as those made with 800 nm. We see small bubble-like defects after a few pulses and then the appearance of laser induced periodic surface structures after about 4 pulses. These ripples then bead up in a direction perpendicular to the long axis of the ripples. After approximately 10 pulses, a two dimensional pattern of beads is established and the microstructures are then dug out around the beads.

The ripples have a spacing close to the central wavelength of the laser pulses (400 nm), one half the wavelength of those shown in Section 3.1. The result is that the density of the final structures is higher than that with 800 nm (approximately two times higher). In addition, the structures after 500 pulses are smaller than those made with 800 nm laser light. The last two panels of Figure 3.17 show the final morphology for structures made with 400 nm (q) and 800 nm (r).

3.5.2 Surface layer structure and composition

At this time we do not have detailed information on the structure of the surface layer and the chemical composition for samples made with 400 nm light. Based on results in the pulse duration section (Section 3.4) and the dependence of melt depth on wavelength [37], we suspect that the disordered surface layer is thinner than the 800 nm irradiated samples.

3.6 Effect of polarization and propagation direction

Two additional laser characteristics that affect microstructure morphology are the polarization and laser propagation direction. In this section, we briefly describe how these

SIONYX1403000030.0032

SAMSUNG EX. 1002 - 2902/4148

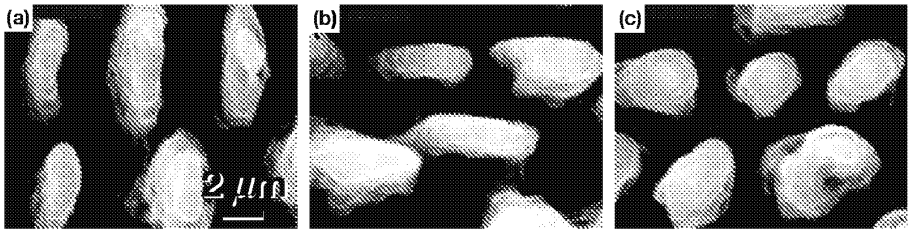


Figure 3.18: Morphology following irradiation with (a) horizontally-polarized, (b) vertically-polarized, and (c) circularly-polarized laser pulses.

two qualities affect the shape and growth direction of the microstructures.

3.6.1 Surface morphology

In Figure 3.6, we see that the base of each microstructure is elliptical, with a long and a short axis; the long axis is perpendicular to the polarization of the laser light. This shape is a result of the higher absorption of p-polarized light over s-polarized light [11, 2]. With the initial bead pattern established, laser light hitting the side of a bead along the horizontal direction (for the scanning electron micrographs in Section 3.1.1 this is the left and right side of the beads) is p-polarized light and light hitting the sides of a bead in the vertical direction (top and bottom) strikes as s-polarized light. Therefore higher absorption, and subsequently more ablation, occurs along the sides in the horizontal direction, where the incident light is p-polarized. Figure 3.18 shows the structure of the microstructures from above for three laser polarizations. Figure 3.18 (a) is our initial case of polarization in the horizontal direction, (b) is for light polarized in the vertical direction, and (c) is for circularly polarized light. When the polarization is rotated 90°, the long axis of the microstructure is also rotated 90°. For circularly polarized light there is no preferential ablation and the base of the microstructures is circular instead of elliptical.

The majority of the data presented in this dissertation is for laser irradiation

SIONYX1403000030.0033

SAMSUNG EX. 1002 - 2903/4148

at normal incidence to the substrate. However, the direction of microstructure growth is always parallel to the direction of incident light, and is independent of the substrate's crystallographic planes [2]. That is, if we irradiate with laser pulses at 45° to the surface, the resulting microstructures point along the direction of the laser, 45° off-normal to the original substrate surface.

3.6.2 Surface layer structure and composition

We do not expect the polarization or the propagation direction to affect the structure or chemical composition of the surface layer.

3.7 Effect of ambient gas

In addition to laser parameters, we vary the gaseous atmosphere in which the sample is microstructured. In this section we examine the morphology for several different gas species at a pressure of 0.67 bar.

3.7.1 Surface morphology

As shown in Figure 3.19, the morphology of the silicon microstructures depends heavily on the gas in which they are formed. Figure 3.19 shows, specifically, the results of laser irradiation in two halogen containing gases, sulfur hexafluoride (SF_6) and chlorine (Cl_2), as well as nitrogen (N_2), air, and vacuum. It should be noted that we used a pressure of 0.67 bar for each gas (except for vacuum, of course), but the laser fluence and shot number were adjusted to yield microstructures with heights of approximately 10–15 μm for each gas. Using SF_6 or Cl_2 leads to sharp-tipped conical structures with a radius of curvature of approximately 500 nm. Structures made in air, N_2, and vacuum are much

SIONYX1403000030.0034

SAMSUNG EX. 1002 - 2904/4148

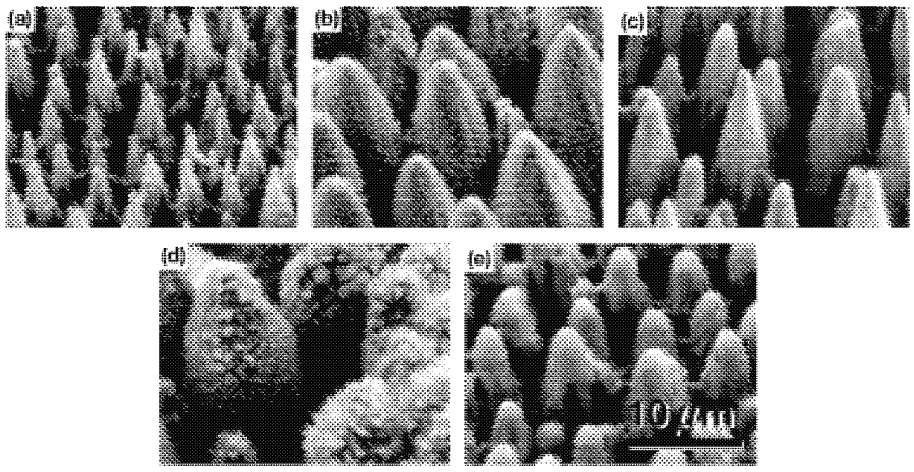


Figure 3.19: Scanning electron micrographs comparing surface morphology for different ambient gas species: (a) sulfur hexafluoride (SF_6), (b) Nitrogen (N_2), (c) Chlorine (Cl_2), (d) air, and (e) vacuum. Each SEM is taken at a 45° angle to the surface with the same magnification.

more rounded than those made in the halogen-containing gases; the radius of curvature of their tips is approximately 2–3 μm.

We examined the effect of ambient gas on the number density of conical structures, as well as partial pressures of SF_6 with N_2 and Cl_2 with N_2 [20]. For a pure ambient gas, higher densities are achieved using SF_6 or Cl_2. Surfaces prepared with SF_6 give the greatest number density, followed by Cl_2. The number densities produced with N_2 and air are approximately equal and are roughly a factor of two less than that of the SF_6-prepared surfaces. The number density of vacuum prepared samples lie roughly halfway between these two cases. In addition, we measured the number density of structures for surfaces patterned in either a SF_6 (Cl_2) alone, or in a mixture of SF_6 (Cl_2) and N_2. We made stationary samples of microstructures in background pressures of 0–0.67 bar of SF_6 (Cl_2). We then made similar stationary samples while varying the partial pressure of the SF_6 (Cl_2), but keeping the total pressure constant at 0.67 atm by adding N_2. In both cases,

SIONYX1403000030.0035

SAMSUNG EX. 1002 - 2905/4148

the number density of microstructures increases with the partial pressure of SF_6 (Cl_2). A plateau is reached for both SF_6 and Cl_2; the maximum number density is reached at roughly 0.13 bar for Cl_2 and 0.54 bar for SF_6.

Some important observations made from varying the ambient gas are that the ambient gas affects the sharpness, density, and ordering of the structures. It is also clear that the nanoscale features on the surface are different for each gas; we will address this shortly. The halogen-containing gases give sharper structures and it seems that reactivity and chemically reactive species in these gases is an important factor. However, recent results using other sulfur containing gases (H_2S) show similar morphologies to the SF_6 samples despite the lack of a highly reactive species.

As we did for the shot number series in SF_6 in Section 3.1, we analyzed the evolution of samples made in vacuum (with no possible contribution from chemical interaction for the ambient environment) to understand in more detail the ambient gas contribution to the final morphology.

Early stage: vacuum

As with SF_6, following the second pulse a distinct, regular ripple pattern appears on the surface. These ripples are laser induced periodic surface structures at the wavelength of the laser light, perpendicular to its polarization. The area covered by ripples is larger for samples made in vacuum than in SF_6, indicating that either the pressure or the surface/gas interaction suppresses the size of the melted/rippled area. Fourier analysis of the horizontal direction shows a strong peak at a frequency corresponding to the ripple period. There is no visible pattern in the vertical direction and, likewise, there is no peak in the Fourier power spectrum.

For vacuum samples, it takes many more pulses for the ripples to give way to

SIONYX1403000030.0036

SAMSUNG EX. 1002 - 2906/4148

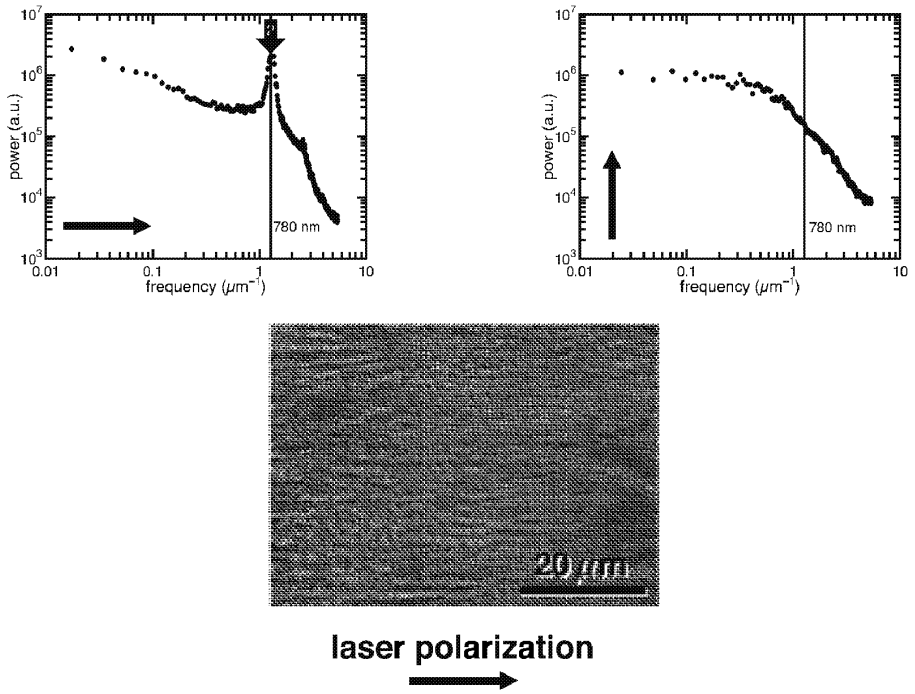


Figure 3.20: Fourier analysis of line-outs taken in the vertical and horizontal direction of a silicon surface after 2 laser pulses in vacuum. The scanning electron micrograph is taken normal to the surface.

beading. In addition, the beads formed during coarsening are much larger in vacuum than in SF_6 (about 2 μm *vs.* 500 nm in diameter). It takes about 50 pulses for the strong peak in the horizontal Fourier power spectrum to decrease. At this point, the beads have a strong periodicity in the direction perpendicular to the laser polarization. Figure 3.21 shows the Fourier transforms after fifty incident pulses in vacuum.

From 50 pulses to several hundred, the peak in the vertical direction broadens and shifts toward longer wavelengths. In addition, a peak in the Fourier power spectrum appears in the horizontal direction. Figure 3.22 shows the Fourier analysis of the surface after two hundred incident pulses. The characteristic spacings for the vacuum structures is constant for higher number of pulses; this marks the end of the early stage of formation.

SIONYX1403000030.0037

SAMSUNG EX. 1002 - 2907/4148

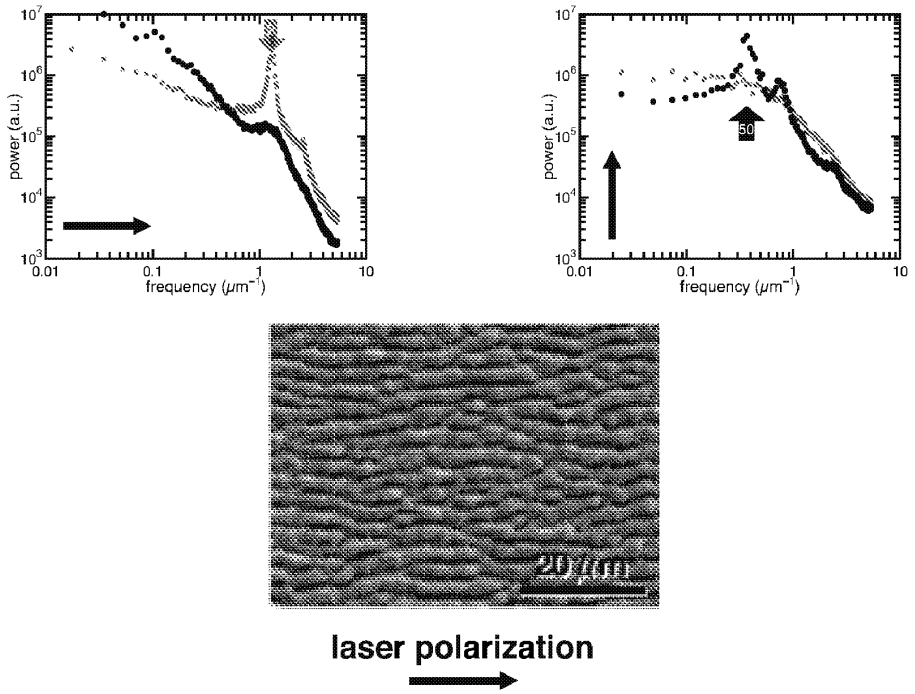


Figure 3.21: Fourier analysis of line-outs taken in the vertical and horizontal direction of a silicon surface after 50 laser pulses in vacuum. The scanning electron micrograph is taken normal to the surface.

Note that it takes 10 to 20 times more pulses for this to occur than in the SF_6 samples. The beads, which become the peaks of the final structures, are much larger and blunter than those in the SF_6 samples.

Although the morphologies are very different and the progression is much slower in vacuum, the stages of formation are similar for vacuum and SF_6 samples. First, a ripple pattern at the wavelength of the laser forms after the second pulse, with the ripples long axis perpendicular to the laser polarization. By the fiftieth pulse, the ripple pattern has coarsened significantly and beads form along the ripples at a spacing larger than the wavelength of the laser. After a few hundred pulses, the beads become more pronounced and a characteristic spacing for both the vertical and horizontal directions emerges. Note

SIONYX1403000030.0038

SAMSUNG EX. 1002 - 2908/4148

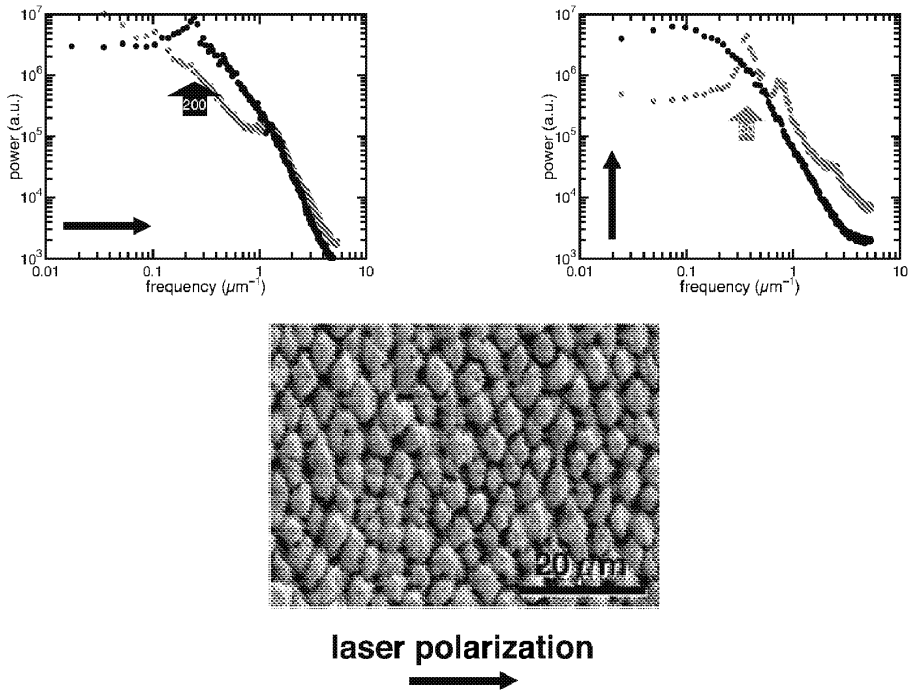


Figure 3.22: Fourier analysis of line-outs taken in the vertical and horizontal direction of a silicon surface after 200 laser pulses in vacuum. The scanning electron micrograph is taken normal to the surface.

that the spatial frequencies in vacuum samples are similar to those with made in SF_6 despite the differing morphologies.

Late stage: vacuum

At the end of the early formation stage, a two dimensional pattern of beads is established. This two dimensional pattern of beads remains in essentially the same arrangement throughout the entire late stage formation. From two hundred pulses to the end of formation, the final conical microstructures are etched out of the surface, with the beads formed at the end of the early stage ending up as the peaks of the cones. As with microstructures formed in SF_6, incident laser pulses preferentially remove material to the

SIONYX1403000030.0039

SAMSUNG EX. 1002 - 2909/4148

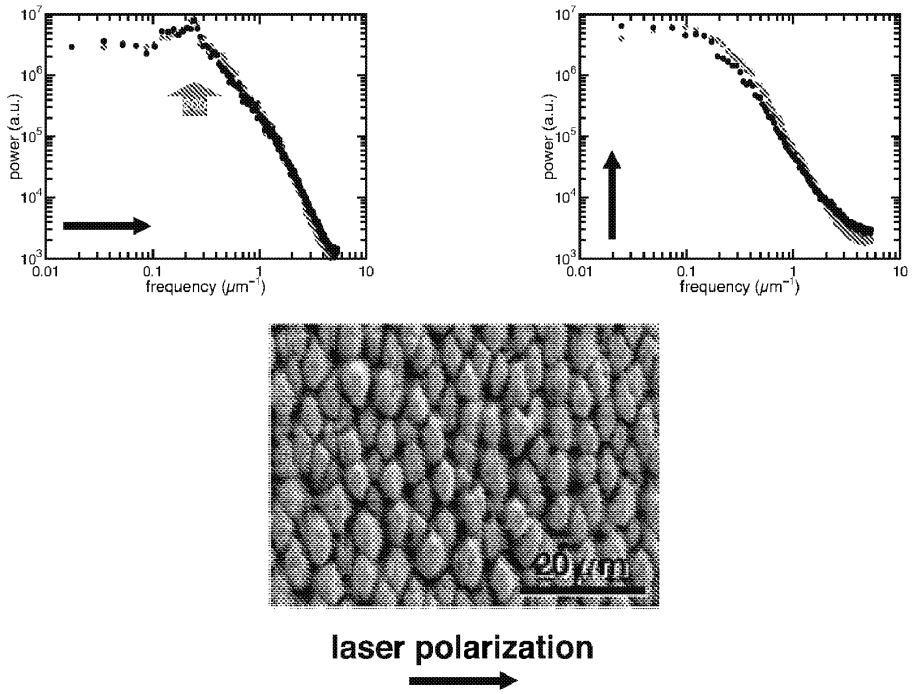


Figure 3.23: Fourier analysis of line-outs taken in the vertical and horizontal direction of a silicon surface after 500 laser pulses in vacuum. The scanning electron micrograph is taken normal to the surface.

sides of the beads, digging out the conical structures with each pulse. Again, the beads from the end of the early stage act as protective caps and focus laser energy into the spaces between them. A final Fourier analysis is shown in Figure 3.23 for a scanning electron micrograph after 500 incident pulses. In summary, the vacuum samples went through the same stages of development as SF_6 samples, but the number of pulses required to reach each stage was higher for vacuum. The final structures are blunter and larger than those formed in SF_6, are less dense, and appear less ordered.

SIONYX1403000030.0040

SAMSUNG EX. 1002 - 2910/4148

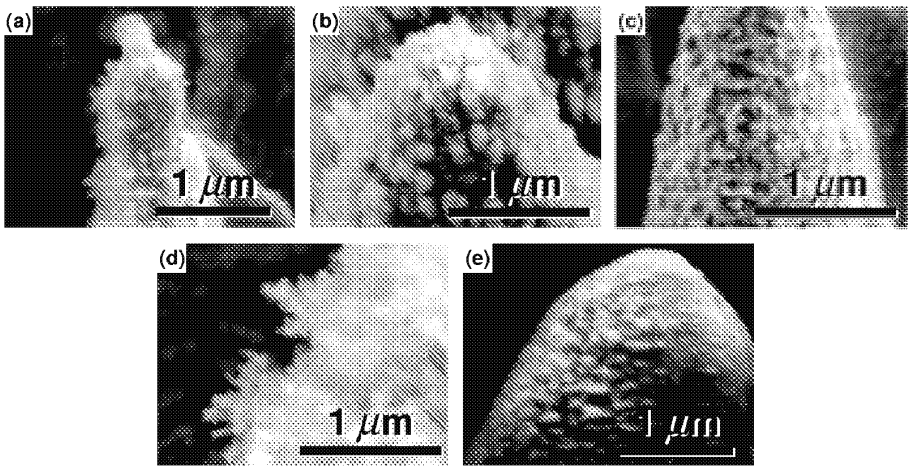


Figure 3.24: Scanning electron micrographs of nanoscale morphology for different ambient gas species: (a) sulfur hexafluoride (SF_6), (b) nitrogen (N_2), (c) chlorine (Cl_2), (d) air, and (e) vacuum.

3.7.2 Surface layer structure and composition

The micrometer-scale morphology varies a great deal depending on the ambient gas, as does the nanoscale structure and chemical composition.

Surface layer structure

At this point, we have been unable to analyze transmission electron micrograph samples of the various gas species. However, high magnification scanning electron micrographs of each surface reveal large differences in the nanoscale structure on the surface (Figure 3.24)[4]. Samples made in SF_6 have the sharpest tips as well as some dendritic nanoscale material on the surface. As mentioned in section 3.2, this material is not present for stationary samples. The nanoscale material is very similar in appearance to material collected from the ejected plume during irradiation in SF_6 [20]. Samples made in N_2 have complex nanoscale features; there are rough, 50-nm clusters of material covering the entire

[4]Each gas sample shown was made while being translated.

SIONYX1403000030.0041

SAMSUNG EX. 1002 - 2911/4148

surface and a visible ripple variation with a period near 800 nm along the sides of the microstructures. Samples made in Cl_2 have a relatively smooth surface with a comparatively small amount of nanoscale material on the surface. There is 5–10 nm scale roughness along the side of each microstructure. Samples made in air are covered in clusters of dendritic material over the microstructures. At high magnification these fractal-like growths look similar to ice crystals or clumps of snow flakes. Lastly, the nanoscale features on the vacuum samples are similar to the Cl_2 samples. There is little nanoscale material on the surface but 10–15 nm roughness along the sides of the microstructures.

Chemical composition

To characterize the chemical species present in each surface, we used secondary ion mass spectrometry (SIMS). Briefly, in SIMS, an energetic beam of ions is used to sputter secondary ions from a surface; the chemical composition of the sputtered material is then analyzed with mass spectrometry. To determine the chemical composition of each microstructured surface, the ratio of the mass spectrometry signal from a given chemical species is normalized relative to silicon using literature values for the relative sensitivity factor of each chemical species in a silicon matrix. The relative sensitivity factors are calculated with data taken from flat silicon surfaces, so the compositions reported are approximate due to the topology of the microstructured silicon.

For each gas, the chemical species present in the ambient gas becomes incorporated into the surface in large amounts; different elements are incorporated at different levels. Figure 3.25 shows the fractional concentration of chemical species in the microstructured silicon surfaces. The smaller amount of fluorine incorporated in the SF_6 samples is attributed to its high reactivity with silicon and likely removal of silicon-fluorine complexes during the microstructure formation process. All of the samples contain oxygen from the

SIONYX1403000030.0042

SAMSUNG EX. 1002 - 2912/4148

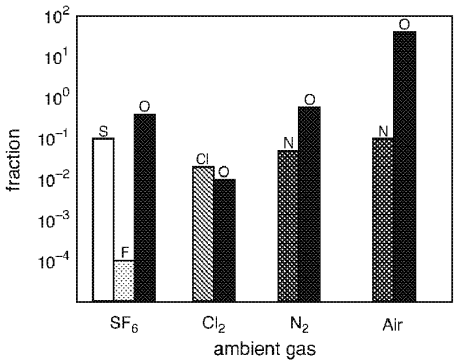


Figure 3.25: Fractional concentration of chemical species as measured by secondary ion mass spectrometry for different ambient gas species: (a) sulfur hexafluoride (SF_6), (b) nitrogen (N_2), (c) chlorine (Cl_2), and (d) air.

native oxide layer that grows on the surface after texturing, but the air sample contains two orders of magnitude more oxygen than the other samples. The high oxygen content and further analysis using Rutherford backscattering spectrometry and transmission electron microscopy suggest that a silicon rich layer of silica, SiO_x (x<2) [38], is formed. The amount of oxygen in the SF_6, Cl_2, and N_2 samples is correlated with surface area (roughness). Samples analyzed with SIMS were not treated with an HF dip and, therefore, the oxygen signal for the SF_6, N_2 and Cl_2 samples is likely due to a native oxide layer. Following an HF dip to remove the native oxide layer and surface contaminants, samples made in vacuum do not show the presence of any elements other than silicon.

3.8 Effect of ambient gas pressure

In this section we examine morphology differences brought about by varying the pressure of SF_6.

SIONYX1403000030.0043

SAMSUNG EX. 1002 - 2913/4148

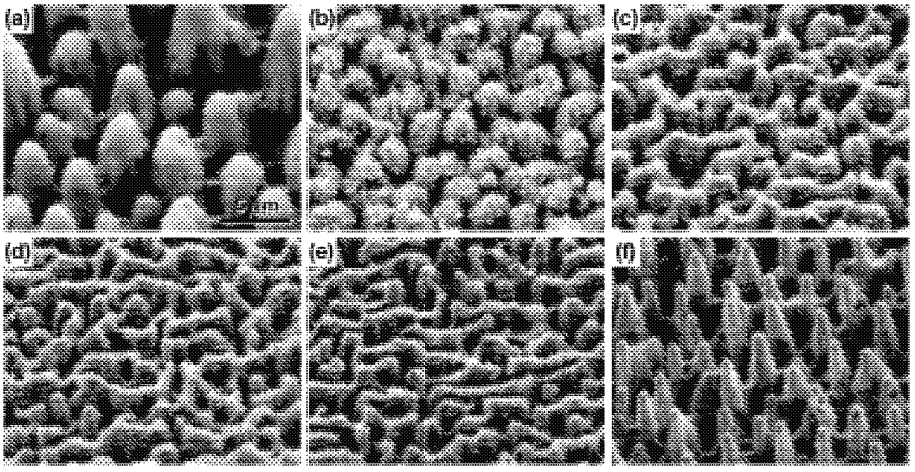


Figure 3.26: Scanning electron micrographs of the surface morphology for different pressures of SF_6: (a) vacuum (10^{-6} torr), (b) 0.007 bar, (c) 0.027 bar, (d) 0.13 bar, (e) 0.40 bar, and (f) 0.67 bar. Each SEM is taken at a 45° angle to the surface with the same magnification.

3.8.1 Surface morphology

Figure 3.26 shows the morphology for microstructures with increasing pressures of SF_6. At a very low pressure of SF_6 (0.007 bar), the surface has a great deal of nanostructure. It looks similar to vacuum samples covered in clumps of nanoparticles. For pressures between 0.027 and 0.40 bar, ridges form and the beginnings of smaller, sharper structures occur. Above 0.533 bar the surface begins to resemble the conical microstructures we see at our standard conditions. Increasing the pressure from 0.67 bar to 1 bar does not affect the final morphology.

3.8.2 Surface layer structure and composition

At this time we do not have data on the effect of gas pressure on the surface layer structure or composition.

SIONYX1403000030.0044

SAMSUNG EX. 1002 - 2914/4148

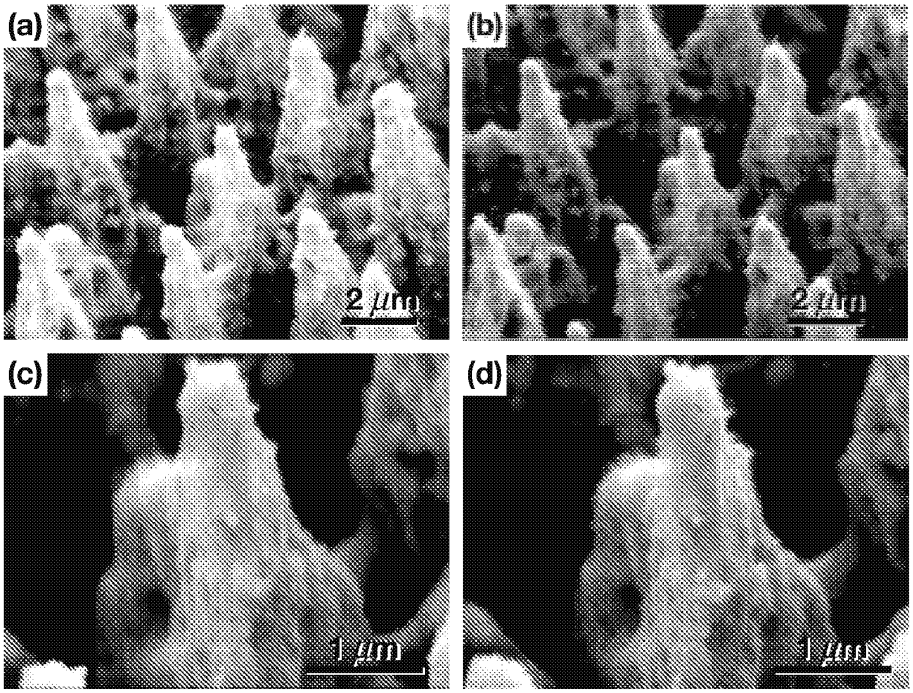


Figure 3.27: Scanning electron micrographs of microstructured silicon ((a) and (c)) before annealing and ((b) and (d)) after annealing at 1075 K for 3 hours.

3.9 Effect of annealing

As a part of our post-processing analysis, we often anneal samples following laser microstructuring. Annealing will be an important step later in this disseratation and here we analyze any morphological or chemical changes brought about by annealing.

3.9.1 Surface morphology

As shown in Figure 3.27, annealing has no visible effect (within the resolution of the SEM) on microstructure morphology or the surface-nanoparticle morphology. The same area of a microstructured surface is shown before and after annealing for 3 hours at 1075 K.

SIONYX1403000030.0045

SAMSUNG EX. 1002 - 2915/4148

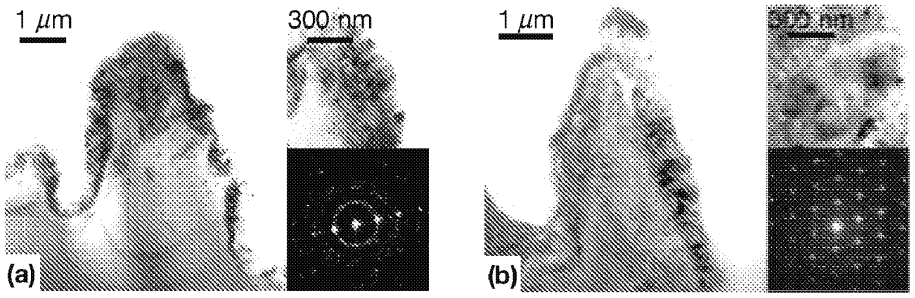


Figure 3.28: Transmission electron micrographs of the surface before (a) and after (b) annealing. The annealed sample has sharper features in the diffraction pattern. Insets: (upper) high-magnification view of the disordered region at the tip of the microstructure and (lower) selected area electron diffraction pattern obtained from the disordered region.

3.9.2 Surface layer structure and composition

Although we do not see any change in the microstructure morphology, there are some effects in both the nanoscale structure and chemical makeup of the surface layer.

Surface layer structure

Figure 3.28 shows transmission electron micrographs of an annealed and a non-annealed sample. The surface layer is similar in thickness and structural composition before and after annealing. However, the diffraction rings are sharper for the annealed sample. The sharper rings most likely indicate that annealing increases the crystallinity of the sample somewhat. Other factors, such as the crystalline plane in focus, could sharpen the diffraction pattern as well.

Chemical composition

We use Rutherford backscattering spectrometry and simulation to characterize the chemical content of the surface before and after annealing. After an anneal of 30 minutes at 725 K, the amount of sulfur in the surface layer drops from about 0.7 at % to

SIONYX1403000030.0046

SAMSUNG EX. 1002 - 2916/4148

0.5 at %. Annealing at 875 K for 30 minutes also results in a concentration of 0.5 at % sulfur. The decrease in the observed sulfur concentration upon annealing most likely reflects sulfur diffusing deeper into the sample than can be observed by Rutherford backscattering spectrometry (RBS)[5]. These results are summarized as a part of Table 3.1 near the end of the chapter.

3.10 Effect of silicon substrate properties

In our work thus far, we have found little, if any, effect on micrometer-scale morphology and chemical composition from the following substrate properties: crystalline orientation, dominant carrier (n- or p-doping), doping level, and presence or absence of a native oxide layer before irradiation.

3.11 Summary of chemical composition (RBS data) and trends

Before moving onto the discussion section, we summarize some of the important information presented in this chapter. Table 3.1 summarizes all of the chemical composition data we have from Rutherford backscattering measurements; the important parameter varied in each section is in bold[6]. Table 3.2 summarizes trends that we see in morphology and composition with experimental parameters. The trends are listed for increasing values of the experimental parameter.

[5]The diffusion length of S in c-Si in 30 minutes at 775K was estimated to be 25 nm by extrapolation from data in [39], p. 68. In microcrystalline or amorphous silicon, the diffusion length may be somewhat different but is unlikely to increase more than threefold.

[6]The RBS spectra may be affected slightly by the changing morphology of the surface, as the surface area of the samples changes as processing conditions change. However, we are confident in comparing the sulfur concentrations for the microstructures made with 2, 3, and 5 laser pulses and the microstructures made with 3, 4, and 5 kJ/m^2 because they are similar in size and shape. As the shape of the microstructures is unchanged by annealing, the concentrations before and after annealing can also be compared with confidence.

SIONYX1403000030.0047

SAMSUNG EX. 1002 - 2917/4148

Average laser fluence (kJ/m^2)	Number of pulses	Annealing temperature (30 minutes)	Pulse duration	Sulfur concentration (±0.1 at. %)
2.5	500	-	100 fs	0.3
3.0	500	-	100 fs	0.3
4.0	500	-	100 fs	0.4
4.9	500	-	100 fs	0.6
8.0	500	-	100 fs	0.7
10.0	500	-	100 fs	0.7
8.0	**2**	-	100 fs	0.2
8.0	**3**	-	100 fs	0.4
8.0	**5**	-	100 fs	0.4
8.0	**10**	-	100 fs	0.5
8.0	**20**	-	100 fs	0.6
8.0	**50**	-	100 fs	0.6
8.0	**500**	-	100 fs	0.7
8.0	500	**725 K**	100 fs	0.5
8.0	500	**875 K**	100 fs	0.5
30.0	1500	-	**30 ns**	0.5
30.0	1500	875 K	**30 ns**	0.4

Table 3.1: Summary of sulfur concentration in samples determined by Rutherford backscattering spectrometry. The bolded values highlight the important parameter being varied from standard conditions.

SIONYX1403000030.0048

SAMSUNG EX. 1002 - 2918/4148

Observables					
Parameter	Morphology			Composition	
	Height	Density	Tip Size	Sulfur	Crystallinity
Shot number	⇑	⇓	⇓	⇑	–
Fluence	⇑	⇓	⇓	⇑	–
Wavelength	⇑	⇓	⇓	–	–
Gas pressure	⇑	⇑	⇓	⇑	–
Anneal temp.	–	–	–	–	⇑

Table 3.2: Summary of the trends in observable morphology and composition characteristics with experimental parameters. The ⇑ symbol indicates that the observable increases as the experimental parameter is increased; the ⇓ symbol indicates a decrease in the observable.

3.12 Discussion

Although a rigorous model for the formation mechanism is not yet determined, we can use the observations made in this chapter to speculate on the mechanisms responsible in creating these quasi-ordered array of microstructures. We hope that this chapter instills in the reader a sense of the large parameter space involved in our experimental procedure. The experimental complexity and intense conditions created in the focal region of the laser make direct observation and modeling rather difficult. However, using the information in this chapter and existing research on similar microstructures formed on a variety of materials (including silicon), we speculate on the important factors for microstructure formation.

Periodic surface ripples, conical microstructures, whisker-like structures, and pyramidal microstructures have all been observed following high-energy ion-bombardment during sputtering experiments [40, 41, 42, 43, 44, 45, 46, 47]. In work that is closely related to our research, conical structures formed after irradiation with nanosecond laser pulses

SIONYX1403000030.0049

SAMSUNG EX. 1002 - 2919/4148

have been observed by several research groups [7, 8, 10, 12, 13, 14, 15, 17, 48, 49, 50]. Although the two means of irradiation (ion-bombardment and laser) are very different, the morphology of the resulting structures is similar. In these papers, there are several proposed formation mechanisms for the microstructures, but there is no complete explanation and most of the papers only address one aspect of the formation mechanism. However, despite the lack of a rigorous explanation, there are four significant factors included in most of the proposed mechanisms: ablation/sputtering, melting, chemical etching/interaction, and redeposition. The degree to which these factors contribute to the final morphology of the surface depends heavily on experimental conditions.

We begin with a chronological description of what occurs during irradiation with each laser pulse. As a laser pulse strikes the surface (at fluences above the ablation threshold), material is ablated from the surface; a thin layer of material that is not ablated, but melts, either by ultrafast melting or thermal melting, is left behind. This melted layer evolves and interacts with its surroundings until it resolidifies. While the surface is melted, chemical species from the ambient gas interacts with the melt layer either through etching or implantation into the surface [51]. Some of the ambient gas molecules inside the focal region of the laser dissociate in the intense electric field [52], so numerous derivatives of the ambient gas could be present at the surface. The possible chemical reactions for our standard conditions are covered in both [18] and [20]. The main chemical interactions between dissociated SF_6 and the melted surface layer are etching of the silicon surface by fluorine and incorporation of sulfur into the silicon surface. Lastly, ablation results in a rich cloud of the the substrate material above the molten surface and redeposition of removed material occurs. After about a microsecond, the surface resolidifies and energy deposited by the laser diffuses out of the focal region. At this point the surface is permanently altered and, when another laser pulse strikes the surface, the process occurs again with different initial

SIONYX1403000030.0050

SAMSUNG EX. 1002 - 2920/4148

conditions.

Before suggesting a formation mechansim, we comment on the significance of observations made earlier in this chapter. The first observation we highlight comes from the effect of fluence (Section 3.3) on our final microstructures. Conical microctructures do not form unless the fluence is above the ablation threshold for silicon. This indicates that ablation is a critical component to the formation mechanism. Pedraza *et al.* observe growth of conical structures while working with nanosecond pulses *below* the ablation threshold. In our attempt to mimic their work, we also used fluences below the ablation threshold and see conical structures form. However, the fluence is an average fluence for a spot hitting a *flat* surface. The surface is only flat for the first few pulses, and, after several hundred pulses, it is far from flat. After a few hundred pulses of nanosecond duration, the surface has protrusions much like the femtosecond case after 10 pulses. These protrusions concentrate light into the pits beside them and, inside these pits, the fluence rises *above* the ablation threshold. In fact, while structuring with nanosecond laser pulses, we do not observe the presence of a plasma spark (a strong indication of ablation) until several hundred laser pulses have struck the surface. Also, Fowlkes *et al.* observe that, at high pulse count, the nanosecond-laser-formed structures begin to decrease in height and eventually end up below the surface; indicating that ablation becomes a more dominant effect once the microstructures are formed [13].

From this information, we conclude that ablation is a necessary condition for microstructure formation. But it is important to keep in mind that, in general, the energy density quoted is an average value for a *flat* surface and that a roughened surface topology can result in higher energy concentrations in places. We feel that energy concentration on a roughened surface is the reason for the similarity in morphology evolution for increasing shot number and fluence. As the structures evolve with shot number, they become sharper

SIONYX1403000030.0051

SAMSUNG EX. 1002 - 2921/4148

and effectively increase the fluence deposited in the pits to the side of the structures. The same morphology is seen with lower fluence and higher shot number as with higher fluence and lower shot number.

Another important observation to be made is that redeposition is definitely occuring during the formation process. The strongest evidence for this is that nanosecond-laser-formed structures are tens of microns above the substrate surface (Section 3.4). From a fluid dynamics discussion, Pedraza *et al.* conclude that capillary motion of molten material cannot yield the microstructure shape we see. They conclude that the dominant mechanism is redeposition of gaseous material (removed from the pits around the structures) at the molten tips. This process is akin to whisker growth by the vapor-liquid-solid (VLS) mechanism [53]. Also, the presence of the spherical tips on both the femtosecond and nanosecond-laser-formed structures is indicative of a VLS process and evidence that redeposition is occurring. It appears that the most dominant change brought about by increasing pulse duration from femtoseconds to nanoseconds is that redeposition becomes dominant over ablation and etching.

For all experiments, the chemical species in the ambient gas are implanted into the surface layer during irradiation (Section 3.7). In the ns-formed structures, sulfur incorporation process is probably similar to gas immersion laser doping (GILD) [54], in which a semiconductor is doped by melting the surface with nanosecond-laser pulses in the presence of a gas that contains the desired dopants. The dopants are incorporated into the melt and the rapid solidification that follows laser melting produces highly supersaturated solid solutions [55]. Sulfur may be incorporated into the femtosecond-formed structures by a similar process.

Also, the final morphology depends a great deal on the ambient gas and the interaction of the chemical environment with the molten surface. For many years, we felt

SIONYX1403000030.0052

SAMSUNG EX. 1002 - 2922/4148

that the reactivity of the elements in the ambient gas was the important factor. However, recent evidence that a non-halogen containing gas (H_2S) yields sharp conical microstructures indicates that perhaps it is the inclusion of elements into the molten surface and the subsequent effect on fluid dynamics that is more important. Incorporation of some elements yields sharp, ordered microstructures (S and Cl), while others yield blunt, disordered structures (O and N).

Lastly, the presence of a molten layer following laser irradiation is necessary for formation of conical microstructures. The femtosecond-laser fluences used are not far above the ablation threshold, and so we expect a molten layer to form at the surface after the laser-induced plasma recombines and the electrons equilibrate with the lattice [51]. The presence of laser induced periodic surface structures after a few pulses leaves little doubt that the surface is molten following irradiation. The way in which this molten surface evolves and interacts with its environment determines the final micrometer-scale morphology, chemical composition, and nanoscale structure of the surface layer. From the evidence we have collected, we feel that it is a combination of fluid dynamics, material removal/redeposition, and implantation of chemical species that yield sharp, conical microstructures [56]. All of these processes require the presence of a molten surface layer.

Using the observations highlighted above, we present a formation process for femtosecond-laser-formed conical microstructures. Following the first laser pulse, the surface is pocked with randomly dispersed defects (Figure 3.1 (a)). These act as scattering centers for the next pulse, resulting in laser induced periodic surface structures through capillary wave excitation in the molten surface. The next few laser pulses strike the surface and melt the ripple pattern. The ripples can be thought of as one half of a silicon column on the surface. A liquid cylinder whose length is larger than its radius is unstable and tends collapse into a row of equally sized and equally spaced drops to reduce surface tension (a

SIONYX1403000030.0053

SAMSUNG EX. 1002 - 2923/4148

phenomenon called cylindrical collapse described by Joseph Plateau in the 1800s) [57]. In our case, the laser melted ripples collapse, or bead-up, along the long axis of the ripple. The periodicity and size of these beads is affected by several parameters. First, the wavelength of the laser induced periodic surface structures is important in the spacing of the beads, which is clearly shown by comparing structures made with 400 nm light with those made with 800 nm light. Furthermore, capillary waves and surface tension influence the evolution of the final bead spacing and size. Surface tension and capillary waves are, in turn, influenced by melt depth, temperature, ambient gas pressure, and inclusion of impurity atoms in the melt layer. We feel that the inclusion of sulfur into the surface and its effects on surface tension are extremely important in creating small, regularly spaced beads. Once the bead pattern is formed, preferential removal of material to the sides of the beads (ablation) takes over as the dominant factor and the final conical microstructures are dug out of the surface. Redeposition continues to occur at the molten tip, but ablation dominates the changes in morphology. At the end of several hundred pulses, we have a quasi-ordered array of sharp conical microstructures.

This proposed formation mechanism is strictly for femtosecond-laser-formed microstructures in the presence of SF_6. Consequently, the mechanism will vary somewhat for different conditions, but the major themes and observations should apply to other experimental conditions.

SIONYX1403000030.0054

SAMSUNG EX. 1002 - 2924/4148

Chapter 4

Optical and electronic properties

In addition to microstructuring the surface, femtosecond-laser irradiation in the presence of SF_6 turns the normally grey, mirror-like surface of silicon into a deep, velvet black. The black surface is clear indication that laser microstructuring alters the optical properties of the silicon surface. In this chapter, we again vary numerous experimental parameters as we did in Chapter 3, but now we examine how experimental parameters affect the optical and electronic properties of microstructured silicon.

Again, our standard conditions are as follows: irradiation of an n-doped silicon wafer (n-Si(111), 260 μm thick, resistivity $\rho = 8 - 12\ \Omega$·m) with an average of 500 laser pulses (100 fs, central wavelength 800 nm, fluence 8 kJ/m^2) in 0.67 bar of SF_6. We vary the number of incident laser pulses, the laser fluence, wavelength, pulse duration, ambient gas species and pressure, substrate doping and crystalline orientation, and annealing temperature. We then measure the effect on the optical and electronic properties of microstructured silicon.

SIONYX1403000030.0055

SAMSUNG EX. 1002 - 2925/4148

4.1 Optical measurements

In order to measure optical properties, we use a Hitachi U-4001 spectrophotometer equipped with an integrating sphere. With the spectrophotometer, we measure the total hemispherical (specular and diffuse) reflectance (R) and transmittance (T) of a sample. The integrating sphere ensures that both specular and diffuse reflectance, as well as both direct and scattered transmittance, are measured accurately. Light from two lamp sources, one for the UV and one for the visible and near-IR, is sent into a monochromator that selects a single wavelength and directs it onto a sample; the amount of light, transmitted or reflected, is then measured relative to a baseline reading taken using a highly reflective titanium oxide blank. The operational wavelength range for this device is 250 nm to 2500 nm.

For reflectance measurements, samples are carefully taped on an optical quality, calcium fluoride window for support; the window is used because samples are smaller than the access ports of the integrating sphere. The calcium fluoride window is then placed on the back port of the integrating sphere in order to reflect light back into the integrating sphere detector. The reflectance of the calcium fluoride window is low ($< 6\%$) in the operational wavelength range [20]. For transmittance, samples are suspended at the front port of the integrating sphere; all transmitted light (scattered or direct) enters the integrating sphere detector. The spectrophotometer setup is described in more detail by Younkin [20].

By measuring both the reflectance (R) and transmittance (T) from 250 nm to 2500 nm, we calculate the absorptance of each sample with

$$A(\lambda) = 1 - T(\lambda) - R(\lambda). \tag{4.1}$$

SIONYX1403000030.0056

SAMSUNG EX. 1002 - 2926/4148

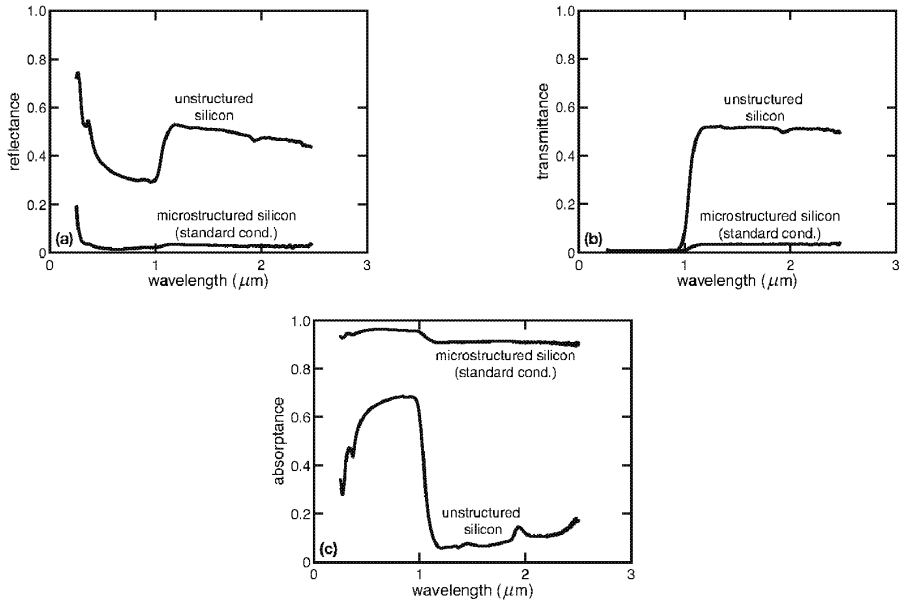


Figure 4.1: (a) Reflectance, (b) transmittance, and (c) the calculated absorptance of microstructured silicon for standard conditions. For reference, the same measurements are shown for unstructured, crystalline silicon.

4.1.1 Optical properties of femtosecond-laser microstructured silicon

Figure 4.1 shows the measured reflectance, transmittance, and calculated absorptance for an unstructured silicon wafer and microstructured silicon. The drop in the absorptance for crystalline silicon near 1100 nm corresponds to the band-gap energy of crystalline silicon (1.07 eV). Light at longer wavelengths does not contain enough energy to promote an electron from the valence band to the conduction band and absorption becomes negligible for crystalline silicon.

Microstructured silicon has a drastically decreased reflectance and transmittance over the entire measured spectrum. The lowered transmittance and reflectance results in near-unity absorptance in the entire wavelength region 250 nm $< \lambda <$ 2500 nm. The increased absorption in the visible is consistent with the black appearance and, indeed, across

SIONYX1403000030.0057

SAMSUNG EX. 1002 - 2927/4148

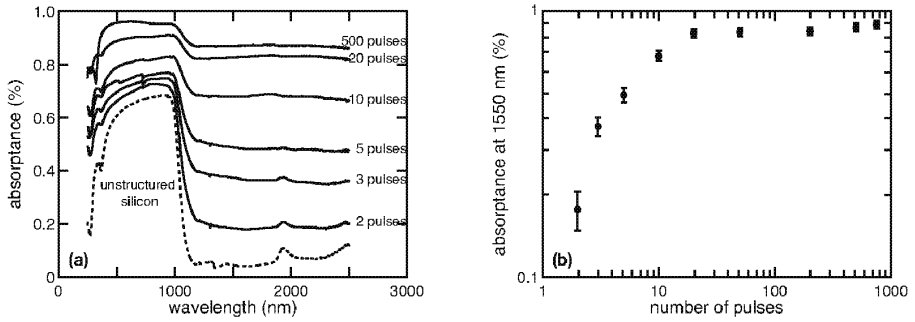


Figure 4.2: (a) Wavelength dependence of absorptance on the number of laser pulses used in microstructuring and (b) the dependence of absorptance at 1550 nm on the number of laser pulses used in microstructuring. All samples were made with 8 kJ/m^2 and 0.67 bar SF_6

this large range of wavelengths the surface is quite "black." By varying experimental parameters we examine what is responsible for the high, featureless absorption. In the following sections, we present only absorptance, which is calculated from a measured reflectance and transmittance (Equation 4.1). All optical measurement samples are made by translating the substrate in order to microstructure a 10 x 10 mm^2 area.

4.1.2 Effect of shot number

In this section, we examine the effect of shot number on the optical properties of microstructured silicon. Figure 4.2 (a) shows that the absorptance increases over the entire wavelength range as the number of laser pulses increases. Figure 4.2 (b) shows that the absorptance at 1550 nm (a below-band gap wavelength) increases strongly with the number of pulses delivered to the sample, up to 20 pulses; additional pulses have little effect. For each microstructured sample, the absorptance is essentially constant and featureless between 1.2 and 2.5 μm, increasing with the number of pulses. It should be noted that the increase in absorptance for below-band gap wavelengths saturates around 20 pulses, the same number of pulses at which the sulfur content saturates (see Table 3.1).

SIONYX1403000030.0058

SAMSUNG EX. 1002 - 2928/4148

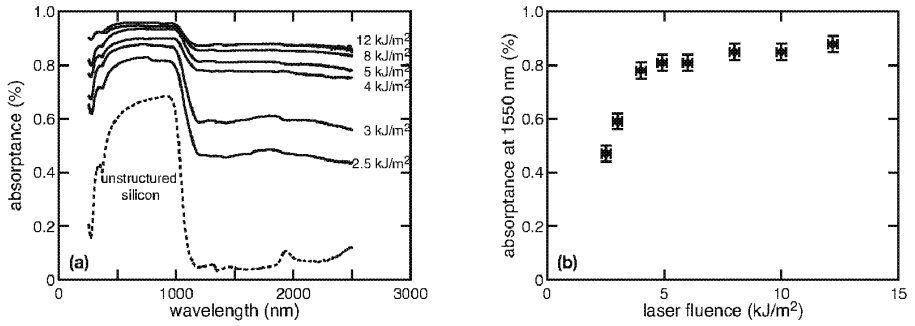


Figure 4.3: (a) Wavelength dependence of absorptance on the laser fluence used in microstructuring and (b) the dependence of the absorptance at 1550 nm on the laser fluence used in microstructuring. All samples were made with 500 laser pulses and 0.67 bar SF_6.

4.1.3 Effect of fluence

In this section, we examine the effect of laser fluence on the optical properties of microstructured silicon. Figure 4.3 (a) shows that absorptance increases with fluence across the entire measured spectrum. Figure 4.3 (b) shows that the absorptance at 1550 nm increases strongly with fluence for fluences up to about 5 kJ/m^2 and increases more slowly for higher fluences. Surfaces made with a fluence of 4 kJ/m^2 or higher display constant absorptance *vs.* wavelength at below-band gap wavelengths; at lower fluences, the absorptance decreases gradually with increasing wavelength. With 500 laser pulses, fluences below 2.5 kJ/m^2 do not produce uniform microstructuring of the surface (see Figure 3.10). Fluences less than 2 kJ/m^2 neither alter the surface nor affect the optical properties. Again, it should be noted that the increase in absorptance at below-band gap wavelengths saturates at around 5 kJ/m^2, the fluence at which the sulfur content saturates (see Table 3.1).

4.1.4 Effect of pulse duration

In this section, we examine the effect of changing the pulse duration from femtoseconds to nanoseconds on the optical properties of microstructured silicon. The femtosecond-

SIONYX1403000030.0059

SAMSUNG EX. 1002 - 2929/4148

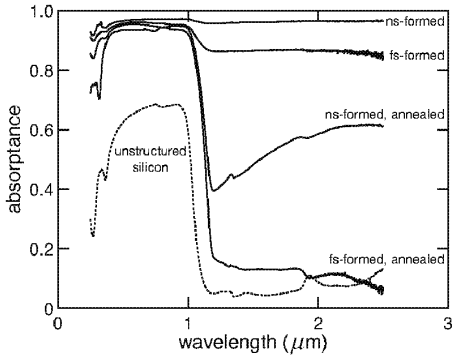


Figure 4.4: Wavelength dependence of absorptance for femtosecond-laser-formed and nanosecond-laser-formed microstructures, before and after thermal annealing at 875 K for 30 minutes (see Section 4.1.8). The absorptance of an unstructured silicon substrate is also shown.

formed structures were made using our standard conditions and the nanosecond-formed structures were made using the conditions listed in Section 3.4.1. Figure 4.4 shows the wavelength dependence of the absorptance of both structured surfaces and of the unstructured substrate silicon. The absorptance of the nanosecond- and femtosecond-formed structures is very similar: near-unity, featureless absorptance from 0.4 μm to 1 μm, a small decrease in absorptance around 1.1 μm (the band edge of ordinary silicon), and strong featureless absorptance from 1.1 μm to 2.5 μm. The absorptance of the nanosecond-structured material (98% in the visible, 95% in the infrared) is somewhat higher than that of the femtosecond-structured material (95% in the visible, 85% in the infrared) across the measured spectral range. Annealing the structured surfaces at 875 K for 30 minutes (see Section 4.1.8) leaves the visible absorptance essentially unchanged, but dramatically decreases the below-band gap absorptance. The below-band gap absorptance of the nanosecond-structured samples changes less with annealing than that of the femtosecond-structured samples; further annealing of the nanosecond-structured samples for up to 12 hours causes little additional

SIONYX1403000030.0060

SAMSUNG EX. 1002 - 2930/4148

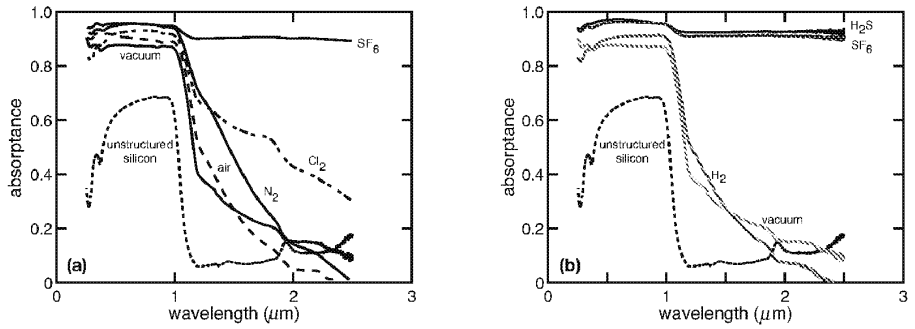


Figure 4.5: (a) Wavelength dependence of absorptance on the gas species used in microstructuring. The gases shown are those used in the morphology study (Section 3.7). The vacuum chamber was at a base pressure of less than 10^{-6} bar for the vacuum sample. (b) Absorptance for a selection of gases that more directly shows the importance of sulfur in the high below-band-gap absorptance. All samples were made with 500 laser pulses and 8 kJ/m^2 laser fluence.

change [1].

4.1.5 Effect of laser wavelength, polarization, and propagation direction

There is no measurable difference between the absorptance of silicon microstructured with 400 nm light and silicon microstructured with 800 nm light. Similarly, changing the polarization and propagation direction of the laser does not affect the measured absorptance.

4.1.6 Effect of ambient gas

In this section, we examine the effect of the ambient gas species on the optical properties of microstructured silicon. We investigate the optical properties of microstructured silicon surfaces prepared in a number of gases (in addition to SF_6). Figure 4.5 (a)

[1] In the 40 μm-deep nanosecond-formed structures, the below-band gap absorptance should be significantly amplified by multiple reflections; geometric effects may be less important to the below-band gap absorption in the femtosecond-formed structures because these infrared wavelengths are not much less than the 8 μm structure depth.

SIONYX1403000030.0061

SAMSUNG EX. 1002 - 2931/4148

shows the absorptance of samples prepared in gases used in Section 3.7 (SF_6, Cl_2, N_2, air, and vacuum). Microstructuring in SF_6 and Cl_2 brings about the most dramatic change in absorptance, with SF_6 having the highest absorptance of all the gases for the entire measured wavelength range. Samples made in air, N_2, and vacuum show increased absorptance relative to unstructured silicon for most of the measured wavelengths (λ <1.5 μm for air, $\lambda < 1.77$ μm for N_2, and $\lambda < 2.3$ μm for vacuum). The reason the absorptance for these gases falls below that of unstructured silicon is unknown.

Although all samples show an increase in infrared absorption over unstructured silicon, samples structured in SF_6 are the only ones with near-unity, featureless absorptance across the entire measured spectrum. For samples made in air, N_2, and vacuum, the gradual decrease of absorptance for wavelengths longer than 1.2 μm is consistent with the presence of band tails of Urbach states due to a high density of defects [58]. Samples microstructured in Cl_2 have significantly increased infrared absorption; the infrared absorption for Cl_2 samples may be a combination of band tails from Urbach states and the large aspect ratio microstructures formed in this gas (Figure 3.19).

From this information, it appears that structuring in SF_6 is critical to the near-unity, below-band gap absorptance. To demonstrate that it is the presence of sulfur in the ambient gas that is critical, we compared the optical properties of samples structured in another set of gases (SF_6, H_2S, H_2, and vacuum). Figure 4.5 (b) shows the absorptance for these gases as compared to unstructured silicon. The most significant chemical difference between H_2 and H_2S is the presence (or lack) of sulfur. As shown in Figure 4.5 (b), the absorptance of H_2S is nearly identical to that of samples made in SF_6, while samples made in H_2 have absorptances that resemble samples made in vacuum. The information shown in Figure 4.5 (b) is compelling evidence that sulfur plays a vital role in the near-unity, below-band gap absorptance.

SIONYX1403000030.0062

SAMSUNG EX. 1002 - 2932/4148

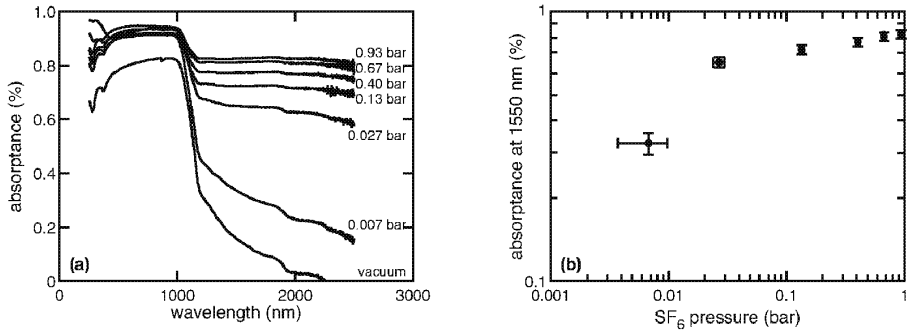


Figure 4.6: (a) Wavelength dependence of absorptance on the pressure of SF_6 used in microstructuring and (b) the dependence of absorptance at 1550 nm on the pressure of SF_6 used in microstructuring. The vacuum chamber was at a base pressure of less than 10^{-6} bar for the vacuum sample.. All samples were made with 500 laser pulses and 8 kJ/m^2 laser fluence.

4.1.7 Effect of gas pressure

In this section, we examine the effect of the pressue of SF_6 on the optical properties of microstructured silicon. Figure 4.6 (a) shows that the absorptance increases with increasing SF_6 pressure. The largest variation in absorptance occurs for below-band gap wavelengths (Figure 4.6 (b)). The greatest rate of increase is observed at low pressures. Above 27 mbar, the below-band gap absorptance does not vary with wavelength, while at lower pressure, it decreases with increasing wavelength.

4.1.8 Effect of annealing

In this section, we examine the effect of annealing on the optical properties of microstructured silicon. Figure 4.7 (a) shows the effect of annealing for thirty minutes at several temperatures on the absorptance of samples made under standard conditions. Annealing at temperatures below 575 K has little effect on the absorptance. Annealing between 575 K and 875 K does not affect absorptance above the band gap, but lowers

SIONYX1403000030.0063

SAMSUNG EX. 1002 - 2933/4148

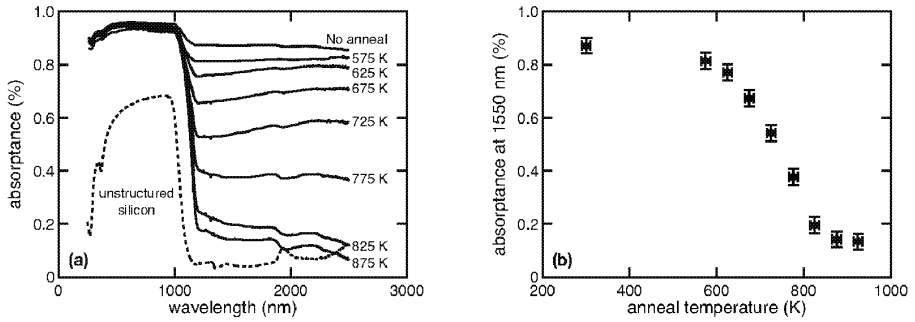


Figure 4.7: (a) Wavelength dependence of absorptance on anneal temperature (following microstructuring). The data point at room temperature (300 K) corresponds to a microstructured sample that was not annealed. (b) The dependence of absorptance at 1550 nm on anneal temperature (following microstructuring). All samples were made with 500 laser pulses and 8 kJ/m^2 laser fluence in 0.67 bar SF_6, and were annealed for 30 minutes.

the below-band gap absorptance; the higher the temperature, the greater the decrease in absorptance (Figure 4.7 (b)). Raising the annealing temperature above 875 K does not produce any additional change. As shown in the last chapter (Figure 3.27), annealing has no visible effect on the shape of either the microstructures or the surface nanoparticles.

It should be noted that sulfur concentrations in the annealed samples, however, do not mirror the below-band gap absorptance (Table 3.1). Annealing is the only parameter (that we have Rutherford backscattering data on) for which below-band gap absorptance does not mirror sulfur concentration. Upon annealing a standard sample at either 725 K or 875 K for 30 minutes, the sulfur content in both cases decreases by only 40%, while the infrared absorptance decreases by almost an order of magnitude. The concentration of sulfur in the annealed samples is comparable to that of the sample made with 4 kJ/m^2 and 500 pulses, or the sample made with ten pulses and 8 kJ/m^2; for these samples, the infrared absorptance is only 20% less than that of a standard sample.

SIONYX1403000030.0064

SAMSUNG EX. 1002 - 2934/4148

4.1.9 Effect of silicon substrate properties

In our work thus far, we have found little, if any, effect on the optical properties of microstructured silicon from the following substrate properties: Crystalline orientation, dominant carrier (*n*- or *p*-doping), dopant concentration (resistivity), and presence or absence of a native oxide layer before irradiation.

4.2 Electronic measurements

For a limited number of parameters, we took a combination of resistivity and Hall effect measurements [59] in order to determine the electronic properties of the disordered surface layer following microstructuring in SF_6. From this information we are able to determine the sheet resistance, dominant carrier sign, sheet carrier density, Hall mobility, and approximate values for resistivity and bulk-carrier density.

4.2.1 Hall effect and resistivity measurements: procedure and apparatus

Much of the information presented in this section, along with design elements for our apparatus, is found at a wonderful online-tutorial from the National Institute of Standards and Technology (NIST) [59]. If the reader is interested in learning more about these measurements, they are strongly recommended to visit this website.

For resistivity and Hall effect measurements, we employ the van der Pauw technique, a widely used technique for accurately determining resistivity of semiconductor samples [60]. Briefly, one uses an arbitrarily shaped, thin-plate sample containing four very small ohmic contacts placed at the edges of the sample and measure two characteristic resistances associated with the contacts. With these characteristic resistances, the sheet resistance and bulk electrical resistivity of the sample can be calculated. The strength of

SIONYX1403000030.0065

SAMSUNG EX. 1002 - 2935/4148

the van der Pauw technique is that it minimizes error from asymmetries in sample geometry and resistances introduced by contacts.

Sample preparation

For the van der Pauw technique, we need to make ohmic electrical contact to four points on the disordered surface layer. For accurate measurements, it is preferable to have a thin sample and to have a suitable geometry for the electrical contacts. We naturally fulfill the first condition because the measurements we are making are for the thin surface layer[2]. For a suitable contact geometry, the average diameters (D) of the contacts, and sample thickness (d) must be much smaller than the distance between the contacts (L). Relative errors caused by non-zero values of D are of the order of D/L. The preferred geometry for the contacts is a cloverleaf setup, but a square or rectangle geometry (with the contacts at the four corners) is acceptable; we use a square geometry for our measurements.

In order to make electrical contact to our samples, we do the following: first a microstructured sample is dipped in a 5% HF solution for 5 minutes to remove the native oxide layer. Next, with a mask covering all but the very corners of 10 x 10 mm^2 microstructured areas, samples are placed in a thermal evaporator and we evaporate chrome/gold (Cr/Au) contacts onto the four corners. We then use a dicing saw to cut 0.25 mm slivers from each side. Cutting the sample edges ensures that the contacts are only connected to the surface layer and do not touch the substrate layer. Finally, we use a wire bonder to connect the contacts on the corner of the samples to four Cr/Au contact pads evaporated onto a glass slide. This arrangement allows us to make repeatable contact to each of the corner contacts on the microstructured surface. For clarity, we number each of the corners

[2]Although not apparent at this point, it is a reasonable assumption that we only measure the properties of the microstructured layer because it has drastically different electronic properties than the substrate wafer. This will become more clear later in this chapter.

SIONYX1403000030.0066

SAMSUNG EX. 1002 - 2936/4148

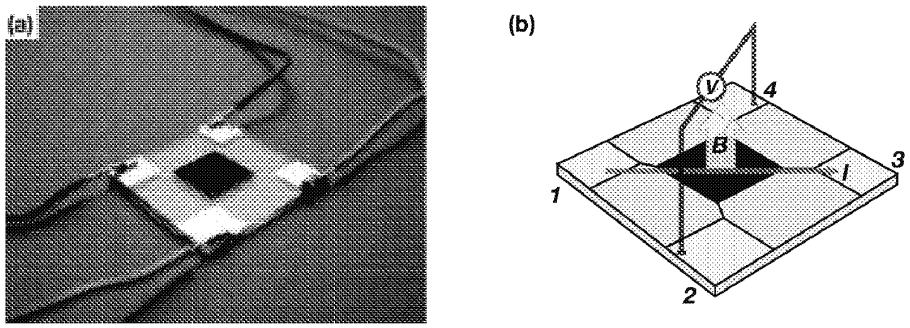


Figure 4.8: (a) A picture of a sample prepared for resistivity and Hall effect measurements. (b) A schematic diagram of how Hall voltage measurements are done. The current flowing through a strong magnetic field creates a voltage normal to both the current and the magnetic field. This is called the Hall effect. The numbers are indices used to keep track of how the current/voltage is being applied/measured.

(1,2,3,4) in counter-clockwise ascending order (See Figure 4.8 (b)). From this point on, when we refer to voltages or currents between two corners we use V and I with the corner numbers as indices. For example, a voltage measured from corner 1 and 2 (V_1 - V_2) is listed as V_{12}. Figure 4.8 (a) shows a sample prepared for measurement.

Resistivity

The procedure for making resistivity (ρ) measurements is as follows: we first apply a small DC current (10 μA) from corner 2 to corner 1(I_{21}). The current should be small enough to ensure that power dissipation is negligible. In general, for a measured resistance R between corners, I should satisfy

$$I < (200R)^{-0.1}. \tag{4.2}$$

We then measure the voltage from corner 3 to corner 4 (V_{34}). We repeat this measurement for the reversed polarity (apply I_{12} and measure V_{43}). Similarly, we measure six more voltages (V_{41}, V_{14}, V_{12}, V_{21}, V_{23}, and V_{32}). From these measurements we calculate eight resistances,

SIONYX1403000030.0067

SAMSUNG EX. 1002 - 2937/4148

$$R_{21,34} = V_{34}/I_{21}, R_{12,43} = V_{43}/I_{12}, \tag{4.3}$$

$$R_{32,41} = V_{41}/I_{32}, R_{23,14} = V_{14}/I_{23}, \tag{4.4}$$

$$R_{43,12} = V_{12}/I_{43}, R_{34,21} = V_{21}/I_{34}, \tag{4.5}$$

$$R_{14,23} = V_{23}/I_{14}, R_{41,32} = V_{32}/I_{41}. \tag{4.6}$$

The second half of this sequence of measurements is redundant. Also, as will become apparent in the next chapter, these measurements should be made in the dark to remove contributions from photovoltaic and photoconductive effects.

From these four measured resistances we calculate two characteristic resistances R_A and R_B,

$$R_A = (R_{21,34} + R_{12,43} + R_{43,12} + R_{34,21})/4, \tag{4.7}$$

$$R_B = (R_{32,41} + R_{23,14} + R_{14,23} + R_{41,32})/4. \tag{4.8}$$

With these characteristic resistances we calculate the sheet resistance, R_S, by numerically solving the van der Pauw equation,

$$e^{-\pi R_A/R_S} + e^{-\pi R_B/R_S} = 1, \tag{4.9}$$

by iteration. The bulk electrical resistivity (ρ) is the sheet resistance (R_S) times the sample thickness (d).

Hall measurements

For readers unfamiliar with the Hall effect or Lorentz force, it is recommended that they visit the NIST website listed above [59]. Briefly, the Lorentz force refers to the force on a charged particle while it moves in an applied magnetic field. Electrons (or holes)

SIONYX1403000030.0068

SAMSUNG EX. 1002 - 2938/4148

moving perpendicular to an applied magnetic force experience a force normal to both the direction of flow and the direction of the applied field; the direction of deflection depends on the sign of the charge. For a current flowing through a semiconductor in the presence of a strong magnetic field, the Lorentz force causes a build up of charge to one side of the semiconductor. The charge build up results in a voltage, the Hall voltage, across the sample in the direction of carrier deflection. By experimentally measuring this voltage, we can determine the sign of the carrier and the sheet carrier density (n_s for electrons and p_s for holes). This, combined with resistivity measurements, can be used to determine the Hall mobility (μ).

Our Hall measurement procedure is as follows: we take the same samples used for resistivity measurements and place them inside a strong applied magnetic field (several thousand gauss). The sample is oriented such that the magnetic field is perpendicular to the silicon surface and defined as positive if the field lines enter the back and leave from the front of the sample. We then apply a small AC current (about 1–2 μA) from contact one to contact three (I_{13}) and measure the voltage across contacts 2 and 4 (V_{24P}, where P indicates a positive magnetic field). Figure 4.8 shows a schematic diagram of this procedure[3]. We then reverse the current (I_{31}) and measure the voltage (V_{42P}). Similarly we measure V_{13P} and V_{31P}, then reverse the direction of the magnetic field, and measure V_{24N}, V_{42N}, V_{13N}, and V_{31N}. With these measurements made we can calculate four characteristic voltages,

$$V_C = V_{24P} - V_{24N}, \tag{4.10}$$

$$V_D = V_{42P} - V_{42N}, \tag{4.11}$$

$$V_E = V_{13P} - V_{13N}, \tag{4.12}$$

$$V_F = V_{31P} - V_{31N}. \tag{4.13}$$

[3]The Hall voltage can be very small at times and, as such, we used a lock-in amplifier, locked to the frequency of the input current, to measure the voltage. In addition, the applied current and magnetic field strength were varied to maximize signal and minimize noise.

SIONYX1403000030.0069

SAMSUNG EX. 1002 - 2939/4148

If the the sum of these four voltages,

$$V_S = V_C + V_D + V_E + V_F, \tag{4.14}$$

is negative, the dominant carriers are electrons (n-type). If the sum is positive, the dominant carriers are holes (p-type). We then calculate the sheet carrier density (in units of cm^{-2}) with

$$p_s = \frac{8 \times 10^{-8} IB}{qV_S} \tag{4.15}$$

$$n_s = \left| \frac{8 \times 10^{-8} IB}{qV_S} \right|, \tag{4.16}$$

where B is the magnetic field in gauss and I is the current in amperes (A). The bulk carrier density is then simply the sheet carrier density (n_s or p_s) divided by the sample thickness (d). With the sheet carrier density and the sheet resistance determined, we calculate the Hall mobility (in units of $\mathrm{cm}^2\mathrm{V}^{-1}\mathrm{s}^{-1}$) with

$$\mu = \frac{1}{qn_s R_S}. \tag{4.17}$$

4.2.2 Results

To ensure that our measurement technique is valid, we performed these measurements on an n-doped, $\rho = 800 - -1200\Omega$·cm, unstructured wafer. We measured a resistivity of 957 Ω·cm and a mobility of 1101.2 $\mathrm{cm}^2\mathrm{V}^{-1}\mathrm{s}^{-1}$ (in close agreement with literature values [39]). The data we present is in the form of sheet carrier density and sheet resistance instead of bulk density and bulk resistivity. We present the data in terms of sheet values rather than bulk values because these are the actual measured quantities and we do not know the thickness (d) of our surface layer with good precision.

SIONYX1403000030.0070

SAMSUNG EX. 1002 - 2940/4148

Original doping	Average fluence (kJ/m^2)	Doping after structuring	Sheet resistance R_S (Ω)	Sheet carrier density n_s (cm^{-2})	Hall mobility μ ($cm^2V^{-1}s^{-1}$)
n	unstructured	-	31931	1.78×10^{11}	1101
n	4.0	n	4865	7.37×10^{12}	174
n	6.0	n	4992	7.15×10^{12}	175
n	8.0	n	6253	4.52×10^{12}	221
n	10.0	n	4554	8.83×10^{12}	155

Table 4.1: Electronic properties of microstructured silicon for several fluences. The original substrate used for all samples is an n-doped, ρ = 800–1200 Ω·cm wafer.

Effect of fluence

There is no recognizable trend in the electronic properties with increasing fluence. The sheet resistance, carrier density, and mobility for all four fluences is similar. However, there are some important results contained withing Table 4.1. Microstructuring silicon results in a higher sheet carrier density than the original substrate, which means that microstructuring n-dopes the surface. We somewhat expected n-doping because sulfur is incorporated into the surface and a sulfur atom has two more valence electrons than silicon. The increase in carrier density is likely the reason for the drop in sheet resistance. Also, the mobility of electrons in the disordered surface layer is an order of magnitude less than the unstructured crystalline wafer. The mobility is decreased because of disorder in the structure of the surface layer; with crystalline order over only tens of nanometers, the carriers' mean free path is greatly diminished compared to the mean free path of carriers in a single crystal substrate.

SIONYX1403000030.0071

SAMSUNG EX. 1002 - 2941/4148

Effect of annealing

Original doping	Average fluence (kJ/m^2)	Annealing temperature (30 minutes)	Sheet resistance R_S (Ω)	Sheet carrier density n_s (cm^{-2})	Hall mobility μ ($cm^2V^{-1}s^{-1}$)
n	4.0	-	4865	7.37×10^{12}	174
n	4.0	825 K	8433	7.34×10^{12}	101
n	4.0	1075 K	2749	1.88×10^{13}	121
n	8.0	-	6253	4.52×10^{12}	221
n	8.0	825 K	6147	1.92×10^{13}	53

Table 4.2: Electronic properties of microstructured silicon for two annealing temperatures. The original substrate used for all samples is an n-doped, ρ = 800–1200 Ω·cm wafer.

Table 4.2 shows the effect of annealing to two different temperatures on the electronic properties of microstructured silicon. Although these data do not represent a large cross section of samples, we see that annealing to high temperatures increases sheet carrier density. We saw in the last chapter that annealing does not change the sulfur content significantly and, if anything, the sulfur content is diminished. However, the level of n-doping increases significantly with annealing at 1075 K. The second observation to note is that an anneal at 825 K does not affect the sheet carrier density significantly but seems to frustrate the conduction of carriers; the resistance increases and the mobility is significantly decreased. Annealing at 1075 K, however, greatly increases the sheet carrier density but does not decrease the mobility as significantly.

SIONYX1403000030.0072

SAMSUNG EX. 1002 - 2942/4148

Effect of original substrate properties

In this section, we examine the effect of using a p-doped substrate (rather than n-doped) and how annealing and fluence affect the electronic properties of structured p-doped substrates.

Original doping (resistivity)	Average fluence (kJ/m^2)	Doping after structuring/annealing	Sheet resistance R_S (Ω)	Sheet carrier density $n_s(p_s)$ (cm^{-2})	Hall mobility μ (cm^{2}V^{-1}s^{-1})
n (ρ=900 Ω·cm)	4.0	n	4865	7.37×10^{12}	174
p (ρ=10 Ω·cm)	4.0	***p***	164	1.4×10^{14}	271
p (ρ=100 Ω·cm)	4.0	***p***	5167	(7×10^{14})	(1)
p (ρ=10 Ω·cm)	3.0	***p***	199	1.34×10^{14}	1392
p (ρ=100 Ω·cm)	3.0	***p***	1492	4.77×10^{13}	27

Table 4.3: Electronic properties of microstructured silicon for p-doped substrates. The measurement for sheet carrier density of a p-doped, 100 Ω·cm substrate and an average fluence of 4.0 kJ/m^2 is likely imprecise.

Table 4.3 shows electronic measurements of p-doped substrates following structuring with two different fluences. The most significant result is that, after microstructuring a p-doped substrate with low fluence (3 or 4 kJ/m^2), the surface remains p-doped . The n-doping from the sulfur-implantation is not enough to cancel out the original p-doping[4]. The measurement of sheet carrier density and mobility of a p-doped (ρ = 100 Ω·cm) sample irradiated with a fluence of 4.0 kJ/m^2 is likely imprecise. The Hall voltage for this sample was extremely small and difficult to distinquish from the noise. We think that this is because these conditions lead to a near perfect cancellation of original hole-doping and

[4]It should be noted that, in order to reach resistivities in p-doped substrates that are comparable to n-doped substrates, the sheet carrier density of holes must be significantly higher due to their lower mobilities [39]

SIONYX1403000030.0073

SAMSUNG EX. 1002 - 2943/4148

implanted electrons. Effectively, the disordered surface layer was near to intrinsic silicon and, combined with the highly disordered structure, the Hall voltage is small and difficult to measure.

Original doping (resistivity)	Average fluence (kJ/m^2)	Doping after structuring/annealing	Sheet resistance R_S (Ω)	Sheet carrier density $n_s(p_s)$ (cm^{-2})	Hall mobility μ (cm^{2}V^{-1}s^{-1})
p (ρ=10 Ω·cm)	4.0	p	164	1.4×10^{14}	271
p (ρ=10 Ω·cm)	4.0 (annealed)	***n***	2080	1.14×10^{14}	26
p (ρ=10 Ω·cm)	3.0	p	199	1.34×10^{14}	1392
p (ρ=10 Ω·cm)	3.0 (annealed)	***n***	1492	1.54×10^{14}	27
p (ρ=100 Ω·cm)	4.0	p	5167	(7×10^{14})	(1)
p (ρ=100 Ω·cm)	4.0 (annealed)	***n***	2607	4.56×10^{13}	53
p (ρ=100 Ω·cm)	3.0	p	1492	4.77×10^{13}	27
p (ρ=100 Ω·cm)	3.0 (annealed)	***n***	3351	3.71×10^{13}	50

Table 4.4: Electronic properties of microstructured silicon for p-doped substrates after annealing. The dominant carrier changes from holes to electrons upon annealing. All annealed samples were annealed to 1075 K for 30 minutes.

Table 4.4 examines the effect of annealing on the electronic properties of microstructured p-doped wafers. Following microstructuring at lower fluences (3 and 4 kJ/m^2) the originally p-doped wafers remain p-doped. However, after annealing at 1075 K for 30 minutes, the surface layer becomes n-doped. The sulfur content does not change significantly, but the change in carrier concentration is so drastic that it *reverses* the sign of the dominant carrier. We believe that this indicates that annealing causes a change in the local bonding/electronic environment of implanted sulfur atoms, increasing the number of

SIONYX1403000030.0074

SAMSUNG EX. 1002 - 2944/4148

free carriers by decreasing the coordination number or annihilating defects. We discuss this further in the following section.

4.3 Discussion

Silicon surfaces microstructured in the presence of SF_6 have interesting and unique optical properties, namely near-unity absorptance from 250 nm to 2500 nm; This spectral range includes wavelengths well below the band-gap of crystalline silicon, which normally pass through silicon unabsorbed. In addition to being scientifically interesting, it is also of great interest in optoelectronic applications (see Chapter 5). For several years, we have tried to identify the mechanism responsible for the remarkable optical properties. We use the information contained in this chapter to speculate on the subject.

For visible wavelengths, the increased absorption is a result of the morphology of the microstructured surface. The conical nature of the microstructures leads to multiple reflections for incoming light. That is, a photon incident onto the structured surface is likely to undergo more than one reflection before leaving the surface. With the steep conical geometry of our microstructures, calculations show that, on average, a photon undergoes approximately four reflections before escaping [20]. At each reflection, incident light absorbed by the intrinsic visible absorptance of ordinary silicon (~65%) quickly raises the total absorptance to over 90%.

Surface roughening is a common method for decreasing reflectance and increasing absorption. For decreasing acoustic reflections, anechoic surfaces are commonly seen in lecture halls and airports. Nature uses roughened surfaces to enhance night vision in nocturnal insects [61] and for more efficient absorption in flower petals [62]. In silicon optoelectronics, many different surface structuring techniques are used to increase absorption, such as wet

SIONYX1403000030.0075

SAMSUNG EX. 1002 - 2945/4148

etching [63, 64], reactive ion etching [65, 66], and thin-films of porous silicon [67].

A roughened surface morphology explains the increased absorption in the visible but does not explain the near-unity absorption for below-band gap wavelengths. Simply roughening a surface does not increase absorption for wavelengths of light that are not absorbed in the first place. For instance, roughened glass still transmits visible light, albeit diffusely, as one sees with frosted glass. At best, the absorptance of crystalline silicon at wavelengths longer than 1.1 μm is 5-6%, and four reflections does not bring the absorptance up to 90%. Therefore, for below-band gap wavelengths, the only way to have near-unity absorptance is if microstructuring alters the band structure of the surface layer. However, determining how the band is altered is not an easy task. It is apparent from information presented in this chapter that sulfur plays a critical role in the high below-band gap absorption (Figure 4.5). We contend that it is not just the presence of sulfur, but, more importantly, the local electronic environment of the sulfur atoms that alters the band structure and leads to the unique optical properties.

There is ample evidence that sulfur is, in some way, responsible for the below-band gap absorption. Samples microctructured in SF_6 or H_2S (Figure 4.5) are the only ones that exhibit near unity absorption across the entire measured spectrum; microstructuring in gases that do not contain sulfur does not produce comparable below-band gap absorption. Changing the pulse duration drastically changes the surface morphology but femtosecond-formed and nanosecond-formed structures have similar optical properties and sulfur content (Figure 4.4). Recently we found that using a powder of elemental sulfur spread across a sample surface has the same effect on the optical properties as using SF_6 as an ambient gas [68]. Chemical composition information from Chapter 3 shows that sulfur is incorporated at very high levels for all experiments with SF_6. We also know that sulfur content and absorptance are intimately connected; both of these values increase with shot number and

SIONYX1403000030.0076

SAMSUNG EX. 1002 - 2946/4148

fluence (and likely with gas pressure).

We are therefore able to assert with confidence that sulfur incorporation is responsible for below-band gap absorptance. However, the way in which sulfur incorporation alters the band structure is more difficult to determine. To propose an answer, we use the information we have on the disordered surface layer structure and chemical composition, and how these factors correlate with optical and electronic properties.

The one particular experimental parameter that sticks out from the others is annealing. It sticks out because, unlike other experimental parameters, annealing causes the below-band gap absorptance to decrease in a manner that does not mirror the sulfur concentration. For example, samples annealed at 725 K and at 875 K have the same sulfur concentration, but the absorptance at 1550 nm of the sample annealed at 725 K is five times that of the sample annealed at 875 K. Also, the observed sulfur concentration in the sample annealed at 875 K is the same as that from the 10-pulse or 4-kJ/m2 samples, but the 10-pulse and 4-kJ/m^2 samples display 80% of the below-band gap absorptance of a standard sample, while the below-band gap absorptance of the sample annealed at 875 K is reduced to essentially the same value as the original substrate silicon.

The most likely explanation of the below-band gap absorption is that laser microstructuring incorporates the sulfur impurities into the silicon matrix in optically active states, and annealing causes bond rearrangement within the silicon matrix that renders the sulfur impurities optically inactive. Following irradiation with an intense shot-pulse laser, the resolidification front of the molten layer is sufficiently fast that it can trap impurity atoms in a nonequilibrium configuration [69]. Indeed, sulfur concentrations we measure in microstructured surfaces exceed the equilibrium solubility of sulfur in crystalline silicon [70] by many orders of magnitude, indicating that sulfur is incorporated through a highly nonequilibrium process. Annealing then allows the lattice to relax toward a more ther-

SIONYX1403000030.0077

SAMSUNG EX. 1002 - 2947/4148

modynamically stable configuration. The optically active states could be the result of any number of defects including changes in coordination number, bond length, and/or bond angle of neighboring atoms. The concentration levels of sulfur we measure in the surface are more than sufficient to create an impurity/defect band of energy levels within the band gap [71]. Deactivation during annealing is likely from rearrangement of these bonding properties or annihilation of defects toward a more stable configuration. Annealing at 875 K for 30 minutes would permit defect annihilation [72] and diffusion of sulfur over several hundred nanometers [39].

Another strong piece of evidence that supports bonding rearrangement and defect annihilation comes from the effect of annealing on the electronic properties. Following microstructuring, p-doped substrates still have holes as their dominant charge carrier, despite the addition of nearly 1 at. % sulfur with two possible donor electrons per atom. However, after annealing, the dominant carrier in the microstructured surfaces switches to electrons. This change in dominant carrier occurs with no significant change in the sulfur content. Before annealing the sulfur is incorporated in the surface in such a way that its donor electrons do not contribute to conduction; the donor electrons are likely locked up in a trap, or perhaps the coordination number of the implanted sulfur is larger than four. Then, during annealing, the bonding arrangements change and donor electrons are freed up to contribute to conduction. The number of electrons being released is large enough to eliminate the holes as charge carriers and turn the surface into an n-doped one with sheet carrier concentrations on the order of 10^{14} cm^{-2}.

We do not expect that crystallinity plays an important role. Annealing temperatures that completely eliminate the below-band gap absorptance are much lower than the temperatures at which significant grain growth would be expected in microcrystalline or polycrystalline silicon [73]. In addition, the pulse duration experiments indicate that the

SIONYX1403000030.0078

SAMSUNG EX. 1002 - 2948/4148

disordered layer covering the femtosecond-formed structures is not essential for below-band gap absorption, as both transmission electron microscopy and Rutherford backscattering spectrometry indicate that the nanosecond-formed structures are nearly single-crystal. The optically active configuration of sulfur may be able to exist in either the single crystal nanosecond-formed structures or the highly disordered femtosecond-formed structures; the optical deactivation process must not require a significant increase in the crystallinity of the femtosecond-formed structures. Alternatively, different optically active configurations of sulfur could be present in the femtosecond-formed and nanosecond-formed structures, although none of our results directly suggest this interpretation. Also, collaborators of ours have been able to demonstrate below-band-gap absorption in a crystalline silicon surface doped with comparable levels of sulfur using ion-implantation followed by laser-annealing [74].

The location and electronic environment of the sulfur atoms before and after annealing is not well known and further work is needed to understand the mechanism by which the sulfur incorporation leads to below-band gap absorption. The disordered surface layer of femtosecond-formed structures is likely to provide a wide variety of possible electronic environments for the sulfur impurities. We are getting much closer to understanding the mechanism and work is ongoing towards solving this problem. We have recently demonstrated that implantation of other chalcogens (selenium and tellurium) also leads to near-unity below-band gap absorptance [68]. From these experiments we are learning a great deal about the local electronic and structural environment of the impurity atoms.

In summary, it is the incorporation of sulfur atoms into an optically active, nonequilibrium, and highly defective configuration that leads to the unique below-band gap absorptance for samples microstructured in SF_6. Annealing causes bond rearrangement and defect annihilation within the silicon matrix that renders the sulfur impurities optically inactive.

SIONYX1403000030.0079

SAMSUNG EX. 1002 - 2949/4148

Chapter 5

Femtosecond-laser microstructured silicon photodiodes

In the previous two chapters, we presented all that we know about how experimental parameters affect the morphology, chemical composition, optical properties, and electronic properties of laser microstructured silicon. Of these results, the near-unity absorptance from ultraviolet wavelengths to the near-infrared for samples microstructured in SF_6 is of particular interest. Extending the spectral range of silicon-based photodetectors is an active area of research because of silicon's low cost and ease of integration with microelectronics. In this chapter, we describe our efforts toward creating a silicon-based photodiode that takes advantage of the extended optical absorption range of silicon microstructured in SF_6. We use the information from the last two chapters to help us design our photodiode and understand the resulting behavior.

We begin the chapter with a basic discussion of photodiode operation by describing the most basic and prevalent type of photodiode, the p-n photodiode. We then describe the procedure for making laser-microstructured silicon photodiodes and examine how ex-

SIONYX1403000030.0080

SAMSUNG EX. 1002 - 2950/4148

perimental parameters affect the performance of these devices. The information from the previous chapters assist us in optimizing and understanding the behavior of our photodiodes.

5.1 Introduction to photodiodes: the *p-n* junction

Before we discuss the creation of laser microstructured silicon photodiodes, we must first describe the basic operation and principles of a photodiode. That is, we must understand the structure of a photodiode and, most importantly, how a photodiode detects light. We present here a basic description of photodiodes and refer the reader to several references for further information on these thoroughly studied devices [39, 75, 36, 76].

There are many types of semiconductor photodiode devices (*p-n* or *p-i-n* photodiodes, avalanche photodiodes, Schottky-barrier photodiodes, heterojunction photodiodes, *etc.*). For the purposes of this dissertation, we discuss one of the more basic devices, the *p-n* photodiode; this particular photodiode is created by the junction between two of the same semiconductor material (a homojunction) with different impurity concentrations. Specifically, a homojunction where the impurity concentration changes abruptly from acceptor impurities (*p*-doped) to donor impurities (*n*-doped)[1]. Although the *p-n* homojunction is a simplified example, the ideas presented can be extended to other photodiode devices and, for that matter, *all* other semiconductor devices.

We begin by considering two separated pieces of similar semiconductor material, one doped with acceptor impurity atoms (*p*-type) and one doped with donor impurity atoms (*n*-type), both electrically neutral. If we bring the two pieces into contact with one another, there will be a large gradient in carrier concentration at the interface (junction).

[1]Much of the basic theory of *p-n* junctions was developed by Shockley shortly after he helped invent the transistor [77].

SIONYX1403000030.0081

SAMSUNG EX. 1002 - 2951/4148

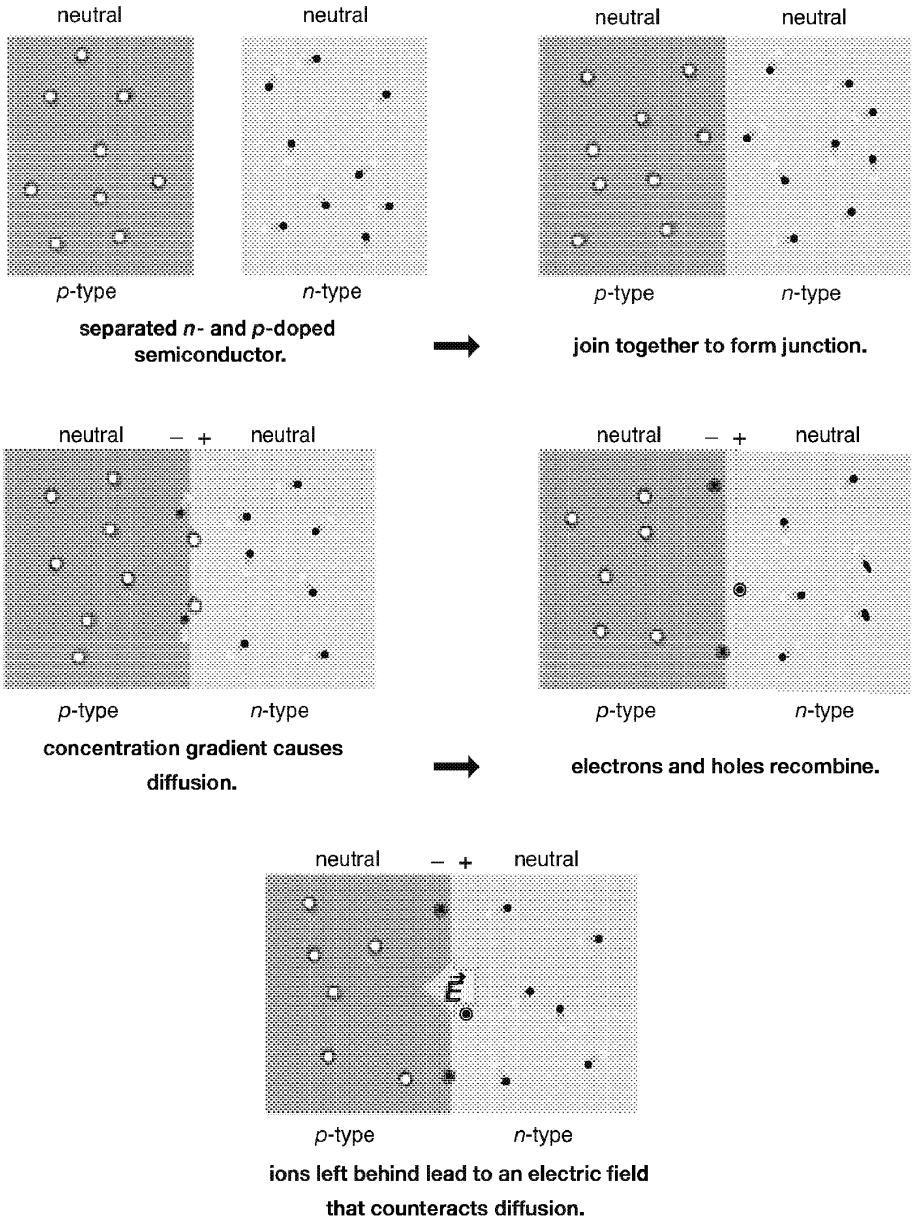


Figure 5.1: Cartoons illustrating the steps that lead to the contact potential and electric field build up in a p-n junction.

After all, one side is doped with electrons and the other, holes. The difference in carrier concentration causes a diffusion potential across the junction; electrons and holes begin to

SIONYX1403000030.0082

SAMSUNG EX. 1002 - 2952/4148

diffuse across the junction to areas of lower concentration. As they cross to the other side of the junction they recombine with their oppositely charged electrical counterparts in the region very close to the junction. The recombined carriers are trapped on the far side of the junction and leave behind immobile ions (called space charges) on the side from which they came. As the number of space-charges increases (positively charged for the n-type side and negatively for the p-type), a potential difference builds up, which results in an electric field in the direction opposite the diffusion potential. If this process progresses to thermal equilibrium, the internal electric field exactly cancels the diffusion potential and charge diffusion stops. Once thermal equilibrium is reached, there is a thin insulating layer near the junction in which all charge carriers have been depleted by recombination (depletion region) and a strong electric field and large potential difference (the contact potential V_c)[2] exist. Figure 5.1 illustrates the steps resulting in the build up of a contact potential and internal electric field. Figure 5.2 shows the junction at thermal equilibrium, along with potential variation near the junction and energy-band diagram. Again, this explanation is conceptual and simplifies the considerations necessary for a rigorous physical description of the p-n-junction.

Now, let us consider what happens if we take the junction out of equilibrium by applying an external electric field[3] (see Figure 5.3). The first case we consider is an applied electric field that reinforces the internal field. The field pushes the holes in the p-doped side to the left and the electrons in the n-doped to the right. This expands the insulating depletion region and increases both the internal electric field and the potential difference across the junction. In this case, no current flows; this arrangement is called the back bias condition. Next, we consider an applied electric field that is opposite the internal field.

[2]Typical potential differences in silicon based devices are around 0.8 V [39] over a depletion region of a few hundred nanometers.

[3]For clarification, the way in which we apply an external electric field is to apply a bias voltage across the two sides of the junction.

SIONYX1403000030.0083

SAMSUNG EX. 1002 - 2953/4148

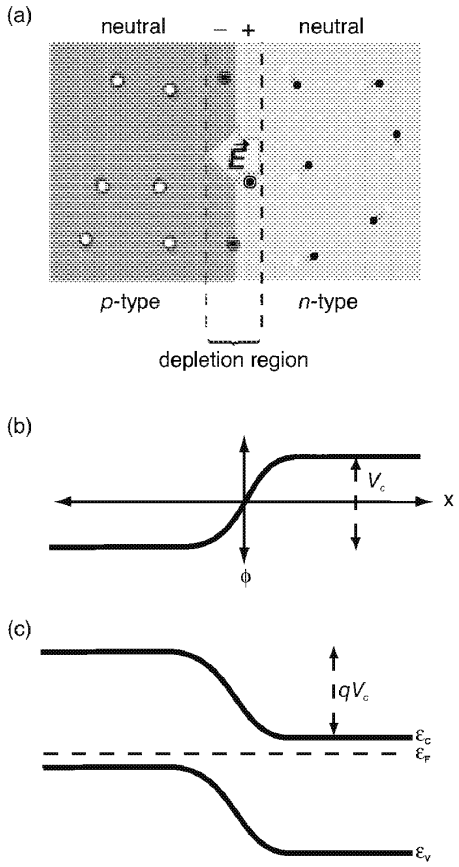


Figure 5.2: (a) A cartoon illustrating the final state of a p-n junction in thermal equilibrium. Also shown are the (b) potential variation with distance and (c) the energy-band diagram. V_c is the contact potential.

In this case, the applied field shrinks the depletion region, diminishing the internal electric field and potential difference across the junction. Current flows with electrons being injected from the right and holes injected (electrons leaving) from the left, replenishing carriers that recombine at the junction. The current increases quickly with increasing external field; this arrangement is called the forward bias condition. From this discussion, we see that the p-n junction allows current to flow in only one direction, *i.e.* it rectifies the current. This is the familiar electronic behavior of a diode. The characteristic current-voltage (I-V) behavior

SIONYX1403000030.0084

SAMSUNG EX. 1002 - 2954/4148

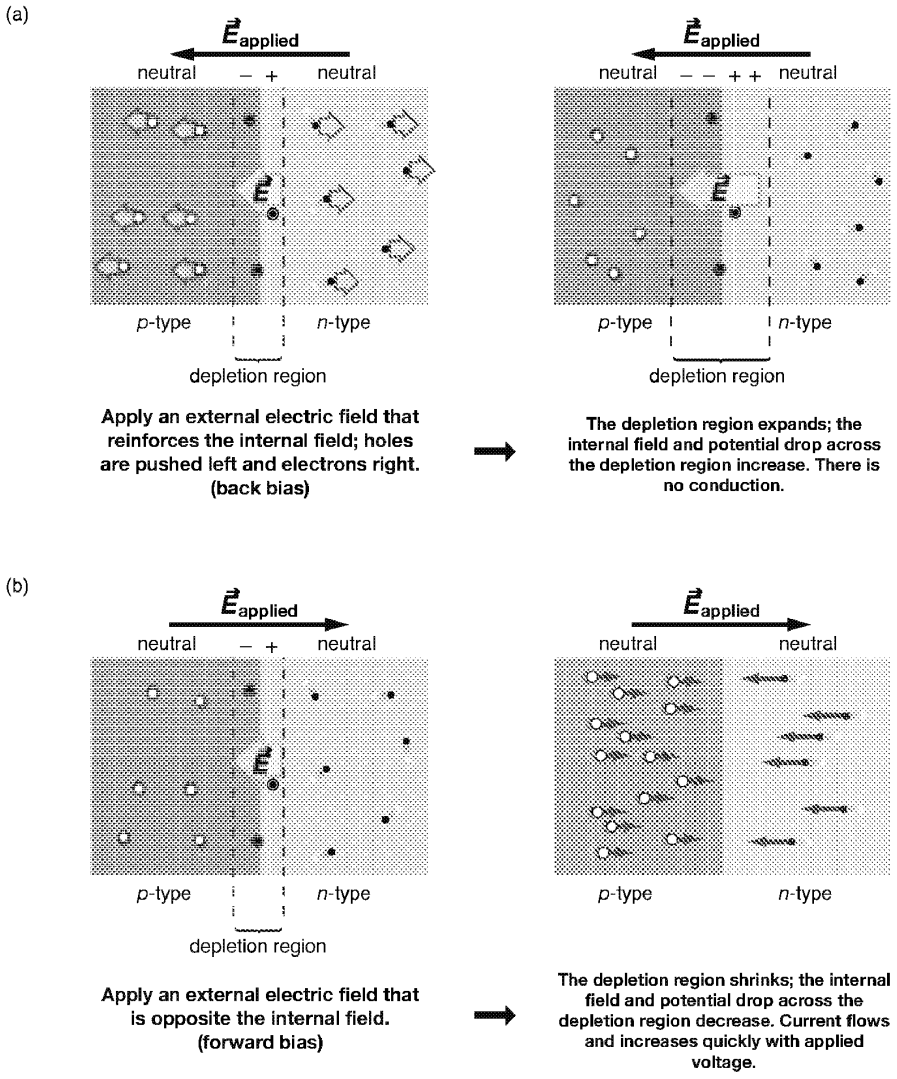


Figure 5.3: (a) Cartoon illustrating a p-n juction under the influence of an externally applied electric field that reinforces the internal field. This is called the back biased condition. (b) Cartoon illustrating a p-n juction under the influence of an externally applied electric field opposite the internal field. This is called the forward biased condition.

of a diode is critical in the operation of photodiodes.

Let us now consider the rectification behavior a little more closely by looking at the factors that contribute to current flow. For this discussion, we define a positive current

SIONYX1403000030.0085

SAMSUNG EX. 1002 - 2955/4148

contribution as that coming from a hole moving from left to right or, similarly, an electron moving from right to left in the above cartoons. In an ideal p-n diode there are two major contributions to the current across the junction. These are the the generation current (I_{gen}) and the recombination current (I_{rec}). The generation current refers to the current from electron-hole pairs that are thermally created within the depletion region. For a given set of conditions (mobility, temperature, carrier lifetime, carrier concentration, *etc.*) there is a statistical rate at which electron-hole pairs are spontaneously generated within the depletion region (thus the name generation current). If an electron-hole pair is created in the depletion region, the strong internal electric field immediately separates the pair and the electron and hole contribute to current flow across the junction. The generation current is negative by our definition, typically small (< 1 μA), and has many names including the saturation current and the dark current. The generation current is, for the most part, independent of the magnitude of the potential difference across the depletion region because *any* potential difference results in an electric field to separate generated carriers. The recombination current comes from the statistical probability that there are electrons (holes) in the n-doped (p-doped) side that have enough thermal energy to surmount the potential barrier at the junction. The number of carriers with enough thermal energy follows Fermi-Dirac statistics and the recombination current has an exponential dependance on the temperature and the size of the potential step. The size of the potential step depends on both the contact potential at thermal equilibrium and the size of the applied voltage. The recombination

SIONYX1403000030.0086

SAMSUNG EX. 1002 - 2956/4148

current is positive based on our definition. So, we have

$$I_{gen} \propto \text{generation rate} \tag{5.1}$$

$$I_{rec} \propto e^{\frac{V_{applied}-V_{contact}}{k_b T}}$$

$$\propto e^{V_{applied}} \tag{5.2}$$

$$I_{tot} = I_{rec} - I_{gen}. \tag{5.3}$$

With no applied field and at thermal equilibrium, the total current flow must be zero and I_{rec} must equal I_{gen}. If we solve for this condition and substitute the solution back in, we have

$$I_{tot} \propto I_{gen}(e^{V_{applied}} - 1). \tag{5.4}$$

From this equation, it easy to see how the characteristic current-voltage (I-V) behavior of a diode is achieved (see Figure 5.4 (a)). If we apply a negative voltage (back bias), the exponential term quickly goes to zero and the total current flow saturates at the small value of $-I_{gen}$. If we apply a positive voltage (forward bias), the current increases exponentially. This result is simply a reiteration of what the cartoon in Figure 5.3 illustrates. That is, a p-n junction only allows current flow in one direction, it rectifies.

Now, let us consider what happens when light is incident onto the junction. If a photon of sufficient energy enters into the depletion region, it is absorbed and creates an electron-hole pair. Again, this electron-hole pair is separated immediately due to the internal electric field in the depletion region and we add negative contribution to the total current; this contribution is the photocurrent (I_L) and it is proportional to the number of incident photons. We return to the equation for the total current and add on the contributing term from the photocurrent,

$$I_{tot} \propto I_{gen}(e^{V_{applied}} - 1) - I_L. \tag{5.5}$$

SIONYX1403000030.0087

SAMSUNG EX. 1002 - 2957/4148

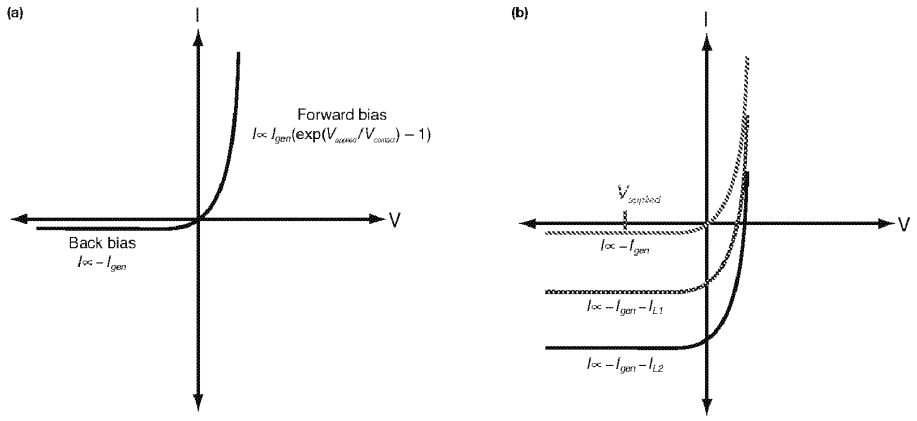


Figure 5.4: (a) The characteristic current-voltage characteristics of a p-n diode. For positive applied voltage the current increases exponentially; this it the forward bias condition. For negative applied voltage the current saturates at a small negative value close to the generation current; this is the back bias condition. (b) If we shine light onto the junction, there will be a negative contribution to the total current from the generated photocurrent. The size of this contribution will be proportional to the power of the incident light. The incident power of L_2 is larger than L_1 and, therefore, the I-V curve drops further.

The photocurrent contribution lowers the I-V curve by an amount proportional to the number of incident photons (incident power). This is how a photodiode works. We set a specific back bias voltage[4] to operate at, shine light at the junction, and measure the contribution to the overall current from the photocurrent. Because the amount of photocurrent is proportional to the power of the incoming light, we can detect the light and determine the relative power. Figure 5.4 (b) illustrates how a photodiode is used to detect light.

5.2 Femtosecond-laser microstructured silicon photodiodes

Silicon is the most commonly used semiconductor in microelectronics and optoelectronic devices. It is widely used for solar cells and photodetectors, but because the band gap of crystalline silicon is 1.07 eV, the absorption and photoresponse decrease precipitously

[4]Operating at a back bias voltage improves detector speed and efficiency by increasing the strength of the internal electric field.

SIONYX1403000030.0088

SAMSUNG EX. 1002 - 2958/4148

for wavelengths longer than 1100 nm. Unfortunately, there are several near-infrared wavelengths longer than 1100 nm that are widely used for both telecommunications and scientific instrumentation. For instance, crystalline silicon photodetectors are insensitive to the two primary telecommunications wavelengths, 1300 nm and 1550 nm. Currently, more expensive and exotic semiconductors, such as germanium and indium gallium arsenide, are used to detect these wavelengths, but a silicon-based near-infrared detector would lower production costs and facilitate integration with other microelectronics. Most researchers have all but given up on using pure silicon in this wavelength range and, consequently, there is a significant amount of research being done on overcoming silicon's shortcomings by using alloys or gradual integrations of more exotic semiconductors with silicon [78, 79, 80, 81, 82, 83].

Although we only discussed the *p*-*n* photodiode, the same principles and ideas hold for all photodiodes. When two dissimilar materials are contacted an internal potential step builds up and a diode is formed; in the case of a *p*-*n* junction, the difference between materials is the impurity carrier concentration. Photocurrent generation contributes to the total current and is a measurable way to detect light. The difference between the two sides of the junction need not come from just carrier concentration differences; there are many ways to make photodiodes. Different doping concentrations, different crystalline structure, dissimilar semiconductor materials (heterojunction), and any combination of these three differences can be used to create a photodiode.

With femtosecond-laser microstructured silicon, we have two distinct layers; the disordered surface layer and the undisturbed crystalline layer below. These two layers are different in crystalline structure, chemical composition, and doping concentration (see Chapters 3 and 4). In addition, the microstructured surface has very unique optical properties with high absorptance from the near ultraviolet deep into the near-infrared (Chapter 4). In following sections, we describe our efforts in making a photodiode that takes advantage

SIONYX1403000030.0089

SAMSUNG EX. 1002 - 2959/4148

of the unique optical properties of silicon microstructured in the presence of SF_6. We aim to use the junction between the sulfur-doped disordered surface layer and the undisturbed silicon substrate to form a diode and then characterize its photoresponse. We use all the information we know about the morphology, chemical composition, optical properties, and electronic properties of microstructured silicon to design and understand our photodiode.

5.2.1 Experimental

All of the photodiodes described in this chapter are silicon substrates microstructured in with a 1-kHz train of 800-nm, 100-fs pulses in 0.67 bar of SF_6. The photodiodes are made while translating the substrates such that an average of 200 laser pulses strike a given area. Except for the section on the effect of original substrate doping, the silicon substrates used are n-doped silicon (n-Si(111), 260 μm thick, resistivity $\rho = 8 - 12\ \Omega\cdot$m).

Fabrication process

We microstructure approximately a 5×5 mm^2 area of silicon in the presence of SF_6. Depending on the experiment, samples are either left alone or annealed for 30 minutes to a specified temperature following microstructuring. We then dip the samples in a 5% HF solution in order to remove the native oxide layer before making electrical contact. With the oxide layer removed, we place the samples in a thermal evaporator and make electrical contact to the microstructured side and the undisturbed substrate by evaporating chromium/gold (Cr/Au) contacts. On the microstructured side, the electrical contact is a finger grid geometry and, on the back side (undisturbed substrate), the entire surface is covered with a Cr/Au layer. Figure 5.5 (a) shows a schematic diagram of the final sample. With this contact structure, we make electrical contact to both sides of the junction and make our measurements across the junction. Figure 5.5 (b) shows a schematic diagram of

SIONYX1403000030.0090

SAMSUNG EX. 1002 - 2960/4148

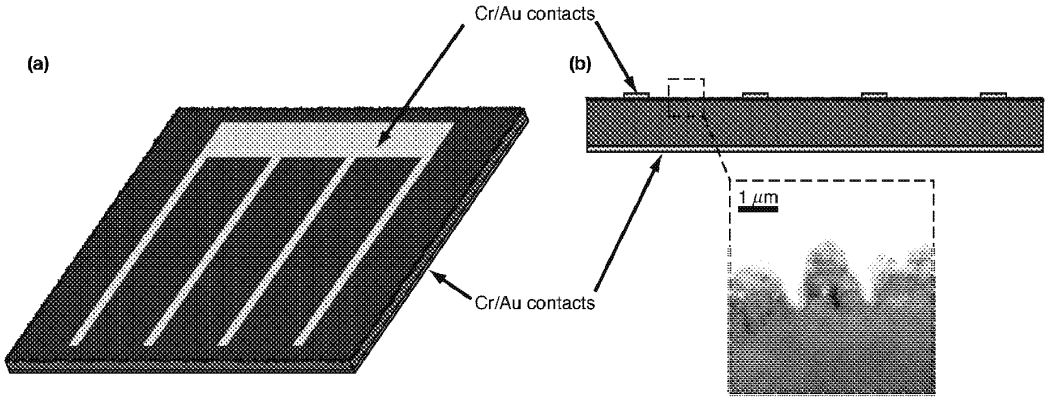


Figure 5.5: (a) A schematic diagram of a microstructured sample with electrical contacts. (b) Cross-section of a microstructured sample showing that we have contacts on either side of the junction between the disordered surface layer and the undisturbed silicon substrate. Inset: Transmission electron micrograph of a typical junction.

a cross section of a finished sample.

Measurements

We present two types of measurement results in this chapter: the current-voltage (I-V) characteristics of the junction and spectral responsivity of the finished photodiode. The I-V measurements are fairly straightfoward. We apply a range of voltages across the junction and measure the resulting current. With this information we plot the I-V curve for each sample. Measurements are done in the dark so no contribution from photocurrent is included. Responsivity is a way of quantifying the sensitivity of a photodiode and is the amount of photocurrent generated per unit of power of incident light (units of A/W). Spectral responsivity is measured using a 300-W xenon arc lamp light source that is passed through a monochromator with a spectral resolution of 0.1 nm. The monochromator is scanned to wavelengths over the range 400 – 1600 nm. Using a calibrated photodiode and a variable neutral density filter, we adjust the power at each wavelength to 1 μW and then

SIONYX1403000030.0091

SAMSUNG EX. 1002 - 2961/4148

measure the generated photocurrent. All samples are at a small back bias of –0.5 volts for responsivity measurements.

5.2.2 Results

The results section is presented in terms of how experimental parameters affect our photodiodes' *I-V* characteristics and responsivity. In general, the logic flow follows our efforts to optimize and understand photodiode performance.

Effect of annealing

Before we can have a photodiode, we must first have a diode. To determine if we indeed have a diode, we perform *I-V* measurements of finished samples. Figure 5.6 (a) shows the *I-V* characteristics for microstructured samples[5] at several anneal temperatures. Immediately following laser microstructuring, with no anneal, *I-V* measurements yield a disappointing result. The *I-V* curve is not diodic and the current and voltage are linearly related. The difference in crystalline structure and inclusion of sulfur in the surface is not sufficient to create a significant junction between the two layers. However, Hall measurements indicate that the number of donor electrons from the microstructuring process increases dramatically with anneal temperature. Therefore, we annealed samples at several temperatures and looked for changes in the shape of the *I-V* curves. An anneal at 725 K shifts the curve slightly and we begin to see different slopes for positive and negative biases. However, the shape is still far from what we would expect from a diode. If we increase our anneal temperature at 825 K, the curve is now diodic, with expontentially increasing current for forward bias and a smaller, less quickly increasing current for back bias. At 1075 K, the *I-V* characteristics are similar to the ideal case, with very small current in the

[5]The samples in the annealing section were microstructured at a fluence of 4 kJ/m^2. The reason for using this fluence as the standard is discussed in the next section.

SIONYX1403000030.0092

SAMSUNG EX. 1002 - 2962/4148

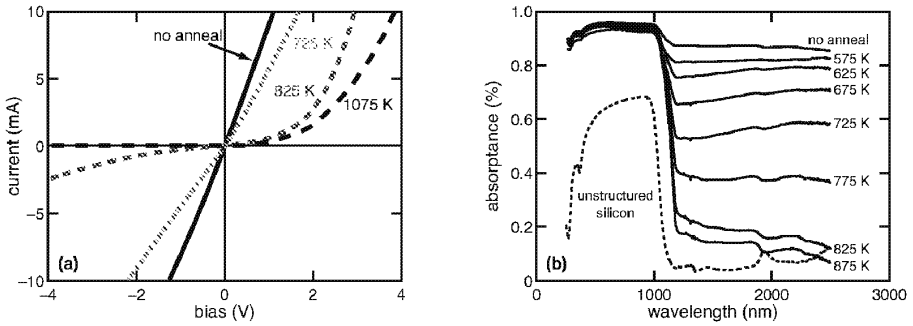


Figure 5.6: (a) The current-voltage characteristics for microstructured samples annealed to four different temperatures. Without annealing, the curve is virtually linear, indicating that the junction is not diodic, but more resistive in nature. The current-voltage characteristics get more like an ideal diode with increasing anneal temperature. (b) Wavelength dependence of absorptance on anneal temperature. Although the diodic characteristics improve with increasing anneal temperature, the near-infrared absorption drops.

back bias condition. However, there is a problem with annealing at high temperatures. The absorptance measurements for increasing anneal temperature are shown in Figure 5.6 (b). The below-band gap absorptance, that we are so interested in, decreases with increasing anneal temperature. Therefore, although we get better diodic behavior with higher anneal temperature, we start to lose the near-infrared absorptance.

The responsivity measurements for four different anneal temperatures (no anneal, 725 K, 825 K, and 1075 K) are shown in Figure 5.7. The responsivity of a commercially available silicon photodiode is also included for reference. The measurement range for the nonannealed sample is limited because the noise is very high and the response is moderate. From Figure 5.6 (a), we see that the *I-V* characteristics for this sample are poor; it is not diodic and the current at –0.5 V bias is significant. The sample annealed at 725 K exhibits very high response but is noisy (see Figure 5.6 (a)), making measurements of responsivity at these low light powers (1 μW) excessively noisy for wavelengths longer than 1200 nm. The responsivity of the sample annealed at 825 K is enormous. It has nearly 100 times

SIONYX1403000030.0093

SAMSUNG EX. 1002 - 2963/4148

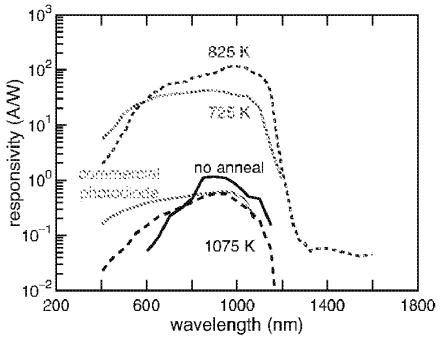


Figure 5.7: Responsivity measurements for samples annealed to four different temperatures. The measurement range for the "no anneal" sample is limited by noise. Similarly, measurements past 1200 nm were too noisy for the sample annealed at 725 K and the response was too small for the sample annealed at 1075 K. For reference, the responsivity of a commercially available silicon photodiode is shown.

larger response than a commercially available photodiode for the visible and responsivity near 100 mA/W in the near-infrared. The *I-V* characteristics are diodic and the current at –0.5 V bias is small. There is a large reduction in responsivity for the sample annealed at 1075 K. The *I-V* characterstics of this sample are the most ideal and therefore the noise during measurement is small, but the response is much lower than the 825 K sample and there is no measurable response at wavelengths longer than 1200 nm. However, the samples annealed to 1075 K have much better responsivity at 0 V bias (quantum efficiency). We will discuss the topic of quantum efficiency *vs.* responsivity at nonzero bias later in this chapter. The commercial silicon photodiode data stops at 1100 nm because responsivity drops steeply to around 10^{-6} A/W for wavelengths longer than 1100 nm [84].

From these results, we see that annealing is a crucial step in producing a photodiode with good rectification and response. Annealing at a temperature that is too low leads to a noisy photodiode, but annealing to too high a temperature lowers the response to both visible and near-infrared wavelengths. For the remaining experiments in this chapter, we present results for samples annealed at 825 K and 1075 K. The samples annealed at 825 K

SIONYX1403000030.0094

SAMSUNG EX. 1002 - 2964/4148

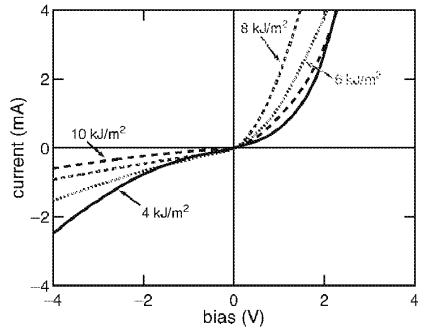


Figure 5.8: Current-voltage characteristics for microstructured samples made with four different fluences and annealed at 825 K. Increasing fluence results in lower dark current for a given back bias.

exhibit the highest response in both the visible and infrared, but the samples annealed at 1075 K are less noisy and their quantum efficiencies are higher.

Effect of fluence

In the previous section, we presented results for annealing samples made with a fluence of 4 kJ/m^2. We will see in this section that this choice of fluence was not arbitrary. Samples made with 4 kJ/m^2 are the best overall photodiodes of the fluences tested. However, it was necessary to discuss annealing before fluence in order to familiarize the reader with the importance of annealing and the reasons behind the anneal temperatures we present in this section.

In this section, we discuss the effect of laser fluence on the photodiode characteristics of microstructured silicon. Figure 5.8 shows the current-voltage characteristics for samples made with four different laser fluences (4 kJ/m^2, 6 kJ/m^2, 8 kJ/m^2, and 10 kJ/m^2) and annealed at 825 K for 30 minutes. Increasing the fluence decreases the amount of dark current for a given back bias. This behavior is likely a result of increased sulfur content in the surface layer with higher fluences (see Section 3.11). Current-voltage characteristics for

SIONYX1403000030.0095

SAMSUNG EX. 1002 - 2965/4148

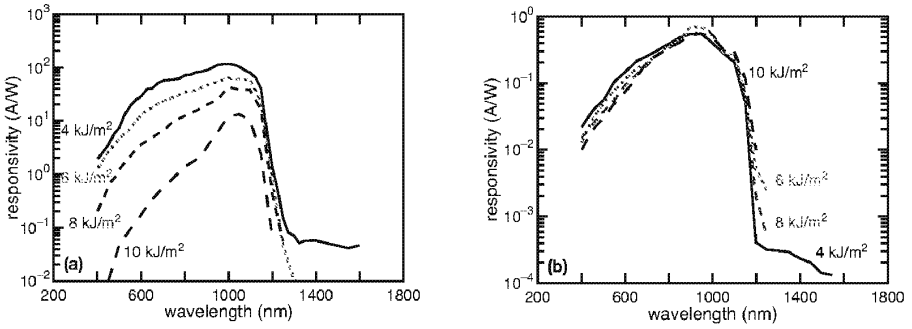


Figure 5.9: (a) Responsivity measurements for samples made with four different fluences and annealed at 825 K for 30 minutes. Samples made with 4 kJ/m^2 have the highest response for both the visible and near-infrared. (b) Responsivity measurements for samples made with four different fluences and annealed at 1075 K for 30 minutes. There is little variation in responsivity with fluence.

samples made with the same fluence but annealed at 1075 K do not vary significantly.

Figure 5.9 shows the responsivity for samples microstructured with four different fluences and annealed at (a) 825 K and (b) 1075 K for 30 minutes. There is a large variation in the responsivity with fluence for samples annealed at 825 K. The responsivity decreases with increasing fluence; samples made with 4 kJ/m^2 have the highest response. In addition, the samples made with 4 kJ/m^2 are the only samples with near-infrared response high enough to be measured with the low incident light power used in our measurements (1 μW). The wavelength of peak response shifts to longer wavelengths with increased fluence. This shift is likely because of a deeper junction depth with higher fluence combined with low mobility for samples annealed to 825 K (see Section 4.2.2). The decrease in responsivity with fluence disappears for samples annealed at 1075 K, as does the shift in peak wavelength. The responsivity for samples annealed at 1075 K is nearly 100 times lower than those annealed at 825 K. However, the samples annealed at 1075 K are less noisy and have higher quantum efficiency. If the fluence is below the ablation threshold (3 kJ/m^2), the current-voltage characteristics and responsivities are very poor. However, these samples were made with

SIONYX1403000030.0096

SAMSUNG EX. 1002 - 2966/4148

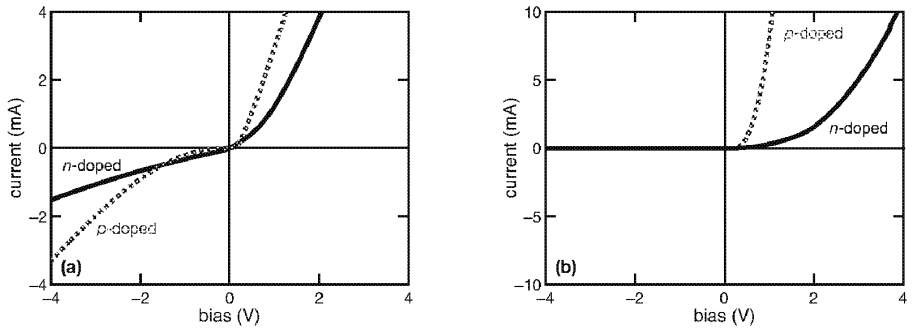


Figure 5.10: (a) Current-voltage characteristics for n-doped and p-doped substrates microstructured with a fluence of 6 kJ/m^2. Samples are annealed at 825 K for 30 minutes following microstructuring. (b) Current-voltage characteristics for n-doped and p-doped substrates microstructured with a fluence of 4 kJ/m^2. Samples are annealed at 1075 K for 30 minutes following microstructuring.

an average shot number of 200 pulses and may improve with larger shot number.

Effect of silicon substrate doping

In this section, we examine the effect of using p-doped (p-Si(100), 350 μm thick, resistivity $\rho > 1$ Ω·m) instead of our standard n-doped substrates. Figure 5.10 shows the current-voltage characteristics for n-doped and p-doped substrates annealed at 825 K and 1075 K for 30 minutes. The p-doped samples annealed at 825 K (Figure 5.10 (a)) have a higher forward bias current than the equivalent n-doped samples. The dark current for back biases also increases more quickly for p-doped samples. Overall, the rectification is not as good for the p-doped samples. However, upon annealing at 1075 K, the p-doped samples exhibit very good diodic properties. The back bias current decreases to the same level as the equivalent n-doped samples. Also, the forward bias current increases more quickly, giving good rectification ratios. As we saw in Section 4.2.2, annealing to higher temperatures increases donor concentration from sulfur doping. The increase in donor concentration likely leads to better rectification for the p-doped samples annealed to higher temperatures.

SIONYX1403000030.0097

SAMSUNG EX. 1002 - 2967/4148

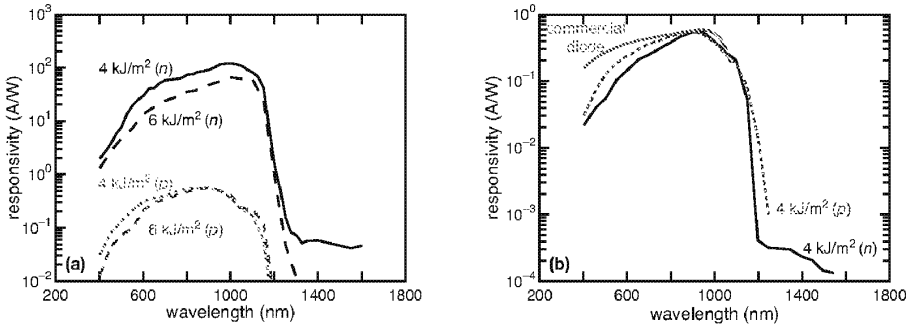


Figure 5.11: (a) Responsivity measurements for microstructured n-doped and p-doped substrates made with two different fluences (4 kJ/m^2 and 6 kJ/m^2) and annealed at 825 K for 30 minutes. Samples made with 4 kJ/m^2 have the highest response for both the visible and near-infrared. (b) Responsivity measurements for microstructured n-doped and p-doped substrates annealed at 1075 K for 30 minutes. The responsivity of a commercial silicon photodiode is shown for reference.

Varying the substrate doping has a more drastic effect on the responsivity. Figure 5.11 (a) shows the responsivity for two n-doped substrates and two p-doped samples annealed at 825 K for 30 minutes. The responsivity for n-doped substrates is much higher over the entire spectral range. The p-doped substrates have no measurable response in the near-infrared. However, if we anneal the microstructured samples at 1075 K (Figure 5.11 (b)), the responsivity for n-doped and p-doped samples is nearly identical. The response for both of these samples is similar to commercial photodiodes. In addition, the spectral responsivity for p-doped samples annealed at 825 K and 1075 K is similar. From these results, we conclude that the substrate doping plays an important role in the responsivity. The microstructured p-doped samples have a lower overall response but have better quantum efficiency.

SIONYX1403000030.0098

SAMSUNG EX. 1002 - 2968/4148

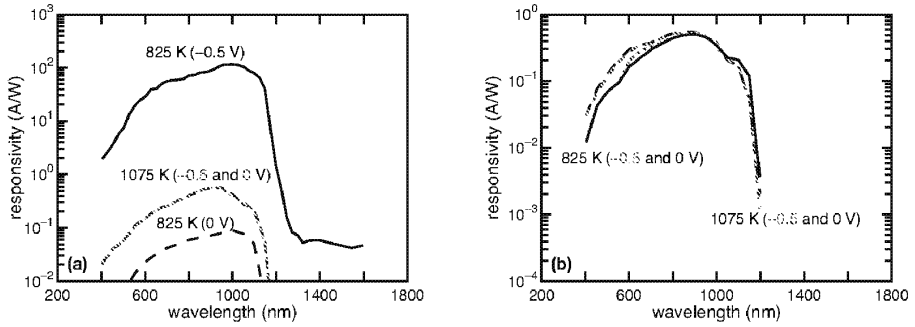


Figure 5.12: (a) Responsivity measurements for microstructured n-doped substrates made with 4 kJ/m^2 and annealed at either 825 K or 1075 K for 30 minutes. Measurements are made with a back bias of –0.5 V or with no applied bias. There is a large difference in the responsivity with a small applied bias for samples annealed at 825 K, but no difference for the samples annealed at 1075 K. (b) Responsivity measurements for microstructured p-doped substrates made with 4 kJ/m^2 and annealed at either 825 K or 1075 K for 30 minutes. There is little difference in the responsivity for either case.

Responsivity, quantum efficiency, and gain

Earlier in this chapter, we made brief reference to a difference between responsivity and quantum efficiency. Quantum efficiency, strictly defined, is the number of electron-hole pairs generated per incident photon at zero applied voltage. The measurements we have presented to this point are made at a back bias of –0.5 V and therefore are not, strictly, quantum efficiency measurements. We showed that samples made with a fluence of 4 kJ/m^2 on n-doped substrates annealed at 825 K have the highest responsivities, but this result does not mean they also have the highest quantum efficiencies.

Figure 5.12 more clearly distinguishes the difference between high responsivity and high quantum efficiency in our photodiodes. Whereas the responsivity of samples made with n-doped substrates at a fluence of 4 kJ/m^2 is much higher than other samples, their responsivity at zero bias (quantum efficiency) is rather low. In fact, if we were to calculate a "quantum efficiency" for these devices at a back bias of –0.5 V, it would be nearly 100.

SIONYX1403000030.0099

SAMSUNG EX. 1002 - 2969/4148

Quantum efficiencies above 1 are not physically meaningful and these high values mean that there is *gain* in these samples. The gain is quite high (>1000 times), especially for such a small bias. The responsivity of samples made on n-doped substrates and annealed to 1075 is lower at –0.5 V, but their quantum efficiency is much higher. There is a small increase in responsivity with back biasing, but it is reasonable to expect a small gain because a bias will slightly increase the depletion region and the photocarrier collection efficiency [36]. The responsivity of samples made on p-doped substrates and annealed at 825 K or 1075 K is also lower, but their quantum efficiencies are higher. The gain disappears with increased anneal temperature or when using a p-doped substrate. The responsivities of these devices is comparable to commercial silicon photodiodes, with no significant response to near-infrared light.

Figure 5.13 shows the increase in responsivity with increasing back bias for an n-doped substrate microstructured with a fluence of 4 kJ/m^2 and annealed at 825 K for 30 minutes. The sample was illuminated with a white light source with an approximate power of 50 μW. The responsivity, and therefore the gain, increases quickly up to –5 V and more slowly up to –15 V. At voltages beyond –15 V the responsivity begins to fall quickly. Although the increase in responsivity is desirable, there is a corresponding increase in noise. Also, the linearity of a photodiode is a measure of how the response changes with changing incident light power. The responsivity of devices that exhibit a large amount of gain is not very linear; the responsivity is higher at lower light powers, probably because the gain is so large that saturation occurs quickly with increasing light power. The response of samples annealed at 1075 K or made with p-doped substrates is more linear because they do not have significant gain with applied bias.

Therefore, it is important to keep in mind that the responsivity of a photodiode does not take into account the quantum efficiency or the noise. Therefore, the best fabrica-

SIONYX1403000030.0100

SAMSUNG EX. 1002 - 2970/4148

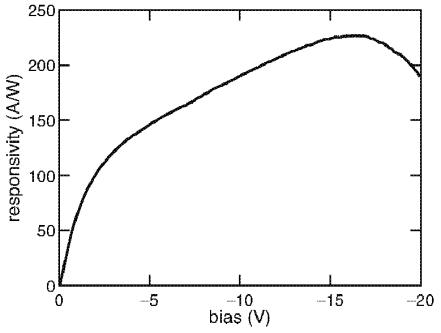


Figure 5.13: Responsivity as a function of back bias for an n-doped substrate microstructured with a fluence of 4 kJ/m^2 and annealed at 825 K for 30 minutes. The sample was illuminated with a white light source with an approximate power of 50 μW.

tion conditions for each sample depends on its intended application. That is, the trade-off between high responsivity and high quantum efficiency should be taken into account.

Effect of temperature

For most photodetectors, it is common practice to cool the detector in order to reduce thermal noise. It is reasonable to expect that cooling our photodiodes would affect noise levels, especially since our samples are sensitive to near-infrared wavelengths[6]. In order to determine the effect of cooling on the characterstics of our photodiodes, we cooled an n-doped sample, made with a fluence of 4 kJ/m^2 and annealed at 825 K, from room temperature down to 80 K. During cooling, we made current-voltage and responsivity measurements at increments of 10 degrees K. The highlights of this analysis are shown in Figure 5.14. Figure 5.14 (a) shows the current-voltage characteristics with decreasing temperature. The current in both the back bias and forward bias condition decreases with temperature. At very low temperatures (below 100 K), conduction becomes very low for both forward and back bias. Figure 5.14 (b) shows the responsivity to 1064 nm light at a back bias of

[6]All of the measurements presented thus far have been performed at room temperature.

SIONYX1403000030.0101

SAMSUNG EX. 1002 - 2971/4148

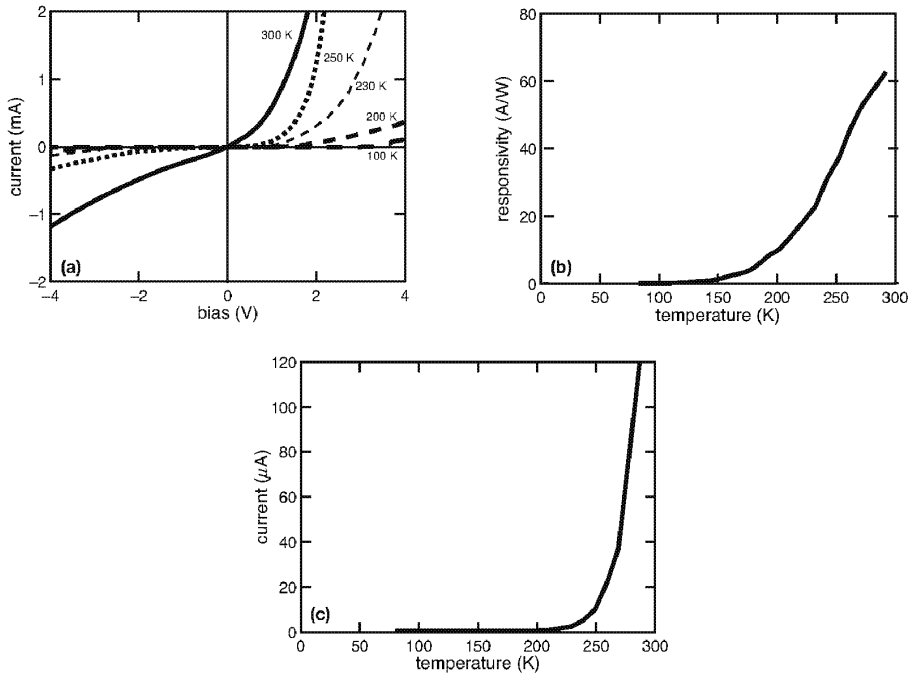


Figure 5.14: (a) The effect of decreasing temperature on the current-voltage characteristics of an n-doped sample made with a fluence of 4 kJ/m^2 and annealed at 825 K. (b) The effect of decreasing temperature on responsivity of the same sample. (c) The dark current at a back bias of –0.5 V with decreasing temperature. The dark current decreases more quickly with temperature than the responsivity.

–0.5 V with decreasing temperature. The responsivity also drops with temperature, which is likely because the wavelength used is close to the band gap of silicon at room temperature and there is an increase in the band gap with decreasing temperature [75]. Figure 5.14 (c) shows the dark current at –0.5 V with decreasing temperature. If we take this measurement to be a rough gauge of the noise in the photodiode, it indicates that the noise decreases much more quickly than the responsivity. This information could be used to optimize device operation but more measurements, especially with below-band gap wavelengths, need to be carried out.

SIONYX1403000030.0102

SAMSUNG EX. 1002 - 2972/4148

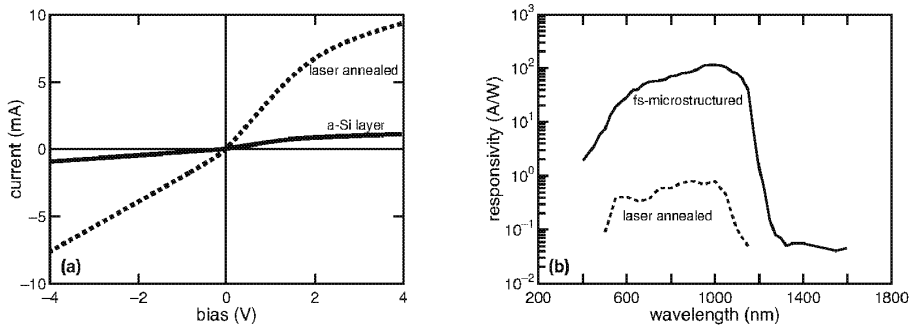


Figure 5.15: (a) The current-voltage charactersitics for a heavily sulfur doped amorphous silicon layer on an n-doped substrate and the same sample after rescrystallization of the amorphous layer with nanosecond laser annealing. (b) Responsivity measurements of the laser annealed surface compared to a femtosecond laser microstructured sample. Both responsivity measurements were taken with a back bias of –0.5 V.

Effect of sulfur inclusion and surface layer structure

A question that comes up in this analysis is whether it is the inclusion of high levels of sulfur alone, the structure of the surface layer, or a combination of the two that leads to the high responsivity and near-infrared sensitivity. In hopes of addressing this question, we performed three experiments trying to deconvolve the contributions of sulfur and structure. First, in collaboration with another research group [74], we prepared a sample that consisted of a thin layer of amorphous silicon with high levels of sulfur doping ($\sim$ 1 at. %) on top of our standard n-doped substrates. We then measured the current-voltage characteristics and responsivity of this sample. The current-voltage characteristics (see Figure 5.15 (a)) are far from diodic and the responsivity is too low to be measured. We then laser annealed the amorphized layer with nanosecond laser pulses in order to recrystallize the amorphized layer, while maintaining the large amount of sulfur doping. The current-voltage characteristics are also far from diodic, but the responsivity is on the level of n-doped femtosecond-laser microstructured samples before anneal. Because the I-V characteristics are so poor, the

SIONYX1403000030.0103

SAMSUNG EX. 1002 - 2973/4148

responsivity measurements are very noisy and we were not able to discern a significant below-band gap response. Figure 5.15 (a) shows the current-voltage characteristics for the amorphous silicon and laser annealed samples. Figure 5.15 (b) shows the responsivity of a laser annealed sample as compared to the n-doped microstructured substrates annealed at 825 K. Although these preliminary results are not very encouraging, this approach might prove fruitful with further experiments and variation of parameters. It is likely that the nanosecond-laser anneal does not perfectly recrystallize the surface layer and its structure has similarities to the disordered surface layer we see with femtosecond-laser microstructured samples. Lastly, we made current-voltage and responsivity measurements for nanosecond-laser microstructured annealed at 825 K for 30 minutes (see Section 3.4) surfaces. The current-voltage characteristics are more reminiscent of a resistor than a diode and noise levels are too high to make meaningful responsivity measurements. The poor performance of nanosecond-laser structured photodiodes is likely because there is no discernable disordered surface layer for these structures (see Section 3.4.1) and therefore no junction is formed. From this information, it seems that the inclusion of sulfur and the structure of the surface layer are both critical for high responsivity in the visible and the near-infrared.

5.3 Optimization and discussion

With the large amount of data presented in the previous sections, the goal and most important result of our experiments may have been lost. We set out to create a silicon-based photodiode that operated in both the visible and near-infrared. In short, we succeeded remarkably well in this goal. Figure 5.16 summarizes some of the main characteristics of our best performaning devices. Thus far, the optimal experimental conditions are microstructuring an n-doped (n-Si(111), 260 μm thick, resistivity $\rho = 8 - 12\ \Omega$·m) with

SIONYX1403000030.0104

SAMSUNG EX. 1002 - 2974/4148

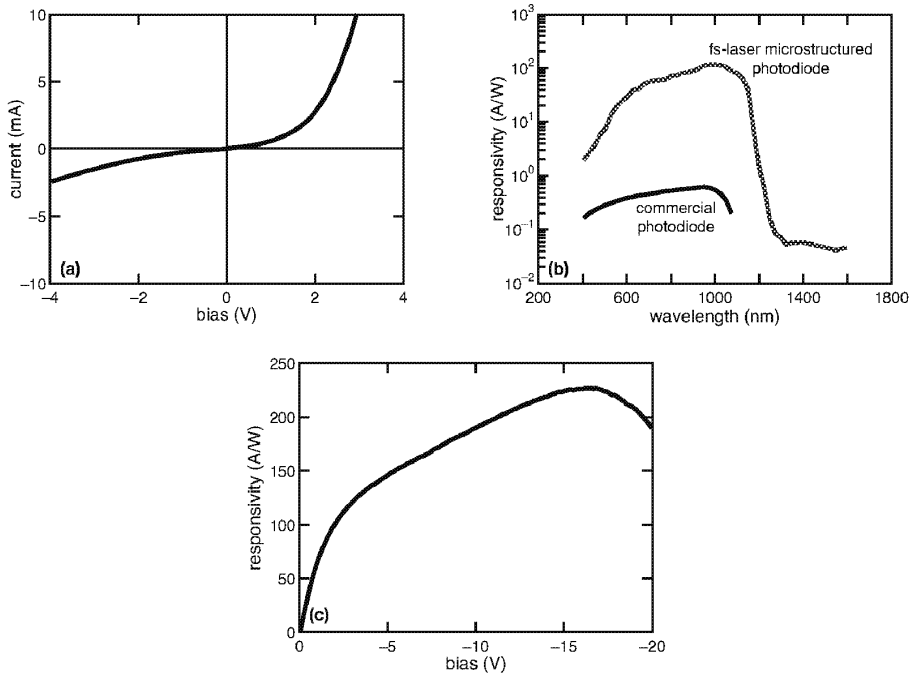


Figure 5.16: (a) The current-voltage charactersitics for our best microstructured photodiode. (b) Responsivity of our best microstructured photodiode compared to a commercial silicon photodiode. (c) Responsivity with increasing applied back bias for our best microstructured photodiode.

a fluence of 4 kJ/m^2 in 0.67 bar of SF_6 and annealing the sample at 825 K for 30 minutes. The responsivity of this sample is nearly two orders of magnitude higher than commercial silicon photodiodes in the visible; this level of sensitivity is much higher than were anticipated. Responsivities for below-band gap wavelengths as long as 1600 nm are on the order of 100 mA/W. This responsivity is only one order of magnitude lower than commercial photodiodes that are currently used in this spectral range, and five orders of magnitude larger than silicon devices in this spectral range [84]. The mobility (μ) of the surface layer made with these conditions is 101 cm^{2}V^{-1}s^{-1}. The response times of the photodiode are 10 ns rise time and 30 ns fall time. The diode capacitance is 63.9 nF at a back bias of –0.5 V.

SIONYX1403000030.0105

SAMSUNG EX. 1002 - 2975/4148

Immediately following laser-microstructuring, our devices do not make very good photodiodes. Their *I-V* characteristics are more representative of a resistor rather than a diode. Their responsivity is on the order of commercial photodiodes but is extremely noisy. It seems that the difference in crystallinity and doping between the disordered surface layer and the undisturbed substrate is not sufficient to create a diodic junction. Annealing dramatically improves both the *I-V* characteristics and the responsivity. It is likely that the annihilation of defects and bond rearrangement during annealing (see Section 4.3) improves the *I-V* characteristics. Removal of defects at the junction interface along with a higher carrier concentration gradient across the junction leads to improved rectification. However, the exact anneal temperature is critical because responsivity drops significantly if we anneal at too high of a temperature. In addition, high temperature anneals result in diminished below-band gap absorptance. Therefore, optimization requires finding an anneal temperature that provides a balance between good *I-V* characteristics and good responsivity.

Arguably, the one characteristic that makes these photodiodes unique is the large gain at very small applied voltages. Our best samples have a large amount of gain (> 1000 times) for an applied bias of –0.5 V. Of all our samples, the ones with high gain have the best responsivity in the visible and, by far, the best responsivity for below-band gap wavelengths. It is likely that the below-band gap absorption only results in a few electron-hole pairs (photocarriers), but the gain is so large that the final photocurrent is brought up to a remarkable level. For samples with little or no gain, we do not see significant below-band gap response.

The gain is present only for certain experimental conditions and therefore we can speculate on the mechanism. For such small applied biases, the gain mechanism one would first expect is photoconductive gain [36]. Photoconductive gain comes from a difference in the recombination lifetime and transit time to the electrodes for electrons and holes.

SIONYX1403000030.0106

SAMSUNG EX. 1002 - 2976/4148

Briefly, we can imagine a scenario in which electrons have a longer lifetime and travel to the electrodes faster than the holes. If this is the case, an electron leaves the semiconductor before the hole recombines and current continuity forces the external circuit to add another electron from the other side of the semiconductor. If the electron and hole recombination lifetimes are sufficiently long, a single photon absorption could result in several electrons contributing to the photocurrent, which amounts to gain. There are several experimental indications that this is not the case for our photodiodes. First, the mobility of the disordered surface layer is significantly less than the crystalline substrate. The disordered layer is the more n-doped side of our junction and the photogenerated electrons travel through the disordered layer on their way to the electrode. If anything, we would expect that the recombination lifetime for these electrons would be so small that we would see quantum efficiencies much less than 1. Secondly, if we anneal samples to higher temperatures, it improves the mobility but removes any gain. This result is counterintuitive to the idea of photoconductive gain because annealing to higher temperatures should remove defects and traps that reduce the recombination lifetime of carriers. The measured mobility for samples annealed at 1075 K is 20% higher than those annealed at 825 K but the responsivity is two orders of magnitude less. For the opposite electronic scenario (*i.e.* long-lifetime holes instead of electrons), it is highly unlikely that photogenerated holes are traveling all the way through the predominantly n-doped substrate and being injected into the disordered layer several times before the photogenerated electrons recombine.

The gain mechanism is more likely the result of an avalanche process from high localized electric fields at defects or collisional ionization at the highly disordered interface. The evidence for this explanation comes from the information contained in Figure 5.11. First, annealing to higher temperatures for microstructured n-doped substrates removes the gain. Annealing at 825 K leads to a small increase in the doping level but also frus-

SIONYX1403000030.0107

SAMSUNG EX. 1002 - 2977/4148

trates conduction and mobility (see Section 4.2.2). Annealing at 1075 K leads to a large increase in the doping level but removes defects and allows for better conduction. The healing of these defects at the interface between the surface layer and the substrate decreases gain but increases quantum efficiency as carriers are more efficiently collected. Secondly, no matter what anneal temperature we use, the microstructured p-doped samples do not exhibit high gain. There is no gain in p-doped samples because the impact ionization rate for holes is nearly 1000 times less than that of electrons at these low electric field strengths [39]. The low response for p-doped samples leads to a subtlety in the conditions needed to produce our best photodiodes. Normally one designs a photodiode to have a large difference in carrier concentration across the junction because this leads to a larger internal electric field and better collection efficiency. So, for an n-doping process, such as our laser microstructuring, we normally want to start with a p-doped substrate. However, from our measurements, it is clear that n-doped substrates yield better responsivities. Therefore, an n-doped substrate is a necessary component of the gain mechanism (collisional ionization). With better understanding of the gain mechanism we can optimize conditions for gain and doping concentration on either side of the junction.

Laser fluence is also an important parameter for optimizing photodiode operation. Lower fluences deposit less energy and do less damage to the surface layer. Lower fluence results in less drastic surface topography for photoelectrons to travel across and shorter distances to electrodes (see Section 3.3). Perhaps with further investigation it may be possible to choose laser parameters that minimize change to the surface morphology and maintain good photodiode characteristics. It is, after all, not the micrometer scale morphology, but the disordered surface layer that is critical to these photodiodes. The decrease in sensivity to shorter wavelengths for increasing laser fluence may prove beneficial for certain applications in which ultraviolet light detection is undesirable.

SIONYX1403000030.0108

SAMSUNG EX. 1002 - 2978/4148

There is still a great deal to improve and learn with these devices. The major omission in this analysis is noise characteristics. The purpose of these experiments was to demonstrate creation of a photodiode using laser microstructured silicon and learning about the material from our measurements. The noise levels need to be reduced in these devices, which is more of an engineering pursuit than a matter of new physics or material behavior. Many improvements can be made in the device design, such as surface passivation to minimize recombination, better isolation of surface currents from leaking around the edges of samples, improved electrical contact and design, operation temperature, and defect removal at the interface without loss of response. Of particular interest for both engineering and material science is a more comprehensive analysis of the effect of annealing on the photodiode characteristics. To date, we do not know if the improvement with annealing is strictly a temperature critical effect or if anneals for longer time periods at lower temperature (kinetics) lead to the same improvement. However, we do know that annealing is a critical step for high responsivity and low noise. Lastly, there is a great deal of information contained within the *I-V* measurements made at room temperature and while cooling. Analysis of these results might contribute to our understanding of the disordered surface layer and the energy levels of donor electrons.

In this chapter, we demonstrated the first application of femtosecond-laser microstructured silicon to create a functioning optoelectronic device. We fabricated photodiodes with sensitivity levels nearly one hundred times greater than their commercial equivalent and an expanded spectral range from 400 nm to 1600 nm. It is the nature of scientists to avoid overstatements of results, but these photodiodes are a very important discovery for the field of semiconductor photodetectors. The ease of integration and low cost of silicon makes it the most attractive and inexpensive material for photodetectors. The extension of silicon's range of spectral sensitivity and increased sensitivity to visible

SIONYX1403000030.0109

SAMSUNG EX. 1002 - 2979/4148

light could find application in numerous devices including photodetectors, charged coupled device (CCD) cameras, and photovoltaics. The fabrication process is relatively simple and lends itself to integration with current silicon device processing techniques. With better physical understanding, we can continue to optimize the photodiodes characteristics and, we hope, apply the underlying principles to create other novel devices.

SIONYX1403000030.0110

SAMSUNG EX. 1002 - 2980/4148

Chapter 6

Solar cells, field emission, and future directions

Since the first experiments involving femtosecond-laser microstructuring of silicon, there were high hopes that the process would find novel application in semiconductor devices. We felt the unique morphology and optical properties would find use in devices such as solar cells and field emission arrays. Toward these goals, we spent a great deal of effort and time gaining an understanding of both the formation mechanisms and properties of the microstructured surface. It is only in the past year that we gained the understanding and insight needed to actually produce operating devices. Our first success, highly sensitive photodiodes for the visible and near-infrared, was covered in the previous chapter, but this is only one of several applications toward which we are working. In this chapter, we present the development of two applications; femtosecond-laser microstructured solar cells and field emission arrays. These are two applications that we have worked on for several years but only had success with and understanding of since the recent photodiode work.

We begin the chapter with a brief background on the workings of solar cells and an

SIONYX1403000030.0111

SAMSUNG EX. 1002 - 2981/4148

update on our recent progress in this pursuit. We then introduce the basic physics of field emission and present early results for femtosecond-laser microstructured field emitters. We also briefly discuss some interesting properties of microstructured silicon that might find application in the future.

6.1 Solar cells and renewable energy

The current political strife and economic climate of the world has reinforced efforts towards using renewable energy sources. Wind power, solar power, and fuel cells are among the many technologies that proponents envision replacing fossil fuel consumption, the current work-horse of the energy business. Unfortunately the energy business is first and foremost concerned with profit and the cost of renewable energy technologies has hindered their implementation. For solar cells in particular, the cost per kilowatt hour (the true figure of merit for businesses) is 5-10 times the average cost of electricity from more traditional suppliers [85]. However, scientific advances and subsidies from conscientious governments are bringing the cost down every year. In the next twenty to thirty years, we hope to witness a transition to renewable energy sources as the dominant provider of electric power.

Efforts to bring down the cost of electricity from solar power are focused on increasing the conversion efficiency of sunlight into electricity and bringing down production costs. Crystalline silicon solar cells comprise the majority of solar cells being used today but the progress in creating more efficient modules at low cost has slowed. Researchers have turned to investigating other forms of silicon (amorphous and microcrystalline) and other materials (conducting polymers and more exotic semiconductors) in order to reduce the cost of solar energy [86, 87, 88, 89, 85, 90]. Progress is steadily being made and the

SIONYX1403000030.0112

SAMSUNG EX. 1002 - 2982/4148

world market for solar cell energy is growing at a healthy pace [85].

6.2 Femtosecond-laser microstructured silicon solar cells

Upon discovering that femtosecond-laser microstructured silicon has near-unity absorption from the visible to the near-infrared, we became excited by possible solar cell applications [91]. First, the increased absorption for visible wavelengths promised to increase the light absorbed by silicon solar cells and, therefore, increase efficiency by reducing losses due to reflection from the silicon surface. Secondly, nearly a third of the sun's energy is at wavelengths longer than 1.1 μm and passes unabsorbed through crystalline silicon solar cells (see Figure 6.1) [92]. Femtosecond-laser microstructured silicon is highly absorbing at these wavelengths and promised to improve efficiency by converting more of the sun's spectrum into electricity. Our initial efforts involved collaboration with solar cell companies to microstructure the surface of completed silicon solar cells. These experiments did not prove fruitful and it is only now, with our recent understanding of the microstructured surface and solar cells themselves, that we understand why did not succeed.

6.2.1 Introduction to solar cells

Before continuing on with the explanation of our initial efforts and getting to our recent progress, it is necessary to understand how a solar cell works. The principles are nearly the same as those we learned for photodetectors in the last chapter (see Section 5.1). Typically a solar cell is a *p*-*n* junction photodiode with high quantum efficiency. The conversion of photons into photocarriers is the physical mechanism by which light is converted into electricity. However, there is a fundamental difference between a photodetector and a solar cell. Photodetectors are generally run in "photoconductive" mode, that is, they have an applied back bias and photocurrent is measured. Applying a bias amounts to putting

SIONYX1403000030.0113

SAMSUNG EX. 1002 - 2983/4148

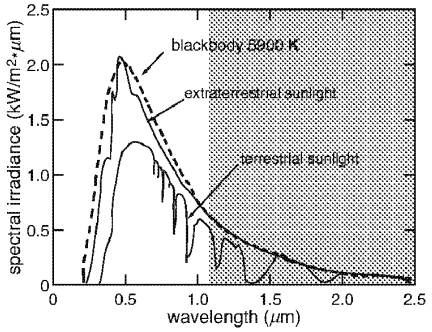


Figure 6.1: Spectral irradiance of the solar spectrum. The solar spectrum above the earth's atmosphere is close to ideal blackbody radiation at 5900 K. Absorption by O_2, H_2O, and CO_2 molecules in the atmosphere result in dips in the terrestrial solar spectrum. The greyed out region of the graph represents the portion of the spectrum that is not absorbed by crystalline silicon solar cells. Adapted from [92].

energy into the system rather than getting energy out. Solar cells, on the other hand, are run in "photovoltaic" mode. Instead of applying a bias, the photodiode is run open circuit mode or attached to a load. Figure 6.2 illustrates the difference between photoconductive and photovoltaic modes.

In photovoltaic mode, it is possible to convert sunlight into electrical energy. As we saw in the last chapter, incident light converted into photocurrent drops the I-V curve of a photodiode an amount proportional to the power of the incident light (Figure 5.4 (b)). When this occurs, portions of the I-V curve lie in the bottom right quadrant of the plot, the so-called fourth quadrant. Operating a photodiode in the fourth quadrant generates electric power. To understand this, we examine the two extreme cases for the I-V curve in this quadrant. The intersection of the I-V curve with the voltage axis represents running a photodiode in open circuit mode (infinite resistance). On a physical level, photogenerated carriers in the depletion region are separated by the internal electric field but, since the circuit loop is open, there is nowhere for them to go. The separated photocarriers result

SIONYX1403000030.0114

SAMSUNG EX. 1002 - 2984/4148

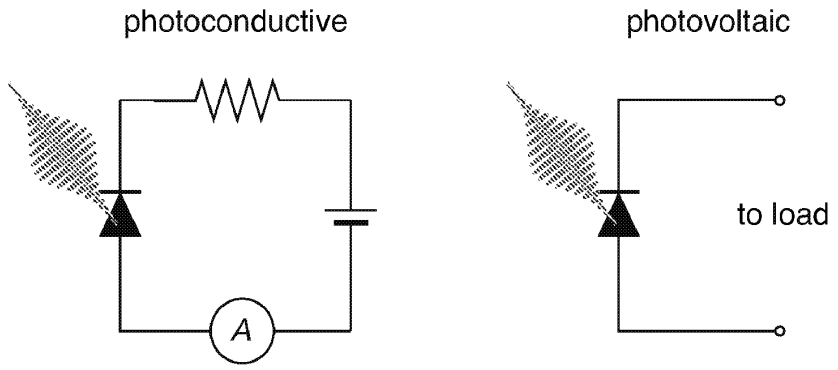


Figure 6.2: Cartoon illustrating the difference between photoconductive and photovoltaic mode.

in a separation of charge and a build up of a potential difference; this potential difference is called the open circuit voltage (V_{OC}). Alternatively, the intersection of the *I-V* curve with the current axis represents running a photodiode in short circuit mode (infinitely small resistance). On a physical level, there is no resistance in the circuit and therefore any photogenerated carriers contribute to the photocurrent; this current is called the short circuit current (I_{SC}). No potential difference builds up in short circuit mode. If we pick a load with *finite* resistance, we end up somewhere along the *I-V* curve in the middle of these two extremes. The resistance of the load determines the actual potential difference and photocurrent by Ohm's law (V=IR. So, with a finite resistance, incident light creates a potential difference and a current, which amounts to electrical power (P=IV).

The figure of merit for a solar cell is the conversion efficiency (η), which is the percentage of incident solar power that gets converted into electrical power. Conversion efficiency, in turn, depends on three other parameters: the short circuit current (I_{SC}), the open circuit voltage (V_{OC}), and the fill factor (FF). We defined short circuit current and open circuit voltage above. Fill factor is the ratio of the maximum power output to the product of the open circuit voltage and the short circuit current. Graphically, the *I-V* curve

SIONYX1403000030.0115

SAMSUNG EX. 1002 - 2985/4148

maps out an area within the fourth quadrant. The total area represents the total electrical power generated by the incident light, but because we have to pick a single load resistance, we are only able to realize a rectangular portion of this area. The largest rectangle we can fit into this area represents the maximum power output (maximum power rectangle) of the solar cell with a maximum voltage (V_m) and maximum current (I_m). The fill factor is the ratio of this realized maximum power over the ideal case of a rectangular area with sides I_{SC} and V_{OC},

$$FF = \frac{P_m}{I_{SC}V_{OC}} = \frac{I_m V_m}{I_{SC}V_{OC}}. \tag{6.1}$$

The maximum power rectangle and fill factor are shown graphically in Figure 6.3. The larger the fill factor, the more efficient the solar cell. The conversion efficiency is the ratio of maximum converted electrical power over the incident light power

$$\eta = \frac{P_m}{P_{in}} = \frac{FFI_{SC}V_{OC}}{P_{in}}. \tag{6.2}$$

So, for a given incident light power, we can use the fill factor, short circuit current, and open voltage to determine the efficiency of a solar cell.

6.2.2 Recent progress

Now that we have a basic understanding of how a solar cell works, we can discuss why our initial efforts to improve efficiency failed. We had hoped that increased absorption in the visible would increase the efficiency of solar cells by reducing the amount of reflected light. However, we now know that femtosecond-laser microstructuring results in a disordered surface layer that has a different carrier concentration than the original substrate. In essence, we are adding another junction and potential step into the finished solar cell. The conversion efficiency and quantum efficiency of a solar cell rely heavily on having no unintentional or extra potential steps introduced from processing steps. The additional

SIONYX1403000030.0116

SAMSUNG EX. 1002 - 2986/4148

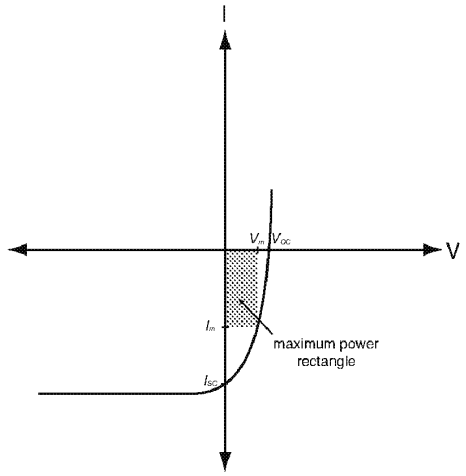


Figure 6.3: Cartoon of the maximum power rectangle of a solar cell. The fill factor is the ratio of this rectangular area over the ideal case of a rectangular area with sides I_{SC} and V_{OC}. The more rectangular the I-V curve, the larger the fill factor and maximum power rectangle.

potential barrier and reduced mobility in the disordered surface layer far outweigh any advantage gained by increased absorption.

The other advantage of femtosecond-laser microstructured silicon for solar cells is the extended absorption range, which may or may not prove increase efficiency. Absorption of additional wavelengths may lead to increased photocurrent, but the open circuit voltage of a semiconductor solar cell is proportional to the semiconductor's band gap. Therefore, the extended absorption range might result in reduced open circuit voltages. In general, there is an inverse relationship between open circuit voltage and short circuit current [39].

With the knowledge we have gained about our surface layer, we are again working toward applying laser microstructuring to creating novel solar cells. Applying the lessons learned while optimizing our photodiodes, we use the p-n junction created during microstructuring to create femtosecond-laser microstructured silicon solar cells. The fabrication process for samples is very similar to those used for photodiodes. We structure

SIONYX1403000030.0117

SAMSUNG EX. 1002 - 2987/4148

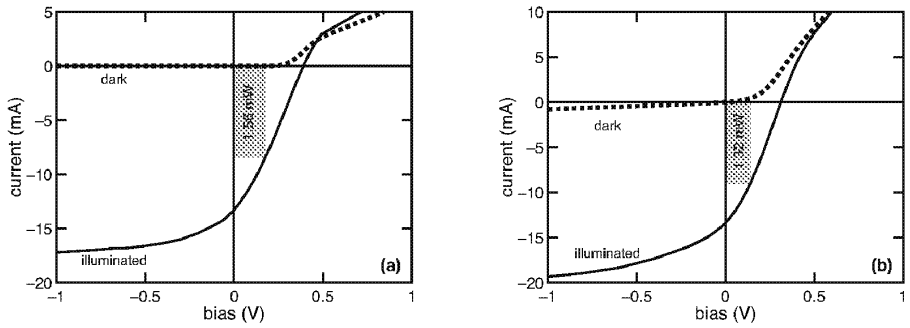


Figure 6.4: (a) The current-voltage characteristics for a high resistivity ($\rho > 1$ Ω·m) microstructured substrate with and without one sun illumination. The maximum output power rectangle is shown along with the maximum power. (b) The current-voltage characteristics for a low resistivity ($\rho = .01 - 0.1$ Ω·m) microstructured substrate with and without one sun illumination. The maximum power rectangle is shown along with the maximum output power.

p-doped crystalline silicon substrates with a fluence of 4 kJ/m^2 and anneal at 1075 K for one hour. The annealing step proves critical in improving the efficiency of our samples. We then evaporate Cr/Au contacts onto the samples; finger grids are evaporated onto the microstructured surface and the contact on unstructured side covers the whole surface. We then use an Oriel^{TM} sun simulator to illuminate the solar cell with the equivalent of one sun at high noon (100 mW/cm^2 average power). Figure 6.4 shows the I-V characteristics for unilluminated and illuminated solar cells made on a high resistivity ($\rho > 1$ Ω·m) and a low resistivity ($\rho = .01 - 0.1$ Ω·m) substrate.

The high resistivity substrate solar cell has an open circuit voltage of 0.4 Volts and a short circuit current of 13.4 mA. The fill factor is rather poor, however, and the overall efficiency is 1.56%. The low resistivity substrate solar cell has an open circuit voltage of 0.31 Volts and a short circuit current of 13.45 mA. The fill factor is also rather poor and the overall efficiency is 1.32%. Considering that these devices are made on crystalline substrates these preliminary results are mediocre. Typical commercial crystalline solar cells

SIONYX1403000030.0118

SAMSUNG EX. 1002 - 2988/4148

have efficiencies around 14 %, depending on the manufacturer. However, we are enthusiastic about the future of this work. After all, the first crystalline solar cells were only 6 % efficient and the first amorphous silicon solar cells were only 2 % efficient [93, 94]. Because we are new to device fabrication, there are several engineering aspects involved in solar cell production that we are not very skilled in. Series resistance added from non ideal electrical contact and the resistance of the substrates can drastically reduce the fill factor. The transition from exponential growth to a linear relationship at forward biases above 0.5 V indicates that series resistances are reducing our fill factors. The numerous methods for improving solar cell efficiency with engineering is beyond the scope of this dissertation [92], but we hope to improve our efficiencies with further work. In the immediate future, we plan to improve efficiency by optimizing laser conditions, substrate doping, and annealing conditions.

Because the microstructuring process leaves the surface layer highly disordered, it is likely that we will pursue application in arenas outside of crystalline silicon solar cells. We are investigating the use of femtosecond-laser microstructured silicon for use in more novel forms of solar cells, such as thin film and hybrid polymer/semiconductor solar cells [86, 95]. Decreasing absorption depths in microcrystalline silicon solar cells could reduce growth times and increase efficiency [89]. In the solar cell research community, there is much excitement about the possibility of producing inexpensive, efficient, and flexible solar cells from conducting polymers combined with nanorods of semiconductor materials such as CdSe. The nanorods are imbedded in the polymer to improve mobility, but have a limited absorption spectra. Imbedding the conical microstructures formed during laser microstructuring with their built in *p*-*n* junction might improve both the spectral absorption and the collection efficiency of these devices.

SIONYX1403000030.0119

SAMSUNG EX. 1002 - 2989/4148

6.3 Field emission from femtosecond-laser microstructured silicon surfaces

Field emission from femtosecond-laser microstructured silicon surfaces was actually the intended topic of the author's dissertation work. Early experiments revealed that the field emission properties of microstructured surfaces were on par with the best technologies in the field. Furthermore, the laser microstructuring process is simpler than the lithographic processes commonly used in other field emission arrays[96]. The results were very encouraging, but there was a problem. In order to understand this problem, we first need an introduction to the basic physics of field emission. As with solar cells, the recent work with photodiodes sheds some light of the problem and recently we began investigating field emission again.

6.3.1 Introduction to field emission

Many of us are familiar with cathode ray tubes (CRT) in older television sets and computer monitors. In these devices, a stream of electrons is generated and accelerated toward a luminescent material on the inside glass of the monitor, lighting up the screen. The supply of electrons is generated by heating up a pointed metal cathode and thereby *thermionically* exciting electrons to energies high enough to escape the metal surface. This hot cathode emission is called thermionic emission. Field emission, in contrast, refers to the application of a large electric field that greatly perturbs the potential barrier electrons encounter at a cathode surface, thereby allowing electrons to tunnel quantum mechanically out of the surface. This process is also referred to as cold cathode emission. Field emitters and field emission arrays have numerous applications [96], but the biggest commercial effort is in using field emission for flat panel displays [97]. In general, field emitters have several

SIONYX1403000030.0120

SAMSUNG EX. 1002 - 2990/4148

advantages over conventional vacuum electron sources. They can produce electron beams with high brightness and current density while operating at low voltages and consuming relatively little power. In addition they can be integrated into small, lightweight devices and operated with high pulse-repetition rates due to their rapid on/off switching speed.

We begin by discussing field emission from a metal surface. The original theory work describing field emission from a metal surface was done by Fowler and Nordheim [98] and is the starting point for understanding field emission from semiconductor surfaces. The following description of field emission comes mainly from the work by Fowler and Nordheim and a more recent summary by Gomer [99]. The reader is encouraged to read these references for a more in depth description.

In a metal, electrons occupy energy levels up to the Fermi energy (E_F). In order for an electron to escape the metal and enter into the surrounding vacuum, it must overcome a potential barrier at the surface. The difference between the lowest energy level above the potential barrier and the Fermi level is called the work function (ϕ)[1]. Figure 6.5 (a) graphically illustrates the energy level arrangement with position. If a strong electric field is applied, the potential barrier is perturbed and, instead of a step function, the barrier decreases linearly with distance from the metal/vacuum interface. If the field is strong enough, the potential barrier becomes thin enough for electrons to escape through quantum mechanical tunneling. Figure 6.5 (b) graphically illustrates the effect of an applied field on the potential barrier at the surface.

We can use the Heisenberg uncertainty principle to estimate the magnitude of the electric field necessary for tunneling. The uncertainty principle states that the uncertainty

[1]The reader might be familiar with work functions from introductory physics experiments with the photoelectric effect.

SIONYX1403000030.0121

SAMSUNG EX. 1002 - 2991/4148

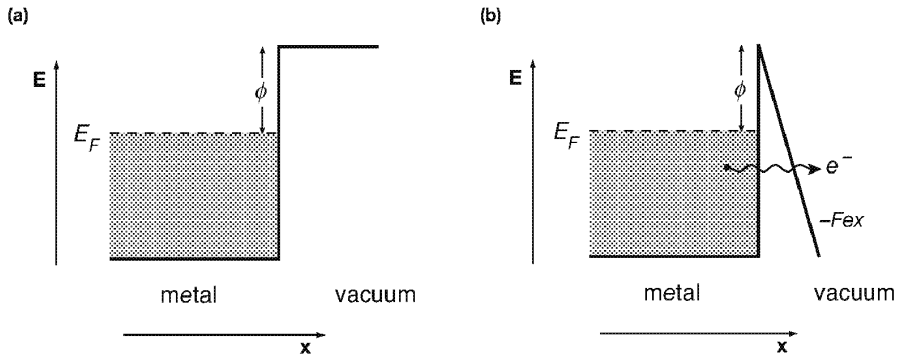


Figure 6.5: Energy level arrangement *vs.* position for field emission from a metal surface (a) without an applied electric field and (b) with an applied field. If the applied field is strong, it can perturb the potential barrier enough for electrons to quantum mechanically tunnel through.

of an electron position (Δx) is related to the uncertainty of the momentum (Δp) by

$$\Delta x \Delta p \geq \hbar. \tag{6.3}$$

If we consider an electron near the Fermi level, the uncertainty in momentum needed to overcome the potential barrier is

$$\Delta p = (2m\phi)^{\frac{1}{2}}. \tag{6.4}$$

For tunneling to occur Δx must equal the width of the perturbed potential barrier. The slope of the potential barrier under appled field F with distance x is $-Fex$. For an electron near the Fermi level, the potential barrier width (Δx) in the applied field is

$$\Delta x = \frac{\phi}{Fe}. \tag{6.5}$$

Plugging this value for Δx into Heisenberg's formula we have

$$\Delta p \geq \frac{\hbar Fe}{\phi}. \tag{6.6}$$

If we set our two formulas for Δp equal to one another we find that

$$F \approx \frac{(2m)^{\frac{1}{2}}\phi^{\frac{3}{2}}}{\hbar e}. \tag{6.7}$$

SIONYX1403000030.0122

SAMSUNG EX. 1002 - 2992/4148

For typical material work functions ($\sim$ 5 eV), field emission requires field strengths on the order of 10^{10} V/m. An electric field of this magnitude is not easily reached, but, electric field strengths are enhanced at sharp points. For this reason field emitters are usually sharp tips; the sharper the better. Geometric enhancement can reduce the necessary macroscopic field strength down to be on the order of V/μm [100, 101]. The sharp, conical microstructures formed during laser microstructuring in the presence of SF_6 are natural candidates for field emitters.

A more rigorous mathematical calculation of field emission current as a function of applied potential difference is carried out by Fowler and Nordheim [98]. Using tunneling probability theory with the WKB (Wentzel, Kramers, and Brillouin) approximation [102], they derive the now classic Fowler-Nordheim formula for field emission from sharp metal tips:

$$J = \frac{(C\beta F)^2}{\phi} e^{-\frac{B\phi^{3/2}}{\beta F}}, \tag{6.8}$$

where J is the current density, F is the applied field, ϕ is the work function, β is the geometric enhancement factor, and B and C are constants. If we substitute in $J = I/A$ (with A the emission area and I the emission current) and $F = \beta V$ (with V the applied potential difference) we arrive at a formula that relates the applied potential difference to the field emission current. Taking the logaritm of both sides of this equation and simplifying we arrive at

$$ln(I/V^2) = ln(a) - b(1/V), \tag{6.9}$$

where a and b are constants. This form of the Fowler-Nordheim equation shows that we expect a linear relation between the $\ln(I/V^2)$ and $1/V$. Plotting measurements in this form allows one to distinguish between field emission and other emission mechanisms, such as thermionic emission.

The theory for field emission from semiconductors is similar to that of metals. The

SIONYX1403000030.0123

SAMSUNG EX. 1002 - 2993/4148

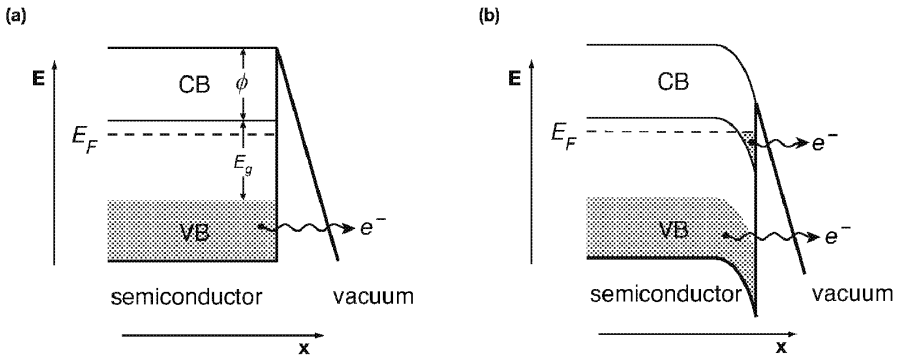


Figure 6.6: Energy level arrangement *vs.* position for field emission from a semiconductor surface in the presence of an electric field (a) without band bending from field penetration (b) and with band bending from field penetration. The conduction band is labeled CB and the valence band is labeled VB.

most significant difference is that the highest significantly occupied energy level is the top of the valence band, rather than at the Fermi level. Therefore, for the simplest case, electrons must overcome an effective work function ϕ_{eff} that includes the band gap energy,

$$\phi_{eff} = E_g + \phi. \tag{6.10}$$

With a large enough applied field, electrons can tunnel from the valence band into vacuum through the perturbed potential barrier. Figure 6.6 (a) illustrates the energy level arrangement *vs.* position for a semiconductor. However, with large applied fields, the electric field penetrates into the surface layer, perturbing the energy band structure near the surface. This phenomenon is called band bending and, if the conduction band bends below the Fermi level, electrons occupy the newly available energy levels just below the Fermi level. These electrons are at a higher energy than those at the top of the valence band and tunnel through at lower electric field strengths. Figure 6.6 (a) illustrates the energy level arrangement *vs.* position for a semiconductor with band bending. Electrons emitted from the surface of a semiconductor also obey the relationships derived in the Fowler-Nordheim

SIONYX1403000030.0124

SAMSUNG EX. 1002 - 2994/4148

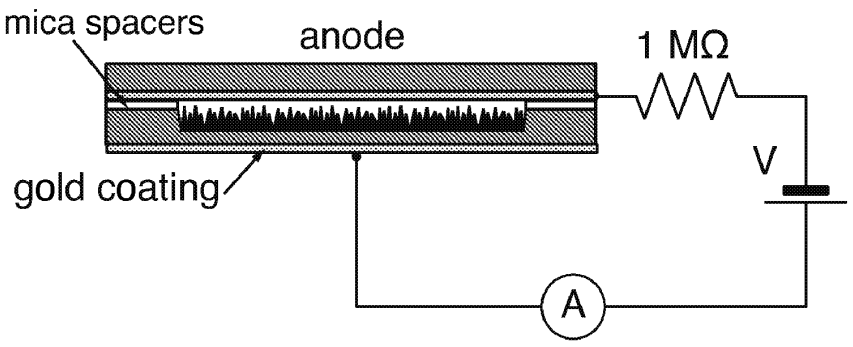


Figure 6.7: Cartoon illustration of the field emission measurement apparatus.

equation (Equation 6.9).

This background information gives us a simplified introduction to field emission theory. The reader is encouraged to refer to the work by Gomer [99] to learn more. We can now present some of our early field emission results as well as discuss the problem we mentioned earlier.

6.3.2 Field emission results

Our experimental procedure begins with femtosecond-laser microstructuring n-doped substrates with a fluence of 8 kJ/m^2. We then evaporate a gold contact onto the back (unstructured) surface of the sample. The sample is then clamped together with a gold-coated silicon wafer, which acts as the anode, with a pair of thin mica spacers (20 μm) between the two wafers. The mica spacers are made by carefully cleaving sheets of mica using the tip of a razor blade. The mounted sample is placed in a vacuum chamber, which is evacuated to a pressure of approximately 10^{-6} torr. Using vacuum feed-throughs, we apply a potential difference between the microstructured sample and the gold-coated anode. Emission current is measured at each applied voltage with a picoammeter; a 1 MΩ

SIONYX1403000030.0125

SAMSUNG EX. 1002 - 2995/4148

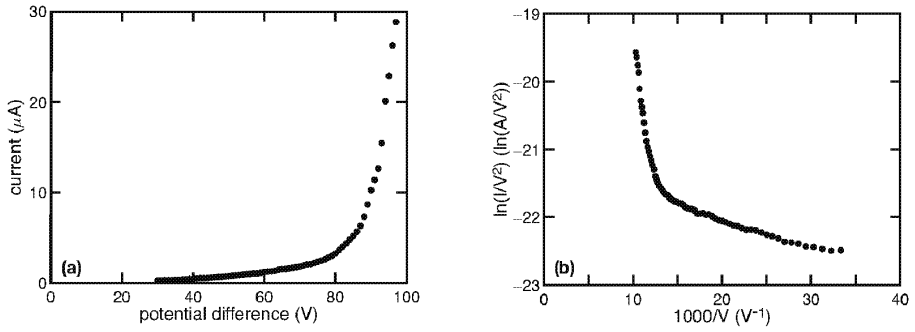


Figure 6.8: (a) Measurement of field emission current as a function of applied potential difference for a silicon surface microstructured in SF_6. (b) Fowler-Nordheim plot of the data contained in (a).

resistor is placed in series to protect the ammeter from unexpected surges in current. Figure 6.7 shows a schematic diagram of the field emission measurement apparatus.

The results of field emission measurements for samples microstructured in SF_6 are show in Figure 6.8. The figures of merit for a field emitting surface are the the turn-on field, defined as the electric field (bias voltage divided by the tip-to-anode spacing) for which a current density of 0.01 μA/mm^2 is observed, and the threshold field, defined as the field at which a current density of 0.1 μA/mm^2 is produced. The turn-on field for substrates microstructured in SF_6 is 1.3 V/μm, and the threshold field is 2.15 V/μm. These are excellent values, on par with carbon nanotubes, the best field emission material to date [100]. The Fowler-Nordheim plot for SF_6 structured samples is shown in Figure 6.8 (b). The two linear regions of the plot indicate that there are two field emission mechanisms contributing, one at low field strength, and one at higher field strengths. Figure 6.9 shows the field emission measurements for substrates microstructured in N_2, and Cl_2, and air. One of the interesting observations from these results is that the surfaces structured in N_2 have better emission characteristics than the surfaces structured in Cl_2. This result is surprising because the surfaces structured in Cl_2 have much sharper mircostructures (see

SIONYX1403000030.0126

SAMSUNG EX. 1002 - 2996/4148

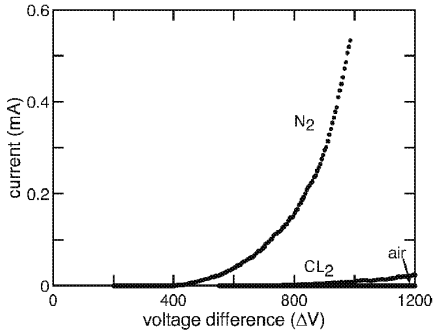


Figure 6.9: Measurements of field emission current as a function of applied potential difference for silicon surfaces microstructured in N_2, Cl_2, and air. The surfaces structured in N_2 have the highest emission currents despite having much blunter microstructures than surfaces structured in Cl_2.

Section 3.7.1). This difference indicates that it might not be geometric effects alone that cause high emission currents for the SF_6 structured surfaces.

These are encouraging results but, as we mentioned, there is a problem. If one looks at the apparatus arrangement shown in Figure 6.7, there should only be current flow for potential differences where the anode is at a higher potential than the cathode. Electrons are only attracted to higher potentials and applying a potential difference in the opposite direction should result in no current flow. However, when we reversed the polarity of our applied potential, we measured a current. It had an exponential dependence on applied potential but increased at a much slower rate than the field emission current. This issue was cause for concern and we speculated that there was a short circuit in our setup and therefore could not definitively claim that our field emission measurements were accurate. The author spent several years investigating the source of this current and, after many attempts to fix the experimental setup, we moved on to investigate other areas. It is only now, after we discovered that we are creating a *p-n* junction during laser microstructuring, that we understand the source of this spurious behavior. By applying a potential difference

SIONYX1403000030.0127

SAMSUNG EX. 1002 - 2997/4148

that is higher at the back side of the microstructured substrate, we are in fact forward biasing the laser created *p-n* junction.

With this new insight we have returned to investigating field emission properties from laser microstructured surfaces. We recently imaged luminescence from a phosphor coated anode; this result indicates that electrons are indeed escaping the silicon surface and traveling to the anode. We are therefore confident that our original results are measurements of field emission current rather than a short circuit. We are also reinforced in this conclusion because other research groups have subsequently investigated field emission from nanosecond-laser microstructured surfaces and measured similar turn-on and threshold fields [103].

6.4 Future directions

In this dissertation we presented results on the application of microstructured silicon surfaces in novel photodetectors, solar cells, and field emission devices. These applications are only a subset of the applications that we are currently investigating or plan to investigate. Among the other applications are photoluminescent surfaces [38], micromanipulation of biomagnetic material, and increased efficiency for drug delivery. We also demonstrated superhydrophylic behavior for microstructured surfaces, and alternatively, superhydrophobic behavior for microstructured surfaces coated with teflon. The increased surface area and electronic properties of substrates microstructured in SF_6 also might find application in biological and chemical sensors. The future is bright with possibilities and we hope that the applications presented in this dissertation are just the beginning.

SIONYX1403000030.0128

SAMSUNG EX. 1002 - 2998/4148

Chapter 7

Summary and outlook

Over the last decade, interdisciplinary work has gained momentum as the paradigm for the future of academic research. The work contained within this dissertation is truly interdisciplinary, representing an intersection between ultrafast optical science, material science, chemistry, and solid state device physics. We begin by creating femtosecond laser pulses with a complicated, multi-stage laser system. We then focus the laser pulses down onto the surface of silicon causing a light-material interaction with enormous intensities and temperatures that rival conditions at the surface of the sun. The resulting new material has unique morphologies, optical, and electronic properties. By investigating the chemical and structural makeup of the newly formed material we then applied our knowledge to design and create novel optoelectronic devices.

This dissertation contains the current state of our understanding of femtosecond-laser microstructured silicon. We presented analysis of the morphology, structural, and chemical composition of microstructured surfaces with varying experimental parameters. This analysis allowed us to determine a more complete picture of formation mechanisms and gain insight into the interaction between the molten silicon surface and the ambient gas

SIONYX1403000030.0129

SAMSUNG EX. 1002 - 2999/4148

environment. We then analyzed the effect of many of the same experimental parameters on optical and electronic properties of microstructured silicon. With this information, combined with structural and chemical measurements, we explained the source of the near-unity below-band gap absorption for surfaces microstructured in SF_6.

With this new found insight into the surface properties, we made the first functioning optoelectronic device using femtosecond-laser microstructured silicon; a highly sensitive silicon-based photodiode for both the visible and near-infrared spectrum. We extended the usable wavelength region of silicon detectors into a previously inaccessible region that has numerous applications in communications and sensing, an accomplishment that might significantly change the commercial landscape for near-infrared detection. We analyzed the effect of experimental parameters on the sensitivity of laser-microstructured photodiodes and identified the presence of a large gain mechanism at small biases. This gain mechanism is critical for the high response of our photodiodes for both the visible and infrared regime. We then presented the beginnings of our work toward using femtosecond-laser microstructured silicon in other devices such as solar cells and field emission arrays. The unique properties of the microstructured surface hold great potential for these and other novel applications.

For each of the areas of research, be it femtosecond laser-material interaction, investigation of material structure after structuring, or novel device design, there are many interesting questions and problems still to be investigated. With each experiment we gain insight into the inner workings of femtosecond-laser microstructured silicon and with each new insight we are better able to take advantage of its unique properties.

I hope that I presented the reader with compelling evidence that the future is bright for this work. Essentially, we have created an entirely new material through the interaction of intense femtosecond laser pulses with silicon in a sulfur containing environment.

SIONYX1403000030.0130

SAMSUNG EX. 1002 - 3000/4148

The resulting chemical and structural makeup are unique to these experimental conditions and, subsequently, the optical and electronic properties are unique as well. Although this accomplishment alone is exciting, I feel that we have just scratched the surface, so to speak. The information in this dissertation deals primarily with the inclusion of a single element, sulfur, into the surface of a single semiconductor, silicon. The true power of our experimental procedure is that we can dope nearly any surface with any element to very high levels in a structurally unique way. The number of possible combinations is enormous and I expect that many more combinations will have novel properties and find useful application. I doubt that we are so lucky as to stumble upon the one important combination with our first attempt.

SIONYX1403000030.0131

SAMSUNG EX. 1002 - 3001/4148

References

[1] T.-H. Her, R. J. Finlay, C. Wu, S. Deliwala, and E. Mazur, "Microstructuring of silicon with femtosecond laser pulses," *Appl. Phys. Lett.*, vol. 73, p. 1673, 1998.

[2] T.-H. Her, *Femtochemistry at gas/solid interfaces.* PhD thesis, Harvard University, 1998.

[3] Z. Ghousheng, P. M. Fauchet, and A. E. Siegman, "Growth of spontaneous periodic surface structures on solids during laser illumination," *Phys. Rev. B*, vol. 26, p. 5366, 1982.

[4] H. M. van Driel, J. E. Sipe, and J. F. Young, "Laser-induced periodic surface structures on solids: a universal phenomenon," *Phys. Rev. Lett.*, vol. 49, p. 1955, 1982.

[5] S. R. Foltyn, "Surface modification of materials by cumulative laser irradiation," in *Pulsed Laser Deposition of Thin Films* (D. B. Chrisey and G. K. Hubler, eds.), New York: Wiley-Interscience, 1994.

[6] J. E. Rothenberg and R. Kelly, "Laser sputtering. Part II. The mechanism of the sputtering of Al_2O_3," *Nucl. Instrum. Meth. Phys. Res. B*, vol. 1, p. 291, 1984.

[7] F. Sanchez, J. L. Morenza, R. Aguiar, J. C. Delgado, and M. Varela, "Whiskerlike structure growth on silicon exposed to ArF excimer laser irradiation," *Appl. Phys. Lett.*, vol. 69, p. 620, 1996.

[8] F. Sanchez, J. L. Morenza, R. Aguiar, J. C. Delgado, and M. Varela, "Dynamics of the hydrodynamical growth of columns on silicon exposed to ArF excimer-laser irradiation," *Appl. Phys. A*, vol. 66, p. 83, 1998.

[9] W. Kautek and J. Krüger, "Femtosecond-pulse laser microstructuring of semiconducting materials," in *Material Science Forum* (D. B. Chrisey and G. K. Hubler, eds.), vol. 173-174, p. 17, Switzerland: Trans Tech Publications Inc., 1995.

[10] A. J. Pedraza, J. D. Fowlkes, and D. H. Lowndes, "Silicon microcolumn arrays grown

SIONYX1403000030.0132

SAMSUNG EX. 1002 - 3002/4148

by nanosecond laser irradiation," *Appl. Phys. Lett.*, vol. 74, p. 2322, 1999.

[11] T.-H. Her, R. J. Finlay, C. Wu, and E. Mazur, "Femtosecond laser-induced formation of spikes on silicon," *Appl. Phys. A*, vol. 70, p. 383, 2000.

[12] A. J. Pedraza, J. D. Fowlkes, S. Jesse, C. Mao, and D. H. Lowndes, "Surface microstructuring of silicon by excimer-laser irradiation in reactive atmospheres," *Appl. Surf. Sci.*, vol. 168, p. 251, 2000.

[13] J. D. Fowlkes, A. J. Pedraza, and D. H. Lowndes, "Microstructural evolution of laser-exposed silicon targets in SF_6 atmospheres," *Appl. Phys. Lett.*, vol. 77, p. 1629, 2000.

[14] V. V. Voronov, S. I. Dolgaev, S. V. Lavrishchev, A. A. Lyalin, A. V. Simakin, and G. A. Shafeev, "Formation of conic microstructures upon pulsed laser evaporation of solids," *Quantum Electron.*, vol. 30, p. 710, 2000.

[15] S. I. Dolgaev, S. V. Lavrishev, A. A. Lyalin, A. V. Simakin, V. V. Voronov, and G. A. Shafeev, "Formation of conical microstructures upon laser evaporation of solids," *Appl. Phys. A*, vol. 73, p. 177, 2001.

[16] J. D. Fowlkes, A. J. Pedraza, D. A. Blom, and H. M. M. III, "Surface microstructuring and long-range ordering of silicon nanoparticles," *Appl. Phys. Lett.*, vol. 80, p. 3799, 2002.

[17] A. J. Pedraza, J. D. Fowlkes, and Y.-F. Guan, "Surface nanostructuring of silicon," *Appl. Phys. A*, vol. 77, p. 277, 2003.

[18] C. Wu, *Femtosecond laser-gas-solid interactions.* PhD thesis, Harvard University, 2000.

[19] C. Wu, C. H. Crouch, L. Zhao, J. E. Carey, R. J. Younkin, J. Levinson, E. Mazur, R. M. Farrel, P. Gothoskar, and A. Karger, "Near-unity below-band gap absorption by microstructured silicon," *Appl. Phys. Lett.*, vol. 78, p. 1850, 2001.

[20] R. Younkin, *Surface studies and microstructure fabrication using femtosecond laser pulses.* PhD thesis, Harvard University, 2001.

[21] D. G. Georgiev, R. J. Baird, I. Avrutsky, G. Auner, and G. Newaz, "Controllable excimer-laser fabrication of conical nano-tips on silicon thin films," *Appl. Phys. Lett.*, vol. 84, p. 4881, 2004.

[22] S. Deliwala, *Time-resolved studies of molecular dynamics using nano- and femtosecond laser pulses.* PhD thesis, Harvard University, 1995.

SIONYX1403000030.0133

SAMSUNG EX. 1002 - 3003/4148

[23] R. J. Finlay, *Femtosecond-laser-induced reactions at surfaces.* PhD thesis, Harvard University, 1998.

[24] J. F. Young, J. E. Sipe, and H. M. van Driel, "Laser-induced periodic surface structure. III. Fluence regimes, the role of feedback, and details of the induced topography in germanium," *Phys. Rev. B*, vol. 30, p. 2001, 1984.

[25] J. F. Young, J. S. Preston, H. M. van Driel, and J. E. Snipe, "Laser-induced periodic surface structure. II. Experiments on Ge, Si, Al, and brass," *Phys. Rev. B*, vol. 27, p. 1155, 1983.

[26] L. S. Dake, D. E. King, J. R. Pitts, and A. W. Czanderna, "Ion beam bombardment effects on solid surfaces at energies used for sputter depth profiling," in *Beam effects, surface topography and depth profiling in surface analysis* (A. W. Czanderna, T. E. Madey, and C. J. Powell, eds.), New York: Plenum Press, 1998.

[27] M. D. Betterton, *Things Fall Apart: Topics in Biophysics and Pattern Formation.* PhD thesis, Harvard University, 2000.

[28] P. Keblinski, S. R. Phillpot, D. Wolf, and H. Gleiter, "Thermodynamically stable amorphous intergranular films in nanocrystalline silicon," *Phys. Lett. A*, vol. 226, p. 205, 1997.

[29] P. L. Liu, R. Yen, N. Bloembergen, and R. T. Hodgson, "Picosecond laser-induced melting and resolidification morphology on silicon," *Appl. Phys. Lett.*, vol. 34, p. 12, 1979.

[30] F. Spaepen and D. Turnbull, "Crystallization processes," in *Laser Annealing of Semiconductors* (J. M. Poate and J. W. Mayer, eds.), New York: Academic Press, 1982.

[31] J. A. Leavitt, L. C. McIntyre, and M. R. Weller, "Backscattering spectrometry," in *Handbook of Modern Ion Beam Analysis* (J. H. Tesmer, C. J. Maggiore, M. Nastasi, J. C. Barbour, and J. W. Mayer, eds.), Pittsburgh: Material Research Society, 1995.

[32] A. J. Garratt-Reed and D. C. Bell, *Energy dispersive X-ray analysis in the electron microscope.* Oxford: BIOS Scientific Publisher, 1st ed., 2003.

[33] *http://www.genplot.com.*

[34] A. Cavalleri, K. Sokolowski-Tinten, J. Bialkowski, M. Schreiner, and D. von der Linde, "Femtosecond melting and ablation of semiconductors studied with time of flight mass spectroscopy," *Journal of Appl. Phys.*, vol. 85, p. 3301, 1999.

[35] M. Meunier, B. Fisette, A. Houle, A. V. Kabashin, S. V. Broude, and P. Miller, "Pro-

SIONYX1403000030.0134

SAMSUNG EX. 1002 - 3004/4148

cessing of metals and semiconductors by a femtosecond laser-based microfabrication system," *Proc. SPIE Vol. 4978*, vol. 4978, p. 169, 2003.

[36] B. Saleh and M. Teich, *Fundamentals of Photonics.* New York: Wiley-Interscience, 1st ed., 1991.

[37] N. Bloembergen, "Fundamentals of laser-solid interactions," in *Laser-Solid Interactions and Laser Processing* (S. D. Ferris, H. J. Leamy, and J. M. Poate, eds.), New York: American Institute of Physics, 1979.

[38] C. Wu, C. H. Crouch, L. Zhao, and E. Mazur, "Visible luminescence from silicon surfaces microstructured in air," *Appl. Phys. Lett.*, vol. 81, p. 1999, 2002.

[39] S. M. Sze, *Physics of Semiconductor Devices.* New York: Wiley-Interscience, 2nd ed., 1981.

[40] R. M. Bradley and J. M. E. Harper, "Theory of ripple topography induced by ion bombardment," *J. Vac. Sci. Technol. A*, vol. 6, p. 2390, 1988.

[41] J. Erlebacher, M. J. Aziz, E. Chason, M. B. Sinclair, and J. A. Floro, "Spontaneous pattern formation on ion bombarded Si(001)," *Phys. Rev. Lett.*, vol. 82, p. 2330, 1999.

[42] J. Erlebacher, M. J. Aziz, E. Chason, M. B. Sinclair, and J. A. Floro, "Nonlinear amplitude evolution during spontaneous patterning of ion-bombarded Si(001)," *J. Vac. Sci. Technol. A*, vol. 18, p. 115, 2000.

[43] Z. X. Jiang and P. F. A. Alkemade, "The complex formation of ripples during depth profiling of Si with low energy, grazing oxygen beams," *Appl. Phys. Lett.*, vol. 73, p. 315, 1998.

[44] G. Carter and V. Vishnyakov, "Roughening and ripple instabilities on ion-bombarded Si," *Phys. Rev. B*, vol. 54, p. 17647, 1996.

[45] T. M. Mayer, E. Chason, and A. J. Howard, "Roughening instability and ion-induced viscous relaxation in SiO_2 surfaces," *J. Appl. Phys.*, vol. 76, p. 1633, 1994.

[46] S. Rusponi, C. Boragno, and U. Valbusa, "Ripple structure on Ag(110) surface induced by ion sputtering," *Phys. Rev. Lett.*, vol. 78, p. 2795, 1997.

[47] E. Chason, T. M. Mayer, B. K. Kellerman, D. T. McIlroy, and A. J. Howard, "Roughening instability and evolution of the Ge(001) surface during ion sputtering," *Phys. Rev. Lett.*, vol. 72, p. 3040, 1994.

[48] A. J. Pedraza, J. D. Fowlkes, and D. H. Lowndes, "Self-organized silicon microcolumn

SIONYX1403000030.0135

SAMSUNG EX. 1002 - 3005/4148

arrays generated by pulsed laser irradiation," *Appl. Phys. A*, vol. 69 [Suppl.], p. S731, 1999.

[49] D. H. Lowndes, J. D. Fowlkes, and A. J. Pedraza, "Early stages of pulsed-laser growth of silicon microcolumns and microcones in air and SF_6," *Appl. Surf. Sci.*, vol. 154-155, p. 647, 2000.

[50] A. J. Pedraza, J. D. Fowlkes, and D. H. Lowndes, "Laser ablation and column formation in silicon under oxygen-rich atmospheres," *Appl. Phys. Lett.*, vol. 77, p. 3018, 2000.

[51] V. I. Emel'yanov and D. V. Babak, "Defect capture under rapid solidification of the melt induced by the action of femtosecond laser pulses and formation of periodic surface structures on a semiconductor surface," *Appl. Phys. A*, vol. 74, p. 797, 2002.

[52] J. H. Sanderson, R. V. Thomas, W. A. Bryan, W. R. Newell, P. F. Taday, and A. J. Langley, "Multielectron-dissociative-ionization of SF_6 by intense femtosecond laser pulses," *J. Phys. B: At. Mol. Opt. Phys.*, vol. 30, p. 4499, 1997.

[53] R. S. Wagner and W. C. Ellis, "Vapor-liquid-solid mechanism of single crystal growth," *Appl. Phys. Lett.*, vol. 4, p. 89, 1964.

[54] P. G. Carey and T. W. Sigmon, "In-situ doping of silicon using the gas immersion laser doping (GILD) process," *Appl. Surf. Sci.*, vol. 43, p. 325, 1989.

[55] R. Reitano, P. M. Smith, and M. J. Aziz, "Solute trapping of group III, IV, and V elements in silicon by an aperiodic stepwise mechanism," *J. Appl. Phys.*, vol. 76, p. 1518, 1994.

[56] M. Y. Shen, C. H. Crouch, J. E. Carey, R. Younkin, M. Sheehy, C. M. Friend, and E. Mazur, "Formation of regular arrays of silicon microspikes by femtosecond laser irradiation through a mask," *Appl. Phys. Lett.*, vol. 82, p. 1715, 2003.

[57] T. M. Rassias, *The problem of Plateau - A tribute to Jesse Douglas and Tibor Radó.* New Jersey: River Edge, 1st ed., 1992.

[58] A. R. Zanatta and I. Chambouleyron, "Absorption edge, band tails, and disorder of amorphous semiconductors," *Phys. Rev. B*, vol. 53, p. 3833, 1996.

[59] *http://www.eeel.nist.gov/812/hall.html.*

[60] L. J. van der Pauw, "A method of measuring the specific resistivity and hall effect on discs of arbitrary shapes," *Philips Res. Repts.*, vol. 13, p. 1, 1958.

SIONYX1403000030.0136

SAMSUNG EX. 1002 - 3006/4148

[61] C. G. Bernhard, "Structural and functional adaptation in a visual system," *Endeavor*, vol. 26, p. 79, 1967.

[62] K. Noda, B. J. Glover, P. Linstead, and C. Martin, "Flower colour intensity depends on specialized cell shape controlled by a Myb-related transcription factor," *Nature*, vol. 269, p. 661, 1994.

[63] E. S. Kolesar, V. M. Bright, and D. M. Sowders, "Optical reflectance reduction of textured silicon surfaces coated with an antireflective thin film," *Thin Solid Films*, vol. 290-291, p. 23, 1996.

[64] J. Zhao, A. Wang, M. Green, and F. Ferrazza, "19.8% efficient honeycomb textured multicrystalline and 24.4% monocrystalline silicon solar cells," *Appl. Phys. Lett.*, vol. 73, p. 1991, 1998.

[65] H. G. Craighead and R. E. Howard, "Microscopically textured optical storage media," *Appl. Phys. Lett.*, vol. 39, p. 532, 1981.

[66] J. I. Gittleman, E. K. S. and. H. W. Lehmann, and R. Widmer, "Textured silicon: A selective absorber for solar thermal conversion," *Appl. Phys. Lett.*, vol. 35, p. 742, 1979.

[67] E. S. Kolesar, V. M. Bright, and D. M. Sowders, "Mid-infrared ($2.5 <= \lambda <= 12.5$ μm) optical absorption enhancement of textured silicon surfaces coated with an antireflective thin film," *Thin Solid Films*, vol. 270, p. 10, 1995.

[68] M. A. Sheehy, "Chalcogen doping of silicon with femtosecond laser irradiation above the ablation threshold." to be submitted, 2004.

[69] M. J. Aziz, "Interface attachment kinetics in alloy solidification," *Metallurgical and Materials Transactions A*, vol. 27A, p. 671, 1996.

[70] F. A. Trumbore, "Solid solubilities of impurity elements in germanium and silicon," *Bell Syst. Tech. Journal*, vol. 39, p. 205, 1960.

[71] J. I. Pankove, *Optical Processes in Semiconductors*. New York: Dover Publications, 1st ed., 1971.

[72] A. Agarwal, H. J. Gossman, D. J. Eaglesham, L. Pelaz, J. M. Poate, and T. E. Haynes, "Critical issues in ion implantation of silicon below 5 keV: Defects and diffusion," *Mater. Sci. Eng. A*, vol. 253, p. 269, 1998.

[73] S. Roorda, S. Saito, and W. C. Sinke, "Solid phase epitaxial regrowth of microcrystalline Si films on a (100) Si substrate," *Mat. Res. Soc. Symp. Proc.*, vol. 100, p. 417,

SIONYX1403000030.0137

SAMSUNG EX. 1002 - 3007/4148

1988.

[74] J. M. Warrender and M. J. Aziz private communication, 2004.

[75] N. W. Ashcroft and N. D. Mermin, *Solid State Physics*. New York: Saunders College Publishing, 1st ed., 1976.

[76] A. Yariv, *Optical Electronics*. New York: Holt, Rinehart, and Winston, 3rd ed., 1985.

[77] W. Shockley, "The theory of *p-n* junctions in semiconductors and *p-n* junction transistors," *Bell. Syst. Tech. J.*, vol. 28, p. 435, 1949.

[78] Z. Lo, R. Jiang, Y. Zheng, L. Zang, Z. Chen, S. Zhu, X. Cheng, and Z. Liu, "Staircase band gap $Si_{1-x}Ge_x$/Si photodetectors," *Appl. Phys. Lett.*, vol. 77, p. 1548, 2000.

[79] M. E. kurdi, P. Boucaud, S. Sauvage, G. Fishman, O. Kermarrec, Y. Campidelli, D. Bensahel, G. Saint-Girons, I. Sagnes, and G. Patriarche, "Silicon-on-insulator waveguide photodetector with Ge/Si self-assembled islands," *J. Appl. Phys.*, vol. 92, p. 1858, 2003.

[80] A. Y. Loudon, P. A. Hiskett, G. S. Buller, R. T. Carline, D. C. Herbert, W. Y. Leong, and J. G. Rarity, "Enhancement of the infrared detection efficiency of silicon photon-counting avalanche photodiodes by use of silicon germanium absorbing layers," *Opt. Lett.*, vol. 27, p. 219, 2002.

[81] G. Masini, L. Colace, G. Assanto, H.-C. Luan, and L. C. Kimerling, "High-performance p-i-n Ge on Si photodetectors for the near infrared: From model to demonstration," *IEEE Trans. Electon Devices*, vol. 48, p. 1092, 2001.

[82] D. Buca, S. Winneri, S. Lenk, S. Mantl, and C. Buchal, "Metal-germanium-metal ultrafast infrared detectors," *J. Appl. Phys.*, vol. 92, p. 7599, 2002.

[83] R. Calarco, M. Fiordelisi, S. Lagomarsino, and F. Scarinci, "Near-infrared metal-semiconductor-metal photodetector integrated on silicon," *Thin Solid Films*, vol. 391, p. 138, 2001.

[84] M. Ghioni, A. Lacaita, G. Ripamonti, and S. Cova, "All-silicon avalanche photodiode sensitive at 1.3 μm with picosecond time resolution," *IEEE J. Quantum Electron.*, vol. 28, p. 2678, 1992.

[85] *http://www.nrel.gov*.

[86] W. U. Huynh, J. J. Dittmer, and A. P. Alivisatos, "Hybrid nanorod-polymer solar cells," *Science*, vol. 295, p. 2425, 2002.

SIONYX1403000030.0138

SAMSUNG EX. 1002 - 3008/4148

[87] N. Jensen, R. M. Hausner, R. B. Bergmann, J. H. Werner, and U. Rau, "Optimization and characterization of amorphous/crystalline silicon heterojunction solar cells," *Prog. Photovolt: Res. Appl.*, vol. 10, p. 1, 2002.

[88] J. Yang, A. Banerjee, and S. Guha, "Amorphous silicon based photovoltaics–from earth to the "final frontier"," *Sol. Energy Mater. Sol. Cells*, vol. 78, p. 597, 2003.

[89] A. V. Shah, J. Meier, E. Vallat-Sauvain, N. Wyrsch, U. Kroll, C. Droz, and U. Graf, "Material and solar cell research in microcrystalline silicon," *Sol. Energy Mater. Sol. Cells*, vol. 78, p. 469, 2003.

[90] M. A. Green, K. Emery, D. L. King, S. Igari, and W. Warta, "Solar cell efficiency tables (version 17)," *Prog. Photovolt: Res. Appl.*, vol. 9, p. 49, 2001.

[91] E. Juengst, "Silicon valleys," *Discover Magazine*, vol. 20, February 1999.

[92] A. Goetzberger, J. Knobloch, and B. Voss, *Crystalline Silicon Solar Cells.* West Sussex: John Wiley and Sons Ltd., 1st ed., 1998.

[93] D. M. Chapin, C. S. Fuller, and G. L. Pearson, "A new silicon p-n junction photocell for converting solar radiation into electrical power," *J. Appl. Phys.*, vol. 25, p. 676, 1954.

[94] D. E. Carlson and C. R. Wronski, "Amorphous silicon solar cell," *Appl. Phys. Lett.*, vol. 28, p. 671, 1976.

[95] W. U. Huynh, J. J. Dittmer, N. Teclemariam, D. J. Milliron, and A. P. Alivisatos, "Charge transport in hybrid nanorod-polymer composite photovoltaic cells," *Phys. Rev. B*, vol. 67, p. 115326, 2003.

[96] I. Brodie and P. Schwoebel, "Vacuum microelectronic devices," *Proc. of the IEEE*, vol. 82, p. 1006, 1994.

[97] A. A. Talin, K. A. Dean, and J. E. Jaskie, "Field emission displays: a critical review," *Solid-State Electron.*, vol. 45, p. 963, 2001.

[98] R. H. Fowler and L. Nordheim, "Electron emission in intense electric fields," *Proc. Roy. Soc. (London) A*, vol. 119, p. 173, 1928.

[99] R. Gomer, *Field Emission and Field Ionization*, vol. 9 of *Harvard Monographs in Applied Science.* Cambridge, Massachusetts: Harvard University Press, 1st ed., 1961.

[100] J.-M. Bonard, M. Croci, C. Klinke, R. Kurt, O. Noury, and N. Weiss, "Carbon nanotube films as electron field emitters," *Carbon*, vol. 40, p. 1715, 2002.

SIONYX1403000030.0139

SAMSUNG EX. 1002 - 3009/4148

[101] H. C. Lo, D. Das, J. S. Hwang, K. H. Chen, C. H. Hsu, C. F. Chen, and L. C. Chen, "SiC-capped nanotip arrays for field emission with ultralow turn-on field," *Appl. Phys. Lett.*, vol. 83, p. 1420, 2003.

[102] E. Merzbacher, *Quantum Mechanics*, ch. 7. New York: John Wiley and Sons, Inc., 3rd ed., 1998.

[103] A. V. Karabutov, V. D. Frolov, E. N. Loubnin, A. V. Simakin, and G. A. Shafeev, "Low-threshold field electron emission of si micro-tip arrays produced by laser ablation," *Appl. Phys. A*, vol. 76, p. 413, 2003.

SIONYX1403000030.0140

SAMSUNG EX. 1002 - 3010/4148

ADVANCED FUNCTIONAL MATERIALS
www.afm-journal.de

Metal-Catalyzed Etching of Vertically Aligned Polysilicon and Amorphous Silicon Nanowire Arrays by Etching Direction Confinement

By *Shih-wei Chang, Vivian P. Chuang, Steven T. Boles,* and *Carl V. Thompson**

A systematic study of metal-catalyzed etching of (100), (110), and (111) silicon substrates using gold catalysts with three varying geometrical characteristics: isolated nanoparticles, metal meshes with small hole spacings, and metal meshes with large hole spacings is carried out. It is shown that for both isolated metal catalyst nanoparticles and meshes with small hole spacings, etching proceeds in the crystallographically preferred <100> direction. However, the etching is confined to the single direction normal to the substrate surface when a catalyst meshes with large hole spacings is used. We have also demonstrated that the metal catalyzed etching method when used with metal mesh with large hole spacings can be extended to create arrays of polycrystalline and amorphous vertically aligned silicon nanowire by confining the etching to proceed in the normal direction to the substrate surface. The ability to pattern wires from polycrystalline and amorphous silicon thin films opens the possibility of making silicon nanowire array-based devices on a much wider range of substrates.

1. Introduction

Silicon nanowires have attracted considerable attention owing to novel properties arising from their quasi-one-dimensional nature.[1] To date, a wide range of applications including electronic devices,[2,3] biochemical sensors,[4] energy storage devices,[5] and thermoelectrics[6] have been demonstrated using silicon nanowires as building blocks. Currently, the most commonly used method to produce silicon nanowires is by vapor-liquid-solid (VLS) growth where metal catalysts such as gold are used to catalyze nanowire growth in a chemical vapor deposition (CVD) process.[7] However, integration of VLS-grown wires with current silicon technology remains challenging due to issues such as in-diffusion of catalyst metal at elevated growth temperatures, and orientation control.[8] In addition, control over wire morphology, which is key to successful property characterization and device applications, is very difficult to achieve using the VLS method.

[*] Dr. S.-W. Chang, Dr. V. P. Chuang, Dr. S. T. Boles, Prof. C. V. Thompson
Department of Materials Science and Engineering
Massachusetts Institute of Technology
Cambridge, MA 02139, USA
E-mail: cthomp@mit.edu

DOI: 10.1002/adfm.201000437

Metal-catalyzed etching provides a promising alternative tool for the fabrication of high-aspect-ratio silicon nanostructures. In this approach metal particles or perforated films are used to facilitate the etching of silicon in a solution consisting of hydrofluoric acid and an oxidant. We and many others have demonstrated the use of metal-catalyzed etching in conjunction with various metal catalyst film patterning techniques for the fabrication of single-crystal silicon nanowires from single-crystal wafers.[9–13] However, despite recent progress in both the fabrication and application of chemically-etched silicon nanowires, relatively little is known about the etching mechanisms. In particular, the crystallographic-orientation dependence of the etching behavior is an important aspect one must understand in order to achieve good orientation control.

Recently, Huang et al.[14] reported a systematic study of the catalyst-morphology dependence of the metal-assisted etching of Si(110) single-crystal substrates.[14] Their results showed that in the case of isolated metal particles or relatively small patches of metal films with perforating nanoholes, the etching direction was predominantly <100>, and in the case of a continuous metal film with perforating holes extending over a sufficiently large area, the direction of etching can be confined to the vertical [$\bar{1}$0] direction. Utilizing this etching suppression behavior, they successfully fabricated vertically aligned silicon nanowires on Si(110) substrates using a porous anodic alumina template as a silver deposition mask. In a similar study on substrate orientation dependence, Zhang et al. also showed that etching proceeded predominantly in the <100> direction when a silver network deposited using electroless deposition was employed as the catalyst.[15]

In this letter, we build upon these results and show that the key to vertical etching lies in other critical dimensions of the metal mesh; i.e. for any given area of the metal mesh, vertical confinement depends on the relative ratio of the hole spacing to the film thickness. The hole spacing in a mesh is defined as the distance between two nearest-neighbor nanoholes for both hexagonal and square arrays, as shown in **Figure 1**. We present a systematic investigation of metal-assisted etching of Si(100), Si(110), and Si(111) substrates using metal catalysts with three varying morphologies: isolated particles, metal mesh with small

© 2010 WILEY-VCH Verlag GmbH & Co. KGaA, Weinheim

SIONYX1403000030.0141

SAMSUNG EX. 1002 - 3011/4148

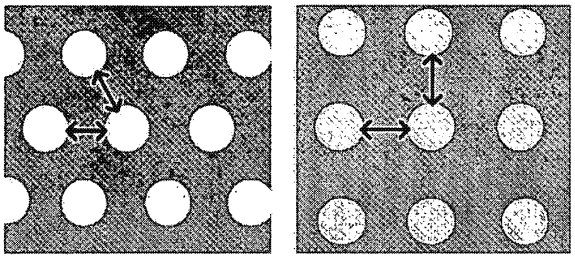


Figure 1. Schematic drawing of metal meshes with hexagonal (left) and square arrays of holes (right). The hole spacing (represented by the arrows) is defined as the nearest-neighbor distance between two nanoholes.

hole spacings, and metal mesh with large hole spacings. We also demonstrated that the metal catalyzed etching method can be extended to the fabrication of vertically aligned one-dimensional polysilicon and amorphous silicon nanostructures.

2. Etching Direction Dependence on Catalyst Geometries

Both n- and p-type silicon substrates with orientations (100), (110), and (111) were used in this study. The general etching behavior was similar for both doping types and only results for n-type silicon are presented in this letter. The resistivity was chosen to be 1–25 Ω cm for all substrates to eliminate any possible effect that the doping level may have on the etching behavior. Au was chosen as the catalyst and was deposited using electron beam (ebeam) evaporation for all three types of catalyst morphologies. For isolated Au particles, 2 nm of Au was deposited directly onto the silicon substrates. The discontinuous Au film morphology is best described as irregularly shaped Au islands of different sizes. For Au meshes with very fine hole spacings, the as-deposited catalyst film was patterned using block copolymer (BCP) lithography, as described in our previous work.[13] The diblock copolymer used was polystyrene (PS)-*block*-polyferrocenyldimethylsilane (PFS) with a molecular weight of 47 kg/mol for PS and 15 kg/mol for PFS. The period was approximately 35 nm and the average diameter of a nanohole was 22 nm, giving a hole spacing of roughly 13 nm. The gold film thickness in this case was 12 nm. Finally, for Au meshes with relatively large hole spacings, interference lithography (IL) was used to pattern the as-deposited catalyst film.[12] A square array of anti-reflection coating (ARC) pillars was first fabricated after a series of exposure and dry etching steps. 12 nm of gold was subsequently deposited through the ARC mask. A gold film with square arrays of perforating holes was obtained after removal of the ARC pillars. The array period was 400 nm and the hole diameter was 140 nm, giving a hole spacing of 260 nm. Scanning electron microscope (SEM) images of the three different Au morphologies are shown in Figure 2.

After catalyst deposition, etching was carried out by immersing the samples in a mixed solution of hydrofluoric acid (HF), hydrogen peroxide (H_2O_2), and water (10 wt% HF and 1.5 wt% H_2O_2) for 5–15 minutes in ambient light. Post-etching drying for the BCP-patterned sample was done in a critical point drier after thoroughly rinsing with alcohol several times, as these high aspect ratio structures otherwise tend to cluster at their tips to form sheaflike structures due to the capillary force present during conventional drying.[13] This was not necessary for the interference-lithography-patterned sample since the aspect ratio of the pillar is smaller, so that the pillars are stiffer and cannot be bent by capillary forces sufficiently to cause tip stiction. The samples were rinsed with isopropanol and blow-dried with nitrogen after the etching procedure.

Figure 3 shows representative SEM images of the silicon nanostructures that resulted from etching. Each of the three columns shows images from substrates of three different crystal orientations–N(100), N(110), and N(111) silicon. Each of the three rows shows images from Au catalysts of three different morphologies–isolated nanoparticles, a fine metal mesh with small hole spacings, and a wide metal mesh with large hole spacings. Comparing silicon nanostructures etched using isolated Au nanoparticles (a, b, and c) and metal meshes with large hole spacings as catalysts (g, h, and i), the former case clearly shows etching in the <100> direction, whereas the latter shows vertical etching. This result is consistent with earlier results presented by Huang et al.[14] in which the crystallographically preferred <100> direction was suppressed and vertical etching resulted for a metal film with perforating nanoholes extending over a large area on the substrate.[14]

By comparing silicon nanostructures etched using metal meshes with large hole spacings (g, h, and i) to those made using very small hole spacings (d, e, and f), we further conclude that the hole spacing also plays an important role in determining the etching direction. In contrast with the vertical etching of the IL-patterned samples, in the case of a BCP-patterned fine metal mesh, etching occurred in the preferred <100> direction. The variation in angle of the fine nanowires in the SEM image is an artifact of cleaving for cross sectional SEM sample preparation. This is different from previous results presented by Huang et al.,[14] in which etching occurred in the <100> direction for small-area patches of metal networks (e.g., a Ag mesh originally covering a large substrate area broken into smaller patches due to Ag dissolution in the etchant solution) and should provide further insight into how to better control the orientation of the etched nanowires. In other words, even if the overall catalyst film area is sufficiently large (in our case over a centimeter-scale area), if the hole spacing is too narrow, inclined etching will still occur. On the

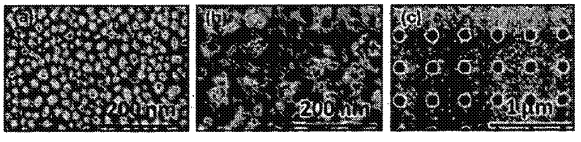


Figure 2. Scanning electron microscopy (SEM) images of metal catalysts of three different morphologies: a) isolated Au islands deposited using direct electron beam (ebeam) evaporation; b) Au mesh with small hole spacings patterned using block copolymer (BCP) lithography; c) Au mesh with relatively large hole spacings patterned using interference lithography (IL).

© 2010 WILEY-VCH Verlag GmbH & Co. KGaA, Weinheim

SIONYX1403000030.0142

SAMSUNG EX. 1002 - 3012/4148

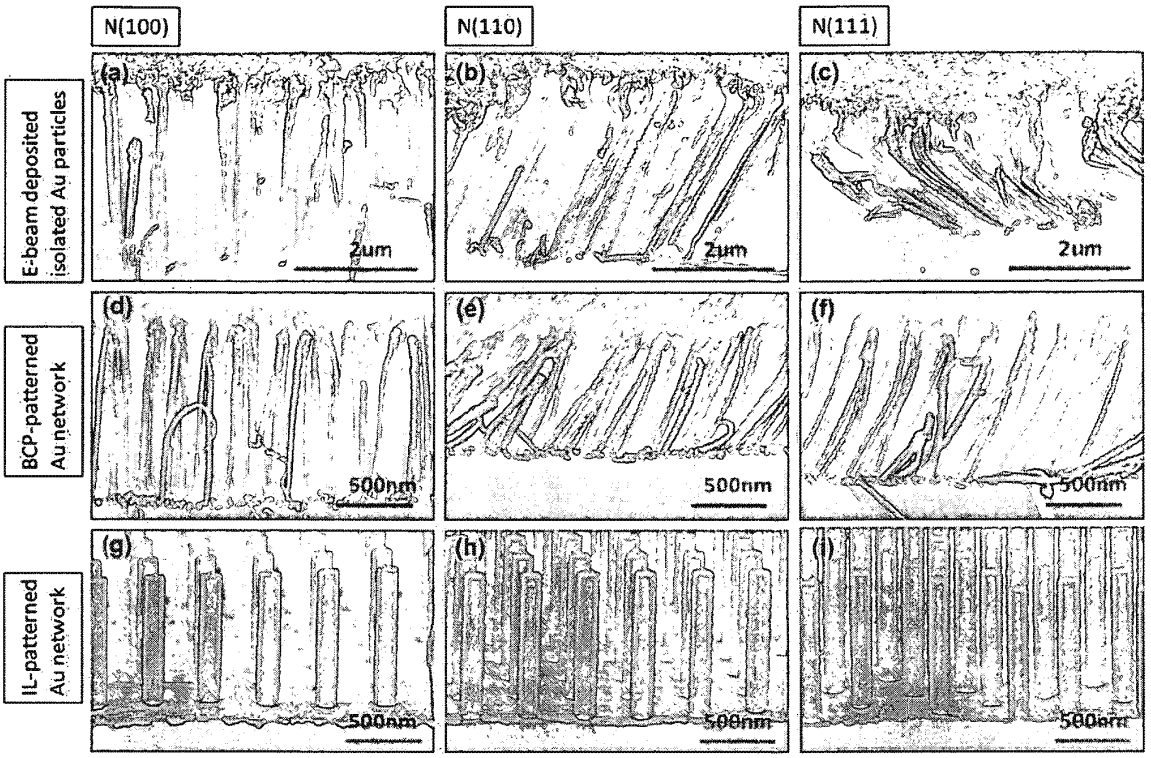


Figure 3. SEM images of etching results from silicon substrates with three different crystallographic orientations and Au catalysts of three differet morphologies: a–c) isolated Au islands deposited using ebeam evaporation on N(100), N(110), and N(111) silicon substrates, respectively; d–f) a Au mesh with small hole spacings patterned using BCP lithography on N(100), N(110), and N(111) silicon substrates, respectively; g–i) a Au mesh with relatively large hole spacings patterned using IL on N(100), N(110), and N(111) silicon substrates, respectively.

other hand, even if the overall catalyst film area is sufficiently small, if the hole spacing is large enough, the etching direction can be confined in the normal direction to the substrate surface. The latter can be further confirmed by patterning a small area Au catalyst mesh with large hole spacings on Si N(110) substrate. Etching was still confined to the vertical direction even though the film was only micrometers in size, as shown in Figure 4.

If we regard the inclined etching as a result of the vector addition of vertical and lateral movement, we expect etching for a large-spacing metal mesh to be confined in the vertical direction as lateral movement is severely restricted. On the other hand, the BCP-patterned fine metal mesh has a hole spacing of 13 nm, comparable to the metal film thickness which was 12 nm; i.e., in cross section, the interconnected Au lines should have roughly the same width as the thickness. As a result, lateral etching is not as restricted as for the IL-patterned mesh, thus allowing etching to proceed in the crystallographically preferred <100> direction. Huang et al.[14] observed well-defined domains for isolated Au particles in which etching occurred in one of the two preferred [$\bar{1}$00] or [0$\bar{1}$0] directions for Si(110) substrates. In our case, no domain formation was observed for etching using the BCP-patterned metal catalyst since the interconnected network forces etching to proceed in one direction over the entire substrate. It should be noted that while Huang et al[11] in earlier work studied the film thickness dependence of wire characteristics for metal catalyzed etching used in conjunction with pre-patterning of the silicon substrate, the film thickness in their case influenced only the hole diameters and did not reveal the behavior reported here.[11]

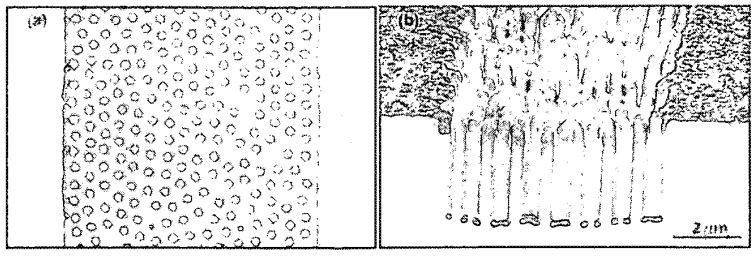


Figure 4. SEM images of (a) a small patch of metal film with perforating hole arrays on a Si N(110) substrate, and (b) vertical silicon nanopillar arrays after metal-assisted etching.

© 2010 WILEY-VCH Verlag GmbH & Co. KGaA, Weinheim

SIONYX1403000030.0143

SAMSUNG EX. 1002 - 3013/4148

3. Fabrication of Amorphous and Polysilicon Nanowire Arrays

By utilizing the confinement effect associated with relatively large hole spacings, we have successfully shown that vertically aligned 1D silicon nanostructures can be obtained regardless of the crystallographic orientation of the silicon from which they are etched, as demonstrated for both n- and p-type Si(100), (110), and (111) substrates. The method can be further extended to fabrication of vertically aligned polycrystalline and amorphous silicon nanostructures by suppressing etching directions other than those normal to the original surface.

To form amorphous and poly-silicon nanostructures, undoped amorphous and poly-silicon thin films were deposited on p-type Si(100) substrates with a film thickness of approximately 1.2 and 1.1 μm, respectively. The amorphous silicon thin film was deposited using ebeam evaporation at room temperature, and the polysilicon thin film was deposited using low pressure chemical vapor deposition (LPCVD) at 625 °C. Both samples were used in the as-deposited state without any further annealing. Figure 5a and b show SEM images of the as-deposited samples.

Au films with nominal thicknesses of 2 nm and in the form of isolated islands were deposited using electron beam evaporation onto both types of substrates. For comparison, Au meshes were patterned using nanosphere lithography.[10] A monolayer of polystyrene spheres with an average diameter of 330 nm was first coated onto the substrates by dip-coating using a home-built dip-coater. A dry etching step was carried out using reactive ion etching (RIE) in an oxygen plasma to reduce the sphere diameter. A gold mesh with a relatively large hole spacings (>120 nm) was obtained after ebeam evaporation of Au through the polystyrene mask and lift-off in toluene to remove the gold-coated spheres. The polystyrene metal deposition mask after RIE and the resulting gold mesh are shown in Figure 5c and d, respectively. Etching was then carried out in a solution consisting of HF, H_2O_2, and water (10 wt% HF, 0.15 wt% H_2O_2). The concentration of the H_2O_2 was reduced by a factor of 10 compared to the etchant concentration used for single-crystal silicon etching to slow down the etch rate as etching occurred very rapidly and violent bubble formation was otherwise observed.

Figure 6 shows etching results for both polycrystalline and amorphous silicon. In the case of isolated gold particles on polycrystalline silicon, etching proceeded in different directions for each particle. As shown in Figure 6a, only under a certain particles did the Au catalyst etch through the polysilicon thin film to continue into the underlying single-crystal Si(100) substrate, where vertical etching was observed. This was expected as isolated catalyst particles tend to move in the <100> direction. As a result of the random etching directions in the polycrystalline silicon, some of the Au particles never reached the polysilicon/substrate interface. For isolated gold particles on amorphous silicon, etching appeared to be mostly vertical with the particles moving collectively in the same direction. Although the actual etching direction could not be determined as the resulting structure lacked structural integrity and collapsed very easily, the vertical etching in the amorphous silicon layer can be confirmed by the relatively high ratio of Au particles that reached the amorphous/substrate interface and continued to catalyze etching into the Si(100) substrate, as shown in Figure 6d. The collective movement suggested some type of interaction with neighboring particles. However, more detailed studies are required to understand the etching behavior in amorphous silicon.

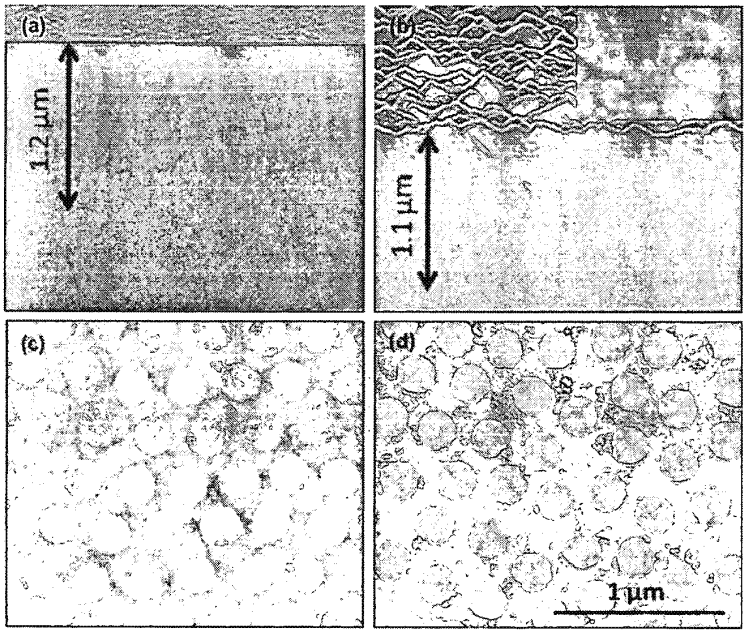


Figure 5. SEM images of (a) an as-deposited amorphous silicon thin film; (b) an as-deposited polysilicon thin film on p-type Si(100) substrates. c–d) SEM images of polystyrene nanospheres with reduced diameter serving as a metal deposition mask, and a gold catalyst film with a hexagonal array of perforating holes, respectively, on a polysilicon sample.

In the case of metal meshes with relatively large hole spacings, etching proceeded in the vertical direction for both polycrystalline and amorphous films, as expected. Figure 6c and 6d show polysilicon and amorphous silicon nanopillars, respectively. These pillar or wire arrays made from polycrystalline and amorphous films are of special interest for device applications because they can be formed on a very wide array of substrates, including large-area, conformable substrates, and are not restricted by the use of costly single crystal wafers. In addition, polycrystalline and amorphous films can be deposited at relatively low temperatures, allowing further flexibility in substrate selection and the possibility of stacking of nanowire arrays without severe constraints. For example, solar cells based on planar amorphous

© 2010 WILEY-VCH Verlag GmbH & Co. KGaA, Weinheim

SIONYX1403000030.0144

SAMSUNG EX. 1002 - 3014/4148

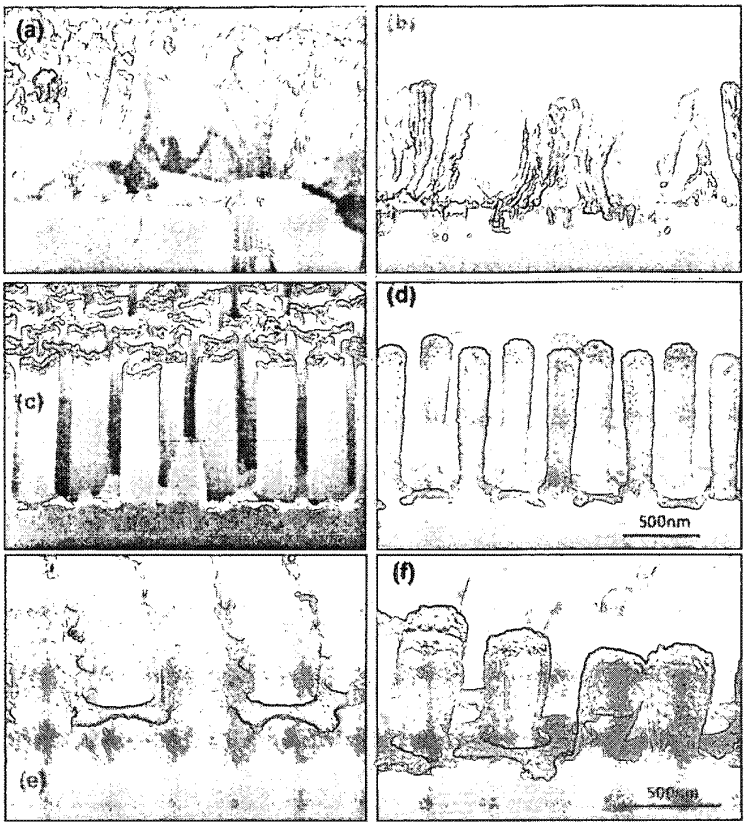


Figure 6. SEM images of results of metal-assisted etching of (a) isolated Au particles on polycrystalline silicon; b) isolated Au particles on amorphous silicon; c) a Au mesh with relatively large hole spacings on polysilicon; d) a Au mesh with relatively large hole spacings on amorphous silicon; e) after etching for only 1 min, with the Au mesh etching only partially through the 300 nm-thick amorphous silicon thin film; f) after etching for 3 min, resulting in the baseball-bat-like shape of the amorphous silicon nanopillars.

silicon[16] and microcrystalline silicon[17] have well-established commercial markets. High surface-to-volume ratio nanostructures based on amorphous and polysilicon patterned arrays may be desirable as potential materials for solar cell photoanodes. Although vertically oriented amorphous nanowires can be synthesized using evaporation methods based on the solid-liquid-solid (SLS) growth mechanism,[18] the high temperature requirement severely limits the substrates that can be used. Polycrystalline silicon nanowire synthesis has also been demonstrated using VLS-based methods.[19] However, this method faces similar challenges as in the case of VLS-grown single crystal silicon nanowires. A room temperature process to achieve these nanostructures such as presented here is therefore particularly attractive.

Upon closer examination, the polysilicon nanopillars are characterized by a vertical side wall similar to their single-crystal counterparts. On the other hand, the amorphous silicon nanopillars exhibit a "baseball bat" shape where the diameter gradually decreases towards the bottom of the pillars. One possible explanation may lie in the extremely fast etch rate of amorphous silicon in comparison to crystalline silicon. For example, for the same etchant concentration (10 wt% HF, 0.15 wt% H_2O_2), the time required to etch approximately 1 μm into the silicon thin films was 3 min for amorphous silicon and 10 min for polycrystalline silicon. As a result of the etch rate difference, the vertical movement of the Au mesh was slowed down significantly when it reached the silicon substrate. It is commonly believed that in metal-assisted etching, the metal significantly enhances the silicon etch rate by catalyzing reduction of the oxidant in the etchant solution. Chartier et al. suggested that one reason that holes are consumed at the perimeter of the catalyst could be that a charge depletion layer exists around the metal catalysts, leading to a lower energy barrier for holes at the interface.[20] They also suggested that since HF must have access to the metal/Si interface during the etching process, the metal/Si contact must be intermittent at best. For amorphous silicon, the dissolution of silicon may have advanced much further into the depletion layer than it would have for crystalline silicon before the metal film loses contact with the sidewalls of the etched structures and proceeds to sink deeper into the silicon thin film. This can be seen in Figure 6(e) where the pillar diameter is clearly smaller than the diameter of the perforating holes in the Au thin film. In this case, since the Au film only moved down partially through the amorphous thin film, the sidewalls of the nanopillars still remained vertical. As the vertical movement of the Au catalyst film was slowed down at the interface, further catalyzed dissolution of the amorphous silicon near the interface can occur for a longer period of time, resulting in the bat-like shape as shown in Figure 6f.

It is worth noting that for device applications, it is desirable that the metal catalysts be removed. For the case of gold, the catalyst can be readily removed by immersing the sample in commercially available iodine-based gold etchants. It is also worth noting that the structure of the amorphous silicon pillars appears to be very spongy and therefore lacked good structural integrity. This may be the result of the low density of amorphous films deposited at room temperature. Similar to the case of high aspect ratio silicon nanowires patterned using BCP lithography, when the surface tension force exerted on the nanowires during drying exceeds the force required to bend the wires, sheaflike structures result as the wires stick together at the tip. Since the amorphous wires are much less stiff in comparison with their crystalline counterparts, the nanostructures easily collapse even at a much smaller aspect ratio. SEM images of such collapsed structures are shown in **Figure 7**. For the case of amorphous silicon nanopillars, the attractive forces between pillars are so great that the

© 2010 WILEY-VCH Verlag GmbH & Co. KGaA, Weinheim

SIONYX1403000030.0145
SAMSUNG EX. 1002 - 3015/4148

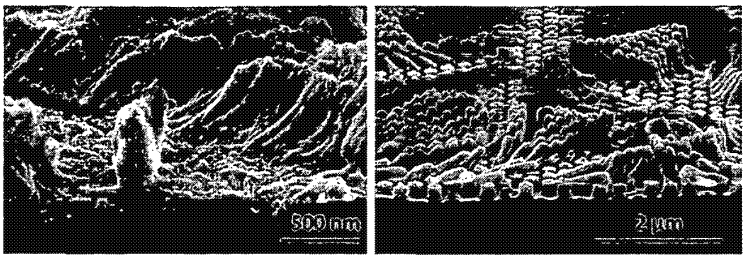


Figure 7. Amorphous silicon etching with both isolated Au nanoparticles (left) and a Au mesh (right) without critical point drying.

pillars detached from the crystalline silicon substrate and stuck together in sheaves. In order to eliminate surface-tension-induced stiction, post-etching drying must be done in a critical point drier.

To further investigate the structure of the polycrystalline and amorphous silicon nanostructures, transmission electron microscopy (TEM) was carried out. Figure 8a shows a typical TEM image of a polysilicon nanopillar array that has not etched all the way through the polysilicon thin film. The grain structure is clearly columnar. The polycrystalline nature of the pillars is further confirmed by the ring pattern in selected area electron diffraction (SAED), as shown in the inset. Figure 8b shows bright- and dark-field TEM images of an amorphous silicon nanopillar array in the same region (top and bottom image, respectively). The amorphous nature of the nanowire array is confirmed by the the much lower intensity in the amorphous region (due to scattering) in the dark field image.

4. Conclusion

In summary, we have demonstrated that in addition to having a meshes structure, the spacing between the perforations (e.g. holes) is a critical factor in determining the catalytic etching direction. For isolated catalyst nanoparticles and catalyst meshes with small hole spacings, etching occurs in the preferential <100> direction. An explanation for the inclined etching was presented. Where both vertical and lateral movement of the catalyst are unrestricted, as in the case for isolated particles and the BCP-patterned films where the hole spacing is comparable to the film thickness, etching in the <100> direction is preferred. By having a meshes with relatively large hole spacings, etching is forced to proceed in a single direction normal to the silicon surface as a result of restricted horizontal movement of the mesh. Based on these results, we have shown, for the first time, that mesh geometries can be chosen for which the crystallographic orientation of the silicon substrate *does not* affect the orientation of the etched wires. This was demosntrated for both n- and p-type Si(100), (110), and (111) substrates.

We have also demonstrated, for the first time, that by properly choosing the mesh geometries, nanowire arrays of polycrystalline and amorphous silicon can be created using metal-catalyzed etching. For isolated Au nanoparticles, etching occurred in different directions for each particle on polycrystalline silicon. On the other hand, collective movement of the catalyst particles in the vertical direction was observed on amorphous silicon substrates. vertically aligned nanopillar arrays were obtained for both poly- and amorphous silicon when mesh with relatively large hole spacings was employed for catalysis. Although we have demonstrated nanopillar fabrication on crystalline silicon substrates, this process can be used to fabricate functional silicon nanowire arrays using silicon films of *any* crystal structure (i.e. single crystal, polycrystalline, or amorphous) deposited on *any* substrate, including those of very large sizes or even flexible plastic substrates. This will enable the use of metal-catalyzed etching for formation of functional silicon nanowire arrays and silicon-nanowire-based devices in much more flexible and much lower-cost ways.

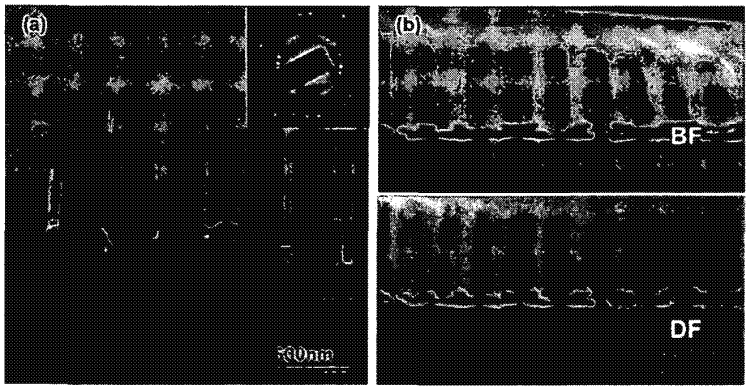


Figure 8. TEM images of (a) polycrystalline silicon nanopillars, and (b) amorphous silicon nanopillars, where the top and bottom images are bright- and dark-field images, respectively. The inset in (a) shows the selected area electron diffraction (SAED) pattern.

5. Experimental Section

Interference-Lithography-Patterned Silicon Nanowire Arrays: First the silicon substrate was coated with BARLi anti-reflection coating (ARC) (200 nm, AZ Electronic Materials, NJ, USA), electron-beam deposited silicon oxide (20 nm), and PFI-88 photoresist (200 nm, Sumitomo Chemical Co., Osaka, Japan). The resist stack was then exposed using a Lloyd's mirror interference lithography system equipped with a 325 wavelength helium-cadmium laser. A square array of posts can be obtained by a two-beam exposure with a rotation angle of 90°. A series of reactive ion etching steps (CF_4 plasma for silicon oxide and He-O_2 plasma for ARC) was carried out to transfer the pattern into the bottom ARC layer which was used as a Au deposition mask. Lift-off was carried out by soaking and sonicating the sample in heated N-Methyl-2-pyrrolidone (NMP). A square array of silicon nanowires is obtained after metal catalyzed etching.

© 2010 WILEY-VCH Verlag GmbH & Co. KGaA, Weinheim

SIONYX1403000030.0146

SAMSUNG EX. 1002 - 3016/4148

Block-Copolymer-Lithography-Patterned Silicon Nanowire Arrays: 60 nm of silicon oxide was first deposited using electron beam evaporation. The diblock copolymer, PS-*b*-PFS, was then spin-coated from a 1.5 wt% toluene solution onto the oxide layer. The spin-coated samples were vacuum-annealed at 140 °C for 44 h to achieve microphase separation into arrays of PFS spheres. Subsequently, the PFS spherical pattern was transferred into the oxide layer by reactive ion etching in CF_4. 12 nm of gold was deposited using e-beam evaporation through the oxide pillar mask. A gold antidot array was obtained after immersion in dilute hydrofluoric acid to remove the oxide pillars. Finally, metal-catalyzed etching was carried out to fabricate ordered arrays of silicon nanowires.

Acknowledgements

This work was financially supported through the Singapore-MIT Alliance and the MIT Energy Initiative. Interference lithography was carried out in MIT's Nanostructures Laboratory.

Received: March 9, 2010
Published online: September 23, 2010

[1] Y. Wu, H. Yan, M. Huang, B. Messer, J. H. Song, P. Yang, *Chem. Eur. J.* **2002**, *6*, 1261.
[2] Y. Cui, Z. Zhong, D. Wang, W. U. Wang, C. M. Lieber, *Nano Lett.* **2003**, *3*, 149.
[3] J. Goldberger, A. I. Hochbaum, R. Fan, P. Yang, *Nano Lett.* **2006**, *6*, 973.
[4] Y. Cui, Q. Wei, H. Park, C. M. Lieber, *Science* **2001**, *293*, 1289.
[5] L.-F. Cui, R. Ruffo, C. K. Chan, H. Peng, Y. Cui, *Nano Lett.* **2009**, *9*, 491.
[6] A. I. Hochbaum, R. Chen, R. D. Delgado, W. Liang, E. C. Garnett, M. Najarian, A. Majumdar, P. Yang, *Nature* **2008**, *8*, 163.
[7] Y. Wu, P. Yang, *J. Am. Chem. Soc.* **2001**, *123*, 3165.
[8] V. Schmidt, S. Senz, U. Gösele, *Nano. Lett.* **2005**, *5*, 931.
[9] K.-Q. Peng, Y. Wu, H. Fang, X. Y. Zhong, Y. Xu, J. Zhu, *Angew Chem. Int. Ed.* **2005**, *44*, 2737.
[10] K.-Q. Peng, M. Zhang, A. Lu, N.-B. Wong, R. Zhang, S.-T. Lee, *Appl. Phys. Lett.* **2007**, *90*, 163123.
[11] Z. Huang, X. Zhang, M. Reiche, L. Liu, T. Shimizu, S. Senz, W. Lee, *Nano Lett.* **2008**, *8*, 3046.
[12] W. K. Choi, T. H. Liew, M. K. Dawood, H. I. Smith, C. V. Thompson, M. H. Hong, *Nano Lett.* **2008**, *8*, 3799.
[13] S.-W. Chang, V. P. Chuang, S. T. Boles, C. A. Ross, C. V. Thompson, *Adv. Funct. Mater.* **2009**, *19*, 2495.
[14] Z. Huang, T. Shimizu, S. Senz, Z. Zhang, X. Zhang, W. Lee, N. Geyer, U. Gösele, *U. Nano Lett.* **2009**, *9*, 2519.
[15] M.-L. Zhang, K.-Q. Peng, X. Fan, J.-S. Jie, R.-Q. Zhang, S.-T. Lee, N.-B. Wong, *J. Phys. Chem. C* **2008**, *112*, 4444.
[16] D. E. Carlson, C. R. Wronski, *Appl. Phys. Lett.* **1976**, *28*, 671.
[17] J. Meier, R. Flückiger, H. Keppner, A. Shah, *Appl. Phys. Lett.* **1994**, *65*, 860.
[18] X. Chen, Y. Xing, J. Xu, J. Xiang, D. Yu, *Chem. Phys. Lett.* **2003**, *374*, 626.
[19] X. B. Zeng, Y. Y. Xu, S. B. Zhang, Z. H. Hu, H. W. Diao, Y. Q. Wang, G. L. Kong, X. B. Liao, *J. Crystal Growth* **2002**, *247*, 13.
[20] C. Chartier, S. Bastide, C. Lévy-Clément, *Electrochim. Acta* **2008**, *53*, 5509.

© 2010 WILEY-VCH Verlag GmbH & Co. KGaA, Weinheim

SIONYX1403000030.0147

SAMSUNG EX. 1002 - 3017/4148

Broadband moth-eye antireflection coatings fabricated by low-cost nanoimprinting

Q. Chen,[1,a] G. Hubbard,[2] P. A. Shields,[1] C. Liu,[1] D. W. E. Allsopp,[1] W. N. Wang,[1] and S. Abbott[2]
[1]*Department of Electronic and Electrical Engineering, University of Bath, Bath BA2 7AY, England*
[2]*MacDermid Autotype Ltd., Grove Road, Wantage OX12 7BZ, England*

(Received 26 February 2009; accepted 17 June 2009; published online 2 July 2009)

Subwavelength scale antireflection moth-eye structures in silicon were fabricated by a wafer-scale nanoimprint technique and demonstrated an average reflection of 1% in the spectral range from 400 to 1000 nm at normal incidence. An excellent antireflection property out to large incident angles is shown with the average reflection below 8% at 60°. Pyramid array gave an almost constant average reflection of about 10% for an incident angle up to 45° and concave-wall column array produced an approximately linear relation between the average reflection and the incident angles. The technique is promising for improving conversion efficiencies of silicon solar cells. © *2009 American Institute of Physics*. [DOI: 10.1063/1.3171930]

Enhancing the energy conversion efficiency will be a key factor in increasing the application range and cost effectiveness of crystalline silicon solar cells. Due to the large refractive index discontinuity at air-silicon interfaces, strong reflection above 30% occurs and causes the additional loss. Various antireflection (AR) techniques have been proposed and investigated, such as single/multilayer films[1,2] and surface texturisation.[3–8] A single layer of deposited quarter-wave silicon nitride AR coating is easy to be fabricated but has limited performance due to the narrow-band and narrow-angle properties.[1] An advanced oblique angle deposition technique was applied to fabricate a multilayer AR coating and demonstrated an important suppression of surface reflection up to 60°.[2] Alkaline etching is the practical technique in industry. Both inverse pyramids formed by masked anisotropic etching of single crystalline silicon and upright random pyramids formed by maskless process are able to reduce the surface reflection because of multiple bounce reflectance.[3–5] Similar texturing technique using acid solution was also applied to multicrystalline silicon.[6] Surface texturization with subwavelength feature size by wet or dry etching attracted wide interests as well and demonstrated impressively enhanced performance.[7,8] Such behavior arises from the behavior arises from the gradual variation in refractive index between air and silicon. This is actually inspired by the naturally evolved cornea of some moths where it comprises of an array of protuberant structures. Research into subwavelength moth-eye structures commenced about 35 years ago when their low reflection over a relatively broad spectral range was first demonstrated.[9] Since then, various methods of fabricating biomimetic moth-eye surfaces have been explored, such as dry etching with spin-coated monolayer colloidal crystals mask[10] and electron-beam lithography.[11] Reflection as low as 2.5% was achieved in the whole solar spectrum[10] but no angle-dependent experimental results was reported, which is important to demonstrate the application potential in sunrise-to-sunset solar cells. In this letter, we report high-performance broadband full-angle AR silicon moth-eye structures fabricated by a high throughput and low-cost nanoimprint technique.[12] Ultralow average reflection of 1% in the spectral range between 400 and 1000 nm was achieved at normal incidence. Up to the incident angle of 60°, the average reflection was still below 8%. The simple technique is compatible with standard microfabrication and has great potential in the application in crystalline silicon solar cells.

Biomimetic nanostructures were fabricated by a soft roller nanoimprint technique, in which the nanoscale structures on a flexible master are sequentially pressed into the UV sensitive resist spin-coated on the wafer as shown in Fig. 1. Then the moth-eye patterns are transferred into the substrate by reactive ion etching or inductively coupled plasma etching with the imprinted resist layer acting as the etch mask. The flexible master is prepared by using a roll-to-roll ultraviolet (UV) replication process from a nickel master, which is molded by a standard electroforming technique in photoresist with moth-eye structure made by two-beam laser interference photolithography (Holotools GmbH). This imprint technique is naturally appropriate for the wafer-scale patterning of even fragile or bowed substrates owing to the use of flexible masters, low imprint force, and the line-contact imprinting process.[12] Residual layer thicknesses less than 20 nm on various substrates are routinely achieved. UV light curing completes the cross linking of the resist rather than thermal curing. Figure 2(a) shows a SEM image of a 450 nm period moth-eye pattern imprinted in the resist on a silicon surface. The inset shows the detail of the nanostructure pseudohexagonal lattice due to the two-light beams in-

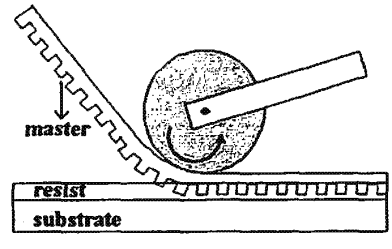


FIG. 1. Schematic of soft roller nanoimprint technique.

[a]Electronic mail: chenqiniscas@gmail.com.

 © 2009 American Institute of Physics

Downloaded 14 Feb 2011 to 128.193.164.203. Redistribution subject to AIP license or copyright; see http://apl.aip.org/about/rights_and_permissions

SIONYX1403000030.0148

SAMSUNG EX. 1002 - 3018/4148

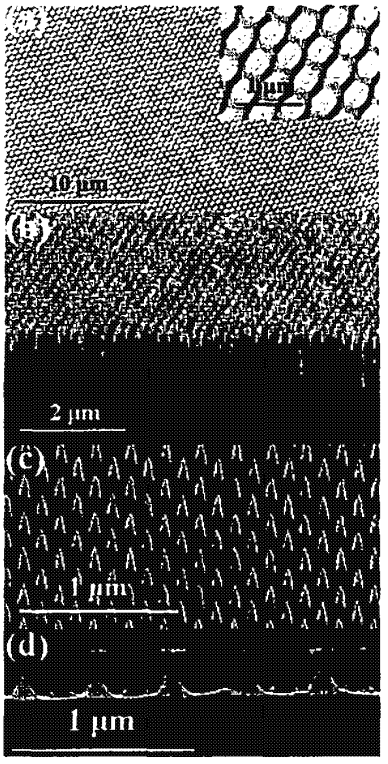


FIG. 2. (a) A SEM image of imprinted moth-eye pattern in 450 nm period in the resist on silicon surface. The detail is shown in the inset. SEM images of silicon *NSs NS1, NS2,* and *NS3* are shown in *(b), (c),* and *(d),* respectively.

terference lithography in master production. This high-quality imprinted pattern was achieved across the entire 4 in. wafer, demonstrating the technique can provide a high-quality nanoscale pattern with high throughput and low cost.

A spectral reflectance system F30 (Filmetrics Inc.) was used to measure the reflection spectra at normal incidence. Results for a bare polished silicon sample and a nanostructured sample (NS) are shown in Fig. 3, where the theoretical result of a SiN_x AR coating and the experiment results in Ref. 4 are also shown for comparison. Sample NS1 as shown in Fig. 2(b) has a surface comprising an array of silicon

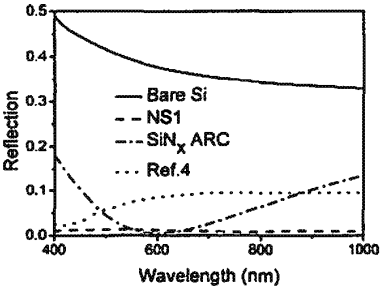


FIG. 3. Measured reflection spectra under normal incidence for a bare polished silicon wafer (bold solid line) and NS1 (dash line). Theoretical reflection spectrum (dash dot line) for a SiN_x AR coating and experiment results (dot line) in Ref. 4 are shown for comparison.

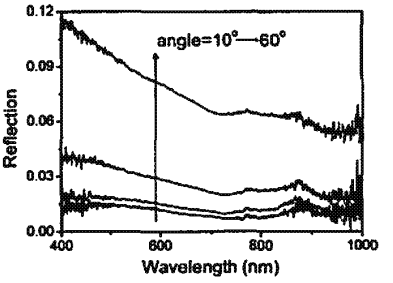


FIG. 4. Measured angle-dependent reflection spectra from NS1 at 10°, 15°, 30°, 45°, and 60°. The spectrum at 15° overlaps with that at 10°.

nanocones with a 230 nm period and a height of about 700 nm. The needle shape silicon columns was achieved by partially isotropic dry etching in a mixture of SF_6 and CHF_3 with the addition of a silicon oxide etch mask underneath the imprinted resist and resulted in a gradual variation in refractive index from air to the flat silicon surface, which was expected to suppress most reflection. Due to the slight dispersion of silicon, the reflectivity from the polished silicon sample (bold solid line) decreases monotonically from 49% to 33% as the wavelength increases from 400 to 1000 nm. NS1 demonstrates a strong reflection suppression effect over the whole spectral range. Notably, the average reflection over a spectral range of 400–1000 nm wavelength is only 1%, a result comparable to that of 16 μm silicon nanocones reported in Ref. 8 albeit for 700 nm nanocones. Although the SiN_x AR coating presents the minimum reflectivity of 0.5% around 600 nm, the reflection over the whole 600 nm wavelength band is much higher. The regular inverse pyramids patterned by KOH etching in Ref. 4 shows an AR effect but the residual reflection is about 10% for the long wavelength range (>700 nm). Most recently, very impressive results were demonstrated in random upright pyramids created by KOH etching with the Langmuir–Blodgett monolayer mask, where reflectivity at normal incidence was less than 2% in the wavelength range from 400 to 1200 nm.[5] Our structures fabricated by nanoimprint technique produce excellent results, which are comparable to these well developed techniques.

For further investigation, angle-dependent reflection was characterized and compared with that of polished silicon. The samples were mounted on an x-ray goniometer and illuminated with a near-collimated, broadband and unpolarized light source. The reflectivity at different incident angles was collected using an integrating sphere connected by an optical fiber to a spectrograph the output of which was detected by a Si-based charge coupled device detector. The aperture of the integrating sphere was approximately three times the size of the reflected beam, ensuring that the full reflected intensity was measured. The measured intensity was normalized to that from a polished silicon surface at the same angle to take account of the response of the optical system. The reflected light from a polished silicon sample was found to have almost the same intensity up to large angles (solid line in Fig. 5) in agreement with Ref. 8. So the reflection spectrum of a polished silicon sample at normal incidence was used to convert the reflected light intensities from the NSs to the absolute reflection spectra.

From Fig. 4, we can see that the absolute reflection from

Downloaded 14 Feb 2011 to 128.193.164.203. Redistribution subject to AIP license or copyright; see http://apl.aip.org/about/rights_and_permissions

SIONYX1403000030.0149

SAMSUNG EX. 1002 - 3019/4148

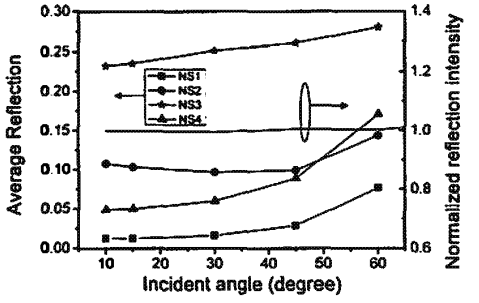


FIG. 5. Measured angle-dependent reflection averaged over the 400–1000 nm wavelength range from NS1, NS2, NS3, and NS4 at 10°, 15°, 30°, 45°, and 60°. The intensity of the reflected light from a bare silicon sample normalized to that at normal incidence is shown as a function of incident angle.

NS1 is less than 4% over the entire usable absorption range of crystalline silicon at the angle of incidence up to 45°. When the incident angle is larger than 45°, the average reflection increases rapidly with the incident angle because the average refractive index profile from air to silicon substrate changes too much from the case at normal incidence, but still less than 8% at 60° (Fig. 5). Such a low-cost process for fabricating high-aspect-ratio silicon nanocones has a considerable potential for the all color, sunrise-to-sunset AR coatings for solar cells.

Other types of moth-eye subwavelength structures were fabricated and characterized, such as silicon pyramids (NS2, 450 nm period and 300 nm height), silicon columns with concave sidewalls (NS3, 230 nm period and 300 nm height) and silicon nanocones (NS4, 230 nm period and 200 nm height). As shown in Fig. 5, an array of silicon pyramids (NS2) has an almost constant average reflection of about 10% for an angle of incidence up to 45°. Although the pyramidlike silicon tapers in NS2 reduce the abrupt refractive index variation at the interface between air and silicon, the small base of each pyramid causes a refractive index gap at the bottom of the pyramids which limits the reflection suppression. Nanocolumns with concave sidewalls (NS3) present a linear relation between the average reflection and the incident angles rather than the exponential one for the nanocones. As a result, the average reflection at an incident angle of 60° for NS3 is 20% greater than at normal incidence, compared to 670% greater for NS1. The quasi-angle-independent reflection for NS3 is due to the similar average refractive index distribution at most angles. A subwavelength structure with both features of NS1 and NS3 might demonstrate an ideal broadband and angle-independent AR effect. NS4 has a similar profile as NS1 and then shows a similar reflection behavior. The relatively larger reflection is caused by the smaller height and larger top of each cone. So a smoother variation in the refractive index from air to the substrate gives a smaller reflection.

In summary, subwavelength silicon moth-eye structures have been fabricated using a soft roller nanoimprint technique. The fabricated nanocone array was found to form a broadband antireflecting surface with an average reflection (400–1000 nm) less than 3% in the spectral range of 400–1000 nm for angles of incidence up to 45°. These coatings greatly increase the amount of sunlight available for conversion to electricity in solar cells and the low-cost and high-throughput technique itself is compatible with standard industrial manufacturing. Its practical application could be a step forward of silicon solar cell.

The authors wish to acknowledge support from the European Union under Framework 6 Contract No. 017481, STREP "N2T2."

[1]P. Doshi, G. E. Jellison, and A. Rohatgi, Appl. Opt. **36**, 7826 (1997).
[2]M.-L. Kuo, D. J. Poxson, Y. S. Kim, F. W. Mont, J. K. Kim, E. F. Schubert, and S.-Y. Lin, Opt. Lett. **33**, 2527 (2008).
[3]A. Parretta, A. Sarno, P. Tortora, H. Yakubu, P. Maddalena, J. Zhao, and A. Wang, Opt. Commun. **172**, 139 (1999).
[4]C.-H. Sun, W.-L. Min, N. C. Linn, and P. Jiang, Appl. Phys. Lett. **91**, 231105 (2007).
[5]J. Hao, N. Lu, H. Xu, W. Wang, L. Gao, and L. Chi, Chem. Mater. **21**, 1802 (2009).
[6]D. Macdonald, A. Cuevas, M. Kerr, C. Samundsett, D. Ruby, S. Winderbaum, and A. Leo, Sol. Energy **76**, 277 (2004).
[7]S. Koynov, M. S. Brandt, and M. Stutzmann, Appl. Phys. Lett. **88**, 203107 (2006).
[8]Y.-F. Huang, S. Chattopadhyay, Y.-J. Jen, C.-Y. Peng, T.-A. Liu, Y.-K. Hsu, C.-L. Pan, H.-C. Lo, C.-H. Hsu, Y.-H. Chang, C.-S. Lee, K.-H. Chen, and L.-C. Chen, Nat. Nanotechnol. **2**, 770 (2007).
[9]P. B. Clapham and M. C. Hutley, Nature (London) **244**, 281 (1973).
[10]C.-H. Sun, P. Jiang, and B. Jiang, Appl. Phys. Lett. **92**, 061112 (2008).
[11]S. A. Boden and D. M. Bagnall, Appl. Phys. Lett. **93**, 133108 (2008).
[12]G. Hubbard, S. J. Abbott, Q. Chen, D. Allsopp, W. N. Wang, C. R. Bowen, R. Stevens, A. Satka, D. Hasko, F. Uherek, and J. Kovac, Physica E (Amsterdam) **41**, 1118 (2009).

Downloaded 14 Feb 2011 to 128.193.164.203. Redistribution subject to AIP license or copyright; see http://apl.aip.org/about/rights_and_permissions

SIONYX1403000030.0150

SAMSUNG EX. 1002 - 3020/4148

Silicon nanocrystal-based photosensor on low-temperature polycrystalline-silicon panels

Wen-Jen Chiang,[a] Chih-Yang Chen, Chrong-Jung Lin, and Ya-Chin King
National Tsing Hua University, 101, Section 2, Kuang-Fu Road, Hsinchu 30013, Taiwan

An-Thung Cho, Chia-Tian Peng, Chih-Wei Chao, Kun-Chih Lin, and Feng-Yuan Gan
AU Optronics Corporation, No. 1, Li-Hsin Road 2, Hsinchu Science Park, Hsinchu 300, Taiwan

(Received 25 January 2007; accepted 9 July 2007; published online 2 August 2007)

A photodetector, comprising a layer of silicon nanocrystals that is sandwiched between two electrodes, is proposed and demonstrated in a photosensing application on low-temperature polysilicon panels. Laser annealing of silicon-rich oxide films can form nanocrystals that respond optimally to a certain absorption spectrum of a light source. These silicon nanocrystals are smaller than 10 nm in diameter, which size determines the effectiveness of their quantum confinement, and promote electron-hole pair generation in the photosensing region because of their direct band gap. Besides obtaining a photosensitivity that is comparable to that of a *p-i-n* diode, which is currently used in low-temperature polysilicon technology, the sensor maximizes the photosensing area of a pixel by its stacked structure. © *2007 American Institute of Physics*. [DOI: 10.1063/1.2767241]

Large amorphous silicon (*a*-Si:H)-based pixel-array sensors that are used in document scanning and low-bit gray imaging have been developed using thin-film transistor technologies.[1,2] In recent years, low-temperature polysilicon (LTPS) has replaced amorphous silicon as the main material for making small panels because of its high mobility, which allows for high-frequency and high-resolution display applications. A *p-i-n*-type photodiode is the most commonly used photodetector in complementary-metal-oxide-semiconductor (CMOS) and *a*-Si:H technologies.[3] Two critical problems are associated with *p-i-n* diodes that are based on LTPS technology. First, the limited substrate thickness, typically around 50 nm, makes their photon absorption efficiency lower than that of photodiodes that are based on conventional CMOS technology.[4] Second, since no effective shielding layer is available in the LTPS process, the output signal is affected by strong backlight illumination, potentially leading to a serious ambient light detection problem. The fill factor (the ratio between photosensing area and total pixel area) of a sensor pixel is another important performance parameter, which is 30%–50% for pixels associated with *p-i-n* photodiodes in general. It greatly influences the actual photon-collecting area as the pixel size is reduced for high-resolution applications.

Silicon nanocrystals have long been developed to store charge in nonvolatile memory devices[5] and light-emitting devices[6–8] and for use in semiconductor lasers.[9] A nanocrystal structure is only effective when the size of the nanocrystal is less than the Bohr radius, such that the quantum confinement effect dominates the original material characteristics. The efficiency of semiconductor lasers is greatly increased because electrons and holes can recombine and release photons in a manner that is similar to that associated with a direct band gap material in small quantum well structures.[10] In this study, a nanocrystal structure is designed as the light absorption layer in a photodetector rather than a light-emitting device.

[a]Electronic mail: wrchiang@well.ee.nthu.edu.tw

The proposed silicon nanocrystal photodetector is stacked above the pixel circuits, which may contain three to five thin-film transistors, as presented in Fig. 1(a). The nanocrystals are formed by the laser annealing of a silicon-rich oxide layer, as shown in Fig. 1(b). The transparent top electrode [indium thin oxide (ITO) layer available in LTPS process] allows ambient light to penetrate and reach the photosensing region. Since the pixel circuits can be placed underneath the photodetector, the fill factor of the silicon nanocrystals pixel can be maximized. Additionally, the metal bottom electrode effectively shields the pixel circuitry, such that the circuit characteristics become more stable. In contrast, the sensor pixel associated with a traditional *p-i-n* pho-

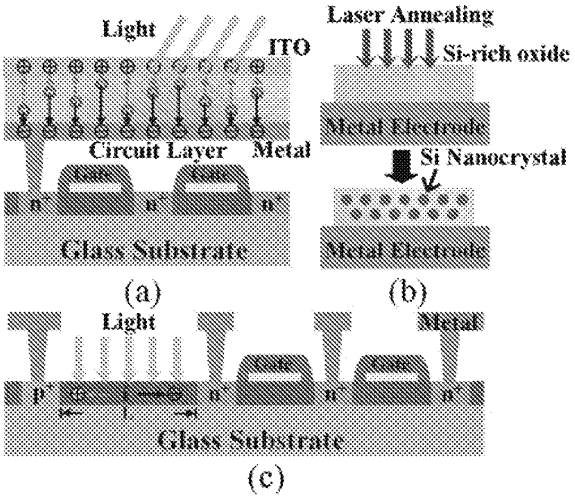


FIG. 1. (Color online) (a) Cross-sectional view of the proposed silicon nanocrystal photosensor; the photosensing area is stacked above the pixel circuits. Electron-hole pairs are generated in the nanocrystal layer by photoexcitation. (b) Silicon nanocrystals are formed by laser annealing of silicon-rich oxide film deposited with PECVD on top of the metal layer. (c) Traditional *p-i-n* photodiode in LTPS technology fabricated by chemical vapor deposition of *a*-Si films, excimer laser crystallization of LTPS, and ion implantation of n^+ and p^+ dopants.

 © 2007 American Institute of Physics

Downloaded 17 Jan 2012 to 140.116.195.188. Redistribution subject to AIP license or copyright; see http://apl.aip.org/about/rights_and_permissions

SIONYX1403000030.0151

SAMSUNG EX. 1002 - 3021/4148

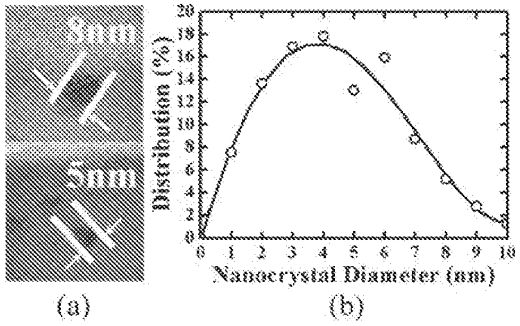


FIG. 2. (a) TEM images of silicon nanocrystals with 5 and 8 nm in diameter, respectively. (b) Distribution of crystal size in the sample with refractive index of 1.8.

todiode, displayed in Fig. 1(c), fabricated using LTPS technology, with the chemical vapor deposition (CVD) of amorphous silicon films, and excimer laser crystallization (ELC) to form polysilicon and implant n^+ and p^+ dopant ions, has a smaller fill factor and suffers from ambient light and backlight noise. Laser annealing of a silicon-rich oxide layer, deposited by plasma-enhanced CVD (PECVD), is performed to produce a layer of silicon nanocrystals on top of a metal electrode. In the silicon-rich oxide film deposition process, the ratio of SiH_4 to N_2O gases is adjusted to obtain a refractive index of this film in the desirable range. This ratio indicates the silicon content in such films.[11] Proper laser annealing of a XeCl laser beam with a width of 0.4 mm, a length of 300 mm, a wavelength of 308 nm, a pulse width of 30 ns, a repetition rate of 300 Hz, and 20 pulses segregates, clusters, and turns the silicon atoms into silicon nanocrystals. Accordingly, the size and density of the nanocrystals can be controlled by the thickness and silicon content of the deposited film as well as the laser annealing power. The transmission electron microscopic (TEM) images in Fig. 2(a) reveal that nanocrystals with diameters from 4 to 10 nm had been fabricated on a glass substrate. Figure 2(b) plots the size distribution of these nanocrystals with a peak population of around 5 nm, obtained on samples whose refractive index equals 1.8 and whose thickness is 100 nm. Figure 3 shows the normalized photocurrents (A/m^2) of these 1.8 refractive index samples for various thicknesses under a light intensity of 35 $\mu W/cm^2$ and a bias voltage of 2.5 V between the top ITO and bottom metal electrodes. Monochromatic visible

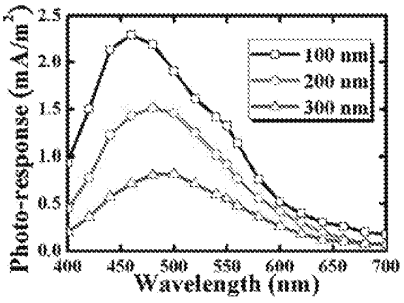


FIG. 3. (Color online) Light absorption spectrum of samples with silicon nanocrystal layers of 100, 200, and 300 nm monochromatically illuminated by a constant optical power of 35 $\mu W/cm^2$ and a bias voltage of 2.5 V. The wavelength that corresponds to the peak photocurrent intensity shifts to green light as the sample thickness changes from 100 to 300 nm.

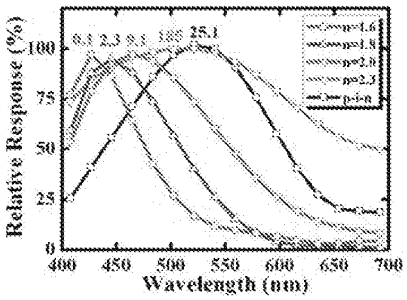


FIG. 4. (Color online) Light absorption spectrum of silicon nanocrystal devices with n=1.6, 1.8, 2.0, and 2.3, and that of a p-i-n device monochromatically illuminated by a constant optical power of 35 $\mu W/cm^2$ and a bias voltage of 2.5 V. The peak response of n=1.6 is 0.1 mA/m^2 at a wavelength of 430 nm, and that of n=1.8 is 2.31 mA/m^2 at 450 nm. The peak responses of n=2.0 and n=2.3 are 9.12 mA/m^2 at 470 nm and 185 mA/m^2 at 510 nm, respectively. The peak value of the p-i-n diode is 25.1 mA/m^2 at a wavelength of 525 nm.

light with wavelengths from 400 to 700 nm, supplied by a halogen lamp with a monochromator, is led into an integration sphere through an optical fiber to provide a stable light source. The incident optical power is fixed at 35 $\mu W/cm^2$ for every single-wavelength measurement. The measurements suggest that the wavelength that corresponds to the peak photocurrent intensity shifts to green as the sample thickness changes from 100 to 300 nm. The quantum microcavity equation[12,13] yields an estimation of peak nanocrystal size of approximately 1.8 nm for the sample with a peak wavelength of 450 nm, suggesting that the effective optical band gap is more affected by interfacial effects than the quantum confinement effect. The interface states and deficiencies, such as neutral oxygen vacancies,[14] substantially increase the corresponding effective optical band gap and may be the main mechanism of the light absorption sensors in the silicon nanocrystals that are formed on a glass panel.

Samples made with a silicon-rich oxide film with various refractive indices and laser annealing powers are prepared to find the optimal conditions and make photosensors with the most favorable features. Since the electrical fields in the silicon-rich oxide layer are higher, 100-nm-thick samples are selected for electrical characterization and performance comparisons with a lateral p-i-n photodiode whose intrinsic region is 100 μm/20 μm wide/long and 50 nm thick. Figure 4 compares the normalized photoresponses (A/m^2) of nanocrystal detectors with refractive indices of 1.6, 1.8, 2.0, and 2.3 with that of a p-i-n diode over the entire visible light spectrum with a constant intensity of 35 $\mu W/cm^2$ and a bias voltage of 2.5 V. The photoresponses are scaled to the same peak value of unity and presented as relative responses to identify clearly the shift of the wavelength of the peak response with the change in the silicon content and compare it with that of the p-i-n diode. The peak response of the sample with n=1.6 is 0.1 mA/m^2 at a wavelength of 430 nm, and that of the sample with n=1.8 is 2.31 mA/m^2 at 450 nm. The peak responses of the samples with n=2.0 and n=2.3 are 9.12 mA/m^2 at 470 nm and 185 mA/m^2 at 510 nm, respectively, while the peak value of the p-i-n diode is 25.1 mA/m^2 at a wavelength of 525 nm. The peak absorption wavelength of the nanocrystal detectors lies between 430 and 510 nm while the absorption spectrum of a p-i-n diode peaks at about 525 nm, indicating that the photosens-

Downloaded 17 Jan 2012 to 140.114.185.188. Redistribution subject to AIP license or copyright; see http://apl.aip.org/about/rights_and_permissions

SIONYX1403000031.0001

SAMSUNG EX. 1002 - 3022/4148

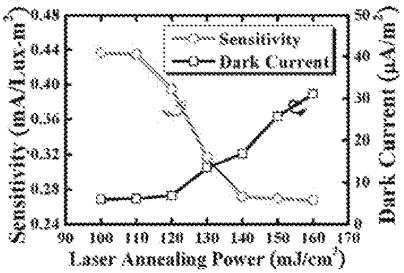


FIG. 5. (Color online) Dark current and sensitivity of nanocrystal sensors underwent different laser annealing energies. The refractive index of silicon-rich oxide film is 1.8 with a thickness of 100 nm. The samples are illuminated by a full spectrum visible light with a 2.5 V bias voltage.

ing mechanisms differ among these samples. The samples with a refractive index between 2.0 and 2.3 can provide a quantum efficiency that is comparable to that of *p-i-n* diodes with a peak wavelength in the range from 470 to 510 nm. Samples with a higher refractive index have higher density of silicon nanocrystals and a correspondingly broader photoresponse spectrum that is closer to that of a polycrystalline silicon film in a *p-i-n* diode. However, samples with a lower density of silicon nanocrystals exhibit a narrower range of absorption bandwidths from only 430–470 nm. Therefore, the absorption characteristics of nanocrystals dominate in samples of lower density with smaller nanocrystals. Figure 5 presents the sensitivity and dark current of nanocrystal detectors that are fabricated using various laser annealing powers and are illuminated by a full spectrum of visible light from 0 to 600 luxes with a 2.5 V bias voltage. The laser annealing power significantly affects the optical sensitivity and dark current of the nanocrystal detectors. The particle lattice and distribution of the nanocrystals are altered as the laser annealing energy is increased,[15] which degrades both the sensitivity and the dark current performances. The experimental results demonstrate that a lower laser annealing power (under 110 mJ/cm^2), promoting the formation of silicon nanocrystals, gives rise to a great photosensor with high sensitivity and low dark current. Further optimization of nanocrystal size, density, and annealing power is expected to enhance the overall performance of sensors in the future.

The silicon nanocrystal photosensor that is developed herein is well demonstrated on a glass substrate by the laser annealing of a silicon-rich oxide film that was deposited using PECVD. Its optical-electrical characteristics are elucidated with comparable sensitivity and a similar dark current level to those associated with the traditional *p-i-n* diodes that are used in LTPS technology. The experimental results indicate that the silicon nanocrystal photosensor can be a profitable, flexible, and functional component of applications on liquid crystal display panel-embedded sensors with the advantages of a large photosensing area, a complete backlight shielding, and a tunable absorption spectrum.

The authors are grateful to the members of the AU Optronics process line for the fabrication of silicon nanocrystal devices. The authors also thank the National Science Council of Taiwan for supporting this research.

[1]G. Yu, G. Srdanov, J. Wang, H. Wang, Y. Cao, and A. J. Heeger, Synth. Met. **111-112**, 133 (2000).
[2]F. Lemmi, M. Mulato, J. Ho, R. Lau, J. P. Lu, and R. A. Street, Appl. Phys. Lett. **78**, 1334 (2001).
[3]C. Xu, C. Shen, W. Wu, and M. Chan, IEEE Trans. Electron Devices **52**, 1110 (2005).
[4]K. Rajkanan, R. Singh, and J. Shewchun, Solid-State Electron. **22**, 793 (1979).
[5]R. Muralidhar, R. F. Steimle, M. Sadd, R. Rao, C. T. Swift, E. J. Prinz, J. Yater, L. Grieve, K. Harber, B. Hradsky, S. Straub, B. Acred, W. Paulson, W. Chen, L. Parker, S. G. H. Anderson, M. Rossow, T. Merchant, M. Paransky, T. Huynh, D. Hadad, K. M. Chang, and B. E. White, Jr., Integrated Circuit Design and Technology, ICICDT '04, International Conference, 2004, pp. 31–35.
[6]T. R. Hebner, C. C. Wu, D. Marcy, M. H. Lu, and J. C. Sturm, Appl. Phys. Lett. **72**, 519 (1998).
[7]P. M. Fauchet, IEEE J. Quantum Electron. **4**, 1020 (1998).
[8]G. Y. Sung, N.-M. Park, T.-Y. Kim, K.-H. Kim, K. S. Cho, and J. H. Shin, Group IV Photonics, 2nd IEEE International Conference , September 21–23, 2005, pp. 51–53.
[9]J. Heitmann, L. Yi, R. Scholz, and M. Zacharias, Quantum Electronics and Laser Science Conference, QELS '02, Technical Digest, 2002, pp. 249–250.
[10]J. Linnros and N. Lalic, Appl. Phys. Lett. **66**, 3048 (1995).
[11]S. J. Shen, C. J. Lin, and C. H. Hsu, Tech. Dig. - Int. Electron Devices Meet. **515** 1996.
[12]T. van Buuren, L. N. Dinh, L. L. Chase, W. J. Siekhaus, and L. J. Terminello, Phys. Rev. Lett. **80**, 3803 (1998).
[13]S. Schuppler, S. L. Friedman, M. A. Marcus, D. L. Adler, Y. H. Xie, F. M. Ross, T. D. Harris, W. L. Brown, Y. J. Chabal, L. E. Brus, and P. H. Citrin, Phys. Rev. Lett. **72**, 2648 (1994).
[14]Y. W. Wang, C. H. Liang, G. W. Meng, X. S. Peng, and L. D. Zhang, J. Mater. Chem. **12**, 651 (2002).
[15]H. Jung, S. D. Cha, J. H. Song, and M. K. Han, Appl. Phys. Lett. **84**, 1287 (2004).

Downloaded 17 Jan 2012 to 140.116.195.188. Redistribution subject to AIP license or copyright; see http://apl.aip.org/about/rights_and_permissions

SIONYX1403000031.0002

SAMSUNG EX. 1002 - 3023/4148

Appl. Phys. A 63, 109–115 (1996)

Applied Physics A Materials Science & Processing

© Springer-Verlag 1996

Femtosecond, picosecond and nanosecond laser ablation of solids

B.N. Chichkov, C. Momma, S. Nolte, F. von Alvensleben, A. Tünnermann

Laser Zentrum Hannover e.V., Hollerithallee 8, D-30419 Hannover, Germany
(Fax: +49-511/2788-100)

Received: 23 February 1996/Accepted: 27 February 1996

Abstract. Laser ablation of solid targets by 0.2–5000 ps Ti:Sapphire laser pulses is studied. Theoretical models and qualitative explanations of experimental results are presented. Advantages of femtosecond lasers for precise material processing are discussed and demonstrated.

PACS: 81.15

Efficient use of lasers for precise material processing is impossible without a thorough knowledge of the fundamental laws governing the interaction of laser radiation with matter. For this goal systematic studies of the laser-matter interaction are necessary. Due to the recent progress of laser systems, especially those based on the chirped pulse amplification (CPA) technique, such systematic studies have become possible in a very broad range of laser parameters. With CPA systems the laser pulse duration can be varied from about one hundred femtoseconds to several nanoseconds leaving other laser parameters unchanged. This allows to perform a very detailed analysis of different nonstationary laser-matter interaction processes. As an example, recent investigations of the damage threshold [1], of the ablation threshold [2], and of the high-intensity laser ablation [3] can be mentioned. Note that such systematic studies have just begun, much more should be done for the understanding and demonstration of the potential of femtosecond laser systems for precise material processing.

Recently several experiments [4–6] comparing laser ablation of solid targets by femtosecond and nanosecond pulses have been performed. In [4] and [5, 6] advantages of femtosecond lasers for precise material processing with dye and excimer laser systems have been demonstrated. In this paper, we present our results on ablation and hole drilling with a commercial, 10 Hz, femtosecond Ti:Sapphire laser system which provides laser pulses at 780 nm with a pulse energy of up to 100 mJ and a variable pulse duration in the range of 0.2 to 5000 ps. Experiments are performed in a low fluence regime, slightly above the evaporation threshold. This regime is most interesting for precise material processing, since in this case the energy deposited into the solid and the heat-affected zones are minimized. We discuss and demonstrate advantages of the femtosecond-pulse lasers. We hope that our results can stimulate new investigations in this field. In Sect. 1, characteristic features of the low fluence laser ablation of metal targets in three different pulse duration regimes: femtosecond, picosecond and nanosecond are considered. The experimental setup and results are presented in Sect. 2.

1 Theoretical background

During the interaction of low intensity short laser pulses with metal targets the laser energy is absorbed by free electrons, due to the inverse Bremsstrahlung. Then the evolution of the absorbed laser energy involves thermalization within the electron subsystem, energy transfer to the lattice, and energy losses due to the electron heat transport into the target. If we assume that the thermalization within the electron subsystem is very fast and that the electron and the lattice subsystems can be characterized by their temperatures (T_e and T_i), the energy transport into the metal can be described by the following one-dimensional, two-temperature diffusion model [7, 8]:

$$C_e \frac{\partial T_e}{\partial t} = -\frac{\partial Q(z)}{\partial z} - \gamma(T_e - T_i) + S, \tag{1}$$

$$C_i \frac{\partial T_i}{\partial t} = \gamma(T_e - T_i), \tag{2}$$

$$Q(z) = -k_e \partial T_e/\partial z, \quad S = I(t)\, A\alpha \exp(-\alpha z). \tag{3}$$

Here z is the direction perpendicular to the target surface, $Q(z)$ is the heat flux, S is the laser heating source term, $I(t)$ is the laser intensity, $A = 1 - R$ and α are the surface transmissivity and the material absorption coefficient, C_e and C_i are the heat capacities (per unit volume) of the electron and lattice subsystems, γ is the parameter characterizing the electron-lattice coupling, k_e is the electron

SIONYX1403000031.0003

SAMSUNG EX. 1002 - 3024/4148

thermal conductivity. In the above equations a thermal conductivity in the lattice subsystem (phonon component) is neglected. The electronic heat capacity is much less than the lattice heat capacity, therefore electrons can be heated to very high transient temperatures. When the electron temperature (in units of energy) remains smaller than the Fermi energy, the electron heat capacity and the nonequilibrium electron thermal conductivity are given by $C_e = C'_e T_e$ (where C'_e is a constant) and $k_e = k_0(T_i) \cdot T_e/T_i$ (where $k_0(T_i)$ is the conventional equilibrium thermal conductivity of a metal) [9–11]. Expressions for the coupling constant γ are given in [7, 12] and results of recent measurements in [11, 13, 14].

Equations (1–3) have three characteristic time scales τ_e, τ_i and τ_L, where $\tau_e = C_e/\gamma$ is the electron cooling time, $\tau_i = C_i/\gamma$ is the lattice heating time ($\tau_e \ll \tau_i$) and τ_L is the duration of the laser pulse. These parameters define three different regimes of the laser-metal interaction which we call femtosecond, picosecond and nanosecond regimes.

Femtosecond pulses

First we consider the case when the laser pulse duration is shorter than the electron cooling time, $\tau_L \ll \tau_e$. For $t \ll \tau_e$, which is equivalent to $C_e T_e/t \gg \gamma T_e$, the electron-lattice coupling can be neglected. In this case (1) can be easily solved. Since the general solution of this equation is quite complicated, we neglect the electron heat conduction term in our formulas. This can be done when the following condition is fulfilled $D_e \tau_L < \alpha^{-2}$, where $D_e = k_e/C_e$ is the electron thermal diffusivity. In this case (1) reduces to

$$C'_e \partial T_e^2/\partial t = 2 I_a \alpha \exp(-\alpha z) \tag{4}$$

and gives

$$T_e(t) = \left(T_0^2 + \frac{2 I_a \alpha}{C'_e} t \exp(-\alpha z) \right)^{1/2}. \tag{5}$$

Here $I(t) = I_0$ is assumed constant, $I_a = I_0 A$, and $T_0 = T_e(0)$ is the initial temperature. At the end of the laser pulse the electron temperature is given by

$$T_e(\tau_L) \simeq \left(\frac{2 F_a \alpha}{C'_e} \right)^{1/2} \exp(-z/\delta), \tag{6}$$

where $T_e(\tau_L) \gg T_0$ is assumed, $F_a = I_a \tau_L$ is the absorbed laser fluence, and $\delta = 2/\alpha$ is the skin depth.

The evolution of the electron and lattice temperatures after the laser pulse is described by (1–3) with $S = 0$. Initial conditions for the electron and lattice temperatures are given by (6) and $T_i = T_0$. After the laser pulse the electrons are rapidly cooled due to the energy transfer to the lattice and heat conduction into the bulk. Since this electron cooling time is very short, (2) can be written as $T_i \simeq T_e(\tau_L)\ t/\tau_i$ (here the initial lattice temperature is neglected). The attainable lattice temperature is determined by the average cooling time of the electrons $\tau_e^a = C'_e T_e(\tau_L)/2\gamma$ and is given by

$$T_i \simeq T_e^2(\tau_L) \frac{C'_e}{2 C_i} \simeq \frac{F_a \alpha}{C_i} \exp(-\alpha z). \tag{7}$$

Note that the problem of the hot electron relaxation dynamics in metals after the excitation by a femtosecond laser pulse has been intensively studied during the last years [14–16]. It has been shown that the time scale for the fast electron cooling and a considerable energy transfer to the lattice is of the order of 1 ps.

The significant evaporation occurs when $C_i T_i$ becomes larger than $\rho\Omega$, where ρ is the density and Ω is the specific (per unit mass) heat of evaporation. Using (7), we can write the condition for strong evaporation in the form

$$F_a \geq F_{th} \exp(\alpha z), \tag{8}$$

where $F_{th} \simeq \rho\Omega/\alpha$ is the threshold laser fluence for evaporation with femtosecond pulses. Then the ablation depth per pulse L is

$$L \simeq \alpha^{-1} \ln(F_a/F_{th}). \tag{9}$$

The logarithmic dependence of the ablation depth on the laser pulse fluence is well known for the laser ablation of organic polymers. Recently the logarithmic dependence of the ablation depth per pulse has been demonstrated for metal targets with femtosecond KrF-laser pulses [5].

Due to the very short time scales involved in the ablation with femtosecond laser pulses the ablation process can be considered as a direct solid-vapor (or solid-plasma) transition. In this case the lattice is heated on a picosecond time scale which results in the creation of vapor and plasma phases followed by a rapid expansion in vacuum. During all these processes thermal conduction into the target can be neglected in a first approximation. These advantages of femtosecond laser pulses allow very precise and pure laser-processing of metals (and other solids) which is experimentally demonstrated below.

Picosecond pulses

Now we turn to the discussion of ablation with picosecond laser pulses when the following condition is fulfilled $\tau_e \ll \tau_L \ll \tau_i$.

At a time $t \gg \tau_e$ which is equivalent to $C_e T_e/t \ll \gamma T_e$, (1) for the electron temperature becomes quasistationary, and (1–3) reduce to

$$\partial/\partial z (k_e \partial T_e/\partial z) - \gamma(T_e - T_i) + I_a \alpha \exp(-\alpha z) = 0, \tag{10}$$

$$T_i = \frac{1}{\tau_i} \int_0^t \exp\left(-\frac{t-\theta}{\tau_i} \right) T_e(\theta)\, d\theta + T_0. \tag{11}$$

Here (2) for the lattice temperature is written in the integral form. These equations describe heating of metal targets by the laser pulses with $\tau_L \gg \tau_e$. When the condition $t \ll \tau_i$ is fulfilled, (11) can be simplified due to the quasistationary character of the electron temperature. Neglecting T_0, we get

$$T_i \simeq T_e(1 - \exp(-t/\tau_i)) \simeq (t/\tau_i) T_e. \tag{12}$$

As can be seen from this expression, in the picosecond regime the lattice temperature remains much less than the

SIONYX1403000031.0004

SAMSUNG EX. 1002 - 3025/4148

electron temperature. This allows to neglect the lattice temperature in (10). The analysis of (10, 12) is especially simple when the condition $k_e T_e \alpha^2 \ll \gamma T_e$ is fulfilled. In this case the electron cooling is due to the energy exchange with the lattice. The electron temperature and the lattice temperature at the end of the laser pulse are given by

$$T_e \simeq \frac{I_a \alpha}{\gamma} \exp(-\alpha z), \quad T_i \simeq \frac{F_a \alpha}{C_i} \exp(-\alpha z). \tag{13}$$

Note that the attainable lattice temperature after the laser pulse is again determined by the electron cooling time. Since $\tau_e \ll \tau_L$, the attainable lattice temperature and the lattice temperature at the end of the laser pulse are approximately equal. In femtosecond and picosecond regimes (7) and (13) give the same expressions for the lattice temperature. Therefore, the condition for strong evaporation given by (8), the fluence threshold and the ablation depth per pulse given by (9) remain unchanged.

Thus, the logarithmic dependence of the ablation depth on the laser pulse fluence is also possible in the picosecond range. In our derivations we have neglected the electron heat conduction into the target. This is a very crude assumption for the description of laser ablation of metal targets in the picosecond regime. Laser ablation in this case is accompanied by the electron heat conduction and formation of a melted zone inside the target. In spite that at the surface we can again consider evaporation as a direct solid-vapor (or solid-plasma) transition, the presence of the liquid phase inside the target reduces the precision of laser processing of metals in this regime (see below).

Nanosecond pulses

Here we briefly discuss ablation with nanosecond laser pulses when the condition $\tau_L \gg \tau_i$ is fulfilled. In this case the electron and lattice temperatures are equal $T_e = T_i = T$, and (1–3) reduce to

$$C_i \partial T/\partial t = \partial/\partial z (k_0 \partial T/\partial z) + I_a \alpha \exp(-\alpha z). \tag{14}$$

Laser heating of metal targets by long laser pulses has been a subject of many experimental and theoretical studies [17–20]. In this regime the absorbed laser energy first heats the target surface to the melting point and then to the vaporization temperature. Note that metals need much more energy to vaporize than to melt. During the interaction the main source of energy losses is the heat conduction into the solid target. The heat penetration depth is given by $l \sim (Dt)^{1/2}$, where D is the heat diffusion coefficient, $D = k_0/C_i$. Note that for long-pulse laser ablation of metal targets the condition $D\tau_L \alpha^2 \gg 1$ is usually fulfilled. The energy deposited inside the target per unit mass is given by $E_m \sim I_a t/\rho l$. When at a certain moment $t = t_{th}$ this energy becomes larger than the specific heat of evaporation Ω, significant evaporation occurs. From the condition $E_m \sim \Omega$ we get $t_{th} \sim D(\Omega\rho/I)^2$ (see [17]). Thus, the condition for strong evaporation, $E_m > \Omega$ (or $\tau_L > t_{th}$), can be written as

$$I > I_{th} \sim \frac{\rho \Omega D^{1/2}}{\tau_L^{1/2}}, \quad F > F_{th} \sim \rho \Omega D^{1/2} \times \tau_L^{1/2} \tag{15}$$

for laser intensity and fluence, respectively. The threshold laser fluence which is necessary for evaporation with long laser pulses grows as $\tau_L^{1/2}$.

In case of ablation with long laser pulses there is enough time for the thermal wave to propagate into the target and to create a relatively large layer of melted material. In this case the evaporation occurs from the liquid metal, which makes precise material processing of metal targets in vacuum with nanosecond pulses very complicated.

2 Experimental setup and results

Now we turn to the discussion of experimental results on a low fluence laser ablation of metals and other solids. In our experiments a commercial femtosecond Ti:Sapphire laser system (BMI Alpha 10A) based on the chirped-pulse amplification (CPA) technique [21] is used. A detailed description of the principal setup is given in [22]. This system provides laser pulses at 780 nm with a variable pulse energy of up to 100 mJ. Due to the CPA technique the pulse duration can be varied from 200 fs up to 400 ps. In this pulse duration range the spectral pulse width remains constant (approximately 8 nm). Pulse duration measurements for pulses shorter than 10 ps are performed by a background free second order autocorrelator and for pulses longer than 10 ps by a picosecond streak camera (Hadland, IMACON 500). Pulse widths of 3–5 ns are obtained when the regenerative amplifier (see [22]) is not seeded by the femtosecond oscillator (Coherent, Mira Basic). In this case the regenerative amplifier operates as an oscillator, and the spectral width of the generated pulses is significantly reduced. The time durations of the nanosecond pulses have been measured by a photodiode in combination with a fast sampling oscillograph and by the streak camera.

Our experiments are performed in the low fluence regime ($F = 0.1$–$5\ \mathrm{J/cm^2}$) with an imaging geometry. An aperture ($d = 5$ mm), mounted in the beam pass, is imaged (with demagnification factor of $\simeq 1/30$) onto the target surface by a $f = 140$ mm suprasil lense. The laser beam diameter is approximately 20 mm. As target materials steel, copper, AlN and silicon plates are used. These plates are attached to a computer controlled x,y,z-translation stage which is mounted in a vacuum cell at a pressure below 10^{-4} mbar. The number of pulses which are necessary to drill through the target plate is controlled by a photodiode mounted behind the targets.

First we present our results on the laser processing of metal targets. We compare holes drilled in 100 μm thick steel foils (in vacuum) with 10^4 laser pulses in three different regimes: femtosecond, picosecond and nanosecond. In Fig. 1 schematic of femtosecond-pulse laser ablation and the hole drilled with 200 fs, 120 μJ, $F = 0.5\ \mathrm{J/cm^2}$ laser pulses are shown. As can be seen, there is no trace of the molten material. Only a vapor dust ring around the hole.

SIONYX1403000031.0005

SAMSUNG EX. 1002 - 3026/4148

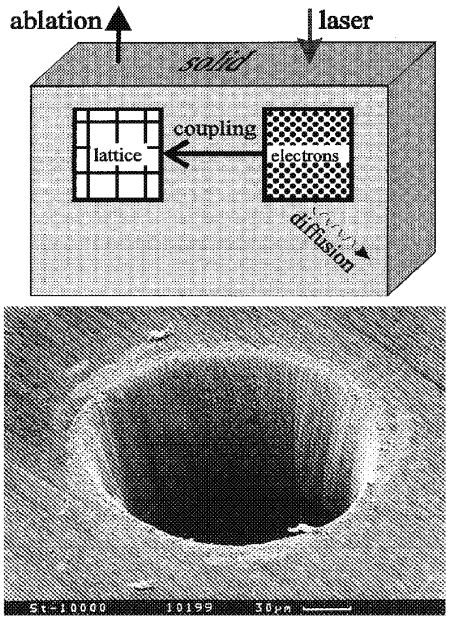


Fig. 1. Schematic of femtosecond-pulse laser ablation and a SEM photograph of a hole drilled in a 100 μm thick steel foil with 200 fs, 120 μJ, $F = 0.5$ J/cm^2 laser pulses at 780 nm

In Fig. 2 schematic of nanosecond-pulse laser ablation and the holes drilled with (a) 80 ps, 900 μJ, $F = 3.7$ J/cm^2; and (b) 3.3 ns, 1 mJ, and $F = 4.2$ J/cm^2 laser pulses are shown. The trace of the molten material can be seen in these figures. The presence of liquid phase leads to an unstable drilling process (see Fig. 2a). In case of ablation with nanosecond pulses there is enough time for the thermal wave to propagate into the metal target and to create a relatively large molten layer. In this case the target material is removed both in vapor and liquid phases, since the vaporization process creates a recoil pressure that expels the liquid. In Fig. 2b a "corona" created due to the recoil vapor pressure is clearly seen. Note that these are the best results which we obtain with 80 ps and 3.3 ns laser pulses at fluences as low as possible. When the laser fluence is reduced further the drilling through the 100 μm steel plate in vacuum becomes impossible.

Comparing Fig. 1 and Fig. 2, the advantages of femtosecond-pulse lasers for precise material processing become evident. Moreover, due to the absence of thermal losses in the femtosecond regime, holes in metal targets can be drilled with much lower laser fluences.

Below we present additional illustrative information on femtosecond-pulse laser ablation of different targets with the second harmonic of Ti:Sapphire laser radiation ($\lambda = 390$). The second harmonic is used to minimize diffraction effects and to improve the quality of image projection. In Fig. 3 the development of the ablation process with the increasing number of 250 fs, 0.5 mJ, and $F = 2.5$ J/cm^2 laser pulses a) 10, b) 100, c) 10^3 and d) 5×10^3 is shown. The target is a 0.5 mm steel plate. In Fig. 3c the creation of characteristic structures is clearly seen. These structures appear due to the instability of a plane evaporation front [23].

In Fig. 4 the evolution of femtosecond-pulse laser ablation of a 1 mm thick copper target is shown with: a) 10, b) 100, c) 10^3, and d) 3×10^4 pulses. In Fig. 5

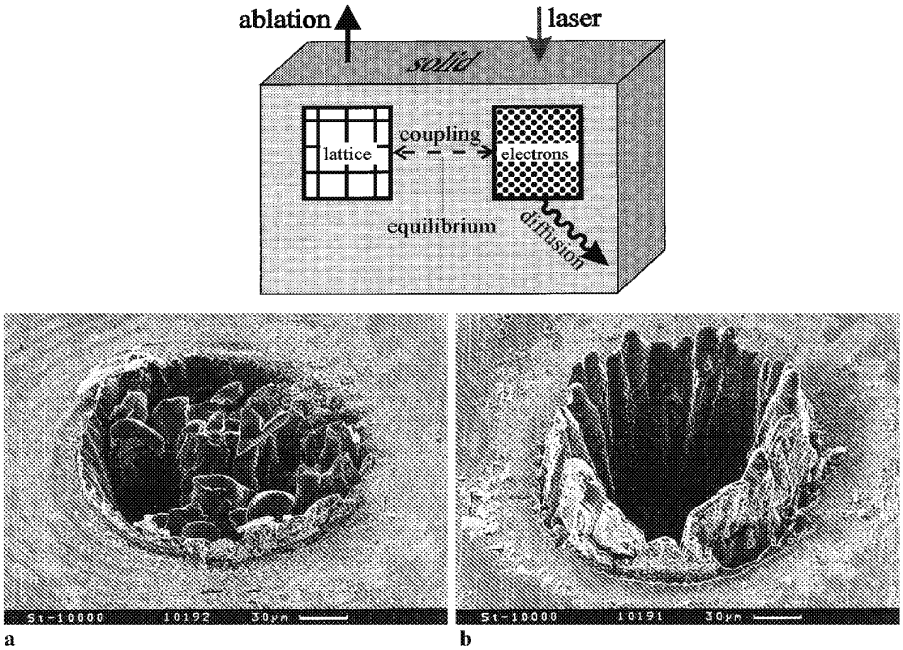


Fig. 2a, b. Schematic of nanosecond-pulse laser ablation and holes drilled in a 100 μm thick steel foil with (**a**) 80 ps, 900 μJ, $F = 3.7$ J/cm^2; and (**b**) 3.3 ns, 1 mJ, and $F = 4.2$ J/cm^2 laser pulses at 780 nm

SIONYX1403000031.0006

SAMSUNG EX. 1002 - 3027/4148

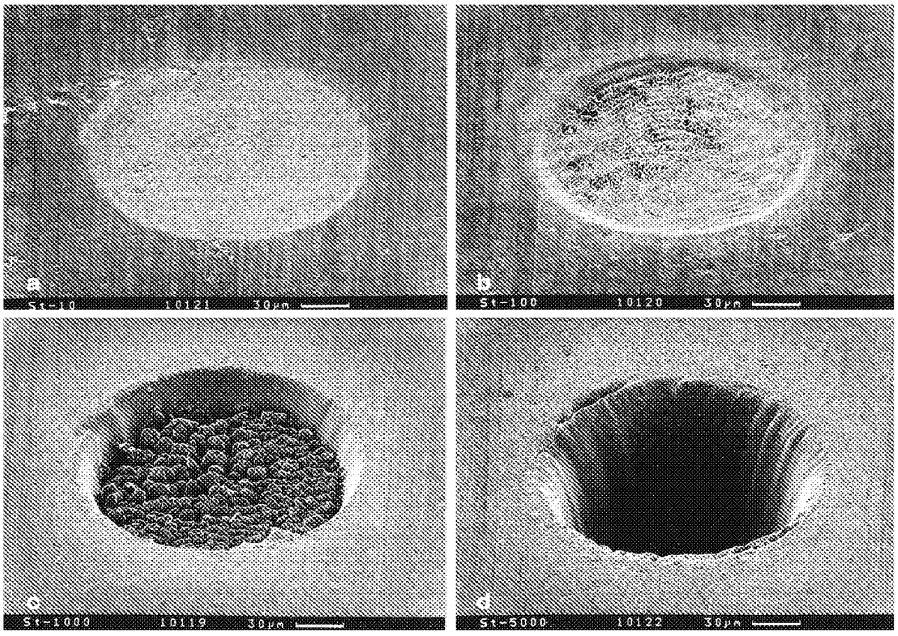


Fig. 3a–d. Femtosecond-pulse laser processing of a 0.5 mm steel plate with 250 fs, 0.5 mJ, and $F = 2.5\ \mathrm{J/cm^2}$ second harmonic radiation ($\lambda = 390$ nm) and different number of pulses: **(a)** 10, **(b)** 100, **(c)** 1000 and **(d)** 5000 laser pulses

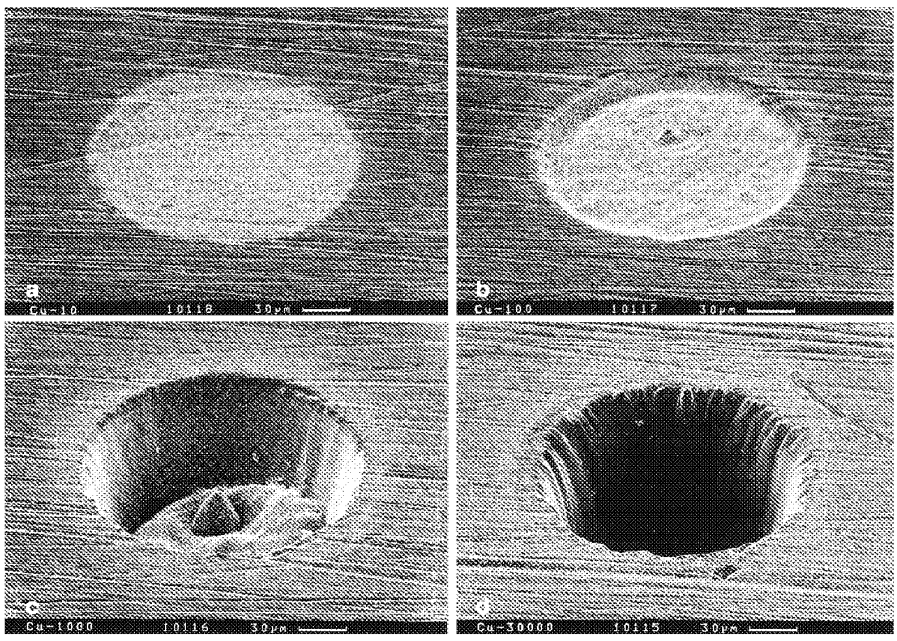


Fig. 4a–d. Evolution of femtosecond-pulse laser ablation of a 1 mm thick copper target with: **(a)** 10, **(b)** 100, **(c)** 10^3, and **(d)** 3×10^4 pulses. Laser parameters are the same as in Fig. 3

results of laser ablation of a 0.3 mm thick silicon target are demonstrated with: a) 10, b) 100, c) 5×10^3, and d) 10^4 pulses. Redeposition of the ablated material on the target surface is much stronger than in the case of metal targets. In Fig. 6 the ablation of a 0.8 mm AlN target with: a) 10, b) 10^3, and c) 3.5×10^4 laser pulses is illustrated. The laser parameters in Figs. 4, 5 and 6 are approximately the same as in Fig. 3.

SIONYX1403000031.0007

SAMSUNG EX. 1002 - 3028/4148

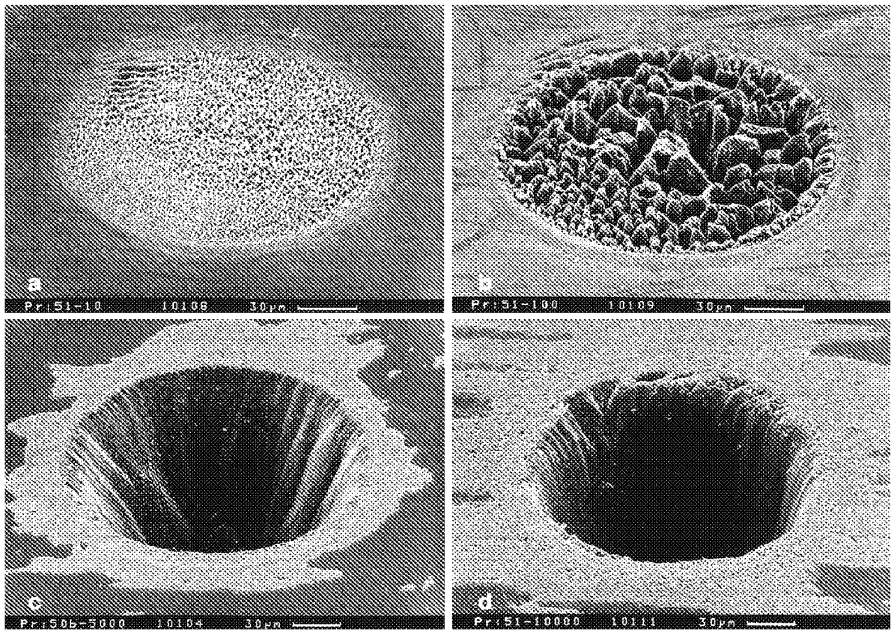


Fig. 5a–d. Laser ablation of a 0.3 mm thick silicon target with: **(a)** 10, **(b)** 100, **(c)** 5×10^3, and **(d)** 10^4 pulses. Laser parameters are the same as in Fig. 3

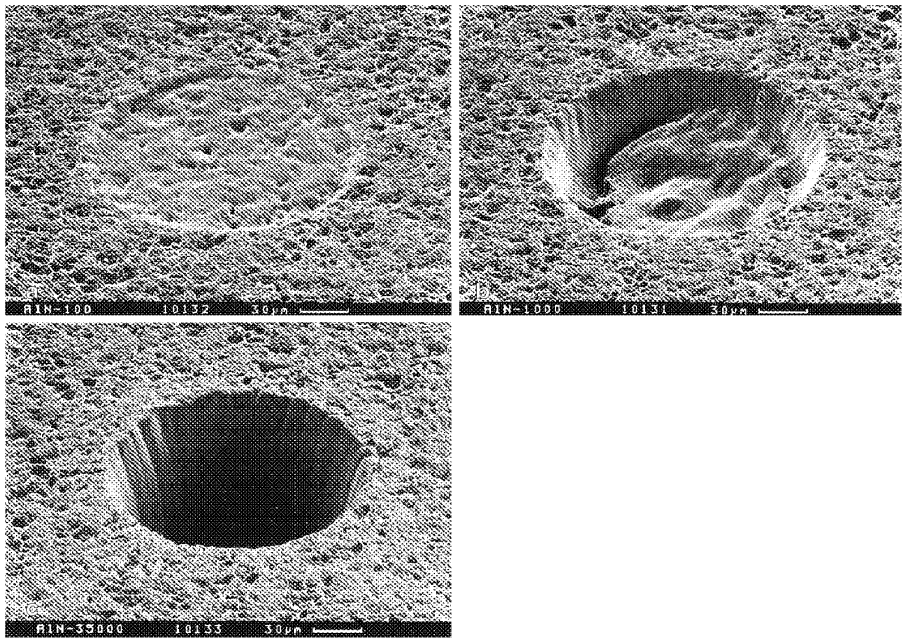


Fig. 6a–c. Ablation of a 0.8 mm AlN target with: **(a)** 10, **(b)** 10^3, and **(c)** 3.5×10^4 laser pulses. Laser parameters are approximately the same as in Fig. 3

Closing this section we summarize the main features of femtosecond laser material processing: very rapid creation of vapor and plasma phases, negligible heat conduction and the absence of liquid phase. The absence of the liquid phase allows better control during the drilling process. Therefore, the reproducibility of our results with femtosecond laser pulses is very good.

SIONYX1403000031.0008

SAMSUNG EX. 1002 - 3029/4148

3 Conclusion

Theoretical models and experimental results on femtosecond, picosecond and nanosecond laser ablation of metal targets are presented. Very pure ablation of metal targets in vacuum with femtosecond laser pulses is demonstrated. Sharp well defined patterns can be ablated in metal and other solid targets by an image projection technique. These advantages of femtosecond lasers are very promising for their future applications in precise material processing.

Acknowledgements. We would like to thank Hanna Jacobs for technical assistance and acknowledge financial support by the German Ministry of Science, Education, Research, and Technology (BMBF, 13N6590/0).

References

1. B.C. Stuart, M.D. Feit, A.M. Rubenchik, B.W. Shore, M.D. Perry: Phys. Rev. Lett. **74**, 2248 (1995)
2. P.P. Pronko, S.K. Dutta, D. Du, R.K. Singh: J. Appl. Phys. **78**, 6233 (1995)
3. C. Momma, B.N. Chichkov, S. Nolte, F. von Alvensleben, A. Tünnermann, H. Welling: Opt. Commun. accepted
4. W. Kautek, J. Krüger: SPIE Proc. **2207**, 600 (1994)
5. S. Preuss, A. Demchuk, M. Stuke: Appl. Phys. A **61**, 33 (1995)
6. J. Ihlemann, A. Scholl, H. Schmidt, B. Wolff-Rottke: Appl. Phys. A **60**, 411 (1995)
7. M.I. Kaganov, I.M. Lifshitz, L.V. Tanatarov: Sov. Phys. –JETP **4**, 173 (1957)
8. S.I. Anisimov, B.L. Kapeliovich, T.L. Perel'man: Sov. Phys. –JETP **39**, 375 (1974)
9. M.B. Agranat, A.A. Benditskii, G.M. Gandel'man, P.S. Kondratenko, B.I. Makshantsev, G.I. Rukman, B.M. Stepanov: Sov. Phys. –JETP **52**, 27 (1980)
10. M.B. Agranat, S.I. Anisimov, S.I. Ashitkov, B.I. Makshantsev, I.B. Ovchinnikova: Sov. Phys. –Solid State **29**, 1875 (1987)
11. P.B. Corkum, F. Brunel, N.K. Sherman, T. Srinivasan-Rao: Phys. Rev. Lett. **61**, 2886 (1988)
12. P.B. Allen: Phys. Rev. Lett. **59**, 1460 (1987)
13. S.D. Brorson, A. Kazeroonian, J.S. Moodera, D.W. Face, T.K. Cheng, E.P. Ippen, M.S. Dresselhaus, G. Dresselhaus: Phys. Rev. Lett. **64**, 2172 (1990)
14. X.Y. Wang, D.M. Riffe, Y.S. Lee, M.C. Downer: Phys. Rev. B **50**, 8016 (1994)
15. R.W. Schoenlein, W.Z. Lin, J.G. Fujimoto, G.L. Eesley: Phys. Rev. Lett. **58**, 1680 (1987)
16. W.S. Fann, R. Storz, H.W.K. Tom, J. Bokor: Phys. Rev. B **46**, 13592 (1992)
17. Y.V. Afanasiev, O.N. Krokhin, G.V. Sklizkov: IEEE J. QE – **2** 483 (1966)
18. J.F. Ready: *Effects of High-Power Laser Radiation* (Academic, New York 1971)
19. V.A. Batanov, F.V. Bunkin, A.M. Prokhorov, V.B. Fedorov: Sov. Phys. –JETP **36**, 311 (1973)
20. A.M. Prokhorov, V.I. Konov, I. Ursu, I.N. Mihailescu: *Laser Heating of Metals* (Adam Hilger, Bristol 1990)
21. D. Strickland, G. Mourou: Opt. Commun. **56**, 219 (1985)
22. J.D. Kmetec, J.J. Macklin, J.F. Young: Opt. Lett. **16**, 1001 (1991)
23. S.I. Anisimov, M.I.Tribel'skii, Ya.G. Epel'baum: Sov. Phys. –JETP **51**, 802 (1980)

SIONYX1403000031.0009

SAMSUNG EX. 1002 - 3030/4148

Copyright © 2003 EBSCO Publishing

Appl. Phys. A 81, 1257–1263 (2005)
DOI: 10.1007/s00339-004-2989-z

Applied Physics A
Materials Science & Processing

C.Y. CHIEN
M.C. GUPTA✉

Pulse width effect in ultrafast laser processing of materials

Applied Research Center, Old Dominion University, Newport News, Virginia 23606, USA

Received: 7 January 2004/Accepted: 12 July 2004
Published online: 31 August 2004 • © Springer-Verlag 2004

ABSTRACT A systematic study of the influence of laser pulse width in ultrafast laser micromachining of silicon and stainless steel was carried out. Experiments were performed using a Ti:sapphire laser with 800 nm and 400 nm (frequency doubling) wavelengths in an air environment with a pulse duration ranging from 110 fs to 10 ps. Hole drilling and line cutting of silicon and stainless steel were studied. Structural details of the machined area were characterized using a number of techniques such as optical microscopy, atomic force microscopy and stylus profilometry. The effect of pulse width on melting was observed at ~ 2.5 ps for stainless steel and at ~ 5 ps for silicon. Also, the polarization effect on the laser machining is reported. The machined quality using femtosecond laser pulses with high energy fluence was found to be limited by the laser intensity contrast.

PACS 79.20Ds; 81.15fg

1 Introduction

The application of ultrashort pulse lasers for precision material processing has been an active area of fundamental and applied research [1–13] due to a growing interest by industry in the technique. When a laser pulse interacts with a solid target, the electrons are heated to a high temperature by the absorption of laser energy. By the electron-phonon interactions, the hot electrons transfer energy to the lattice on a few picosecond time scale for most materials [14–16]. However, for the femtosecond laser pulse, energy is transferred to the electrons on a time scale much faster than the transfer time of this energy to the lattice of the material. Consequently, the ultrashort machining process is highly precise with minimal lateral thermal damage or heat-affected zone. There have been a number of experiments [17–20] on comparing laser ablation of solid targets in three different pulse regimes, femtosecond, picosecond, and nanosecond. However only few systematic studies on the influence of pulse duration to the material processing in a time frame of femto- to pico- seconds are reported. Also, in the case of laser-solid target interactions, one critical issue is the laser intensity contrast ratio, which is the ratio of the peak intensity to that of the prepulses or background. These prepulses, which are pedestals with relatively low intensity ($10^{10} - 10^{11}$ W/cm^2), could pre-heat the target before the arrival of the main pulse [21]. Therefore, it is difficult to have melt-free material processing using an ultrashort laser pulse with a low intensity contrast.

The primary aim of this research is to study the influence of the pulse width in the femto- to pico- second time regimes on laser machining and to determine an optimum pulse duration for material processing. In this paper, we analyzed and compared the drilled holes and cut lines in silicon and stainless steel with laser pulse durations ranging from 110 fs to 10 ps. The machined structures were examined using an atomic force microscope (AFM), an optical microscope and a stylus profilometer.

2 Experimental

The experiments were performed with a commercial, femtosecond Ti:sapphire laser system (Spectra Physics, Spitfire). The laser system delivered pulses at a repetition rate of 1 kHz with an energy up to 2 mJ at a wavelength of 800 nm. The system was based on the chirped-pulse amplification (CPA) technique, and by altering the distance of the compressor grating, the pulse width could be varied from 110 fs to 10 ps or more without changing any other laser parameters. Pulse duration was measured with a background free, scanning second-order autocorrelator. The temporal profile of 110 fs laser pulse (assuming a Gaussian pulse shape) was measured with a high-dynamic range second-order autocorrelator as shown in Fig. 1. The peak-to-background intensity contrast ratio was around 10^3 : 1 at 1 ps pulse duration. The intensity contrast was further improved by Type-I frequency doubling using a 250 μm thick BBO crystal. Frequency doubling by second harmonic generation (SHG) could suppress the low-intensity wings and almost square the intensity contrast of the laser pulse [22]. The SHG pulse width has been investigated theoretically and experimentally by several research groups [23, 24]. These results indicate that the pulse width of SHG should not broaden due to group velocity dispersion by using a 250 μm BBO crystal. The 800 nm wavelength and 8 mm diameter laser beam was focused on the sample with an uncoated singlet $f/20$ lens. The diameter of the focal spot measured using an imaging system coupled with a CCD cam-

✉ Fax: +1-757/269-5644, E-mail: mgupta@odu.edu

SIONYX1403000031.0011

SAMSUNG EX. 1002 - 3032/4148

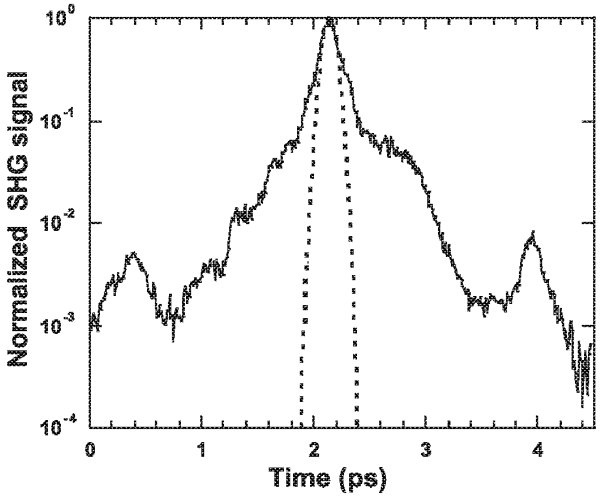


FIGURE 1 Measured temporal profile of a 110 fs laser pulse. The *solid line* is the normalized second harmonic signal and the peak-to-background intensity contrast ratio is around 10^3 : 1 at 1 ps. The *dotted line* is an ideal Gaussian pulse fit with duration of 110 fs

era (Cohu 6400) was 45 μm ± 2.5 μm (at $1/e^2$). An energy controller (a half-wave plate and a polarizer with a contrast ratio 1000 : 1) was used to adjust the pulse energy. During the experiments, a fast mechanical shutter (Uniblitz, model VS14, Vincent Associates) was used to control the number of laser pulses. For the single pulse experiment, even though the exposure time of this shutter was 1.5 ms, the repetition rate of the laser system was adjusted to make sure that only one single pulse passed through the shutter. Samples of *n*-type silicon (100) wafers (Southwest Silicon) and stainless steel (Goodfellow, AISI 304) with a thickness of 500 μm were used. They were cleaned with methanol before mounting on a motorized linear translation stage (Melles Griot). The ablation experiments were performed by translating the samples across the focused laser beam at a linear speed of 0.5 mm/sec.

For polarization studies, the polarization state was changed relative to sample motion as shown in Fig. 2. The experimental setup for assist gas studies included a glass tube with interior diameter of 25 mm placed between the focusing lens and the target as shown in Fig. 3. The end of tube near the sample holder was open while the other end was sealed with a thin (150 μm) cover glass to prevent gas from escaping. Industrial grade helium gas (99.995%) was used in the experiments. The pure gas was fed into the side of sealed end, then leaked through the gap between the tube and sample holder.

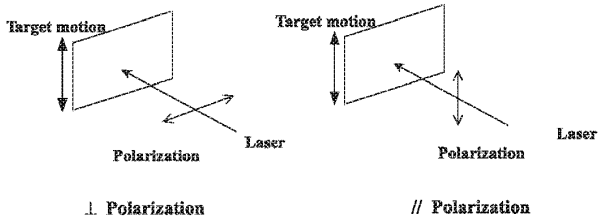


FIGURE 2 Laser beam polarization with respect to target motion direction

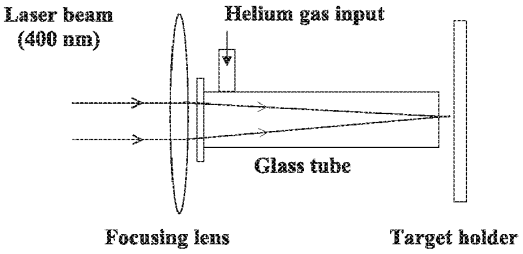


FIGURE 3 Assist gas experimental setup

The focused laser beam passed through the ambient pressure helium gas. After machining, all samples were cleaned in an ultrasonic bath of methanol for a few minutes to remove any loose debris. The machined samples were examined with an atomic force microscope (Digital Instrument, Nanoscope III), a stylus profilometer (Tencor alphastep-200) and optical microscope (Olympus, CK40M).

3 Results and discussion

3.1 *Pulse width effect in material processing*

To make a meaningful comparison of thermal effects, holes were drilled in a 500 μm thick silicon wafer with 110 fs laser pulses at wavelength of 800 nm to determine an optimum laser energy. The characteristics of the drilled holes were recorded as a function of laser energy and the number of pulses (with a duration of 110 fs) used to drill each hole. Figure 4a and b shows two AFM images of two craters, one ablated with ten shots at 50 μJ/shot and the other ablated with fifty shots at 10 μJ/shot. The total energy for each was ~ 500 μJ. As can be seen in Fig. 4b, a well-defined molten rim formed around the crater of the hole drilled with ten 50 μJ/shots. Such machined characteristics are similar to ones obtained using 3.3 ns, 1 mJ laser pulses [19, Fig. 2b]. At this laser energy, the laser peak intensity is $\sim 3.2 \times 10^{13}$ W/cm^2. With a near 10^3 : 1 intensity contrast ratio, the intensity of the long pedestal is high enough to ablate the material. This could explain the rim structure even when ablated with ultrashort (e.g., 110 fs) laser pulses. Therefore, a picosecond contrast measurement is essential to support this claim. Unfortunately, the second order autocorrelator provides a symmetrical measurement (no distinction between prepulse and post pulse). Polarization gate frequency resolved optical gating (FROG) could measure pulse width and chirp (phase) but typically does not have enough dynamic range. The temporal profile of the laser pulse could be measured with a high dynamic range third-order correlator [25], which was not available at the time for this study. To avoid the pedestal effect, the maximum laser energy used in the experiments was 10 μJ.

First we present the results on laser processing of silicon. We compare line cutting using a 800 nm wavelength and an energy of 10 μJ. The surface morphologies and material removal rates of silicon were characterized as a function of pulse duration and the number of cut passes. The machined samples were examined using a stylus profilometer. Cross sections of the machined lines using a single-pass cut at different pulse widths are shown in Fig. 5. With the exception of some ab-

SIONYX1403000031.0012

SAMSUNG EX. 1002 - 3033/4148

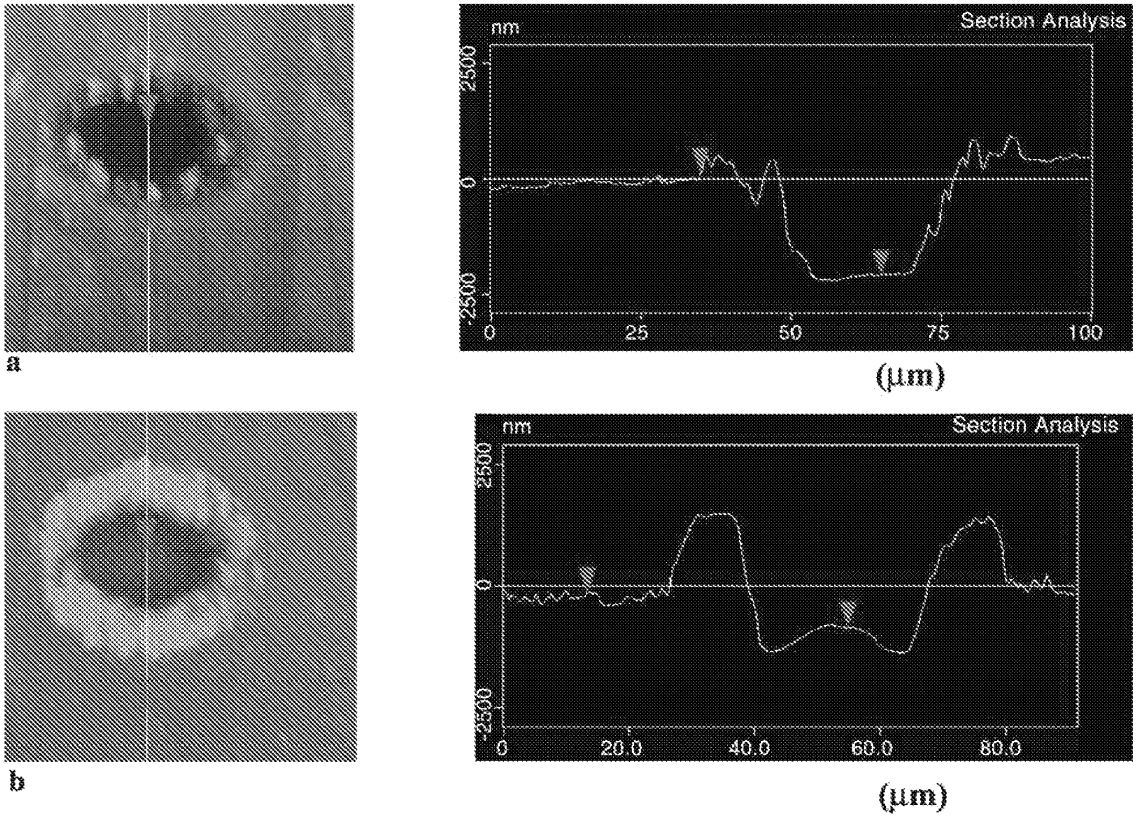


FIGURE 4 Typical AFM images of two craters formed with a femtosecond laser pulse ($\tau_p = 110$ fs, $\lambda = 800$ nm), **a** fifty shots with 10 μJ/shot, **b** ten shots with 50 μJ/shot

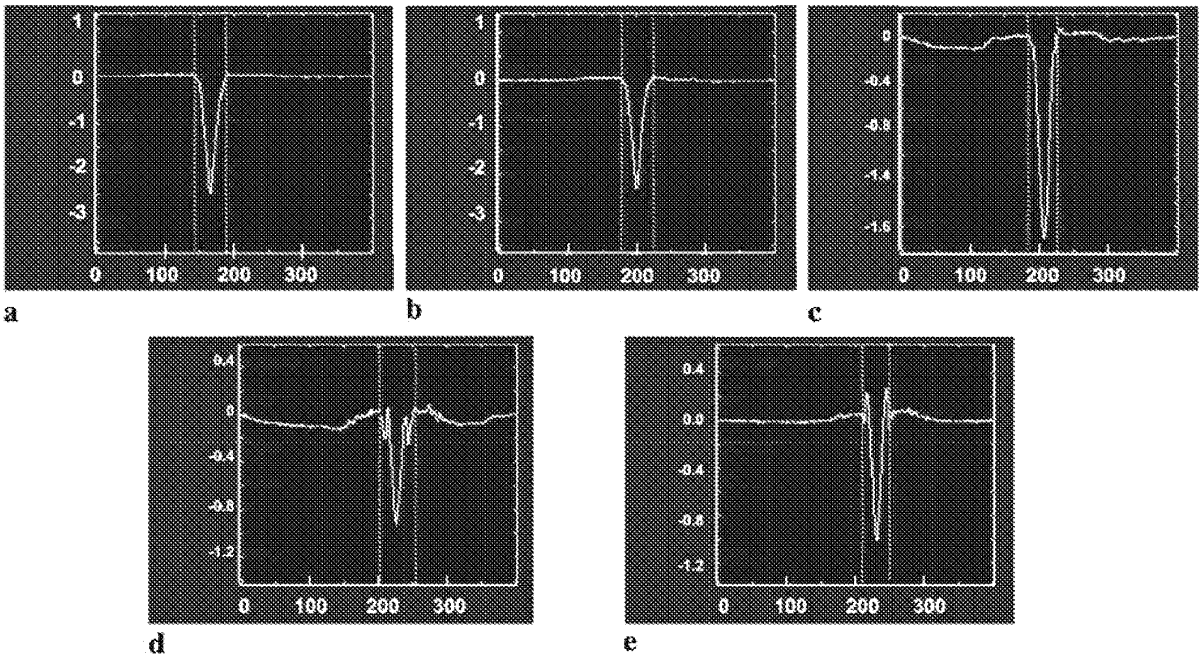


FIGURE 5 Surface profiles of single-pass cut lines on silicon for pulse durations of **a** 110 fs, **b** 500 fs, **c** 1 ps, **d** 5 ps, **e** 10 ps

SIONYX1403000031.0013

SAMSUNG EX. 1002 - 3034/4148

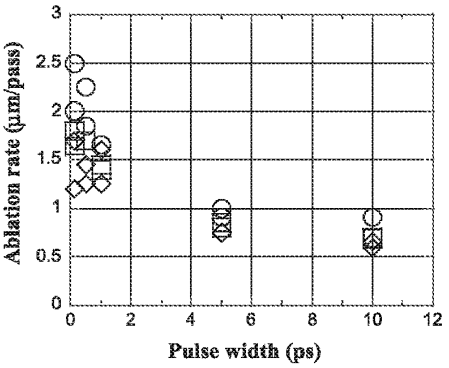


FIGURE 6 Ablation rate as a function of pulse duration for various cut passes, single pass (*open circles*), 5-pass (*open squares*), 10-pass (*open diamonds*). The measurement uncertainty was ±10%

lated debris, traces for a 1 ps laser pulse width or less show no molten material along the machined line. However, at 5 ps, the image shows variations along the machined area. The presence of molten structure indicated that lattice melting occurs around 5 ps. At a pulse duration of 10 ps, a rim structure, which is similar to that which occurs from ablation with a long laser pulse [19], is clearly observed. Figure 6 shows plots of the ablation rate as a function of pulse width and the number of passes. As the pulse duration increased, the ablation rate decreased due to the decrease in laser peak intensity. Also, the ablation rate decreased as the number of cutting passes increased. This could be due to a reduction in the effective fluence on the wall of the machined structure.

Next we present the experimental results on laser ablation of silicon and stainless steel using a laser wavelength of 400 nm. The contrast ratio of the laser pulse was further improved due to frequency doubling. Also a beam delivery system, filled with helium gas at ambient pressure, was set up to maintain the quality of the focus spot. The cutting lines were compared for pulse durations ranging from 110 fs to 10 ps. Figure 7 shows the profiles of single-pass cuts in silicon with pulse durations of 110 fs, 5 ps, and 10 ps at energies of 5 μJ/pulse and 10 μJ/pulse. The cut width (kerf width) is plotted as a function of pulse width and laser energy in Fig. 8a. At the pulse energy of 5 μJ, the cut width is approximated to be 30 μm and is almost the same for all pulse durations. However, at an energy of 10 μJ, the cut width starts to increase at a pulse width of 5 ps. The increase of the cut width indicates the melting effect starts around 5 ps. The melting behavior as a function of pulse width observed for stainless steel is similar to that observed for silicon. The single-pass cut width of stainless steel is plotted as a function of pulse duration and laser pulse energy in Fig. 8b. The cut width starts to increase at a pulse width longer than 2.5 ps with a laser energy of 10 μJ. The data indicate melting damage starts to occur at around 2.5 ps. Based on the experimental data, significant pulse width related melting damage can be avoided if the pulse duration for laser material processing of silicon is less than 5 ps and is less than 2.5 ps for stainless steel.

3.2 *Polarization effect*

Several research groups have demonstrated the influence of the laser polarization on the quality of ultrashort

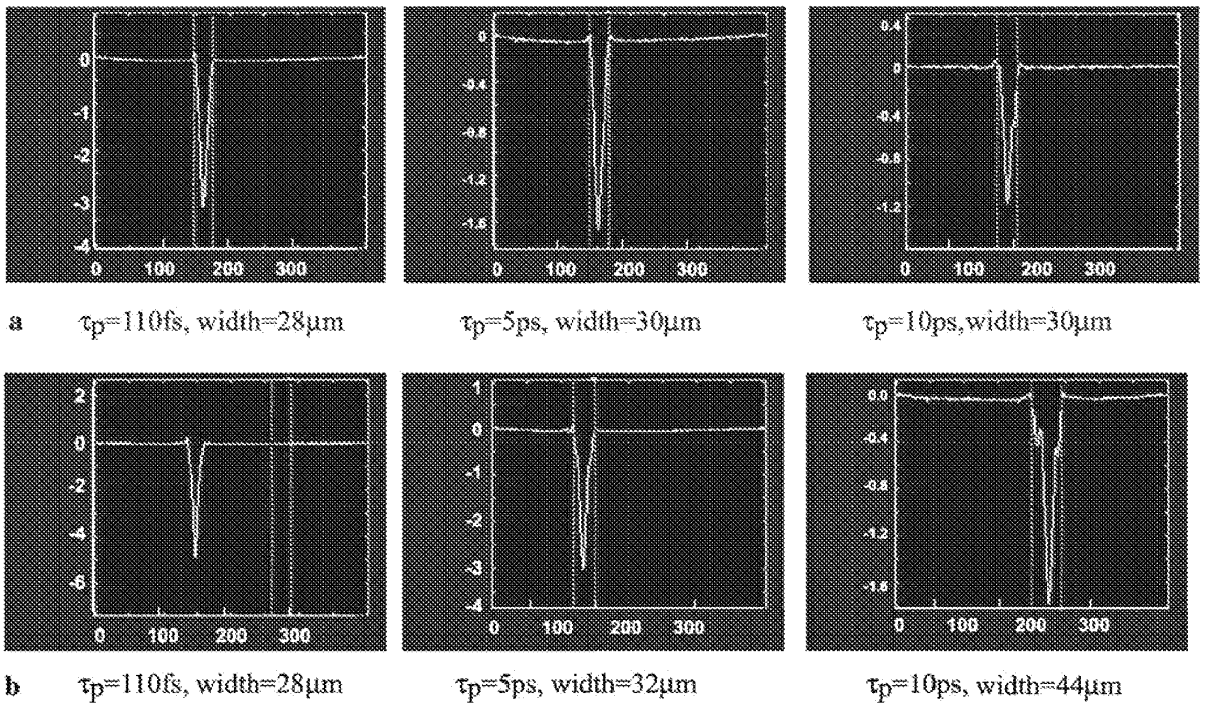


FIGURE 7 Surface profiles of single-pass cut on silicon in a helium environment with $\lambda = 400$ nm, pulse energies of **a** 5 μJ/pulse, and **b** 10 μJ/pulse

SIONYX1403000031.0014

SAMSUNG EX. 1002 - 3035/4148

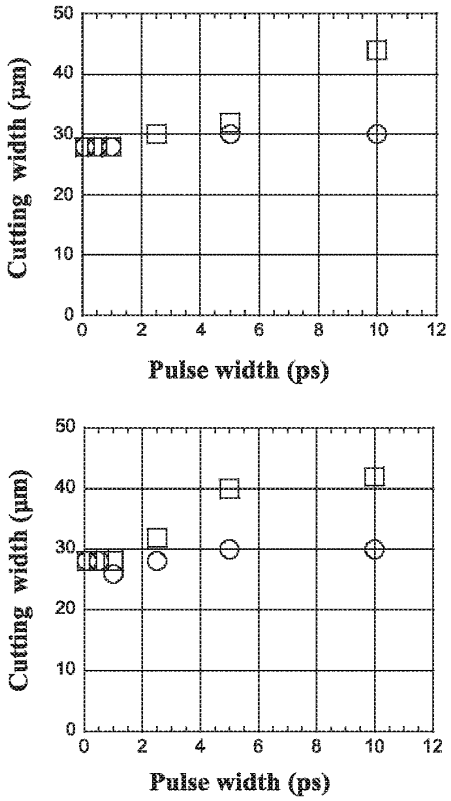


FIGURE 8 Cutting width as a function of pulse width for **a** silicon, **b** stainless steel at the energy of 5 μJ/shot (*open circles*), and 10 μJ/shot (*open squares*). The measurement uncertainty was ±10%

laser hole drilling [5, 26–28]. The effect of polarization on reflectivity can be calculated using Fresnel equations. For typical hole drilling configurations, the reflectivity of *p*-polarized light was found to be two times smaller than that of the *s*-polarized light due to the light reflected from the walls. In this section, the results of polarization effect on the laser cutting of silicon with a femtosecond laser ($\tau_p = 110$ fs, $\lambda = 800$ nm, 10 μJ) are presented. The samples were machined with the same process parameters except for a change in polarization state and were examined with an optical microscope. A half wave plate was used to change the state of the polarization. Figure 9 shows optical microscope pictures of the entrance of the machined areas as a function of the number of passes. The pictures show irregular cut edge if the polarization is parallel to the cutting motion and the irregularities are increased with number of passes. Also, the data for cut depth as a function of the number of passes are shown in Fig. 10. At a 10-pass laser cut, the cut depth drops about 25%–30% for laser polarization parallel to the cutting direction. These results show the important impact of polarization effects on edge roughness and cutting efficiency.

3.3 *Effect of assist gas*

Ultrashort laser pulses have been demonstrated to possess unique advantages for precise materials processing such as the creation of melt and burr-free structures and reduced material redeposition over longer laser pulses. In order to further improve laser machining performance, we applied the concept of assist gas during laser cutting [13, 29] which gas pressure typical of several atmospheres. The main challenge for high intensity laser pulse propagation in air is phase front distortion on the envelop of pulse due to an intensity-dependent nonlinear refractive index, which could degrade the ability to focus the beam. To assess beam quality, the integrated nonlinear index along the beam path is characterized by the so called B integral [30]. Using a rare gas such as helium, which has a nonlinear refractive index 10 times lower than air [31], would minimize the beam distortion. A flowing helium gas was used during the experiments to improve the quality of laser focus and to reduce the redeposition of ab-

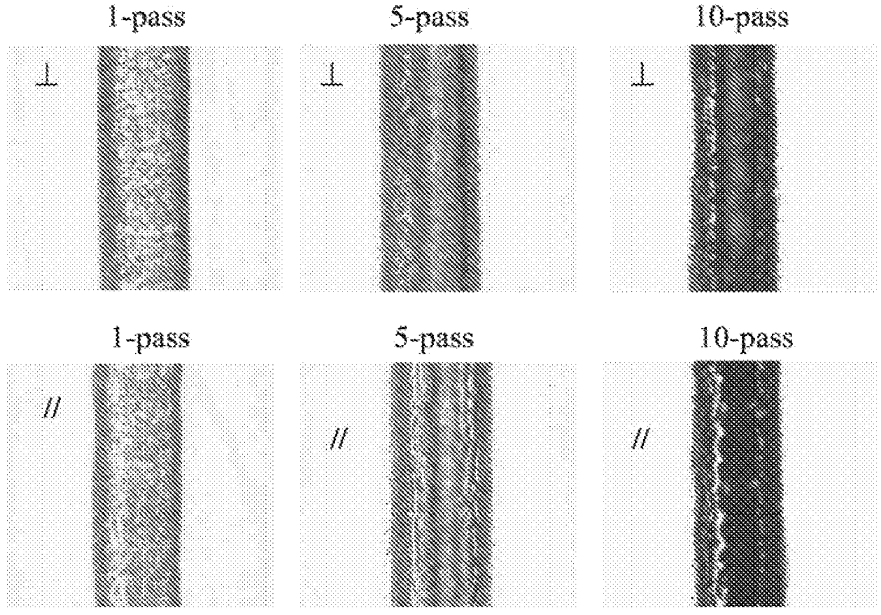


FIGURE 9 Optical microscope images of the machined silicon for differing numbers of passes and laser polarization (parallel and perpendicular)

SIONYX1403000031.0015

SAMSUNG EX. 1002 - 3036/4148

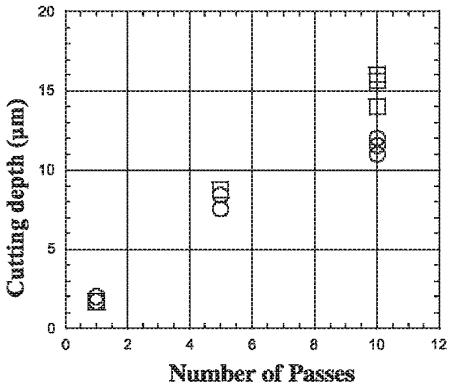


FIGURE 10 Cutting depth as a function of the number of passes and laser polarization. *Open squares* show the laser polarization perpendicular to the cutting motion and *open circles* show the laser polarization parallel to the cutting motion

lated material on the surface. To compare machined quality, a silicon sample was cut in both helium and air at ambient pressure. Figure 11 shows the typical optical microscope images of the surface of the machined silicon with air and helium gas and before and after an ultrasonic cleaning. The quality was significantly improved with helium assist gas and ultrasonic cleaning. Instead of using helium gas, dry air was also tested during the experiments and shown to have similar results. These results indicate that by applying a gas flow (close to ambient pressure), the redeposition of the ablated material can be reduced significantly.

4 Conclusions

The quality of the fs laser ablation-produced marks depended on the pulse energy, intensity contrast ratio, polarization, pulse duration, and material properties. A pulse width related melting effect was observed. Based on the experimental results, the pulse duration for laser material processing to avoid significant melting damage was ~ 5 ps for silicon and ~ 2.5 ps for stainless steel. It is important to arrange the polarization perpendicular to the cutting direction to have efficient and high quality laser machining. Also, a technique based on flowing gas on the target surface to reduce the redeposition and improve laser material processing was demonstrated. The presence of a prepulse is a major concern for material processing using femtosecond lasers with high fluences.

ACKNOWLEDGEMENTS The authors thank Brandt Robertson and Patrick Woodworth for help with the AFM images and stylus profilometer. We are grateful to Don Lijana (Spectra Physics) for fs laser technical support. This work was supported by Spectra-Physics through the NSF Industry-University Cooprative Research Center for Lasers and Plasmas for Advanced Manufacturing at the Applied Research Center of Old Dominion University. We also thank NSF for the femtosecond laser equipment grant.

REFERENCES

1 D. Bauerle: *Laser processing and Chemistry*, 3rd edn. (Springer-Verlag, Berlin, Heidelberg 2000)
2 W.M. Steen: *Laser Material processing*, 2nd edn. (Springer-Verlag, London 1998)
3 J. Ihlemann, A. Scholl, H. Schmidt, B. Wolff-Rottke: Appl. Phys. A **60**, 411 (1995)
4 P.P. Pronko, S.K. Dutta, J. Squier, J.V. Rudde, D. Du, G. Mourou: Opt. Commun. **114**, 106 (1995)

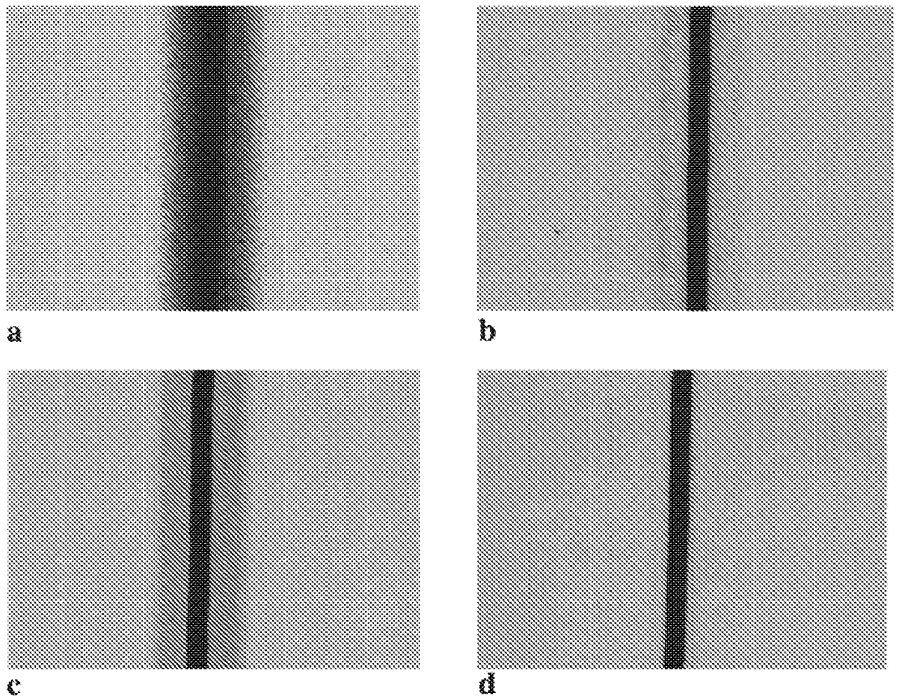


FIGURE 11 Optical microscope images of the machined surface of silicon. **a** sample processed in ambient air, **b** same as **a** with ultrasonic cleaning. **c** sample processed in helium gas, **d** same as **c** with ultrasonic cleaning

SIONYX1403000031.0016

SAMSUNG EX. 1002 - 3037/4148

5 D. Ashkenasi, A. Rosenfeld, H. Varel, M. Wahmer, E.E.B. Campbell: Appl. Surf. Sci. **120**, 65 (1997)
6 M.D. Perry, B.C. Stuart, P.S. Banks, M.D. Feit, V. Yanovsky, A.M. Rubenchik: J. Appl. Phys. **85**, 6803 (1999)
7 S. Nolte, G. Kamlage, F. Korte, T. Bauer, T. Wagner, A. Ostendorf, C. Fallnich, H. Welling: Adv. Eng. Mater. **2**, 23 (2000)
8 N. Barsh, K. Korrber, A. Ostendorh, K.H. Tonshoff: Appl. Phys. A **77**, 237 (2003)
9 R.F.W. Herrmann, J. Gerlach, E.E.B. Campbell: Appl. Phys. A **66**, 35 (1998)
10 V. Hertel, R. Stoian, A. Rosenfeld, D. Ashkenasi, E.E.B. Campbell: Riken Review **32**, 23 (2001)
11 A.A. Bugayev, M.C. Gupta: Opt. Lett. **28**, 1463 (2003)
12 M. El-Bandrawy, K. Nagarathnam, M.C. Gupta, C. Hamann, J. Horsting: J. Laser Appl. **15**, 101 (2003)
13 M. El-Bandrawy, M.C. Gupta: Proc. SPIE **4977**, 219 (2003)
14 X.Y. Wang, D.M. Riffe, Y.S. Lee, M.C. Downer: Phys. Rev. B **50**, 8016 (1994)
15 R.W. Schoenlein, W.Z. Lin, J.G. Fujimoto, G.L. Eesley: Phys. Rev. Lett. **58**, 1680 (1987)
16 W.S. Fann, R. Storz, H.W. K Tom, J. Bokor: Phys. Rev. B **46**, 13592 (1992)
17 W. Kautek, J. Kruger: Proc. SPIE **2207**, 600 (1994)
18 S. Preuss, A. Demchuk, M. Stuke: Appl. Phys. A **61**, 33 (1995)
19 B.N. Chichkov, C. Momma, S. Notle, F. Alvensleben, A. Tünnermann: Appl. Phys. A **63**, 109 (1996)
20 P.S. Banks, D.D. Feit, A.M. Rubenchik, B.C. Stuart, M.D. Perry: Appl. Phys. A **69**, S377 (1999)
21 M.M. Murnanem H.C. Kapteyn, R.M.W. Falcone: Phys. Rev. Lett. **62**, 155 (1989)
22 J. Queneuille, F. Druon, A. Maksimchuk, G. Cheriaux, G. Mourou, K. Nemoto: Opt. Lett. **25**, 508 (2000)
23 J.Y. Zhang, J. Huang, H. Wang, K.S. Wong, G.K. Wong: J. Opt. Soc. Am. B **15**, 200 (1998)
24 Y. Tamaki, M. Obara, K. Midorikawa: Jpn. J. Appl. Phys. **37**, 4801 (1998)
25 G. Albrecht, A. Antnetti, G. Mourou: Opt. Commun. **40**, 59 (1981)
26 S. Nolte, C. Momma, G. Kamlage, A. Ostendorf, C. Fallnich, F. von Alvensleben, H. Welling: Appl. Phys. A **68**, 563 (1999)
27 H.K. Tonshoff, A. Ostendorf, T. Wagner: Proc. SPIE **4274**, 88 (2001)
28 K. Venkatakrishnan, B. Tan, P. Stanley, N.R. Sivakumar: J. Appl. Phys. **92**, 1604 (2002)
29 K. Fargoo, A. Kar: J. Appl. Phys. **83**, 7467 (1998)
30 A. Siegman: *Lasers* (University Science Books, Mill Valley, CA 1986) pp. 385
31 E.T.J. Nibbering, G. Grillon, M.A. Franco, F.S. Prade, A. Mysyrowicz: J. Opt. Soc. Am. B **14**, 650 (1997)

SIONYX1403000031.0017

SAMSUNG EX. 1002 - 3038/4148

An Evaluation of MOS Interface-Trap Charge Pump as an Ultralow Constant-Current Generator

Uğur Çilingiroğlu, Adriana Becker-Gómez, and Kenton T. Veeder, *Member, IEEE*

***Abstract*—In this work, we explore the MOS interface-trap charge-pump as an ultralow constant-current generator for analog CMOS applications. Charge pumping techniques in general are more suitable than conventional continuous-time techniques for ultralow current generation because the linear controllability of current by frequency is maintained regardless of the level of current. An interface-trap pump has the same property but the minimum charge it puts out per cycle is at least two orders of magnitude smaller than that of a switched-capacitor charge pump. This helps generate the same current more accurately at a much higher frequency with a much smaller filter capacitance. The paper presents a simplified model of the terminal characteristics of the interface-trap pump and an evaluation of its performance as a stand-alone current generator. Cascoding and complementary pumping are introduced as measures of performance improvement. Temperature sensitivity, pulse feedthrough, controllability, matching, reliability, and trimming issues are addressed. Transconductor circuits built with the charge pump are presented and experimentally evaluated.**

***Index Terms*—Charge pumping, CMOS transconductors, interface-traps, ultralow current generation.**

I. Introduction

THE low-current frontier of analog CMOS remained mostly unexplored until the beginning of 1990s. Since then, it has been challenged indirectly by a growing demand for low-power/low-voltage architectures and directly by the emergence of MOSFET log-domain processors and fully integrated low-frequency continuous-time filters [1]–[3]. Bias levels have already been reduced to the order of nanoamps in numerous applications [4]–[7] and the downward trend is likely to continue particularly in ultralow-frequency continuous-time filter applications. Traditionally, these filters are used in biomedical signal processing but, considering the ongoing diversification of system-on-chip applications, we can expect their application domain to expand significantly in the future.

Theoretically, the lower limit of controllable constant-current generation is set by device leakage currents to the order of picoamps or less. Reaching this limit with conventional continuous-time techniques, however, is not a trivial task. In practice, even nanoamp constant-current generation relies on some specific and costly current division or cancellation techniques mainly because: 1) the very strong sensitivity of subthreshold conductance to gate voltage, device parameters and temperature precludes the MOSFET as a simple voltage-controlled subnanoamp current source and 2) there exists no integrable and stable resistive element with which this level of reference current can be generated. An alternative is the switched-capacitor (SC) technique, which has already been adopted in a number of architectures generating conventional levels of reference current [8]–[10]. The current $I_P = fQ_P$ of an SC can be scaled down by decreasing the clock frequency f or the charge Q_P pumped per cycle. Decreasing Q_P is highly desirable also because the current ripple of a subthreshold MOSFET biased by an SC is an exponentially increasing function of Q_P, as described approximately by $\Delta I_O/I_O = \exp(2.3Q_P/SC_F) - 1$, where S is the MOSFET subthreshold slope in V/decade and C_F is the filter capacitance. Unfortunately, the cost of generating a slow clock generally increases significantly with a decreasing f and the accuracy of I_P degrades as Q_P approaches its physical limit. Therefore, the key to generating a given ultralow current with a high f, a small C_F, and a high accuracy is to have a low physical limit for Q_P, which, in a conventional SC is determined solely by the parasitic capacitance of a pair of minimized MOSFET switches. Assuming a few hundred millivolts of reference voltage, this limit is no less than several femtocoulombs in a typical 0.5-μ CMOS technology. Even if Q_P is lowered to this limit, it takes at most a kilohertz frequency to generate a picoamp current and at least several picofarads of capacitance to filter the ripple below 1%. This work evaluates the MOSFET interface-trap charge-pumping (ITCP) effect as a possible ultralow constant-current generating technique overcoming these difficulties by offering at least two orders of magnitude reduction in the physical limit of Q_P.

ITCP was discovered in 1969 [11], fully modeled in the 1980s [12]–[15], and since then has become the most popular test tool for MOSFET Si-SiO_2 interface characterization. It also found a few digital circuit applications in the distant past [16]–[19]. Its use as a low-current source was suggested in [20] but, to the best of our knowledge, it has never enjoyed any analog circuit application.

We present in Section II a simplified model of its terminal characteristics pertaining to circuit applications. Its properties as a stand-alone current generator are experimentally evaluated in Section III. Improving its performance by cascoding is discussed in Section IV. Sections V and VI are devoted to temperature sensitivity and pulse feedthrough analyses, respectively. Also presented in Section VI is a complementary pumping scheme for ripple suppression. Controllability, matching, reliability, and trimming issues are addressed in Section VII. Transconductor circuits built with the charge pump are presented and experimentally evaluated in Section VIII. Finally, the conclusions are summarized in Section IX.

Manuscript received March 13, 2002; July 23, 2002.

The authors are with the Department of Electrical Engineering, Texas A&M University, College Station, TX 77843-3128 USA (e-mail: uciling@ee.tamu.edu).

Digital Object Identifier 10.1109/JSSC.2002.806282

0018-9200/03$17.00 © 2003 IEEE

SIONYX1403000031.0018

SAMSUNG EX. 1002 - 3039/4148

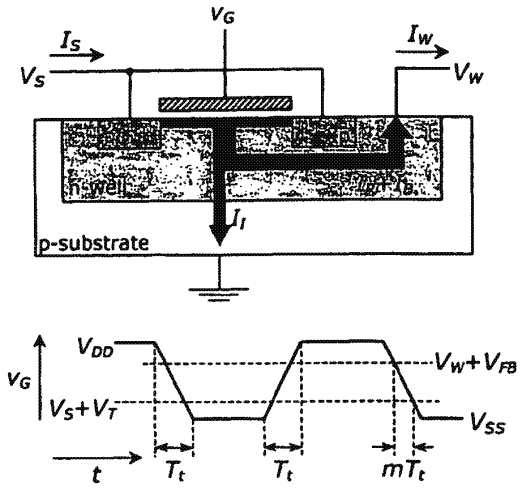


Fig. 1. PMOS transistor configured as an interface-trap charge pump.

II. Primary Model of ITCP

ITCP is a transient recombination effect activated by cycling the $Si\text{-}SiO_2$ interface of a MOSFET between accumulation and inversion. For a brief explanation of its primary model, consider the PMOS device shown in Fig. 1. Note that the source and drain junctions are interconnected to form a single source terminal, whose voltage with respect to ground is V_S. The n-well constitutes a second current conducting terminal, whose voltage is represented by V_W. Gate voltage v_G is pulsed periodically between the rails V_{DD} and V_{SS}, which induce accumulation and inversion, respectively, provided that the following conditions are met:

$$V_W < V_{DD} - V_{FB} \quad \text{(for accumulation)} \tag{1}$$

$$V_S > V_{SS} - V_T \quad \text{(for inversion)} \tag{2}$$

where V_{FB} is the flatband voltage and V_T is the threshold voltage. During each cycle, the midgap interface traps distributed within an energy range ΔE are filled in the accumulation phase by capturing electrons, which are supplied by the well terminal and are emptied in the inversion phase by capturing holes, which are supplied by the source terminal. Acting as recombination centers, these traps transfer from source to well a net charge of

$$Q_P = qD_{it}A\Delta E \tag{3}$$

where q is the electronic charge, A is the gate area, and D_{it} is the trap density per unit area per unit energy, which can be assumed to be energy-independent without much loss of accuracy for circuit applications. The primary model of ITCP predicts

$$\Delta E = 2kT \ln \frac{\tau}{mT_t} \tag{4}$$

where kT is the thermal energy, τ is a time constant, T_t is the transition time of v_G, and mT_t represents the time spent in depletion during each transition of v_G. As depicted in Fig. 1, m is given by

$$m \equiv \frac{V_W + V_{FB} - (V_S + V_T)}{V_{DD} - V_{SS}}. \tag{5}$$

The average current resulting from the periodic transfer of Q_P from source to well is defined as the ITCP current and is described by

$$I_P = 2kTqD_{it}Af \ln \frac{\tau}{mT_t} \tag{6}$$

where f is the frequency of gate excitation.[1]

I_P is not the sole current resulting from pulsing the gate. Some of the mobile holes released from the channel during the upward transition of v_G move into the well instead of returning to source. Most of these are transported to the substrate through the reverse biased well-substrate junction resulting in an injection current I_I flowing from source to substrate, but a fraction recombines with electrons within the well giving rise to a bulk recombination current I_B which adds on to the source and well terminal currents [21], [22]. This injection/bulk-recombination phenomenon is actually a transient bipolar effect, where I_I and I_B respectively correspond to the collector and base currents of a vertical pnp. The current gain of this pnp makes I_B a fraction of I_I. These two currents can be suppressed by making the source more attractive than the well as the destination of all mobile holes released from the channel. This can be done by increasing the well–source reverse bias $V_W - V_S$ and the transition time T_t and/or by shortening the channel.

According to the ongoing analysis, the well and source terminal currents of the PMOS interface-trap charge pump can be expressed as

$$I_W = I_P + I_B \tag{7}$$

$$I_S = I_P + I_B + I_I. \tag{8}$$

Note that the leakage currents flowing across the well–source and well–substrate junctions are not indicated in these formulations.

The pump is characterized by experimentally extracting the two interface-trap parameters D_{it} and τ, relying on (6). This is done by setting the conditions (1) and (2), taking all precautions to minimize I_B and measuring the well current I_W as a function of T_t. Assuming that I_W closely approximates I_P, D_{it} is extracted from the slope of the plot of I_W versus $\ln T_t$ and τ is obtained from the x intercept of the same plot. The reason for selecting I_W and not I_S for parameter extraction is that the latter is more severely corrupted by the presence of I_I.

At this point the reader may wonder why the ongoing review is presented on a PMOS pump rather than an NMOS. The reason is that the latter is less favorable in an n-well bulk-CMOS circuit application because the common substrate being biased to V_{SS} and V_{FB} being negative, it is impossible to accumulate an NMOS device even weakly unless v_G is reduced below V_{SS}. PMOS devices usually have a positive V_{FB} but, regardless of

[1]Note that I_P flows from the lower potential source terminal to the higher potential well terminal through the device. Therefore, the charge pump is indeed a *current generator*.

SIONYX1403000031.0019

SAMSUNG EX. 1002 - 3040/4148

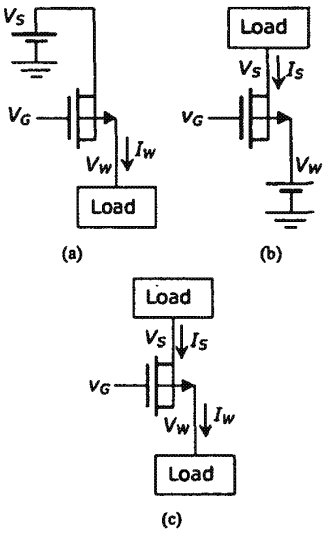


Fig. 2. Bare pump current-generator configurations. (a) Current source. (b) Current sink. (c) Floating current generator.

the polarity of V_{FB}, the well can be biased properly to ensure accumulation for $v_G = V_{DD}$. Furthermore, both the source and well are available as current-conducting terminals in a PMOS pump. Therefore, a PMOS pump can be configured not only as a current source or sink but also as a floating current generator.

III. Well and Source Terminal Characteristics of a Bare Pump

The pump in its simplest "bare" form of a single PMOS device can be configured into a current source by dc biasing the source with V_S and designating the well as the output terminal as shown in Fig. 2(a). Transposing the roles of these two terminals as in Fig. 2(b) results in a current-sink configuration. Since neither terminal needs to be tied to a supply rail, it is also possible to utilize the pump as a floating current-generator as depicted in Fig. 2(c), provided that an acceptable equality between I_W and I_S is achieved by minimizing I_I in (8). The dc behavior of the pump is represented in all these applications by the terminal characteristics I_W-V_W and I_S-V_S. In this section, we discuss these dc characteristics in detail with the support of experimental data extracted from a set of bare pumps fabricated in AMIS 0.5-μm n-gate/n-well CMOS technology, in which zero-bias threshold voltage and well body-factor are specified as $V_{T0} = -0.94$ V and $\gamma_W = 0.56$ V$^{1/2}$, the gate-oxide thickness is 14 nm, the well doping concentration is around 6×10^{16} cm^{-3}, and V_{FB} is estimated to be 0.35 V. Rail levels have been kept at $V_{SS} = 0$ and $V_{DD} = 5$ V and a trapezoidal gate waveform of identical rise and fall times has been used in all tests.

Shown in Fig. 3 are the values of D_{it} and τ extracted from a pump of $A = 194$ μm^2 at $f = 1$ MHz and plotted as a function of well–source bias for four different values of V_W. D_{it} is seen to be highly independent of bias conditions as expected. τ, on the other hand, appears to be a significantly decreasing function of well–source bias. This is a result of the presence

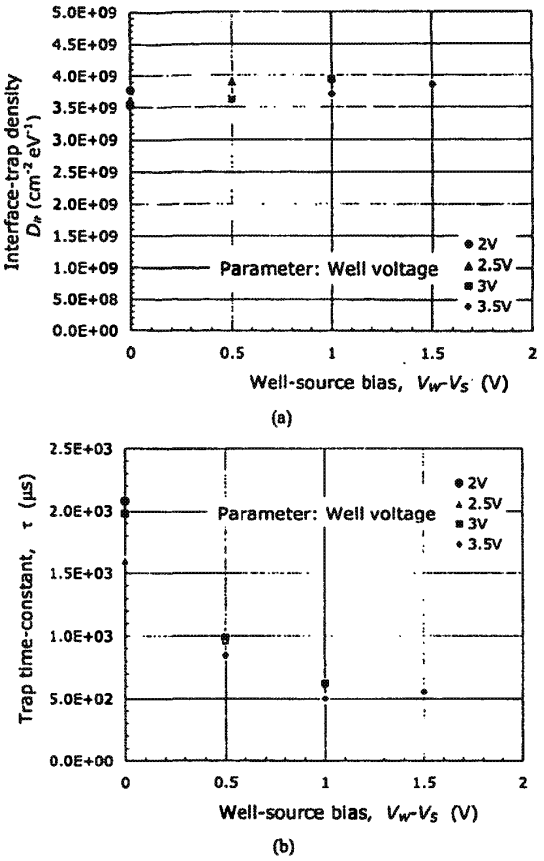


Fig. 3. Experimentally extracted values of charge-pump parameters. (a) Interface-trap density (D_{it}). (b) Trap time-constant (τ).

of I_B at the well terminal. However small this current may be, the exponential sensitivity of the τ-extraction procedure to the terminal current as indicated by (6) leads to an overestimation of τ for small values of $V_W - V_S$ for which I_B attains its largest value.

Assuming a charge pump of minimum area 0.5 μm × 2.5 μm and a typical energy range $\Delta E \approx 0.5$ eV, the extracted value of D_{it} yields $Q_P \approx 3.5$ aC (22 electrons per cycle) from (3). As stated in Section I, the minimum charge pumped by a conventional SC built in the same technology is on the order of femtocoulombs. Quite obviously, the interface-trap charge pump offers at least two orders of magnitude reduction in Q_P.

Shown in Fig. 4 is a set of well–terminal characteristics relevant to current-source applications. These have been extracted from the same $A = 194$ μm^2 pump at $f = 1$ MHz for three different values of T_t. The source bias is fixed at 2 V, which causes sufficiently strong inversion to satisfy (2). Three distinct regions of operation can be identified on these characteristics as explained next.

For any value of V_W beyond 4.65 V, the accumulation condition (1) is not met. The vanishing surface concentration of electrons at the top level of v_G becomes the limiting factor of charge pumping and consequently the current sharply declines with an increasing V_W in this *nonsaturation region*. For V_W less than

SIONYX1403000031.0020

SAMSUNG EX. 1002 - 3041/4148

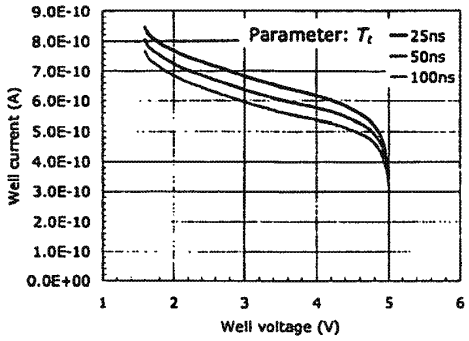


Fig. 4. Bare-pump well–terminal characteristics for $A = 194\ \mu m^2$ and $f = 1$ MHz. Channel length: 5.3 μm.

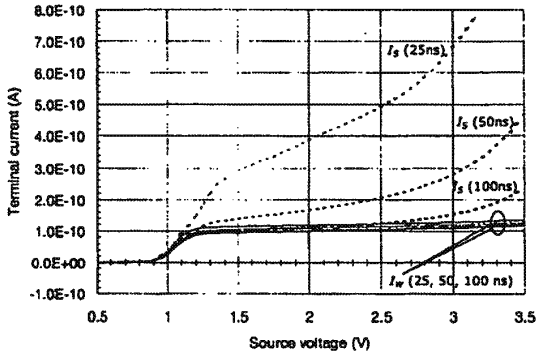


Fig. 5. Variation of the bare-pump source and well currents with well voltage for $A = 251\ \mu m^2$ and $f = 100$ kHz. Channel length: 5.3 μm.

4.65 V, the pump is fully activated and, as predicted by (6), I_W becomes a logarithmic function of T_t and exhibits much reduced sensitivity to V_W in comparison with the nonsaturation region. For $T_t = 100$ ns and $V_W = 3.5$ V, the measured value of the inverse voltage-coefficient $I_W(dV_W/dI_W)$ is around 10 V. Not only the bias dependence of m but also that of I_B via τ contributes to this low value. The pump remains in this *saturation region* of operation as long as $V_W > V_S$, i.e, larger than 2 V in the case of Fig. 4. Any further reduction of V_W forward biases the source–well junction and thus forces the pump into a BJT forward-active region. For all practical purposes, therefore, V_S sets the lower limit of applicable terminal voltage V_W.

A set of source–terminal characteristics I_S-V_S relevant to current-sink applications is given in Fig. 5 which also includes the plots of I_W. These results belong to a pump of $A = 251\ \mu m^2$ driven with $f = 100$ kHz for three different values of T_t. V_W is fixed at 3.5 V to induce strong accumulation to satisfy (1). This also sets an upper limit of 3.5 V to V_S. For V_S less than about 0.9 V, pumping is disabled because the interface cannot be inverted even weakly. A nonsaturation region limited by weak inversion is observed for $0.9\ \text{V} < V_S < 1.3$ V, where I_S and I_W rapidly increase with V_W. No significant disparity between the two currents is observed in this region because the inverting hole population of the channel is too small to generate any significant I_I. The pump enters a saturation region once the inversion becomes strong enough around $V_S = -V_T = 1.3$ V so that condition (2) is satisfied. In this region, the terminal currents become significantly disparate due to the presence of I_I and the difference increases with a decreasing bias $V_W - V_S$ and a decreasing T_t as predicted in Section II. The inverse voltage coefficient of the source-terminal characteristic is also significantly lowered by the presence of I_I.

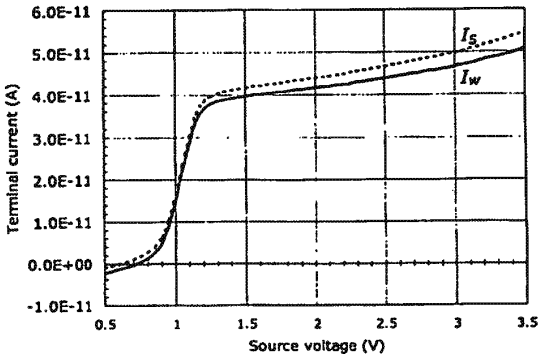


Fig. 6. Variation of bare-pump source and well currents with well voltage for $A = 80.6\ \mu m^2$, $f = 100$ kHz and $T_t = 25$ ns. Channel length: 1.7 μm.

The channel length of the pump on which the data of Fig. 5 have been extracted is 5.3 μm. Shown in Fig. 6 is the source–terminal characteristic extracted for $T_t = 25$ ns on a pump of channel length 1.7 μm and gate area of 80.6 μm^2. The conditions of operation are otherwise the same as those of Fig. 5. A comparison with the I_S (25 ns) curve of Fig. 5 reveals that I_I is indeed a strongly increasing function of channel length, as predicted in Section II.

A further set of experimentation, whose results are not presented here in graphical form, has shown that the parity of I_S and I_W is achievable also with weak accumulation even if inversion is strong. This is not surprising because, unless accumulation is strong enough to satisfy (1), the polarity of the transversal electric field at the channel during the top level of v_G is unfavorable for hole injection away from the interface.

In summary, the dc terminal characteristics of a bare pump exhibit the following properties pertaining to current source/sink/generator applications.

- In a current-source application, the compliance voltage $V_{DD} - V_{W(\max)}$ is around V_{FB}. In an n-gate PMOS, where V_{FB} is small, a current source can therefore operate up close to V_{DD} as verified by the experimental results. In a dual-gate technology, a larger V_{FB} and therefore a larger compliance voltage should be expected. The current sink configuration has a sizeable compliance voltage $V_{S(\min)} - V_{SS}$ around $-V_T$, which generally is inflated by the body effect.
- In all applications, a severe limitation is placed on the terminal voltage by the well-source junction nonforward bias requirement $V_W \geq V_S$.
- Generally, terminal currents are in disparity. However, parity is achieved if inversion or accumulation is weak and/or T_t is long, the channel is short, and $V_W - V_S$ is large.

SIONYX1403000031.0021

SAMSUNG EX. 1002 - 3042/4148

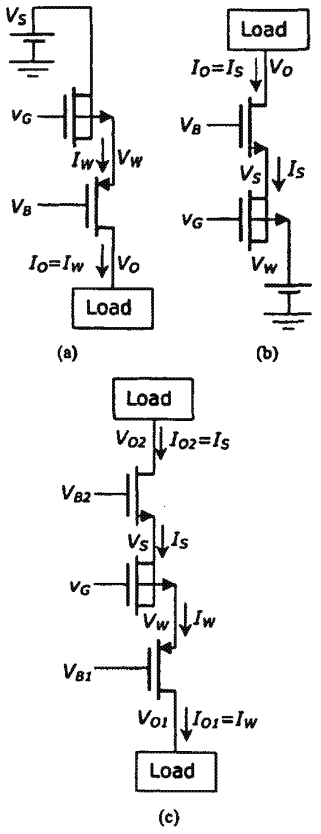


Fig. 7. Cascoded pump current-generator configurations. (a) Current source. (b) Current sink. (c) Floating current generator.

- The inverse voltage-coefficient is low in current-source applications and very low in current-sink applications.

IV. Cascoded Pump

The shortcomings of the bare pump in current source/sink/generator applications are obvious from the properties just itemized. By cascoding the pump, however, all of these can be either eliminated or vastly improved. Shown in Fig. 7 are the schematics of a cascoded pump for all three applications.

A typical set of cascoded current-source I_O-V_O terminal characteristics measured for $f = 1$ MHz and $T_t = 100$ ns are given in Fig. 8. They belong to the same pump whose bare characteristics are shown in Fig. 4. Quite obviously, not only the terminal current is made virtually insensitive to the terminal voltage but also the nonforward biasing requirement is now satisfied without imposing a minimum limit on the terminal voltage. Indeed, as long as V_B keeps V_W above V_S, the terminal voltage can now be freely reduced all the way to ground. Note that the inverse voltage-coefficient is now boosted above 200 V. It is also worth noting that, although cascoding desensitizes the current against variations in the terminal voltage, the sensitivity of the current to the binary levels of the gate excitation remains to be determined solely by the bare pump.

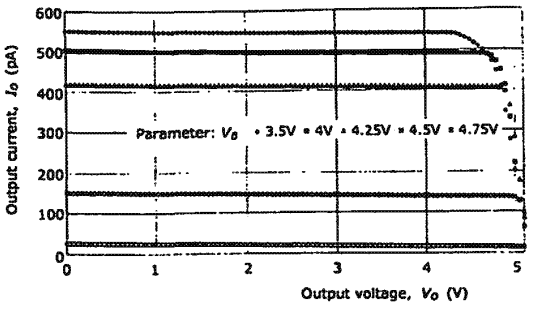


Fig. 8. Cascoded current-source terminal characteristics for $A = 194\ \mu m^2$, $f = 1$ MHz, and $T_t = 100$ ns. Channel length: 5.3 μm. V_B is the cascode bias.

The cascode bias V_B is influential on the performance in a number of different ways. First of all, the higher the V_B, the smaller the compliance voltage. It is obvious from Fig. 8 that a sufficiently high V_B can even eliminate compliance because the pump remains operative even for a well voltage exceeding V_{DD} by a few hundred millivolts as required by the saturated operation of the cascode device. It is also obvious that the higher the V_B, the more pronounced the effect of weak accumulation. This makes the current not only more dependent on the top level of v_G but also less predictable because of the relatively strong dependence on the well voltage in this nonsaturation region. On the other hand, weak accumulation helps decrease the disparity between I_S and I_W as concluded in Section III. The equality of I_S and I_W may be important only in a floating current-generator application but the effect of some degree of weak accumulation on temperature sensitivity can also benefit other applications, as discussed next.

V. Temperature Sensitivity

The temperature coefficient $TC_c \equiv dI_O/I_O dT$ of the output current of a cascoded pump operating as a current source can be expressed as

$$TC_c = TC_b + VC_b \frac{dV_W}{dT} \tag{9}$$

where $TC_b \equiv \partial I_W/I_W \partial T$ and $VC_b \equiv \partial I_W/I_W \partial V_W$ are, respectively, the temperature and voltage coefficients of the bare pump, whereas dV_W/dT represents the temperature sensitivity of the source–gate voltage of the cascoding MOSFET.

Assuming $I_W = I_P$, TC_b is attributible to the temperature sensitivity of ΔE. If accumulation and inversion are not too weak, so that (6) is applicable, then the main factors of this sensitivity are the thermal energy kT and the time constant τ [23]. The latter is inversely proportional to the thermal velocity $v_{th} = \sqrt{3kT/m}$ and the intrinsic carrier concentration $n_i = CT^{3/2} \exp(-E_g/2kT)$, where m is the effective mass, C a constant, and E_g the silicon bandgap. Ignoring the temperature dependence of E_g, TC_b can be expressed as

$$TC_b = -\frac{1}{T}\left(\frac{E_g + 4kT}{\Delta E} - 1\right)$$

which, for $T = 300$ °C and a typical energy range of one half the bandgap, predicts a coefficient around -0.4% per degree. Re-

SIONYX1403000031.0022

SAMSUNG EX. 1002 - 3043/4148

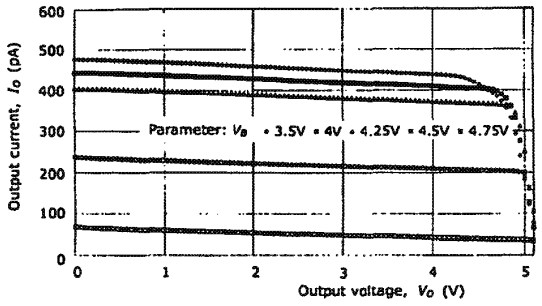


Fig. 9. Cascoded current-source high temperature (70 °C) terminal characteristics for $A = 194\ \mu m^2$, $f = 1$ MHz, and $T_t = 100$ ns. Channel length: 5.3 μm. V_B is the cascode bias.

turning to the last term in (9) and considering that the cascoding MOSFET operates in the subthreshold mode due to the low level of current, we typically expect $dV_W/dT \approx -4$ mV/°C [24], [25]. Therefore, it seems possible to achieve a zero TC_c by biasing the pump around the point of its well–terminal characteristic where $VC_b \approx -100\%$ per volt. Shown in Fig. 9 are the $T = 70$°C terminal characteristics of the cascoded pump whose room-temperature characteristics are given in Fig. 8. A comparison between the two not only verifies the expected temperature sensitivity of the bare pump but also clearly shows that, indeed, a temperature-insensitive current is available for a bias around $V_B = 4.25$ V.

VI. Pulse Feedthrough and Complementary Pumping

The mobile charge exchanged between the channel and source/well nodes during each transition of v_G is many orders of magnitude larger than the charge Q_P pumped via interface traps. The resulting pulse feedthrough makes the bare pump totally useless as an integrated current source/sink because the terminal capacitance required for suppression is prohibitively large. This problem is greatly facilitated by cascoding alone and is virtually eliminated if cascoding is combined with complementary pumping. For a quantitative evaluation of pulse feedthrough, first, consider the cascoded current source given in Fig. 10(a). The simulated transient response of the circuit to the trapezoidal gate drive of Fig. 10(b) is shown in the rest of the same figure.

During the downward transition of v_G, initially the accumulating electrons are transported to the well until the flatband condition is reached. From then on, the expansion of the depletion region continues transporting electrons to the well up until the onset of inversion. The rate of charge transfer is represented by the negative well–current pulse observed in Fig. 10(c) and the resulting drop in well voltage is identified as ΔV_W in Fig. 10(d). The magnitude of the total charge transported can be estimated from

$$Q_W = AC_{ox}(V_{DD} - V_W - V_{FB}) + AC_{ox}\gamma_W\sqrt{V_W - V_S - 2\phi_{FW}} \quad (10)$$

where C_{ox} is the oxide capacitance per unit area and ϕ_{FW} is the (negative) equilibrium Fermi potential of the well. The first term on the right-hand side of (10) is the accumulation charge. The second term represents the electron charge displaced by the expansion of the depletion region. During the upward transition of v_G, the channel not only receives the ITCP charge Q_P from the well but also reclaims Q_W. Since the latter is many orders of magnitude larger than the former, the drop ΔV_W on the well voltage is determined almost solely by the bilateral Q_W and is given by

$$\Delta V_W = \frac{Q_W}{C_W} \quad (11)$$

where C_W represents the total capacitance of the well node. ΔV_W forces the channel current of the cascoding MOSFET to drop from an $I_{O(max)}$ to an $I_{O(min)}$ as observed in Fig. 10(e). Considering the fact that the cascoding MOSFET operates in the subthreshold mode, the ratio of these two current levels can be described as

$$\frac{I_{O(max)}}{I_{O(min)}} = \exp\left(\frac{2.30}{S}\Delta V_W\right) \quad (12)$$

where S denotes the subthreshold slope. Also, the average of these two levels equals I_P, i.e.,

$$\frac{1}{2}\left[I_{O(min)} + I_{O(max)}\right] = I_P. \quad (13)$$

Finally, assuming that the ripple on the load current i_L is much smaller than $I_{O(max)} - I_{O(min)}$, so that $i_L \approx I_P$, the ripple ΔV_O on the output voltage can be expressed as

$$\Delta V_O = \left[I_{O(max)} - I_P\right]\frac{T}{2C_O} \quad (14)$$

where $T = 1/f$ is the period of gate excitation and C_O is total output capacitance. Assuming a single MOSFET load operating under subthreshold conditions, which also represents the worst case of ripple in a differential-pair load,[2] the relative ripple on the load current can be expressed as

$$\frac{\Delta I_L}{I_L} = \exp\left(2.3\frac{\Delta V_O}{S}\right) - 1 \quad (15)$$

which indicates ΔV_O as a direct measure of the pulse feedthrough performance of the current source. Using (11)–(14), we relate ΔV_O to its driving force Q_W as follows:

$$\Delta V_O = \frac{TI_P}{2C_O}\frac{\exp\left(\frac{2.3Q_W}{SC_W}\right) - 1}{\exp\left(\frac{2.3Q_W}{SC_W}\right) + 1}. \quad (16)$$

To identify the most feasible approach to suppressing the pulse feedthrough effect, first consider the effect of C_W on ΔV_O. For $C_W < 2.3Q_W/S$, this capacitance is virtually ineffective on ΔV_O and the latter is well approximated by

$$\Delta V_O = \frac{TI_P}{2C_O}. \quad (17)$$

ΔV_O becomes inversely proportional to C_W for $C_W > 2.3Q_W/S$, but this condition implies a capacitance far in

[2]The output current of a differential pair carries the largest ripple when one of the two branches is cut off and the other conducts the entire bias current.

SIONYX1403000031.0023

SAMSUNG EX. 1002 - 3044/4148

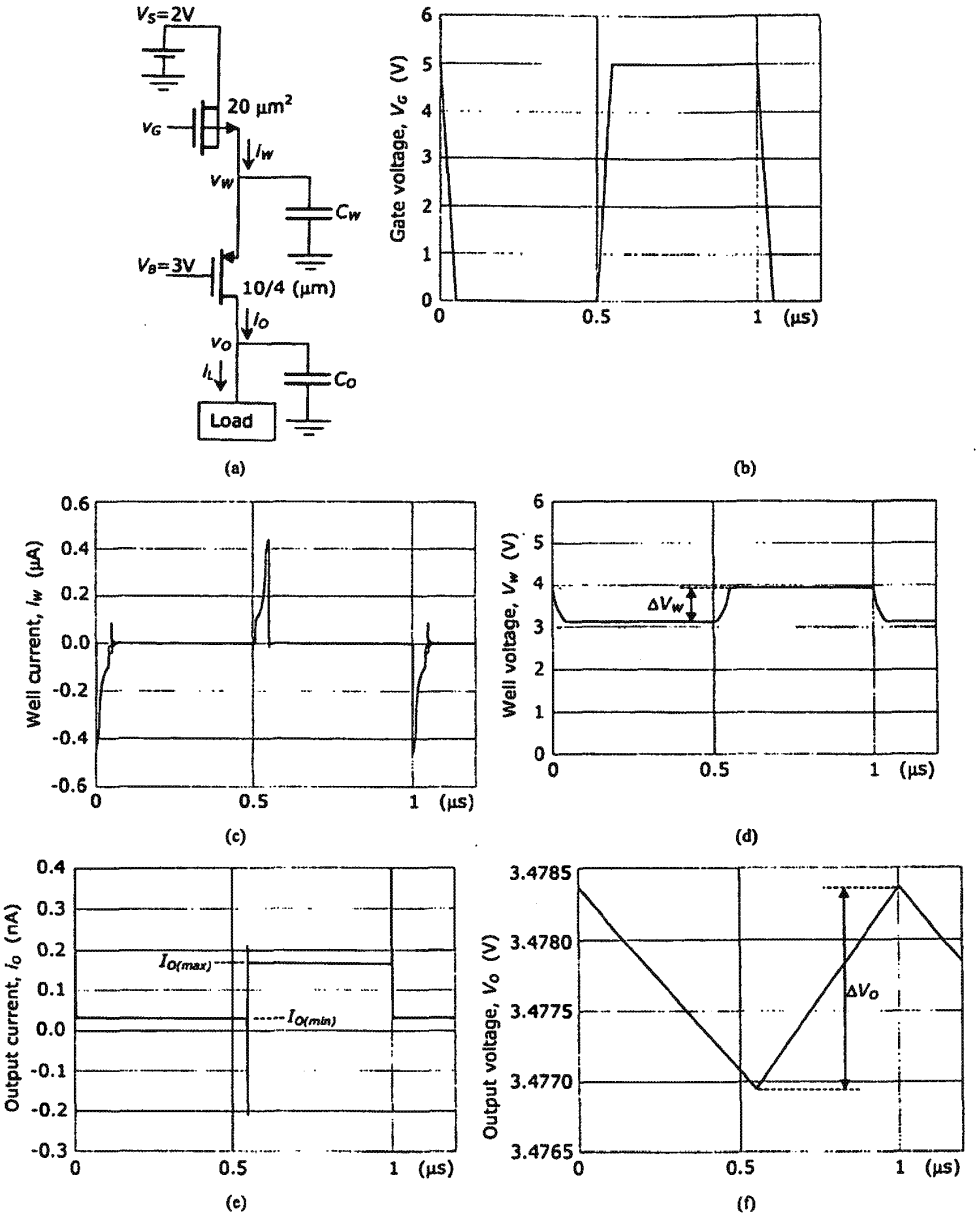


Fig. 10. Spice-simulated waveforms of a cascoded current source. (a) Circuit schematic. (b) Gate voltage. (c) Well current. (d) Well voltage. (e) Output current. (f) Output voltage.

excess of the parasitic capacitance of the well node. The simulated pump of Fig. 10, for example, puts out $Q_W = 80$ fC as calculated from (10), which, for $S = 80$ mV/decade, sets a lower effective limit of 2.3 pF for C_W. Even for the unrealistically optimistic biasing conditions $V_{DD} - V_W - V_{FB} \approx 0$ and $V_W = V_S$ causing a negligible accumulation and a minimum depletion volume, respectively, C_W must be at least 0.65 pF to have any significant effect on ΔV_O. Considering the fact that the parasitic C_W of the simulated circuit is less than 0.1 pF, it is necessary to add a sizeable capacitor to the well node if C_W is to be a meaningful instrument of feedthrough suppression. If this costly approach is abandoned, then ΔV_O will be determined by C_O alone as indicated by (17). The simulated circuit, whose load is a 20 μm/4 μm PMOS device emulating the twin drivers of a differential pair, has a parasitic C_O around 40 fF for which (17) yields $\Delta V_O = 1.25$ mV, which agrees well with Fig. 10(f). For better suppression, C_O can be augmented with additional capacitance but there exists an alternative which manipulates the duration of the dip in v_W to suppress the feedthrough. In this scheme two identical pumps operate in parallel with complementary gate excitation as shown in Fig. 11(a) and (b). The waveforms shown in the rest of Fig. 11

SIONYX1403000031.0024

SAMSUNG EX. 1002 - 3045/4148

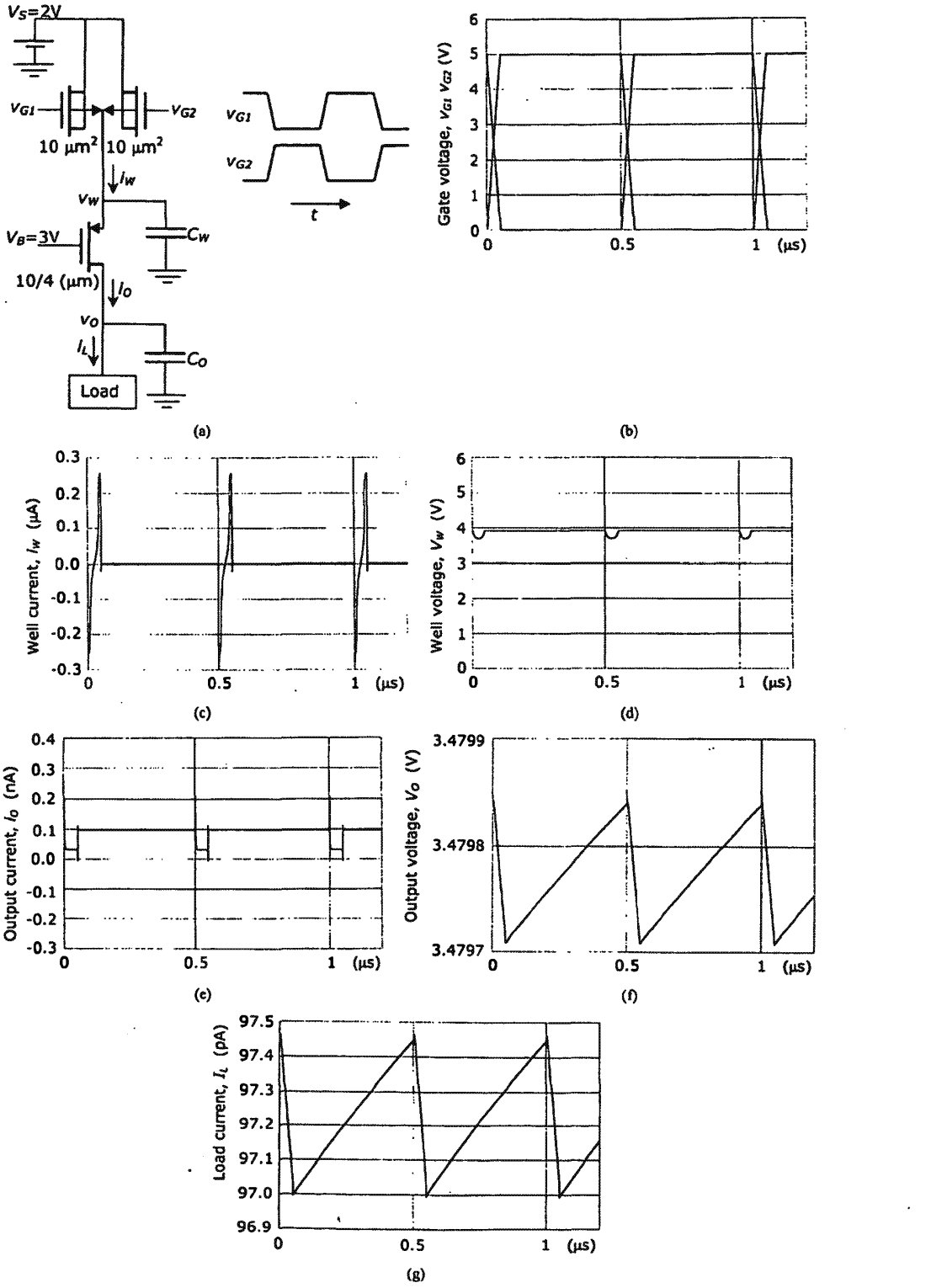


Fig. 11. Spice-simulated waveforms of a cascoded complemetary current source. (a) Circuit schematic. (b) Gate voltage. (c) Well current. (d) Well voltage. (e) Output current. (f) Output voltage. (g) Load current.

SIONYX1403000031.0025

SAMSUNG EX. 1002 - 3046/4148

are simulated with the same conditions as Fig. 10 with the only exception that two 10-μm^2 pumps are deployed instead of one 20-μm^2. A comparison between the well–current waveforms of Figs. 10(c) and 11(c) clearly indicates that Q_W is considerably reduced by mobile charge sharing between the two pumps. This causes a smaller ΔV_W as observed in Fig. 11(d), but, more importantly, the duration of ΔV_W is now reduced from $T/2$ to the transition time T_t. The resulting ΔV_O is given by

$$\Delta V_O = \frac{T_t I_P}{C_O} \tag{18}$$

where I_P is the total of two pump currents. A comparison between (17) and (18) indicates that the pulse feedthrough admitted by complementary pumping is a factor of $T/2T_t$ smaller than its single-pump counterpart. The waveform in Fig. 11(f), indicating $\Delta V_O = 125\ \mu V$, verifies this prediction for the simulated circuit. The corresponding load-current relative ripple, as calculated from (15), is about 5000 ppm, which is also verified by the waveform shown in Fig. 11(g). These figures exemplify the level of suppression attainable even with parasitic capacitances when cascoding is combined with complementary pumping. It is also interesting to note that the load-current ripple in the case of complementary pumping is independent of the magnitude of the root cause, Q_W. The reason is that, unless the well node is equipped with a very large C_W, even a very small Q_W is more than enough to effectively suppress I_O during the transition periods, as seen in Fig. 11(e). The ripple is, therefore, determined mainly by the duty factor of the resulting I_O pulses. This is why the geometrical features and bias conditions of the pumps have no significant effect on ripple suppression, as indicated by (18).

As a final word of caution about feedthrough in the current-source configurations of Figs. 10(a) and 11(a), we emphasize the importance of building the cascoding PMOS in an individual well tied to a dc voltage, say V_{DD}, because if it shares the same well with the pumps the capacitive coupling between the common well and the output node will create another path for pulse feedthrough.

The analyses and arguments presented here for pulse feedthrough in a current-source application of the cascoded pump is valid also for current-sink applications; the only difference is the composition of the charge dumped. The complementary pumping scheme is, therefore, equally useful for suppressing this effect in current-sink applications.

VII. Controllability, Matching, Reliability, and Trimming

Gate area and charge pumping frequency provide two degrees of freedom for setting and controlling the current with a reasonable linearity in a wide range. Shown in Fig. 12 is the variation of I_W with channel length for a fixed channel width of 23.7 μm. The linear relationship predicted by (6) between the current and area holds with the exception of the smallest pump of 0.5 μm in length. This deviation is attributible to the spatial variation of D_{it}, which is known to increase near the source/drain junctions of a MOSFET. As shown in Section III, channel length is also an influential parameter of the disparity between I_W and

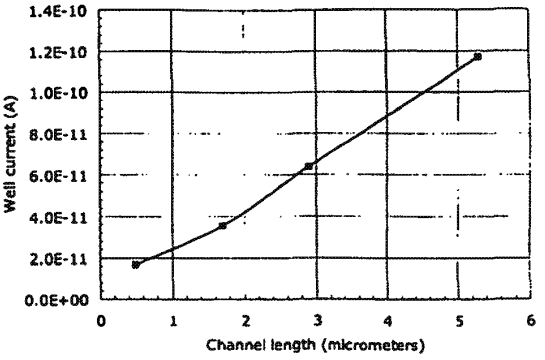


Fig. 12. Variation of well current with pump channel length. Channel width is fixed at 23.7 μm.

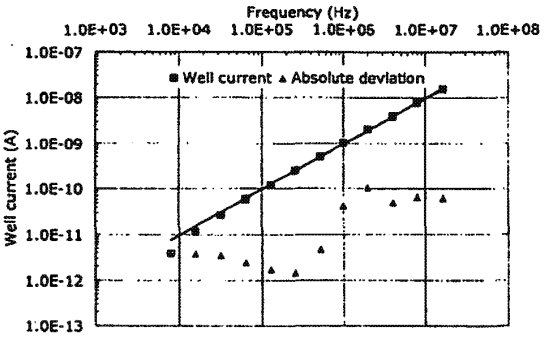


Fig. 13. Variation of well current with frequency. Channel width is fixed at 23.7 μm. Also shown are the regression line and absolute deviation from linearity.

I_S. Although biasing the pump to weak accumulation or inversion with the cascode MOSFET greatly reduces the disparity, it is still prudent to minimize the channel length if parity is crucial and then adjust the channel width to set the desired area.

The I_W-f characteristic of our 194-μm^2 test pump extracted for $T_t = 5$ ns is given in Fig. 13 together with the regression line $I_W = 0.96\ (\text{fA/Hz})f$. The same figure also includes the plot of absolute deviation from linearity. The relative deviation remains less than 5% for more than two decades at the upper end of the range and increases rapidly under the influence of leakage currents below $f = 64$ kHz. Although not shown in Fig. 13, the linear range actually extends into higher frequencies and eventually starts breaking down as the accumulation and inversion half periods become too short for the traps to complete carrier capture processes. Weak accumulation or inversion lowers the upper limit of the linear range by slowing down the rate of these processes. Needless to say, selecting a long T_t for the purpose of matching I_W and I_S will decrease the frequency at which these phenomena become effective. Nevertheless, the range and linearity of control by frequency is a very valuable asset of the charge pump because it adds precise tunability to the circuit biased with the pump.

Repeatibility and matching properties of the interface-trap charge pump are most likely to be determined by the distribution of D_{it}, which is not one of the tightly controlled parameters of

SIONYX1403000031.0026

SAMSUNG EX. 1002 - 3047/4148

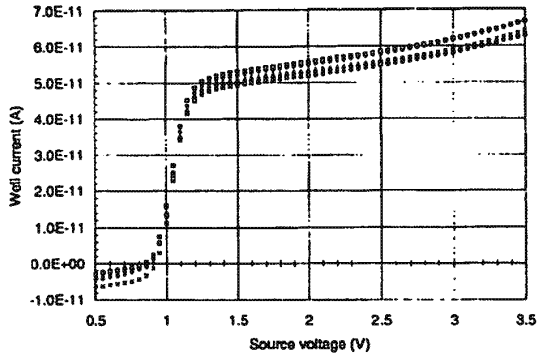


Fig. 14. Variation of well current with source voltage for $A = 194\ \mu m^2$ and $f = 100$ kHz on five different chips of the same run.

MOS devices. Although it may have order-of-magnitude variation between different technologies depending on the annealing processes applied, we expect it to be relatively repeatible in a given technology as long as the annealing procedures remain unchanged. Shown in Fig. 14 are the experimental I_W-V_S characteristics of our 194-μm^2 pump as extracted for $f = 100$ kHz on five different chips of the same run. Note that the negative current indicated for about $V_S < 0.8$ V is due to leakage only. Full pumping is enabled for $V_S > 1.3$ V and the difference between the charge-pumping and leakage currents flows as a positive I_W. Clearly, the observed spread is attributible more to leakage than charge pumping. Still, the relative standard deviation of I_W is less than 3% even without any correction for leakage. Although this result is indicative of a matching performance better than those of on-chip MOSFETs of comparable area operating under subthreshold conditions [26], the number of samples examined in this work is too small to generalize this conclusion with any degree of confidence.

It is well known that hot-carrier injection can lead to interface-trap generation in MOSFETs, creating long-term reliability problems [27]. This is not expected to be a concern in the case of the present application because the pump does not support any high-velocity carrier motion in the channel. The Fowler–Nordheim (FN) tunneling process is also known to generate interface traps if the gate-oxide field is large enough to activate it [27]. For an operation complying with the rated supply limits this should not be a problem either. On the contrary, FN may possibly be exploited as an instrument of trimming the pump after fabrication.

VIII. Transconductor and Low-Frequency OTA-C Filter Applications

We have built single-ended and fully differential OTA circuits biased with complementary cascoded charge pumps. Shown in Fig. 15 is the circuit schematic of the single-ended OTA. All devices, including charge pumps, are sized $W/L = 23.7\ \mu m/4.2\ \mu m$. The measured transconductance characteristics are given in Fig. 16 for $T_t = 25$ ns and f varying in octaves in the range 15 kHz–16 MHz corresponding to a bias-current tuning range of 16 pA–6 nA. As discussed in Section VII, the linearity of tuning by frequency deteriorates

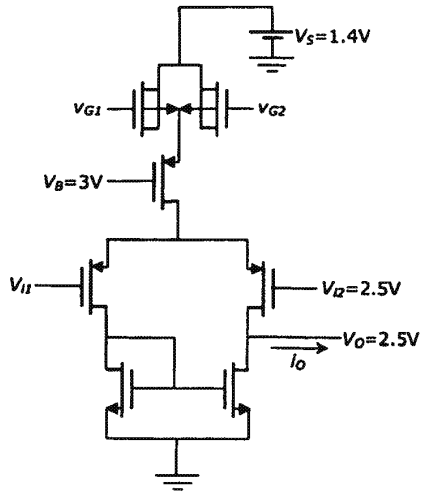


Fig. 15. Circuit schematic of the single-ended transconductor circuit biased with a cascoded complementary charge-pump current source.

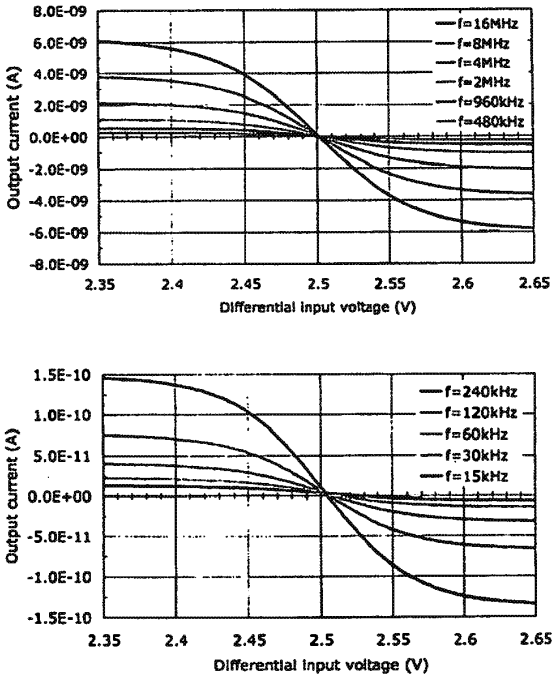


Fig. 16. Characteristics of the transconductor of Fig. 15.

due to leakage at the lower end and due to incomplete capture processes at the higher end. The measured input offset of the OTA is plotted in Fig. 17 as a function of bias current. Despite the large disparity between the drain-source voltages of the current-mirror load devices, the offset remains smaller than 5 mV for any bias greater than 80 pA. The rapidly increasing offset observed for smaller bias is due to leakage.

We have also put to test the floating current-generator property of the complementary cascoded charge pump by biasing a fully differential OTA with it, as shown in

SIONYX1403000031.0027

SAMSUNG EX. 1002 - 3048/4148

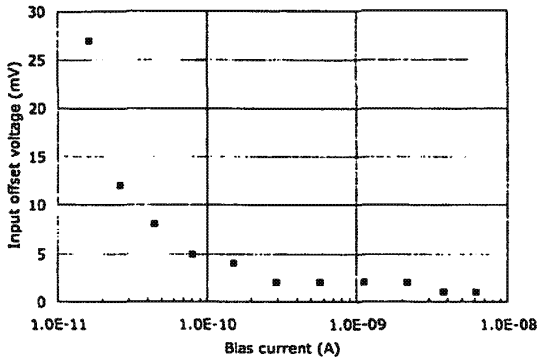


Fig. 17. Input-referred offset of the transconductor of Fig. 15.

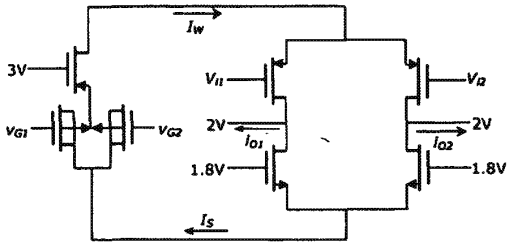


Fig. 18. Circuit schematic of the fully differential transconductor circuit biased with a cascoded complementary floating charge-pump current generator.

Fig. 18. Again, all devices including charge pumps are sized $W/L = 23.7\ \mu m/4.2\ \mu m$ and the frequency is 1 MHz. Note that the circuit is powered only by the pulsed excitation of the complementary charge pump gates and no supply connection is made to V_{DD} or V_{SS}. Each of the two NMOS transistors conducts $I_S/2$, while each of the driver PMOS transistors is biased with $I_W/2$. The experimental bias conditions indicated on the schematic force the pumps to operate with strong inversion and accumulation. As explained in Section III, selecting a short T_t under these conditions may result in a significant disparity between I_S and I_W and therefore lead to a current offset when the OTA is balanced with identical input voltages. Such an offset of about -60 pA is clearly observable on the experimental transconductance characteristics extracted for $T_t = 25$ ns by varying V_{i1} for a constant $V_{i2} = 2.475$ V and shown in Fig. 19. When the experiment is repeated for $T_t = 100$ ns, however, the offset virtually disappears, as shown in Fig. 20.

As a further step of experimental evaluation, we have designed first-order low-pass and high-pass OTA-C filter sections with charge-pump biased single-ended and floating OTAs and 15-pF capacitors and used them to build a fully differential bandpass OTA-C filter. Shown in Fig. 21 is the photomicrograph of the 2.2 mm × 2.2 mm MOSIS tiny chip carrying this fully integrated filter in addition to stand-alone filter sections, OTAs, and charge-pump current generator structures. Also shown is a blow-up of a typical cascoded current source built with complementary charge pumps. The corner frequencies of the low-pass and high-pass sections of the filter are independently tunable by means of two separate pump drives. Tests

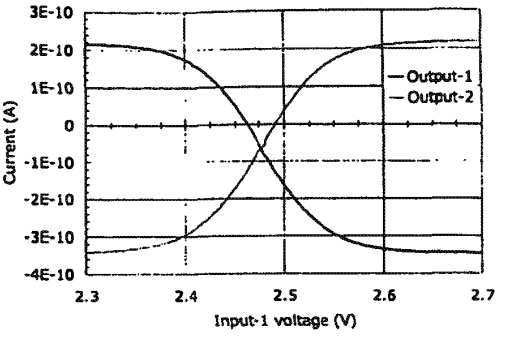


Fig. 19. Characteristics of the transconductor of Fig. 18 for $T_t = 25$ ns.

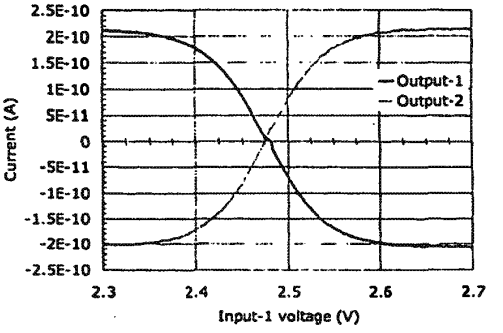


Fig. 20. Characteristics of the transconductor of Fig. 18 for $T_t = 100$ ns.

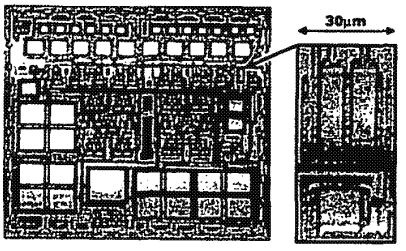


Fig. 21. Photomicrograph of the AMIS 0.5-μm CMOS chip containing an OTA-C bandpass filter in addition to stand-alone low-pass and high-pass filter sections, OTAs, and charge-pump current generator structures. The blow-up shows a typical cascoded current source built with complementary charge pumps.

indicate a linearly tunable range of two decades above 0.3 Hz. Design details and experimental evaluation of this filter are beyond the scope of this paper and will be published elsewhere.

IX. Conclusion

In this work, we have explored the MOS interface-trap charge pump as an ultralow current generator for analog CMOS applications. Charge pumping techniques in general are suitable for ultralow current generation because the linear controllability of current by frequency is maintained regardless of the level of current. What is fundamentally attractive about the interface-trap pump is that it exhibits the same property but the minimum charge it puts out per cycle is at least two orders of magnitude

SIONYX1403000031.0028

SAMSUNG EX. 1002 - 3049/4148

smaller than that of a conventional SC core for a given technology. This helps generate the same current more accurately at a much higher frequency with a much smaller filter capacitance.

Our work shows that a bare pump in the form of single PMOSFET hardly qualifies as a constant-current generator because of its excessive pulse feedthrough, low output resistance, and the restrictions imposed on its terminal voltages by the compliance and nonforward bias conditions. When cascoded, however, these shortcomings are removed. Cascoding also enables biasing for weak inversion or accumulation, which in turn not only effectively eliminates the disparity of the two terminal currents but also makes a temperature-insensitive biasing possible. The effect of pulse feedthrough is virtually eliminated with parasitic capacitances when two pumps are operated in a complementary fashion. Our tests on a 194-μm^2 pump indicates less than 3% mismatch, but the small number of samples examined prevents us from reaching a general conclusion about the matching properties of the charge pump. The tests on single-ended and fully differential transconductor circuits biased with cascoded complementary charge pump constant-current generator configurations indicate full functionality over a bias range more than two decades wide.

REFERENCES

[1] C. C. Enz and E. A. Vittoz, "CMOS low-power analog circuit design," *Designing Low Power Digital Systems, Emerging Technologies*, pp. 79–133, 1996.

[2] A. G. Andreou, "Exploiting device physics in circuit design for efficient computational functions in analog VLSI," in *Low-Voltage/Low-Power Integrated Circuits and Systems*, E. S. Sinencio and A. G. Andreou, Eds. New York: IEEE Press, 1999, pp. 85–132.

[3] Y. Papananos, T. Georgantas, and Y. Tsividis, "Design considerations and implementation of very low frequency continuous-time CMOS monolithic filters," *IEE Proc.-Circuits Devices Syst.*, vol. 144, pp. 68–74, 1997.

[4] M. Steyaert, P. Kinget, W. Sansen, and J. Van der Spiegel, "Full integration of extremely large time constants in CMOS," *Electron. Lett.*, vol. 27, pp. 790–791, 1991.

[5] J. S. Martinez and J. S. Sufier, "Very low frequency IC filters," in *Proc. 38th IEEE Midwest Symp. Circuits and Systems*, vol. 2, 1996, pp. 1325–1328.

[6] C.-C. Hung, K. Halonen, M. Ismail, and V. Porra, "Micropower CMOS GM-C filters for speech signal processing," in *Proc. 1997 IEEE Int. Symp. Circuits Syst.*, vol. 3, 1997, pp. 1972–1975.

[7] S. S. Bustos, J. S. Martinez, F. Maloberti, and E. S. Sinencio, "A 60-dB dynamic-range CMOS sixth-order 2.4-Hz low-pass filter for medical applications," *IEEE Trans. Circuits Syst. II*, vol. 47, pp. 1391–1398, 2000.

[8] A. Olesin, K. K. L. Luke, and R. D. Lee, "Switched Capacitor Precision Current Source," US Patent 4 373 357, 1983.

[9] G. Torelli and A. de la Plaza, "Tracking switched-capacitor CMOS current reference," *IEE Proc.-Circuits Devices Syst.*, vol. 145, pp. 44–47, 1998.

[10] B. Razavi, *Design of Analog CMOS Integrated Circuits*. New York: McGraw-Hill, 2001, p. 392.

[11] J. S. Brugler and P. G. A. Jespers, "Charge pumping in MOS devices," *IEEE Trans. Electron Devices*, vol. ED-16, pp. 297–302, 1969.

[12] G. Groeseneken, H. E. Maes, N. Beltran, and R. F. de Keersmaecker, "A reliable approach to charge-pumping measurements in MOS transistors," *IEEE Trans. Electron Devices*, vol. ED-31, pp. 42–53, 1984.

[13] U. Çilingiroğlu, "A general model for interface-trap charge-pumping effects in MOS devices," *Solid-State Electron.*, vol. 28, pp. 1127–1141, 1985.

[14] G. Gibhaudo and N. S. Saks, "A time domain analysis of the charge pumping current," *J. Appl. Phys.*, vol. 64, pp. 4751–4754, 1988.

[15] ——, "Investigation of the charge pumping current in metal-oxide-semiconductor structures," *J. Appl. Phys.*, vol. 65, pp. 4311–4318, 1989.

[16] M. S. Ebel, J. Gionis, and W. M. Regitz, "A 4096-bit high-speed emitter-coupled-logic (ECL) compatible random-access memory," *IEEE J. Solid-State Circuits*, vol. SC-10, pp. 262–267, 1975.

[17] U. Çilingiroğlu, "A charge-pumping-loop concept for static MOS/RAM cells," *IEEE J. Solid-State Circuits*, vol. SC-14, pp. 599–603, 1979.

[18] ——, "A two-device bistable memory circuit without feedback loop," *IEEE J. Solid-State Circuits*, vol. SC-17, pp. 593–596, 1982.

[19] ——, "Bistable storage in pulsed gate-controlled diodes," *IEEE Electron Device Lett.*, vol. 12, pp. 338–340, 1991.

[20] T. P. Chen, "Frequency-controlled low-level current source based on charge pumping," *Electron. Lett.*, vol. 37, pp. 1046–1047, 2001.

[21] G. Van den bosch, G. Groeseneken, and H. E. Maes, "On the geometric component of charge-pumping current in MOSFETs," *IEEE Electron Device Lett.*, vol. 14, pp. 107–109, 1993.

[22] P. Habaš, G. Groeseneken, and G. Van den bosch, "Geometric current component in charge-pumping measurements," in *Proc. Int. Conf. Microelectronics*, 1997, pp. 599–604.

[23] G. Van den bosch, G. V. Groeseneken, P. Heremans, and H. E. Maes, "Spectroscopic charge pumping: A new procedure for measuring interface trap distributions on MOS transistors," *IEEE Trans. Electron Devices*, vol. 38, pp. 1820–1831, 1991.

[24] F. S. Shoucair, "Scaling, subthreshold and leakage current matching characteristics in high temperature 25°C–250°C VLSI CMOS devices," *IEEE Trans. Comp., Hybrids Manufact. Technol.*, vol. 12, pp. 780–788, 1989.

[25] E. P. Vandamme, Ph. Jansen, and L. Deferm, "Modeling the subthreshold swing in MOSFETs," *IEEE Electron Device Lett.*, vol. 18, pp. 369–371, 1997.

[26] F. Forti and M. E. Wright, "Measurement of MOS current mismatch in the weak inversion region," *IEEE J. Solid-State Circuits*, vol. 29, pp. 138–142, 1994.

[27] J.-H. Shiue, J. Y.-M. Lee, and T.-S. Chao, "A study of interface trap generation by Fowler-Nordheim and substrate-hot-carrier stresses for 4-nm thick gate oxides," *IEEE Trans. Electron Devices*, vol. 46, pp. 1705–1710, 1999.



Uğur Çilingiroğlu received the M.Sc. degree in electronics engineering from Istanbul Technical University, Istanbul, Turkey, in 1973, and the Ph.D. degree in microelectronics from Southampton University, Southampton, U.K., in 1978.

He held Assistant and Associate Professor positions at Istanbul Technical University between 1978–1988. He has been a Professor at Istanbul Technical University since 1991. He is also currently a Professor in the Department of Electrical Engineering, Texas A&M University, College Station, where he was a Member of Faculty during 1985–1986 and 1988–1991. Prior to 1984, he was a Consultant with the Turkish Scientific and Technological Research Council, where he contributed to the planning and implementation of a semiconductor laboratory. From 1986 to 1988, he was a Consultant to Teletas (now Alcatel), where he organized industrial training courses on CMOS technology and ASIC design. He spent the summer of 1990 with Hewlett Packard, Manufacturing Test Division, where he invented the capacitive in-circuit testing technique known today as TestJet Technology. He also held the position of Academic Coordinator with the ETA ASIC Design Center from 1991 to 1999, where he was responsible for the management of about 15 industrial ASIC design projects. He also was Head of the Department of Electronics and Communication Engineering, Istanbul Technical University, in 1998. He holds seven patents and is the author of *Systematic Analysis of Bipolar and MOS Transistors* (Norwood, MA: Artech House, 1993). His research activity spans all aspects of microelectronics, ranging from device physics and technology to integrated circuit design.

Dr. Çilingiroğlu held a Fulbright Research Fellowship in the Department of Electrical Engineering, Texas A&M University, in 1984. He received a CENTO Scholarship in 1973 and an Eta Kappa Nu Outstanding Professor Award in 1990.

SIONYX1403000031.0029

SAMSUNG EX. 1002 - 3050/4148



Adriana Becker-Gómez was born in Mexico City, Mexico, in 1966. She received the B.S.E.E. degree from Universidad Iberoamericana, Mexico, in 1989 and the M.S. degree in electrical engineering from Texas A&M University, College Station.

She worked as a Research and Development Engineer from 1989 to 1993, developing quality control systems for the automotive industry. She also was a Lecturer and a Teaching Assistant of microprocessor architectures, digital systems, and structured programming from 1992 to 1996. She also worked as an Assistant to the dean of the Graduate Studies of Engineering Division at Universidad Nacional Autonoma de Mexico. She worked in the Preamp R&D SP Group at Texas Instruments, Dallas, TX, as a Design Engineer on high-precision comparator circuit design from September of 2001 to January of 2002. Her research interests are in the design of analog and mixed signal circuits, sensors, and signal processing.

She was a recipient of a Ministry of Education Scholarship during her bachelor studies. She received a Texas Instruments ADC Grant during her first year and then became a CONACYT scholarship recipient.



Kenton T. Veeder (S'96–M'01) received the B.S. degree in electrical engineering from the University of Idaho, Ames, in 1999 and the M.S. degree in electrical engineering from Texas A&M University, College Station, in 2001.

While in the Analog & Mixed-Signal Group at Texas A&M University, he concentrated on analog IC design and solid-state device phenomena. He is currently a Senior Electrical Engineer with Raytheon Infrared Operations (RIO, formerly Hughes Santa Barbara Research Center), Santa Barbara, CA. He is leading an IC design team in the pursuit of very large imaging arrays with on-chip data conversion. His research interests at RIO involve analog-to-digital conversion for imaging arrays, low-power readout techniques, and complete SoC integration.

SIONYX1403000031.0030

SAMSUNG EX. 1002 - 3051/4148

Electronic Acknowledgement Receipt

EFS ID:	26311677
Application Number:	14747875
International Application Number:	
Confirmation Number:	1722
Title of Invention:	Pixel Isolation Elements, Devices and Associated Methods
First Named Inventor/Applicant Name:	Martin U. Pralle
Customer Number:	136549
Filer:	Andrew W. Schultz
Filer Authorized By:	
Attorney Docket Number:	143705.05211
Receipt Date:	11-JUL-2016
Filing Date:	23-JUN-2015
Time Stamp:	16:25:04
Application Type:	Utility under 35 USC 111(a)

Payment information:

Submitted with Payment	no

File Listing:

Document Number	Document Description	File Name	File Size(Bytes)/ Message Digest	Multi Part /.zip	Pages (if appl.)
1	Foreign Reference	JP2003163360A.pdf	1535726 a6e4244c57506669f2af5829ffc18217cfa1e84b	no	25
Warnings:					

SIONYX1403000031.0031

Information:					
2	Foreign Reference	JP2004273886A.pdf	561439 bf24d5c77c819f42dc5745d9d1bf8e3c8cf8a53d	no	13
Warnings:					
Information:					
3	Foreign Reference	JP2004273887.pdf	4197377 1f7a61c1413d897fe3726558efddc0d2b4280051	no	12
Warnings:					
Information:					
4	Foreign Reference	JPH06267868.pdf	282377 d229a95d4f27149940385d5a6821b8c2ccc1535b	no	7
Warnings:					
Information:					
5	Foreign Reference	JP2007180642.pdf	369136 5bdb534131ce04bfcadbaa4a598b5cf0d7daaec78	no	10
Warnings:					
Information:					
6	Foreign Reference	JP2007180643.pdf	1322159 54b4fa964d5c319cb8220b67a03b5ccb1d2dadc2	no	23
Warnings:					
Information:					
7	Foreign Reference	JP2007305675.pdf	655388 4bcab694c9bcd8154b021b6342a127bff11ac7da	no	11
Warnings:					
Information:					
8	Foreign Reference	JP2008187003_FujitsuLtd.pdf	328750 0b5834e6dc5d5d9c81b7cea594c249f9717ec256	no	16
Warnings:					
Information:					

9	Foreign Reference	JPH07183484.pdf	325806 4bdce2973241c72c79bbdc162c2f053400e6e468	no	9
Warnings:					
Information:					
10	Foreign Reference	JP2011091128.pdf	616124 140619fcbc4f5939794e8ad0de7585d5983ae0f8	no	13
Warnings:					
Information:					
11	Foreign Reference	JP9148594.pdf	842204 f28986516ce871286044b0fc200983cccd1ba95c	no	7
Warnings:					
Information:					
12	Foreign Reference	JPH09298308_SharpKK.pdf	354791 2f65b811d7c832a8ef40d0f5c2b96fb0410779e0	no	12
Warnings:					
Information:					
13	Foreign Reference	JPH06104414.pdf	618760 08b918c9c2c93229e8f5b71dc7b7aa4c28c936b2	no	13
Warnings:					
Information:					
14	Foreign Reference	JP11077348.pdf	537832 a0d6af0a3d440ce92a2d59af24d6f17e62cc6028	no	8
Warnings:					
Information:					
15	Foreign Reference	JP11097724.pdf	418030 388cf460be12ae7b4f3e22a0d80a7074841fefbd	no	5
Warnings:					
Information:					

16	Foreign Reference	JP2001189478.pdf	988458 7c05ae25d1f85455a612ccdc71e87ea064eaa34f	no	9
Warnings:					
Information:					
17	Foreign Reference	JP2001339057.pdf	917067 bdb90a215a9643ddd48da1a7c0e971aca0d8c1c2	no	11
Warnings:					
Information:					
18	Foreign Reference	JP2006173381.pdf	549271 bc7c846bcd6bc839839d4854f211956ec0f20517	no	14
Warnings:					
Information:					
19	Foreign Reference	JP2007165909.pdf	555922 4e79efe47b9cb4449af3fa5dd66fcefb0b3de0ec	no	14
Warnings:					
Information:					
20	Foreign Reference	JP2008283219.pdf	1000268 a8298045817e1ebeecf458223c02e73dc633ddf8	no	23
Warnings:					
Information:					
21	Foreign Reference	JP2009021479.pdf	1424319 1a74de12636ea4bcd9c9e5e35f2ee55ffd829235	no	19
Warnings:					
Information:					
22	Foreign Reference	JP2010278472.pdf	412252 b8d1fc94e5f63cc03f3e7a3c274d82c0b5cb6e4c	no	14
Warnings:					
Information:					

23	Foreign Reference	KR20060052278.pdf	371228 61ac679b5c6e054bfeb19bfafdde510f551cc4c5	no	27
Warnings:					
Information:					
24	Foreign Reference	KR100825808B1.pdf	646102 06d2e3325f454fa224d492eebbe50e6c5da62c9e	no	13
Warnings:					
Information:					
25	Foreign Reference	KR20010061058.pdf	382021 578d2f6ed2af52f66736a7374840d3fd43965de6	no	16
Warnings:					
Information:					
26	Foreign Reference	KR2005039273.pdf	1115809 07563e87b3c4d6f2a05b4e27ecf99b69cf227f47	no	39
Warnings:					
Information:					
27	Foreign Reference	KR20100118864.pdf	268807 0a1cd0ccef1218d45b4b5fd0ae8997928027852b	no	13
Warnings:					
Information:					
28	Foreign Reference	WO_9114284.pdf	5452711 189679f5621a455b6c38ac4cca2f695e859399f4	no	33
Warnings:					
Information:					
29	Foreign Reference	WO200241363A2.pdf	3954769 fdf8da7c36bf84ac437465b352821625caec57bb	no	30
Warnings:					
Information:					

30	Foreign Reference	WO_03059390.pdf	4604279 50bdb2a5f65667047c40a327bac5d5db5fe ed734	no	29
Warnings:					
Information:					
31	Foreign Reference	WO2006086014.pdf	689136 8d86c664a5ef2585eae6dfb1d8269877d2f2 b988	no	61
Warnings:					
Information:					
32	Foreign Reference	WO2008091242.pdf	1996072 8b967f6443619361b1029c1babb559580d9 5fbb0	no	59
Warnings:					
Information:					
33	Foreign Reference	WO_2008145097.pdf	3206168 4043358df938cf664885a917c4d47c4790d5 d00c	no	20
Warnings:					
Information:					
34	Foreign Reference	WO2010033127A1.pdf	622855 a52a3f6d0a61c39eddd0e6f957989f399043 790f	no	17
Warnings:					
Information:					
35	Foreign Reference	WO2008099524.pdf	11122587 3c184d7936aff409c80f5b811a56deffd01cd 9e8	no	72
Warnings:					
Information:					
36	Non Patent Literature	Arndt_1975.pdf	5226628 0d0185ac7fc60ac7348695ec7d6a14dd794 78a48	no	4
Warnings:					
Information:					

37	Non Patent Literature	Asom_1987.pdf	650131 b0461a684fd86192233bd4b8087286a575d7f6c9	no	3
Warnings:					
Information:					
38	Non Patent Literature	Berger_2007.pdf	10393363 6f15165b55cd5da88bb0d253daf96a8fe6921286	no	7
Warnings:					
Information:					
39	Non Patent Literature	Berger_2008.pdf	78627 69bdc1b3b72154ce327726eb9ac4002bb355e081	no	3
Warnings:					
Information:					
40	Non Patent Literature	Betta_1997.pdf	6003554 032e1625b6ea814b677ddb06b0a1b0882847605d	no	5
Warnings:					
Information:					
41	Non Patent Literature	Boden_2008.pdf	125597 22b56de86fbd70764f40a9a6f3e15c2185a01398	no	4
Warnings:					
Information:					
42	Non Patent Literature	Bogue_2007.pdf	7466615 6fef78a5bd90149c062df971f384b8da5ae8652a	no	4
Warnings:					
Information:					
43	Non Patent Literature	Borghesi_1995.pdf	21304314 9eacafa33b7b3f077cb834f0944ef1e23c8d3e0f	no	76
Warnings:					
Information:					

44	Non Patent Literature	Born_1999.pdf	490424 4c34933101608eab317d17662c7610be44b57870	no	10
Warnings:					
Information:					
45	Non Patent Literature	Brieger_2006.pdf	318787 ace8e08c3384158ee56a46b0218be89cf9cf3ce3	no	4
Warnings:					
Information:					
46	Non Patent Literature	Buttgen_2006.pdf	11984389 d8d598c17a8e038f9156c587bca5fa6540ce143d	no	7
Warnings:					
Information:					
47	Non Patent Literature	Carey_2001_CLEO.pdf	87071 ea4b6338834aa9acf933dd0fcf3ba030567232b2	no	2
Warnings:					
Information:					
48	Non Patent Literature	Carey_2001_IVMC.pdf	4021770 b97419a0a09cce2ff1552267b8800ddcd0aa6238	no	69
Warnings:					
Information:					
49	Non Patent Literature	Carey_2002_LEOS.pdf	5724195 7a81b5ade8914998ef1581738918f108dd3a0b20	no	91
Warnings:					
Information:					
50	Non Patent Literature	Carey_2003_LEOS.pdf	6389237 7045366d21ff0001646365e7feff20843d49a7bd	no	85
Warnings:					
Information:					

51	Non Patent Literature	Carey_2003_OpticalSocietyOfAmerica.pdf	99005 938470d354f4c7b687b054e1dc431c23b8f20489	no	2
Warnings:					
Information:					
52	Non Patent Literature	Carey_2003_OpticsPhotonicsNews.pdf	286881 6adbf66ea87508bd80cfcafbb2fa88bd04472c8b	no	6
Warnings:					
Information:					
53	Non Patent Literature	Carey_2004_HarvardThesis.pdf	1509556 0f0dc525c09bdca5e36ec430a972810b77f852c1	no	162
Warnings:					
Information:					
54	Non Patent Literature	Chang_2010.pdf	1233972 7c22e525b9c9e150f213c52f1fa4c84809a8954e	no	7
Warnings:					
Information:					
55	Non Patent Literature	Chen_2009.pdf	282475 6732229a99c304b891ac1492c7444aec3f30df30	no	3
Warnings:					
Information:					
56	Non Patent Literature	Chiang_2007.pdf	449554 e7f2557d452669a6571be7bc63b6d55d4aa2580c	no	3
Warnings:					
Information:					
57	Non Patent Literature	Chichkov_1996.pdf	2871709 0d47f42b9b4387b43fc0f6de428beadbc5acc10a	no	8
Warnings:					
Information:					

SAMSUNG EX. 1002 - 3060/4148

58	Non Patent Literature	Chien_2005.pdf	1126333 1f0ee9107bbaaec16ee66deea9e515457ca0b38f	no	7
Warnings:					
Information:					
59	Non Patent Literature	Cilingiroglu_2003.pdf	1002943 1af8738802475b46acab093247d9bf15136879f3	no	13
Warnings:					
Information:					
			Total Files Size (in bytes):	142373130	

This Acknowledgement Receipt evidences receipt on the noted date by the USPTO of the indicated documents, characterized by the applicant, and including page counts, where applicable. It serves as evidence of receipt similar to a Post Card, as described in MPEP 503.

New Applications Under 35 U.S.C. 111
If a new application is being filed and the application includes the necessary components for a filing date (see 37 CFR 1.53(b)-(d) and MPEP 506), a Filing Receipt (37 CFR 1.54) will be issued in due course and the date shown on this Acknowledgement Receipt will establish the filing date of the application.

National Stage of an International Application under 35 U.S.C. 371
If a timely submission to enter the national stage of an international application is compliant with the conditions of 35 U.S.C. 371 and other applicable requirements a Form PCT/DO/EO/903 indicating acceptance of the application as a national stage submission under 35 U.S.C. 371 will be issued in addition to the Filing Receipt, in due course.

New International Application Filed with the USPTO as a Receiving Office
If a new international application is being filed and the international application includes the necessary components for an international filing date (see PCT Article 11 and MPEP 1810), a Notification of the International Application Number and of the International Filing Date (Form PCT/RO/105) will be issued in due course, subject to prescriptions concerning national security, and the date shown on this Acknowledgement Receipt will establish the international filing date of the application.

UNITED STATES PATENT AND TRADEMARK OFFICE

UNITED STATES DEPARTMENT OF COMMERCE
United States Patent and Trademark Office
Address: COMMISSIONER FOR PATENTS
P.O. Box 1450
Alexandria, Virginia 22313-1450
www.uspto.gov

APPLICATION NO.	FILING DATE	FIRST NAMED INVENTOR	ATTORNEY DOCKET NO.	CONFIRMATION NO.
14/747,875	06/23/2015	Martin U. Pralle	143705.05211	1722

136549 7590 07/22/2016

Pepper Hamilton LLP/SiOnyx LLC
Attn: Boston IP Docketing Department
125 High Street
19th Floor
Boston, MA 02110-2736

EXAMINER	
PHAM, LONG	

ART UNIT	PAPER NUMBER
2814	

NOTIFICATION DATE	DELIVERY MODE
07/22/2016	ELECTRONIC

Please find below and/or attached an Office communication concerning this application or proceeding.

The time period for reply, if any, is set in the attached communication.

Notice of the Office communication was sent electronically on above-indicated "Notification Date" to the following e-mail address(es):

docketingbn@pepperlaw.com
davisdr@pepperlaw.com

Office Action Summary	Application No. 14/747,875	Applicant(s) PRALLE ET AL.	
	Examiner LONG PHAM	Art Unit 2814	AIA (First Inventor to File) Status No

-- The MAILING DATE of this communication appears on the cover sheet with the correspondence address --

Period for Reply

A SHORTENED STATUTORY PERIOD FOR REPLY IS SET TO EXPIRE 3 MONTHS FROM THE MAILING DATE OF THIS COMMUNICATION.

- Extensions of time may be available under the provisions of 37 CFR 1.136(a). In no event, however, may a reply be timely filed after SIX (6) MONTHS from the mailing date of this communication.
- If NO period for reply is specified above, the maximum statutory period will apply and will expire SIX (6) MONTHS from the mailing date of this communication.
- Failure to reply within the set or extended period for reply will, by statute, cause the application to become ABANDONED (35 U.S.C. § 133). Any reply received by the Office later than three months after the mailing date of this communication, even if timely filed, may reduce any earned patent term adjustment. See 37 CFR 1.704(b).

Status

1)☒ Responsive to communication(s) filed on *6/22/16*.

☐ A declaration(s)/affidavit(s) under **37 CFR 1.130(b)** was/were filed on _____.

2a)☐ This action is **FINAL**. 2b)☒ This action is non-final.

3)☐ An election was made by the applicant in response to a restriction requirement set forth during the interview on _____; the restriction requirement and election have been incorporated into this action.

4)☐ Since this application is in condition for allowance except for formal matters, prosecution as to the merits is closed in accordance with the practice under *Ex parte Quayle*, 1935 C.D. 11, 453 O.G. 213.

Disposition of Claims*

5)☒ Claim(s) *1,2,4-6,8-10,12-14,17,19 and 34-40* is/are pending in the application.

5a) Of the above claim(s) _____ is/are withdrawn from consideration.

6)☐ Claim(s) _____ is/are allowed.

7)☒ Claim(s) *1,2,4-6,9-14,17,19 and 37-40* is/are rejected.

8)☒ Claim(s) *9-10 and 34-36* is/are objected to.

9)☐ Claim(s) _____ are subject to restriction and/or election requirement.

* If any claims have been determined allowable, you may be eligible to benefit from the **Patent Prosecution Highway** program at a participating intellectual property office for the corresponding application. For more information, please see http://www.uspto.gov/patents/init_events/pph/index.jsp or send an inquiry to PPHfeedback@uspto.gov.

Application Papers

10)☐ The specification is objected to by the Examiner.

11)☐ The drawing(s) filed on _____ is/are: a)☐ accepted or b)☐ objected to by the Examiner.

Applicant may not request that any objection to the drawing(s) be held in abeyance. See 37 CFR 1.85(a).

Replacement drawing sheet(s) including the correction is required if the drawing(s) is objected to. See 37 CFR 1.121(d).

Priority under 35 U.S.C. § 119

12)☐ Acknowledgment is made of a claim for foreign priority under 35 U.S.C. § 119(a)-(d) or (f).

Certified copies:

a)☐ All b)☐ Some** c)☐ None of the:

1.☐ Certified copies of the priority documents have been received.

2.☐ Certified copies of the priority documents have been received in Application No. _____.

3.☐ Copies of the certified copies of the priority documents have been received in this National Stage application from the International Bureau (PCT Rule 17.2(a)).

** See the attached detailed Office action for a list of the certified copies not received.

Attachment(s)

1) ☒ Notice of References Cited (PTO-892)

2) ☒ Information Disclosure Statement(s) (PTO/SB/08a and/or PTO/SB/08b) Paper No(s)/Mail Date *7/11/16*.

3) ☐ Interview Summary (PTO-413) Paper No(s)/Mail Date. _____ .

4) ☐ Other: _____.

The present application is being examined under the pre-AIA first to invent provisions.

DETAILED ACTION

Election/Restrictions

Applicant's election without traverse of claims 1, 2, 4, 5, 6, 9, 10, 12-14, 17, 19, and 34-40 in the reply filed on 6/22/16 is acknowledged.

Claim Objections

Claim 17 is objected to because of the following informalities: Claim 17 depends on cancelled claim 16. Appropriate correction is required.

Claim Rejections - 35 USC § 102

The following is a quotation of the appropriate paragraphs of pre-AIA 35 U.S.C. 102 that form the basis for the rejections under this section made in this Office action:

> A person shall be entitled to a patent unless –
>
> (e) the invention was described in (1) an application for patent, published under section 122(b), by another filed in the United States before the invention by the applicant for patent or (2) a patent granted on an application for patent by another filed in the United States before the invention by the applicant for patent, except that an international application filed under the treaty defined in section 351(a) shall have the effects for purposes of this subsection of an application filed in the United States only if the international application designated the United States and was published under Article 21(2) of such treaty in the English language.

Claim(s) 1, 3, 12-14, 19, 38-40 is/are rejected under pre-AIA 35 U.S.C. 102(e) as being anticipated by Velichko (US pub 20130200251).

SAMSUNG EX. 1002 - 3064/4148

With respect to claim 1, Velichko teach a light trapping device, comprising (see figs. 1-23 and associated text):

at least one light sensitive pixel 34 having a light incident surface, a backside surface opposite the light incident surface, and a peripheral sidewall extending at least partially around the pixel periphery;

a backside light trapping material 42 at least partially covering the backside surface; and

a peripheral light trapping material 36 substantially covering the peripheral sidewall,

a reflective layer 50 coupled to the light incident side and having an aperture to allow entry of light into the pixel:

wherein the reflective layer is operable to reflect at least a portion of light impinging thereupon from inside the pixel back into the pixel back into the pixel.

With respect to claim 2, Velichko teach at least one of the backside light trapping material and the peripheral light trapping material reflects light incident thereon back into the pixel.

With respect to claim 12, Velichko teach the peripheral sidewall extends completely around the pixel periphery.

With respect to claim 13, Velichko teach the peripheral sidewall extends from the light incident surface to the backside surface.

With respect to claim 14, Velichko teach said aperture has an effective surface area of less than about 90% of total area of the incident light surface.

With respect to claim 19, Velichko teach at least one of the backside light trapping material and the peripheral light trapping material is a metal layer.

With respect to claim 38, Velichko teach the backside light trapping material substantially covers the backside surface.

With respect to claim 39, Velichko teach the backside light trapping material completely covers the backside surface.

With respect to claim 40, Velichko teach said peripheral sidewall extends through the pixel substantially from the light incident surface to the backside surface.

Claims 4-6, 17 rejected under pre-AIA 35 U.S.C. 103(a) as being unpatentable over Velichko (US pub 20130200251) as applied to claims 1, 3, 12-14, 19, 38-40 above, and further in view of Yanagisawa (JP 403183037) (a reference cited by the applicant).

With respect to claims 4-6, Velichko teaches the peripheral light trapping material is reflective but fails to teach the peripheral light

trapping material is made of silicon oxide or having a refractive index of less than about 2.1.

Yanagisawa teaches a reflective made of silicon oxide or having a refractive index of less than about 2.1 to improve reflectivity. See English abstract.

It would have been obvious to one of ordinary skill in the art of making semiconductor devices to incorporate the teaching of Yanagisawa into the device of Velichko to achieve the above benefit.

With respect to claim 17, Velichko fails to teach coupling a lens to aperture to the pixel to focus incident light.

However, the coupling of a lens to aperture to a pixel to focus incident light is well-known in semiconductor art.

With respect to claim 37, Velichko fails to teach the peripheral light trapping material is made of aluminum oxide.

However, the use of aluminum oxide as reflective material is well-known in semiconductor art.

Allowable Subject Matter

Claims 9-10 and 34-36 are objected to as being dependent upon a rejected base claim, but would be allowable if rewritten in independent form including all of the limitations of the base claim and any intervening claims.

Conclusion

Any inquiry concerning this communication or earlier communications from the examiner should be directed to LONG PHAM whose telephone

number is (571)272-1714. The examiner can normally be reached on Mon-Frid, 10am to 5pm.

If attempts to reach the examiner by telephone are unsuccessful, the examiner's supervisor, Wael Fahmy can be reached on 571-272-1705. The fax phone number for the organization where this application or proceeding is assigned is 571-273-8300.

Information regarding the status of an application may be obtained from the Patent Application Information Retrieval (PAIR) system. Status information for published applications may be obtained from either Private PAIR or Public PAIR. Status information for unpublished applications is available through Private PAIR only. For more information about the PAIR system, see http://pair-direct.uspto.gov. Should you have questions on access to the Private PAIR system, contact the Electronic Business Center (EBC) at 866-217-9197 (toll-free). If you would like assistance from a USPTO Customer Service Representative or access to the automated information system, call 800-786-9199 (IN USA OR CANADA) or 571-272-1000.

Long Pham
Primary Examiner
Art Unit 2814

/LONG PHAM/
Primary Examiner, Art Unit 2814

SAMSUNG EX. 1002 - 3068/4148

Notice of References Cited	Application/Control No. 14/747,875	Applicant(s)/Patent Under Reexamination PRALLE ET AL.	
	Examiner LONG PHAM	Art Unit 2814	Page 1 of 1

U.S. PATENT DOCUMENTS

*		Document Number Country Code-Number-Kind Code	Date MM-YYYY	Name	CPC Classification	US Classification
*	A	US-2013/0200251 A1	08-2013	Velichko; Sergey	H01L31/02327	250/208.1
	B	US-				
	C	US-				
	D	US-				
	E	US-				
	F	US-				
	G	US-				
	H	US-				
	I	US-				
	J	US-				
	K	US-				
	L	US-				
	M	US-				

FOREIGN PATENT DOCUMENTS

*		Document Number Country Code-Number-Kind Code	Date MM-YYYY	Country	Name	CPC Classification
	N					
	O					
	P					
	Q					
	R					
	S					
	T					

NON-PATENT DOCUMENTS

*		Include as applicable: Author, Title Date, Publisher, Edition or Volume, Pertinent Pages)
	U	
	V	
	W	
	X	

*A copy of this reference is not being furnished with this Office action. (See MPEP § 707.05(a).)
Dates in MM-YYYY format are publication dates. Classifications may be US or foreign.

EAST Search History

EAST Search History (Prior Art)

Ref #	Hits	Search Query	DBs	Default Operator	Plurals	Time Stamp
S2	84	US-3035052-$.DID. OR US-20030029495-$.DID. OR US-20040222187-$.DID. OR US-20050127401-$.DID. OR US-20050227390-$.DID. OR US-20060011955-$.DID. OR US-20060079062-$.DID. OR US-20060118781-$.DID. OR US-20060180885-$.DID. OR US-20060231914-$.DID. OR US-20070145505-$.DID. OR US-20080026550-$.DID. OR US-20080036022-$.DID. OR US-20080044943-$.DID. OR US-20080076240-$.DID. OR US-20080099804-$.DID. OR US-20080178932-$.DID. OR US-20080258604-$.DID. OR US-20090065051-$.DID. OR US-20090142879-$.DID. OR US-20090160983-$.DID. OR US-20090194671-$.DID. OR US-20090200586-$.DID. OR US-20090213883-$.DID. OR US-3487223-$.DID. OR US-4277793-$.DID. OR US-4419533-$.DID. OR US-4493942-$.DID. OR US-4514582-$.DID. OR US-4536608-$.DID. OR US-4663188-$.DID. OR US-4829013-$.DID. OR US-5080725-$.DID. OR US-5081049-$.DID. OR US-5100478-$.DID. OR US-5114876-$.DID. OR US-5164324-$.DID. OR US-5322988-$.DID. OR US-5346850-$.DID. OR US-5597621-$.DID. OR US-5714404-$.DID. OR US-5731213-$.DID. OR US-5792280-$.DID. OR US-6147297-$.DID. OR US-6498336-$.DID. OR US-6580053-$.DID. OR US-6583936-$.DID. OR US-6667528-$.DID. OR US-6759262-$.DID. OR US-6800541-$.DID. OR US-	US-PGPUB; USPAT; USOCR; JPO; IBM_TDB	OR	ON	2014/06/25 14:14

SAMSUNG EX. 1002 - 3070/4148

		7057256-$.DID. OR US-7091411-$.DID. OR US-7109517-$.DID. OR US-7247527-$.DID. OR US-7314832-$.DID. OR US-7354792-$.DID. OR US-7390689-$.DID. OR US-7442629-$.DID. OR US-7456452-$.DID. OR US-7482532-$.DID. OR US-7498650-$.DID. OR US-7504325-$.DID. OR US-7504702-$.DID. OR US-7511750-$.DID. OR US-7745901-$.DID. OR US-7781856-$.DID. OR US-7816220-$.DID. OR US-7847253-$.DID. OR US-7884439-$.DID. OR US-7884446-$.DID. OR US-8030726-$.DID. OR US-8058615-$.DID. OR US-8207051-$.DID. OR US-8476681-$.DID. OR US-3666484-$.DID. OR US-2030766-$.DID. OR JP-07173484-$.DID. OR JP-071734840721-$.DID. OR JP-2008187003-$.DID. OR JP-2011091128-$.DID. OR JP-2152226-$.DID. OR JP-63116421-$.DID. OR JP-9298308-$.DID. OR KR-20010061058-$.DID. OR KR-20100118864-$.DID. OR WO-2006086014-$.DID. OR WO-2009100023-$.DID. OR WO-2011035188-$.DID. OR WO-2011119618-$.DID.				
S3	7768	(light adj2 (trapping or trapped))	US-PGPUB; USPAT; USOCR; FPRS; EPO; JPO; DERWENT; IBM_TDB	OR	ON	2014/06/25 14:16
S4	11	S2 and S3	US-PGPUB; USPAT; USOCR; FPRS; EPO; JPO; DERWENT; IBM_TDB	OR	ON	2014/06/25 14:16
S5	2251	(reflector or Bragg) and S3	US-PGPUB; USPAT; USOCR;	OR	ON	2014/06/25 15:40

SAMSUNG EX. 1002 - 3071/4148

			FPRS; EPO; JPO; DERWENT; IBM_TDB			
S6	14	(reflector or Bragg) and S2	US-PGPUB; USPAT; USOCR; FPRS; EPO; JPO; DERWENT; IBM_TDB	OR	ON	2014/06/25 15:41
S7	888	(reflector or Bragg) near3 backside	US-PGPUB; USPAT; USOCR; FPRS; EPO; JPO; DERWENT; IBM_TDB	OR	ON	2014/06/25 15:55
S8	51623	(reflector or Bragg) near3 (side or sidewall or edge or wall)	US-PGPUB; USPAT; USOCR; FPRS; EPO; JPO; DERWENT; IBM_TDB	OR	ON	2014/06/25 15:55
S9	112640	pixel near5 (side or sidewall or edge or wall)	US-PGPUB; USPAT; USOCR; FPRS; EPO; JPO; DERWENT; IBM_TDB	OR	ON	2014/06/25 15:56
S10	143	S7 same S8	US-PGPUB; USPAT; USOCR; FPRS; EPO; JPO; DERWENT; IBM_TDB	OR	ON	2014/06/25 15:56
S11	2	S9 same4 S10	US-PGPUB; USPAT; USOCR; FPRS; EPO; JPO; DERWENT; IBM_TDB	OR	ON	2014/06/25 15:56
S12	3	S9 and S10	US-PGPUB; USPAT; USOCR; FPRS; EPO; JPO;	OR	ON	2014/06/25 15:57

SAMSUNG EX. 1002 - 3072/4148

			DERWENT; IBM_TDB			
S13	1	S12 not S11	US-PGPUB; USPAT; USOCR; FPRS; EPO; JPO; DERWENT; IBM_TDB	OR	ON	2014/06/25 15:57
S14	179	S7 same4 S8	US-PGPUB; USPAT; USOCR; FPRS; EPO; JPO; DERWENT; IBM_TDB	OR	ON	2014/06/25 15:58
S15	145	S14 and (photodiode or pixel or light)	US-PGPUB; USPAT; USOCR; FPRS; EPO; JPO; DERWENT; IBM_TDB	OR	ON	2014/06/25 15:59
S16	129	S14 same10 (photodiode or pixel or light)	US-PGPUB; USPAT; USOCR; FPRS; EPO; JPO; DERWENT; IBM_TDB	OR	ON	2014/06/25 15:59
S17	128	S14 same8 (photodiode or pixel or light)	US-PGPUB; USPAT; USOCR; FPRS; EPO; JPO; DERWENT; IBM_TDB	OR	ON	2014/06/25 15:59
S18	1204	(reflector or Bragg) near5 backside	US-PGPUB; USPAT; USOCR; FPRS; EPO; JPO; DERWENT; IBM_TDB	OR	ON	2014/06/25 16:09
S19	71202	(reflector or Bragg) near5 (side or sidewall or edge or wall)	US-PGPUB; USPAT; USOCR; FPRS; EPO; JPO; DERWENT; IBM_TDB	OR	ON	2014/06/25 16:09

SAMSUNG EX. 1002 - 3073/4148

S20	280	S18 same4 S19	US-PGPUB; USPAT; USOCR; FPRS; EPO; JPO; DERWENT; IBM_TDB	OR	ON	2014/06/25 16:09
S21	195	S20 same4 (photodiode or pixel or light)	US-PGPUB; USPAT; USOCR; FPRS; EPO; JPO; DERWENT; IBM_TDB	OR	ON	2014/06/25 16:09
S22	7	S18 same2 S9	US-PGPUB; USPAT; USOCR; FPRS; EPO; JPO; DERWENT; IBM_TDB	OR	ON	2014/06/25 16:10
S23	7	S22 same4 (photodiode or pixel or light)	US-PGPUB; USPAT; USOCR; FPRS; EPO; JPO; DERWENT; IBM_TDB	OR	ON	2014/06/25 16:10
S24	217	S18 same S19	US-PGPUB; USPAT; USOCR; FPRS; EPO; JPO; DERWENT; IBM_TDB	OR	ON	2014/06/25 16:13
S25	0	(light adj2 sensitive adj2 pixel) same4 S24	US-PGPUB; USPAT; USOCR; FPRS; EPO; JPO; DERWENT; IBM_TDB	OR	ON	2014/06/25 16:14
S26	0	(light adj2 sensitive adj2 pixel) and S24	US-PGPUB; USPAT; USOCR; FPRS; EPO; JPO; DERWENT; IBM_TDB	OR	ON	2014/06/25 16:14
S27	14	pixel same4 S24	US-PGPUB;	OR	ON	2014/06/25 16:14

			USPAT; USOCR; FPRS; EPO; JPO; DERWENT; IBM_TDB			
S28	7	S27 and index	US-PGPUB; USPAT; USOCR; FPRS; EPO; JPO; DERWENT; IBM_TDB	OR	ON	2014/06/25 16:18
S29	26925	(high adj2 index) near3 (layer or film)	US-PGPUB; USPAT; USOCR; FPRS; EPO; JPO; DERWENT; IBM_TDB	OR	ON	2014/06/26 12:48
S30	27823	(low adj2 index) near3 (layer or film)	US-PGPUB; USPAT; USOCR; FPRS; EPO; JPO; DERWENT; IBM_TDB	OR	ON	2014/06/26 12:48
S31	12802	S29 near10 S30	US-PGPUB; USPAT; USOCR; FPRS; EPO; JPO; DERWENT; IBM_TDB	OR	ON	2014/06/26 12:48
S32	1170	(reflector or Bragg) same S31	US-PGPUB; USPAT; USOCR; FPRS; EPO; JPO; DERWENT; IBM_TDB	OR	ON	2014/06/26 12:49
S33	611	(reflector or Bragg) near10 S31	US-PGPUB; USPAT; USOCR; FPRS; EPO; JPO; DERWENT; IBM_TDB	OR	ON	2014/06/26 12:49
S34	4200	S30 near5 ("between")	US-PGPUB; USPAT; USOCR;	OR	ON	2014/06/26 12:49

SAMSUNG EX. 1002 - 3075/4148

			FPRS; EPO; JPO; DERWENT; IBM_TDB			
S35	1972	S34 near10 S29	US-PGPUB; USPAT; USOCR; FPRS; EPO; JPO; DERWENT; IBM_TDB	OR	ON	2014/06/26 12:50
S36	81	(reflector or Bragg) near10 S35	US-PGPUB; USPAT; USOCR; FPRS; EPO; JPO; DERWENT; IBM_TDB	OR	ON	2014/06/26 12:50
S37	188	S29 near5 (polysilicon or polycrystalline or poly or (amorphous adj2 silicon) or germanium)	US-PGPUB; USPAT; USOCR; FPRS; EPO; JPO; DERWENT; IBM_TDB	OR	ON	2014/06/26 12:53
S38	2500	S30 near5 (oxide or nitride or oxynitride or oxynitrides)	US-PGPUB; USPAT; USOCR; FPRS; EPO; JPO; DERWENT; IBM_TDB	OR	ON	2014/06/26 12:53
S39	14	S37 near20 S38	US-PGPUB; USPAT; USOCR; FPRS; EPO; JPO; DERWENT; IBM_TDB	OR	ON	2014/06/26 12:53
S40	0	(reflector or Bragg) same S39	US-PGPUB; USPAT; USOCR; FPRS; EPO; JPO; DERWENT; IBM_TDB	OR	ON	2014/06/26 12:54
S41	0	S39 near20 ("between")	US-PGPUB; USPAT; USOCR; FPRS; EPO; JPO;	OR	ON	2014/06/26 12:54

SAMSUNG EX. 1002 - 3076/4148

			DERWENT; IBM_TDB			
S42	51	backside near6 (textured near2 (layer or film))	US-PGPUB; USPAT; USOCR; FPRS; EPO; JPO; DERWENT; IBM_TDB	OR	ON	2014/06/26 13:12
S43	10	S42 AND ((H01L21/02686 OR H01L27/1214 OR H01L21/02532 OR H01L21/02595 OR H01L31/0236 OR H01L21/0237 OR H01L21/02403 OR H01L21/0243 OR H01L21/02472 OR H01L21/02483 OR H01L21/02494 OR H01L21/02554 OR H01L21/02565 OR H01L21/02573 OR H01L21/02587 OR H01L21/02609 OR H01L21/0262 OR H01L21/365 OR H01L2224/16 OR H01L27/14625 OR H01L27/14627 OR H01L27/14629 OR H01L27/1463 OR H01L27/14685 OR H01L31/02168 OR H01L31/022425 OR H01L31/02363 OR H01L31/042 OR H01L31/0527 OR H01L31/0682 OR H01L31/18 OR H01L31/1804 OR H01L33/0087 OR H01L33/22 OR H01L33/24 OR H01L33/28 OR H01L33/385 OR H01L33/405 OR H01L33/483 OR H01L33/60 OR H01L33/62).CPC.)	US-PGPUB; USPAT; USOCR; FPRS; EPO; JPO; DERWENT; IBM_TDB	OR	ON	2014/06/26 13:25
S44	5	S39 AND ((H01L21/02686 OR H01L27/1214 OR H01L21/02532 OR H01L21/02595 OR H01L31/0236 OR H01L21/0237 OR H01L21/02403 OR H01L21/0243 OR H01L21/02472 OR H01L21/02483 OR H01L21/02494 OR H01L21/02554 OR	US-PGPUB; USPAT; USOCR; FPRS; EPO; JPO; DERWENT; IBM_TDB	OR	ON	2014/06/26 13:25

SIONYX1403000031.0056

SAMSUNG EX. 1002 - 3077/4148

		H01L21/02565 OR H01L21/02573 OR H01L21/02587 OR H01L21/02609 OR H01L21/0262 OR H01L21/365 OR H01L2224/16 OR H01L27/14625 OR H01L27/14627 OR H01L27/14629 OR H01L27/1463 OR H01L27/14685 OR H01L31/02168 OR H01L31/022425 OR H01L31/02363 OR H01L31/042 OR H01L31/0527 OR H01L31/0682 OR H01L31/18 OR H01L31/1804 OR H01L33/0087 OR H01L33/22 OR H01L33/24 OR H01L33/28 OR H01L33/385 OR H01L33/405 OR H01L33/483 OR H01L33/60 OR H01L33/62).CPC.)				
S45	2	S36 AND ((H01L21/02686 OR H01L27/1214 OR H01L21/02532 OR H01L21/02595 OR H01L31/0236 OR H01L21/0237 OR H01L21/02403 OR H01L21/0243 OR H01L21/02472 OR H01L21/02483 OR H01L21/02494 OR H01L21/02554 OR H01L21/02565 OR H01L21/02573 OR H01L21/02587 OR H01L21/02609 OR H01L21/0262 OR H01L21/365 OR H01L2224/16 OR H01L27/14625 OR H01L27/14627 OR H01L27/14629 OR H01L27/1463 OR H01L27/14685 OR H01L31/02168 OR H01L31/022425 OR H01L31/02363 OR H01L31/042 OR H01L31/0527 OR H01L31/0682 OR H01L31/18 OR H01L31/1804 OR H01L33/0087 OR H01L33/22 OR H01L33/24 OR H01L33/28 OR H01L33/385 OR H01L33/405 OR	US-PGPUB; USPAT; USOCR; FPRS; EPO; JPO; DERWENT; IBM_TDB	OR	ON	2014/06/26 13:25

SIONYX1403000031.0057

SAMSUNG EX. 1002 - 3078/4148

		H01L33/483 OR H01L33/60 OR H01L33/62).CPC.)				
S46	1	("20140138785").PN.	US-PGPUB; USPAT; USOCR	OR	OFF	2015/01/05 11:26
S47	3930	(257/432).CCLS.	US-PGPUB; USPAT; USOCR	OR	OFF	2015/01/05 11:54
S48	218	(257/228).CCLS.	US-PGPUB; USPAT; USOCR	OR	OFF	2015/01/05 11:54
S50	1	("9373732").PN.	US-PGPUB; USPAT; USOCR	OR	OFF	2016/07/13 15:10
S51	1	("9373732").PN.	US-PGPUB; USPAT; USOCR	OR	OFF	2016/07/15 10:13
S52	395	reflective near3 (aluminum adj oxide)	US-PGPUB; USPAT; USOCR; FPRS; EPO; JPO; DERWENT; IBM_TDB	OR	ON	2016/07/15 13:07

EAST Search History (Interference)

Ref #	Hits	Search Query	DBs	Default Operator	Plurals	Time Stamp
S49	1	(257/432).CCLS.		OR	OFF	2015/01/05 11:54

7/15/2016 1:49:52 PM
C:\Users\lpham\Documents\EAST\Workspaces\14-747,875.wsp

SIONYX1403000031.0058

SAMSUNG EX. 1002 - 3079/4148

Substitute for Form 1449/PTO				Complete if Known	
INFORMATION DISCLOSURE STATEMENT BY APPLICANT				Application No.:	14/747,875
				Filing Date:	June 23, 2015
				First Named Inventor:	Martin U. Pralle
				Group Art Unit:	2814
(use as many sheets as necessary)				Examiner Name:	Long Pham
Sheet	1	of	20	Attorney Docket No.:	143705.05211

U. S. PATENT DOCUMENTS

Examiner's Initials	Cite No.	U.S. Patent Document Number Kind Code (if known)	Name of Patentee or Applicant of Cited Document	Date of Publication of Cited Document MM-DD-YYYY	Pages, Columns, Lines, Where Relevant Passages or Relevant Figures Appear	
	A1	3487223	St. John	12/30/1969		
	A2	3922571	Smith	11/25/1975		
	A3	3973994	Redfield	8/10/1976		
	A4	3994012	Warner, Jr.	11/23/1976		
	A5	4017887	Davies et al.	4/12/1977		
	A6	4149174	Shannon	4/10/1979		
	A7	4176365	Kroger	11/27/1979		
	A8	4201450	Trapani	5/6/1980		
	A9	4242149	King et al.	12/30/1980		
	A10	4253882	Dalal	3/3/1981		
	A11	4277793	Webb	7/7/1981		
	A12	4322571	Stanbery	3/30/1982		
	A13	4419533	Czubatyj et al.	12/6/1983		
	A14	4452826	Shields et al.	6/5/1984		
	A15	4493942	Sheng et al.	1/15/1985		
	A16	4514582	Tiedje et al.	4/30/1985		
	A17	4536608	Sheng et al.	8/20/1985		
	A18	4568960	Petroff et al.	2/4/1986		
	A19	4593303	Dyck et al.	6/3/1986		
	A20	4593313	Nagasaki	6/3/1986		
	A21	4617593	Dudley	10/14/1986		
	A22	4630082	Sakai	12/16/1986		
	A23	4648936	Ashby et al.	3/10/1987		
	A24	4663188	Kane	5/5/1987		
	A25	4672206	Suzuki	6/9/1987		
	A26	4673770	Mandelkorn	6/16/1987		
	A27	4679068	Lillquist et al.	7/7/1987		
	A28	4751571	Lillquist	6/14/1988		
	A29	4775425	Guha et al.	10/4/1988		
	A30	4777490	Sharma et al.	10/11/1988		
	A31	4829013	Yamazaki	5/9/1989		
	A32	4883962	Elliot	11/28/1989		
	A33	4887255	Handa et al.	12/12/1989		
	A34	4894526	Bethea et al.	1/16/1990		
	A35	4910568	Taki, et al.	3/20/1990		
	A36	4910588	Kinoshita, et al.	3/20/1990		
	A37	4964134	Westbrook et al.	10/16/1990		
Examiner Signature		/LONG PHAM/		Date Considered	07/15/2016	

EXAMINER: Initial if reference considered, whether or not citation is in conformance with MPEP 609. Draw line through citation if not in conformance and not considered. Include copy of this form with next communication to Applicant.

ALL REFERENCES CONSIDERED EXCEPT WHERE LINED THROUGH. /L.P./

SAMSUNG EX. 1002 - 3080/4148

Substitute for Form 1449/PTO				Complete if Known	
INFORMATION DISCLOSURE STATEMENT BY APPLICANT				Application No.:	14/747,875
				Filing Date:	June 23, 2015
				First Named Inventor:	Martin U. Pralle
				Group Art Unit:	2814
(use as many sheets as necessary)				Examiner Name:	Long Pham
Sheet	2	of	20	Attorney Docket No.:	143705.05211

	A38	4965784	Land et al.	10/23/1990		
	A39	4968372	Maass	11/6/1990		
	A40	4999308	Nishiura et al.	3/12/1991		
	A41	5021100	Ishihara et al.	6/4/1991		
	A42	5021854	Huth	6/4/1991		
	A43	5080725	Green et al.	1/14/1992		
	A44	5081049	Green et al.	1/14/1992		
	A45	5100478	Kawabata	3/31/1992		
	A46	5114876	Weiner	5/19/1992		
	A47	5127964	Hamakawa et la.	7/7/1992		
	A48	5164324	Russell et al.	11/17/1992		
	A49	5208822	Haus et al	5/4/1993		
	A50	5223043	Olson et al.	6/29/1993		
	A51	5234790	Lang, et al.	8/10/1993		
	A52	5244817	Hawkins et al.	9/14/1993		
	A53	5296045	Banerjee et al.	3/22/1994		
	A54	5309275	Nishimura et al.	5/3/1994		
	A55	5322988	Russell et al.	6/21/1994		
	A56	5346850	Kaschmitter et al.	9/13/1994		
	A57	5370747	Noguchi et al.	12/6/1994		
	A58	5373182	Norton	12/13/1994		
	A59	5381431	Zayhowski	1/10/1995		
	A60	5383217	Uemura	1/17/1995		
	A61	5390201	Tomono et al.	2/14/1995		
	A62	5413100	Barthelemy et al.	5/9/1995		
	A63	5449626	Hezel	9/12/1995		
	A64	5454347	Shibata et al.	10/3/1995		
	A65	5502329	Pezzani	3/26/1996		
	A66	5523570	Hairston	6/4/1996		
	A67	5559361	Pezzani	9/24/1996		
	A68	5569615	Yamazaki et al.	10/29/1996		
	A69	5578858	Mueller et al.	11/26/1996		
	A70	5580615	Itoh et al.	12/3/1996		
	A71	5589008	Kepper	12/31/1996		
	A72	5589704	Levine	12/31/1996		
	A73	5597621	Hummel et al.	1/18/1997		
	A74	5627081	Tsuo et al.	5/6/1997		
	A75	5640013	Ishikawa, et al.	6/17/1997		
	A76	5641362	Meier	6/24/1997		
	A77	5705413	Harkin et al.	1/6/1998		
	A78	5705828	Noguchi et al.	1/6/1998		
	A79	5708486	Miyawaki et al.	1/13/1998		
	A80	5710442	Watanabe et al.	1/20/1998		
	A81	5714404	Mititsky et al.	2/3/1998		

Examiner Signature	/LONG PHAM/	Date Considered	07/15/2016

EXAMINER: Initial if reference considered, whether or not citation is in conformance with MPEP 609. Draw line through citation if not in conformance and not considered. Include copy of this form with next communication to Applicant.

ALL REFERENCES CONSIDERED EXCEPT WHERE LINED THROUGH. /L.P./

SAMSUNG EX. 1002 - 3081/4148

Substitute for Form 1449/PTO				Complete if Known	
INFORMATION DISCLOSURE STATEMENT BY APPLICANT				Application No.:	14/747,875
				Filing Date:	June 23, 2015
				First Named Inventor:	Martin U. Pralle
				Group Art Unit:	2814
(use as many sheets as necessary)				Examiner Name:	Long Pham
Sheet	3	of	20	Attorney Docket No.:	143705.05211

	A82	5731213	Ono	3/24/1998		
	A83	5751005	Wyles et al.	5/12/1998		
	A84	5758644	Diab et el.	6/2/1998		
	A85	5766127	Pologe et al.	6/16/1998		
	A86	5766964	Rohatgi et al.	6/16/1998		
	A87	5773820	Osajda, et al.	6/30/1998		
	A88	5779631	Chance	7/14/1998		
	A89	5781392	Clark	7/14/1998		
	A90	5792280	Ruby et al	8/11/1998		
	A91	5808350	Jack et al	9/15/1998		
	A92	5859446	Nagasu et al.	1/12/1999		
	A93	5861639	Bernier	1/19/1999		
	A94	5923071	Saito	7/13/1999		
	A95	5935320	Graf et al.	8/10/1999		
	A96	5942789	Morikawa	8/24/1999		
	A97	5943584	Shim et al	8/24/1999		
	A98	5963790	Matsuno et al	10/5/1999		
	A99	5977603	Ishikawa	11/2/1999		
	A100	6071796	Voutsas	6/6/2000		
	A101	6072117	Matsuyama et al.	6/6/2000		
	A102	6080988	Ishizuya et al.	6/27/2000		
	A103	6097031	Cole	8/1/2000		
	A104	6106689	Matsuyama	8/22/2000		
	A105	6107618	Fossum et al.	8/22/2000		
	A106	6111300	Cao et al.	8/29/2000		
	A107	6147297	Wettling et al.	11/14/2000		
	A108	6160833	Floyd et al.	12/12/2000		
	A109	6168965	Malinovich, et al.	1/2/2001		
	A110	6194722	Fiorini et al.	2/27/2001		
	A111	6229192	Gu	5/8/2001		
	A112	6252256	Ugge et al.	6/26/2001		
	A113	6290713	Russell	9/18/2001		
	A114	6291302	Yu	9/18/2001		
	A115	6313901	Cacharelis	11/6/2001		
	A116	6320296	Fujii et al.	11/20/2001		
	A117	6331445	Janz et al	12/18/2001		
	A118	6372591	Mineji et al.	4/16/2002		
	A119	6372611	Horikawa	4/16/2002		
	A120	6379979	Connolly	4/30/2002		
	A121	6420706	Lurie, et al.	7/16/2002		
	A122	6429036	Nixon, et al.	8/6/2002		
	A123	6429037	Wenham et al.	8/6/2002		
	A124	6465860	Shigenaka, et al.	10/15/2002		
	A125	6475839	Zhang, et al.	11/5/2002		

Examiner Signature	/LONG PHAM/	Date Considered	07/15/2016

EXAMINER: Initial if reference considered, whether or not citation is in conformance with MPEP 609. Draw line through citation if not in conformance and not considered. Include copy of this form with next communication to Applicant.

ALL REFERENCES CONSIDERED EXCEPT WHERE LINED THROUGH. /L.P./

SAMSUNG EX. 1002 - 3082/4148

Substitute for Form 1449/PTO				Complete if Known	
INFORMATION DISCLOSURE STATEMENT BY APPLICANT				Application No.:	14/747,875
				Filing Date:	June 23, 2015
				First Named Inventor:	Martin U. Pralle
				Group Art Unit:	2814
(use as many sheets as necessary)				Examiner Name:	Long Pham
Sheet	4	of	20	Attorney Docket No.:	143705.05211

	A126	6483116	Kozlowski et al.	11/19/2002		
	A127	6483929	Marakami et al.	11/19/2002		
	A128	6486522	Bishay et al.	11/26/2002		
	A129	6493567	Krivitski et al.	12/10/2002		
	A130	6498336	Tian et al.	12/24/2002		
	A131	6500690	Yamagishi et al.	12/31/2002		
	A132	6504178	Carlson et al.	1/7/2003		
	A133	6580053	Voutsas	6/17/2003		
	A134	6583936	Kaminsky et al.	6/24/2003		
	A135	6597025	Lauter et al	7/22/2003		
	A136	6607927	Ramappa et al.	8/19/2003		
	A137	6624049	Yamazaki	9/23/2003		
	A138	6639253	Duane et al.	10/28/2003		
	A139	6667528	Cohen et al.	12/23/2003		
	A140	6677655	Fitzgerald	1/13/2004		
	A141	6677656	Francois	1/13/2004		
	A142	6683326	Iguchi, et al.	1/27/2004		
	A143	6689209	Falster et el.	2/10/2004		
	A144	6753585	Kindt	6/22/2004		
	A145	6759262	Theil et al.	7/6/2004		
	A146	6790701	Shigenaka, et al.	9/14/2004		
	A147	6800541	Okumura	10/5/2004		
	A148	6801799	Mendelson	10/5/2004		
	A149	6803555	Parrish et al.	10/12/2004		
	A150	6815685	Wany	11/9/2004		
	A151	6818535	Lu et al.	11/16/2004		
	A152	6822313	Matsushita	11/23/2004		
	A153	6825057	Heyers, et al.	11/30/2004		
	A154	6864156	Conn	3/8/2005		
	A155	6864190	Han et al.	3/8/2005		
	A156	6867806	Lee et al.	3/15/2005		
	A157	6900839	Kozlowski et al.	5/31/2005		
	A158	6911375	Guarini et al.	6/28/2005		
	A159	6919587	Ballon et al.	7/19/2005		
	A160	6923625	Sparks	8/2/2005		
	A161	6927432	Holm, et al.	8/9/2005		
	A162	6984816	Holm, et al.	1/10/2006		
	A163	7008854	Forbes	3/7/2006		
	A164	7041525	Clevenger et al.	5/9/2006		
	A165	7057256	Carey, III et al.	6/6/2006		
	A166	7075079	Wood	7/11/2006		
	A167	7091411	Falk et al.	8/15/2006		
	A168	7109517	Zaidi	9/19/2006		
	A169	7126212	Enquist et al.	10/24/2006		

Examiner Signature	/LONG PHAM/	Date Considered	07/15/2016

EXAMINER: Initial if reference considered, whether or not citation is in conformance with MPEP 609. Draw line through citation if not in conformance and not considered. Include copy of this form with next communication to Applicant.

ALL REFERENCES CONSIDERED EXCEPT WHERE LINED THROUGH. /L.P./

SAMSUNG EX. 1002 - 3083/4148

Substitute for Form 1449/PTO				Complete if Known	
INFORMATION DISCLOSURE STATEMENT BY APPLICANT				Application No.:	14/747,875
				Filing Date:	June 23, 2015
				First Named Inventor:	Martin U. Pralle
				Group Art Unit:	2814
(use as many sheets as necessary)				Examiner Name:	Long Pham
Sheet	5	of	20	Attorney Docket No.:	143705.05211

	A170	7132724	Merrill	11/7/2006		
	A171	7202102	Yao	4/10/2007		
	A172	7211501	Liu et al	5/1/2007		
	A173	7235812	Chu, et al.	6/26/2007		
	A174	7247527	Shimomura et al.	7/24/2007		
	A175	7247812	Tsao	7/24/2007		
	A176	7256102	Nakata, et al.	8/14/2007		
	A177	7271445	Forbes	9/18/2007		
	A178	7271835	Iizuka et al.	9/18/2007		
	A179	7285482	Ochi	10/23/2007		
	A180	7314832	Kountz et al.	1/1/2008		
	A181	7354792	Carey, III et al.	4/8/2008		
	A182	7358498	Geng et al.	4/15/2008		
	A183	7375378	Manivannan et al.	5/20/2008		
	A184	7390689	Mazur et al.	6/24/2008		
	A185	7432148	Li et al.	10/7/2008		
	A186	7442629	Mazur et al.	10/28/2008		
	A187	7446359	Lee, et al.	11/4/2008		
	A188	7446807	Hong	11/7/2008		
	A189	7456452	Wells et al.	11/25/2008		
	A190	7482532	Yi et al.	1/27/2009		
	A191	7498650	Lauxtermann	3/3/2009		
	A192	7504325	Koezuka et al.	3/17/2009		
	A193	7504702	Mazur et al.	3/17/2009		
	A194	7511750	Murakami	3/31/2009		
	A195	7521737	Augusto	4/21/2009		
	A196	7528463	Forbes	5/5/2009		
	A197	7542085	Altice, Jr. et al.	6/2/2009		
	A198	7547616	Fogel et al.	6/16/2009		
	A199	7551059	Farrier	6/23/2009		
	A200	7560750	Niira et al.	7/14/2009		
	A201	7564631	Li, et al.	7/21/2009		
	A202	7582515	Choi et al.	9/1/2009		
	A203	7592593	Kauffman, et al.	9/22/2009		
	A204	7595213	Kwon et al.	9/29/2009		
	A205	7605397	Kindem et al.	10/20/2009		
	A206	7615808	Pain, et al.	11/10/2009		
	A207	7618839	Rhodes	11/17/2009		
	A208	7619269	Ohkawa	11/17/2009		
	A209	7629582	Hoffman, et al.	12/8/2009		
	A210	7648851	Fu, et al.	1/19/2010		
	A211	7649156	Lee	1/19/2010		
	A212	7705879	Kerr et al.	4/27/2010		
	A213	7731665	Lee et al	6/8/2010		

Examiner Signature	/LONG PHAM/	Date Considered	07/15/2016

EXAMINER: Initial if reference considered, whether or not citation is in conformance with MPEP 609. Draw line through citation if not in conformance and not considered. Include copy of this form with next communication to Applicant.

ALL REFERENCES CONSIDERED EXCEPT WHERE LINED THROUGH. /L.P./

SAMSUNG EX. 1002 - 3084/4148

Substitute for Form 1449/PTO				Complete if Known	
				Application No.:	14/747,875
INFORMATION DISCLOSURE STATEMENT BY APPLICANT				Filing Date:	June 23, 2015
				First Named Inventor:	Martin U. Pralle
				Group Art Unit:	2814
(use as many sheets as necessary)				Examiner Name:	Long Pham
Sheet	6	of	20	Attorney Docket No.:	143705.05211

	A214	7741666	Nozaki, et al.	6/22/2010		
	A215	7745901	McCaffrey et al	6/29/2010		
	A216	7763913	Fan et al	7/27/2010		
	A217	7772028	Adkisson et al	8/10/2010		
	A218	7781856	Mazur et al.	8/24/2010		
	A219	7800192	Venezia, et al.	9/21/2010		
	A220	7816220	Mazur et al.	10/19/2010		
	A221	7828983	Weber et al	11/9/2010		
	A222	7847253	Carey et al.	12/7/2010		
	A223	7847326	Park, et al.	12/7/2010		
	A224	7855406	Yamaguchi et al	12/21/2010		
	A225	7875498	Elbanhawy, et al.	1/25/2011		
	A226	7880168	Lenchenkov	2/1/2011		
	A227	7884439	Mazur et al.	2/8/2011		
	A228	7884446	Mazur et al.	2/8/2011		
	A229	7910964	Kawahito et al.	3/22/2011		
	A230	7923801	Tian et al.	4/12/2011		
	A231	7968834	Veeder	6/28/2011		
	A232	8008205	Fukushima et al.	8/30/2011		
	A233	8013411	Cole	9/6/2011		
	A234	8030726	Sumi	10/4/2011		
	A235	8035343	Seman Jr.	10/11/2011		
	A236	8058615	McCaffrey	11/15/2011		
	A237	8080467	Carey et al.	12/20/2011		
	A238	8088219	Knerer et al.	1/3/2012		
	A239	8093559	Rajavel	1/10/2012		
	A240	8164126	Moon, et al.	4/24/2012		
	A241	8207051	Sickler et al.	6/26/2012		
	A242	8247259	Grolier et al.	8/21/2012		
	A243	8259293	Andreou et al.	9/4/2012		
	A244	8288702	Veeder	10/16/2012		
	A245	8476681	Haddad et al.	7/2/2013		
	A246	8564087	Yamamura et al.	10/22/2013		
	A247	8603902	Mazer et al.	12/10/2013		
	A248	8629485	Yamamura et al.	1/14/2014		
	A249	8680591	Haddad et al.	3/25/2014		
	A250	8742528	Yamamura et al.	6/3/2014		
	A251	8884226	Miyazaki, et al.	11/11/2014		
	A252	8916945	Sakamoto et al	12/23/2014		
	A253	8994135	Yamamura et al.	6/31/2015		
	A254	9190551	Yamamura et al.	11/17/2015		
	A255	RE43169	Parker	2/7/2012		
	A256	20010017344	Aebi	8/30/2001		
	A257	20010022768	Takahashi	9/20/2001		

Examiner Signature	/LONG PHAM/	Date Considered	07/15/2016

EXAMINER: Initial if reference considered, whether or not citation is in conformance with MPEP 609. Draw line through citation if not in conformance and not considered. Include copy of this form with next communication to Applicant.

ALL REFERENCES CONSIDERED EXCEPT WHERE LINED THROUGH. /L.P./

SAMSUNG EX. 1002 - 3085/4148

Substitute for Form 1449/PTO				Complete if Known	
				Application No.:	14/747,875
INFORMATION DISCLOSURE STATEMENT BY APPLICANT				Filing Date:	June 23, 2015
				First Named Inventor:	Martin U. Pralle
				Group Art Unit:	2814
(use as many sheets as necessary)				Examiner Name:	Long Pham
Sheet	7	of	20	Attorney Docket No.:	143705.05211

	A258	20010044175	Barret et al.	11/22/2001		
	A259	20020020893	Lhorte	2/21/2002		
	A260	20020024618	Imai	2/28/2002		
	A261	20020056845	Iguchi et al.	5/16/2002		
	A262	20020060322	Tanabe et al.	5/23/2002		
	A263	20020079290	Holdermann	6/27/2002		
	A264	20020117699	Roy	8/29/2002		
	A265	20020148964	Dausch et al.	10/17/2002		
	A266	20020182769	Campbell	12/5/2002		
	A267	20030029495	Mazur et al.	2/13/2003		
	A268	20030030083	Lee et al.	2/13/2003		
	A269	20030045092	Shin	3/6/2003		
	A270	20030057357	Uppal et al.	3/27/2003		
	A271	20030111106	Nagano et al.	6/19/2003		
	A272	20030210332	Frame	11/13/2003		
	A273	20030213515	Sano et al.	11/20/2003		
	A274	20040014307	Shin et al.	1/22/2004		
	A275	20040016886	Ringermacher et al.	1/29/2004		
	A276	20040041168	Hembree et al.	3/4/2004		
	A277	20040046224	Rossel et al.	3/11/2004		
	A278	20040077117	Ding et al.	4/22/2004		
	A279	20040080638	Lee	4/29/2004		
	A280	20040130020	Kuwabara et al.	7/22/2004		
	A281	20040161868	Hong	8/19/2004		
	A282	20040222187	Lin	11/11/2004		
	A283	20040252931	Belleville et al.	12/16/2004		
	A284	20050051822	Manning	3/10/2005		
	A285	20050062041	Terakawa et al.	3/24/2005		
	A286	20050101100	Kretchmer et al.	5/12/2005		
	A287	20050101160	Garg et al.	5/12/2005		
	A288	20050127401	Mazur et al.	6/16/2005		
	A289	20050134698	Schroeder et al.	6/23/2005		
	A290	20050150542	Madan	7/14/2005		
	A291	20050158969	Binnis et al.	7/21/2005		
	A292	20050211996	Krishna, et al.	9/29/2005		
	A293	20050227390	Shtein et al.	10/13/2005		
	A294	20060006482	Rieve, et al.	1/12/2006		
	A295	20060011954	Ueda et al.	1/19/2006		
	A296	20060011955	Baggenstoss	1/19/2006		
	A297	20060060848	Chang et al.	3/23/2006		
	A298	20060071254	Rhodes	4/6/2006		
	A299	20060079062	Mazur et al.	4/13/2006		
	A300	20060097172	Park	5/11/2006		
	A301	20060231914	Carey et al.	10/19/2006		

Examiner Signature	/LONG PHAM/	Date Considered	07/15/2016

EXAMINER: Initial if reference considered, whether or not citation is in conformance with MPEP 609. Draw line through citation if not in conformance and not considered. Include copy of this form with next communication to Applicant.

ALL REFERENCES CONSIDERED EXCEPT WHERE LINED THROUGH. /L.P./

SAMSUNG EX. 1002 - 3086/4148

Substitute for Form 1449/PTO				Complete if Known	
				Application No.:	14/747,875
INFORMATION DISCLOSURE STATEMENT BY APPLICANT				Filing Date:	June 23, 2015
				First Named Inventor:	Martin U. Pralle
				Group Art Unit:	2814
(use as many sheets as necessary)				Examiner Name:	Long Pham
Sheet	8	of	20	Attorney Docket No.:	143705.05211

	A302	20090097290	Chandrasekaran	4/16/2009		
	A303	20060118781	Rhodes	6/8/2006		
	A304	20060121680	Tanaka	6/8/2006		
	A305	20060132633	Nam, et al.	6/22/2006		
	A306	20060138396	Lin, et al.	6/29/2006		
	A307	20060145148	Hirai, et al.	7/6/2006		
	A308	20060145176	Lee	7/6/2006		
	A309	20060160343	Chong et al.	7/20/2006		
	A310	20060166475	Mantl	7/27/2006		
	A311	20060175529	Harmon et al.	8/10/2006		
	A312	20060180885	Rhodes	8/17/2006		
	A313	20060181627	Farrier	8/17/2006		
	A314	20060210122	Cleveland	9/21/2006		
	A315	20060214121	Schrey et al.	9/28/2006		
	A316	20060228897	Timans	10/12/2006		
	A317	20060231914	Carey, III et al.	10/19/2006		
	A318	20060238632	Shah	10/26/2006		
	A319	20060244090	Roy, et al.	11/2/2006		
	A320	20060255340	Manivannan et al.	11/16/2006		
	A321	20060257140	Seger	11/16/2006		
	A322	20070035849	Li et al.	2/15/2007		
	A323	20070035879	Hall,et al.	2/15/2007		
	A324	20070051876	Sumi et al.	3/8/2007		
	A325	20070052050	Dierickx	3/8/2007		
	A326	20070076481	Tennant	4/5/2007		
	A327	20070115554	Breitung et al	5/24/2007		
	A328	20070123005	Hiura et al.	5/31/2007		
	A329	20070138590	Wells, et al.	6/21/2007		
	A330	20070145505	Kim et al.	6/28/2007		
	A331	20070178672	Tanaka, et al.	8/2/2007		
	A332	20070187670	Hsu et al.	8/16/2007		
	A333	20070194356	Moon, et al.	8/23/2007		
	A334	20070194401	Nagai, et al.	8/23/2007		
	A335	20070195056	Lloyd	8/23/2007		
	A336	20070200940	Gruhlke et al.	8/30/2007		
	A337	20070201859	Sarrat	8/30/2007		
	A338	20070235827	Altice	10/11/2007		
	A339	20070247414	Roberts	10/25/2007		
	A340	20070262366	Baek et al.	11/15/2007		
	A341	20070290283	Park et al.	12/20/2007		
	A342	20070296060	Tanabe et al.	12/27/2007		
	A343	20080002863	Northcott	1/3/2008		
	A344	20080020555	Shimomura et al.	1/24/2008		
	A345	20080026550	Werner et al.	1/31/2008		

Examiner Signature	/LONG PHAM/	Date Considered	07/15/2016

EXAMINER: Initial if reference considered, whether or not citation is in conformance with MPEP 609. Draw line through citation if not in conformance and not considered. Include copy of this form with next communication to Applicant.

ALL REFERENCES CONSIDERED EXCEPT WHERE LINED THROUGH. /L.P./

SAMSUNG EX. 1002 - 3087/4148

Substitute for Form 1449/PTO				Complete if Known	
INFORMATION DISCLOSURE STATEMENT BY APPLICANT				Application No.:	14/747,875
				Filing Date:	June 23, 2015
				First Named Inventor:	Martin U. Pralle
				Group Art Unit:	2814
(use as many sheets as necessary)				Examiner Name:	Long Pham
Sheet	9	of	20	Attorney Docket No.:	143705.05211

	A346	20080036022	Hwang et al.	2/14/2008		
	A347	20080044943	Mazur et al.	2/21/2008		
	A348	20080076240	Yannick Veschtti et al.	3/27/2008		
	A349	20080099804	Venezia	5/1/2008		
	A350	20080121280	Carnel et al.	5/29/2008		
	A351	20080121805	Tweet et al.	5/29/2008		
	A352	20080170173	Park et al.	7/17/2008		
	A353	20080174685	Shan et al.	7/24/2008		
	A354	20080178932	Willem Den Boer et al.	7/31/2008		
	A355	20080179762	Cho et al.	7/31/2008		
	A356	20080191310	Wu et al.	8/14/2008		
	A357	20080192132	Bechtel et al.	8/14/2008		
	A358	20080196761	Nakano et al.	8/21/2008		
	A359	20080198251	Xu et al.	8/21/2008		
	A360	20080202576	Hieslmair	8/28/2008		
	A361	20080213936	Hatai	9/4/2008		
	A362	20080223436	den Boer et al.	9/18/2008		
	A363	20080242005	Dozen et al.	10/2/2008		
	A364	20080257409	Li et al.	10/23/2008		
	A365	20080258604	Mazur et al.	10/23/2008		
	A366	20080266435	Agranov et al.	10/30/2008		
	A367	20080266434	Sugawa et al.	10/30/2008		
	A368	20080281174	Dietiker	11/13/2008		
	A369	20080309913	Fallon	12/18/2008		
	A370	20090002528	Manabe et al.	1/1/2009		
	A371	20090050944	Hong	2/26/2009		
	A372	20090014056	Hockaday	1/15/2009		
	A373	20090038669	Atanackovic	2/12/2009		
	A374	20090039397	Chao	2/12/2009		
	A375	20090056797	Barnett et al.	3/5/2009		
	A376	20090057536	Hirose	3/5/2009		
	A377	20090065051	Chan et al.	3/12/2009		
	A378	20090078316	Khazeni et al.	3/26/2009		
	A379	20090095887	Saveliev	4/16/2009		
	A380	20090109305	Dai et al.	4/30/2009		
	A381	20090142879	Isaka et al.	6/4/2009		
	A382	20090146240	Carey III et al.	6/11/2009		
	A383	20090160983	Lenchenkov	6/25/2009		
	A384	20090180010	Adikisson et al.	7/16/2009		
	A385	20090194671	Nozaki et al.	8/6/2009		
	A386	20090200454	Barbier et al.	8/13/2009		
	A387	20090200586	Mao et al.	8/13/2009		
	A388	20090200626	Qian, et al.	8/13/2009		
	A389	20090200631	Tai, et al.	8/13/2009		

Examiner Signature	/LONG PHAM/	Date Considered	07/15/2016

EXAMINER: Initial if reference considered, whether or not citation is in conformance with MPEP 609. Draw line through citation if not in conformance and not considered. Include copy of this form with next communication to Applicant.

ALL REFERENCES CONSIDERED EXCEPT WHERE LINED THROUGH. /L.P./

SAMSUNG EX. 1002 - 3088/4148

Substitute for Form 1449/PTO				Complete if Known	
				Application No.:	14/747,875
INFORMATION DISCLOSURE STATEMENT BY APPLICANT				Filing Date:	June 23, 2015
				First Named Inventor:	Martin U. Pralle
				Group Art Unit:	2814
(use as many sheets as necessary)				Examiner Name:	Long Pham
Sheet	10	of	20	Attorney Docket No.:	143705.05211

	A390	20090206237	Shannon et al.	8/20/2009		
	A391	20090211627	Meier et al.	8/27/2009		
	A392	20090213883	Mazur et al.	8/27/2009		
	A393	20090218493	McCaffrey et al.	9/3/2009		
	A394	20090223561	Kim et al.	9/10/2009		
	A395	20090227061	Bateman et al.	9/10/2009		
	A396	20090242032	Yamazaki et al.	10/1/2009		
	A397	20090242933	Hu, et al.	10/1/2009		
	A398	20090256156	Hsieh	10/15/2009		
	A399	20090256226	Tatani	10/15/2009		
	A400	20090261255	Nakamura et al.	10/22/2009		
	A401	20090283807	Adkisson et al.	11/19/2009		
	A402	20090294787	Nakaji, et al.	12/3/2009		
	A403	20090308450	Adibi et al.	12/17/2009		
	A404	20100000597	Cousins	1/7/2010		
	A405	20100013036	Carey	1/21/2010		
	A406	20100013039	Qian, et al.	1/21/2010		
	A407	20100013593	Luckhardt	1/21/2010		
	A408	20100024871	Oh et al.	2/4/2010		
	A409	20100032008	Adekore	2/11/2010		
	A410	20100037952	Lin	2/18/2010		
	A411	20100038523	Venezia et al.	2/18/2010		
	A412	20100038542	Carey et al.	2/18/2010		
	A413	20100040981	Kiesel et al.	2/18/2010		
	A414	20100044552	Chen	2/25/2010		
	A415	20100051809	Onat et al.	3/4/2010		
	A416	20100052088	Carey	3/4/2010		
	A417	20100053382	Kuniba	3/4/2010		
	A418	20100055887	Piwczyk	3/4/2010		
	A419	20100059385	Li	3/11/2010		
	A420	20100059803	Gidon et al.	3/11/2010		
	A421	20100072349	Veeder	3/25/2010		
	A422	20100074396	Schmand et al.	3/25/2010		
	A423	20100083997	Hovel	4/28/2010		
	A424	20100084009	Carlson et al	4/8/2010		
	A425	20100096718	Hynecek, et al.	4/22/2010		
	A426	20100097609	Jaeger, et al.	4/22/2010		
	A427	20100102206	Cazaux et al.	4/29/2010		
	A428	20100109060	Mao, et al.	5/6/2010		
	A429	20100116312	Peumans et al.	5/13/2010		
	A430	20100117181	Kim et al.	5/13/2010		
	A431	20100118172	McCarten et al.	5/13/2010		
	A432	20100128937	Yoo et al.	5/27/2010		
	A433	20100133635	Lee et al.	6/3/2010		

Examiner Signature	/LONG PHAM/	Date Considered	07/15/2016

EXAMINER: Initial if reference considered, whether or not citation is in conformance with MPEP 609. Draw line through citation if not in conformance and not considered. Include copy of this form with next communication to Applicant.

ALL REFERENCES CONSIDERED EXCEPT WHERE LINED THROUGH. /L.P./

SAMSUNG EX. 1002 - 3089/4148

Substitute for Form 1449/PTO				Complete if Known	
				Application No.:	14/747,875
INFORMATION DISCLOSURE STATEMENT BY APPLICANT				Filing Date:	June 23, 2015
				First Named Inventor:	Martin U. Pralle
				Group Art Unit:	2814
(use as many sheets as necessary)				Examiner Name:	Long Pham
Sheet	11	of	20	Attorney Docket No.:	143705.05211

	A434	20100140733	Lee et al.	6/10/2010		
	A435	20100143744	Gupta	6/10/2010		
	A436	20100147383	Carey et al.	6/17/2010		
	A437	20100219506	Gupta	9/2/2010		
	A438	20100224229	Pralle et al.	9/9/2010		
	A439	20100240169	Petti et al.	9/23/2010		
	A440	20100245647	Honda et al.	9/30/2010		
	A441	20100258176	Kang et al.	10/14/2010		
	A442	20100264473	Adkisson et al.	10/21/2010		
	A443	20100289885	Lu et al.	11/18/2010		
	A444	20100290668	Friedman et al.	11/18/2010		
	A445	20100300505	Chen	12/2/2010		
	A446	20100300507	Heng et al.	12/2/2010		
	A447	20100313932	Kroll et al.	12/16/2010		
	A448	20110056544	Ji et al.	3/10/2011		
	A449	20110073976	Vaillant	3/31/2011		
	A450	20110095387	Carey et al.	4/28/2011		
	A451	20110104850	Weidman et al.	5/5/2011		
	A452	20110127567	Seong	6/2/2011		
	A453	20110140221	Venezia et al.	6/16/2011		
	A454	20110220971	Haddad	9/15/2011		
	A455	20110227138	Haddad	9/22/2011		
	A456	20110251478	Wieczorek	10/13/2011		
	A457	20110260059	Jiang et al.	10/27/2011		
	A458	20110266644	Yamamura et al.	11/4/2011		
	A459	20110303999	Sakamoto et al.	12/15/2011		
	A460	20120024363	Carey et al.	2/2/2012		
	A461	20120024364	Carey, III et al.	2/2/2012		
	A462	20120038811	Ellis-monaghan et al	2/16/2012		
	A463	20120043637	King et al.	2/23/2012		
	A464	20120049242	Atanackovic et al.	3/1/2012		
	A465	20120111396	Saylor et al.	5/10/2012		
	A466	20120171804	Moslehi et al.	7/5/2012		
	A467	20120187190	Wang et al.	7/26/2012		
	A468	20120222396	Clemen	9/6/2012		
	A469	20120291859	Vineis et al.	11/22/2012		
	A470	20120300037	Laudo	11/29/2012		
	A471	20120305063	Moslehi et al.	12/6/2012		
	A472	20120312304	Lynch et al.	12/13/2012		
	A473	20120313204	Haddad et al.	12/13/2012		
	A474	20120313205	Haddad et al.	12/13/2012		
	A475	20120326008	Mckee et al.	12/27/2012		
	A476	20130001553	Vineis et al.	1/3/2013		
	A477	20130082343	Fudaba, et al.	4/4/2013		

Examiner Signature	/LONG PHAM/	Date Considered	07/15/2016

EXAMINER: Initial if reference considered, whether or not citation is in conformance with MPEP 609. Draw line through citation if not in conformance and not considered. Include copy of this form with next communication to Applicant.

ALL REFERENCES CONSIDERED EXCEPT WHERE LINED THROUGH. /L.P./

SAMSUNG EX. 1002 - 3090/4148

Substitute for Form 1449/PTO				Complete if Known	
INFORMATION DISCLOSURE STATEMENT BY APPLICANT				Application No.:	14/747,875
				Filing Date:	June 23, 2015
				First Named Inventor:	Martin U. Pralle
				Group Art Unit:	2814
(use as many sheets as necessary)				Examiner Name:	Long Pham
Sheet	12	of	20	Attorney Docket No.:	143705.05211

	A478	20130168792	Haddad et al.	7/4/2013		
	A479	20130168803	Haddad et al.	7/4/2013		
	A480	20130200251	Velichko	8/8/2013		
	A481	20130207214	Haddad et al.	8/15/2013		
	A482	20130285130	Ting	10/31/2013		
	A483	20140247378	Sharma et al.	9/4/2014		

FOREIGN PATENT DOCUMENTS

Examiner's Initials	Cite No.	Foreign Patent Document Number Kind Code (if known)	Name of Patentee or Applicant of Cited Document	Date of Publication of Cited Document MM-DD-YYYY	Pages, Columns, Lines, Where Relevant Passages or Relevant Figures Appear			T
	B1	AU 3666484	Wenham et al.	6/27/1985				
	B2	EP 0473439	Cooper Industries	3/4/1992				
	B3	EP 0566156	Terumo Kabushiki Kaisha	10/20/1993				
	B4	EP 1630871	Matsushita Electric Industrial Co. Ltd.	1/3/2006				
	B5	EP 1873840	Neil, et al.	1/2/2008				
	B6	EP 2073270	Hirota, et al.	5/16/2012				
	B7	FR 2827707	FR De Detecteurs Infrarouges S	1/24/2003				
	B8	GB 2030766	Plessey Co. Ltd.	4/10/1980				
	B9	JP H04318970	Mitsubishi Electric Corp.	11/10/1992				
	B10	JP S57173966	Fuji Photo Film Co. Ltd.	10/26/1982				
	B11	JP S63116421	Mitsubishi Electric Corp.	5/20/1988				
	B12	JP H02152226	Fujitsu Ltd.	6/12/1990				
	B13	JP H02237026	Sony, Corp.	9/19/1990				
	B14	JP H03183037	Nec Corp.	8/9/1991				
	B15	JP H06275641	Semiconductor Energy Lab Co. LTD.	9/30/1994				
	B16	JP S5771188	Mitsubishi Electric Corp.	5/1/1982				
	B17	JP 2000164914	Electrowatt Technol Innov AG	6/16/2000				
	B18	JP 2001007381	Japan Broadcasting Corp.	1/12/2001				
	B19	JP 2002043594	Sharp KK	2/8/2002				
	B20	JP 2002134640	United Test CT Inc.	5/10/2002				
	B21	JP 2003163360	Seiko Epson Corp.	6/6/2003				
	B22	JP 2004273886	Hatachi Cable	9/3/2004				
	B23	JP 2004273887	Hatachi Cable Ltd.	9/30/2004				
	B24	JP H06267868	Fuji Electric Co LTD	9/22/1994				
	B25	JP 2007180642	SWCC Showa Device Tech Co. Ltd.	7/12/2007				

Examiner Signature	/LONG PHAM/	Date Considered	07/15/2016

EXAMINER: Initial if reference considered, whether or not citation is in conformance with MPEP 609. Draw line through citation if not in conformance and not considered. Include copy of this form with next communication to Applicant.

ALL REFERENCES CONSIDERED EXCEPT WHERE LINED THROUGH. /L.P./

SAMSUNG EX. 1002 - 3091/4148

Substitute for Form 1449/PTO				Complete if Known	
				Application No.:	14/747,875
INFORMATION DISCLOSURE STATEMENT BY APPLICANT				Filing Date:	June 23, 2015
				First Named Inventor:	Martin U. Pralle
				Group Art Unit:	2814
(use as many sheets as necessary)				Examiner Name:	Long Pham
Sheet	13	of	20	Attorney Docket No.:	143705.05211

	B26	JP 2007180643	Sony Corp.	7/12/2007				
	B27	JP 2007305675	Sony, Corp.	11/22/2007				
	B28	JP 2008187003	Fujitsu Ltd.	8/14/2008				
	B29	JP H07183484	FR Telecom	7/21/1995				
	B30	JP 2011091128	Cannon KK	5/6/2011				
	B31	JP 9148594	Sanyo Electric Co.	6/6/1997				
	B32	JP H09298308	Sharp KK	11/18/1997				
	B33	JP H06104414	Toshiba Corp.	4/15/1994				
	B34	JP 11077348	Cannon KK	3/23/1999				
	B35	JP 11097724	Citizen Watch Co. Ltd.	4/9/1999				
	B36	JP 2001189478	Sanyo Electric Co.	7/10/2001				
	B37	JP 2001339057	Fuji Xerox Co. Ltd.	12/7/2001				
	B38	JP 2006173381	Toyota Motor Corp.	6/29/2006				
	B39	JP 2007165909	Icemos Technology Corp.	6/28/2007				
	B40	JP 2008187003	Fujitsu Ltd.	8/14/2008				
	B41	JP 2008283219	Toshiba Corp.	11/20/2008				
	B42	JP 2009021479	Omron Tteisi Electronics Co.	1/29/2009				
	B43	JP 2010278472	Sony, Corp.	12/9/2010				
	B44	KR 20060052278	Sony Corp.	5/16/2016				
	B45	KR 100825808	Samsung Electronics CO. Ltd.	4/29/2008				
	B46	KR 20010061058	Hynix Semiconductor Inc.	4/7/2001				
	B47	KR 2005039273	Jin- Sin Lee	4/29/2005				
	B48	KR 20100118864	Hyosung Corp	11/8/2010				
	B49	WO 91/14284	Theden, Ulrich	9/19/1991				
	B50	WO 2002041363	Solarflex Technologies Inc.	5/23/2002				
	B51	WO 03/059390	Dong Wha Pharm Ind Co. Ltd	7/24/2003				
	B52	WO 2006/086014	President and Fellows of Harvard College	8/17/2006				
	B53	WO 2008091242	UVA Patent Foundation	7/31/2008				
	B54	WO 2008099524	Mitsubishi Heavy Industries Ltd.	8/21/2008				
	B55	WO 2008145097	Fraunhofer-Gesellschaft Zur Faurderung Der Angewandten	12/8/2008				
	B56	WO 2010033127	Sionyx, Inc.	3/25/2010				
	B57	WO 2009100023	President and Fellows of Harvard College	8/13/2009				
	B58	WO 2009147085	Thiel et al.	12/10/2009				
	B59	WO 2011003871	International Business Machines Corporation	1/13/2011				

Examiner Signature	/LONG PHAM/	Date Considered	07/15/2016

EXAMINER: Initial if reference considered, whether or not citation is in conformance with MPEP 609. Draw line through citation if not in conformance and not considered. Include copy of this form with next communication to Applicant.

ALL REFERENCES CONSIDERED EXCEPT WHERE LINED THROUGH. /L.P/

SAMSUNG EX. 1002 - 3092/4148

Substitute for Form 1449/PTO **INFORMATION DISCLOSURE STATEMENT BY APPLICANT** (use as many sheets as necessary)				**Complete if Known**	
				Application No.:	14/747,875
				Filing Date:	June 23, 2015
				First Named Inventor:	Martin U. Pralle
				Group Art Unit:	2814
				Examiner Name:	Long Pham
Sheet	14	of	20	Attorney Docket No.:	143705.05211

	B60	WO 2011035188	Sionyx, Inc.	3/24/2011				
	B61	WO 2011119618	Sionyx, Inc.	3/22/2011				

OTHER ART (Including Author, Title, Date, Pertinent Pages, Etc.)			
Examiner's Initials	**Cite No.**	**Include name of the author (in CAPITAL LETTERS), title of the article (when appropriate), title of the item (book, magazine, journal, serial, symposium, catalog, etc.), date, page(s), volume-issue number(s), publisher, city and/or county where published**	T
	C1	International Search Report, mailed August 18, 2014, in corresponding PCT/US2014/024964 (3 pages).	
	C2	International Preliminary Report on Patentability and Written Opinion, mailed August 18, 2014, in corresponding PCT/US2014/0024964 (6 pages).	
	C3	A. Arndt, J.F. Allison, J.G. Haynos, and A. Meulenberg, Jr., "Optical Properties of the COMSAT Non-reflective Cell," 11th IEEE Photovoltaic Spec. Conf., p. 40, 1975	
	C4	Asom et al., Interstitial Defect Reactions in Silicon; Appl. Phys. Lett.; 07/27/1987; pp. 256-258; vol. 51(4); American Institute of Physics.	
	C5	BERGER, Michael; Moth Eyes Inspire Self-Cleaning Antireflection Nanotechnology Coatings; 2008; 3 pages; Nanowerk LLC	
	C6	Berger, O., Inns, D. and Aberle, A.E. "Commercial White Paint as Back Surface Reflector for Thin-Film Solar Cells", Solar Energy Materials & Solar Cells, vol. 91, pp. 1215-1221,2007.	
	C7	Betta et al.; Si-PIN X-Ray Detector Technology; Nuclear Instruments and Methods in Physics Research; 1997; pp. 344-348; vol. A, No. 395; Elsevier Science B.V. cited by applicant.	
	C8	BODEN, S.A. et al.; Nanoimprinting for Antireflective Moth-Eye Surfaces; 4 pages; 2008	
	C9	Bogue: "From bolometers to beetles: the development of the thermal imaging sensors;" sensor Review; 2007; pp. 278-281; Emerald Group Publishing Limited (ISSN 0260-2288).	
	C10	Borghesi et al.; "Oxygen Precipitation in Silicon," J. Appl. Phys., v. 77(9), pp. 4169-4244 (May 1, 1995).	
	C11	Born, M. and E.Wolf, "Princip les of Optics, 7th Ed.", Cambridge University Press, 1999, pp. 246-255.	
	C12	Brieger,S., O.Dubbers, S.Fricker, A.Manzke, C.Pfahler, A.Plettl, and P.Zlemann, "An Approach for the Fabrication of Hexagonally Ordered Arrays of Cylindrical Nanoholes in Crystalline and Amorphous Silicon Based on the Self-Organization of Polymer Micelles", Nanotechnology, vol. 17, pp. 4991-4994, 2006, doi:10.1088/0957-4884/17/19/036.	
	C13	Buttgen, B.; "Demodulation Pixel Based on Static Drift Fields"; IEEE Transactions on Electron Devices, vol. 53, No. 11, Nov. 2006.	
	C14	Carey et al., "Femtosecond-Laser-Assisted Microstructuring of Silicon Surfaces", Optics and Photonics News, 2003. 14, 32-36.	
	C15	Carey, et al. "Femtosecond Laser-Assisted Microstructuring of Silicon for Novel Detector, Sensing and Display Technologies", LEOS 2003, 481-482, Tuscon, AR.	
	C16	Carey, et al. "Femtosecond Laser-Assisted Microstructuring of Silicon for Novel Detector, Sensing and Display Technologies", LEOS; 2002, 97-98, Glasgos, Scotland, 2002.	
	C17	Carey, et al., "Fabrication of Micrometer-Sized Conical Field Emitters Using Femtosecond Laser-Assisted Etching of Silicon," Proc. IVMC 2001, 75-76, UC Davis, Davis, CA.	
	C18	Carey, et al., "Field Emission from Silicon. Microstructures Formed by Femtosecond Laser Assisted Etching," Proc. CLEO 2001 (Baltimore, MD 2001) 555-557.	
	C19	Carey, et al., "High Sensitivity Silicon-Based VIS/NIR Photodetectors", Optical Society of America (2003) 1-2.	

Examiner Signature	/LONG PHAM/	Date Considered	07/15/2016

EXAMINER: Initial if reference considered, whether or not citation is in conformance with MPEP 609. Draw line through citation if not in conformance and not considered. Include copy of this form with next communication to Applicant.

ALL REFERENCES CONSIDERED EXCEPT WHERE LINED THROUGH. /L.P./

SAMSUNG EX. 1002 - 3093/4148

Substitute for Form 1449/PTO				Complete if Known	
INFORMATION DISCLOSURE STATEMENT BY APPLICANT				Application No.:	14/747,875
				Filing Date:	June 23, 2015
				First Named Inventor:	Martin U. Pralle
				Group Art Unit:	2814
(use as many sheets as necessary)				Examiner Name:	Long Pham
Sheet	15	of	20	Attorney Docket No.:	143705.05211

	C20	CAREY, III; "Femtosecond-laser Microstructuring of Silicon for Novel Optoelectronic Devices"; Harvard University, July 2004; (Thesis)	
	C21	Chang, S.W., V.P.Chuang, S.T.Boles, and C.V.Thompson, "Metal-Catalyzed Etching of Vertically Aligned Polysilicon and Amorphous Silicon Nanowire Arrays by Etching Direction Confinement", Advanced Functional Materials, vol. 20, No. 24, pp. 4364-4370, 2010	
	C22	CHEN, Q. et al.; Broadband moth-eye antireflection coatings fabricated by low-cost nanoimprinting; Applied Physics Letters 94; pgs. 263118-1 - 263118-3; 2009; American Institute of Physics	
	C23	Chien et al, "Pulse Width Effect in Ultrafast Laser Processing of Materials," Applied Physics A, 2005, 1257-1263, 81, Springer Berlin, Heidelberg, Germany.	
	C24	CHIANG, Wen Jen Et al., "Silicon Nanocrystal-Based Photosensor on Low-Temperature Polycrystalline-Silicone Panels", Applied Physics Letters, 2007, 51120-1-51120-3, Ltt. 91, American Inst. Of Physics, Melville, NY.	
	C25	CHICHKIV, B.N. et al, "Femtosecond, picosecond and nanosecond laser ablation of solids" Appl. Phys. A 63, 109-115; 1996.	
	C26	CILINGIROGLU et al., "An evaluation of MOS Interface-Trap Charge Pump as and Ultralow Constant-Current Generator," IEEE Journal of Solid-State Circuit, 2003, Vol. 38, No. 1, Jan. 2003, 71-83.	
	C27	CMOSIS; "Global Shutter Image Sensors for Machine Vision Application"; Image Sensors Europe 2010, Mar. 23-25, 2010; .COPYRGT. copyright 2010.	
	C28	Cotter, Jeffrey E.; Optical intensity of light in layers of silicon with rear diffuse reflectors; Journal of Applied Physics; Jul. 1, 1998; pp. 618-624; vol. 84, No. 1; American Institute of Physics.	
	C29	Crouch et al., "Comparison of Structure and Properties of Femtosecond and Nanosecond Laser-Structured Silicon" Appl. Phys. Lett., 2004, 84,1850-1852.	
	C30	Crouch et al., "Infrared Absorption by Sulfur-Doped Silicon Formed by Femtosecond Laser Irradiation", Appl. Phys. A, 2004, 79, 1635-1641.	
	C31	Despeisse, et al.; "Thin Film Silicon Solar Cell on Highly Textured Substrates for High Conversion Efficiency"; 2004.	
	C32	Detection of X-ray and Gamma-ray Photons Using Silicon Diodes; Dec. 2000; Detection Technology, Inc.; Micropolis, Finland.	
	C33	DEWAN, Rahul et al.; Light Trapping in Thin-Film Silicon Solar Cells with Submicron Surface Texture; Optics Express; Vol. 17, No. 25; December 7, 2009; Optical Society of America	
	C34	Deych et al.; Advances in Computed Tomography and Digital Mammography; Power Point; Nov. 18, 2008; Analogic Corp.; Peabody, MA	
	C35	Dobie, et al.; "Minimization of reflected light in photovoltaic modules"; Mar. 1, 2009.	
	C36	DOBRZANSKI, L.A. et al.; Laser Surface Treatment of Multicrystalline Silicon for Enhancing Optical Properties; Journal of Materials Processing Technology; page 291 - 296; 2007; Elsevier B.V.	
	C37	Dolgaev et al., "Formation of Conical Microstructures Upon Laser Evaporation of Solids", Appl. Phys. A, 2001, 73, 177-181.	
	C38	Duerinckx, et al.; "Optical Path Length Enhancement for >13% Screenprinted Thin Film Silicon Solar Cells"; 2006.	
	C39	Dulinski, Wojciech et al.; Tests of backside illumincated monolithic CMOS pixel sensor in an HPD set-up; Nuclear Instruments and methods in Physics Research; Apr. 19, 2005; pp. 274-280; Elsevier B.V.	
	C40	FORBES; "Texturing, reflectivity, diffuse scattering and light trapping in silicon solar cells"; 2012	
	C41	Forbes, L. and M.Y. Louie, "Backside Nanoscale Texturing to Improve IR Response of Silicon Photodetectors and Solar Cells," Nanotech, vol. 2, pp. 9-12, Jun. 2010.	
	C42	Fowlkes et al., "Surface Microstructuring and Long-Range Ordering of Silicon Nanoparticles",	

Examiner Signature	/LONG PHAM/	Date Considered	07/15/2016

EXAMINER: Initial if reference considered, whether or not citation is in conformance with MPEP 609. Draw line through citation if not in conformance and not considered. Include copy of this form with next communication to Applicant.

ALL REFERENCES CONSIDERED EXCEPT WHERE LINED THROUGH. /L.P/

SAMSUNG EX. 1002 - 3094/4148

Substitute for Form 1449/PTO				Complete if Known	
INFORMATION DISCLOSURE STATEMENT BY APPLICANT				Application No.:	14/747,875
				Filing Date:	June 23, 2015
				First Named Inventor:	Martin U. Pralle
				Group Art Unit:	2814
(use as many sheets as necessary)				Examiner Name:	Long Pham
Sheet	16	of	20	Attorney Docket No.:	143705.05211

		Appl. Phys. Lett., 2002, 80 (20), 3799-3801.	
	C43	Gjessing, J. et al.; 2D back-side diffraction grating for impored light trapping in thin silicon solar cells; Optics Express; vol. 18, No. 6; pp. 5481-5495; Mar. 15, 2010; Optical Society of America.	
	C44	Gjessing, J. et al.; 2D blazed grating for light trapping in thin silicon solar cells; 3 pages; 2010; Optical Society of America.	
	C45	Gloeckler et al. Band-Gap Grading in CU(In,GA)Se2 Solar Cells, Journal of Physics and Chemistry of Solids; 2005; pages 189-194; vol. 66.	
	C46	Goetzberger, et al.; "Solar Energy Materials & Solar Cells"; vol. 92 (2008) pp. 1570-1578.	
	C47	HAN et al., "Evaluation of a Small Negative Transfer Gate Bias on the Performance of 4T CMOS Image Sensor Pixels," 2007 International Image Sensor Workshop, 238-240, Ogunquit, Maine.	
	C48	HAUG, et al.; "Light Trapping effects in thin film silicon solar cells"; 2009	
	C49	Her et al., "Microstructuring of Silicon with Femtosecond Laser Pulses," Applied Physics Letters, 1998, 1673-1675, vol. 73, No. 12, American Institute of Physics.	
	C50	Her et al., "Novel Conical Microstructures Created in Silicon With Femtosecond Laser Pulses", CLEO 1998, 511-512, San Francisco, CA.	
	C51	Her, et al., "Femtosecond laser-induced formation of spikes on silicon," Applied Physics A, 2000, 70, 383-385.	
	C52	HERMANN, S. et al.; Impact of Surface Topography and Laser Pulse Duration for Laser Ablation of Solar Cell Front Side Passivating SiNx Layers; Journal of Applied Physics; Vol. 108, No. 11; pages 114514-1 - 114514-8; 2010; American Institute of Physics	
	C53	High--Performance Technologies for Advanced Biomedical Applications; .COPYRGT. 2004Brochure; pp. 1-46; PerkinElmerOptoelectronics	
	C54	Holland; Fabrication of Detectors and Transistors on High-Resistivity Silicon; Nuclear Instruments and Methods in Physics Research, vol. A275, pp. 537-541 (1989).	
	C55	HONG et al., "Cryogenic processed metal-semiconductor-metal (MSM) photodetectors on MBE grown ZnSe,", 1999, IEEE Transactions on Electron Devices, vol. 46, No. 6, pp. 1127-1134.	
	C56	HSIEH et al., "Focal-Plane-Arrays and CMOS Readout Techniques of Infrared Imaging Systems," IEE Transactions on Circuits and Systems for Video Technology, 1997, vol. 7, no. 4, Aug. 1997, 594-605.	
	C57	Hu et al., "Solar Cells from Basic to Advanced Systems," McGraw Hill Book Co., 1983, 39, New York, New York.	
	C58	HUANG, et al.; "Microstructured silicon photodetector"; Applied Physics Letters 89, 033506; 2006 American Institute of Physics; 2006	
	C59	HÜPKES, J. et al.; Light Scattering and Trapping in Different Thin Film Photovoltaic Devices; 24th European Photovoltaic Solar Energy Conference, Hamburg, Germany (Sept. 21-25, 2009); pgs. 2766-2769	
	C60	Igalson et al. Defect States in the CIGS Solar cells by Photocapacitance and Deep Level Optical Spectroscopy; Bulletin of the Polish Academy of Sciences Technical Sciences; 2005; pp. 157-161; vol. 53(2).	
	C61	"Infrared Absorption by Sulfur-Doped Silicon formed by Femtosecond Laser Irradiation"; Springer Berline/Heidelberg, vol. 79, Nov. 2004.	
	C62	Job et al., "Doping of Oxidized Float Zone Silincon by Thermal Donors - A low Thermal Budget Doping Method for Device Applications?" Mat. Res. Soc. Symp. Pro.; v. 719, F9.5.1-F9.5.6 (2002).	
	C63	Joy, T. et al.; Development of a Production-Ready, Back-Illuminated CMOS Image Sensor with Small Pixels; Electron Devices Meeting; pp. 1007-1010; 2007; IEEE.	
	C64	Juntunen et al.; Advanced Photodiode Detector for Medical CT Imaging: Design and Performance; 2007; pp. 2730-2735; IEEE.	

Examiner Signature	/LONG PHAM/	Date Considered	07/15/2016

EXAMINER: Initial if reference considered, whether or not citation is in conformance with MPEP 609. Draw line through citation if not in conformance and not considered. Include copy of this form with next communication to Applicant.

ALL REFERENCES CONSIDERED EXCEPT WHERE LINED THROUGH. /L.P./

SAMSUNG EX. 1002 - 3095/4148

Substitute for Form 1449/PTO				Complete if Known	
INFORMATION DISCLOSURE STATEMENT BY APPLICANT				Application No.:	14/747,875
				Filing Date:	June 23, 2015
				First Named Inventor:	Martin U. Pralle
				Group Art Unit:	2814
(use as many sheets as necessary)				Examiner Name:	Long Pham
Sheet	17	of	20	Attorney Docket No.:	143705.05211

	C65	KIM et al.; "Strong Sub-Band-Gap Infrared Absorption in Silicon Supersaturated with Sulfur"; 2006 Appl. Phys. Lett. 88, 241902-1 – 241902-3	
	C66	Kolasinski et al., "Laser Assisted and Wet Chemical Etching of Silicon Nanostructures," J. Vac. Sci. Technol., A 24(4), Jul/Aug 2006, 1474-1479.	
	C67	Konstantatos et al., "Engineering the Temproal Response of Photoconductive Photodetectors via Selective Introduction of Surface Trap States," Nano Letters, v. 8(5), pp. 1446-1450 (Apr. 2, 2008).	
	C68	Konstantatos et al., "PbS Colloidal Quantum Dot Photoconductive Photodetectors: Transport, Traps, and Gain," Appl. Phys. Lett., v. 91, pp. 173505-1-173505-3 (Oct. 23, 2007).	
	C69	Kray, D. et al.; Laser-doped Silicon Soalr Cells by Laser Chemical Processing (LCP) exceeding 20% Efficiency; 33rd IEEE Photovoltaic Specialist Conference; 3 pages; May 2008; IEEE.	
	C70	Kroning et al.; X-ray Imaging Systems for NDT and General Applications; 2002; Fraunhofer Institute for Nondestructive Testing; Saarbrucken and Dresden, Germany.	
	C71	Kryski; A High Speed 4 Megapixel Digital CMOS Sensor; 2007 International Image Sensor Workshop; Jun. 6-10, 2007.	
	C72	Li, "Design and Simulation of an Uncooled Double-Cantilever Microbolometer with the Potential for .about.mK NETD," 2004, Sensors and Actuators A, 351-359, vol. 112, Elsevier B.V.	
	C73	Li et al., "Gettering in High Resistive Float Zone Silicon Wafers," Transaction on Nuclear Science," vol. 36(1), pp. 290-294 (Feb. 1, 1989).	
	C74	Li, Hongsong et al.; An experimental study of the correlation between surface roughness and light scattering for rough metallic surfaces; Advanced Characterization Techniques for Optics, Semiconductors, and Nanotechnologies II; 2005; pp. 25780V-1-25780V-15; vol. 5878; SPIE Bellingham, WA.	
	C75	Lin, A. et al.; Optimization of Random Diffraction Gratings in Thin-Film Solar Cells Using Genetic Algorithms; 2007; 1 page; SSEL Annual Report. cited by applicant .	
	C76	Low Dose Technologies; Power Point	
	C77	Madzharov, et al.; "Light trapping in thin-firm silicon solar cells for superstrate and substrate configuration" Abstract #1614, 218.sup.th ECS Meeting .COPYRGT. 2010 the Electrochemical Society.	
	C78	"Masimo Rainbow SET Pulse CO-Oximetry," 2010, Masimo Corporation, Irvine, California, http://www.masimo.com/Rainbow/about.htm.	
	C79	Mateus; C.F.R. et al.; Ultrabroadband Mirror Using Low-Index Cladded Subwavelength Grating; Photonics Technology Letters; vol. 16, Issue No. 2; pp. 518-520; Feb. 2004; IEEE.	
	C80	Matsuno, Shigeru et al.; Advanced Technologies for High Efficiency Photovoltaic Systems; Mitsubishi Electric Advance; vol. 122; pp. 17-19; Jun. 2008	
	C81	Meynants, et al.; "Backside illuminated global shutter COMOS image sensors"; 2011 International Image Sensor Workshop; Jun. 11, 2011.	
	C82	MOLONEY, A.M. et al.; Novel Black Silicon PIN Photodiodes; 8 pages; January 25, 2006; SPIE.	
	C83	Moon et al. Selective emitter using porous silicon for crystalline silicon solar cells. Solar Energy Materials & Solar Cells, v. 93, pp. 846-850 (2009).	
	C84	Moses; Nuclear Medical Imaging--Techniques and Challenges; Power Point; Feb. 9, 2005; Lawrence Berkeley National Laboratory Department of Functional Imaging.	
	C85	Murkin, JM and Arangol, M, "Near Infrared spectroscopy as an index of rain and tissue oxygenation," Bri. J. of Anathesia (BJA/PGA Supplement):13-il3 (2009).	
	C86	Munday, J.N. et al.; Large Integrated Absorption Enhancement in Plasmonic Solar Cells by Combining Metallic Gratings and Antireflection Coatings; Nano Letters; vol. 11, No. 6; pp. 2195-2201; Oct. 14, 2010; American Chemical Society	
	C87	Myers, Richard et al., "Enhancing Near-IR Avalanche Photodiodes Performance by Femtosecond Laser Microstructuring" Harvard Dept. Of Physics.	

Examiner Signature	/LONG PHAM/	Date Considered	07/15/2016

EXAMINER: Initial if reference considered, whether or not citation is in conformance with MPEP 609. Draw line through citation if not in conformance and not considered. Include copy of this form with next communication to Applicant.

ALL REFERENCES CONSIDERED EXCEPT WHERE LINED THROUGH. /L.P/

SAMSUNG EX. 1002 - 3096/4148

Substitute for Form 1449/PTO				Complete if Known	
INFORMATION DISCLOSURE STATEMENT BY APPLICANT				Application No.:	14/747,875
				Filing Date:	June 23, 2015
				First Named Inventor:	Martin U. Pralle
				Group Art Unit:	2814
(use as many sheets as necessary)				Examiner Name:	Long Pham
Sheet	18	of	20	Attorney Docket No.:	143705.05211

	C88	Nauka et al., Intrinsic Gettering in Oxygen-Free Silicon; App. Phys. Lett., vol. 46(7), Apr. 4, 1985.	
	C89	Nauka et al., "New Intrinsic Gettering Process in Silicon Based on Interactions of Silicon Interstitials," J. App. Phys., vol. 60(2), pp. 615-621, July 15, 1986.	
	C90	Nayak et al, "Semiconductor Laesr Crystallization of a--Si:H," SPIE Digital Library, 2003, 277-380, vol. 4977, Bellingham, Washington. 2003.	
	C91	Nayak et al, "Ultrafast-Laser-Assisted Chemical Restructuring of Silicon and Germanium Surfaces," Applied Surface Science, 2007, 6580-6583, vol. 253, Issue 15, Elsevier B.V.	
	C92	Nayak et al, "Semiconductor Laser Crystallization of a--Si:H on Conducting Tin-Oxide-Coated Glass for Solar Cell and Display Applications," Applied Physics A, 2005, 1077-1080, 80, Springer Berlin, Heidelberg, Germany	
	C93	NAYAK, B.K. et al.; Ultrafast Laser Textured Silicon Solar Cells; Mater. Res. Soc. Symp. Proc.; Vol. 1123; 6 pages; 2009; Materials Research Society	
	C94	NAYAK, et al.; "Efficient light trapping in silicon solar cells by ultrafast-laser-induced self-assembled micro/nano structures"; Progress in Photovoltaics: Research and Applications; 2011	
	C95	Oden, et al.; "Optical and Infrared Detection Using Microcantilevers;" SPIE Digital Library on Oct. 13, 2010; vol. 2744; 10 pages.	
	C96	Pain, Bedabrata; Backside Illumination Technology for SOI-CMOS Image Sensors; 2009 IISW Symposium on Backside Illujination of Solid-State Image Sensors, Bergen Norway; Jun. 25, 2009; pp. 1-23.	
	C97	Pain, Bedabrata; "A Back-Illuminated Megapixel CMOS Image Sensor"; http://hdl.handle.net/2014/39312; May 1, 2005	
	C98	Palm et al. CIGSSe Thin Film PB Modules: From Fundamental Investigators to Advanced Performance and Stability; Thin Solid Films; 2004; pp. 544-551; vol. 451-2.	
	C99	Payne, D.N.R. et al.; Characterization of Experimental Textured ZnO:Al Films for Thin Film Solar Cell Applications and Comparison with Commercial and Plasmonic Alternatives; Photovoltaic Specialists Conference (PVSC); pp. 1560-1564; 2010; IEEE.	
	C100	Pedraza et al., "Silicon Microcolumn Arrays Grown by Nanosecond Pulsed-Excimer Laser Irradiation", Appl. Phys. Lett., 1999, 74 (16), 2322-2324, American Institute of Physics. cited by applicant .	
	C101	Pedraza et al., "Surface Nanostructuring of Silicon", Appl. Phys. A, 2003, 77, 277-284.	
	C102	Rashkeev et al., "Hydrogen passivation and Activation of Oxygen Complexes in Silicon," American Institute of Physics, vol. 78(11), pp. 1571-1573 (Mar. 12, 2001).	
	C103	RUSSELL, et al.; "Nanosecond Eximer Laser Processing for Novel Microelectronic Fabrication"; Nanosecond Excimer Laser Processing; 6 pages; 1989	
	C104	Russell, Ramirez and Kelley, "Nanosecond Excimer Laser Processing for Novel Microelectronic Devices," US Navy, SPAWAR, San Diego, Techical Report, 2003.	
	C105	Russell, Ramirez, Kelley, "Nanosecond Excimer Laser Processing for Novel Microelectronic Fabrication," SSC Pacific Technical Reports , pp. 228-233, 2003, vol. 4, US Navy.	
	C106	Sai, H. et al.; Enhancement of Light Trapping in Thin-Film Hydrogenated Microcrystalline Si Solar Cells Using Back Reflectors with Self-Ordered Dimple Pattern; Applied Physics Letters; vol. 93; 2008; American Institute of Physics.	
	C107	Sanchez et al., "Whiskerlike Structure Growth on Silicon Exposed to ArF Excimer Laser Irradiation", Appl. Phys. Lett., 1996, 69 (5), 620-622.	
	C108	Sanchez et al., "Dynamics of the Hydrodynamical Growth of Columns on Silicon Exposed to ArF Excimer-Laser Irradiation ", Appl. Phys. A, 66, 83-86 (1998). cited by other .	
	C109	Samet et al.; "Femtosecond laser for black silicon and photovoltaic cells"; February 21, 2008, Proc. Of SPIE; Vol. 6881; pags 1-15	
	C110	Senoussaoui, N. et al.; Thin-Film Solar Cells with Periodic Grating Coupler; Thin Solid Films; pp.	

Examiner Signature	/LONG PHAM/	Date Considered	07/15/2016

EXAMINER: Initial if reference considered, whether or not citation is in conformance with MPEP 609. Draw line through citation if not in conformance and not considered. Include copy of this form with next communication to Applicant.

ALL REFERENCES CONSIDERED EXCEPT WHERE LINED THROUGH. /L.P./

SAMSUNG EX. 1002 - 3097/4148

Substitute for Form 1449/PTO				Complete if Known	
INFORMATION DISCLOSURE STATEMENT BY APPLICANT				Application No.:	14/747,875
				Filing Date:	June 23, 2015
				First Named Inventor:	Martin U. Pralle
				Group Art Unit:	2814
(use as many sheets as necessary)				Examiner Name:	Long Pham
Sheet	19	of	20	Attorney Docket No.:	143705.05211

		397-401; 2003; Elsevier B.V.	
	C111	Serpenguzel et al., "Temperature Dependence of Photluminescence in Non-Crystalline Silicon", Photonics West (San Jose, CA, 2004) 454-462.	
	C112	Shen et al., "Formation of Regular Arrays of Silicon Micorspikes by Femotsecond Laser Irradiation Through A Mask", Appl. Phys. Lett., 82, 1715-1717 (2003).	
	C113	Solar Energy Research Institute, "Basic Photovoltaic Principles and Methods," Van Nostrand Reinhold Co., NY 1984, pp. 45-47 and 138-142.	
	C114	Solhusvik, J. et al. "A 1280x960 3.75um pixel CMOS imager with Triple Exposure HDR," Proc. of 2009 International Image Sensor Workshop, Bergen, NORWAY, June 22-28, 2009.	
	C115	Stone et al.; The X-ray Sensitivity of Amorphous Selenium for Mammography;.Am. Assoc. Phys. Med.; Mar. 2002; pp. 319-324; vol. 29 No. 3; Am. Assoc. Phys. Med.	
	C116	Szlufcik, J. et al.; Simple Integral Screenprinting process for selective emitter polycrystalline silicon solar cells; Applied Physics Letters; vol. 59, No. 13; Sep. 23, 1991; American Institute of Physics.	
	C117	TABBAL et al., "Formation of Single Crystal Sulfur Supersaturated Silicon Based Junctions by Pulsed Laser Melting". 2007, J. Vac. Sci. Technol. B25(6), 1847-1852	
	C118	Takayanagi, et al.; "A 600.times.600 Pixel, 500, fps CMOS Image Sensor with a 4.4 jum Pinned Photodiode 5-Transistor Global Shutter Pixel"; 2007 International Image Sensor Workshop; Jun. 6-10, 2007.	
	C119	Tower, John R. et al.; Large Format Backside Illuminated CCD Imager for Space Surveillance; IEEE Transactions on Electron Devices, vol. 50, No. 1; Jan. 2003; pp. 218-224.	
	C120	TULL; "Femtosecond Laser Ablation of Silicon: Nanoparticles, Doping and Photovotaics"; Harvard University, June 2007 (Thesis)	
	C121	UEHARA et al., "A High-Sensitive Digital Photosensor Using MOS Interface-Trap Charge Pumping," IEICE Electronics Express, 2004, vol. 1, no. 18, 556-561.	
	C122	Wilson, "Depth Distributions of Sulfur Implanted Into Silicon as a Function of Ion energy, Ion Fluence, and Anneal Temperature," 1984, Appl. Phys. 55(10, 3490-3494.	
	C123	Winderbaum, S. et al.; Reactive ion etching (RIE) as a method for texturing polycrystalline silicon solar cells; Solar Energy Materials and Solar Cells; 1997; pp. 239-248; Elsevier Science B.V.	
	C124	Wu et al., "Black Silicon" Harvard UPS 1999	
	C125	Wu et al., "Black Silicon: A New Light Absorber," APS Centennial Meeting (Mar. 23, 1999).	
	C126	Wu et al., "Femtosecond laser-gas-solid interactions," Thesis presented to the Department of Physics at Harvard University, pp. 1-113, 126-136, Aug. 2000.	
	C127	Wu et al., "Visible Luminescence From Silicon Surfaces Microstructured in Air". Appl. Phys. Lett., vol. 81, No. 11, 1999-2001 (2002).	
	C128	Wu, et al "Near-Unity Below-Band-Gap Absorption by Microstructured Silicon," 2001, Applied Physics Letters, 1850-1852, vol. 78, No. 13, American Institute of Physics.	
	C129	Xu, Y., et al, "Infrared Detection Using Thermally Isolated Diode," Sensors and Actuators A, Elsevier Sequoia S.A., 1993, vol. 36, 209-217, Lausanne, Switzerland.	
	C130	Yablonovitch, et al.; "Intensity Enhancement in Textured Optical Sheets for Solar Cells"; .COPYRGT. 1982 IEEE.	
	C131	YAMAMOTO, K. et al.; NIR Sensitivity Enhancement by Laser Treatment for Si Detectors; Nuclear Instruments and Methods in Physics Research A; pages 520 - 523; March 31, 2010; Elsevier	
	C132	Yan, B.; Light Trapping Effect from Randomized Textures of Ag/ZnO Back Reflector on Hyrdrogenated Amorphous and Nanocrystalline Silicon Based Solar Cells; Thin Film Solar Technology II; vol. 7771; 2010; SPIE.	
	C133	Yasutomi, et al.; "Two-Stage Charge Transfer Pixel Using Pinned Diodes for Low-Noise Global	

Examiner Signature	/LONG PHAM/	Date Considered	07/15/2016

EXAMINER: Initial if reference considered, whether or not citation is in conformance with MPEP 609. Draw line through citation if not in conformance and not considered. Include copy of this form with next communication to Applicant.

ALL REFERENCES CONSIDERED EXCEPT WHERE LINED THROUGH. /L.P./

SAMSUNG EX. 1002 - 3098/4148

Substitute for Form 1449/PTO **INFORMATION DISCLOSURE STATEMENT BY APPLICANT** (use as many sheets as necessary)				**Complete if Known**	
				Application No.:	14/747,875
				Filing Date:	June 23, 2015
				First Named Inventor:	Martin U. Pralle
				Group Art Unit:	2814
				Examiner Name:	Long Pham
Sheet	20	of	20	Attorney Docket No.:	143705.05211

		Shutter Imaging"; 2009 International Image Sensor Workshop; Mar. 28, 2009.	
	C134	Younkin et al., "Infrared Absorption by Conical Silicon Microstructures Made in a Variety of Background Gases Using Femtosecond-Laser Pulses", J. Appl. Phys., 93, 2626-2629 (2003).	
	C135	Younkin, "Surface Studies and Microstructure Fabrication Using Femtosecond Laser Pulses," Thesis presented to the Division of Engineering & Applied sciences at Harvard University (Aug. 2001).	
	C136	YUAN, et al.; "Efficient black silicon solar cell with a density-graded nanoporous surface: Optical properties, performance limitations, and design rules"; American Institute of Physics; Applied Physics Letters 95. 1230501 (2009) 3 pages	
	C137	Zaidi, S.H. et al.; Diffraction Grating Structures in Solar Cells; Photovoltaic Specialists Conference, 2000; 4 pages; Sep. 2000; IEEE.	
	C138	Zhang et al, "Ultra-Shallow P+-Junction Formation in Silicon by Excimer Laser Doping: a Heat and Mass Transfer Perspective," Int. J. Heat Mass Transfer, 1996, 3835-3844, vol. 39, No. 18, Elsevier Science Ltd., Great Britain.	
	C139	Zhu et al., "Evolution of Silicon Surface Microstructures by Picosecond and Femtosecond Laser Irradiations," Applied Surface Science, 2005, 102-108, Elsevie, Amsterdam, NL.Ultra-Shallow P+-Junction Formation in Silicon by Excimer Laser Doping: a Heat and Mass Transfer Perspective," Int. J. Heat Mass Transfer, 1996, 3835-3844, vol. 39, No. 18, Elsevier Science Ltd., Great Britain.	

Examiner Signature	/LONG PHAM/	Date Considered	07/15/2016

EXAMINER: Initial if reference considered, whether or not citation is in conformance with MPEP 609. Draw line through citation if not in conformance and not considered. Include copy of this form with next communication to Applicant.

ALL REFERENCES CONSIDERED EXCEPT WHERE LINED THROUGH. /L.P./

SAMSUNG EX. 1002 - 3099/4148

Index of Claims	Application/Control No.	Applicant(s)/Patent Under Reexamination
	14747875	PRALLE ET AL.
	Examiner	Art Unit
	LONG PHAM	2814

✓	Rejected	-	Cancelled	N	Non-Elected	A	Appeal
=	Allowed	÷	Restricted	I	Interference	O	Objected

☐ Claims renumbered in the same order as presented by applicant ☐ CPA ☐ T.D. ☐ R.1.47

CLAIM		DATE								
Final	Original	04/17/2016	07/15/2016							
	1	÷	✓							
	2	÷	✓							
	3	÷	-							
	4	÷	✓							
	5	÷	✓							
	6	÷	✓							
	7	÷	-							
	8	÷	-							
	9	÷	O							
	10	÷	O							
	11	÷	-							
	12	÷	✓							
	13	÷	✓							
	14	÷	✓							
	15	÷	-							
	16	÷	-							
	17	÷	✓							
	19	÷	✓							
	20	÷	-							
	34		O							
	35		O							
	36		O							
	37		✓							
	38		✓							
	39		✓							
	40		✓							

To: docketingbn@pepperlaw.com,davisdr@pepperlaw.com,
From: PAIR_eOfficeAction@uspto.gov
Cc: PAIR_eOfficeAction@uspto.gov
Subject: Private PAIR Correspondence Notification for Customer Number 136549

Jul 22, 2016 05:25:48 AM

Dear PAIR Customer:

Pepper Hamilton LLP/SiOnyx LLC
Attn: Boston IP Docketing Department
125 High Street
19th Floor
Boston, MA 02110-2736
UNITED STATES

The following USPTO patent application(s) associated with your Customer Number, 136549 , have new outgoing correspondence. This correspondence is now available for viewing in Private PAIR.

The official date of notification of the outgoing correspondence will be indicated on the form PTOL-90 accompanying the correspondence.

Disclaimer:
The list of documents shown below is provided as a courtesy and is not part of the official file wrapper. The content of the images shown in PAIR is the official record.

Application	Document	Mailroom Date	Attorney Docket No.
14747875	CTNF	07/22/2016	143705.05211
	892	07/22/2016	143705.05211
	1449	07/22/2016	143705.05211

To view your correspondence online or update your email addresses, please visit us anytime at https://sportal.uspto.gov/secure/myportal/privatepair.

If you have any questions, please email the Electronic Business Center (EBC) at EBC@uspto.gov with 'e-Office Action' on the subject line or call 1-866-217-9197 during the following hours:

Monday - Friday 6:00 a.m. to 12:00 a.m.

Thank you for prompt attention to this notice,

UNITED STATES PATENT AND TRADEMARK OFFICE

PATENT APPLICATION INFORMATION RETRIEVAL SYSTEM

IN THE UNITED STATES PATENT AND TRADEMARK OFFICE

In re Application of: Martin U. Pralle Application No.: 14/747,875 Filed: June 23, 2015 For: PIXEL ISOLATION ELEMENTS, DEVICES, AND ASSOCIATED METHODS	Confirmation No.: 1722 Art Unit: 2814 Examiner: Long Pham

Commissioner for Patents
P. O. Box 1450
Alexandria, VA 22313-1450

Certificate of Mailing

I hereby certify that this correspondence is being electronically filed via EFS-Web to the Commissioner for Patents, P.O. Box 1450, Alexandria, VA 22313-1450.

January 23, 2017	Electronic Signature: /Andrew W. Schultz/
Dated	Andrew Schultz, Reg. No. 66,869

AMENDMENT AND RESPONSE TO NON-FINAL OFFICE ACTION

Dear Sir,

This paper is filed in response to the non-final Office Action dated July 22, 2016. A three month extension of time is filed concurrently herewith.

Amendments to the Claims begin on page 2 of this paper.

Arguments begin on page 7.

SAMSUNG EX. 1002 - 3102/4148

LISTING OF CLAIMS

1. (Currently Amended) A light trapping device, comprising:

at least one light sensitive pixel having a light incident surface, a backside surface opposite the light incident surface, and a peripheral sidewall extending at least partially around the pixel periphery;

a backside light trapping material at least partially covering the backside surface; ~~and~~

a peripheral light trapping material substantially covering the peripheral sidewall, wherein said peripheral light trapping material is doped with a dopant to create a surface field; and

a reflective layer coupled to the light incident side and having an aperture to allow entry of light into the pixel;

wherein the reflective layer is operable to reflect at least a portion of light impinging thereupon from inside the pixel back into the pixel back into the pixel.

2. (Previously Presented) The device of claim 1, wherein at least one of the backside light trapping material and the peripheral light trapping material reflects light incident thereon back into the pixel.

3. (Canceled)

4. (Previously Presented) The device of claim 1, wherein said peripheral light trapping material has a refractive index of less than about 2.1.

5. (Previously Presented) The device of claim 1, wherein said peripheral light trapping material includes a member selected from the group consisting of an oxide, a nitride, oxynitrides, a gas, at least a partial vacuum, and combinations thereof.

6. (Previously Presented) The device of claim 5,wherein said peripheral light trapping material is selected from the group consisting of silicon oxide, silicon nitride, silicon dioxide, and combinations thereof.

7-9. (Canceled)

10. (Currently Amended) The device of claim [[9]] 10, wherein the dopant is boron or antimony.

11. (Canceled)

12. (Original) The device of claim 1, wherein the peripheral sidewall extends completely around the pixel periphery.

13. (Original) The device of claim 1, wherein the peripheral sidewall extends from the light incident surface to the backside surface.

14. (Previously Presented) The device of claim 1, wherein said aperture has an effective surface area of less than about 90% of total area of the incident light surface.

15. (Canceled)

16. (Canceled)

17. (Currently Amended) The device of claim [[16]] 1, further comprising a lens functionally coupled to the aperture and operable to focus incident light through the aperture and into the pixel.

18. (Canceled)

19. (Original) The device of claim 1, wherein at least one of the backside light trapping material and the peripheral light trapping material is a metal layer.

20-33. (Canceled)

34. (Previously Presented) The device of claim 1, further comprising a textured region positioned to interact with light incident thereon to increase quantum efficiency of the device.

35. (Previously Presented) The device of claim 34, wherein said textured region comprises a textured film layer.

36. (Previously Presented) The device of claim 35, wherein said textured film layer comprises any of silicon dioxide, silicon nitride, amorphous silicon, polysilicon, a metal and

SIONYX1403000031.0083

SAMSUNG EX. 1002 - 3104/4148

combinations thereof.

37. (Previously Presented) The device of claim 1, wherein the peripheral light trapping material comprises any of aluminum oxide and hafnium oxide.

38. (Previously Presented) The device of claim 1, wherein the backside light trapping material substantially covers the backside surface.

39. (Previously Presented) The device of claim 1, wherein the backside light trapping material completely covers the backside surface.

40. (Previously Presented) The device of claim 1, wherein said peripheral sidewall extends through the pixel substantially from the light incident surface to the backside surface.

41. (New) A light trapping device, comprising:

at least one light sensitive pixel having a light incident surface, a backside surface opposite the light incident surface, and a peripheral sidewall extending at least partially around the pixel periphery;

a backside light trapping material at least partially covering the backside surface;

a peripheral light trapping material substantially covering the peripheral sidewall;

a textured region positioned to interact with light incident thereon to increase quantum efficiency of the device; and

a reflective layer coupled to the light incident side and having an aperture to allow entry of light into the pixel;

wherein the reflective layer is operable to reflect at least a portion of light impinging thereupon from inside the pixel back into the pixel back into the pixel.

42. (New) The device of claim 41, wherein at least one of the backside light trapping material and the peripheral light trapping material reflects light incident thereon back into the pixel.

43. (New) The device of claim 41, wherein said peripheral light trapping material has a refractive index of less than about 2.1.

44. (New) The device of claim 41, wherein said peripheral light trapping material includes a

member selected from the group consisting of an oxide, a nitride, oxynitrides, a gas, at least a partial vacuum, and combinations thereof.

45. (New) The device of claim 44,wherein said peripheral light trapping material is selected from the group consisting of silicon oxide, silicon nitride, silicon dioxide, and combinations thereof.

46. (New) The device of claim 41, wherein said peripheral light trapping material is doped with a dopant to create a surface field.

47. (New) The device of claim 46, wherein the dopant is boron or antimony.

48. (New) The device of claim 41, wherein the peripheral sidewall extends completely around the pixel periphery.

49. (New) The device of claim 41, wherein the peripheral sidewall extends from the light incident surface to the backside surface.

50. (New) The device of claim 41, wherein said aperture has an effective surface area of less than about 90% of total area of the incident light surface.

51. (New) The device of claim 41, further comprising a lens functionally coupled to the aperture and operable to focus incident light through the aperture and into the pixel.

52. (New) The device of claim 41, wherein at least one of the backside light trapping material and the peripheral light trapping material is a metal layer.

53. (New) The device of claim 41, wherein said textured region comprises a textured film layer.

54. (New) The device of claim 53, wherein said textured film layer comprises any of silicon dioxide, silicon nitride, amorphous silicon, polysilicon, a metal and combinations thereof.

55. (New) The device of claim 41, wherein the peripheral light trapping material comprises any of aluminum oxide and hafnium oxide.

SIONYX1403000031.0085

SAMSUNG EX. 1002 - 3106/4148

56. (New) The device of claim 41, wherein the backside light trapping material substantially covers the backside surface.

57. (New) The device of claim 41, wherein the backside light trapping material completely covers the backside surface.

58. (New) The device of claim 41, wherein said peripheral sidewall extends through the pixel substantially from the light incident surface to the backside surface.

SIONYX1403000031.0086

SAMSUNG EX. 1002 - 3107/4148

REMARKS

The pending Office Action addresses claims 1, 2,4-6, 8-10, 12-14, 17, 19 and 34-40, of which claims 1, 2, 4-6, 9-14, 17, 19 and 37-40 stand rejected. The Office Action objects to claims 9, 10, and 34-36 as being dependent on a rejected based, but are indicated as being allowable if rewritten in independent form. Reconsideration and allowance are respectfully requested in light of the above amendments and following remarks.

Allowable Subject Matter

Applicant thanks the Examiner for the indication that claims 9, 10, and 34-36 would be allowable if rewritten in independent form. As discussed below, the independent claims are amended in accordance with the Examiner's indication of allowable subject matter.

Amendments to the Claims

Applicant presents the following claim amendments solely to expedite prosecution. These amendments should not be construed as Applicant's acceptance of the Examiner's rejection. Applicant reserves the right to prosecute any of the former claims in a continuing application.

As shown on the attached sheets, independent claim 1 is amended to incorporate the recitations of allowable claim 9 (which is hereby canceled). Claim 10 is amended to depend from claim 1 in light of the cancellation of claim 9. Claim 17 is amended to correct its dependency in light of the previous cancellation of claim 16. Additionally, Applicant submits herewith new independent claim 41, which represent allowable claim 34, rewritten in independent form to include all limitations from claim 1 from which claim 34 depended. New dependent claims 42-58 are additionally presented and represent the subject matter of pending dependent claims that depended from claim 1. Support for the amendments can be found throughout the application as filed, for example, within the original claims. No new matter is added.

Rejections Pursuant to 35 U.S.C. § 102

The Office Action rejects claims 1, 3, 12-14, 19, 38-40 pursuant to 35 U.S.C. § 102 as being anticipated by U.S. Pub. No. 20130200251 of Velichko ("Velichko"). As indicated above,

independent claim 1 is amended to incorporate the recitations of allowable claim 9, thereby obviating the bases of these rejections.

Rejections Pursuant to 35 U.S.C. § 103

The Office Action rejects claims 4-6 and 17 pursuant to 35 U.S.C. § 103 as being obvious over Velichko in view of JP Patent JP 403183037 of Yanagisawa ("Yanagisawa"). In light of the amendments to claim 1, claims 4-6 and 17 are believed to be allowable over Velichko and Yanagisawa for at least the same reasons as allowable claim 1.

Conclusion

Applicant believes that all claims are in proper condition for allowance and allowance thereof is respectfully requested. The Examiner is encouraged to telephone the undersigned attorney for Applicants if such communication is deemed to expedite prosecution of this application.

The Director is hereby authorized to charge any fees that may be associated with this filing and/or credit any overpayments to our Deposit Account No. 50-0436, under Docket No. 143705.05211.

Dated: January 23, 2017

Respectfully submitted,
Electronic Signature: /Andrew W. Schultz/
Andrew W. Schultz, Reg. No. 66,869
Attorney for Applicants
Pepper Hamilton LLP
125 High Street
19th Floor, High Street Tower
Boston, MA 02210
Tel: (617) 204-5176
Fax: (617) 204-5150

Electronic Patent Application Fee Transmittal

Application Number:	14747875
Filing Date:	23-Jun-2015
Title of Invention:	Pixel Isolation Elements, Devices and Associated Methods
First Named Inventor/Applicant Name:	Martin U. Pralle
Filer:	Andrew W. Schultz/Jillian Stockel
Attorney Docket Number:	143705.05211

Filed as Small Entity

Filing Fees for Utility under 35 USC 111(a)

Description	Fee Code	Quantity	Amount	Sub-Total in USD($)
Basic Filing:				
Pages:				
Claims:				
CLAIMS IN EXCESS OF 20	2202	3	40	120
Miscellaneous-Filing:				
Petition:				
Patent-Appeals-and-Interference:				
Post-Allowance-and-Post-Issuance:				

Description	Fee Code	Quantity	Amount	Sub-Total in USD($)
Extension-of-Time:				
Extension - 3 months with $0 paid	2253	1	700	700
Miscellaneous:				
		Total in USD ($)		**820**

SAMSUNG EX. 1002 - 3111/4148

Electronic Acknowledgement Receipt	
EFS ID:	28140352
Application Number:	14747875
International Application Number:	
Confirmation Number:	1722
Title of Invention:	Pixel Isolation Elements, Devices and Associated Methods
First Named Inventor/Applicant Name:	Martin U. Pralle
Customer Number:	136549
Filer:	Andrew W. Schultz/Jillian Stockel
Filer Authorized By:	Andrew W. Schultz
Attorney Docket Number:	143705.05211
Receipt Date:	23-JAN-2017
Filing Date:	23-JUN-2015
Time Stamp:	17:10:43
Application Type:	Utility under 35 USC 111(a)

Payment information:

Submitted with Payment	yes
Payment Type	CARD
Payment was successfully received in RAM	$820
RAM confirmation Number	012417INTEFSW17132500
Deposit Account	
Authorized User	
The Director of the USPTO is hereby authorized to charge indicated fees and credit any overpayment as follows:	

File Listing:

Document Number	Document Description	File Name	File Size(Bytes)/ Message Digest	Multi Part /.zip	Pages (if appl.)
1	Transmittal Letter	IDSTransmittal.pdf	102270 0634a3d63db021fada9bd1071ee0074d1fa3d533	no	2
Warnings:					
Information:					
2	Information Disclosure Statement (IDS) Form (SB08)	SuppIDS.pdf	1036703 6ce02bd544f378686b95c0fc0e75ceb7b5ff0d7f	no	7
Warnings:					
Information:					
3	Foreign Reference	JP2001024936.pdf	5288640 c6f11fc9cd44d28a3b0c609ba6d66e686e3e018a	no	12
Warnings:					
Information:					
4	Foreign Reference	JP2001257297.pdf	13660736 d359ed018147937f5654fa4114e2f7e09a0f0841	no	25
Warnings:					
Information:					
5	Foreign Reference	JP2003242125.pdf	12132549 484fee5dcca5e19f65e696ccdbf2dbd26f0b3dd3	no	25
Warnings:					
Information:					
6	Foreign Reference	JP2003308130.pdf	7000104 82757cd0d2df829b8b0099d29e5be682ff2a6e85	no	15
Warnings:					
Information:					

SAMSUNG EX. 1002 - 3113/4148

7	Foreign Reference	JP2005339425.pdf	3497322 c853968fb9dc2c074cfbf31219cdbf9a5af80540	no	12
Warnings:					
Information:					
8	Foreign Reference	JP2006255430A.pdf	7701610 f2a80de81ab0a0d1e091c507a4595a9f5c114b2b	no	22
Warnings:					
Information:					
9	Foreign Reference	JPH06244444.pdf	956529 f2a974a722b52f8278c52d4dbaa977127a7750d9	no	16
Warnings:					
Information:					
10	Foreign Reference	WO0031679A1.pdf	1809838 91b7b7738e44c2d154638f529ed64adef47c8dea	no	43
Warnings:					
Information:					
11	Foreign Reference	WO2009016846A1.pdf	7613140 cb8d24461d6ade239d4403edd12b10b65d0c4290	no	62
Warnings:					
Information:					
12	Non Patent Literature	Huang_2013.pdf	1050684 0036c290c8cf0e7ed24b136d7dd7c871f59d0a33	no	5
Warnings:					
Information:					
13	Non Patent Literature	Jansen_1995.pdf	688378 e1755ead34e70893c1e020bcd10ea0f37343eb51	no	6
Warnings:					
Information:					

14	Non Patent Literature	Koh_2000.pdf	554663 a71c512b3b509d821356eb91d7cebdb2e7c1eec1	no	5
Warnings:					
Information:					
15	Non Patent Literature	Zhong_2016.pdf	836183 9728b3e8721f1bec9517e3c826e9b33ce1db0c62	no	11
Warnings:					
Information:					
16		ResponseToOA.pdf	136623 1345b083ce09238f7f59e20af542db36f1eb2ba3	yes	8
	Multipart Description/PDF files in .zip description				
	Document Description		**Start**	**End**	
	Amendment/Req. Reconsideration-After Non-Final Reject		1	1	
	Claims		2	6	
	Applicant Arguments/Remarks Made in an Amendment		7	8	
Warnings:					
Information:					
17	Fee Worksheet (SB06)	fee-info.pdf	32265 9ff48b0c3344a8439a7ca4a7a1fa00af79b4ebc2	no	2
Warnings:					
Information:					
			Total Files Size (in bytes):	64098237	

SAMSUNG EX. 1002 - 3115/4148

This Acknowledgement Receipt evidences receipt on the noted date by the USPTO of the indicated documents, characterized by the applicant, and including page counts, where applicable. It serves as evidence of receipt similar to a Post Card, as described in MPEP 503.

New Applications Under 35 U.S.C. 111
If a new application is being filed and the application includes the necessary components for a filing date (see 37 CFR 1.53(b)-(d) and MPEP 506), a Filing Receipt (37 CFR 1.54) will be issued in due course and the date shown on this Acknowledgement Receipt will establish the filing date of the application.

National Stage of an International Application under 35 U.S.C. 371
If a timely submission to enter the national stage of an international application is compliant with the conditions of 35 U.S.C. 371 and other applicable requirements a Form PCT/DO/EO/903 indicating acceptance of the application as a national stage submission under 35 U.S.C. 371 will be issued in addition to the Filing Receipt, in due course.

New International Application Filed with the USPTO as a Receiving Office
If a new international application is being filed and the international application includes the necessary components for an international filing date (see PCT Article 11 and MPEP 1810), a Notification of the International Application Number and of the International Filing Date (Form PCT/RO/105) will be issued in due course, subject to prescriptions concerning national security, and the date shown on this Acknowledgement Receipt will establish the international filing date of the application.

Docket No.: 143705.05211
(PATENT)

IN THE UNITED STATES PATENT AND TRADEMARK OFFICE

In Re Application of: Martin U. Pralle	Confirmation No.: 1722
Application No.: 14/747,875	Art Unit: 2814
Filed: June 23, 2015	Examiner: Long Pham
For: PIXEL ISOLATION ELEMENTS, DEVICES, AND ASSOCIATED METHODS	

VIA EFS-WEB
Commissioner for Patents
P. O. Box 1450
Alexandria, VA 22313-1450

Certificate of Mailing
I hereby certify that this correspondence is being electronically filed via EFS-Web to the Commissioner for Patents, P.O. Box 1450, Alexandria, VA 22313-1450.

January 23, 2017 (Dated)
Electronic Signature: /Andrew W. Schultz/
Andrew Schultz, Reg. No. 66,869

INFORMATION DISCLOSURE STATEMENT (IDS)

Dear Sir:

Pursuant to 37 CFR 1.56, 1.97 and 1.98, the attention of the Patent and Trademark Office is hereby directed to the references listed on the attached PTO/SB/08. It is respectfully requested that the information be expressly considered during the prosecution of this application, and that the references be made of record therein and appear among the "References Cited" on any patent to issue therefrom.

This Information Disclosure Statement is filed more than three months after the U.S. filing date, OR more than three months after the date of entry of the national stage of a PCT application, AND after the mailing date of the first Office Action on the merits, but before the mailing date of a Final Office Action or Notice of Allowance (37 CFR 1.97(c)). This IDS is accompanied with the fee set forth in 37 C.F.R. 1.17(p).

SAMSUNG EX. 1002 - 3117/4148

In accordance with 37 CFR 1.98(a)(2)(ii), Applicant has not submitted copies of U.S. patents and U.S. patent applications. Applicant submits herewith copies of foreign patents and non-patent literature in accordance with 37 CFR 1.98(a)(2).

In accordance with 37 CFR 1.97(g), the filing of this Information Disclosure Statement shall not be construed to mean that a search has been made or that no other material information as defined in 37 CFR 1.56(a) exists. In accordance with 37 CFR 1.97(h), the filing of this Information Disclosure Statement shall not be construed to be an admission that the information cited in the statement is, or is considered to be, material to patentability as defined in § 1.56 (b).

It is submitted that the Information Disclosure Statement is in compliance with 37 CFR 1.98 and the Examiner is respectfully requested to consider the listed references.

The Director is hereby authorized to charge any deficiency in the fees filed, asserted to be filed or which should have been filed herewith (or with any paper hereafter filed in this application by this firm) to our Deposit Account No. 50-0436, under Order No. 143705.05211.

Dated: January 23, 2017

Respectfully submitted,
Electronic Signature: /Andrew W. Schultz/
Andrew W. Schultz, Reg. No. 66,869
Attorney for Applicants
Pepper Hamilton LLP
125 High Street
19th Floor, High Street Tower
Boston, MA 02210
Tel: (617) 204-5176
Fax: (617) 204-5150

#42516501 v1

PTO/SB/08a (03-15)
Approved for use through 07/31/2016. OMB 0651-0031
U.S. Patent and Trademark Office; U.S. DEPARTMENT OF COMMERCE

Under the Paperwork Reduction Act of 1995, no persons are required to respond to a collection of information unless it contains a valid OMB control number.

INFORMATION DISCLOSURE STATEMENT BY APPLICANT

(Not for submission under 37 CFR 1.99)

Application Number	14747875
Filing Date	2015-06-23
First Named Inventor	Martin U. Pralle
Art Unit	2814
Examiner Name	Long Pham
Attorney Docket Number	14705.05211

U.S.PATENTS Remove

Examiner Initial*	Cite No	Patent Number	Kind Code[1]	Issue Date	Name of Patentee or Applicant of cited Document	Pages,Columns,Lines where Relevant Passages or Relevant Figures Appear
	1	5101260		1992-03-31	Nath	
	2	5600130		1997-02-04	VanZeghbroeck	
	3	5626687		1997-05-06	Campbell	
	4	5635089		1997-06-03	Singh et al.	
	5	6082858		2000-07-04	Grace et al.	
	6	6204506		2001-03-20	Akahori et al.	
	7	6907135		2005-06-15	Gifford	

If you wish to add additional U.S. Patent citation information please click the Add button. Add

U.S.PATENT APPLICATION PUBLICATIONS Remove

INFORMATION DISCLOSURE STATEMENT BY APPLICANT (Not for submission under 37 CFR 1.99)		
	Application Number	14747875
	Filing Date	2015-06-23
	First Named Inventor	Martin U. Pralle
	Art Unit	2814
	Examiner Name	Long Pham
	Attorney Docket Number	14705.05211

Examiner Initial*	Cite No	Publication Number	Kind Code[1]	Publication Date	Name of Patentee or Applicant of cited Document	Pages,Columns,Lines where Relevant Passages or Relevant Figures Appear
	1	20030214595		2003-11-20	Mabuchi	
	2	20030228883		2003-12-11	Kusakari et al.	
	3	20050093100		2005-05-05	Tze-Chiang et al.	
	4	20060086956		2006-04-27	Furukawa et al.	
	5	20060128087		2006-06-15	Bamji et al.	
	6	20070189583		2007-08-16	Shimada et al.	
	7	20070237504		2007-10-11	Nakashiba	
	8	20080158398		2008-07-03	Yoel et al.	
	9	20080192133		2008-08-14	Takahiro et al.	
	10	20080284884		2008-11-20	Eiji et al.	

INFORMATION DISCLOSURE STATEMENT BY APPLICANT (Not for submission under 37 CFR 1.99)		
	Application Number	14747875
	Filing Date	2015-06-23
	First Named Inventor	Martin U. Pralle
	Art Unit	2814
	Examiner Name	Long Pham
	Attorney Docket Number	14705.05211

	11	20090308457		2009-12-17	Smith et al.	
	12	20100200658		2010-08-12	Olmstead et al.	
	13	20110292380		2011-12-01	Bamji	

If you wish to add additional U.S. Published Application citation information please click the Add button. Add

FOREIGN PATENT DOCUMENTS Remove

Examiner Initial*	Cite No	Foreign Document Number[3]	Country Code[2] i	Kind Code[4]	Publication Date	Name of Patentee or Applicant of cited Document	Pages,Columns,Lines where Relevant Passages or Relevant Figures Appear	T[5]
	1	2001024936	JP		2001-01-26	Matsushita Electric Industrial Co. Ltd.		
	2	2001257927	JP		2001-09-21	Technosonic KK		
	3	2003242125	JP		2003-08-29	Cannon KK		
	4	2003308130	JP		2003-10-31	Matsushita Electric Industrial Co. Ltd.		
	5	2005339425	JP		2005-12-08	Sanyo Electric Co.		
	6	2006255430	JP		2006-09-28	Fujitsu Ltd.		

INFORMATION DISCLOSURE STATEMENT BY APPLICANT (Not for submission under 37 CFR 1.99)		
	Application Number	14747875
	Filing Date	2015-06-23
	First Named Inventor	Martin U. Pralle
	Art Unit	2814
	Examiner Name	Long Pham
	Attorney Docket Number	14705.05211

	7	200031967	WO		2000-06-02	Iriscan Inc.			
	8	2009016846	WO		2009-02-05	Panasonic Corp.			
	9	6244444	JP		1994-09-02	Hatachi Ltd.			

If you wish to add additional Foreign Patent Document citation information please click the Add button Add

NON-PATENT LITERATURE DOCUMENTS Remove

Examiner Initials*	Cite No	Include name of the author (in CAPITAL LETTERS), title of the article (when appropriate), title of the item (book, magazine, journal, serial, symposium, catalog, etc), date, pages(s), volume-issue number(s), publisher, city and/or country where published.	T5
	1	Huang, et al.; "Key Technique for texturing a uniform pyramid structure with a layer of silicon nitride on monocrystalline silicon wafer" Applied Surface Science; 2013 pp. 245-249.	
	2	Jansen, H. et al., "The Black Silicon Method: a universal method for determining the parameter setting of a flourine-based reactive ion etcher in deep silicon trench etching with profile control",J. Micromech. Microeng. Vol. 5, 1995 pp.115-120.	
	3	Koh et al., "Simple nanostructuring on silicon surface by means of focused beam patterning and wet etching", Applied Surface Science, 2000 pp. 599-603.	
	4	Zhong, S. et al. "Excellent Light Trapping in Ultrathin Solar Cells," AFM-Journal, May 2016 pp. 1-11.	

If you wish to add additional non-patent literature document citation information please click the Add button Add

EXAMINER SIGNATURE

Examiner Signature		Date Considered	

*EXAMINER: Initial if reference considered, whether or not citation is in conformance with MPEP 609. Draw line through a citation if not in conformance and not considered. Include copy of this form with next communication to applicant.

INFORMATION DISCLOSURE STATEMENT BY APPLICANT (Not for submission under 37 CFR 1.99)		
	Application Number	14747875
	Filing Date	2015-06-23
	First Named Inventor	Martin U. Pralle
	Art Unit	2814
	Examiner Name	Long Pham
	Attorney Docket Number	14705.05211

[1] See Kind Codes of USPTO Patent Documents at www.USPTO.GOV or MPEP 901.04. [2] Enter office that issued the document, by the two-letter code (WIPO Standard ST.3). [3] For Japanese patent documents, the indication of the year of the reign of the Emperor must precede the serial number of the patent document. [4] Kind of document by the appropriate symbols as indicated on the document under WIPO Standard ST.16 if possible. [5] Applicant is to place a check mark here if English language translation is attached.

INFORMATION DISCLOSURE STATEMENT BY APPLICANT (Not for submission under 37 CFR 1.99)		
	Application Number	14747875
	Filing Date	2015-06-23
	First Named Inventor	Martin U. Pralle
	Art Unit	2814
	Examiner Name	Long Pham
	Attorney Docket Number	14705.05211

CERTIFICATION STATEMENT

Please see 37 CFR 1.97 and 1.98 to make the appropriate selection(s):

That each item of information contained in the information disclosure statement was first cited in any communication from a foreign patent office in a counterpart foreign application not more than three months prior to the filing of the information disclosure statement. See 37 CFR 1.97(e)(1).

OR

☐ That no item of information contained in the information disclosure statement was cited in a communication from a foreign patent office in a counterpart foreign application, and, to the knowledge of the person signing the certification after making reasonable inquiry, no item of information contained in the information disclosure statement was known to any individual designated in 37 CFR 1.56(c) more than three months prior to the filing of the information disclosure statement. See 37 CFR 1.97(e)(2).

See attached certification statement.

☒ The fee set forth in 37 CFR 1.17 (p) has been submitted herewith.

☒ A certification statement is not submitted herewith.

SIGNATURE

A signature of the applicant or representative is required in accordance with CFR 1.33, 10.18. Please see CFR 1.4(d) for the form of the signature.

Signature	/Andrew W. Schultz/	Date (YYYY-MM-DD)	2017-01-23
Name/Print	Andrew W.Schultz	Registration Number	66869

This collection of information is required by 37 CFR 1.97 and 1.98. The information is required to obtain or retain a benefit by the public which is to file (and by the USPTO to process) an application. Confidentiality is governed by 35 U.S.C. 122 and 37 CFR 1.14. This collection is estimated to take 1 hour to complete, including gathering, preparing and submitting the completed application form to the USPTO. Time will vary depending upon the individual case. Any comments on the amount of time you require to complete this form and/or suggestions for reducing this burden, should be sent to the Chief Information Officer, U.S. Patent and Trademark Office, U.S. Department of Commerce, P.O. Box 1450, Alexandria, VA 22313-1450. DO NOT SEND FEES OR COMPLETED FORMS TO THIS ADDRESS. **SEND TO: Commissioner for Patents, P.O. Box 1450, Alexandria, VA 22313-1450.**

Privacy Act Statement

The Privacy Act of 1974 (P.L. 93-579) requires that you be given certain information in connection with your submission of the attached form related to a patent application or patent. Accordingly, pursuant to the requirements of the Act, please be advised that: (1) the general authority for the collection of this information is 35 U.S.C. 2(b)(2); (2) furnishing of the information solicited is voluntary; and (3) the principal purpose for which the information is used by the U.S. Patent and Trademark Office is to process and/or examine your submission related to a patent application or patent. If you do not furnish the requested information, the U.S. Patent and Trademark Office may not be able to process and/or examine your submission, which may result in termination of proceedings or abandonment of the application or expiration of the patent.

The information provided by you in this form will be subject to the following routine uses:

1. The information on this form will be treated confidentially to the extent allowed under the Freedom of Information Act (5 U.S.C. 552) and the Privacy Act (5 U.S.C. 552a). Records from this system of records may be disclosed to the Department of Justice to determine whether the Freedom of Information Act requires disclosure of these record s.

2. A record from this system of records may be disclosed, as a routine use, in the course of presenting evidence to a court, magistrate, or administrative tribunal, including disclosures to opposing counsel in the course of settlement negotiations.

3. A record in this system of records may be disclosed, as a routine use, to a Member of Congress submitting a request involving an individual, to whom the record pertains, when the individual has requested assistance from the Member with respect to the subject matter of the record.

4. A record in this system of records may be disclosed, as a routine use, to a contractor of the Agency having need for the information in order to perform a contract. Recipients of information shall be required to comply with the requirements of the Privacy Act of 1974, as amended, pursuant to 5 U.S.C. 552a(m).

5. A record related to an International Application filed under the Patent Cooperation Treaty in this system of records may be disclosed, as a routine use, to the International Bureau of the World Intellectual Property Organization, pursuant to the Patent Cooperation Treaty.

6. A record in this system of records may be disclosed, as a routine use, to another federal agency for purposes of National Security review (35 U.S.C. 181) and for review pursuant to the Atomic Energy Act (42 U.S.C. 218(c)).

7. A record from this system of records may be disclosed, as a routine use, to the Administrator, General Services, or his/her designee, during an inspection of records conducted by GSA as part of that agency's responsibility to recommend improvements in records management practices and programs, under authority of 44 U.S.C. 2904 and 2906. Such disclosure shall be made in accordance with the GSA regulations governing inspection of records for this purpose, and any other relevant (i.e., GSA or Commerce) directive. Such disclosure shall not be used to make determinations about individuals.

8. A record from this system of records may be disclosed, as a routine use, to the public after either publication of the application pursuant to 35 U.S.C. 122(b) or issuance of a patent pursuant to 35 U.S.C. 151. Further, a record may be disclosed, subject to the limitations of 37 CFR 1.14, as a routine use, to the public if the record was filed in an application which became abandoned or in which the proceedings were terminated and which application is referenced by either a published application, an application open to public inspections or an issued patent.

9. A record from this system of records may be disclosed, as a routine use, to a Federal, State, or local law enforcement agency, if the USPTO becomes aware of a violation or potential violation of law or regulation.

Espacenet

Bibliographic data: JP2001024936 (A) — 2001-01-26

IMAGE FETCHING DEVICE

Inventor(s): HIRAMA YUICHI ± (HIRAMA YUICHI)

Applicant(s): MATSUSHITA ELECTRIC IND CO LTD ± (MATSUSHITA ELECTRIC IND CO LTD)

Classification: **- international:** ***G06T1/00; H04N5/232;*** (IPC1-7): G06T1/00; H04N5/232

- cooperative:

Application number: JP19990196142 19990709

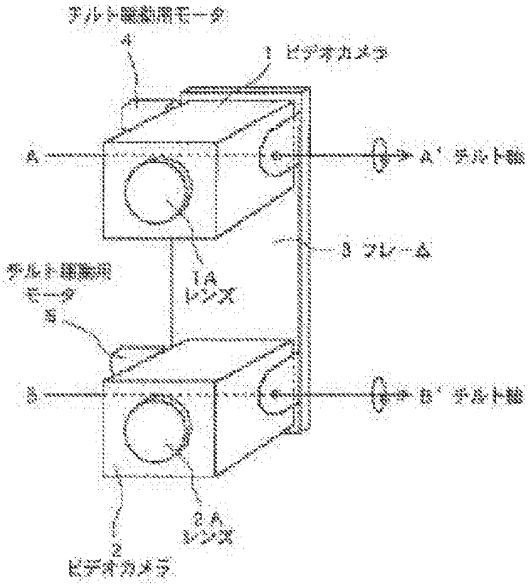
Priority number (s): JP19990196142 19990709

Abstract of JP2001024936 (A)

PROBLEM TO BE SOLVED: To calculate an exact position and to prevent the reduction of a recognition rate caused by the dispersion of height differences when fetching the image of the iris or the like for recognizing it. SOLUTION: An imaging device having a high pixel number is built in both video cameras 1 and 2. Besides, lenses 1A and 2A having zoom focus functions are provided. The video cameras 1 and 2 are attached to the surface of a frame 3 while keeping a prescribed vertical interval. The video cameras 1 and 2 can be oscillated around respective tilt shafts A-A' and B-B' by motors 4 and 5 for tilt drive. Because of positioning based on two video cameras, the exact position can be calculated. Further, since the image of the iris can be fetched while selecting upper and lower video cameras, the image of the iris can be fetched from the front and the reduction of the recognition rate caused by the dispersion of height differences can be prevented.

SIONYX1403000031.0105

SAMSUNG EX. 1002 - 3126/4148



SIONYX1403000031.0106

SAMSUNG EX. 1002 - 3127/4148